

AD-A161 247

OM85 BASIC PROPERTIES OF OPTICAL MATERIALS SUMMARIES OF  
PAPERS(U) NATIONAL BUREAU OF STANDARDS GAITHERSBURG MD  
A FELDMAN MAY 85 NBS-SP-697 AFOSR-RR-85-0902

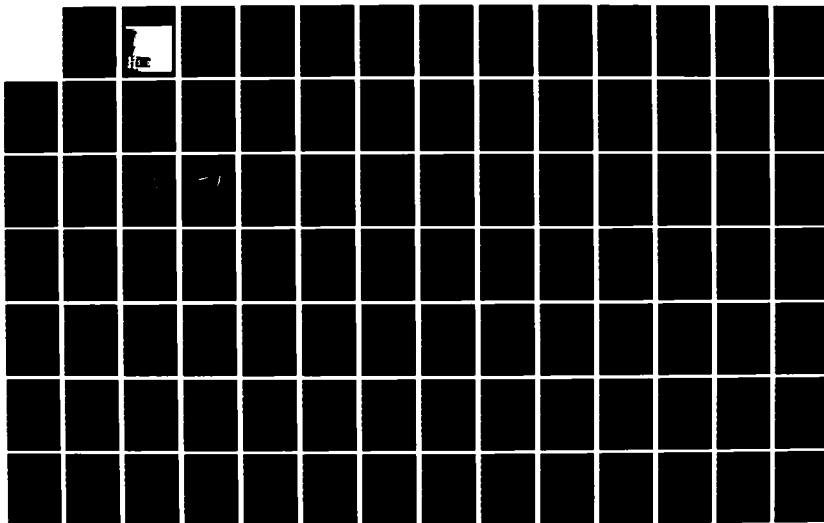
1/1

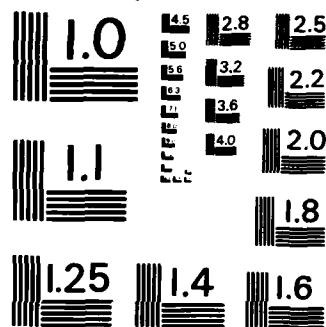
UNCLASSIFIED

AFOSR-ISSA-85-00052

F/G 20/6

NL





MICROCOPY RESOLUTION TEST CHART  
NATIONAL BUREAU OF STANDARDS-1963-A

AFOSR 28

①



# NBS SPECIAL PUBLICATION 697

U.S. DEPARTMENT OF COMMERCE National Bureau of Standards

AD-A161 247

DTIC  
ELECTE  
NOV 14 1985  
S D

**T**he National Bureau of Standards<sup>1</sup> was established by an act of Congress on March 3, 1901. The Bureau's overall goal is to strengthen and advance the nation's science and technology and facilitate their effective application for public benefit. To this end, the Bureau conducts research and provides: (1) a basis for the nation's physical measurement system, (2) scientific and technological services for industry and government, (3) a technical basis for equity in trade, and (4) technical services to promote public safety. The Bureau's technical work is performed by the National Measurement Laboratory, the National Engineering Laboratory, the Institute for Computer Sciences and Technology, and the Center for Materials Science.

### ***The National Measurement Laboratory***

Provides the national system of physical and chemical measurement; coordinates the system with measurement systems of other nations and furnishes essential services leading to accurate and uniform physical and chemical measurement throughout the Nation's scientific community, industry, and commerce; provides advisory and research services to other Government agencies; conducts physical and chemical research; develops, produces, and distributes Standard Reference Materials; and provides calibration services. The Laboratory consists of the following centers:

- Basic Standards<sup>2</sup>
- Radiation Research
- Chemical Physics
- Analytical Chemistry

### ***The National Engineering Laboratory***

Provides technology and technical services to the public and private sectors to address national needs and to solve national problems; conducts research in engineering and applied science in support of these efforts; builds and maintains competence in the necessary disciplines required to carry out this research and technical service; develops engineering data and measurement capabilities; provides engineering measurement traceability services; develops test methods and proposes engineering standards and code changes; develops and proposes new engineering practices; and develops and improves mechanisms to transfer results of its research to the ultimate user. The Laboratory consists of the following centers:

- Applied Mathematics
- Electronics and Electrical Engineering<sup>2</sup>
- Manufacturing Engineering
- Building Technology
- Fire Research
- Chemical Engineering<sup>2</sup>

### ***The Institute for Computer Sciences and Technology***

Conducts research and provides scientific and technical services to aid Federal agencies in the selection, acquisition, application, and use of computer technology to improve effectiveness and economy in Government operations in accordance with Public Law 89-306 (40 U.S.C. 759), relevant Executive Orders, and other directives; carries out this mission by managing the Federal Information Processing Standards Program, developing Federal ADP standards guidelines, and managing Federal participation in ADP voluntary standardization activities; provides scientific and technological advisory services and assistance to Federal agencies; and provides the technical foundation for computer-related policies of the Federal Government. The Institute consists of the following centers:

- Programming Science and Technology
- Computer Systems Engineering

### ***The Center for Materials Science***

Conducts research and provides measurements, data, standards, reference materials, quantitative understanding and other technical information fundamental to the processing, structure, properties and performance of materials; addresses the scientific basis for new advanced materials technologies; plans research around cross-country scientific themes such as nondestructive evaluation and phase diagram development; oversees Bureau-wide technical programs in nuclear reactor radiation research and nondestructive evaluation; and broadly disseminates generic technical information resulting from its programs. The Center consists of the following Divisions:

- Inorganic Materials
- Fracture and Deformation<sup>3</sup>
- Polymers
- Metallurgy
- Reactor Radiation

<sup>1</sup>Headquarters and Laboratories at Gaithersburg, MD, unless otherwise noted; mailing address Gaithersburg, MD 20899.

<sup>2</sup>Some divisions within the center are located at Boulder, CO 80303.

<sup>3</sup>Located at Boulder, CO, with some elements at Gaithersburg, MD.



UNCLASSIFIED

SECURITY CLASSIFICATION OF THIS PAGE

AD-A16147

## REPORT DOCUMENTATION PAGE

1a. REPORT SECURITY CLASSIFICATION UNCLASSIFIED		1b. RESTRICTIVE MARKINGS	
2a. SECURITY CLASSIFICATION AUTHORITY		3. DISTRIBUTION/AVAILABILITY OF REPORT Approved for public release; distribution unlimited.	
2b. DECLASSIFICATION/DOWNGRADING SCHEDULE		4. PERFORMING ORGANIZATION REPORT NUMBER	
5. MONITORING ORGANIZATION REPORT NUMBER AFOSR-TR-		6a. NAME OF PERFORMING ORGANIZATION National Bureau of Standards	
6b. OFFICE SYMBOL (If applicable)		7a. NAME OF MONITORING ORGANIZATION Air Force Office of Scientific Research	
6c. ADDRESS (City, State and ZIP Code) Dept of Commerce Gaithersburg MD 20899		7b. ADDRESS (City, State and ZIP Code) Bldg 410 Bolling AFB DC 20332-6448	
8a. NAME OF FUNDING/SPONSORING ORGANIZATION AFOSR		8b. OFFICE SYMBOL (If applicable) NE	
9. PROCUREMENT INSTRUMENT IDENTIFICATION NUMBER AFOSR-ISSA-85-00052		10. SOURCE OF FUNDING NOS	
8c. ADDRESS (City, State and ZIP Code) Bldg 410 Bolling AFB DC 20332-6448		PROGRAM ELEMENT NO 61102F	PROJECT NO 2306
		TASK NO B2	WORK UNIT NO
11. TITLE (Include Security Classification) TOPICAL CONFERENCE ON BASIC PROPERTIES OF OPTICAL MATERIALS			
12. PERSONAL AUTHOR(S) Albert Feldman			
13a. TYPE OF REPORT Final	13b. TIME COVERED FROM 07 MAY 85 TO 01 SEP 85	14. DATE OF REPORT (Yr., Mo., Day) May 1985	15. PAGE COUNT 294
16. SUPPLEMENTARY NOTATION Library of Congress Catalog Card Number 85-600534 <i>Held at National Bureau of Standards, Gaithersburg, Md., May 7-9, 1985</i>			
17. COSATI CODES		18. SUBJECT TERMS (Continue on reverse if necessary and identify by block number)	
FIELD	GROUP	SUB GR	
		Glasses; infrared; modulated structures; nonlinear optics; metals; organics; optical constants; optical waveguides; photorefractive effect; polymers; semiconductors; thin films	
19. ABSTRACT (Continue on reverse if necessary and identify by block number) See Back			
20. DISTRIBUTION/AVAILABILITY OF ABSTRACT UNCLASSIFIED/UNLIMITED <input checked="" type="checkbox"/> SAME AS RPT. <input type="checkbox"/> DTIC USERS <input type="checkbox"/>		21. ABSTRACT SECURITY CLASSIFICATION UNCLASSIFIED	
22a. NAME OF RESPONSIBLE INDIVIDUAL KEVIN J MALLOY, Capt, USAF		22b. TELEPHONE NUMBER (Include Area Code) (202) 767-4931	22c. OFFICE SYMBOL NE

This Special Publication contains summaries of papers to be presented at the Topical Conference on Basic Properties of Optical Materials to be held at the National Bureau of Standards in Gaithersburg, Maryland on May 7-9, 1985. The conference is sponsored by the National Bureau of Standards, the Air Force Office of Scientific Research, and the American Physical Society in cooperation with the Optical Society of America and SPIE-The International Society for Optical Engineering. This publication contains summaries of 70 papers which include 17 invited papers.

The purpose of the conference is to bring together researchers from industry, academia, and government to discuss the physical and structural properties of optical materials as they affect optical performance. The scope of the conference includes the measurement and theory of basic properties of optical materials in bulk and in thin film form and the dependence of these properties on atomic structure, morphological structure, impurity content, and inhomogeneity.

Approved For	
NTIS - Case #	<input checked="" type="checkbox"/>
DTIC - TAB	<input type="checkbox"/>
Unannounced	<input type="checkbox"/>
Justification	
By	
Distribution/	
Availability Codes	
Dist	Avail and/or Special
A-1	



**OM85**

# **Basic Properties of Optical Materials Summaries of Papers**

---

Presented at the  
Topical Conference on  
Basic Properties of Optical Materials

Held at the National Bureau of Standards  
Gaithersburg, Maryland, May 7-9, 1985

Edited by:

Albert Feldman

Center for Materials Science  
Inorganic Materials Division  
National Bureau of Standards  
Gaithersburg, Maryland 20899

Sponsored by:

U.S. Department of Commerce  
National Bureau of Standards  
Center for Materials Science  
Inorganic Materials Division  
Center for Electronics and Electrical Engineering  
Semiconductor Materials and Processes Division  
American Physical Society  
Air Force Office of Scientific Research

In Cooperation with:

Optical Society of America  
SPIE—The International Society for Optical Engineering



U.S. DEPARTMENT OF COMMERCE, Malcolm Baldrige, Secretary  
NATIONAL BUREAU OF STANDARDS, Ernest Ambler, Director

Issued April 1985

1

NOV 14 1985

This document has been approved  
for public release and sale; its  
distribution is unlimited.

Library of Congress Catalog Card Number: 85-600534

National Bureau of Standards Special Publication 697  
Natl. Bur. Stand. (U.S.), Spec. Publ. 697, 294 pages (Apr. 1985)  
CODEN: XNBSAV

U.S. GOVERNMENT PRINTING OFFICE  
WASHINGTON: 1985

For sale by the Superintendent of Documents, U.S. Government Printing Office, Washington, DC 20402

## Foreword

This Special Publication contains summaries of papers to be presented at the Topical Conference on Basic Properties of Optical Materials to be held at the National Bureau of Standards in Gaithersburg, Maryland on May 7-9, 1985.

The use of optical materials in advanced applications such as optical signal processing, optical computing, integrated optics, optical coatings, optical domes, and laser windows is placing increasingly stringent requirements on material performance. The purpose of this conference is to bring together researchers from industry, academia, and government to discuss the physical and structural properties of optical materials as they affect performance. The scope of the conference includes the measurement and theory of basic properties of optical materials in bulk and in thin film form and the dependence of these properties on atomic structure, morphological structure, impurity content, and inhomogeneity. The principal topical areas are:

- Influence of microstructure on properties
- Waveguide materials, guided modes, surface plasmons
- Nonlinear phenomena, bistability, photorefractive effect
- Semiconductors and modulated structures
- Thin films
- Organics and polymers
- Glasses
- Metals
- Electro-optic, magneto-optic materials
- Optical constants and other properties
- Ultraviolet, visible, infrared properties
- Optical spectroscopies

The importance of optical materials to the international research community is attested to by the large number of papers from abroad.

This publication contains summaries of 70 papers which include 17 invited papers. The manuscripts have been prepared by the authors in camera-ready form, and any questions pertaining to their content should be addressed to those authors.

Albert Feldman  
Chairperson

### Program and Editorial Committee

Albert Feldman - Chairperson  
National Bureau of Standards

Michael I. Bell  
National Bureau of Standards

Bernard Bendow  
The BDM Corporation

H. E. Bennett  
Naval Weapons Center

Samuel Ditman  
Naval Surface Weapons Center

H. P. R. Frederikse  
Bureau of Standards

Alastair M. Glass  
AT&T Bell Laboratories

Arthur H. Guenther  
Air Force Weapons Laboratory

H. Angus Macleod  
University of Arizona

Edward Palik  
Naval Research Laboratory

Armand R. Tanguay, Jr.  
University of Southern California

Van Wood  
Battelle Memorial Institute

### Acknowledgments

We wish to thank the following individuals for their invaluable assistance in preparing for the conference and this summary: Kathy Kilmer, Mary Nestor, Susan Roth, Carolyn Sladic, Kathy Stang, Lillian Ware, Judy Wilson. Special thanks are due to Jane Walters, Kathy Gallo, and Brenda Kefauver for typing the conference program, for retyping several of the manuscripts, and for assembling and editing the completed Summary of Papers.

### Disclaimer

Certain commercial equipment, instruments, or materials may be identified in this publication in order to adequately specify the experimental procedure. In no case does such identification imply recommendation or endorsement by the National Bureau of Standards, nor does it imply that the material or equipment identified is necessarily the best available for the purpose.

## CONTENTS

	Page
Foreword . . . . .	iii
Keynote Address--Progress in Optical Materials Research . . . . .	1
*I. P. Kaminow	

### EFFECTS OF MICROSTRUCTURE

Determination of Microstructure from Spectrophotometry and Spectroellipsometry . . . . .	5
*D. E. Aspnes	
Light Scattering from Dielectric and Metallic Microstructures . . . . .	11
*R. K. Chang and P. W. Barber	
Characterization of Optical Materials and Surfaces Using Time-Domain Reflectometry . . . . .	17
A. G. Lieberman	
Theory of Light Scattering from a Rough Surface with a Nonlocal Inhomogeneous Dielectric Permittivity . . . . .	21
J. M. Elson	

### INFRARED MATERIALS

Optical Properties of Metals in the Infrared - the Drude Model, Problems with It, and Non-Local Optics . . . . .	24
*D. W. Lynch	
Separation of Drude and Band-to-Band Spectra in Polyvalent Metals . . . . .	28
D. Y. Smith and B. Segall	
Status of Materials for Transmissive and Reflective Infrared Components . . . . .	32
*H. E. Bennett	
Dimensional Stability . . . . .	36
W. Primak	

### ORGANIC MATERIALS AND POLYMERS

Nonlinear Optical Properties of Organic Polymer Materials . . . . .	40
*G. M. Carter, Y. J. Chen, M. F. Rubner, M. K. Thakur, S. K. Tripathy, J. P. Georger, and J. V. Hryniewicz	
Preparation of Organic Nonlinear Optical Materials for Second Harmonic Generation . . . . .	46
C. W. Dirk, R. J. Twieg, and G. Wagniere	

\*Invited Presentation

	Page
Optical Phase Transitions in Organo-Metallic Compounds . . . . .	50
T. O. Poehler and R. S. Potember	
A Review of the Optical Data Analysis for Phthalocyanine Conducting Polymer and Molecular-Metal Systems . . . . .	54
W. J. McCarthy, C. R. Kannewurf, T. Inabe, T. J. Marks, and R. L. Burton	
Optical Properties of PBS . . . . .	58
M. W. Williams, D. W. Young, J. C. Ashley, and E. T. Arakawa	

#### WAVEGUIDE MATERIALS AND SURFACE PLASMONS

Optical Constants and Harmonic Generation by Surface Plasmons . . . . .	60
*H. J. Simon	
Low Loss Thin Film Materials for Integrated Optics . . . . .	65
*H. E. Jackson and J. T. Boyd	
Quantitative Sampling in Planar Waveguides . . . . .	71
P. W. Bohn	

#### THIN FILMS

Relationship of Microstructure to Optical Properties of Thin Films . . . . .	74
*H. A. Macleod	
The Microstructure and Optical Properties of Thin Films Prepared by Molecular Beam Techniques . . . . .	80
K. L. Lewis, A. M. Pitt, J. A. Savage, A. G. Cullis, N. G. Chew, and L. Charlwood	
A Simple Model of Inhomogeneity in Optical Thin Films . . . . .	84
G. Deniau, F. Flory, and E. Pelletier	
Optical Properties of Diamondlike Carbon Films on Semiconductors . . . . .	86
G. H. Bu-Abbud, J. D. Lamb, J. E. Oh, and J. A. Woollam	
Temperature Dependent Optical Properties of Silver Sulfide Thin Films . . . . .	89
R. L. Burton, H. Buhay, M. Nisar, J. L. Grieser, and N. P. Murarka	
Molecular Bonding in Optical Films Deposited by Ion-Beam Sputtering . . . . .	93
*C. Y. She	



POSTER PAPERS

Highly Transparent Metal Films: Pt on InP . . . . .	99
D. E. Aspnes, A. Heller, J. D. Porter, T. T. Sheng, and R. G. Vadimsky	
Calculation of the Electronic Structure of $As_4S_4$ and $As_4Se_4$ Molecules . . . . .	103
D. Babic and S. Rabii	
Free-Carrier Absorption in a Thin Film Silver Sulfide Galvanic Cell . . . . .	106
R. L. Burton, H. Buhay, J. L. Grieser, and N. P. Murarka	
Synthesis and Characterization of Stoichiometric $CdPS_3$ . . . . .	110
J. Covino, P. Dragovich, and C. Lowe-Ma	
Optical Characterization of Thin Semiconducting Films on Transparent Substrates . . . . .	115
B. Edgerton and D. Shortt	
Laser Propagation Through Fibers with Biquadratic Refractive Index (Closed Form Solution) . . . . .	119
F. Z. El-Halafawy, A. Y. Rezk, and E-S. A. El-Badawy	
Densification of Zirconia Films by Coevaporation with Silica . . . . .	122
A. Feldman and E. N. Farabaugh	
Temperature Dependence of the VUV Optical Spectra and Band Structure of $Al_2O_3$ . . . . .	126
R. H. French and R. L. Coble	
Raman Spectra of $LiYF_4$ Crystal . . . . .	130
F. X. Gan and H. Y. Chen	
EPR Studies of Infrared-Transmitting Sulfide Ceramics . . . . .	133
D. C. Harris, M. E. Hills, J. Covino, C. K. Lowe-Ma, and R. W. Schwartz	
Elastic Properties of Chemically Vapor-Deposited ZnS and ZnSe . . . . .	137
C. A. Klein and C. B. Willingham	
Radiation Effects in a Glass-Ceramic (Zerodur) . . . . .	141
N. Koumvakalis, M. G. Jani, and L. E. Halliburton	
Infrared Characterization of Defect Centers in Quartz . . . . .	145
H. G. Lipson	

	Page
The Importance of Electron-Electron Correlation in the Calculation of Second-Order Nonlinear Optical Properties of Organic Molecules. The Case of Urea . . . . .	150
B. M. Pierce	
Diffuse Multilayer Analysis Using a Multiflux Method . . . . .	154
S. O. Sari	
Optical Absorption in the Band Gap in High Purity Silicon . . . . .	158
R. T. Swimm	
Properties of Guided Modes in Bidirectional Anisotropic Media . . . . .	160
O. Schwelb	
Calorimetric Measurement of Optical Absorption in Sapphire at Visible, Near IR, and Near UV Wavelengths . . . . .	164
A. B. Villaverde, R. T. Swimm, and M. Bass	
Optical Properties of Ion Beam Irradiated Molybdenum Laser Mirrors as Studied by Ellipsometry . . . . .	167
J. A. Woollam, G. H. Bu-Abbud, D. L. Mathine, D. Poker, D. Ingram, and P. Pronko	
Crystal Field Energy Levels and Optical Absorption Intensities of $\text{Ni}^{2+}:\text{MgF}_2$ . . . . .	169
B. Zhang, J-K. Zhu, and S-H. Liu	

#### PROPERTIES FROM MILLIMETER TO X-RAY WAVELENGTHS

Status of Optical Constants of Solids from X-Ray to MM-Wave Region. . . . .	171
*E. D. Palik	
Optical Constants at X-Ray Wavelengths . . . . .	177
D. Y. Smith, A. E. Williamson, and T. I. Morrison	
Vacuum Ultraviolet Loss in Magnesium Fluoride Films . . . . .	181
O. R. Wood, II, P. J. Maloney, H. G. Craighead, and J. E. Sweeney	
Surface Erosion Induced by Electronic Transitions . . . . .	184
R. F. Haglund, Jr., and N. H. Tolk	

#### SEMICONDUCTORS AND QUANTUM WELL STRUCTURES

Dielectric Function and Interband Transitions in Semiconductors . . . . .	188
*M. Cardona	

	Page
Band Structure and Density of States Changes for Doped Gallium Arsenide . . . . .	194
H. S. Bennett	
Micro-Raman Study of Laser-Induced Damage . . . . .	198
P. M. Fauchet, I. H. Campbell, and F. Adar	
Optical Effects in Quantum Well Structures and Superlattices . . . . .	202
*D. S. Chemla	
Photoreflectance in GaAs/AlGaAs Multiple Quantum Wells . . . . .	214
O. J. Glembocki, B. V. Shanabrook, N. Bottka, W. T. Beard, and J. Comas	
Picosecond Carrier Dynamics in a-Si . . . . .	218
A. I. D'Souza, M. G. Roe, P. E. Wigen, and R. Messier	
 <u>NONLINEAR OPTICAL MATERIALS AND THE PHOTOREFRACTIVE EFFECT</u>	
Photorefractive and Nonlinear-Optical Properties of New Electrooptic Materials . . . . .	222
*P. Gunter	
Measurement of Defect and Transport Properties of Electro-Optic Materials Using the Photorefractive Effect . . . . .	226
M. B. Klein and G. C. Valley	
Analysis of Scattering Patterns and Decay Dynamics of Photorefractive Gratings in LiNbO <sub>3</sub> Crystals . . . . .	229
J. K. Tyminski, R. C. Powell, H. C. Chow, and M. J. Kleiwer	
Use of Optical Phase Conjugation for Understanding Basic Materials Properties . . . . .	232
*R. W. Hellwarth	
Measurement of Dielectric Properties of KTa <sub>1-x</sub> Nb <sub>x</sub> O <sub>3</sub> . . . . .	234
D. Rytz, M. B. Klein, B. Bobbs, M. Matloubian, and H. Fetterman	
Refractive Indices and Thermo-Optic Coefficients of Nonlinear Crystals Isomorphic to KH <sub>2</sub> PO <sub>4</sub> . . . . .	238
K. W. Kirby, C. S. Hofer, and L. G. DeShazer	
Bismuth Silicon Oxide: Sample Variability Studied with Thermally Stimulated Conductivity and Thermoluminescence . . . . .	242
B. W. Holmes, J. E. Ludman, and C. L. Woods	

NONLINEAR OPTICS AND BISTABILITY

Materials Requirements for Optical Logic and Bistable Devices . . . . .	246
*N. Peyghambarian and H. M. Gibbs	
Mirrorless Optical Bistability in CdS . . . . .	249
J. W. Haus, C. C. Sung, C. M. Bowden, and J. M. Cook	
Nonlinear Optical Effects in Liquid Crystals . . . . .	251
D. Armitage and S. M. Delwart	
A Study of Second Harmonic Generation Coefficients and Ultraviolet Absorption Edge of Barium Borate Crystal . . . . .	255
J-K. Zhu, B. Zhang, and S-H. Liu	
Soliton Transmission in Inhomogeneous Media with W-Tailored Refractive Index . . . . .	256
F. Z. El-Halafawy, E-S. A. El-Badawy, M. A. El-Gammal, and M. H. Aly	

GLASSES

Comparison of Vibrational Spectra of Heavy Metal Fluoride Glasses with Those of "Common" Glasses . . . . .	260
*B. Bendow	
Sol Gel Coatings for Optical Applications . . . . .	(Paper not Available)
*D. R. Uhlmann	
The Verdet Constant of Optical Glasses . . . . .	266
H. J. Hoffman, W. W. Jochs, and G. Przybilla	
Temperature Dependence of Magneto optic Effects in Mid-Infrared Fibers . . . . .	270
H. Sato, Y. Azumai, and M. Saito	
Optical Characterization of Devitrification for $\text{Cr}^{3+}$ -Doped Zr-Ba-La-Al Fluoride Glass . . . . .	274
W. J. Miniscalco, L. J. Andrews, B. T. Hall, and D. E. Guenther	
Optical Study of Ge-P-Te and Ge-Se-Te Chalcogenide Glasses . . . . .	278
L. Boehm, A. Bornstein, and S. Arie	
Author Index . . . . .	282

## PROGRESS IN OPTICAL MATERIALS RESEARCH (KEYNOTE TALK)

Ivan P. Kaminow  
AT&T Bell Laboratories  
Crawford Hill Laboratory  
Holmdel, New Jersey 07733

The advent of the laser in 1960 stimulated the need for research in high quality optical materials. The last 25 years are peppered with both great successes and disappointments in the quest for practical materials for novel applications. I will review a few examples pertinent to telecommunications applications with an eye to future needs.

The initial challenge is usually to find any material that exhibits a unique optical property to demonstrate a new phenomenon or device. But a first success then leads to more stringent demands on the material. Not only must the unique property be enhanced, but, at the same time, ancillary properties essential for practical implementation must also be realized.

Optical Fibers: Perhaps the most dramatic illustration of success in optical materials research is the low-loss optical fiber now widely used for telecommunications. It was well-known in the 1960s that light -- including laser light -- could be guided by an optical fiber with a high refractive index core and lower index cladding. However, all the handbooks indicated losses due to absorption in the most transparent glasses to be about 1000 dB/km -- much too large for long haul communications. Then it was recognized that if impurities could be reduced sufficiently (parts/billion), the transparency could be improved to practical levels. The bulk oxides from which glasses were made could not be economically purified to the required level. However, chemical vapor techniques already known in the glass and silicon industries led naturally to high purity silica glasses. The starting materials,  $\text{SiCl}_4$  and  $\text{O}_2$ , could be obtained as high-purity reagents and the vapor pressures of remnant transition metal chlorides in the liquid  $\text{SiCl}_4$  were low enough that they were not transferred with the  $\text{SiCl}_4$  vapor. The demonstration of losses of 20 dB/km in 1970 marked the start of the practical phase of fiber materials research. Over the past 15 years, not only has the loss been reduced to 0.16 dB/km -- near the theoretical limit -- but a host of ancillary material problems have been addressed; including, high mechanical strength, new plastic coatings, efficient production methods, minimal OH impurities, and new dopants for changing the refractive index of silica.

Further applications call for entirely new fiber materials that will transmit wavelengths,  $\lambda$ , longer than  $1.55\mu\text{m}$ , where the silica fibers have their minimum loss. Since the loss due to Rayleigh scattering decreases as  $\lambda^{-4}$ , the hope is to realize losses much less than 0.16 dB/km. But one must find glasses with weak lattice vibration absorption at these wavelengths that can be manufactured free of impurities (particularly OH), and later, learn to make them strong, robust and cheap.

Semiconductor Lasers: Another example of success is the development of methods for epitaxial growth of semiconductor alloys to be employed in lasers and photodiodes to operate with the low-loss silica fibers. The first important step toward a practical device was the recognition of the need for a heteroepitaxial structure to confine the photons and electrons to the same thin region. A liquid phase epitaxial (LPE) method for growing a suitable double heterostructure (DH) AlGaAs/GaAs wafer was developed and a low-threshold laser operating at  $0.8\mu\text{m}$  was demonstrated in 1970. The next requirement was to find a semiconductor compound with a bandgap corresponding to the low-loss region --  $1.2\text{--}1.5\mu\text{m}$  -- of the silica fibers. In 1976,  $\text{In}_{1-x}\text{Ga}_x\text{As}_{1-y}\text{P}_y$ , which can cover the desired wavelength range, was grown lattice-matched to InP, and was used in a long-wavelength DH laser. Following the demonstration of laser operation at that time, much effort has been devoted to growing reproducible, large wafers without defects and with well-controlled layer thickness and composition. A variety of epitaxial methods have been studied: liquid phase, vapor phase (VPE and MOVPE) and molecular beam epitaxy (MBE). And, of course, as these techniques have been perfected they suggest and permit still more sophisticated applications, which in turn put more demands on the material -- on both its optical and non-optical properties. The most recent advance is the development of multi-quantum well structures.

Electrooptics and Non-linear Optics: The non-linear optical materials in some sense represent a disappointment. KDP -- or, chemically,  $\text{KH}_2\text{PO}_4$  -- and its isomorphs were known as piezoelectric, ferroelectric and electrooptic materials in 1935, well before the invention of the laser. When the laser came along, they were obvious choices for the first high-speed modulators and for the demonstration of optical second harmonic generation, since both applications require non-centrosymmetric (piezoelectric) transparent crystals. After 25 years of research, there is still no substitute for  $\text{KD}_2\text{PO}_4$  in many important applications. True, the available size of the crystals has increased substantially from about  $1\text{ cm}^2$  in cross-section to  $10^3\text{ cm}^2$ . But still one would prefer a non-water soluble crystal with larger non-linear optical coefficients -- while retaining the excellent optical quality, UV transparency, freedom from optical damage, high resistivity, and low dielectric constant. During the 1960s, I and others hunted

through mineralogical collections looking for natural crystals with the required symmetry and range of transparency to test for their electrooptic and non-linear optical coefficients. In the few cases that led to interesting materials, one then had the problem of finding or growing large crystals with good physical and electrical properties. Meanwhile, crystal growers set out to synthesize oxides with suitable symmetry and transparency - often following the clues offered by the previously-known synthetic piezoelectric and ferroelectric oxides, such as  $\text{BaTiO}_3$ ,  $\text{KNbO}_3$ ,  $\text{LiNbO}_3$  and  $\text{LiTaO}_3$ , all of which had been synthesized in the 1940s as a result of research on high dielectric constant and ferroelectric materials. Their large linear polarizabilities suggested large non-linear polarizabilities. Many  $\text{ABO}_3$  crystals and their solid solutions were synthesized and studied. The solutions never really worked well because uniform crystal growth was not possible. Some compound oxides showed large electrooptic coefficients due to the proximity of the ferroelectric Curie temperature to the operating temperature. However, the corresponding high dielectric constant lead to poor high frequency modulator performance. Finally, after many years of study,  $\text{LiNbO}_3$  and  $\text{LiTaO}_3$  have emerged as the best materials for many electrooptic and non-linear optic applications, because they exhibit reasonably large non-linear coefficients and can be grown in large crystals of good quality. Still, these crystals have many shortcomings for the sophisticated device applications that had been proposed in the 1960s and 1970s: the non-linear coefficients are too small for efficient tunable parametric oscillators or harmonic generators and the materials suffer an optical damage (photorefractive) effect at wavelengths of interest.

In the 1970s, I had hoped that an understanding of the microscopic origins of the electrooptic and non-linear optic coefficients would provide guidance to synthesizing the optimum crystal -- and I understand that some researchers still have this hope -- but, practically speaking, only the "seat-of-the-pants" approach has worked. That is, intuitive people have guessed at compounds that might exhibit the desired optical property and still be growable, and then have tried them out.

Photonic Structures: In the absence of the ideal material, one can also look for innovations in the device structure. Since these non-linear effects are strong functions of field strength, the interaction efficiency can be improved by confining the interaction to the smallest allowed cross-section and assuring good overlap of all the fields involved. The use of optical waveguides eliminates diffraction and allows uniform interaction over a path of many wavelengths. Thus, in the 1970s researchers looked for methods to make waveguides in non-linear materials. The most widely used process for waveguide electrooptic modulators has turned out to be diffusion of titanium into

$\text{LiNbO}_3$ , since it is simple to employ using standard photolithographic methods. Although it has been on the horizon for a long time, it now looks as though integrated optics devices employing  $\text{Ti:LiNbO}_3$  waveguides are on the verge of application in telecommunications. Here again however,  $\text{Ti:LiNbO}_3$  was one of the early combinations tried and demonstrated, and subsequent efforts have not improved matters. Thus, we were not able to make metal-diffused guides in any other electrooptic oxides or semiconductors.

Certainly efforts to make good waveguides in semiconductor materials as conveniently as the  $\text{Ti:LiNbO}_3$  guides, in such a way that they will be compatible with the heteroepitaxial lasers mentioned above, offers a worthy challenge to the optical materials community. Not only could such electrooptic waveguide devices be integrated with semiconductor lasers and detectors, they could all be integrated together on the same chip with the transistor circuits to drive them -- the so called "integrated optoelectronic structure". Further down the road is the "photonic structure" in which optical signals switch other optical signals leading to pure optical logic and switching. Such devices will depend upon extremely large non-linear optical interactions.

Optical materials research has had a remarkable record of success in making lightwave telecommunications a reality. As the field becomes more sophisticated, many challenges remain, and others are sure to develop, that require new approaches to making high performance materials while working within the physical constraints defined by the periodic table.



## DETERMINATION OF MICROSTRUCTURE FROM SPECTROPHOTOMETRY AND SPECTROELLIPSOMETRY

D. E. Aspnes

Bell Communications Research, Inc., Murray Hill, N.J. 07974

That microstructure can profoundly influence optical properties of materials has been known essentially from the first investigations of the electromagnetic response of macroscopic media.<sup>1,2</sup> "Microstructure" is used here in the standard materials science sense, referring to spatial inhomogeneities on the scale of about 1 to 25 nm. These are inhomogeneities large enough so that the separate regions possess their own dielectric identity, yet small compared to the wavelength of light.

Can one reverse the procedure and use optical properties to determine microstructure? Yes, within limits. The major difficulty is that optical data take the form of transmitted or reflected intensities or of ratios of complex reflectances, whereas one really wants to know microstructural properties such as average compositions, void fractions, and interface and surface region thicknesses. To go from optical data to microstructure one needs to model, that is, to devise idealized mathematical representations for given samples that allow their optical properties to be calculated analytically in terms of available data and the sample parameters of interest. Given a model, one can either use the optical data as a template and apply least-squares regression to systematically best-fit the model parameters to the data, or else use the optical data as input to allow the model equations to be solved explicitly for one or more of the parameters of the model. Complicated samples are usually analyzed by the first approach, while the determination of oxide thicknesses is an example of the second approach. With present capabilities it is now possible to analyze composite bulk or thin film samples that are anisotropic, macroscopically inhomogeneous, microscopically rough, covered with adsorbed layers, or have finite interface and surface region thicknesses.

The present summary deals primarily with the modeling problem, and will cover topics that in my opinion have not been adequately discussed elsewhere. References to more detailed treatments of specific topics will be given as needed. I shall be concerned with the analysis of spectral data taken with the sample under static conditions, the usual situation for materials characterization, rather than single-wavelength data taken under dynamic conditions, the usual situation for process characterization.

The essential requirements for accurate microstructural analysis are accurate data for the sample and all possible constituents, and an accurate model of the sample. Recent advances in instrumentation, in particular the development of fast, automatic spectroellipsometers, have virtually solved the instrumentation and data accuracy problems, and recent needs for nondestructive, in situ analyses of materials, surfaces, and interfaces in semiconductor technology have greatly expanded the data base needed for model calculations. These data have also been essential to the development of analytical procedures,

which can also be considered a solved problem.

In contrast, the determination of the model that accurately represents a given sample is an open-ended problem that is definitely not solved. McPhedran et al.<sup>3</sup> have recently discussed some aspects of this topic as it applies to spectrophotometry. In brief, one faces a challenge analogous to the black-box problem of electrical engineering: the microstructural details of the sample are not known but must be deduced from available data. Mathematicians term this a problem of the inverse type, loosely describable as a situation where one is given the answer and asked to find the problem. Difficulties include the possible existence of different but apparently equally valid models, overlooked models, inadequate data, no confidence in the parameters determined, convergence to a wrong solution, and doubts that all relevant sample properties have actually been included in the model. Considerable physical insight may also be needed to construct the model. The recommended procedure is to start with the simplest possible model until it proves to be inadequate and to take advantage of all the information available, whether it comes from optical data or from other sources.

At present, the primary objectives of optical microstructural analysis are to establish the reliability of specific models and confidence in the results. That these are now the main challenges represents considerable progress, as anyone who recalls the Ellipsometry Conferences of the 1960's and 1970's can attest. Reliability and confidence are established by successful overdetermination, that is, by showing that data taken under different conditions lead to the same parameters, or equivalently by showing that optical properties calculated from model parameters determined under one set of conditions accurately predict optical properties observed under another. Different conditions are obtained by varying parameters under direct experimental control such as the angle of incidence or the wavelength of light.

An inspection of the optical characterization literature in, e.g., *Applied Optics* or in any of a number of reviews,<sup>4</sup> will show that almost anything that can be varied has been varied, including not only wavelength and angle of incidence but also film thickness, ambient refractive index, and numbers and types of overlayers. The most useful, convenient, and powerful variable by far is the wavelength of light, not only because it can be changed without affecting the sample but also because optical properties are themselves strong functions of wavelength through intrinsic polarizabilities, long-range order, interference, and other phenomena. In fact, a wavelength scanning capability is almost mandatory for any serious microstructural analysis effort because single-wavelength measurements do not return enough information to allow models to be cross-checked. Since optical properties are generally slow functions of the angle of incidence, a consequence of Snell's Law is going from less dense to more dense media, this parameter is much less useful than the wavelength in establishing independent conditions although it does affect sensitivities to interface regions under optically thick films.<sup>5</sup> The use of film thickness as a variable is risky because microstructure tends to evolve with deposition. The use of different ambients also cannot be recommended because of the tendency of porous films to absorb ambient material, a well known phenomenon in the optical coatings field.<sup>6</sup>

The model is the weak link in any optical microstructural analysis, so the following limita-

tions should be kept in mind. A model is an idealized representation of a sample and consequently is an approximation. As such, it can always be pushed too far, even if it accurately describes all major observable sample characteristics. If adequate data are not available, the model may not represent the sample properly. Models are usually expressed in terms of macroscopic parameters, which are themselves averages over microscopic phenomena that may be extremely complex. While macroscopic parameters are very useful for practical purposes (consider the relative advantages of working with pressure and temperature or with the position and velocity of each molecule in a macroscopic sample of a gas), many problems can only be solved by using techniques such as transmission electron microscopy that are destructive but have the spatial resolution necessary to access microstructure directly. Also, the values of macroscopic parameters such as compositions deduced from effective medium theory depend on microscopic properties such as grain shapes that cannot be studied directly by optical techniques. However, limit theorems<sup>7-9</sup> can be used to determine the ranges of uncertainty of such parameters even if nothing is known about the microstructure in detail.

Also, the values obtained depend on the accuracy of the data base. For example, Johnson and Christy<sup>10</sup> used reflectance and transmittance measurements to determine the dielectric properties of a number of metal films deposited on room-temperature substrates by evaporation at moderate ( $10^{-5}$  torr) pressures. These data probably differ from the true bulk dielectric responses of the respective metals by amounts of the order of 10% due to the inefficient packing of the metal grains in the films. Any microstructural analysis using these data as reference data must take this uncertainty into account. As materials preparation procedures improve, reference data become more accurate, but the process is an evolutionary one. As another example, the maximum amplitude of the "best" dielectric function spectrum of amorphous Si has increased gradually from 20 to about 30 over the past 15 years, primarily because of improvements in deposition procedures. Indications that the intrinsic dielectric properties of a-Si may have finally been obtained follow because the dielectric properties of material prepared by three different ways in three different laboratories (and measured by two different optical techniques) are now in very good agreement.<sup>11</sup> But the possibility of further improvements cannot be ruled out.

I now consider specific details, beginning with available information and its determination. The optical probe is polarized light, which carries four pieces of information in the form of the amplitudes and phases of the two orthogonal components of the electric field. Reflection or transmission changes these amplitudes and phases to new values. Consequently, four pieces of data can be obtained in principle about a sample during any single optical measurement. In reflectance measurements these four data are expressed as two complex reflectances,  $r_s$  and  $r_p$ , which describe the effect of the sample on the electric field components parallel and perpendicular, respectively, to the plane of incidence. The fact that only four data are available is a severe limitation and shows that multiple measurements are necessary. The actual situation is even less favorable: photometric techniques (reflectometry) that deal with intensities determine only two data (in two separate measurements), the amplitudes of  $r_s$  and  $r_p$ , and ellipsometric measurements that deal with polarization states also determine only two data (in a single measurement), the complex reflectance ratio  $r_p/r_s$ . The latter quantity is analogous to an impedance. Because it is

easier to accurately measure impedances than power levels, and because such measurements are less susceptible to experimental artifacts, it is easier to reach a given level of accuracy with ellipsometry than with reflectometry even though the ultimately attainable levels of accuracy are the same.

The biggest experimental impediment to accuracy is not instrumentation but sample preparation. For example, careful sample preparation is the reason why the dielectric properties of single-crystal Ge determined by Archer<sup>12</sup> from discrete-wavelength ellipsometric data and those determined by Donovan et al.<sup>13</sup> from reflectance data agree within several percentage points of each other and with those determined from recent spectroellipsometric data<sup>14</sup> in a field where discrepancies of 10-20% are not uncommon. Ideally, samples should be clean, flat, and damage-free, and maintained that way by keeping them in an inert atmosphere during measurement. Proper sample preparation simplifies microstructural analysis by eliminating complexity at the experimental level rather than forcing it to be dealt with during data analysis. The real-time data acquisition capabilities and better submonolayer sensitivities of presently operating automatic spectroellipsometers allow surface conditions to be assessed during the sample preparation process, guaranteeing that the best possible surfaces can be obtained before spectral data are acquired for analysis. A comprehensive discussion of methods of obtaining accurate data by ellipsometry has been given elsewhere.<sup>15</sup>

The theoretical tools needed for microstructural characterization are the n-phase model, effective medium theory, and least-squares regression analysis.<sup>16</sup> The n-phase model is the mathematical prescription for calculating complex reflectances and transmittances from the Fresnel reflection and propagation equations for a stratified medium consisting of the substrate, (n-2) overlayers, and the ambient. Each layer is assumed to be uniform, but graded interfaces can be accommodated by subdividing them into thin laminations. The most convenient, comprehensive, and practical treatment of the n-phase model is that recently given by Yeh.<sup>17</sup> All necessary equations are provided in a form readily adaptable to numerical analysis, and are completely general in that optically anisotropic materials are treated as well. Numerical analysis is necessary because of the arcane nature of the calculations and because almost all quantities involved are complex.

The purpose of effective medium theory (EMT) is to describe the dielectric function,  $\epsilon$ , of a composite in terms of those of its constituents and microstructure. The physical basis is straightforward: the application of an external field causes local displacements of charge within the material which manifests itself as screening charge at the boundaries of the separate microscopic regions. This screening charge modifies the local electric and displacement field  $\vec{e}(\vec{r})$  and  $\vec{d}(\vec{r})$  and therefore the average or macroscopic fields  $\vec{E}$  and  $\vec{D}$  that are actually observed. For any medium,  $\epsilon$  can be calculated (at least in principle) by solving the microscopic field problem exactly, and then spatially averaging the solution. The dielectric function is then obtained from the relation  $\vec{D} = \epsilon \vec{E}$ .

This prescription is simple, but it shows why the biggest theoretical impediment to accuracy is the EMT. It shows that each sample has its own EMT, and since the local fields depend on the relative values of the dielectric functions of the constituents, the EMT is different in principle for each wavelength. Since this challenge is too much to accommo-

date in practice, one resorts to idealized microstructures for which analytic solutions are available. The Maxwell Garnett (MG) model<sup>1</sup> is derived from the electrostatic solution for isolated spheres in an infinite host dielectric and approximately describes cermet or coated-sphere microstructures, while the Bruggeman effective medium approximation<sup>18</sup> (EMA) is derived from the MG theory by a self-consistency assumption that allows it to be applied to aggregate or random microstructures. While the derivation of the MG expression implies that its range of validity is limited to small volume fractions of the inclusion phase, Smith<sup>19</sup> has shown that it also applies for coated spherical ellipsoidal or spherical particles such that the dipolar component of the field outside the coated particle vanishes. The big difference between the MG and the EMA theories from a conceptual point of view is that the MG theory represents a microstructure for which the internal field pattern is always stationary, consisting of spatially fixed dipolar corrections to a background uniform field, whereas the self-consistency inherent in the EMA is an attempt to represent a microscopic field pattern that changes with the relative dielectric function values of the separate constituents. The dielectric function for a two-phase composite can be written in general as<sup>20</sup>

$$\frac{\epsilon - \epsilon_h}{\epsilon + \kappa \epsilon_h} = f_a \frac{\epsilon_a - \epsilon_h}{\epsilon_a + \kappa \epsilon_h} + f_b \frac{\epsilon_b - \epsilon_h}{\epsilon_b + \kappa \epsilon_h}; \quad (1a)$$

$$\epsilon = \frac{q\epsilon_a\epsilon_b + (1-q)\epsilon_h(f_a\epsilon_a + f_b\epsilon_b)}{(1-q)\epsilon_h + q(f_a\epsilon_b + f_b\epsilon_a)}; \quad (1b)$$

where  $\epsilon_a$ ,  $\epsilon_b$ , and  $\epsilon_h$  are the dielectric functions of the separate phases a, b and the host phase h,  $f_a$  and  $f_b$  are the respective volume fractions, and  $q = 1/(1 + \kappa)$  is the depolarization factor that takes the values 0, 1/3, 1/2, and 1 for no screening, three dimensionally isotropic, two dimensionally isotropic, and maximum screening, respectively. The host dielectric function has the values  $\epsilon_a$  or  $\epsilon_b$  for the MG theories and  $\epsilon$  for the EMA. Arbitrary degrees of freedom in composition and microstructure do not lead to arbitrary values of  $\epsilon$  because the parameters themselves have limited ranges, as described in simple geometrical constructions by various limit theorems<sup>7-9</sup> discussed elsewhere.<sup>20</sup> The limit theorems are written in terms of macroscopic observables such as relative volume fractions and isotropy in two or three dimensions and can be used to establish the intrinsic uncertainties in the parameters obtained by the application of Eqs. (1) to optical data.

In principle  $q$ ,  $f_a$  (or  $f_b$ ), and  $\epsilon_h$  all have the status of adjustable parameters, but some assumptions are usually made. These typically take the form of specific values, such as  $q = 1/3$  for systems that are expected to be isotropic in three dimensions, and/or the EMA approximation  $\epsilon_h = \epsilon$  for systems that are expected to have a random or aggregate microstructure. Although the MG and EMA theories are identical to first order when the volume fraction of one of the phases becomes small, for comparable volume fractions the predicted spectral lineshapes for  $\epsilon$  are sufficiently different so that the two microstructures are usually readily distinguishable from optical spectra. The EMA is found to describe rather well the dielectric properties of a wide range of thin film systems owing to their essentially random microstructure, but not surprisingly, there are numerous examples where neither simple theory is adequate to describe the data. Au-SiO<sub>2</sub> cermets discussed

by Gittleman and Abeles<sup>21</sup> fall into this category, as do the Rh films recently measured by Arndt et al.<sup>22</sup> Equation (1b) shows that  $q$  and  $\epsilon_h$  are not independent, but that the assumption of a particular form for  $\epsilon_h$  will affect  $q$  and vice versa. Since the choice of  $\epsilon_h$  is not always clearcut, uncertainties are introduced in the optically determined values of  $q$ . The limit theorems show that particle shapes become particularly important whenever the dielectric functions of the constituents are significantly different, as might be expected from the relative efficiencies by which needle- and disc-shaped inclusions screen themselves from externally applied fields. When the dielectric functions of the constituents are similar, then compositional differences are the important variables.

The final step is to determine the best fit parameters by linear regression analysis.<sup>16</sup> A number of applications can be found in two recent reviews by the author.<sup>23,24</sup>

## REFERENCES

1. J. C. M. Garnett, *Philos. Trans. R. Soc. London* **203**, 385 (1904); A205, 237 (1906).
2. H. A. Lorentz, *Theory of Electrons*, 2nd ed. (Teubner, Leipzig, 1916).
3. R. C. McPhedran, L. C. Botter, D. R. McKenzie, and R. P. Netterfield, *Appl. Opt.* **23**, 1197 (1984).
4. F. Abeles, in *Physics of Thin Films 6*, ed. by G. Hass and R. E. Thun (Academic, New York 1971).
5. J. B. Theeten and D. E. Aspnes, *Thin Solid Films* **60**, 183 (1979).
6. J. P. Borgogno, F. Flory, P. Roche, B. Schmitt, G. Albrand, E. Pelletier and H. A. Macleod, *Appl. Opt.* **23**, 3567 (1984).
7. Z. Hashin and S. Shtrikman, *J. Appl. Phys.* **33**, 3125 (1962).
8. D. J. Bergman, *Phys. Rev. Lett.* **44**, 1285 (1980).
9. G. W. Milton, *Appl. Phys. Lett.* **37**, 300 (1980).
10. P. B. Johnson and R. W. Christy, *Phys. Rev.* **B6**, 4370 (1972); **B9**, 5056 (1974).
11. D. E. Aspnes, A. A. Studna, and E. Kinsbron, *Phys. Rev.* **B29**, 768 (1984).
12. R. J. Archer, *Phys. Rev.* **110**, 354 (1958).
13. T. M. Donovan, E. J. Ashley, and H. E. Bennett, *J. Opt. Soc. Am.* **53**, 1403 (1963).
14. D. E. Aspnes and A. A. Studna, *Phys. Rev.* **B27**, 985 (1983).
15. D. E. Aspnes, in *Handbook of Optical Constants of Solids*, ed. E. E. Palik (Academic, New York, 1985).
16. D. E. Aspnes, J. B. Theeten, and F. Hottier, *Phys. Rev.* **B20**, 3292 (1979).
17. P. Yeh, *J. Opt. Soc. Am.* **69**, 742 (1979); *Surface Sci.* **96**, 41 (1980).
18. D. A. G. Bruggeman, *Ann. Phys. (Leipzig)* **24**, 636 (1935).
19. G. B. Smith, *J. Phys.* **D10**, L39 (1977).
20. D. E. Aspnes, *Thin Solid Films* **89**, 249 (1982).
21. J. I. Gittleman and B. Abeles, *Phys. Rev.* **B15**, 3273 (1977).
22. D. P. Arndt et al., *Appl. Opt.* **23**, 3571 (1984).
23. D. E. Aspnes, *J. de Physique Colloque* **C10**, 3 (1983).
24. D. E. Aspnes, *SPIE Proc.* **452**, 60 (1983).

# LIGHT SCATTERING FROM DIELECTRIC AND METALLIC MICROSTRUCTURES

Richard K. Chang

Yale University  
Section of Applied Physics and Center for Laser Diagnostics  
New Haven, Connecticut 06520

and

Peter W. Barber

Clarkson University  
Department of Electrical and Computer Engineering  
Potsdam, New York 13676

## Introduction

The generalized Lorenz/Mie formalism can be used to calculate the elastic scattering (e.g., extinction and scattering cross sections) and the internal electromagnetic field distributions<sup>1</sup> of axisymmetric micro-objects (e.g., cylinders, spheres, and spheroids) with complex refractive index ( $\tilde{n} = n + ik$ ) and characteristic size  $a$ . The electromagnetic fields inside and on the surface of the microparticles can be enhanced at specific values of the size parameter  $x = 2\pi a/\lambda$  (where  $\lambda$  is the optical wavelength). For dielectric microparticles with  $x \gg 1$ , morphology-dependent resonances occur at nearly regularly spaced wavelength intervals. For metallic microparticles, even with  $x < 1$ , localized surface plasmon resonances can occur at several wavelengths with vastly different electromagnetic field enhancement factors and spectral linewidths.

Recent experimental interests have been directed toward the exploitation of the enhanced electromagnetic field intensity at these resonances. For dielectric microparticles in particular, morphology-dependent resonances have been applied to the determination of the following properties of individual droplets flowing in a linear stream: (a) evaporation and condensation rates; (b) interfacial surface tension and bulk viscosity; and (c) nonlinear optical properties such as lasing and coherent Raman processes. For metallic microparticles, localized surface plasmon resonances have been applied to the species determination of molecular adsorbates via the surface enhanced Raman scattering. In this presentation, research results from collaborative work at Yale, Cornell, and Clarkson Universities will be briefly reviewed.

## Dielectric Microparticles

### Evaporation and Condensation Rates

Shifts in the wavelength of the morphology-dependent resonances have been used to measure extremely small changes in the radius of spherical liquid droplets. A modified Berglund-Liu vibrating orifice droplet generator was used to generate highly monodispersed (1 part in  $10^5$ ) liquid droplets with

a radius in the 10-50  $\mu\text{m}$  range. Since the morphology-dependent resonances associated with fluorescence emission are spectrally narrower than those associated with elastic scattering, the droplets were impregnated with fluorescent dyes and excited by a pulsed UV  $\text{N}_2$  laser. The resonances from different droplets successively further downstream of the orifice were noticed to shift monotonically to shorter wavelengths indicative of a decrease in the radius due to evaporation, as shown in Figs. 1(a) and 1(b). These resonances shifted to longer wavelengths when the droplets increased in radius as a result of being in a saturated vapor environment, as shown in Fig. 1(c). The wake of preceding droplets in the linear stream significantly decreased the evaporation rate of individual droplets relative to that of an isolated droplet. Small radius changes of 1 part in  $10^4$  have been observed.<sup>2</sup>

#### Interfacial Surface Tension and Bulk Viscosity

A spherical droplet which has been perturbed by a laser pulse (impulse function) distorts a droplet from a sphere to an equal volume spheroid. The freely damped oscillation of the droplet shape (from a sphere to an oblate and/or prolate spheroid) has a characteristic frequency and a damping constant (as shown in Fig. 2), which are related to the interfacial surface tension and bulk viscosity of the droplet.<sup>3</sup> Small amplitude shape distortions of 1 part in  $10^4$  have been observed.

#### Nonlinear Optical Properties

The incident wavelength or the internally generated radiation at a shifted wavelength can be tuned to be commensurate with one of the many morphology-dependent resonances, i.e., single resonance conditions (with either input or output waves) or double resonance conditions (with both input and output waves) can be satisfied. At the input resonance, the large internal electromagnetic field can increase nonlinear optical phenomena. At the output resonance, the liquid-air interface can provide a wavelength selective optical feedback (with high  $Q$ ) which greatly lowers the input intensity necessary to achieve lasing<sup>4</sup> or stimulated Raman scattering.<sup>5</sup> Molecular composition identification by stimulated Raman scattering and other coherent Raman processes<sup>6</sup> in droplets will be compared with those processes for an equal volume sample without an optical boundary.

#### Metallic Microparticles

The surface-averaged electromagnetic intensity of metallic spheres<sup>7</sup> and spheroids<sup>8</sup> can be greatly enhanced for certain combinations of incident wavelength. For metals with a small imaginary component of the bulk dielectric constant [ $\epsilon(\omega) = \epsilon_1(\omega) + i\epsilon_2(\omega)$ ], the largest enhancement factor is calculated to occur when the size of the microparticle is much less than the incident wavelength (the electrostatic limit). For metals with larger  $\epsilon_2(\omega)$ , the maximum enhancement occurs when the size extends well into the electrodynamic region. However, the enhancement in the latter case is greatly reduced from that in the former case. Recent calculations of the enhanced surface field for a few catalytically important metals will be compared with those for Ag,<sup>9</sup> which is known to exhibit surface enhanced Raman scattering. For example, Fig. 3 shows the enhancement at the tip of a 2:1 Pt spheroid as a function of size and incident wavelength. For the



size range shown, the maximum enhancement of 76 occurs at  $a = 101$  nm and  $\lambda = 710$  nm. Preliminary experimental results on the inelastic emission from discrete 2000 Å-sized metal microstructures designed and fabricated by e-beam lithography at the National Research and Resources Facilities for Submicron Structures at Cornell University will be presented.<sup>10</sup>

We wish to acknowledge the collaboration of our colleagues at Yale (M. B. Long, S.-X. Qian, B. Schlicht, J. B. Snow, H.-M. Tzeng, and K. F. Wall), at Cornell (E. D. Wolf), and Clarkson (M. P. Cline). We also acknowledge the partial support of this work by the Air Force Office of Scientific Research (Grant No. F49620-82-K-005), the Army Research Office (Grants No. DAAG29-82-K004 at Yale and DAAG29-84-K-0054 at Clarkson), and the Gas Research Institute (Basic Research Grant No. 5083-260-0795).

#### References

1. M. Kerker, The Scattering of Light and Other Electromagnetic Radiation (Academic, New York, 1969); C. F. Bohren and D. R. Huffman, Absorption and Scattering of Light by Small Particles (Wiley, New York, 1983).
2. H.-M. Tzeng, K. F. Wall, M. B. Long, and R. K. Chang, Opt. Lett. **9**, 273 (1984).
3. H.-M. Tzeng, M. B. Long, R. K. Chang, and P. W. Barber, "Laser-Induced Distortions of Flowing Droplets Deduced from Morphology-Dependent Resonances in Fluorescence Spectra," submitted to Opt. Lett.
4. H.-M. Tzeng, K. F. Wall, M. B. Long, and R. K. Chang, Opt. Lett. **9**, 499 (1984).
5. J. B. Snow, S.-X. Qian, and R. K. Chang, "Stimulated Raman Scattering from Individual Water and Ethanol Droplets at Morphology-Dependent Resonances," Opt. Lett., in press.
6. S.-X. Qian, J. B. Snow, and R. K. Chang, "Coherent Raman Mixing and Coherent Anti-Stokes Raman Scattering from Individual Micron-Sized Droplets," to be published.
7. B. J. Messinger, K. U. von Raben, R. K. Chang, and P. W. Barber, Phys. Rev. B **24**, 649 (1981).
8. P. W. Barber, R. K. Chang, and H. Massoudi, Phys. Rev. Lett. **50**, 997 (1983); ibid., Phys. Rev. B **27**, 7251 (1983).
9. M. P. Cline, P. W. Barber, and R. K. Chang, "Surface-Enhanced Electric Fields on Pt, Ir, Ni, Pd, and Rh Spheroids," to be published.
10. Burghard Schlicht (Yale) and Edward D. Wolf (Cornell), private communication.

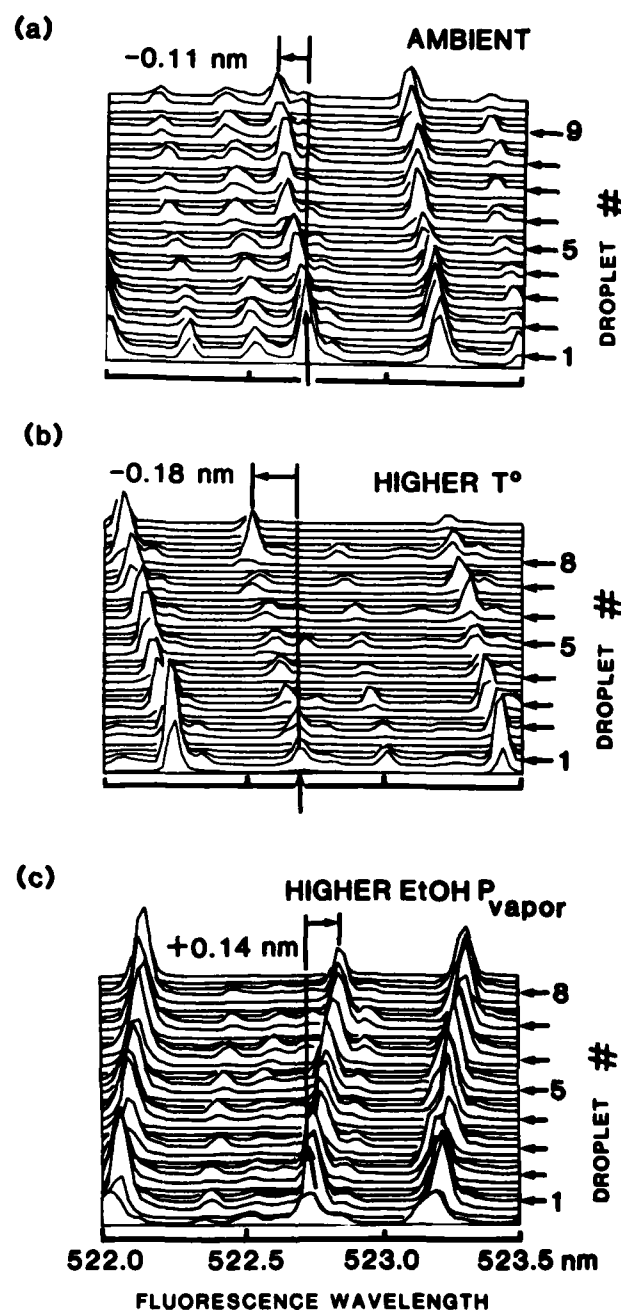


Fig. 1. The single laser shot fluorescence spectra from 8 to 10 spatially resolved droplets emerging from a Berglund-Liu generator into several different environments: (a) ambient, (b) higher temperature, and (c) high ambient ethanol vapor pressure (EtOH  $P_{\text{vapor}}$ ) at room temperature. Shifts to shorter wavelengths and longer wavelengths correspond to evaporation and condensation, respectively. [Figure from ref. 2.]

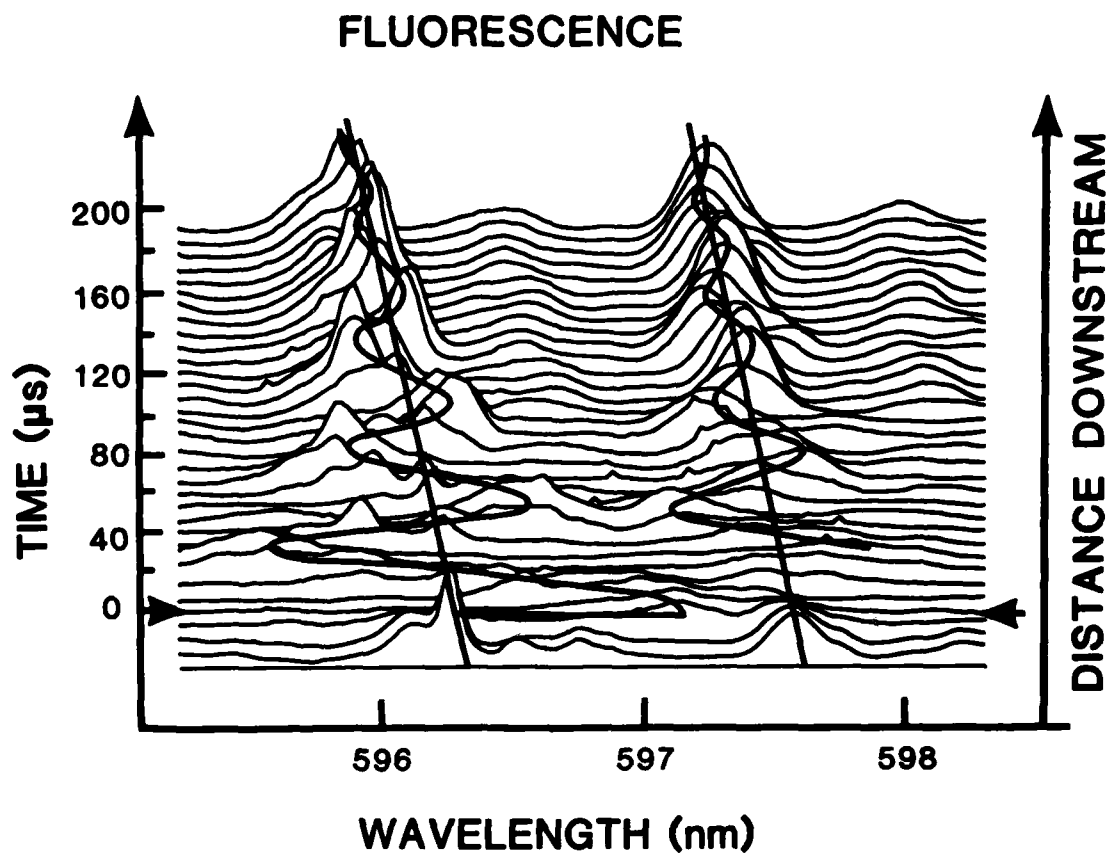


Fig. 2. Fluorescence spectra from laser-perturbed droplets downstream from the Berglund-Liu generator. Each droplet is perturbed by two counterpropagating  $\text{Ar}^+$  laser beams at locations indicated by the two arrows. The subsequent freely damped oscillations of morphology-dependent resonances from droplets downstream yield a shape oscillation frequency and damping constant corresponding to a quadrupole shape distortion with  $L = 2$  and  $m = 0$ . [Figure from ref. 3.]

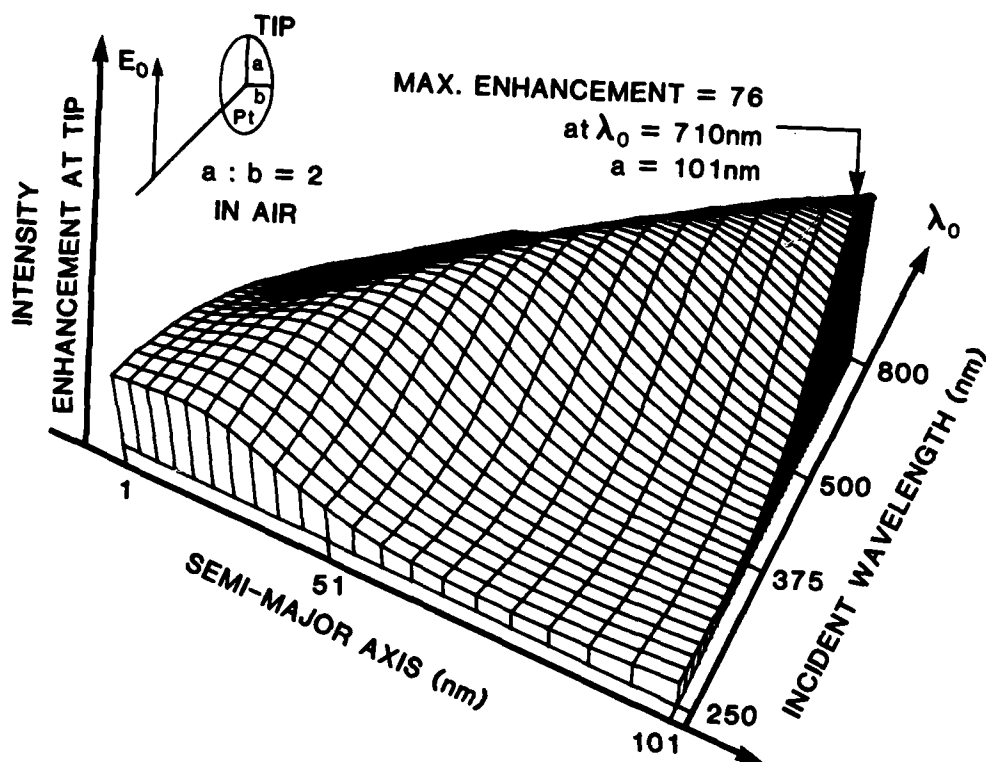


Fig. 3. Electrodynamic results of the intensity enhancement at the tip of a Pt spheroid. The dependence of this enhancement on the semi major axis length ( $a$ ) and the incident wavelength ( $\lambda_0$ ) is plotted for a Pt spheroid with  $a:b = 2$  and immersed in air.

## CHARACTERIZATION OF OPTICAL MATERIALS AND SURFACES USING TIME-DOMAIN REFLECTOMETRY

A. G. Lieberman  
National Bureau of Standards  
Gaithersburg, Maryland 20899

The generation of femtosecond duration laser pulses containing only a few oscillations of coherent light has recently been achieved using pulse compression techniques (1). Such ultrashort pulses have broad spectral bandwidths which may encompass the material and structural resonances of a reflecting medium. The effects of these resonances upon the reflected waveform could provide a novel method for characterizing the optical properties of a material or evaluating the surface finish of a manufactured object. The purpose of this paper is to explore the features of time-dependent optical pulse scattering from dispersive materials having smooth surfaces, from perfect conductors having randomly rough surfaces, and from materials exhibiting both dispersion and surface roughness.

For optical pulses structured as planewaves of a particular polarization the scattering process can be entirely characterized by a single entity, the impulse response function. This function, denoted  $R(t)$ , is physically equivalent to the field induced on the scattering surface by the incidence of a planewave of impulsive form. In the present analysis the electric field is assumed to be polarized perpendicular to the plane of incidence and the scattering medium is treated as a homogeneous material half-space. For a material having a perfectly smooth surface, the impulse response function is the inverse Fourier or Laplace transform of the Fresnel reflection coefficient for the electric field. For a material having a randomly rough surface, a statistically defined scattering coefficient is used instead.

The Green's function describing the propagation of the reflected or scattered impulsive field is obtained by retarding the impulse response function. That is to say, the argument of  $R(t)$  must be delayed by the time it would take for a wave leaving the surface and traveling with speed  $c$  in the direction of specular reflection to reach a given observation point. For a planewave of arbitrary waveform, the scattered field is simply the convolution in time of the waveform with the Green's function.

In practice, the required inverse transformations are not usually available in mathematical handbooks because the contour integrals are extremely difficult or impossible to evaluate exactly. An algorithm was consequently devised for expanding the reflection or scattering coefficient into a series of terms which could be individually transformed from the frequency domain to the time domain (2). The results of applying this algorithm to a number of model materials are shown in the accompanying table. The first four examples describe materials having smooth surfaces; the last example relates to a perfect conductor having a randomly rough surface.

The Debye material model is useful for treating relaxation phenomena in polar dielectrics and semiconductors. Reflection is characterized by the relaxation time  $\tau$ , the static susceptibility function  $\chi(0)$ , and the angle of incidence  $\theta_i$ . The impulse response waveform is shown for normal incidence ( $\theta_i = 0$ ). The Lorentz model treats resonant dispersion in non-polar dielectrics and other materials whose molecules (atoms or electrons) behave as harmonic oscillators (as opposed to rigid rotators). In this case, the binding frequency  $\omega_0$ , the oscillator strength  $\omega_p$ , and the viscous damping rate (linewidth)  $\nu$ , characterize a specific resonance of the medium. The waveform displayed in the figure corresponds to  $\nu = \omega_p/8$ ,  $\omega_0 = \omega_p$ , and  $\theta_i = 0$ . The Drude model for electronic conduction in a metal or a semiconductor results from setting the binding frequency  $\omega_0$  to zero in the Lorentz model. The oscillator strength  $\omega_p$  now represents the plasma frequency for a collective oscillation of the free electron gas. By further eliminating the viscous damping the impulse response of a cold, collisionless plasma results.

A metal surface characterized as smooth, lossless and infinitely conducting ( $\nu = 0$  and  $\omega_p = \infty$ ) is an ideal reflector incapable of dispersing an incident waveform, i.e.,  $R(t) = -\delta(t)$ . As such it provides a useful, but fictitious, comparison standard for evaluating the dispersive effects of surface roughness. The final entry in the accompanying table describes the impulse response for scattering in the direction of specular reflection by a randomly rough perfect conductor. Conditions of normal incidence are assumed so that no surface element is shadowed from the incident radiation by any other element. Also, the distribution of surface heights about the mean surface plane is assumed to be Gaussian with root-mean-square height  $a_{rms}$ . The usual Fresnel-Kirchoff diffraction formula (3) has been applied to evaluate the scattering of a unit intensity, monochromatic planewave. In performing the integration, the tilt of the surface normal on each element of the rough surface relative to the normal to the mean plane has been disregarded. This would appear to limit the application of the theory to surfaces of small  $a_{rms}$  or gentle slopes, and has the effect of treating the surface as a phase screen. Namely, the field-induced surface current has the same magnitude as that induced upon a plane reflector occupying the mean surface, whereas the phase at each location varies proportionately with the random surface height. The application of the inverse Fourier transform to the scattered monochromatic field gives  $R(t)$ . Note from the expression in the table that in the limit of a perfectly smooth surface ( $a_{rms} \rightarrow 0$ ),  $R(t) \rightarrow -\delta(t)$ , as it should.

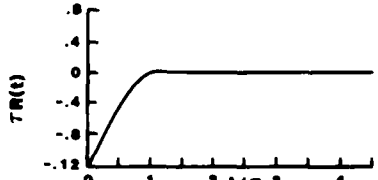
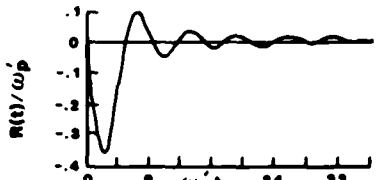
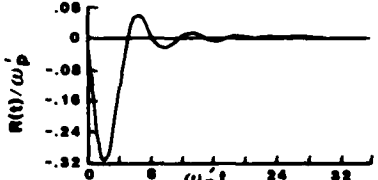
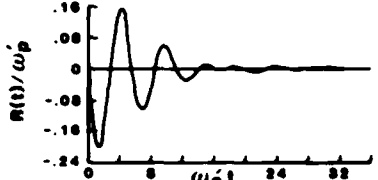
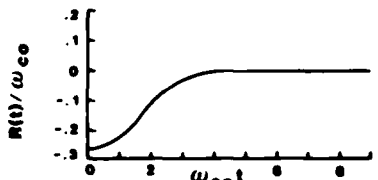
The foregoing expressions may be applied as follows to materials which are simultaneously dispersive and rough. For conditions of normal incidence and normal scattering, the Fresnel-Kirchoff formula is easily generalized to account for the reflectivity of the medium. Since the Fresnel reflection coefficient for a perfect conductor is -1, the generalization is accomplished by multiplying the scattered field amplitude by the negative value of the Fresnel reflection coefficient for the dispersive medium. (Describing the reflectivity by a Fresnel coefficient is an approximation consistent with the phase screen approximation.) In the time domain, the impulse response function for the simultaneously rough and dispersive medium is given by the convolution of the impulse response for the rough, perfect conductor with the negative of  $R(t)$  for the dispersive bulk material.

The waveform upon reflection for an actual optical pulse is evaluated as a convolution of this incident signal with the overall impulse response of the medium. Since an incident physical pulse would have finite bandwidth, shortcomings in the derivation of  $R(t)$  for large and small  $a_{rms}/\lambda$  tend to become suppressed in the computation of the reflected pulse.

#### References

- (1) Halbout, J.-M.; Grischowski, D. 12 femtosecond compressed laser pulses. J. Opt. Soc. Am. 74: 1337; 1984.
- (2) Lieberman, A. G. Transient state analysis of plane electromagnetic waves reflected from dispersive material surfaces. Nat. Bur. Stand. (U.S.) Tech. Note 1202; 1985. 69 p.
- (3) Born, M.; Wolf, E. Principles of optics. New York: Pergamon Press; 1980. 375-382.

# IMPULSE RESPONSE FUNCTIONS

<p><b>DEBYE POLAR DIELECTRIC</b></p> $\tau R(t) = -\left(\frac{t}{\tau}\right)^{-1} I_1\left(\frac{t}{2\tau}\right) \exp\left[-\left(\frac{1}{\tau} + \frac{1}{2\tau}\right)t\right]$ $\tau' = \tau \cos^2 \theta_1 / X(0)$	
<p><b>COLLISIONLESS PLASMA</b></p> $R(t)/\omega_p' = -(2/\omega_p' t) J_2(\omega_p' t)$ $\omega_p' = \omega_p / \cos \theta_1$	
<p><b>DRUDE METAL</b></p> $R(t)/\omega_p' = -\frac{1}{4}(\omega_p' t) \sum_{n=0}^{\infty} (-1)^n \frac{(3/2, n)}{(3, n) n!} \left[ \frac{(\omega_p' t)^2}{\nu t} \right]^n I_n(\nu t/2) e^{-\nu t/2}$	
<p><b>LORENTZ DIELECTRIC</b></p> $R(t)/\omega_p' = -\frac{1}{4}(\omega_p' t) \sum_{n=0}^{\infty} (-1)^n \frac{(3/2, n)}{(3, n) n!} \left[ \frac{(\omega_p' t)^2}{2\omega_c t} \right]^n I_n(\omega_c t) e^{-\nu t/2}$ $\omega_c = \sqrt{\omega_0^2 - (\nu/2)^2}$	
<p><b>ROUGH PERFECT CONDUCTOR</b></p> $R(t)/\omega_{co} = \frac{-1}{2\sqrt{\pi}} \exp\left[-(\omega_{co} t)^2/4\right]$ $\omega_{co} = c/\sqrt{2} a_{rms}$	



# THEORY OF LIGHT SCATTERING FROM A ROUGH SURFACE WITH A NONLOCAL INHOMOGENEOUS DIELECTRIC PERMITTIVITY

J. M. Elson

Michelson Laboratory, Physics Division  
Naval Weapons Center, China Lake, California 93555

First-order perturbation theory can be used to predict the combined effect of surface roughness and dielectric inhomogeneities on the scattering of light from optical surfaces. Figure 1 shows  $\log_{10}[(dP/d\Omega)/P_0]$  versus polar angle of scattering, where  $(dP/d\Omega)/P_0$  is the differential scattered power  $dP$  per unit solid angle  $d\Omega$  normalized to incident power  $P_0$ . The angle of incidence is 60 deg from the normal, and the wavelength is 6328 Å. The circles and squares are scattered light measurements for a mirror with an evaporated silver coating. The measurements were taken in the plane of incidence for p- and s-polarized light, respectively. They may be compared to the theoretical predictions (solid and dashed curves) for angle-resolved scattering due to surface roughness only, with p- and s-polarization incident, respectively. The data and curves to the right of the specular direction of 60 deg are for scattering directions away from the specular and toward the incident beam (backscattering). The angle -60 deg is literally the retroscattering direction. The data and curves to the left of 60 deg are in directions beyond the specular direction and away from the incident beam (forward scattering). Careful examination shows that in the backscattering direction the predicted polarization ratio is larger than the measured data. In the forward direction, the predicted polarization ratio is smaller than the measured data. Thus, in order to obtain better agreement between roughness scattering theory and these experimental data, the theory curves need to be brought closer together in the backscattering direction and further apart in the forward scattering direction. Such a discrepancy as this is frequently seen in practice, and so Figure 1 does not represent a unique situation.<sup>1</sup>

First-order perturbation methods of roughness-induced light scattering do not offer an opportunity to correct this discrepancy, as can be seen by the following argument. The ensemble-averaged, angle-resolved scattering formula can be written

$$\frac{1}{P_0} \left\langle \frac{dP_r}{d\Omega} \right\rangle = [ |p_r|^2 + |s_r|^2 ] g_r \quad , \quad (1)$$

where  $|p_r|^2 g_r$  and  $|s_r|^2 g_r$  are the contributions to scattering intensity which are p- and s-polarized, respectively. The r subscript refers to roughness as a source of scattering. The  $p_r$  and  $s_r$  are independent of surface topography; whereas,  $g_r$  is the power spectral density of surface roughness. The polarization ratio of scattered light can thus be written

$$R_r = |p_r/s_r|^2 \quad , \quad (2)$$

which is independent of surface roughness, since the power spectral density cancels out. In other words, the  $R_r$  is independent of roughness statistics. Thus, the prediction from Eq. (2) is that  $R_r$  will be the same for different mirrors provided that such parameters as angles of incidence and scattering, optical constants, and wavelength are held constant. However, polarization ratio measurements do vary between samples of the same material. An additional source of scattering may be the explanation for this disagreement between roughness scattering theory and measured data.

If it is assumed that dielectric inhomogeneities, in addition to roughness, are present, then perturbation theory may be applied to calculate the scattered fields due to both sources. In this case, the angle-resolved scattering depends on the autocorrelation properties of the surface roughness [as in Eq. (1)], the dielectric inhomogeneities [analogous to Eq. (1)], and the statistical cross-correlation between the roughness and dielectric random variables. In this case, the angle-resolved scattering formula may be written in the general form

$$\frac{1}{P_0} \left\langle \frac{dP_{rd}}{d\Omega} \right\rangle = A g_r + B g_d + C g_{rd} \quad , \quad (3)$$

where  $g_r$ ,  $g_d$ , and  $g_{rd}$  are the power spectral densities associated with the autocorrelation properties of the roughness, dielectric inhomogeneities, and the cross-correlation properties between the roughness and dielectric perturbations, respectively. The d subscript refers to dielectric inhomogeneity. The resulting polarization ratio has the general form

$$R_{rd} = \frac{|p_r|^2 g_r + b g_d + c g_{rd}}{|s_r|^2 g_r + e g_d + f g_{rd}} \quad , \quad (4)$$

which is now dependent on the statistical properties of a given mirror. By juggling the roughness and dielectric statistics, especially the cross-correlation between them,  $R_{rd}$  can be increased or decreased relative to the roughness-only result, and the experimental reflectance curves can be accurately fitted by theory. If  $g_d = g_{rd} = 0$ , Eq. (4) reduces to the roughness-only result, as discussed previously.<sup>2</sup>

## References

1. J. M. Bennett, J. M. Elson, and J. P. Rahn, Proc. SPIE 401, 234 (1983).
2. J. M. Elson, Phys. Rev. B 30, 5460 (1984).

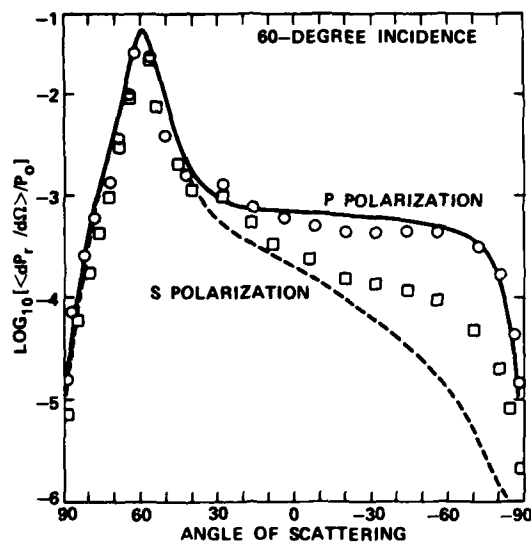


FIGURE 1. Roughness Theory-Experiment Discrepancy.

# OPTICAL PROPERTIES OF METALS IN THE INFRARED - THE DRUDE MODEL, PROBLEMS WITH IT, AND NON-LOCAL OPTICS

David W. Lynch  
Department of Physics and Ames Laboratory-USDOE  
Iowa State University  
Ames, Iowa 50011

The infrared optical properties of metals are frequently described by a free-electron gas model, the Drude model. This model has only two parameters, an electron scattering time,  $\tau$ , and the plasma frequency,  $\omega_p = (4\pi Ne^2/m)^{1/2}$ . It can be derived simply from a classical picture for the electrons, or from the Boltzmann equation. Quantum mechanically, it represents the photoexcitation of a conduction electron accompanied by the scattering of the electron by a phonon or impurity. The frequency-dependent dielectric function is given by

$$\tilde{\epsilon}(\omega) = \epsilon_1 + i\epsilon_2 = 1 - \frac{\omega_p^2 \tau^2}{1 + \omega^2 \tau^2} + i \frac{\omega_p^2 \tau}{\omega(1 + \omega^2 \tau^2)}$$

The conductivity, a material function alternate to  $\tilde{\epsilon}$ , has a real part

$$\sigma(\omega) = \frac{\sigma(0)}{1 + \omega^2 \tau^2} \quad \text{with} \quad \sigma(0) = \frac{Ne^2 \tau}{m} = \frac{\omega_p^2 \tau}{4\pi}.$$

A common test for the applicability of this model is a plot of  $\omega\epsilon_2$  vs.  $\epsilon_1 - 1$ , which should be a straight line. In many cases, when data over a limited wavelength region are used, the plot yields a satisfactory straight line, even for materials for which the free-electron contribution to  $\tilde{\epsilon}$  is known not to be the only one. In such cases the parameters derived from the data will not be meaningful. We discuss several situations for which the Drude model is known not to be valid, despite its use in the literature.

The infrared is taken here to mean the region between 1 and 50  $\mu\text{m}$  wavelength, and we assume temperatures are around room temperature, except as noted below. In this range the excitations of the free electrons are the only excitations to consider only if interband transitions are negligible. There are just a few elemental metals for which this is so, and all are monovalent: the five alkali metals and the three noble metals. In principle, all polyvalent metals have interband transitions extending to arbitrarily low energies. The practical problem here is to whether the low-energy interband contributions to  $\tilde{\epsilon}$  are negligible with respect to the Drude contribution in a given spectral region and at a particular temperature. For the transition metals and rare earths, and presumably the actinides, the region of strong interband contributions to  $\tilde{\epsilon}$  depends primarily on the crystal structure, and is roughly the region above 1 eV for b.c.c.-structured metals, above 0.1 eV for h.c.p.-structured metals, and above 0.05 eV for f.c.c. structured materials. In principle, all these metals have interband transitions at still lower energies, but their contribution to  $\tilde{\epsilon}$  is relatively small compared to the Drude term. Despite this, the Drude model has been fit successfully over a limited energy range to optical data for

some of the transition metals. There appears to be no simple structure-based rule for the polyvalent simple metals. If we take aluminum as an example, there is an interband absorption peak around 0.5 eV, which has a tail extending to lower energy. In fact, band structure calculations show that there are regions in the Brillouin zone where two bands cross at the Fermi energy, leading to intraband absorption at arbitrarily low energies. The 0.55 eV interband structure is difficult to detect at room temperature because of the dominance of the Drude contribution. It probably has not affected significantly the fit to the Drude model. At lower temperatures the Drude contribution diminishes, and the interband term becomes relatively more important.

There have been a number of studies of the alkali metals, which should have a well-defined threshold for interband transitions, predictable from reliable Fermi surface measurements. Significant absorption has been found below this energy, some of it reproducible. Until the origin of this is clear, one must be suspicious of Drude parameters obtained in the spectral region near this "anomalous" absorption. A recent suggestion is that it arises from excitations to or from surface states, and a calculation indicates that the expected magnitude is correct. Similar optical effects of surface states have been seen in electrodielectric measurements on Ag around 1 eV, i.e., well inside the Drude region. In this case, however, the observed effects are very small and require that the surface be predominantly 100 or 110 planes. Such effects of surface states probably do not affect the extraction of Drude parameters from data on Ag, but they could have an effect on the alkali metals.

We now discuss some limited aspects of non-local optics at the surface of a metal and how this affects the interpretation of optical measurements. We assume the metal can be described by a single dielectric function, later to be extended to two functions. This implies that the metal is completely homogeneous right up to the surface, where it terminates. We thereby ignore surface relaxation and the tail-off of the electron distribution into the vacuum. We simplify the above free-electron dielectric function for two regions in the infrared, where  $\omega \ll \omega_p$ . If  $\omega\tau \ll 1$

$$\epsilon_1 \approx 1 - \omega_p^2 \tau^2 \quad \epsilon_2 \approx \omega_p^2 \tau / \omega$$

$$\sigma(\omega) \approx \sigma(0)$$

$$A = 1 - R \approx \frac{2}{\omega_p} \sqrt{\frac{2\omega}{\tau}}$$

(R and A are reflectance and absorbance at normal incidence on a semi-infinite sample.) This is the Hagen-Rubens or classical skin effect region. If  $\omega\tau \gg 1$  we have the relaxation region in which

$$\epsilon_1 \approx 1 - \frac{\omega_p^2}{\omega^2} \quad \epsilon_2 \approx \frac{\omega_p^2}{\omega^3 \tau}$$

$$\sigma(\omega) \approx \frac{\sigma(0)}{\omega^2 \tau^2}$$

$$A = \frac{2}{\omega_p \tau}$$

In a relatively pure metal,  $\tau$  will increase by a large factor, the resistivity ratio, as the sample is cooled to 4.2 K. The measured absorbance falls only a little as the sample is cooled, and the low temperature value of  $A$  is far larger than the Drude theory predicts. Classically, the radiation penetrates to a depth characterized by the classical skin depth,  $\delta_0 = c/(2\pi\omega\sigma(0))^{1/2}$ . At room temperature the mean free path of the electrons,  $l = v_F\tau$ , is much shorter than  $\delta_0$ . At low temperatures, the mean free path can be much larger, depending on the impurity and defect concentration in the individual sample.  $l$  can even be larger than  $\delta = \delta_0\omega\tau$ , in the relaxation region. When the mean free path is not much less than the classical skin depth, we speak of the region of the anomalous skin depth, and non-local optics must be introduced. Local optics uses a local constitutive relation, e.g.,  $\vec{J} = \sigma\vec{E}$ . (Cubic crystals are assumed.) This means that at each point  $\vec{r}$  in space and  $t$  in time the current density is proportional to the electric field at that  $\vec{r}$  and  $t$ . The constant of proportionality contains an average of the electron velocity, i.e., the response of the electrons to the applied field  $\vec{E}$  at  $\vec{r}$  and  $t$ . When the mean free path is large compared to the skin depth, the velocity at a point  $\vec{r}$ ,  $t$  is not proportional to the field there, but rather depends on the field at other points and earlier times, going back along its trajectory to its previous collision. The electric field is not constant over this path. The relationship between  $\vec{J}$  and  $\vec{E}$  is now an integral one

$$\vec{J}(\vec{r}, t) = \frac{3Ne^2}{4\pi m v_F} \int \frac{\vec{R}[\vec{R} \cdot \vec{E}(\vec{r}', t')]}{|\vec{R}|^4} \exp(-|\vec{R}|/\ell) d^3R$$

with  $\vec{R} = \vec{r} - \vec{r}'$  and  $t' = t - |\vec{R}|/v_F$ , a retarded time. Important contributions come only from a volume around  $\vec{r}$  of the order of the mean free path in radius. This is a non-local relationship, and to the extent that the effect is a large one, it means that one can no longer define a local constitutive relation,  $\vec{J} = \sigma\vec{E}$ , that has any meaning. Just as the time dependence of the electronic response can be Fourier transformed to give individual frequency components, in a periodic solid, the  $\vec{r}, \vec{r}'$  dependence becomes the simpler dependence on  $\vec{r} - \vec{r}'$ , which Fourier transforms to a wave vector dependence. This means that for non-local optics, the conductivity depends separately on the frequency and wave vector. A measurement at a fixed frequency involves a response function that is integrated over all wave vectors.

A second reason for the introduction of non-local optics is the occurrence of surface charge induced on the surface of the metal by p-polarized radiation at non-normal incidence. The boundary condition on the normal component of  $\vec{D}$  leads to a surface charge density, one of zero thickness in classical electromagnetism. The uncertainty principle dictates that this will spread into a finite thickness, often of the order of the Thomas-Fermi screening length, about 1 Å for metals. When one Fourier analyzes this spatial distribution, a large spread of wave vectors results, and these must be summed to get the response to an incident wave of a single frequency.

The surface charge density gives rise to longitudinal electric fields, while the fields of the electromagnetic wave are transverse. Two dielectric functions are now needed, a longitudinal and a transverse, except at normal

incidence. Both depend on both frequency and wave vector, but in the limit of zero wave vector, they become equal. However, for non-normal incidence, both are needed. Both dielectric functions may be obtained from calculations of varying degrees of sophistication. Once obtained, they may be used for comparison with experiment, but because  $\tilde{\epsilon}(\omega, k)$  is not measured in the infrared (although some high resolution electron energy loss measurements are approaching this) a measurable quantity must be calculated from the dielectric functions. This is the surface impedance  $\tilde{Z}$ ,  $4\pi/c$  times the ratio of the surface electric to magnetic fields, from which the reflectance can be calculated as

$$R = \left| \frac{\tilde{Z} - \frac{4\pi}{c}}{\tilde{Z} + \frac{4\pi}{c}} \right|^2, \quad \text{If } A \ll 1 \quad A \approx \frac{c}{\pi} \operatorname{Re}(\tilde{Z})$$

$\tilde{Z}$  may be calculated. It not only depends on the model for the electron gas and the surface, but on a boundary condition imposed on the electron momentum at the surface. A fraction  $p$  of the electrons is assumed to scatter specularly at the surface, with the remainder scattering perfectly diffusely. At normal incidence in the Hagen-Rubens region the absorbance is

$$A = \frac{2}{\omega_p} \sqrt{\frac{2\omega}{\tau}} \left[ 1 + (1 - p) \frac{3}{8} \frac{v_F}{c} \omega_p \tau \right]$$

which agrees with the Drude result if all scattering is specular. The result for the relaxation region is

$$A = p \frac{1}{2} \left( \frac{\omega_p}{\omega} \right)^2 \left( \frac{v_F}{c} \right)^3 + (1 - p) \frac{3}{4} \frac{v_F}{c}$$

in which the scattering time does not even appear. Holstein pointed out that there is an additional process contributing to  $A$ , a second-order one in which a photon excites an electron and a momentum-conserving phonon. It contributes an additive term to  $A$  of

$$A_H = \frac{4}{5} \frac{\theta_D}{T} \frac{1}{\omega_p \tau}$$

in which  $\theta_D$  is the Debye temperature and  $T$  is a relatively high temperature (not that of the measurement of  $A$ ) at which the electron-phonon scattering time is  $\tau$ .

The anomalous skin effect completely dominates the low temperature infrared optical properties of pure metals. At room temperature it produces a correction that is of the order of a few percent at most (in  $A$ , still less in  $R$ ), depending on wavelength. To the extent that it is present, it weakens the concept of a frequency-dependent function to describe the optical properties. The use of such a function, e.g.,  $\tilde{\epsilon}$ , to predict optical properties other than the one from which it was derived, can lead to errors.

# SEPARATION OF DRUDE AND BAND-TO-BAND SPECTRA IN POLYVALENT METALS

D. Y. Smith\*  
Argonne National Laboratory  
Argonne, Illinois 60439  
and  
B. Segall  
Case Western Reserve University  
Cleveland, Ohio 44106

The problem of separating intra- and interband contributions to optical properties has been reexamined with the goal of minimizing the dependence of the separation on specific models. This was prompted by a desire to compare the recently published<sup>1</sup> theoretical interband spectrum of aluminum with reflectance measurements. Unfortunately, such a comparison is complicated because intra- and interband effects are almost inextricably intermeshed in the data. Several prior analyses<sup>2-8</sup> have involved restrictive assumptions regarding the interband component. However, we present here an approach that uses general qualitative features of the theory combined with experimental data over a wide energy range that reduces the assumptions required and yields a more reliable separation.

Interband absorption arises from electron-hole excitations and may be treated in one-electron theory. Band structure calculations show that for aluminum there are two principal interband excitations<sup>9,10</sup> arising from transitions between pairs of parallel bands<sup>4,9</sup> near zone boundaries. These parallel-band absorptions have sharp onsets at the zone-boundary energy gaps--estimated from Fermi-surface data to lie at ~0.5 and ~1.6 eV--followed by long high-energy tails. In addition, detailed band calculations<sup>1,11</sup> predict a weak absorption extending to zero energy and substantial broadening of the parallel-band transitions.

Intraband absorption involves creation of an electron-hole pair within a band and its simultaneous scattering by phonons. For  $\omega \gg \omega(\text{Debye})$ , the intraband contribution to the dielectric function has the "free-electron" Drude form<sup>12</sup>

$$\epsilon^f(\omega) = 1 - \Omega_p^2 / \omega(\omega + i/\tau) . \quad (1)$$

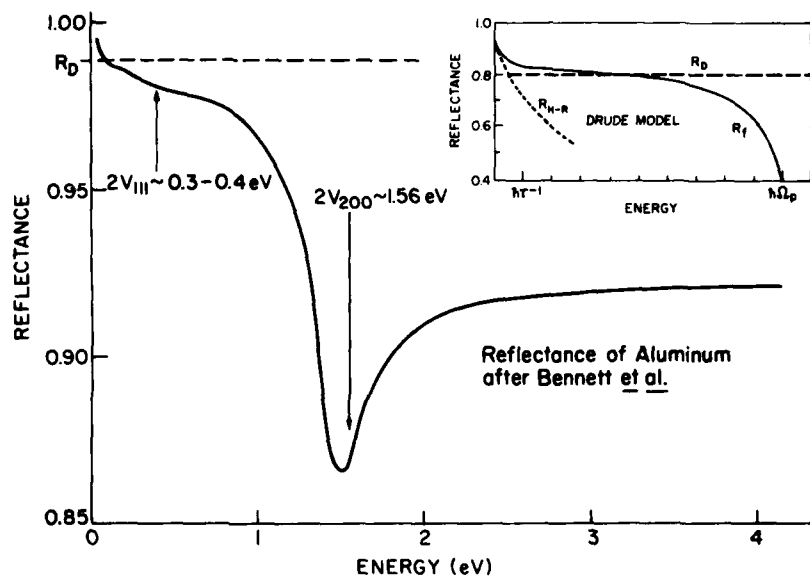
$\Omega_p$  &  $\tau$ , the intraband plasma frequency and relaxation time, are constants.

In principle, the intra- and interband contributions may be separated because, below the lowest parallel-band absorption, the Drude term dominates. The reflectance of unoxidized aluminum films at room temperature is shown in Fig. 1 after Bennett et al.<sup>3</sup> That of a good Drude "metal" is given in the inset. Comparison of the two suggests that the measured spectrum is Drude-like below ~0.2 eV in accord with the theoretical expectations. For  $2\hbar\omega(\text{Debye}) = 0.07 \text{ eV} \ll \hbar\omega \ll 0.2 \text{ eV}$  the reflectance has a frequency dependence intermediate between a Hagens-Rubens form-- $\ln [R_{HR}(\omega)] \approx - (2\omega/\pi\sigma_0)^{1/2}$ ,  $\omega \ll \tau^{-1} \ll \Omega_p$ --and the Dingle value-- $\ln [R_D(\omega)] \approx - \Omega_p / 2\pi\sigma_0$ ,  $\tau^{-1} < \omega \ll \Omega_p$ --

\*Work supported by the U. S. Department of Energy.



Fig. 1. Reflectance of metallic aluminum at room temperature after Bennett et al. The principal interband transitions are indicated by arrows. The insert shows the reflectance of a Drude "metal."



where  $\sigma_0$  is the dc conductivity. In this intermediate regime the reflectance may be fit using the modified Kronig formula<sup>13</sup>

$$\ln [R_K(\omega)] \approx - (2\omega/\pi\sigma_0)^{1/2} [(1+\omega^2\tau^2)^{1/2} - \omega\tau]^{1/2}. \quad (2)$$

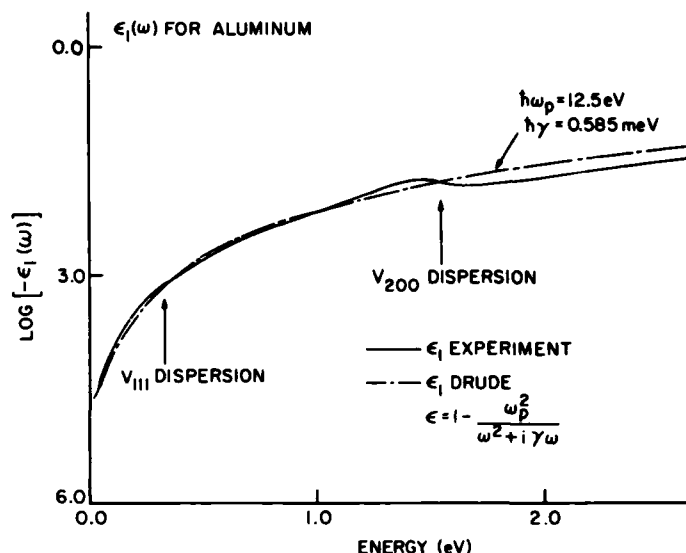
However, even the small ( $\pm 0.1\%$ ) error in the reflectance data of Bennett et al. translates into a large uncertainty in the Drude parameters, namely:  $12 \text{ eV} \leq \hbar\omega_p \leq 29 \text{ eV}$  and  $0.06 \text{ eV} \leq \hbar\tau^{-1} \leq 0.2 \text{ eV}$ . Note that the Dingle plateau (indicated by a dashed line) does not develop because of the onset of the strong interband transitions.

An alternative is to seek a separation of the intra- and interband components of the dielectric function  $\epsilon(\omega) = \epsilon'(\omega) + i\epsilon''(\omega)$  obtained from an analysis of the reflectance measurements. The  $\epsilon(\omega)$  for Bennett et al.'s<sup>3</sup> data has been given by Shiles et al.<sup>14</sup> One approach employs theoretical guidance as to the form of the interband contribution. An obvious choice is the analytical model of Ashcroft and Sturm<sup>10</sup> which, together with a Drude term, may be fit to  $\epsilon(\omega)$ . This method has been applied previously<sup>7,8</sup> and was tested here. Our experience was that, if no interrelation was assumed between the various parameters, a broad and poorly defined minimum--especially for lifetimes--occurred in the least-squares fitting. Moreover, the two-band model does not account for interaction with other bands and introduces a bias into the separation.

To avoid these problems we employed the general, rather than the specific features of the interband spectrum, in particular the dominant parallel-band absorptions at  $\sim 0.5$  and  $\sim 1.6$  eV. These make distinctive contributions to  $\epsilon'(\omega)$  in the form of regions of anomalous dispersion. Hence, one expects the total  $\epsilon'(\omega)$  consists of (a) the Drude contribution with (b) two superimposed oscillatory dispersions at each of the parallel-band absorptions; see Fig. 2.

The fitting procedure consists of searching for values of the Drude parameters that give an intraband contribution to  $\epsilon'(\omega)$  which (a) fits the experimental  $\epsilon'(\omega)$  curve in the Drude region below 0.2 eV; but which (b) passes through the

Fig. 2. Comparison of the experimental  $\epsilon'(\omega)$  after Shiles et al. with a trial Drude contribution satisfying the criteria of fitting experiment at low energies, and passing through regions of anomalous intraband dispersion. Note  $\gamma = \tau^{-1}$ .



experimental  $\epsilon'(\omega)$  curve near the expected positions of the parallel-band absorptions so as to form a monotonically increasing "background" on which the anomalous interband dispersions are superimposed. In ambiguous cases the regions where the crossings occur may be located using  $d[\epsilon'(\omega)]/d\omega$ . These requirements were found to be highly constraining for aluminum yielding  $\hbar\Omega_p = 12.5 \pm 0.3$  eV, and  $\tau = 1.06 \pm 0.12 \times 10^{-14}$  sec.

A comparison with literature values is given in Table 1. Early studies, such as that of Mendlowitz,<sup>2</sup> involved fits above 2-2.5 eV and forced all the conduction-band oscillator strength into the Drude term; the resulting  $\tau$  is too small. Bennett et al.<sup>3</sup> assumed both  $\Omega_p$  and  $\sigma_0$  from independent experiments. Ehrenreich et al.<sup>4</sup> and Powell<sup>5</sup> separated the 1.5 eV transition, but included the 0.5 eV transition in their Drude term. Dresselhaus et al.<sup>6</sup> and Mathewson and Myers<sup>7</sup> (M & M) accounted for both principal interband transitions; the latter via a fit of the Ashcroft-Sturm model<sup>10</sup> to ellipsometric measurements from 0.7 - 2.5 eV. Benbow and Lynch<sup>8</sup> also accounted for both transitions, but assumed  $\Omega_p$  (via the optical mass) following Ashcroft and Sturm.<sup>10</sup>

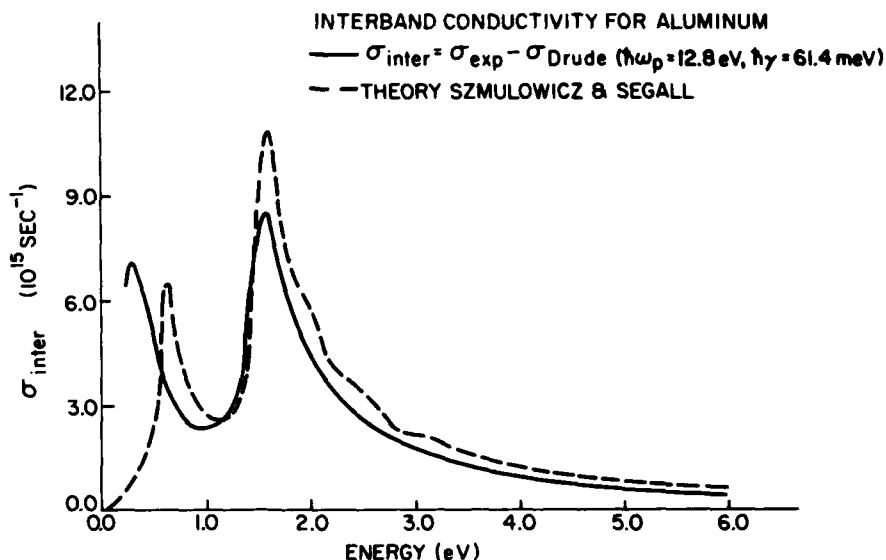
The present room temperature results and those of M & M agree nearly within the estimated uncertainty. M & M's high value of  $\Omega_p$  may arise because their measurements extended to only 0.7 eV--well above the Drude region. However,

Table I. Aluminum Drude Parameters and Oscillator Strength  $f_f$  (in electrons/atoms)

Source	Temp (K)	$\hbar\Omega_p$ (eV)	$\tau$ ( $10^{-14}$ sec)	$f_f$ (e/a)	$\sigma_{opt}(e)$ ( $10^{17}$ sec $^{-1}$ )
Mendlowitz (1960), Ref. 2	RT	14.1	0.12	2.40	0.44
Bennett et al. (1966), Ref. 3	RT	14.7	0.801	2.60	3.18
Ehrenreich et al. (1963) Ref. 4	RT	12.7	0.512	1.94	1.52
Powell (1970), Ref. 5	RT	12.2	0.66	1.80	1.81
Dresselhaus et al. (1971), Ref. 6	RT	12.9 $\pm$ 0.7	0.5 $\pm$ 0.2	2.0 $\pm$ 0.2	1.60 $\pm$ 0.8
Mathewson and Myers (1972), Ref. 7	RT	13.0	1.02	2.03	3.14
Benbow and Lynch (1975), Ref. 8	4.2	12.7	1.10	1.94	3.25
Smith and Segall (present work)	RT	12.5 $\pm$ 0.3	1.06 $\pm$ 0.12	1.88 $\pm$ 0.09	3.00 $\pm$ 0.30
Electrical Conductivity, Ref. 15	RT				3.18-3.39

in both cases the optical ( $\sigma_o = \Omega_p^2 \tau / 4\pi$ ) and electrical conductivities are equal to within the uncertainty of the separation. The values of  $\tau$  and  $\sigma_o$  given by Dresselhaus *et al.*<sup>6</sup> is in disagreement with M & M and the present work; the reason is not clear from their publication.

Fig. 3. Interband conductivity of aluminum. The experimental curve is for the room-temperature reflectance data of Bennett *et al.* as analyzed by Shiles *et al.* The theoretical results of Szmulowicz and Segall are based on parameterized APW band calculations.



The experimental interband conductivity obtained by subtraction of the Drude contribution is given in Fig. 3. The position and shape of the 1.6 eV transition are independent of  $\Omega_p$  and  $\tau$  within the range of the Drude parameters. The position of the low-energy peak varies between 0.3 and 0.35 eV, its height is uncertain by  $\pm 20\%$ . The predictions of Szmulowicz and Segall<sup>1</sup> are given in Fig. 3 for comparison. These were made for aluminum at 4 K; at higher temperatures broadening and a red shift is expected. Consequently, agreement between theory and experiment is considered quite good.

#### References

1. F. Szmulowicz and B. Segall, *Phys. Rev. B* **24**, 892 (1981).
2. H. Mendlowitz, *Proc. Phys. Soc.* **75**, 664 (1960).
3. H. E. Bennett, M. Silver, and E. J. Ashley, *J. Opt. Soc. Am.* **53**, 1089 (1963).
4. H. Ehrenreich, H. R. Philipp, and B. Segall, *Phys. Rev.* **132**, 1918 (1963).
5. C. J. Powell, *J. Opt. Soc. Am.* **60**, 78 (1970).
6. G. Dresselhaus, M. S. Dresselhaus, and D. Beaglehole, in *Electronic Density of States*, edited by L. H. Bennett, NBS Special Publication 323, National Bureau of Standards, Washington, DC (1971).
7. A. G. Mathewson and H. P. Myers, *J. Phys. F* **2**, 403 (1972).
8. R. L. Benbow and D. W. Lynch, *Phys. Rev. B* **12**, 5615 (1975).
9. W. H. Harrison, *Phys. Rev.* **147**, 467 (1966).
10. N. W. Ashcroft and K. Sturm, *Phys. Rev. B* **3**, 1898 (1971).
11. D. Brust, *Phys. Rev. B* **2**, 818 (1970).
12. G. P. Mahan, *Many Particle Physics* (Plenum, New York, 1981).
13. F. Modine and D. Y. Smith, *J. Opt. Soc. Am.*, in press.
14. E. Shiles, T. Sasaki, M. Inokuti, and D. Y. Smith, *Phys. Rev. B* **22**, 1612 (1980).
15. *Handbook of Chemistry & Physics*, R. C. Weast, ed. (CRC, Boca Raton, 1972 & 1983) 52nd and 64th ed.

## STATUS OF MATERIALS FOR TRANSMISSIVE AND REFLECTIVE INFRARED COMPONENTS

H. E. Bennett

Michelson Laboratory, Physics Division  
Naval Weapons Center, China Lake, California 93555

The search for better infrared materials for transmissive and reflective optics has been ongoing for at least 70 years. Alkali halides were developed as infrared transmitting materials for spectrometers before 1950, but achieved very low absorption only in the 1970s. In response to the requirements of the laser community, alkali halide optics were produced with infrared absorption coefficients two orders of magnitude lower than had previously been available. For example, at the CO<sub>2</sub> lasing wavelength of 10.6  $\mu\text{m}$ , absorption coefficients of KCl as low as  $8 \times 10^{-5} \text{ cm}^{-1}$  have been reported.<sup>1</sup> In the process of achieving this low absorption, a better understanding of the absorption process was achieved. As illustrated in Figure 1, the absorption of a typical dielectric reaches a maximum in the far and intermediate infrared as a result of infrared excitation of the molecular vibration or reststrahlen bands. At shorter wavelengths, the absorption falls off at a rate which in many materials is a nearly exponential function of wavenumber<sup>2</sup> (and hence nearly linear on a semilog plot, as illustrated in Figure 1). This multiphonon absorption is intrinsic to the material and can only be changed by changing the material or its crystal structure.

As the wavelength decreases, the absorption levels off and becomes nearly independent of wavelength. By removing or compensating for impurities, reducing grain boundary absorption, reducing distortion in the crystal lattice, minimizing lattice defects, and lowering surface absorption, this extrinsic absorption can be reduced, sometimes dramatically. To obtain a low absorption infrared material, the technique is then to pick a material (and ideally a crystal structure, although this option is usually not available) which has low intrinsic absorption in the wavelength region of interest and then through process control reduce the extrinsic absorption to the desired level.

In addition to optical absorption, various other parameters must be considered in selecting an infrared transmitting material for a given application. In many cases, fracture toughness, resistance to thermal shock, and insensitivity to environmental agents such as water are of great importance. KCl and many of the other alkali halides are very soluble in water. To overcome this difficulty, high-purity ZnSe was developed in a multimillion-dollar program lasting several years. Eventually, an absorption at 10.6  $\mu\text{m}$  in this material comparable to purified KCl was achieved. ZnSe, although hydrophobic, shares with KCl and most of the other alkali halides the problem of being extremely soft with low-fracture toughness. To obtain a stronger, low-absorption material, work began on purifying ZnS. The well-known yellow cast was removed, leaving a water-clear material, and the infrared absorption coefficient was reduced from about  $5 \times 10^{-2} \text{ cm}^{-1}$  to  $2 \times 10^{-3}$ , a factor of 25 times, in the extrinsic absorption region.<sup>3</sup>

Unfortunately, ZnS has multiphonon structure in the 10 to 20  $\mu\text{m}$  wavelength region arising from excitation of the  $3\omega_{\text{TO}}$  phonon.<sup>4</sup> This absorption is intrinsic and thus cannot be removed. The material, although harder than ZnSe and surprisingly resistant to thermal shock, is still relatively soft, with low-fracture toughness. A harder material with lower absorption in the 8 to 12  $\mu\text{m}$  wavelength region would be useful. The ternary sulfides offer promise here, and  $\text{CaLa}_2\text{S}_4$ , a cubic material with a thorium phosphide structure, has been under development for several years. The progress made in reducing extrinsic absorption in this material and a comparison to ZnSe and ZnS are shown in Figure 2.

A compromise must be made between physical properties such as fracture toughness and low infrared absorption. Strong, high-melting materials typically are formed by small, light atoms with low coordination numbers (i.e., number of nearest neighbors) and covalent (directional) bonding. The atoms are thus tightly bound, have high vibrational frequencies, and hence have significant intrinsic multiphonon absorption even in the short wavelength infrared. Transparent infrared materials typically contain large, heavy atoms with high coordination numbers and ionic (nondirectional) bonding. They thus have low vibrational frequencies but also tend to be soft with low melting temperatures.

As one proceeds from longer to shorter infrared wavelengths, vibrational frequencies can increase and harder, tougher materials should become available. Sapphire, a very hard infrared transmitting material with high fracture toughness and good thermal shock properties, is still intrinsic at a wavelength of 3.5  $\mu\text{m}$ . It also is hexagonal and hence slightly birefringent. A cubic crystal structure can be obtained by substituting a nitrogen atom for one of the oxygen atoms. Techniques of growing this crystal,<sup>5</sup> which has physical properties approaching sapphire and is commonly called ALON or "cubic sapphire," have now been developed. Its absorption spectrum is shown in Figure 3. Other novel infrared transmitting materials in Figure 3 of interest in the 3 to 5  $\mu\text{m}$  wavelength range, where an atmospheric window exists, are hot-pressed spinel,<sup>6</sup> and sintered yttrium oxide.<sup>7</sup> Their absorption may be compared to ITRAN 1 (hot-pressed magnesium fluoride), a more traditional material for this wavelength region, and to water-clear CVD zinc sulfide. Another interesting material is zirconium oxide,<sup>7</sup> which is exceedingly hard and durable. Unlike  $\text{Y}_2\text{O}_3$ , its absorption cannot be reduced further in the 4 to 5  $\mu\text{m}$  band since it does not become extrinsic until about 4  $\mu\text{m}$ . The fluoride glasses, one of which, zirconium barium lanthanum aluminum fluoride or ZBLA, is shown in Figure 3, are also of interest in this region,<sup>8</sup> particularly in waveguide applications.

Mirrors as well as windows are often used as infrared components. Recently, interest has centered on the insensitivity of the mirror substrates to heating or cooling and to creep. Low-expansion glasses such as ULE or Zerodur are frequently used as substrate materials. Their low-expansion coefficients over a range of temperatures near ambient and the excellent optical figure and low microroughness which can be produced by optically polishing these materials make them very attractive. It has been shown that ULE and Zerodur are among the most stable materials known,<sup>9</sup> provided they are maintained at ambient temperature. However, if they are thermally shocked, Zerodur may not return

to its initial shape upon cooling.<sup>10-12</sup> The optical figure of the mirror is thus degraded, and in critical applications this small effect can become important. Reasons for this behavior are currently under study.

## References

1. J. W. Davisson et al., Third Conference on High Power Infrared Laser Window Materials-1973, Air Force Cambridge Research Laboratory, Report No. AFCRL-TR-0085, Vol. I, pp. 31-42.
2. T. F. Deutsch, J. Phys. Chem. Solid 34, 2091 (1973).
3. C. A. Klein and C. Willingham, Raytheon Research Division, Lexington, Mass. (to be published).
4. C. A. Klein and R. N. Donadio, J. Appl. Phys. 51, 797 (1980).
5. J. W. McCauley and N. D. Corbin, J. Am. Ceram. Soc. 62, 476 (1979); N. D. Corbin and J. W. McCauley, Proc. SPIE 297, 19-23 (1981).
6. D. W. Roy, Proc. SPIE 297, 13-18 (1981).
7. W. H. Rhodes and E. A. Trickett, Proc. SPIE 505 (1984) (in press).
8. B. Bendow and D. Martin, *ibid.*; C. T. Moynihan, A. J. Bruce, S. R. Loehr, S. M. Opalka, R. Mossadegh, and N. Perazzo, *ibid.*
9. J. W. Berthold III, S. F. Jacobs, and M. A. Norton, Appl. Opt. 15, 1898 (1976).
10. J. J. Shaffer and H. E. Bennett, Appl. Opt. 23, 2852 (1984).
11. H. E. Bennett, J. J. Shaffer, and D. K. Burge, *ibid.*, p. 2734.
12. S. F. Jacobs, S. C. Johnston, and G. A. Hansen, *ibid.*, p. 3014.

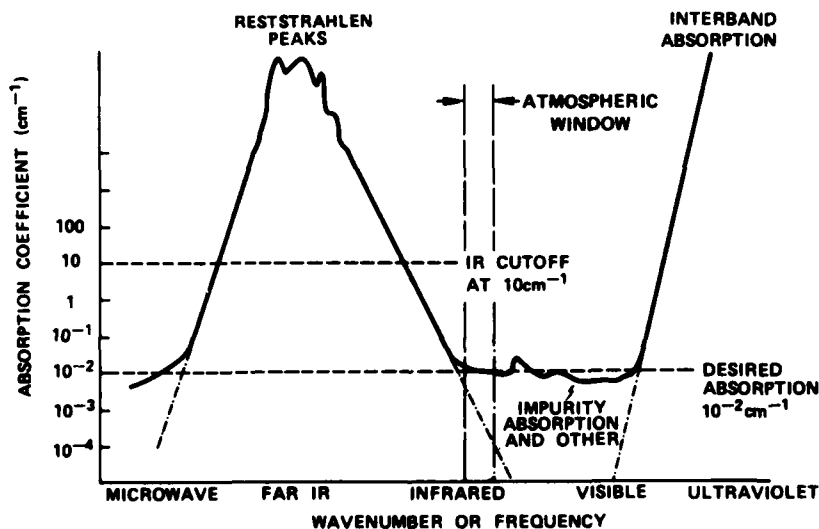


FIG. 1. Absorption Spectrum of a Typical Dielectric. The reststrahlen absorption and its multiphonon tail seen on the left side of the figure and the interband absorption with its Urbach tail seen on the right side are intrinsic to the material and can sometimes be removed.

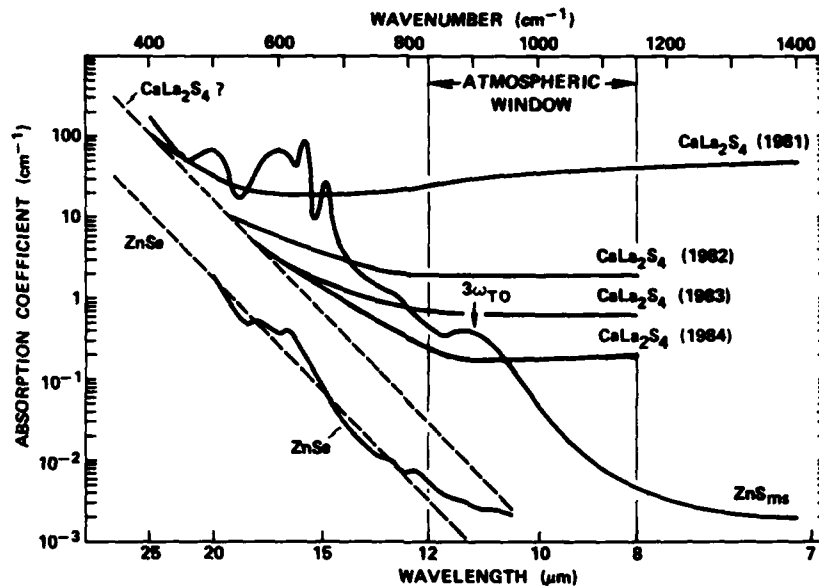


FIG. 2. Multiphonon Edges of Some Useful 8 to 12  $\mu\text{m}$  Materials. The absorption of  $\text{CaLa}_2\text{S}_4$  is extrinsic in this region and has been reduced by over 100 times in the past three years. At 7  $\mu\text{m}$  the absorption of water-clear multispectral ZnS has been reduced by about 25 times. It is now intrinsic in the 8 to 12  $\mu\text{m}$  region, and additional decreases in absorption are not expected here.

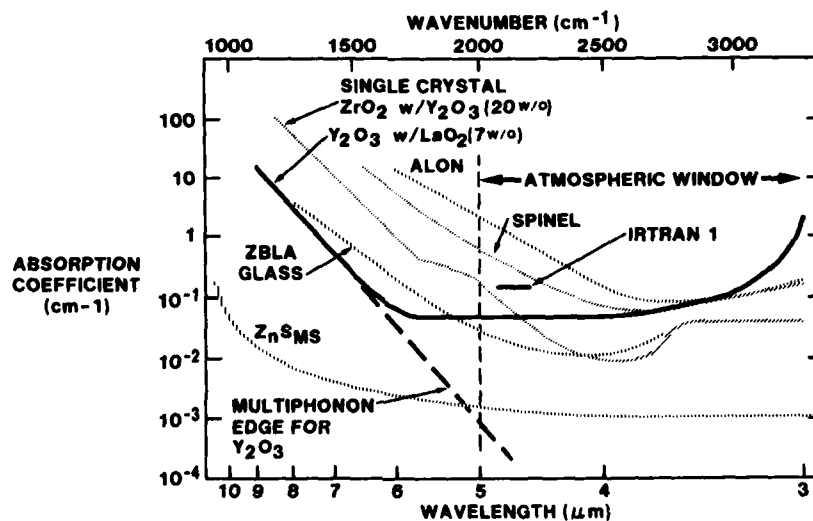


FIG. 3. Absorption of Some Useful 3 to 5  $\mu\text{m}$  Materials. The absorption of  $\text{Y}_2\text{O}_3$  in this region is largely extrinsic as is that of the fluoride glass ZBLA and of water-clear multispectral ZnS. These absorption levels can thus, at least in theory, be further reduced.

## DIMENSIONAL STABILITY

William Primak  
Wolfe Loeb & Co.  
735 S. Quincy St., Hinsdale, IL 60521

A few years ago, after I had succeeded in interpreting the large viscoelastic stress relaxation which was observed in my laboratory in the 60's upon irradiating vitreous silica, a NASA subcontractor contacted me about the possible dimensional instability in the Space Telescope from the radiation in the space environment. When I learned that the specification for the mirror was 1/60th wave, I asked whether the mirror was that stable even in the absence of radiation, for this is an interferometric tolerance. There are all sorts of precautions which are given in the literature of interferometry on the proper handling of mirrors, and even a few reports of changes of this magnitude in their figures. It was not until much later that I learned the specification was only an rms one, hence a more relaxed one than the absolute specifications I was accustomed to, but, in the meantime I became interested in the literature of the subject. Except for a few investigations of grinding and polishing, annealing, and thermal cycling, I was unfamiliar with any scientific investigations of the dimensional stability, which I attributed to optical specialists feeling constrained to handling their optics very gently. I have learned since about a few attempts to assess the temporal stability of a few candidate materials for the telescope application. While the results lend some assurances for that project, apart from any questions about precision, the major criticism of the investigations is that they were not directed toward determining the effects of specific conditions or treatments, hence they are of little value in guiding the manufacture of the materials or the fabrication of components made from them.

The observations which are available are of the alteration of the figures of plates, changes in internal stress measured photoelastically, alterations in surface composition measured by refractive index and other means, changes in the lengths of blocks or rods, and surface scattering measurements. Additional information about surfaces has been obtained by etching.

Emerson(1) reported a 1/60th wave alteration in the figure of an optical flat subjected to a small stress (resulting from its own weight), but Primak (2) considered the change to be too large to attribute it to a bulk viscoelastic deformation, and suspected another cause or an error of measurement. Dew(3) found that hard crown glass flats were not dimensionally stable. He hypothesized a stress relaxation was occurring, but he was unable to measure any stresses. Primak(2) suggested that alkali mobility might have been the cause of the instability. Dew did not find this instability in vitreous silica.

Justice(4) measured length changes of two glass ceramics, ULE, and vitreous silica with a Zeiss gauge block interferometer; and Jacobs and co-workers (5) employed a stabilized laser cavity to study these and some other materials. Most of the measurements indicated a small shrinkage, but those for the ce-



ramics, Zerodur and Cervit showed expansions. The measurements were not of the bodies themselves, but of the distance between plates wrung to, or contacted to, the bodies of interest. Some of the changes were shown to be contact changes (5), and it is possible that the changes in the ceramics may have been caused by surface deterioration. Although the preparation of the bodies is described, no characterization of them is reported.

Angel(6) informed me that after 40 years, the 100 in. Mount Wilson telescope still has a  $\frac{1}{4}$  arc second resolution. The precision of this measurement is rather less than the interferometric studies described above since it could be achieved with a  $1/10$  wave rms surface, and its significance for viscoelastic stress relaxation is questionable since, according to Oke(7), this mirror was figured in the horizontal position and tested in the vertical position, the mounting being cleverly designed so that the figure of the mirror would not be altered significantly by the change in position, hence the stresses associated with the aging data could be insignificant.

Surface scattering associated with various treatments of the surface, ultrasonic cleaning, acid treatment, polishing are reported by Stowell and Orazio (8). Stowell also informed me of a severe temporal instability of polished Cervit, and in other materials, of the areas surrounding very light scratches (9). Reversible alterations in the figure of flats caused by thermal changes have been considered by Dew(3) who placed thermocouples on the front and back faces of his plates. The author(2) pointed out that the typical thermal distributions in transverse heat flow should not alter the figure of flats; the alterations are associated with lateral heat flow. Permanent changes caused by thermal cycling were studied by Jacobs(10) and others(11). Attempts to measure a bulk viscoelastic deformation in silicate glasses at room temperature have been unsuccessful. This is not surprising since the viscosity extrapolated from higher temperatures is over  $10^{50}$  poise, and the maximum feasible measurement would be about  $10^{30}$  poise. The highest value in the literature known to this author,  $10^{25}$  poise, seems suspect.

What is needed to establish a science of dimensional stability is relating changes to forces and to molecular alterations. A step in this direction occurred when this author interpreted the stress relaxation of vitreous silica during irradiation (12). The stresses were known, for they had been measured in the course of determining the radiation-induced dilatation, and the molecular processes occurring were known to cause bond cleavage in the glass, and after irradiation some centers remained. The stress relaxation could be accounted for by an apparent viscosity of  $10^{14}$  poise during ion bombardment (13),  $10^{16}$  poise during electron bombardment (14), and  $10^{21}$  poise following ion bombardment. A further quantification of the process could be obtained if the number of centers present could be evaluated. To understand this method of investigation, it is necessary to appreciate the distribution of internal stresses in a body associated with a surface strain. This is presented in numerous of the author's papers (12). The solution is a linear stress distribution balancing the stresses associated with the surface strain. Thus, it is possible to determine the surface strain and the associated stress from the surface being held in constraint by the rest of the body. This can be done either by measuring the strain birefringence (if the material is suitable for this purpose and in suitable orientation) or by measuring the deformation of the surface associated with this stress distribution.

Another step in this direction occurred in the author's investigation of the grinding and polishing stresses (15). The thickness of the layer affected was determined by etching it away and measuring the residual stress. Grinding was found to develop surface stresses in excess of  $10^5$  psi which seemed too great to be accounted for by macroscopic fractures, hence it was attributed to breaking bonds on the atomic scale. It was pointed out by Twyman(16) that these stresses are sufficient to alter the figure of a plate very significantly, in our experience by several fringes. Here are present all of the elements required for stress relaxation to take place: the cleaved bonds and the high stresses; hence for dimensional instability; but I am not familiar with any investigation of this possibility. It should be appreciated that any surface damage may alter the figure of a plate.

The alkali in the complex silicate glasses becomes very mobile not very far above room temperature, and it is possible to electrolyze it with quite low voltage drops. In the author's studies (17), large dimensional changes accompanied the ion depletion in this process, and similar results have been reported by others (18). Elastic aftereffects have been attributed to displacement of alkali in these glasses. Both leaching and incorporation of foreign ions occur in the grinding and polishing of glass, and it is possible that dimensional changes may accompany these. The author is unaware of any investigation of dimensional instability which may accompany such processes, but he has suggested they may be responsible for some of the effects reported by Dew(3).

In the author's examination of figured marble surfaces, large changes in the figure were encountered after relatively mild thermal cycling, that associated with cleaning in hot organic solvents (19). Additionally, a deterioration of the surface finish occurred. Even as little as a minute of ultrasonic cleaning was sufficient to cause a noticeable deterioration of the surface finish of the marble. Marble is a random conglomerate of small calcite crystals. There is a very large anisotropy in the thermal expansions of calcite and also in its elastic constants. The dimensional changes probably were caused by an intergranular ratcheting mechanism, much as has been described for the behavior of uranium fuel elements. It seems likely that this kind of process occurs in Cervit and should be anticipated in all inhomogeneous materials. The high silica borosilicate glasses such as have been favored for large terrestrial telescope mirrors are inhomogeneous because small compositional variations remain in manufacture because of the high viscosity at the manufacturing temperature. These inhomogeneities are typically present on the millimeter scale and are readily seen in a polarimeter. They are called "cords" in the trade. The birefringence results from differences in thermal expansion when cooling below the strain point. Stresses approaching 1000 psi have been observed for these regions (20). This writer is not familiar with any studies of dimensional instability which may be associated with these cords.

While surface studies do not typically relate behavior to forces, they are valuable in understanding structure and composition. Notable among these studies are Rawstron's(21) by etching in which he showed that the structure seen in etching of polished hard crown glass is not associated with the prior grinding, but rather with the action of the polisher in dragging polishing particles across the surface. Evidence of a special polish layer was found by Stowell and Orazio(8) in studies of light scattering from the surface.

Many of the studies which have been reported here were funded in other connections. They could be extended to provide valuable insights into the dimensional instabilities of optical materials and yield the kind of information which would be helpful in improving the materials in manufacture and in their performance when fabricated, but no funding for such investigations has yet been forthcoming. I have not mentioned the dimensional changes caused by radiation, a subject which should be of concern for space applications, because this could provide a whole talk by itself, but I should mention it appears that an important component will be the low energy flux about which there is only limited information (22). It would be very desirable therefore to place a material like vitreous silica (whose radiation behavior has been explored extensively) into the space environment and examine it afterward. There is a great deal of information about radiation effects at high fluxes, but there is little for the low fluxes and low fluences which would apply in these applications. Although there is considerable information about the radiation behavior of vitreous silica, to the best of my knowledge, the behavior of the low expansion materials (22) has not been investigated.

#### REFERENCES

1. W. B. Emerson, J. Res. (NBS), 49(1952)241
2. W. Primak, Opt. Eng., 23(1984)806
3. G. D. Dew, Opt. Acta, 21(1974)609
4. B. Justice, J. Res. (NBS), 79A(1975)545
5. J. W. Berthold III, S. F. Jacobs, M. H. Norton, Appl. Opt., 15(1976)1398
6. J. R. P. Angel, Priv. Comm. (1984)
7. B. Oke, Priv. Comm. (1984)
8. W. K. Stowell, F. D. Orazio, SPIE paper no. 406-04 (1984)
9. W. K. Stowell, Priv. Comm., (1984)
10. S. F. Jacobs, S. C. Johnston, G. A. Hansen, Appl. Opt., 23(1984)3014
11. J. J. Shaffer, H. E. Bennett, Appl. Opt., 23(1984)2852
12. W. Primak, J. Appl. Phys., 53(1982)7331
13. W. Primak, J. Appl. Phys., 55(1984)852
14. W. Primak, J. Appl. Phys., 55(1984)3315
15. W. Primak, Phys. Chem. Glasses, 43(1981)43
16. F. V. Twyman, "Prism and Lens Making", Hilger & Watts, 2nd Ed.(1952)p318
17. W. Primak, E. Monahan, J. Electrochem. Soc., 126(1979)2196
18. D. E. Carlson, K. W. Hang, G. F. Stockdale, J. Am. Ceram. Soc., 57(1974)295
19. W. Primak, Report submitted by C. A. Youngdahl to NAPAP Group G Stone Subcommittee (10/22/1984)
20. H. Hagy, Priv. Comm. (1984)
21. G. O. Rawstron, Trans. Soc. Glass Techn., 42(1953)253
22. W. Primak to J. Osantowski, (3/19/1984), (4/2/1984)
23. S. Pearson, J. Soc. Glass Technol., 36(1952)105T
24. F. W. Preston, Glass Technology, 14(1973)20

#### ADDENDUM

Hagy (20) informed me of pertinent investigations (23, 24) of stress deformation of high alkali silicate glass bodies (non-optical) having high aspect ratios. Surface affects were shown by effects of humidity; elastic after-effects were seen.

## NONLINEAR OPTICAL PROPERTIES OF ORGANIC POLYMER MATERIALS

G.M. Carter, Y.J. Chen, M.F. Rubner, M.K. Thakur, S.K. Tripathy,  
J. P. Georger, and J.V. Hryniewicz  
GTE Laboratories, Inc.  
40 Sylvan Road, Waltham, Mass. 02254

Research into the nonlinear optical properties of organic polymers includes such phenomena as harmonic generation, Raman scattering, difference frequency generation, and the Kerr effect as well as including a wide variety of materials (available through organic synthesis) in various forms (e.g. solution, liquid crystal, and solid).<sup>1</sup> In order to realize practical applications from such research an interdisciplinary approach is necessary. As an example, optical signal processing schemes require materials that have large nonlinear optical coefficients combined with desirable linear optical properties (e.g. low loss, low scatter) as well as being processible in desired forms (e.g. waveguides). In order to examine the interdisciplinary nature of the research, we will restrict our discussion to a class of polymers, the polydiacetylenes (PDA's),  $\text{---}[\text{R}-\text{C}\equiv\text{C}-\text{C}(\text{R}')\text{---}]_n$ . The PDA's have the potential to be such a material system when their third order optical nonlinearity is suitably employed.<sup>2</sup> In the solid state, the PDA's have the largest measured nonresonant third order nonlinear susceptibility  $\chi^{(3)}$  ( $\approx 10^{-10}$  esu).<sup>2</sup> In addition, they are obtainable for a large number of side groups (molecules) R and R' which determine the structural properties of the PDA's, and in many examples can be grown in single crystalline form. The large nonlinear coefficient is attributed to the one-dimensional delocalized ( $\pi$ ) electronic states of the carbon backbone,<sup>3</sup> and as such has led to the prediction of subpicosecond response times for these nonlinear coefficients.<sup>2</sup> However, to assess the usefulness of these materials for signal processing more research is needed. All of the measurements in the solid state have been on the nanosecond time scale with no time resolution,<sup>4,5,6,7</sup> and recent theoretical research has indicated that the strong coupling between the electronic and vibrational states in the PDA's may increase the response time of the optical nonlinearity to  $>$  picosecond.<sup>8</sup> Further it is not clear what effect material form has on the results. Two of the measurements were in bulk crystals,<sup>4,5</sup> and two of them were in thin films<sup>6,7</sup> one of which yielded a much smaller value for  $\chi^{(3)}$  than the other three.<sup>6</sup> In the following we present some recent research results from our laboratory that are aimed at providing information to help assess the PDA's as a nonlinear optical materials system.

To obtain high optical quality PDA thin films in the form of planar waveguides used in our nonlinear optical measurements, we use the Langmuir Blodgett

(LB) technique to form a diacetylene monomer  $[R=CH_3-(CH_2)_{15}; R'=(CH_2)_8-COOH]$  monolayer on an inert gas-water interface to polymerize the material while still at the interface and to subsequently deposit the polymer monolayer onto the substrate. Recently we have been able to "grow" mono-phase high optical density films with either the "blue" or "red" spectrum<sup>9</sup> as shown in Fig.1. The "blue" form was prepared by polymerizing the monomer monolayer for 90 sec at 12.5°C at the gas-water interface followed by transfer of the partially polymerized monolayer to the substrate. After the multilayer of the desired thickness was formed, the film was further polymerized for 150 sec. at 12.5°C (optical density per monolayer of 0.004 at 630nm). The "red" form was prepared by polymerizing the monomer monolayer 9 min. at the gas-water interface followed by the transfer of the polymer monolayer to the substrate. The final multilayer assembly was heat annealed at 70° C for 2 min. to insure a completely "red" form (optical density per monolayer of 0.008 at 500nm.). The nonlinear coefficient reported in our earlier work was a mixture of the two phases, and since on theoretical grounds one would expect the red phase (a more localized PDA phase) to have a significantly smaller optical nonlinearity, the "blue" phase films prepared by the technique described above should yield larger optical nonlinearities.

To study the LB multilayer growth process we have carried out surface enhanced and resonant Raman scattering (SERS and RRS) on mono- and multilayers of our LB "grown" films. Fig. 2 shows Raman spectra using a 6328Å HeNe laser line for one, two, and three bilayers of a PDA film grown on a roughened silver substrate. The Raman spectrum of a single monolayer (attributed to the SERS mechanism) is the same as that for one bilayer, and matches that obtained from a bulk "red" phase material while the subsequent multilayer spectrum matches that of the "blue" phase. RRS data is consistent with this phase assignment of the first two layers relative to the subsequent layers. Our experiments show that: 1. The preparation of the monolayer film is important in obtaining high optical quality "blue" phase films; 2. A lot more defects were present for the first bilayer than for the subsequent bilayers; 3. To obtain phase matched interfaces two or more bilayer growth is needed for the LB process.

Since no dynamical information exists of the PDA excited states for optical excitations near their absorption maximum (typically 600-650nm), we have initiated pump-probe (saturated transmission) experiments in thin film PDA's to help understand the excited state processes in these materials and to examine the limitations imposed on the optical nonlinearity by these processes. These experiments used an intense (>1 kW peak power), transform limited (6 psec duration) optical pulse from a tunable synchronously pumped cavity dumped dye laser system. In the LB films we obtained data from 6200-6700Å. As shown in Fig. 3 for wavelengths shorter than the "blue" absorption maximum ( $\approx 6300\text{Å}$ ), we observed that the pump beam did not change the transmission of the weaker probe beam (derived from the same laser pulse) when the two beams did not overlap in time. However when the incident wavelength was changed to 6400Å (and other wavelengths longer than the absorption maximum) the probe transmission was affected by the pump when the probe arrival time at the sample was delayed relative to the pump. This "memory" effect

had  $\approx 1$  nsec time constant. We have observed a similar time constant for thin samples of the PDA, TCDU. Note that the spike near zero relative time delay in Fig. 3 is a coherence (self-scattering) effect, and only lasts for the pulse duration. Thus in this spectral region the excited state processes observable by this technique have wavelength dependent decay times which are either long ( $\approx 1$  nsec) or short compared to our pulse duration, 6 psec (and thus not resolved). We are now experimentally and theoretically concentrating on relating these excited state time constants to the response time of  $\chi^{(3)}$  for the PDA's.

To summarize, the polydiacetylenes are an interesting nonlinear optical materials system, and current research is addressing the interrelation between their structural and the time dependent excited state properties to provide a knowledge base for potential applications. Yet the polydiacetylenes are just one interesting class of organic nonlinear optical materials. The present investigation of the nonlinearities in the PDA's can clearly set the broad direction for the investigation of other molecularly engineered organic systems for practical exploitation.

#### References

1. A good general reference is the book Nonlinear Optical Properties of Organic and Polymeric Materials, ed. by David J. Williams, Published by The American Chemical Society, Washington, D.C. (1983).
2. P. W. Smith, Bell Sys. Tech. J. 61, 1975(1982).
3. G. P. Agrawal, C. Cojan, and C. Flytzanis, Phys. Rev. B17, 776(1978).
4. C. Sauteret, J. P. Hermann, R. Frey, F. Pradere, J. Ducuing, R. H. Baughman, and R. R. Chance, Phys. Rev. Lett. 36, 956(1976).
5. J. P. Hermann and P. W. Smith, Digest of Technical Papers from XI International Quantum Electronics Conference, Boston, Massachusetts, June 23-26 (1980) (IEEE, New York, 1980), Paper T6, pp.656-657.
6. F. Kajzar, J. Messier, J. Zyss, and I. Ledoux, Opt. Commun. 45, 133 (1983).
7. G. M. Carter, Y. J. Chen, and S. K. Tripathy, Appl. Phys. Lett. 43, 891(1983).
8. C. Flytzanis, Chapter 8, Nonlinear Optical Properties of Organic and Polymeric Materials, Ed. by D. J. Williams, American Chemical Society, Wash., D.C. (1983).
9. B. Tieke, G. Lieser, and G. Wegner, J. Polym. Sci., Polym. Chem. Ed. 17, 1631(1979).

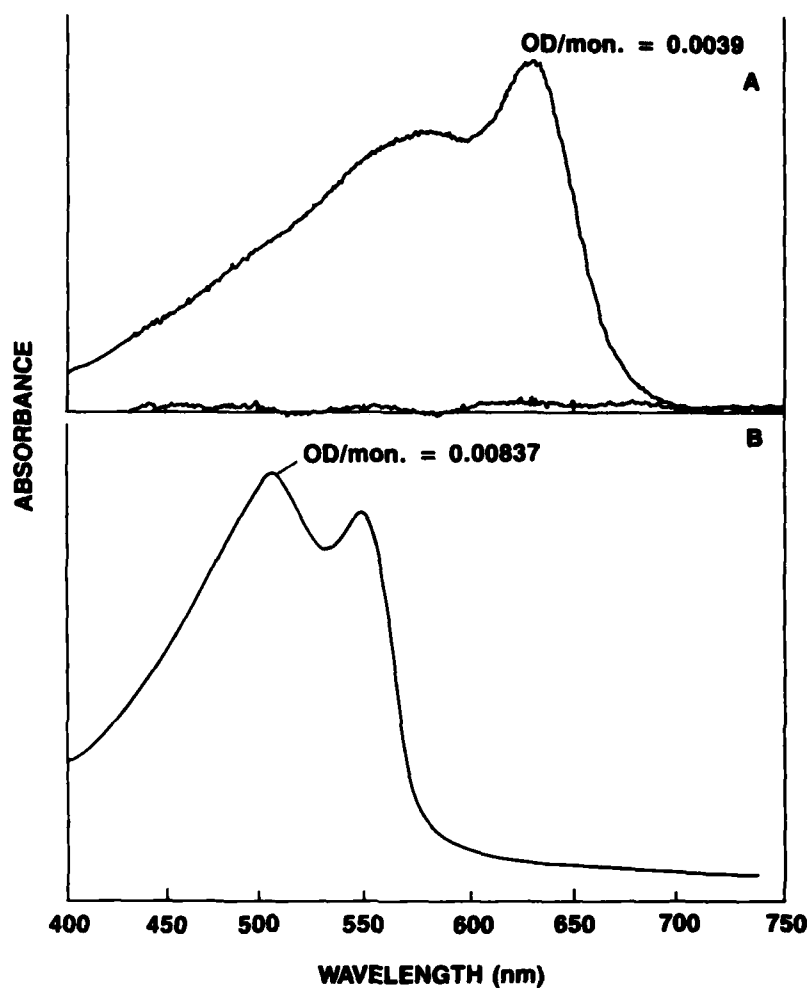


Figure 1 Absorbance vs wavelength for high optical quality "blue" phase (curve A) and "red" phase (curve B) polydiacetylene films "grown" by the Langmuir Blodgett technique described in the text.

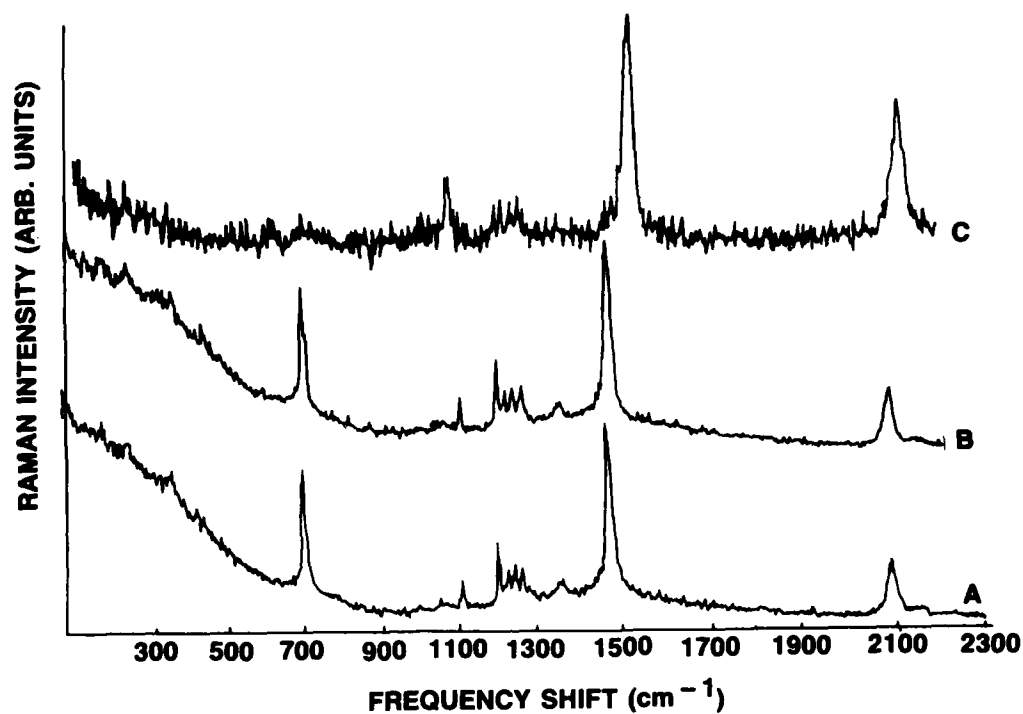


Figure 2 Raman spectra of a two-bilayer (A), a three-bilayer (B), and a one-bilayer (C) polydiacetylene film that were deposited on a rough silver island film. Note that the peaks near  $1500\text{ cm}^{-1}$  and  $2100\text{ cm}^{-1}$  are shifted in the one bilayer film relative to the other bilayers. The frequency shift in  $\text{cm}^{-1}$  is measured relative to the incident HeNe laser line at  $6328\text{ \AA}$ .



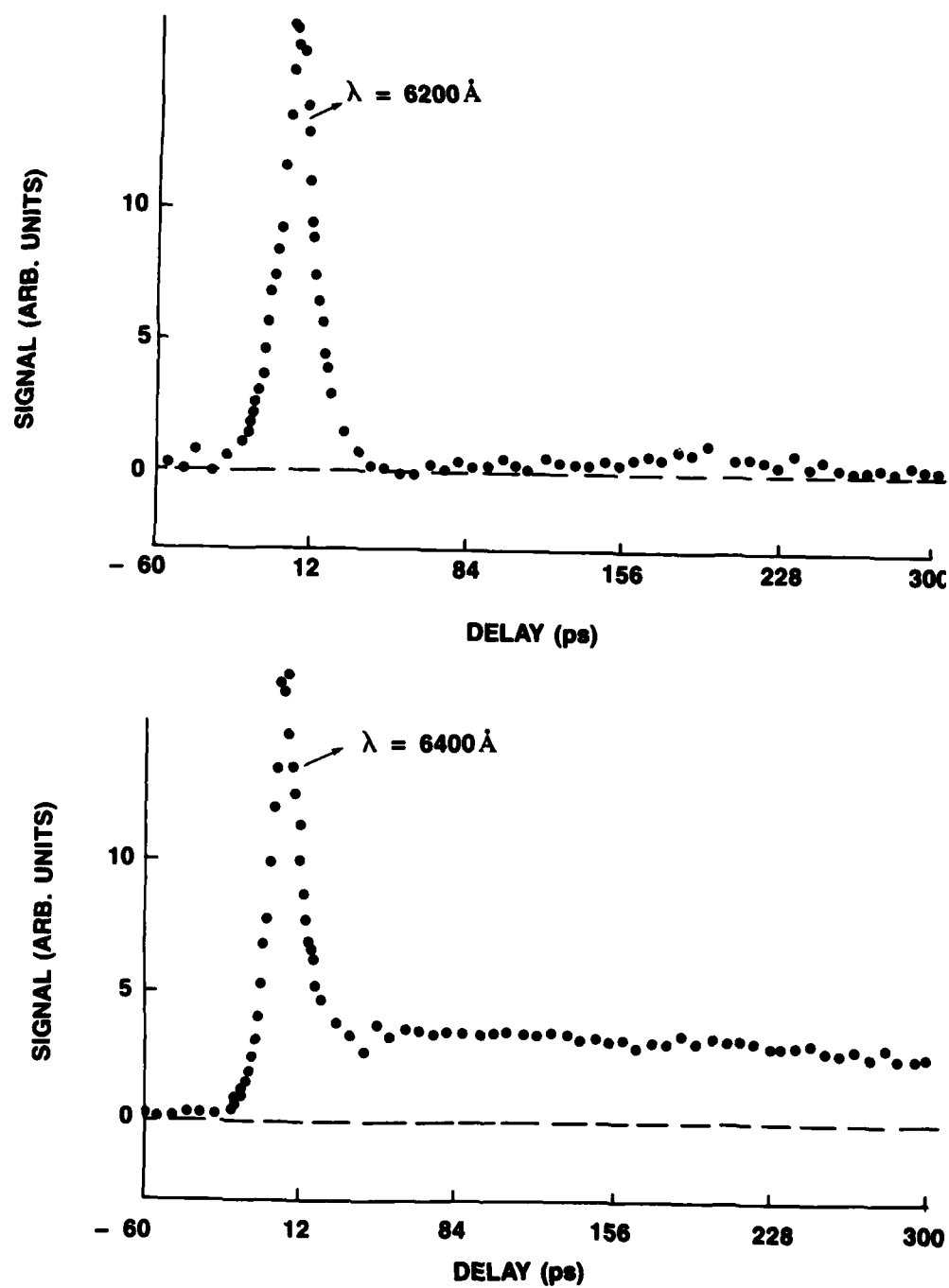


Figure 3 The signal is the difference between the values of the transmitted probe power when the pump is present and when absent. The delay is the difference between probe and the pump beam arrival time (in picoseconds). The two curves were obtained at different incident laser wavelengths.

## PREPARATION OF ORGANIC NONLINEAR OPTICAL MATERIALS FOR SECOND HARMONIC GENERATION

Carl W. Dirk,\* Robert J. Twieg,\* Georges Wagniere\*\*

IBM Research Laboratory\*  
K42/282  
5600 Cottle Road  
San Jose, California 95123

Institute of Physical Chemistry\*\*  
University of Zurich  
Winterhurerstrasse 190  
CH 8057 Zurich, Switzerland

The proliferation of lasers has permitted, by way of their large optical electric fields, the observation and investigation of optical nonlinearities in many materials. Applied and basic research in lasers has necessitated the use of optically nonlinear materials as component tools, as well as being problems of primary study. Examination of the vector equation of the microscopic polarizability permits some insight as to the source of the nonlinearities:

$$P = \alpha E + \beta E^2 + \gamma E^3 + \dots$$

The first term,  $\alpha E$ , linear in the optical electric field, is responsible for the familiar processes of reflection, refraction, and Raman scattering. The second term,  $\beta E^2$ , is the lowest order nonlinear term. Fields of the same or different frequency can mix by way of this term, giving rise to parametric generation, d.c. rectification, the linear electro-optic effect, and sum and difference frequency mixing, second harmonic generation (SHG) being a special case of the latter. The second nonlinear term,  $\gamma E^3$ , is responsible for CARS, third harmonic generation (THG), two photon absorption, and the quadratic electro-optic effect. The tensors  $\alpha, \beta, \gamma$  typically differ by six to ten orders of magnitude, decreasing in the order given. Obviously, only the large optical electric fields of lasers can permit observation of nonlinear effects.

Second harmonic generation is mediated by the  $\beta$  tensor. This tensor is a 27 component third rank polar tensor which possesses the property that it must be zero under centrosymmetry. This places a severe symmetry requirement upon systems potentially useful for SHG since most compounds tend to crystallize centrosymmetrically. Early investigation of SHG focused on inorganic compounds, such as lithium niobate and KDP (potassium hydrogen phosphate), which are the best recognized examples and are the two crystals most often employed as practical frequency doubling components.

The ever increasing use of lasers in communications, energy related (e.g., laser fusion) fields and others requires the fabrication of a variety of frequency doubling components with a wide range of physical sizes, efficiencies, and phase matching characteristics dependent on the specific application. Cost, ease of fabrication (i.e., crystal growth), poor conversion efficiency, and stringency of phase matching conditions tend to restrict further use of the common inorganics. Organic materials can offer higher conversion efficiencies, and more importantly, device configurations other than single crystals (e.g., thin films are envisioned). In addition, the diversity of structures and synthetic methodology available make organic systems especially attractive for the purposes of iterative modification.

There has been much recent interest in the nonlinear optical properties of organics.<sup>1</sup> Compounds such as urea, 2-methyl-4-nitroaniline (MNA), 3-methyl-4-nitropyridine-1-oxide (POM), and methyl-(2,4-dinitrophenyl)-aminopropanoate (MAP) have been extensively investigated.<sup>1</sup> From these studies, a general understanding has emerged with respect to the factors concerned with maximizing the hyperpolarizability tensor and thus optimizing the resulting SHG. The  $\beta$  tensor is defined by excited state processes and thus the largest components of the  $\beta$  tensor are roughly proportional to the change in dipole moment upon going from the ground to first excited state.<sup>2</sup> Generally, compounds with large ground state dipoles experience large dipole changes upon excitation. Therefore, one strategy is to concentrate on molecules with large ground state dipole moments. Zyss and Oudar<sup>3</sup> have further determined an orientational dependence to  $\beta$  with respect to its projection on the macroscopic tensor  $d$ , and have also arrived at a dependence by  $\beta$  on crystal point symmetry. These complex geometry and symmetry requirements are further aggravated by the aforementioned need for noncentrosymmetry. The severe structural restrictions have little effect on the chemists optimization of a molecule's intrinsic hyperpolarizability, but take hold due to the uncontrollable orientations and symmetries brought about by crystallization. Many a compound possessing the correct electronic structure has failed because it crystallized inappropriately.

Our effort in producing SHG from organic systems began with efforts to optimize the molecular hyperpolarizability by use of chemical intuition, but recognition of the supra-molecular structural factors has caused us to assume three different strategies: First, an exhaustive search of the Cambridge Crystallographic File (CCF) has been undertaken to sort out all compounds which crystallize noncentrosymmetrically. Many of these compounds are to be prepared and tested for SHG. Hopefully, new SHG active moieties can be found and perhaps more importantly, classes of noncentrosymmetrically crystallizing compounds can be identified and rendered SHG active by suitable synthetic modification. Second, in conjunction with the above investigation as well as an aid to intuitive synthesis, a calculational method for  $\beta$  has been prepared.<sup>4</sup> Use of a PPP-SCF-CI routine permits calculation of the eigenstates and transition moments necessary for use of Flytzanis'<sup>5</sup> perturbational derivation for  $\beta_{ijk}$ :

$$\beta_{ijk} = \frac{1}{2} \sum_p \sum_{ee'} \frac{\langle 0 | \mu_i | e \rangle \langle e | \mu_j | e' \rangle \langle e' | \mu_k | 0 \rangle}{[(E_e - E_0) - 2\hbar\omega][(E_{e'} - E_0) - \hbar\omega]}$$

Calculational procedures of this type are valuable in saving time in synthetic efforts. Many compounds from the Cambridge File search can thus be 'tested' without actual synthesis. Obviously, molecules — as yet unknown — can also be tested, thus obviating needless synthesis. In addition, the procedure has been configured such that collections of molecules can be calculated and the tensor components vector summed to give a net  $\beta$  for a crystal fragment. Third, since crystal growth is difficult in its own right, investigations into SHG active thin films have been initiated.

### Results

Of the 29052 compounds present in the Cambridge File as of *ca.* 1980-81, 8004 in noncentrosymmetric space groups have been sorted out. Of these, 3828 or 48% crystallize in the optimal<sup>3</sup> space groups. From the total of 8004, ~60 compounds have been tested to date with the result that ~60-70% show some activity and seven possess powder SHG of the order or greater than urea:

<u>Compound</u>	<u>SHG (x urea)</u>	<u>Spacegroup</u>
p-aminobenzamide	3	P2 <sub>1</sub>
sulfisomidine	2	Pca2 <sub>1</sub>
o-nitrobenzaldehyde	~urea	P2 <sub>1</sub>
2,4-bis(phenylthio)nitrobenzene	4	P2 <sub>1</sub>
5-iodouracil	~urea	P2 <sub>1</sub>
triethylphosphine sulfide	~urea	P6 <sub>3</sub> mc
l-N-acetylcysteine	~urea	P1

Some of the compounds above are quite unique or represent new variations on the typical<sup>1</sup> donor-acceptor theme. The most intriguing is the triethylphosphine sulfide. The SHG active moiety is extremely compact and considering the short dipole length, the change in charge distribution must be fairly large upon excitation. This compound grows large crystals relatively easily and is colorless. Examination of other phosphine sulfides, oxides, and selenides has not revealed any other compounds with analogous activity. The compound 5-iodouracil is, formally, a urea derivative, and represents the second uracil to display significant activity. The 5-nitro derivative has been known to be strongly SHG active.<sup>6</sup> Calculations (*vide infra*) indicate that 5-fluorouracil should be comparably active. The Cambridge File holds 267 uracils, ~25% of which are noncentrosymmetric. Many of these compounds are being tested.

Of primary interest are classes of compounds which tend to crystallize noncentrosymmetrically. Compounds with large dipoles (suitable to maximize  $\beta$ ) tend to crystallize with dipoles opposed often promoting a center of symmetry; any steric influence which can generally reverse this behavior would be a valuable moiety to add to many SHG active molecules. Chiral centers represent one approach.<sup>1</sup> One small class of

noncentrosymmetric compounds uncovered in the Cambridge Search are the 2,6-di-*t*-butylphenols. The attraction of this class is the presence of the hydroxy donor and the extremely bulky sterically dominating *t*-butyls. Addition of a strong acceptor should produce a large dipole moment but might not offset the action of the *t*-butyls, which presumably will cause the molecule to crystallize noncentrosymmetrically. When either a nitro or formyl acceptor are placed in the 4-position the resulting crystalline solids display strong SHG. More compounds of this type are being investigated as well as related classes of compounds.

Computational procedures for the determination of  $\beta$  have been employed previously.<sup>1</sup> Results from the PPP-SCF-CI method used here are shown below:

<u>Compound</u>	<u><math>\beta</math> calc<sup>a,c</sup></u>	<u><math>\beta</math> calc<sup>b,c</sup></u>	<u><math>\beta</math> exp<sup>c,1</sup></u>
urea	-7.0	1.44	2.3
p-nitroaniline	35.3	26.8	34.3
m-nitroaniline	12.9	8.1	6
o-nitroaniline	26.4	9.2	10.2
5-nitrouracil		5.6	
5-fluorouracil		-7.0	

<sup>a</sup>Ref. 4, crystallographic data used for urea, nitroanilines were calculated using uniform benzene rings and all other bond lengths invariant from compound to compound, resonance integrals unchanged throughout.

<sup>b</sup>Crystallographic data used for all compounds, resonance integrals scaled using Linderberg's procedure.<sup>7</sup>

<sup>c</sup>Average  $\beta$ 's, units =  $10^{-30}$  esu.

Examination of these results indicate good agreement with experiment. As stated earlier, 5-fluorouracil is calculated to be not significantly different from 5-nitrouracil. The fluorouracil result indicates the utility of these calculations in that it crystallizes centrosymmetrically thus preventing an actual powder determination. The calculation suggests, along with the 5-iodouracil measurement (vide supra), that the uracils may be a generally good class for SHG.

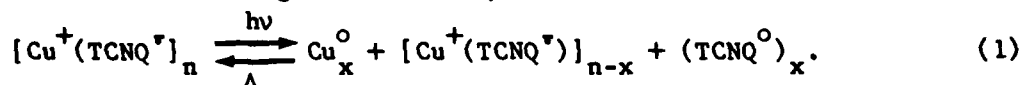
#### References

1. (a) D. J. Williams, ed., "Nonlinear Optical Properties of Organic and Polymeric Materials" *ACS Symposium Series*, No. 233 (American Chemical Society, Washington, D.C. 1983); (b) D. J. Williams, *Angew. Chem. Int. Ed. Eng.* **23**, 690-703 (1984).
2. J. L. Oudar and D. S. Chemla, *J. Chem. Phys.* **66**, 2664-2668 (1977).
3. J. Zyss, J. and J. L. Oudar, *Phys. Rev. A* **26**, 2028-2048 (1982).
4. G. Wagniere, manuscript in preparation.
5. C. Flytzanis, "Nonlinear Optics, Part A", in *Quantum Electronics: A Treatise*, Vol. I H. Rabin and C. L. Tang, eds. (Academic Press 1975), pp. 9-207
6. J. Jerphagnon, *IEEE J. Quant. Chem.* **7**, 42-43 (1971).
7. J. Linderberg, *Chem. Phys. Lett.* **1**, 39-41 (1967).

# OPTICAL PHASE TRANSITIONS IN ORGANO-METALLIC COMPOUNDS

T. O. Poehler and R. S. Potember  
 Johns Hopkins University, Applied Physics Laboratory  
 Johns Hopkins Road  
 Laurel, Maryland 20707

We have recently reported optical and optoelectronic switching between two states in polycrystalline organo-metallic semiconductor films<sup>1-4</sup> using the 488.0 and 457.9 nm lines of an argon ion laser<sup>5</sup>. Although the optical measurements have largely concerned films of copper or silver complexed with the electronic acceptor tetracyanoquinodimethane (TCNQ), results on other acceptors indicate similar effects. It has been demonstrated that the effect of the applied electric field on the initial charge-transfer salt (e.g., CuTCNQ) is to induce a phase transition resulting in the formation of a non-stoichiometric complex salt containing neutral TCNQ:



The reaction shown in Eq. (1) is reversible and the initial phase can be easily reformed by heating the film. The reaction proceeds readily because simple  $\text{Cu}^+(\text{TCNQ}^-)$  has been shown to be thermodynamically more stable than the complex salt containing neutral TCNQ ( $\text{TCNQ}^0$ ).<sup>6</sup>

The previous results on optical switching in the class of semiconducting organo-metallic films such as copper and silver tetracyanoquinodimethane (CuTCNQ and AgTCNQ) have been extended to show that switching can be erased using CO<sub>2</sub> laser radiation. The effect can be observed by Raman spectroscopy and direct observation. Results on the wavelength and irradiance dependence of the optical switching threshold show the optical switching occurs over a wide spectral range and can be interpreted in light of proposed switching mechanisms in these organic materials.

Two switching effects in the organo-metallic films can be induced by optical radiation, depending on the irradiance (W/cm<sup>2</sup>) of the incident laser beam. At low irradiance levels, optoelectronic switching from a high to a low electrical impedance state can be induced, while at higher irradiance levels, high-contrast patterns can be generated by forming macroscopic amounts of  $\text{TCNQ}^0$ . Both these effects remain stable until the film is heated, which causes  $\text{TCNQ}^0$  molecules and the corresponding metal atoms to undergo a solid-state reaction, Eq. (1), and form the original metal-TCNQ charge-transfer complex.

We have now demonstrated that defocused laser radiation can be used as a source of thermal energy to reverse or erase switched regions of the film. Shown in Figure 1 are the results on reversing the optical switching using a CO<sub>2</sub> laser as a source of thermal energy. The high and low impedance states exhibit marked differences in the Raman spectrum, especially in the 1300 to 1500 cm<sup>-1</sup> region due to the  $\nu_4$  band (C=C stretching).<sup>5,7</sup> In this spectral region, the initial charge-transfer complex in the high impedance (insulating) state has only one strong Raman band at 1375 cm<sup>-1</sup> corresponding to the TCNQ anion species (Fig. 1a). In all cases, the laser power of the probe beam was

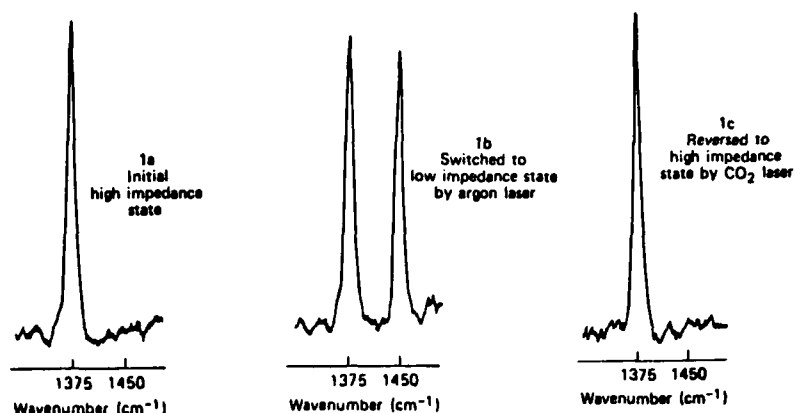


FIGURE 1. Raman spectra in the 1300-1500  $\text{cm}^{-1}$  region demonstrating the use of  $\text{CO}_2$  laser radiation to reverse the optoelectronic switching.

sufficiently low that the equilibrium state of the film was not perturbed. After irradiation with an argon laser, the film is switched to the low impedance (conducting) state, and an additional band is observed at  $1450 \text{ cm}^{-1}$  corresponding to  $\text{TCNQ}^\circ$  (Fig. 1b). The film in the conducting state can be driven back to the original insulating state using defocused  $\text{CO}_2$  laser radiation as shown in Figure 1c. For thin  $\text{CuTCNQ}$  films on a copper substrate, the  $\text{CO}_2$  laser irradiance required to reverse the film state was approximately  $200 \text{ W/cm}^2$ . It should be emphasized that this exposure was necessary because of the efficient heat dissipation from the film to the metal substrate. Much lower exposures, however, can be used when the films are on thermally insulating substrates. Other defocused laser sources can also be used as a source of thermal energy to reverse the reaction [Eq. (1)].  $\text{CO}_2$  laser radiation can also be used to erase high-contrast patterns which contain macroscopic amounts of  $\text{TCNQ}^\circ$ .

The wavelength dependence of the optical switching threshold for  $\text{CuTCNQ}$  and  $\text{AgTCNQ}$  was studied to obtain information about the switching mechanism. Wavelengths from three different CW lasers were used: 457.9, 488.0, and 514.5 nm from an argon ion laser; 632.8 nm from a helium-neon laser and 10,600 nm from a carbon dioxide laser. At each wavelength, the metal-organic films were irradiated at various laser powers and at several locations on the film. The switching threshold (i.e., the laser irradiance at which neutral  $\text{TCNQ}$  was produced) was measured by Raman spectroscopy. By varying the laser spot size, it was determined that the threshold was dependent on the irradiance and not on the laser power. The results are presented in Table I. Variations in the observed thresholds are due largely to spatial inhomogeneities in the film, with the exception of the value at 10,600 nm for  $\text{CuTCNQ}$ . It is evident that the optical switching threshold for  $\text{AgTCNQ}$  is approximately one-half the value for  $\text{CuTCNQ}$ . The threshold for  $\text{AgTCNQ}$  is essentially independent of wavelength, while the threshold for  $\text{CuTCNQ}$  is relatively constant in the visible spectral region, but is approximately four times higher in the infrared.

Work in progress has also involved a variety of thin films of semiconducting charge-transfer complexes different from the typical  $\text{AgTCNQ}$  and  $\text{CuTCNQ}$  for which many of the previous results have been reported. Other salts which are members of the class are those formed of metal donor atoms and the organic acceptor molecule such as TCNE,  $\text{TCNQ}$ , methyl  $\text{TCNQ}$ , and TNAP.

TABLE I. Optical switching threshold at various wavelengths.

Laser Source	Wavelength nm	Photon Energy eV	Laser Irradiance Threshold (W/cm <sup>2</sup> )	
			AgTCNQ	CuTCNQ
Argon Ion	457.9	2.71	800	1500
	488.0	2.54	600	1500
	514.5	2.41	1000	1500
Helium Neon	632.8	1.96		2000
Carbon Dioxide	10600.0	0.12	600	8000

Many copper complexes are observed to exhibit switching behavior with thresholds varying over almost two orders of magnitude (Table II). Complexes such as CuTNAP and CuTCNQ (OMe) (O-*i*pr) switch at irradiances similar to that required for CuTCNQ. On the other hand, CuTCNQ (OEt)<sub>2</sub> exhibits a switching threshold at least one order of magnitude lower than CuTCNQ.

TABLE II. Optical switching thresholds of various copper complexes. Beam area approximately  $2 \times 10^{-5}$  cm<sup>2</sup>.

Compound	Wavelength (nm)	Incident Power (mW)	Irradiance (W/cm <sup>2</sup> )
CuTCNQ(OEt) <sub>2</sub>	458	3	150
CuTCNQ(OEt) <sub>2</sub>	458	15	750
CuTNAP	488	30	1500
CuTCNQ(OMe)(O- <i>i</i> pr)	488	30	1500
CuDTF	458	15	750
CuTCNQ( <i>i</i> -pr) <sub>2</sub>	488	40	2000
CuTCNQF <sub>4</sub>	488	150	7500

An area of significant interest is the change in macroscopic optical properties of the CuTCNQ films in a radiation field. The potential for large changes in transmission and reflection in CuTCNQ and other members of this family under intense radiation fields are of significant practical interest.

We have begun to investigate the transmission spectra of irradiated thin films formed on glass substrates. As shown in Figure 2, a typical CuTCNQ film formed by solid state diffusion is rather poorly transmitting from the mid-visible into the near infrared in the vicinity of 1100 nm, and there is a substantial increase in transmission extending into the infrared. Upon irradiating the CuTCNQ film with a Nd:YAG laser at 532 nm scanned over a sufficient region to perform simple transmission measurements, one observes a large change in the transmission as also shown on Figure 2. A significant increase in transmission throughout the spectrum from the mid-visible to the IR is observed. Extremely dramatic increases are observed in the red end of the spectrum and the near IR, particularly those regions which are of interest with respect to many of the principal laser sources. These preliminary transmission measurements demonstrate a very large change in the optical transmission which is clearly of practical interest.



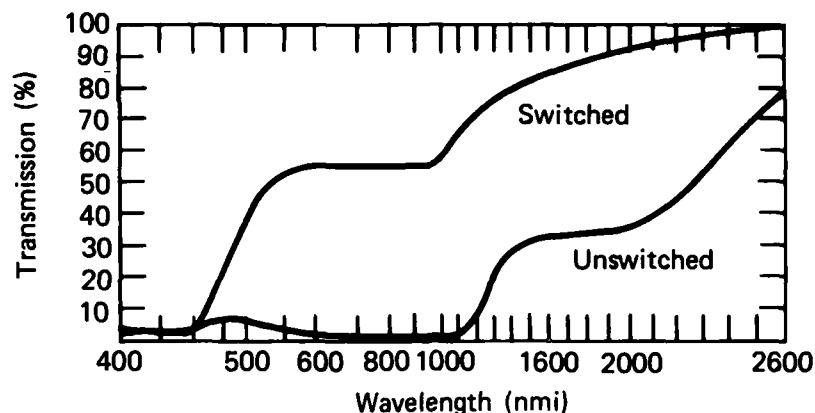


FIGURE 2. CuTCNQ transmission switch - 30 mJ pulses from frequency doubled Nd:YAG laser (532 nm).

The transmission properties of an AgTCNQ film are shown in Figure 3. In contrast to the changes observed in CuTCNQ, the switched and unswitched films are quite similar in the infrared portion of the spectrum. However, large changes in transmission are noted in the visible part of the spectrum between 400 and 600 nm. The switched AgTCNQ becomes strongly transmitting in a band centered at 500 nm while the unirradiated film is poorly transmitting in the same region.

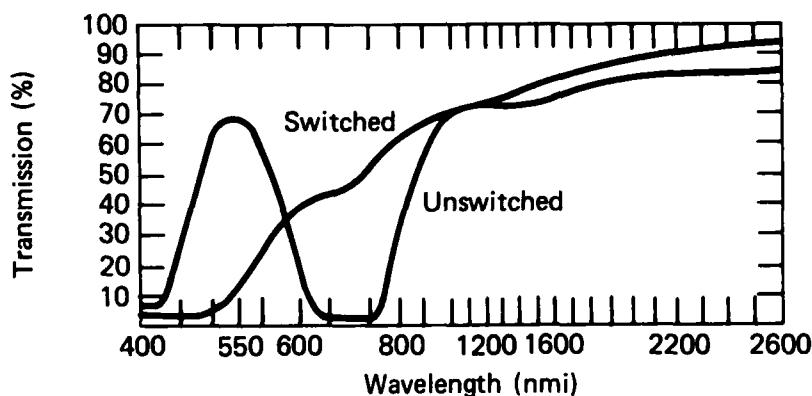


FIGURE 3. AgTCNQ transmission switch - 45 mJ laser pulses at 532 nm.

#### References

1. R. S. Potember, T. O. Poehler, and D. O. Cowan, *Appl. Phys. Lett.* **34**, 405 (1979).
2. R. S. Potember, T. O. Poehler, A. Rappa, D. O. Cowan, and A. N. Bloch, *J. Am. Chem. Soc.* **103**, 3659 (1980).
3. R. S. Potember, T. O. Poehler, D. O. Cowan, A. N. Bloch, P. Brant, and F. L. Carter, *Chemica Scripta* **17**, 219 (1981).
4. R. S. Potember, T. O. Poehler, D. O. Cowan, and A. N. Bloch, *Proc. of NATO Conf. on Chemistry and Physics of One-Dimensional Materials*, L. Alcácer, ed. (D. Reidel Publishing Co., Boston 1980), pp. 419-428.
5. R. S. Potember, T. O. Poehler, and R. C. Benson, *Appl. Phys. Lett.* **41**, 548 (1982).
6. S. Aronson and J. S. Mittelman, *J. Solid-State Chem.* **36**, 221 (1981).
7. E. I. Kamitos, C. H. Tzinis, and W. M. Risen, *Solid State Commun.* **42**, 561 (1982).

A REVIEW OF THE OPTICAL DATA ANALYSIS FOR PHTHALOCYANINE CONDUCTING  
POLYMER AND MOLECULAR-METAL SYSTEMS\*

W.J. McCarthy and C.R. Kannewurf  
Department of Electrical Engineering and Computer Science  
and the Materials Research Center  
Northwestern University, Evanston, Illinois 60201

T. Inabe and T.J. Marks  
Department of Chemistry and the Materials Research Center  
Northwestern University, Evanston, Illinois 60201

R.L. Burton  
Electro-Optics Division, IIT Research Institute  
Chicago, Illinois 60616

During the past decade a number of interesting low-dimensional materials have been prepared which have been found to exhibit a combination of unusual properties that are not generally observed in the conventional inorganic semiconductor and metallic systems. Optical diagnostics have provided a key method for obtaining important information about both molecular-metal and conducting polymer systems. For many of these systems the optical measurements and the methods of analysis have been carried out by D.B. Tanner,<sup>[1]</sup> C.S. Jacobsen<sup>[2]</sup> and their respective co-workers.

At this laboratory the principal effort in this area has been devoted to the development of phthalocyanine based systems with various doping agents<sup>[3]</sup>. It has been found that the phthalocyanine polymers possess a rather unique blend of properties that show considerable promise for applications. Optical reflectance studies have also provided valuable information about the phthalocyanine systems, but for many compounds single crystal samples have not been successfully prepared as yet. Thus the majority of the optical measurements have been performed on polycrystalline pressed powder compactions. Such specimens also have been used to provide information in other systems that could not be obtained from single crystal data alone<sup>[4]</sup>.

In previous work with other systems the analysis of polycrystalline compositions generally has been developed on the assumption that the principal contribution to the specular reflectance, where the metallic-like features dominate, comes from the high conduction direction parallel to the stacking axis. Therefore, if  $\theta$  is the angle between this direction and the electric field vector of the optical radiation, then a total metallic reflection would correspond to  $\langle \cos^2 \theta \rangle = 1/3$ ; the average is performed over all orientations of the stacking axis in the sample. However, it has been found in the various phthalocyanine samples that the  $\langle \cos^2 \theta \rangle$  can actually vary from 0.28 to 0.5. The purpose of the present paper is to examine some alternative methods for the data processing of polycrystalline samples with a comparison to the results obtained from single crystal samples of the same compound.

\* This research was supported by the NSF-MRL Program through the Materials Research Center of Northwestern University (Grant DMR82-16972) and by the Office of Naval Research.

The data presented here was obtained for the metal-free molecular metal  $H_2(Pc)I$ . This is a system for which samples are available in the form of single crystals, fibers and thin ribbons; and it is a system which can be used as a model for many other phthalocyanine compounds. It is also the system for which the most extensive single crystal optical data is currently available. [5]

In Figure 1 a computer generated plot is shown of the polarized reflectance both parallel and perpendicular to the conducting axis. This plot is developed from the actual single crystal data for  $H_2(Pc)I$  after the data has been fit to a model for the variation of the dielectric function with frequency. [5] A principal feature of the reflectance data parallel to the conducting axis is the plasma-like edge for frequencies less than  $4400\text{cm}^{-1}$ . In this region the dielectric function can be fit to a simple Drude model, [6]

$$\epsilon(\omega) = \epsilon_{\infty} - \omega_p^2 / (\omega^2 + i\omega/\tau), \quad (1)$$

where  $\epsilon_{\infty}$  is the high frequency dielectric constant,  $\omega_p$  is the plasma frequency and  $\tau$  is the electronic relaxation time. At frequencies above  $10,000\text{cm}^{-1}$  the dielectric function for both polarizations can be fit to a Lorentz oscillator model, with a single oscillator in the  $R_{||}$  data and a sum of two oscillators in the  $R_{\perp}$  data. The identification of these oscillators for phthalocyanine systems is well known. [3]

Since most of the low-dimensional phthalocyanine systems of interest have a tetragonal crystal structure, the dielectric function can be described by a term  $\epsilon_{||}$  for the conducting (or stacking) axis and a term  $\epsilon_{\perp}$  for the direction normal to this axis. In processing polycrystalline samples these terms cannot be directly extracted from the reflectance data. The upper curve in Figure 2 shows the actual reflectance data obtained from a pressed pellet of  $H_2(Pc)I$ . The plasma edge and the possibility of several Lorentz oscillators at higher frequencies are readily observable, but the data does not really fit either curve of Figure 1 very closely. It should be pointed out that for frequencies less than approximately  $1300\text{cm}^{-1}$  a large number of molecular oscillators appear in the polycrystalline data. These are absent in Figure 1 since the single crystal data is currently available only above  $1200\text{cm}^{-1}$ , and therefore the computer generated curves show no such features in the low frequency region.

One of the major reasons for a relatively poor fit of the polycrystalline data to the single crystal curve in various regions is that from x-ray diffraction studies the  $\langle \cos^2\theta \rangle$  for  $H_2(Pc)I$  powder compactions was determined to be as large as 0.5. Since this factor can be independently determined, it is possible to use the following expression for the average dielectric function, that has been employed by Tanner et al. [4] for the analysis of polycrystalline films.

$$\langle \epsilon(\omega) \rangle = \epsilon_{\perp}(\omega) + \frac{Cf\epsilon_{\perp}(\omega) [\epsilon_{||}(\omega) - \epsilon_{\perp}(\omega)]}{\epsilon_{\perp}(\omega) + G(1-Cf) [\epsilon_{||}(\omega) - \epsilon_{\perp}(\omega)]} \quad (2)$$

Here  $C = \langle \cos^2\theta \rangle$ ,  $f$  is the filling factor of the compaction, and  $G$  is the depolarization factor of the crystallites. Eq. (2) has been developed through effective-medium theory based on the original Maxwell-Garnett Model of isotropic spheres imbedded in an insulating matrix. [7]

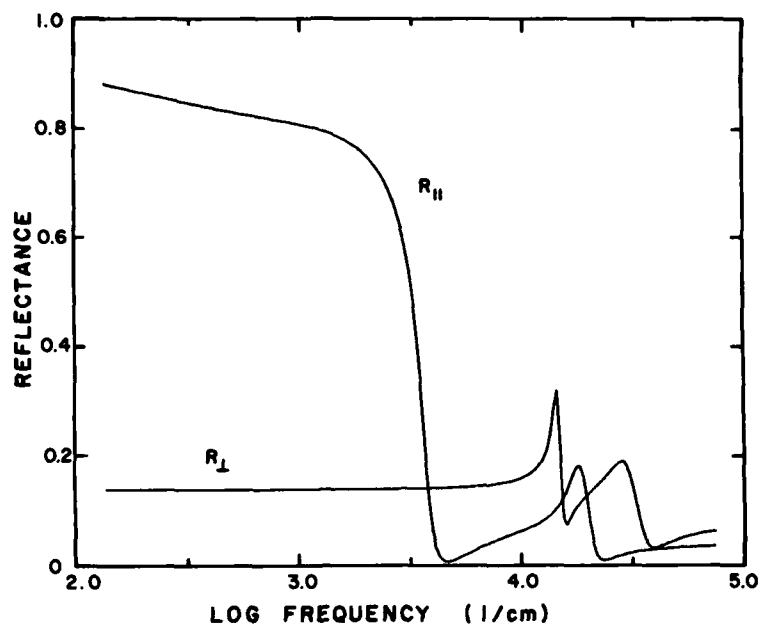


Figure 1. Computer generated curves for the polarized reflectance versus frequency which are calculated from the optical parameters determined from the single crystal reflectance data for  $H_2(Pc)I$ .

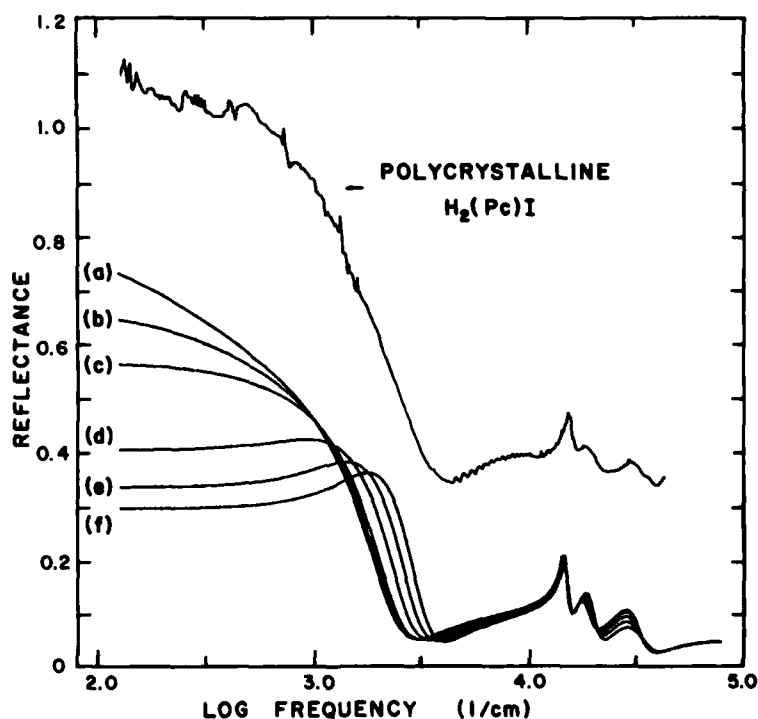


Figure 2. Upper Curve: Reflectance data versus frequency for a polycrystalline compaction of  $H_2(Pc)I$ , this curve is displaced +0.3 reflection units vertically from the origin for the lower curves. Curves (a) through (f): Computer generated plots of reflectance versus frequency for polycrystalline material with the depolarization factor selected as follows: (a),  $G=0.01$ ; (b),  $G=0.05$ ; (c),  $G=0.1$ ; (d),  $G=0.3$ ; (e),  $G=0.5$ ; (f),  $G=0.7$ .

To show that from Eq. (2) a reflectance spectrum can be developed which is similar to the polycrystalline data of Figure 2, the  $\epsilon_{||}(\omega)$  and  $\epsilon_{\perp}(\omega)$  values were directly obtainable from the single crystal spectra of Figure 1. The set of curves (a) through (f) in Figure 2 are computer generated from Eq. (2). The depolarization factor is the parameter starting with  $G = 0.01$  for curve (a) and increasing to  $G = 0.7$  for curve (f). Work now in progress is being carried out to determine typical crystalline dimensions so that an independent  $G$  factor can be used in the analysis. For all curves  $C = 0.5$ , and  $f$  was assumed to be unity. At high frequencies the three oscillators generated from Eq. (2) now show a close similarity to their appearance in the polycrystalline data; in this region the variation in  $G$  has little effect.

Two noticeable differences between the polycrystalline and single crystal data are the slope of the plasma edge and the value of the reflectance at the minimum of the plasma edge. One important parameter of the fit that can influence both of these changes is the relaxation time defined in Eq. (1). It has been found that the relaxation time for polycrystalline phthalocyanine samples is approximately one-third of the single crystal value.<sup>[8]</sup> This is attributed to the stress produced by the mechanical force used to prepare the powder compactions. Thus the computer generated curves of Figure 2 are calculated using the lower relaxation time. The low frequency behavior of the depolarization factor and the obvious shift of the plasma edge with a change in depolarization factor will be discussed in conjunction with the influence of other parameters on these same features.

The set of curves in Figure 2 is typical of a large number of such plots that can be generated for the various terms of Eq. (2). Particular attention has been given to the influence of all these terms on the parameters of the plasma edge since these parameters yield important information about the electronic carriers and energy band structure of low dimensional systems. For phthalocyanine materials a superior fit to the polycrystalline optical data is possible through the use of Eq. (2) in conjunction with additional parameter measurements.

#### REFERENCES

1. D.B. Tanner in Extended Linear Chain Compounds, Vol. 2, edited by J.S. Miller (Plenum, New York, 1982), p. 205 and references therein.
2. For example: C.S. Jacobsen, D.B. Tanner, and K. Bechgaard, *Phys. Rev. B* **28**, 7019 (1983).
3. B.N. Diel, T. Inabe, J.W. Lyding, K.F. Schoch, Jr., C.R. Kannewurf, and T.J. Marks, *J. Am. Chem. Soc.* **105**, 1551 (1983).
4. D.B. Tanner, C.S. Jacobsen, A.F. Garito, and A.J. Heeger, *Phys. Rev. B* **13**, 3381 (1976).
5. R.L. Burton, T. Inabe, J.W. Lyding, W.J. McCarthy, G.M. Reisner, F.H. Herbstein, C.R. Kannewurf, and T.J. Marks, (submitted for publication).
6. F. Wooten, Optical Properties of Solids (Academic, New York, 1972) Ch.3.
7. D.B. Tanner, A.J. Sievers, and R.A. Buhrman, *Phys. Rev. B* **11**, 1330 (1975) and references therein.
8. R.L. Burton, M.S. Thesis (Northwestern U., 1984); R.L. Burton, W.J. McCarthy, T. Inabe, T.J. Marks, and C.R. Kannewurf, (manuscript in preparation).

## OPTICAL PROPERTIES OF PBS\*

M. W. Williams, D. W. Young,<sup>†</sup> J. C. Ashley, and E. T. Arakawa  
Health and Safety Research Division  
Oak Ridge National Laboratory  
Oak Ridge, Tennessee 37831

PBS, or poly(butene-1-sulfone) with a formula of  $\{C_4H_8SO_2\}_n$ , is a fast electron-resist used in microlithography. To understand, and to be able to predict, the resolution attainable with this system, it is necessary to know the optical properties of the resist material over the range of photon energies associated with the oscillator strength of the valence electrons. Electron mean free paths in the material can be calculated from these data as a function of incident electron energy. Energy deposition and details of track structure can then be calculated for incident electron beams. Predictions of the sharpness and resolution in the resulting microstructures can be compared with those obtained experimentally.

We have obtained the optical properties of PBS over the range of incident photon energies,  $h\nu$ , from 2.5 to 41.0 eV. Liquid resist (1) was spin-coated onto glass substrates and the films obtained were then heat treated at 80°C for 30 mins to evaporate the solvent. Above  $\sim 5.9$  eV these films were essentially opaque and normal incidence reflectance,  $R_n$ , was obtained over the range of energies from 5.9 to 10.3 eV using a Seya-Namioka monochromator and from 8.0 to 41.0 eV using a grazing-incidence monochromator (McPherson, Model 247). Below  $\sim 5.9$  eV PBS becomes transparent and the real and imaginary parts,  $n$  and  $k$  respectively, of the complex refractive index were obtained from separate observations. The refractive index,  $n$ , was obtained from critical angle measurements. A thick film of PBS was formed on the plane surface of a

\*Research sponsored jointly by the Solid State Sciences Division, Rome Air Development Center, under Interagency Agreement DOE No. 40-226-70 and the Office of Health and Environmental Research, U.S. Department of Energy, under contract DE-AC05-84OR21400 with Martin Marietta Energy Systems, Inc.

<sup>†</sup>Oak Ridge Science Semester student participating in the Great Lakes Colleges Association/Associated Colleges of the Midwest from DePauw University, Greencastle, Indiana.

sapphire semicylinder. Reflectance at the sapphire-PBS interface was measured as a function of angle of incidence and  $n$  was then calculated from the observed value of the critical angle. The extinction coefficient,  $k$ , for a given photon energy was obtained from observations of the transmittance as a function of film thickness. For these observations liquid PBS was allowed to flow down a quartz microscope slide which was held at an angle of  $\sim 15^\circ$  from the vertical. The resulting film increased in thickness towards the bottom. After all transmittance measurements had been obtained, the variation of thickness along the film was determined interferometrically. For each incident photon energy, a least squares fit to Fresnel's equations for transmittance as a function of film thickness yielded values of  $n$  and  $k$ . This method gave reliable values of  $k$  but not of  $n$ . In the energy range from 2.5 to 5.9 eV, the values of  $n$  from critical angle measurements and the values of  $k$  from transmittance vs film thickness were used to calculate values of  $R_n$ . These values were then combined with the measured values of  $R_n$  from 5.9 to 41.0 eV. A Kramers-Kronig analysis, over all photon energies, was then performed using the  $R_n$  values from 2.5 to 41.0 eV. Below 2.5 eV, the  $R_n$  values were smoothly extrapolated to  $R_n = 0.04$  at zero energy. Above 41.0 eV, a smooth extrapolation of the data in the vicinity of 41.0 eV was achieved by a  $(\hbar\omega)^{-4}$  variation to infinite photon energy. This analysis yielded  $n$  and  $k$  values over the range of photon energies from 2.5 to 41.0 eV. The density of the PBS films was found by the sink-float method to be  $(1.39 \pm 0.02) \text{ g.cm}^{-3}$ . As expected this density is greater than that of the liquid resist.

The values obtained for  $R_n$ ,  $n$  and  $k$ , over the experimental range of photon energies, will be presented. It will be shown how sum rule calculations, of the effective number of valence electrons participating in excitations, using these data agree with theoretical predictions for PBS. In these calculations core-valence electron coupling will be taken into consideration. Values of electron inelastic mean free path,  $\Lambda$ , as a function of incident electron energy,  $E$ , will be derived using the experimental values of  $n$  and  $k$ .

(1) We gratefully acknowledge Mead Technologies, Inc., Rolla, Missouri 65401 for making the liquid PBS available to us.

## OPTICAL CONSTANTS AND HARMONIC GENERATION BY SURFACE PLASMONS

H. J. Simon  
Department of Physics and Astronomy  
The University of Toledo  
Toledo, OH 43606

Over fifteen years ago the first demonstration of the prism method of surface plasmon (SP) excitation for studying the linear optical properties of metal films was reported.<sup>1</sup> Today there exists a large literature on the application of SP's in linear optics.<sup>2</sup> A sophisticated example of the sensitivity that may be obtained with SP's is demonstrated in the use of the modulated SP resonance for adsorption studies.<sup>3</sup> The SP resonance on high-reflectivity metals is very sensitive to changes in the optical properties of the surface region, in particular, to the effects of adsorbed molecules. The SP resonance on noble metal films is excited using the Kretschmann configuration and detected via the surface-roughness scattered light. By modulating the angle of incidence of the exciting laser beam and using the electronically differentiated signals to track and monitor the resonance, the complex dielectric constant of the film and the strength of the surface-roughness scattering may be measured as a function of time. A schematic drawing of the apparatus is shown in Fig. 1. This technique was used to study the chemisorption of  $O_2$  on Cu and Ag. A compilation of the SP response for various  $O_2$  exposures on Cu is shown in Fig. 2. The straight line is the extrapolation of the linear dependence associated with the oxide growth back into the linear regime. Values of adsorbed film thickness and optical constants are determined from a self-consistent fit to the Lorentzian SP profile. From these data it is estimated that about 0.6% of a monolayer of O atoms on a Cu surface may be determined.

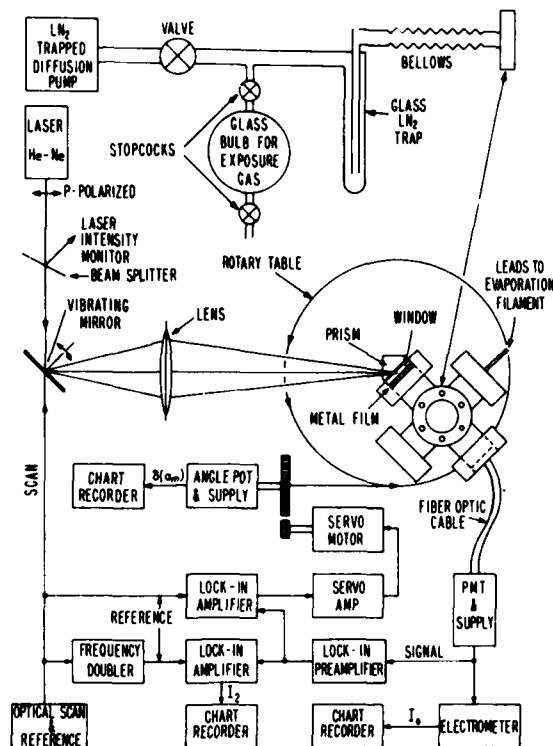
The resonant SP mode may be used to drive the nonlinear polarization sources at the interface between a metal and a dielectric thereby producing enhanced optical second-harmonic generation (SHG). In the first experiment, reported ten years ago, a pulse of light from a ruby laser was incident through a prism on a 500 Å silver film in air (the Kretschmann configuration and enhanced reflected SHG was observed at the angle for laser excitation on the SP.<sup>4</sup> An example of recent data taken with a Nd glass laser is shown in Fig. 3a where the experimental nonlinear SHG reflectance is plotted on an absolute scale and the theoretical curve is calculated from Sipe's hydrodynamical model for the harmonic nonlinearity of a free electron gas.<sup>5</sup> From such experiments the harmonic normal surface current parameters, which cannot be easily calculated, may be determined. If the SP is excited at the interface between a metal film and a nonlinear dielectric then even larger SHG resonances due to SP excitation may be observed. The experimental results obtained with a quartz crystal which are shown in Fig. 3b agree well with the theoretical curve. When a similar experiment is repeated with a polished hygroscopic crystal such as KDP, however, the resonance is broadened and reduced by an order of magnitude, thus demonstrating the sensitivity of this technique to crystal surface quality.<sup>6</sup>



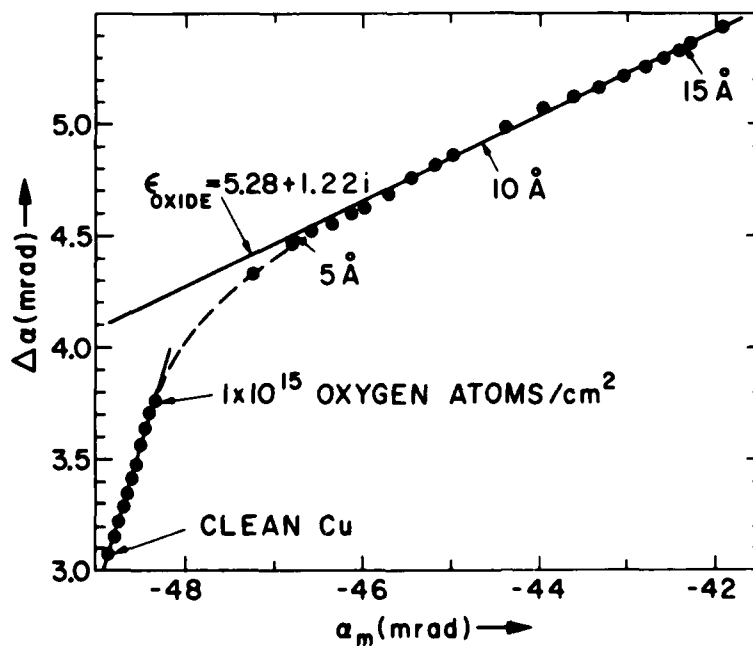
The recent prediction of the properties of a new long range surface plasmon (LRSP) mode on the two surfaces of a thin metal film bounded by index-matched dielectrics has stimulated theoretical and experimental interest in this new mode.<sup>7</sup> When the fundamental mode of this plasmon is excited on both surfaces of a thin silver film bounded by a nonlinear quartz crystal and an index-matched liquid, the SHG is over two orders of magnitude larger than that due to the single-boundary SP as illustrated in Fig. 4a. The first observation of nonlinear coupling to a harmonic LRSP mode is demonstrated by the middle peak of the angular scan data displayed in Fig. 4b. SHG with simultaneously phase-matched fundamental short-range and harmonic long-range SP modes has also been observed. Since the frequency-dispersion curve for the LRSP mode falls close to the light line, the SHG is produced in the radiative region of the curve. This feature has been exploited to observe transmitted SHG with fundamental LRSP excitation.<sup>8</sup> By using a crystal with a larger nonlinear susceptibility, one can predict SHG conversion efficiencies of 1%. In conclusion, the highly resonant and localized nature of the LRSP mode will make this mode a useful new probe for studying linear and nonlinear optical properties of metal-dielectric interfaces.

#### REFERENCES

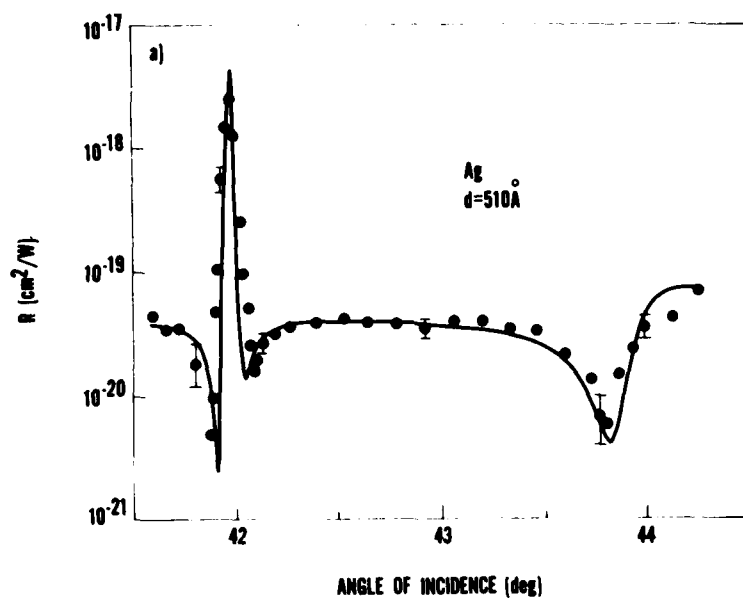
1. A. Otto, Z. Phys. 216, 398 (1968); E. Kretschmann and H. Raether, Z. Naturforsch. Teil A23, 2135 (1968).
2. Surface Polaritons, edited by V. M. Agranovich and A. A. Maradudin (North-Holland, Amsterdam, 1982); Electromagnetic Surface Modes, edited by A. D. Boardman (John Wiley and Sons, Chichester, 1982).
3. C. F. Eagan, and W. H. Weber, Phys. Rev. B19, 5068 (1979).
4. H. J. Simon, D. E. Mitchell, and J. G. Watson, Phys. Rev. Lett. 33, 1531 (1974).
5. J. E. Sipe, V.C.Y. So, M. Fukui, and G. I. Stegeman, Phys. Rev. B21, 4389 (1980).
6. H. J. Simon, R. E. Benner, and J. G. Rako, Opt. Commun. 23, 245 (1977); J. G. Rako, J. C. Quail, and H. J. Simon, Phys. Rev. B30, 5552 (1984).
7. D. Sarid, Phys. Rev. Lett. 47, 1927 (1981); J. C. Quail, J. G. Rako, and H. J. Simon, Opt. Lett. 8, 377 (1983); A. E. Craig, G. A. Olson, and D. Sarid, Opt. Lett. 8, 380 (1983); Y. Kuwamura, M. Fukui, and O. Tado, J. Phys. Soc. Jpn 52, 2350 (1983).
8. J. C. Quail, J. G. Rako, H. J. Simon, and R. T. Deck, Phys. Rev. Lett. 50, 1987 (1983); J. C. Quail, and H. J. Simon, J. Appl. Phys. 56, 2589 (1984); J. C. Quail and H. J. Simon, J. Opt. Soc. Am. B1, 319 (1984).



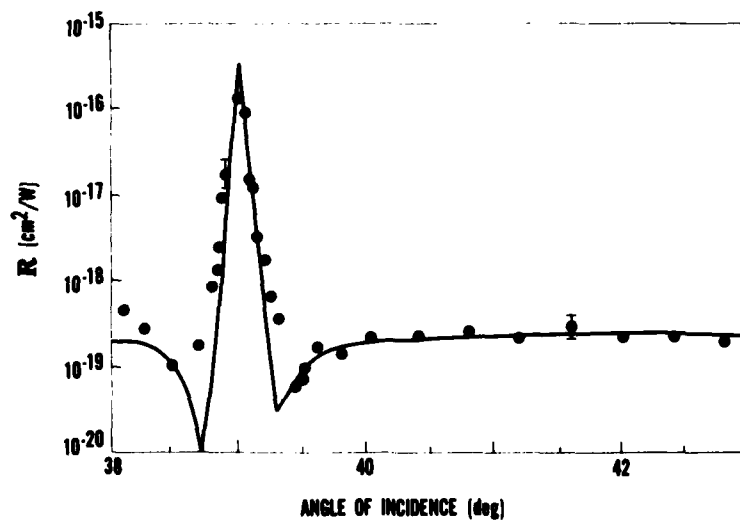
1. Schematic drawing of electronic, optical, and vacuum systems employed in angle-modulated SP studies. (Courtesy of Dr. W. H. Weber, Ford Motor Co.)



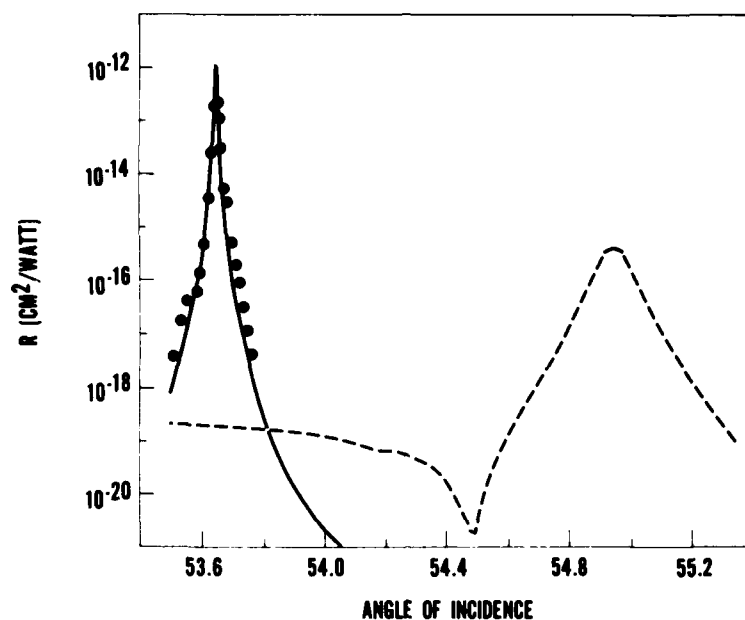
2. Compilation of the SP response for various  $\text{O}_2$  exposures on Cu. (Courtesy of Dr. W. H. Weber, Ford Motor Co.)



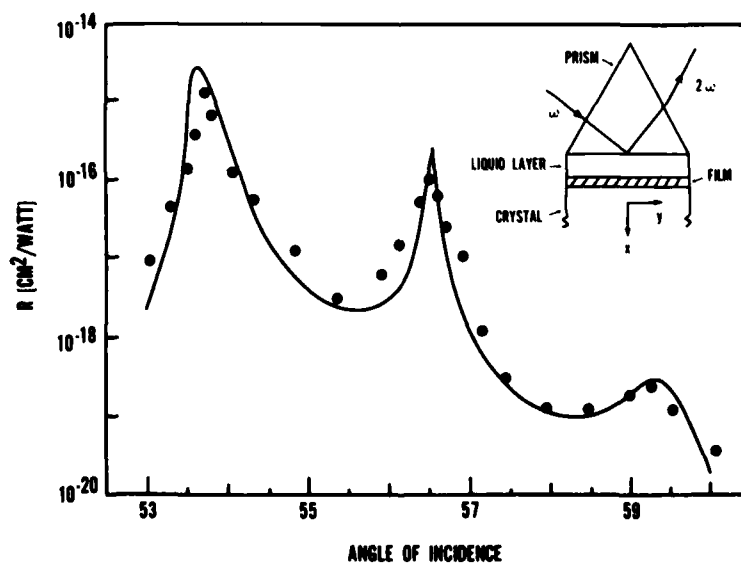
3a. Nonlinear SHG reflectance versus internal angle of incidence from a silver film ( $d=510 \text{ \AA}$ ) on a BK-7 prism. Solid curve is calculated from hydrodynamic theory for free electron gas with  $a=0.9$ .



3b. Nonlinear SHG reflectance vs. interior angle of incidence for rutile prism/550 Å Ag film/X-cut quartz crystal substrate.



4a. Nonlinear SHG reflectance vs. interior angle of incidence from SF-59 prism/ $3\mu$  index-matching liquid layer/ $135 \text{ \AA}$  Ag film/X-cut quartz crystal substrate illustrating optimal excitation of the fundamental LRSP mode. The dotted curve displays the case for a single-boundary SP for comparison purposes only.



4b. Reflected SHG demonstrating excitation of the fundamental LRSP, the nonlinearly excited harmonic LRSP, and the fundamental SRSP modes vs. the interior angle of incidence. Inset shows prism geometry.

## LOW LOSS THIN FILM MATERIALS FOR INTEGRATED OPTICS

Howard E. Jackson and J. T. Boyd  
Department of Physics and Solid State Electronics  
Laboratory, Department of Electrical and Computer Engineering  
University of Cincinnati, Cincinnati, Ohio 45221

In this paper we review our recent efforts to obtain low loss planar optical waveguides using both novel fabrication and laser annealing techniques. Scattering of light which occurs in thin-film optical waveguides represents a loss mechanism and, more importantly, such scattering can limit the performance obtainable in integrated optical signal processing and sensing devices. Reduction of scattering is thus desirable, allowing higher levels of performance and making optical signal and sensing processing devices more competitive with other approaches. The possibility of an integrated version of an optical fiber interferometer would require extremely low loss channel waveguides. To obtain low loss thin film optical waveguides, we have utilized the technique of laser annealing to obtain optical attenuation values below 1 dB/cm for a number of materials with potential for use in integrated optics. In addition, we have fabricated several types of graded-index waveguides which display low scattering characteristics.

For each of the thin-film waveguide materials discussed here, the substrate material is silicon. Silicon as a substrate provides an excellent surface for formation of a variety of waveguide structures. In addition, the use of silicon allows the integration of guided wave structures and electronic devices on the same substrate. In what follows we shall discuss first the use of laser annealing to achieve low loss waveguides and then several graded-index structures.

### Laser Annealing of Optical Thin-Film Waveguides

We have achieved considerable success in using the technique of laser annealing to reduce scattering in a variety of thin-film waveguides deposited onto thermally oxidized silicon substrates. We associate a reduction in waveguide scattering with an improvement in quality of either the bulk film, the film surface, the film-SiO<sub>2</sub> interface, or combinations of these. In each case values of optical attenuation less than 1 dB/cm were achieved, and in two cases the low value of 0.01 dB/cm was obtained. After briefly describing the experimental set-up for the laser annealing and for the measurement of low values of optical attenuation, we present results which show improvement in waveguide loss for five different waveguide films: Corning 7059 glass, ZnO, Si<sub>3</sub>N<sub>4</sub>, Nb<sub>2</sub>O<sub>5</sub> and Ta<sub>2</sub>O<sub>5</sub>.

Each of the waveguides was annealed by scanning a focused CO<sub>2</sub> laser beam of wavelength 10.6  $\mu$ m horizontally across the waveguide surface at a rate of 1 cm/sec. Typical vertical translation increments varied from 100 to 150  $\mu$ m. A 6.4 cm focal length lens provided power densities from  $9 \times 10^2$  W/cm<sup>2</sup> to  $3 \times 10^5$  W/cm<sup>2</sup>, with the lower power densities obtained by moving the sample away from the focal point.

The waveguide loss or the optical attenuation was determined for each of the waveguides by careful measurement of the out-of-plane scattering

before and after laser annealing. HeNe laser light was prism coupled into the waveguide, and the intensity of light scattered out of the waveguide was measured as a function of distance along the axis of propagation. The measurements were performed using a scanning photometric microscope incorporating a 50  $\mu\text{m}$  aperture optical fiber probe within the microscope and a 10x microscope objective. This allowed precise positioning of the probe with respect to the waveguide surface. To obtain an individual data point for the out-scattered light, the microscope was defocused

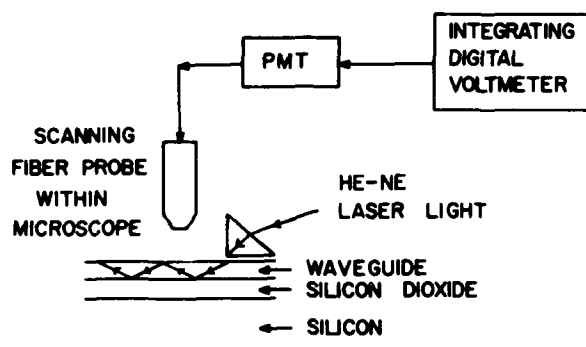


Fig. 1. Schematic of the experimental arrangement for measurement of out-of-plane waveguide scattering loss.

by 3mm, the fiber probe was scanned a distance of 1mm transverse to the propagation axis at a rate of 1mm/min, and an integrating digital voltmeter was used to integrate the signal over the scan. A schematic of the experimental arrangement is given in Fig. 1. In addition, for the very low loss measurements, the laser power was monitored with a precision of  $\pm 0.05\%$ , and the data normalized accordingly. Using these averaging techniques has allowed consistent measurement of waveguide attenuation values as low as 0.01 dB/cm.

Corning 7059 glass has been the most widely used thin-film waveguide, and is advantageous for many applications because of its value of refractive index and its ease of fabrication.  $\text{CO}_2$  laser annealing of Corning 7059 glass waveguides fabricated on thermally oxidized substrates has been shown to significantly reduce scattering losses in these waveguides<sup>1</sup>. The initial laser experiments reduced the waveguide attenuation from 17.4 dB/cm before laser annealing to 0.6 dB/cm afterwards. More recent laser annealing experiments carried out at optimized power densities of  $3\text{--}4 \times 10^3 \text{ W/cm}^2$  have resulted in improvements from initial values of 3 to 8 dB/cm to values as low as .05 dB/cm after laser annealing.

Dark field photomicrographs taken before and after laser annealing indicate clearly that surface, and possibly bulk, defects in these waveguides have been reduced substantially after laser annealing. To substantiate these observations, we have carried out a series of experiments using index-matched liquid surface coatings to quantify changes in both surface and bulk contributions to waveguide attenuation after laser annealing. Table 1 summarizes the results. By comparing the bulk ( $\alpha_b$ ) and surface ( $\alpha_s$ ) attenuation coefficients shown in Table 1 before and after laser annealing, we conclude that both bulk and surface contributions to the

Table 1. Effect of laser annealing on surface and bulk scattering in waveguides.

	Sample No.	$\alpha$ without film	$\alpha$ with film	$\alpha_b$	$\alpha_s$
Unannealed	1	1.8 cm <sup>-1</sup>	0.6 cm <sup>-1</sup>	0.6 cm <sup>-1</sup>	1.2 cm <sup>-1</sup>
waveguides	2	0.9 cm <sup>-1</sup>	0.1 cm <sup>-1</sup>	0.1 cm <sup>-1</sup>	0.8 cm <sup>-1</sup>
Laser-annealed	3	0.3 cm <sup>-1</sup>	0.1 cm <sup>-1</sup>	0.1 cm <sup>-1</sup>	0.2 cm <sup>-1</sup>
waveguides	4	0.05 cm <sup>-1</sup>	0.002 cm <sup>-1</sup>	~0 cm <sup>-1</sup>	~0.05 cm <sup>-1</sup>

waveguide scattering are significantly reduced. To achieve permanently the extremely low attenuation values obtained with the liquid index-matching film, we have substituted a spin-on liquid film on the laser annealing waveguide which can be solidified upon baking. In one waveguide, the attenuation coefficient was reduced from 4.0 dB/cm to 0.05 dB/cm after laser annealing, and finally to the extremely low value of 0.01 dB/cm after adding the solid film.<sup>2</sup>

Thin films of ZnO are important for their current use in both bulk and surface acoustic wave (SAW) devices and for their potential use in integrated optical devices. Use of ZnO in integrated optical devices allows excitation of surface acoustic waves and thus allows implementation of the guided wave acousto-optic effect on substrates either lacking or having a very weak piezoelectric effect, such as Si or GaAs. Use of Si as a substrate material is desirable, as it allows integration of photodetector arrays and utilization of the very low-loss thin-film waveguides. We have laser annealed ZnO thin-film optical waveguides deposited on an amorphous SiO<sub>2</sub> layer thermally grown on Si. Previously, values of waveguide attenuation as low as 0.5 dB/cm for ZnO films deposited on crystalline sapphire substrates and 1.0 dB/cm for ZnO films deposited on amorphous oxidized silicon substrates have been observed. We have obtained improvement in loss from several dB/cm before laser annealing to values as low as 0.01 dB/cm after laser annealing for ZnO films deposited on amorphous oxidized silicon substrates.<sup>3</sup>

The ZnO waveguides were annealed in a similar manner to the Corning 7059 glass waveguides, with the CO<sub>2</sub> laser scanned at 1 cm/s with power densities of  $2.0 - 2.3 \times 10^5$  W/cm<sup>2</sup>. ZnO is nearly transparent to the CO<sub>2</sub> laser wavelength (10.6  $\mu$ m), while the SiO<sub>2</sub> layer absorbs strongly. Thus, we expect that heating of the ZnO film will occur primarily at the ZnO-SiO<sub>2</sub> interface, a region characterized by a relatively large defect density.

Waveguide attenuation measurements are presented in Table 2 for two different waveguide thicknesses and for the first three TE waveguide modes. The data for the TE<sub>1</sub> waveguide mode for one sample is displayed before and after laser annealing in Fig. 2. Laser annealing of sample #1 reduced the waveguide attenuation coefficient from 4.6 dB/cm before laser annealing to the low value of 0.02 dB/cm. In sample #2 the significant reduction measured in the TE<sub>1</sub> and TE<sub>2</sub> mode losses following laser annealing supports the suggestion of substantial improvements in the ZnO-SiO<sub>2</sub> interfacial region. A possible decrease in the surface acoustic wave attenuation after laser annealing is being investigated.

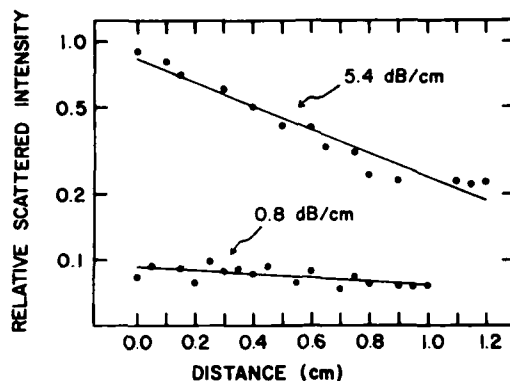


Fig. 2. Logarithm of relative scattered intensity is plotted vs distance along the ZnO waveguide for the TE<sub>1</sub> mode before (upper line) and after (lower line) laser annealing.

Table 2. Effect of laser annealing on ZnO waveguide attenuation.

Sample number	ZnO film thickness (μm)	Waveguide	attenuation coefficient (dB/cm)			Annealing power density (W/cm <sup>2</sup> )
			TE <sub>0</sub>	TE <sub>1</sub>	TE <sub>2</sub>	
1	0.93	Before anneal	4.6	10.0	16.0	2.0 x 10 <sup>5</sup>
		After anneal	0.02	8.7	6.5	
2	0.93	Before anneal	2.5	7.0	9.3	2.3 x 10 <sup>5</sup>
		After anneal	0.01	12.4	13.9	
3	0.71	Before anneal	1.0	5.4	7.1	2.3 x 10 <sup>5</sup>
		After anneal	0.03	0.8	1.6	

Rutherford backscattering (RBS) measurements were used in the case of both Corning 7059 glass and ZnO waveguides to help elucidate the mechanisms responsible for the reductions in scattering loss observed after laser annealing. RBS measurements indicate that no redistribution of implanted impurities takes place during laser annealing. Thus no melting occurs and the annealing occurs in the solid phase.<sup>4</sup>

We have also used CO<sub>2</sub> laser annealing to significantly reduce waveguide scattering losses in waveguides composed of several other materials of potential use in integrated optics including Si<sub>3</sub>N<sub>4</sub>, Nb<sub>2</sub>O<sub>5</sub>, and Ta<sub>2</sub>O<sub>5</sub>. The lowest values of optical attenuation achieved were 0.1 dB/cm for Si<sub>3</sub>N<sub>4</sub>, 0.6 dB/cm for Nb<sub>2</sub>O<sub>5</sub>, and 0.4 dB/cm for Ta<sub>2</sub>O<sub>5</sub>.

#### Graded Index Waveguides

Graded-index planar SiO<sub>2</sub> optical waveguides might be expected to have many of the advantages associated with graded-index fibers including low loss. We have observed extremely low scattering in planar graded-index SiO<sub>2</sub> waveguides formed by thermally oxidizing silicon wafers for periods up to several weeks resulting in waveguide thicknesses of up to 15 microns.<sup>6</sup> The graded refractive index results from some unknown combination of composition, impurity, density, and stress distributions in the SiO<sub>2</sub> layer.



The losses in these optical waveguides were characterized in several ways, but perhaps the most telling was the attempt to measure scattering losses in a manner similar to that described above. The amount of out-of-plane scattering observed using an input power of 160 mW to excite a TE mode was consistent with the observation of inelastic scattering from phonons ( $<2$  cps), i.e. with the observation of no elastic scattering from defects or inhomogeneities in the waveguide. Waveguide attenuation, of course, can also be determined by measuring the transmitted intensity as a function of distance along the waveguide. Such measurements yielded the low, but not extraordinarily low, values of 0.3-0.6 dB/cm. Since the out-of-plane scattering was demonstrably exceedingly low, the loss of 0.3-0.6 dB/cm is ascribed to substrate absorption. Thus we expect that if we can provide stronger field confinement for these graded-index waveguides, the waveguide attenuation would indeed be exceedingly small.

We have attempted to provide stronger field confinement in two different ways. First, phosphorous doping was used, as the presence of phosphorus increases the refractive index of  $\text{SiO}_2$ . Stronger field confinement was observed, along with losses of 1 dB/cm, for total oxide thicknesses of about 6 microns. Second, we have formed graded-index waveguides in  $\text{SiO}_2$  by oxidizing silicon wafers under time-varying conditions. The index of refraction of a layer of  $\text{SiO}_2$  is dependent on the growth temperature and the water content of the ambient oxygen. In a variety of experimental circumstances, all resulting in strong enough field confinement so that calculated substrate absorption loss was  $\leq 0.1$  dB/cm, the lowest value of waveguide attenuation was still about 0.6 dB/cm. The loss values were thus much larger than expected.

A second kind of graded index guide has recently been investigated by Naik.<sup>7</sup> Nitrogen implantation of a thermally grown  $\text{SiO}_2$  layer on Si was followed by annealing yielded waveguides with the very low waveguide attenuation of 0.1 dB/cm. Very preliminary results are reported here for three

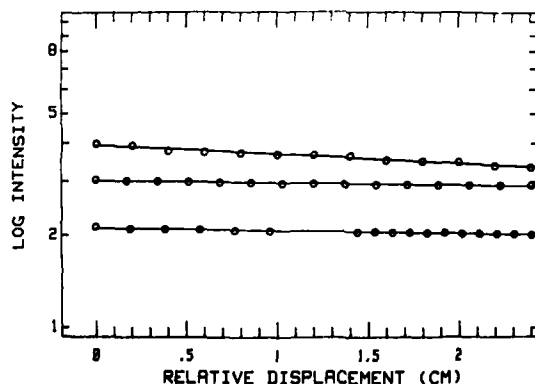


Fig. 3. The logarithm of the relative outcoupled intensity is plotted vs distance along the waveguide for three waveguides. Loss decreases for increasing thermal nitridation times.

graded-index guides formed using a thermal nitridation process.<sup>8</sup> The waveguide attenuation values for these samples were obtained by outcoupling the guided wave for various distances along the waveguide, in contrast to the out-of-plane scattering measurements discussed above. Waveguide attenuation measurements for the three waveguides are displayed in Fig.3. Values of the optical attenuation range from 0.29 dB/cm (uppermost line) to 0.08 dB/cm (lowest line). For longer thermal nitridation times, which might reasonably correspond to stronger field confinement and lower substrate absorption loss, we observe lower values of loss. Clearly much remains to be done here.

#### Summary

We have reviewed our recent efforts to obtain low loss planar waveguides for potential use in integrated optics. Employing both novel fabrication and laser annealing techniques, we have achieved values of waveguide attenuation substantially below 1 dB/cm for a variety of waveguide materials. In several cases values below 0.1 dB/cm were achieved, with efforts to achieve even lower values of waveguides attenuation continuing.

This research was supported in part by the Air Force Office of Scientific Research and the National Science Foundation.

#### References.

1. S. Dutta, H. E. Jackson, and J. T. Boyd, Appl. Phys. Lett. 37, 512 (1980).
2. S. Dutta, H. E. Jackson, and J. T. Boyd, J. Appl. Phys. 52, 3873 (1981).
3. S. Dutta, H. E. Jackson, J. T. Boyd, F. S. Hickernell and R. L. Davis, Appl. Phys. Lett. 39, 206 (1981).
4. S. Dutta, H. E. Jackson, J. T. Boyd, and C. W. White, J. Appl. Phys. 54, 2125 (1983).
5. S. Dutta, H. E. Jackson, J. T. Boyd, R. L. Davis and F. S. Hickernell, IEEE Quant. Electron. QE-18, 800 (1982).
6. D. E. Zelmon, H. E. Jackson, J. T. Boyd, A. Nauman and D. B. Anderson, Appl. Phys. Lett. 42, 565 (1983).
7. I. K. Naik, Appl. Phys. Lett. 43, 519 (1983).
8. D. E. Zelmon, H. E. Jackson and J. T. Boyd (to be published).

## QUANTITATIVE SAMPLING IN PLANAR WAVEGUIDES

Paul W. Bohn

Department of Chemistry and Materials Research Laboratory, University of Illinois, 1209 W. California, Urbana, Illinois 61801

Realization of the goal of direct quantitative analysis of molecules bound in the matrix of a thin film may be approached by using the thin film of interest as the active waveguiding medium in a three or four layer asymmetric slab dielectric waveguide. In these structures the spatial asymmetry of the electric field amplitude distribution perpendicular to the film plane and the fact that these profiles may be calculated exactly from simple knowledge of the thickness and dielectric constants of the layers mean that fluorescence or Raman scattering, monitored outside the waveguide, will automatically contain information about the spatial distribution of the molecules being probed (1,2). In order for this phenomenon to be exploited however it is necessary that the characteristic signals being recorded be related to the concentration of the probe species in a simple manner. In solution the signal in a Raman scattering experiment is linearly proportional to concentration of scatterers at low irradiances (3). Thus the solid solution thin films under investigation in these experiments should be characterized by scattering signals which are proportional to the product of the electric field intensity distribution and the molecular concentration distribution, summed over the thin film thickness and the area sampled by the collection optics as shown in equation 1,

$$I_i = \text{const.} \times \int_0^t E_i^2(z) N(z) dz \quad (1)$$

where  $I_i$  = Raman scattering intensity measured for the  $i$ th mode,  $E_i^2(z)$  = electric field intensity distribution in the direction perpendicular to the film plane, and  $N(z)$  = molecular concentration profile.

In the simplest case, that of a spatially homogeneous concentration profile,  $N(z)$  is a constant and the integral of equation 1 can be solved analytically for any layer of either a three or four layer structure (4). The results can be expressed as a normalized p-matrix, the elements of which are the normalized portions of the total irradiance resident in each layer for each mode. In the spatially homogeneous case then the scattering intensities for excitation of different modes of the waveguide should just be proportional to the elements of the p-matrix for that mode. As an example of a spatially homogeneous matrix a three layer structure composed of a 1.96  $\mu\text{m}$  atactic poly(styrene) film on glass was investigated at 514.5 nm in a prism coupled configuration. The normalized TE p-matrix for this structure is given in Table I. In the table the  $j$  values are the modes of the waveguide and the  $i$  values are the layers starting with substrate ( $i=1$ ) and ending with superstrate ( $i=3$ ). These values should then be proportional to the scattering signals from any vibration characteristic of the poly(styrene) repeat unit.

Table I

	i=1	i=2	i=3
j=0	0.0043	0.9954	0.0003
j=1	0.0189	0.9800	0.0011
j=2	0.0511	0.9465	0.0024
j=3	0.1536	0.8424	0.0040

The ring breathing mode at  $1004\text{ cm}^{-1}$  was chosen and the results are shown in Figure 1. Two striking results are observed. First as the observations are made further from the coupling position, the shape of the curve changes, becoming less linear. In addition the plots for different observation points are displaced downward for each mode observed. These observations are consistent with and typical of other organic polymer thin films studied using both fluorescence (for doped films) and Raman scattering (for undoped films) probes. Thus the simple model invoked above wherein the signal strength is proportional to a weighted average of the probe molecule concentration fails in this most simple test case.

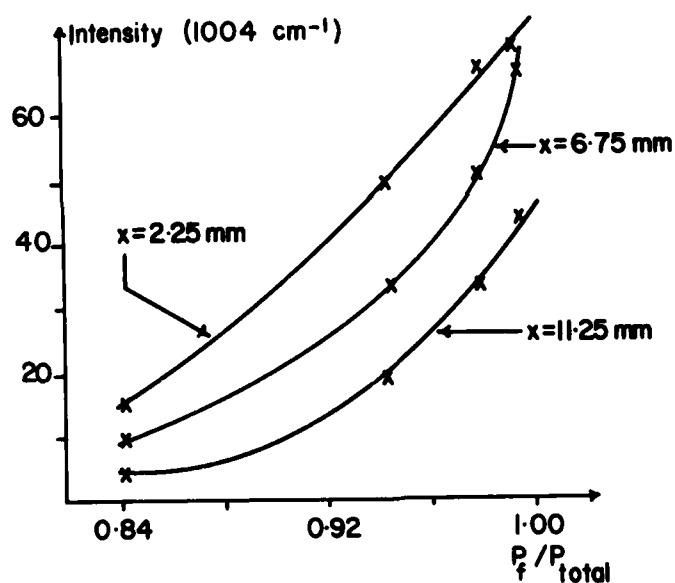


Figure 1. Plot of the Raman scattering intensity of the  $1004\text{ cm}^{-1}$  ring breathing mode in poly(styrene) as a function of the normalized irradiance within the waveguiding layer.

The reasons for the failure of the simple model are that it leaves out both elastic scattering contributions to the overall optical loss in transmission through these thin films and mode dependent coupling efficiency effects in the prism coupled configuration. Several models have been put forth in the literature to explain the effects of surface and volume scattering on the

optical loss function. Although differing in detail they all agree that the surface scattering loss pathway should increase dramatically at higher modes. Thus if observation of a signal is made at a particular distance away from the coupling prism, this signal should be weaker for higher modes, because the irradiance is smaller at that point than it is when lower order modes are excited. This then explains the curvature in Figure 1. Higher order modes are characterized by smaller normalized irradiances in the main waveguiding film and appear on the left part of the abscissa. The curvature in the plot roughly parallels the curvature in the total loss vs. mode plot as given by Tien (5). If these same data are plotted vs. distance from the coupling prism for each mode, the resulting familiar plot can be used to estimate the overall optical loss coefficient,  $\alpha_T$ , from the slope. When this plot is extrapolated to the coupling prism it is seen that the different modes have different initial intensities, i.e. the coupling efficiency is mode dependent as predicted by Ulrich (6). Thus this effect will also contribute to a decrease in the available excitation power for spectroscopic experiments at higher order modes.

A simple model for quantitative spectroscopic sampling in thin films has been advanced and compared with experiment for the simple case of spatially homogeneous scatterers. Agreement with theoretical scattering intensities demands a treatment which takes into account both surface and volume elastic scattering and mode dependent coupling efficiency effects.

#### References

- 1) J.N. Polky and G.L. Mitchell, J. Opt. Soc. Am. 64, 274 (1974).
- 2) J.F. Rabolt, R. Santo, N.E. Schlotter, and J.D. Swalen, IBM J. Res. Devel. 26, 209 (1982).
- 3) D.A. Long, "Raman Spectroscopy," (McGraw-Hill, London, 1977).
- 4) P.W. Bohn, "Theory of Spectroscopic Sampling in Thin Amorphous Films," submitted to Anal. Chem.
- 5) P.K. Tien, Appl. Opt. 10, 2395 (1971).
- 6) R. Ulrich, J. Opt. Soc. Am. 60, 1337 (1970).

## RELATIONSHIP OF MICROSTRUCTURE TO OPTICAL PROPERTIES OF THIN FILMS

H. A. Macleod  
Optical Sciences Center  
University of Arizona  
Tucson, AZ 85721

### Introduction

Although the properties of materials in thin-film form are broadly similar to those of bulk materials, there are often significant differences. Frequently the level of performance that can be achieved with thin films is inferior to that predicted from simple bulk properties. Great progress has been made in closing the gap between real thin-film properties and bulk properties but a gap still remains and much of it is a direct consequence of the effects of microstructure on the optical, mechanical and chemical properties of thin films. Here we are concerned solely with the optical properties and we limit the discussion to dielectric films.

### Microstructure

Thin-film microstructure is complex, and there are different levels of structure. In order to relate the structure to the film properties we need a model that retains the essential features of the real structure but which is more amenable to calculation and easier to visualise. The principal detail of film microstructure is its columnar form of the grains and the simple model, shown in figure 1, which was devised originally by H. K. Pulker (1) and elaborated by Ogura (2) (3), enables us to discuss and understand a wide range of microstructure-related effects.

The most important parameter relating to the microstructure is the packing density  $p$  given by

$$p = \frac{\text{Volume of the solid part of the film (i.e. columns)}}{\text{Total volume of film (i.e. columns plus voids)}}$$

$p$  is usually in the range of 0.8 to 0.95 for most thin-film material deposited by thermal evaporation in vacuo.

### Measurements

Optical inhomogeneity is a feature of those models with varying columnar cross section and indeed is a frequent feature of optical thin films. Cryolite and zinc sulphide films have been measured in situ by Netterfield (4). Inhomogeneity in titanium oxide and its agreement with the columnar model has been considered by Harris et al (3). Borgogno et al (5) have made measurements on a wide range of inhomogeneous films.

Birefringence in thin films is another microstructure-related area. In 1957, Bousquet (6) published an analytical treatment for the calculation of the

optical properties of an anisotropic thin film. In the same year he reported (7) calcium fluoride films that were uniaxial with optic axis perpendicular to the surface with  $(n_o - n_e) = 2.5 \times 10^{-1}$ . With Rouard in 1960 he warned (8) of the problems caused by birefringence in measurement of optical constants involving obliquely incident light. Rouard (9) had already noted that if the axes of the grains in the films were normal to the boundaries, then measurements at only normal incidence would not be perturbed. Recently King and Talim (10) compared various techniques of optical constant measurement. Guided waves showed a significant difference between indices for TE modes, 1.9887, from those for TM, 2.0015, at 632.8nm in zirconium dioxide.

The columnar nature of the films strongly suggests that they should be birefringent with the principal axes of the dielectric tensor along the columnar direction ( $n_z$ ), and normal to the columns both in the plane of incidence of the vapor ( $n_1$ ), and normal to the plane of vapor incidence ( $n_2$ ). For films that are evaporated at normal incidence we would expect the birefringence to be uniaxial with optic axis normal to the film surface and not detectable by purely normal incidence measurements. Normal incidence measurements would, however, permit us to infer the presence of birefringence in obliquely deposited films where we would expect biaxial birefringence with the optic axes in the plane of incidence of the vapor during the film growth. Because obliquely deposited columns are less closely spaced in the plane of vapor incidence than normal to the plane, we would expect the birefringence usually to be characterised by a maximum index along the columns and by a minimum normal to the columns in the plane of incidence. The optic axes for a biaxial film would therefore be in the plane of vapor incidence.

Some measurements of anisotropic behaviour in zirconium dioxide and titanium dioxide films have recently been made (11) (12). Zirconium dioxide films evaporated at very high angles of incidence were found to be anisotropic with an effective  $\Delta n = 0.042$  for propagation through the film at normal incidence (16) (17). The measurements assumed that the orientation of the columns in the films was known through the tangent rule (13) connecting the angle of vapor incidence,  $\alpha$ , and the column orientation angle,  $\beta$ ,

$$\tan \alpha = 2 \tan \beta$$

Results are given in Table 1 (12) for wavelengths in the region of 630 nm.

TABLE 1

Material	$\alpha$	$\beta$	$n_1$	$n_2$	$n_z$
Zirconium oxide	30°	16.1°	1.948	1.966	2.033
Zirconium oxide	65°	47.0°	1.502	1.575	1.788
Titanium oxide	30°	16.1°	2.437	2.452	2.552

#### Calculation of optical constants

Since the film is made up of solid parts and voids, we can expect that the refractive index will be reduced below that for a film made up entirely of

solid material. Many attempts have been made at deriving a relationship between packing density and refractive index. An early attempt by J.C. Maxwell-Garnett (14) (15) based on the Lorentz-Lorenz polarization theory, can be written (3)

$$n_f = \frac{(1-p)(n_s^2+2)n_v^2 + p(n_v^2+2)n_s^2}{(1-p)(n_s^2+2) + p(n_v^2+2)} \quad (1)$$

where  $n_f$  is the index of the composite film,  $n_s$  is the index of the solid material of the film, and  $n_v$  is the index of the voids in the film, usually unity. The possibility that the particles of the film might depart from the spherical form assumed in the Maxwell-Garnett theory has been included in an analysis by Bragg and Pippard (16). Assuming cylindrical particles and manipulating the expressions somewhat, we arrive at the expression (3)

$$n_f = \frac{(1-p)n_v^2 + (1-p)n_v^2 n_s^2}{(1+p)n_v^2 + (1-p)n_s^2} \quad (2)$$

where the same symbols have been used. An alternative expression for the index of a composite film based on an interpolation between two limits, is that of Kinoshita and Nishibori (17)

$$n_f = (1-p)n_v + pn_s \quad (3)$$

The accuracy of these expressions has been investigated by Harris et al (3) using a finite difference approach to calculate the dielectric permittivity of a hexagonal array of columns. The linear interpolation is surprisingly good for low index films but poor for high index films. For intermediate values of packing density it was found that the Bragg and Pippard expression gave better agreement than the Maxwell-Garnett. An alternative approach by McPhedran and McKenzie (18) (19) used a computer to permit the inclusion of terms of very high order in series expansions based on work by Raleigh.

For packing densities in the region from around 0.75 to 1.0 finite elements are more suitable. In this region, Harris (20) obtained results of which those in figure 2 are typical showing a transition from the Bragg and Pippard law to the linear interpolation at around  $p=0.8$ , the details of this behaviour depending on the precise columnar shape. This result could explain the difficulty of controlling materials like titanium oxide and zirconium oxide both of which have packing densities in the critical region. Recently some experimental evidence of such an effect was obtained by Martin et al (21) for zirconium dioxide films produced by ion-assisted deposition with packing densities varying from around 0.7. to 1.0 (Figure 3).

### Conclusion

This has been a necessarily short and incomplete survey of some of the relationships between microstructure and the optical properties of dielectric thin films. Work to date has been almost entirely from the point of view of adverse effects, that is a reduction of the performance of



coatings below what we could expect from bulk materials and major research effort is now being devoted to attempts to modify the microstructure so that the films are more like bulk material. Little attention appears to have been devoted to the opposite question of using some of the special properties of thin films to our advantage.

#### References

1. H.K. Pulker and E. Jung, "Correlation between film structure and sorption behaviour of vapor deposited ZnS, cryolite and MgF<sub>2</sub> films," Thin Solid Films, Vol.9, pp 57-66, 1971
2. S. Ogura, "Some features of the behaviour of optical thin films," PhD Thesis, Newcastle-Upon-Tyne Polytechnic, 1975
3. M. Harris, H.A. Macleod, S. Ogura, E. Pelletier and B. Vidal, "The relationship between optical inhomogeneity and film structure," Thin Solid Films, Vol.57, pp 173-178, 1979
4. R.P. Netterfield, "Refractive indices of zinc sulphide and cryolite in multilayer stacks," Applied Optics, Vol.15, pp 1969-1973, 1976
5. J.P. Borgogno, B. Lazarides and E. Pelletier, "Automatic determination of the optical constants of inhomogeneous thin films," Applied Optics, Vol.21, pp 4020-4029, 1982
6. P. Bousquet, "Theoretical study of the optical properties of thin transparent films," Ann Phys (Paris), Vol.2, pp 5-15, 1957
7. P. Bousquet and Y. Delacourt, "Evidence of the birefringence of calcium fluoride thin layers obtained by vacuum evaporation", J. Phys. Rad., Vol.18, pp 447-452, 1957
8. P. Bousquet and P. Rouard, "Constantes optiques et structure des couches minces," J. Phy. Rad., Vol.21, pp 873-892, 1960
9. P. Rouard, "Determination of the optical constants of thin films." J. Opt. Soc. Am., Vol.46, p 370, 1956 (Abstract)
10. R.J. King and S.P. Talim, "A comparison of thin film measurement by guided waves, ellipsometry and reflectometry", Optica Acta, Vol.28, pp 1107-1123, 1981
11. F. Horowitz and H.A. Macleod, "Form birefringence in thin films," Proc. SPIE, Vol.380, pp 83-87, 1983
12. F. Horowitz, "Structure-induced optical anisotropy in thin films," PhD Dissertation, University of Arizona, Optical Sciences Center, 1983
13. A.G. Dirks and H.J. Leamy, "Columnar microstructure in vapor-deposited thin films," Thin Solid Films, Vol.47, pp 219-233, 1977
14. J.C. Maxwell-Garnet, "Colours in metal glasses and in metallic films,"

Roy. Soc. Phil. Trans., Vol.203, pp 385-420, 1904

15. J.C. Maxwell-Garnett, "Colours in metal glasses, in metallic films and in metallic solutions," Roy. Soc. Phil. Trans., 205, pp 237-288, 1906

16. W.L. Bragg and A.B. Pippard, "The form birefringence of macromolecules." Acta Cryst., Vol.6, pp 865-867, 1953

17. K. Kinoshita and M. Nishibori, "Porosity of MgF<sub>2</sub> films - evaluation based on changes in refractive index due to adsorption of vapors," J. Vac.Sci. Technol., Vol.6, pp 730-733, 1969

18. R.C. McPhedran and D.R. McKenzie, "The conductivity of lattices of spheres. I. The simple cubic lattice," Proc. Roy., Soc. London, A, Vol.359, pp 45-63, 1978

19. D.R. McKenzie, R.C. McPhedran and G.H. Derrick, "The conductivity of lattices of spheres. II. The body centred and face centred cubic lattices," Proc. Roy. Soc. London, A, Vol.362, pp 211-232, 1978

20. M. Harris, M. Bowden and H.A. Macleod, "Refractive index calculations for a thin film with columnar structure," Optics Comm., Vol.51, pp 29-32, 1984

21. P.J. Martin, R.P. Netterfield and W.G. Sainty, "The modification of the optical and structural properties of dielectric ZrO<sub>2</sub> films by ion-assisted deposition", J. Appl. Phys., Vol.55, pp 235-241, 1984

### Figures

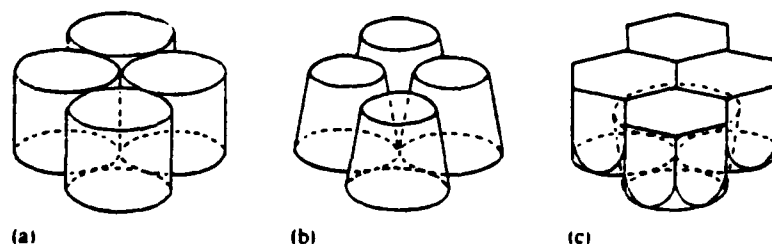


Fig 1. The three principal variations of the model of the columnar structure of thin films: (a) the cylindrical model,  $p = 0.9069$ ; (b) contracting columns,  $p < 0.9069$ ; (c) expanding columns,  $p > 0.9069$ . (After Ogura<sup>2</sup>.)

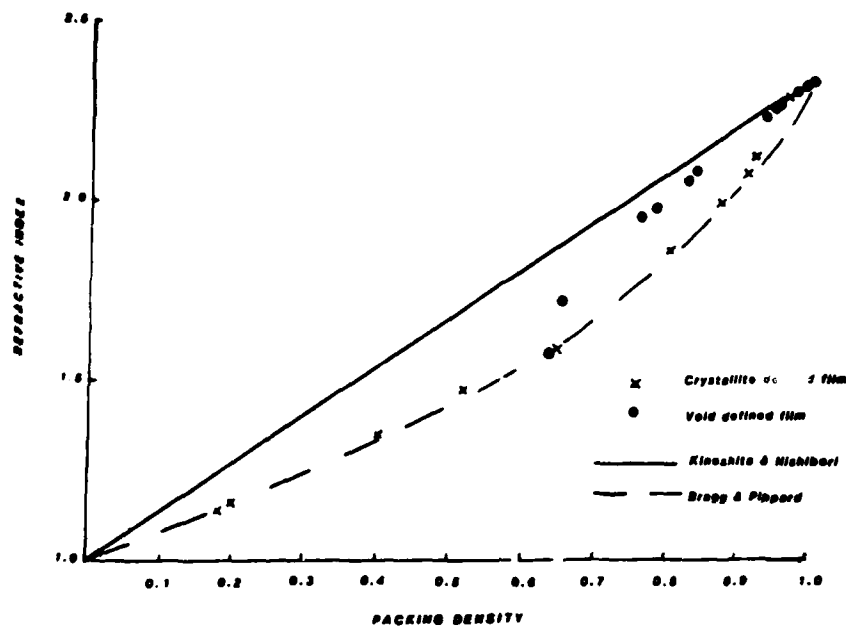


Fig.2. Numerical and analytical solutions for refractive index as a function of packing density.

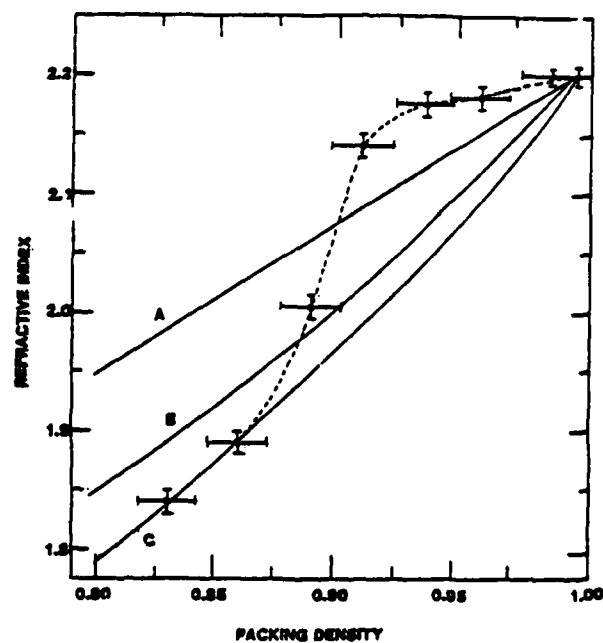


Fig.3 The refractive index of  $ZrO_2$  films produced by ion-assisted deposition as a function of packing density. A-linear relationship(3), B-(1), C-(3). After Martin et al (21).

THE MICROSTRUCTURE AND OPTICAL PROPERTIES OF THIN FILMS  
PREPARED BY MOLECULAR BEAM TECHNIQUES

K. L. Lewis, A. M. Pitt, J. A. Savage,  
A. G. Cullis, N. G. Chew and L. Charlwood

Royal Signals and Radar Establishment  
Malvern, Worcestershire  
England WR14 3PS

Introduction

A common factor in the failure of optical coatings under laser irradiation has been the lack of perfection and the relatively low purity of the coating material. Optical absorption levels are frequently too high and the refractive index uniformity of the film difficult to control. This is a consequence of several contributing factors. In the first instance, the film may contain a high concentration of impurity species arising from its fabrication in conventional evaporators at background pressures in the region of  $10^{-6}$  mbar, where the dominant species present is  $H_2O$  due to outgassing of the coating chamber walls and substrate assembly. Even for a partial pressure of  $H_2O$  of  $4.5 \times 10^{-9}$  mbar, which is some way below that achievable in conventional equipment, a film of ZnSe produced at a growth rate of  $2\mu\text{m/hr}$  would contain approximately 0.05%  $H_2O$  which implies an absorption coefficient of about  $0.5\text{cm}^{-1}$ . The problem is not restricted to  $H_2O$  - other molecular species, e.g.,  $CO_3$ ,  $SO_4$ ,  $SO_3$ ,  $CO_2$ ,  $CH_n$  are commonly produced as a result of reactions during deposition and give rise to significant absorption at  $10.6\mu\text{m}$ .

A second contributory factor may be associated with a degree of nonstoichiometry in the film which can result in the generation of free charge carriers which interact strongly with radiation at long wavelengths. Walsh and Bertke (1) have found that significant variations in the Zn:Se ratio of ZnSe can occur during RF sputtering, paralleling the results of O'Brien (2) who suggests that the Zn/Se ratio increases at higher deposition rates resulting in higher IR absorption.

The presence of further impurity species at the substrate/film or film/film interfaces contributes to poor adhesion of films and may also act as nucleation sites for the formation of pores and other undesirable morphological features. At short laser pulses (100nsec or less) coatings fail either as a result of heating microscopic coating defects or by electron avalanche processes in the coating material itself. It may be argued that the most serious coating defects are voids, from the point of view that they cannot be controlled by attention to cleanliness, dust control, etc. The presence of open porosity results in a high susceptibility to water ingress and inevitably a lower laser damage threshold.

The morphology of thin films plays an important part in determining resistance to laser induced damage. Films prepared by conventional evaporation techniques exhibit a polycrystalline morphology with a characteristic columnar structure (3). It has long been asserted that void formation is enhanced at grain boundaries in thin films and that diffusion of impurities especially water readily proceeds along such paths. The segregation of heterogeneous impurities at such grain boundaries also results in the generation of compressive stresses in the film (4,5). An immediate solution would appear to avoid producing films with polycrystalline columnar morphology, and to deposit films with an epitaxial relationship to the substrate. Unfortunately this requires a close match of the crystallographic parameters of the film and substrate and it may be too much to hope that this can be achieved with simultaneous satisfaction of refractive index criteria in any one film/substrate combination. The requirements of high interface perfection to ensure good epitaxy cannot be met in other than a UHV system employing ion beam cleaning and annealing/surface reconstruction techniques, or in chemical vapour deposition equipment where high substrate temperatures/gaseous etchants can be employed. The alternative solution, the adoption of pseudo amorphous morphologies may offer some potential since the coating need not be lattice matched to the substrate.

### Experimental

The present work assesses the potential of molecular beam techniques for the deposition of improved optical coatings. This growth technique allows a high degree of control over the deposition process and in situ assessment techniques such as Auger and XPS allow the characterization of the surfaces produced. By combining Knudsen evaporation with RF sputtering processes in a dedicated UHV facility, it is possible to fabricate coating structures containing a wide range of different materials including sulphides, selenides, tellurides, arsenides, phosphides, fluorides, chlorides, oxides and nitrides without necessarily having to break vacuum and risk the creation of contaminated interfaces. The coatings discussed in this paper were fabricated in a 3 chambered UHV facility incorporating Knudsen sources, a small RF plasma source, a molecular beam sampling spectrometer, Auger spectrometer and ion guns for substrate cleaning. Details are presented in previous publications (6,7). The morphology of the coatings was examined in detail by cross-sectional transmission electron microscopy (XTEM) at 120KV using specimens prepared by sequential mechanical polishing/low voltage AR<sup>+</sup> ion milling. Laser damage thresholds were determined using a short cavity TEA laser (33nsec FWHM with tail extending to 1700nsec) and a grating tuned hybrid laser (340nsec FWHM) as described previously at 10.6 $\mu$ m.

### Morphology

The MBE produced coatings were mirror smooth and replicated the topography of the substrates used. Some inclusions were evident in ZnS films deposited on Ge substrates, but these were also present in uncoated regions of the substrates and were attributed to polishing debris. XTEM micrographs of 0.7 $\mu$ m thick ZnSe films grown on GaAs at 50°C clearly reveal columnar grains some 250Å in diameter running throughout the thickness of the film. The crystalline structure within the material is highly defective with a high density of stacking faults each running perpendicular to the direction of

growth. X-ray diffraction measurements show that the material is highly ordered with cubic (111) planes lying parallel to the surface. Careful examination of the grain boundary regions reveals the complete absence of any voids within the scale of resolution available (20Å). A transition region some 1500Å in height above the substrate is also evident where growth of the columnar grains is clearly unstable and new grains are being nucleated. Also evident is a narrow 60Å amorphous region at the surface of the substrate resulting from ion beam damage during substrate cleaning. The morphology of ZnSe produced at 192°C is essentially similar to that of the films deposited at 50°C with the exception of a greatly increased grain size of 1000Å. The grain boundaries are, however, less well defined in the 192°C film and stacking faults in neighbouring grains tend to merge into one another. No voids are detected.

XTEM micrographs of SiO<sub>x</sub> films produced by RF sputtering under ultra-clean conditions at ambient temperatures are essentially featureless with faint contrast barely discernable due to ion beam thinning artifacts. The films are amorphous and contain no voids.

#### Optical Properties and Discussion

A direct comparison has been carried out of film deposition in conventional vacuum environments ( $p(\text{H}_2\text{O})$   $2.5 \times 10^{-6}$  mbar) and UHV ( $p(\text{H}_2\text{O})$   $2 \times 10^{-10}$  mbar) using the same equipment under otherwise identical conditions. Infra-red spectral analysis of the resulting films clearly shows the presence of OH species in ZnS films produced in poor vacuum whilst UHV grown ZnS is essentially free from such impurities. There are also significant differences in the adhesion of such films with the UHV produced films adhering to the substrate more strongly especially during laser pulse irradiation.

The laser induced damage thresholds (LIDT) of UHV produced ZnSe films on ZnSe substrates for 33nsec pulses were in the range 60-73J/cm<sup>2</sup> (1/e<sup>2</sup> radius 102µm). This was in excess of the value of 50-60J/cm<sup>2</sup> measured on uncoated regions of the same samples, with the uncoated region always damaging at a lower incident energy. This was attributed to the presence of residual surface impurities on the substrate which had been removed by pre-deposition ion cleaning. At longer pulse length (340nsec) the LIDT value for such a film was 31-38J/cm<sup>2</sup> (1/e<sup>2</sup> radius 180µm) with damage initiated at discrete microscopic inclusions resulting in craters some 10µm in diameter. The uncoated rear surface of the substrate always damaged at these energy densities. Refractive indices of such films are in the range 2.39 to 2.40 in the IR demonstrating the near theoretical density of the film material. The damage thresholds are significantly in excess of values of the order of 20J/cm<sup>2</sup> reported for sputtered ZnSe on KCl (8), and are attributed largely to the pore-free nature of the films.

Films of ZnS have been deposited on ZnS, ZnSe and Ge. In these cases, film stoichiometry was considered to be an additional problem since the sticking coefficient of sulphur from an S<sub>2</sub> flux is likely to be less than that of Zn. Experiments have therefore been carried out to assess the importance of this effect by supplying additional sulphur (specifically S<sub>2</sub>) from a second source. This was conveniently provided by a Knudsen source containing sul-

AD-A161 247

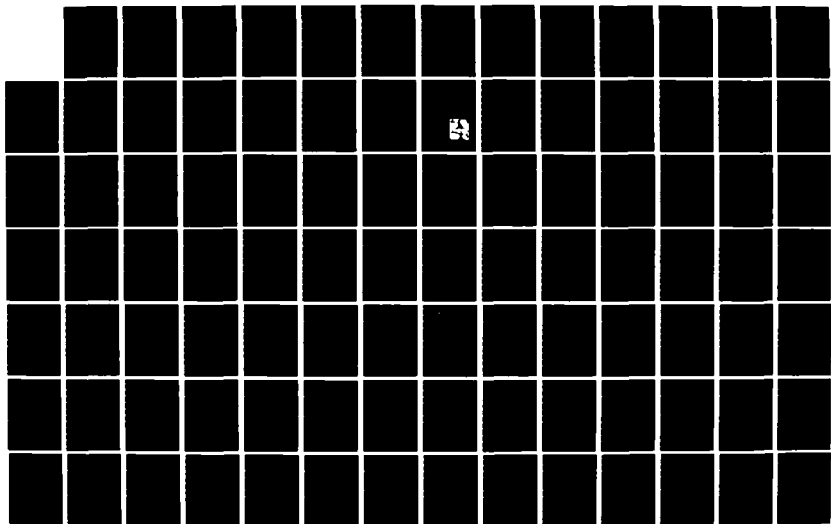
ON05 BASIC PROPERTIES OF OPTICAL MATERIALS SUMMARIES OF  
PAPERS(U) NATIONAL BUREAU OF STANDARDS GAITHERSBURG MD  
A FELDMAN MAY 85 NBS-SP-697 AFOSR-RR-85-0902  
AFOSR-ISSA-85-00032

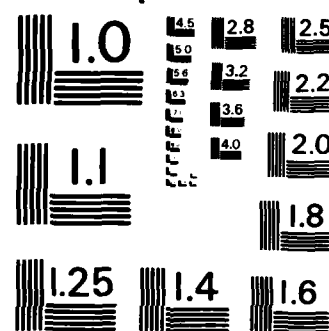
2/4

UNCLASSIFIED

F/G 20/6

NL





MICROCOPY RESOLUTION TEST CHART  
NATIONAL BUREAU OF STANDARDS-1963-A



sulphide which dissociates to produce  $S_2$  and Ag fluxes in the ratio of about  $10^4$ . Provided that this source is purely used as a 'top-up' measure, significant contamination of the ZnS with Ag is likely to be negligible.

ZnS films deposited in UHV at temperatures of  $50^\circ\text{C}$  without the supply of additional sulphur are slightly colored demonstrating a degree of nonstoichiometry in the material. However, laser damage thresholds are high -  $70\text{J}/\text{cm}^2$  (33nsec,  $1/e^2$  radius  $70\mu\text{m}$ ) when deposited on multispectral ZnS substrates and  $79\text{J}/\text{cm}^2$  when deposited on ZnSe. Comparative LIDT values for the uncoated substrates for these spot widths were  $193\text{J}/\text{cm}^2$  (ZnS) and  $66\text{J}/\text{cm}^2$  (ZnSe), respectively. The enhancement in LIDT observed for ZnS windows compared with that of ZnSe has been reported by others (9) and appears to be real despite the fact that the absorption coefficient of the ZnS at  $10.6\mu\text{m}$  ( $0.2\text{cm}^{-1}$ ) is significantly greater than that of the ZnSe ( $0.003\text{cm}^{-1}$ ).

When deposited at  $50^\circ\text{C}$  from fluxes containing an excess of  $S_2$ , ZnS films are no longer colored, demonstrating achievement of the correct stoichiometry. However the laser damage thresholds of such films so far examined are very similar to those produced without the sulphur excess, suggesting that the damage mechanism is dependent on factors other than the degree of optical absorption in the film.

#### References

1. D. A. Walsh and R. S. Bertke: Proc. Boulder Laser Damage Symposium 271 (1977).
2. D. F. O'Brien: Proc. Boulder Laser Damage Symposium 276 (1977).
3. K. H. Guenther and H. K. Pulker: Appl. Optics 15, 2992 (1976).
4. H. K. Pulker: Thin Solid Films 58, 371 (1979).
5. H. K. Pulker: Proc. SPIE 325, 84 (1982).
6. K. L. Lewis and J. A. Savage: Proc. Boulder Laser Damage Symposium (1983).
7. K. L. Lewis, J. A. Savage, A. G. Cullis, N. G. Chew, L. Charlwood and D. W. Craig: Proc. Boulder Laser Damage Symposium (1984).
8. A. Golubovic, J. Fitzgerald, I. Berman, J. Bruce, R. Bradbury, J. J. Comer, W. S. Ewing and H. G. Lipson: Proc. Boulder Laser Damage Symposium 271 (1976).
9. R. M. Wood, P. Waite and S. K. Sharma: Proc. Boulder Laser Damage Symposium (1983).

## A SIMPLE MODEL OF INHOMOGENEITY IN OPTICAL THIN FILMS

G. Deniau, F. Flory, and E. Pelletier  
Ecole Nationale Supérieure de Physique de Marseille  
Laboratoire Associé au C.N.R.S.  
13397 Marseille Cedex 13 - France

Most materials used in thin-film optical coatings exhibit optical inhomogeneity that is frequently so large that it cannot be neglected. The inhomogeneity is directly related to the layer microstructure that can be observed in electron micrographs. This leads directly to the consideration of a layer model that can be used to represent this inhomogeneity and can be used in calculations. Its usefulness decreases with its complexity and it should therefore be as simple as possible but nevertheless it should also reflect the real behavior of the films. The unprecedented precision with which multilayer deposition can now be controlled coupled with the possibility of accurate in situ property measurement makes the time ripe for a reexamination of this problem.

The simplest possible model, at first sight, would be a layer with a linear variation of index with optical thickness throughout the layer from rear to front surface, the front surface being identified as corresponding to the material deposited at the termination of the layer. A single extra parameter  $\Delta n/n$  can then be added to the other layer parameters usually used in calculations such as  $n$  and  $d$ .  $\Delta n$  represents the change in index from the initial to the final, or rear to front, surface and therefore a negative value of  $\Delta n/n$  implies an index that decreases as the layer thickness increases. While such a model appears simple, it leads to calculation difficulties and to ease these we modify the model so that it becomes a combination of ten sublayers of equal thickness, each being homogeneous and having indices that form a regular progression such that their indices are exactly that given by the intercepts of their center lines and the linear variation through the optical thickness of the layers. The parameter  $\Delta n/n$  can therefore still be used to represent this model.

To the refractive index we add a single value of extinction coefficient that remains constant throughout the ten sublayers.

We have already examined the validity of this model for normal incidence calculations. The calculation method developed by BORGOGNO et al. [1] is used for the extraction of the various model parameters from experimental measurements of  $R$  and  $T$ . Measurements on complete films can be well reproduced by the model [2]. Further, in situ measurements during deposition, which yield actual profiles of the index as a function of layer thickness, show that a linear variation of index is a reasonable assumption [3]. It is important that this study should be continued so that layers with as large a variation of index as possible might be studied and the validity of the model tested in such cases.

All this so far has dealt with near normal incidence. We have recently examined layers of  $\text{TiO}_2$  in both polarizations at  $45^\circ$  and been able to reproduce accurately the results using model parameters derived at normal incidence. Guided wave techniques give us another opportunity of testing the validity of the model at oblique incidence.

We used a method based on the measurement of the coupling angles or m-lines [4] [5]. The principle is simple. A prism coupler permits accurate measurement of the coupling angles of the various modes of the film and hence their propagation constants. If the inhomogeneous model is used for the layer then  $n$ ,  $\Delta n/n$  and the geometrical thickness can be extracted from these constants. The calculations are fairly complicated and involve successive approximations and it is not always possible to find a unique solution. Most of our work so far has been with TE waves. Provided we have used fairly thick layers ( $nd \approx 6$  to  $8 \lambda/4$ ), the values of index gradient that have been obtained show very satisfactory agreement with measurements made by the other techniques.

There can sometimes be an ambiguity in the sign of  $\Delta n/n$  but this can very readily be resolved by the use of classical spectroscopy. When the layers are rather thinner ( $nd \approx 4$  to  $6 \lambda/4$ ), two modes only can be observed, insufficient to determine  $n$  and  $\Delta n/n$  simultaneously. It is possible to use the value of  $\Delta n/n$  obtained by spectrometry and calculate  $n$  and  $d$  when excellent agreement with the other measurements of these parameters is obtained. When TM measurements are added to the TE, the interpretation becomes still further complicated and an anisotropy of the index as well as inhomogeneity becomes detectable in some materials such as titanium oxide. It should be stressed that the guided wave measurements are effectively at very high angles of incidence. We conclude that the layer model works well. The next step is to consider the inclusion of anisotropy.

- [1] J. P. Borgogno, B. Lazarides, E. Pelletier, *Applied Optics*, 21, 4020-4029, (1982).
- [2] J. P. Borgogno, F. Flory, P. Roche, B. Schmitt, G. Albrand, E. Pelletier, H. A. MacLeod, *Applied Optics*, 23, 3567-3570, (1984).
- [3] F. Flory, B. Schmitt, E. Pelletier, H. A. Macleod, *Proc. SPIE*, vol 401, 109-116, (1983).
- [4] P. K. Tien, *Applied Optics*, 10, 2385-2389, (1971).
- [5] M. Olivier, J. C. Peuzin, *Applied Phys. Lett.* 32, 386-388, (1978).

## OPTICAL PROPERTIES OF DIAMONDLIKE CARBON FILMS ON SEMICONDUCTORS

George H. Bu-Abbud,<sup>1,2</sup> Joel D. Lamb,<sup>1</sup> and J. E. Oh<sup>1</sup>  
Department of Electrical Engineering, University of Nebraska  
Lincoln, NE 68588-0511  
and  
John A. Woollam<sup>1,2,3</sup>  
Universal Energy Systems  
Dayton, OH 45432

Diamonlike carbon (DLC) films have been described by various authors as being hard, resistant to various chemicals, highly insulating, and adherent to a wide variety of materials (1). We have recently been investigating the usefulness of these materials in various applications including dielectrics for integrated circuits and coatings for optical (especially infrared) materials (2-4). The purpose of the present paper is to describe the optical properties of DLC films deposited on several technologically important semiconductors. Specifically, we have used spectroscopic ellipsometry and absorption spectroscopy to determine the index of refraction and extinction coefficient over the wavelength range from 220 nm to 3.39 microns. Substrate materials include flat, polished, oriented single crystals of silicon, indium phosphide, cadmium telluride, mercury cadmium telluride, germanium, and quartz.

All substrate materials are cleaned in trichlorethylene, acetone, methanol, deionized water, and blow dried with nitrogen gas, prior to insertion in the DLC deposition system. The deposition chamber is a small diffusion pumped (base pressure  $<2 \times 10^{-6}$  torr) bell jar which contains the parallel plate, capacitor-coupled rf plasma system. The rf generator operates at a frequency of 136 MHz which is tuned such as to deliver up to 100 watts to the plasma. The electrode on which the sample is placed can be electrically biased up to several hundred volts, and can be heated to several hundred degrees C, as well.

The plasma is a mixture of hydrocarbon and argon gases operating in the millitorr pressure range. Usually the hydrocarbon is methane but methane, propane, and ethane were used as well. Deposition rates are on the order of 50 Angstroms per minutes, and thicknesses are usually in the range from 300 Angstroms to 2000 Angstroms.

Routine measurements of absorption vs wavelength are made, using quartz substrates and a uv-vis spectrometer. From these data we find that the optical bandgap is in the 2 to 3 electron volt range, depending on deposition parameters and hydrocarbon gas. The highest bandgap is 2.8 electron volts.

1. Supported by Grant NAG-3-154 from NASA Lewis Research Center.
2. Supported by Contract DAAG-46-84-C-0057 from the Army Materials and Mechanics Research Center.
3. Also: Department of Electrical Engineering, University of Nebraska.

A rotating analyzer automated spectroscopic ellipsometry is used to determine the index of refraction and extinction coefficient as a function of wavelength (5). Data from a typical sample are shown in Figure 1. Note that the index of refraction is near 2.0, and the extinction coefficient shows a rapid rise starting in the range of 550 to 600 nm. A plot of the square root of absorption coefficient times photon energy vs photon energy yields a straight line with an intercept of 2 eV (equal to the optical gap) for this sample.

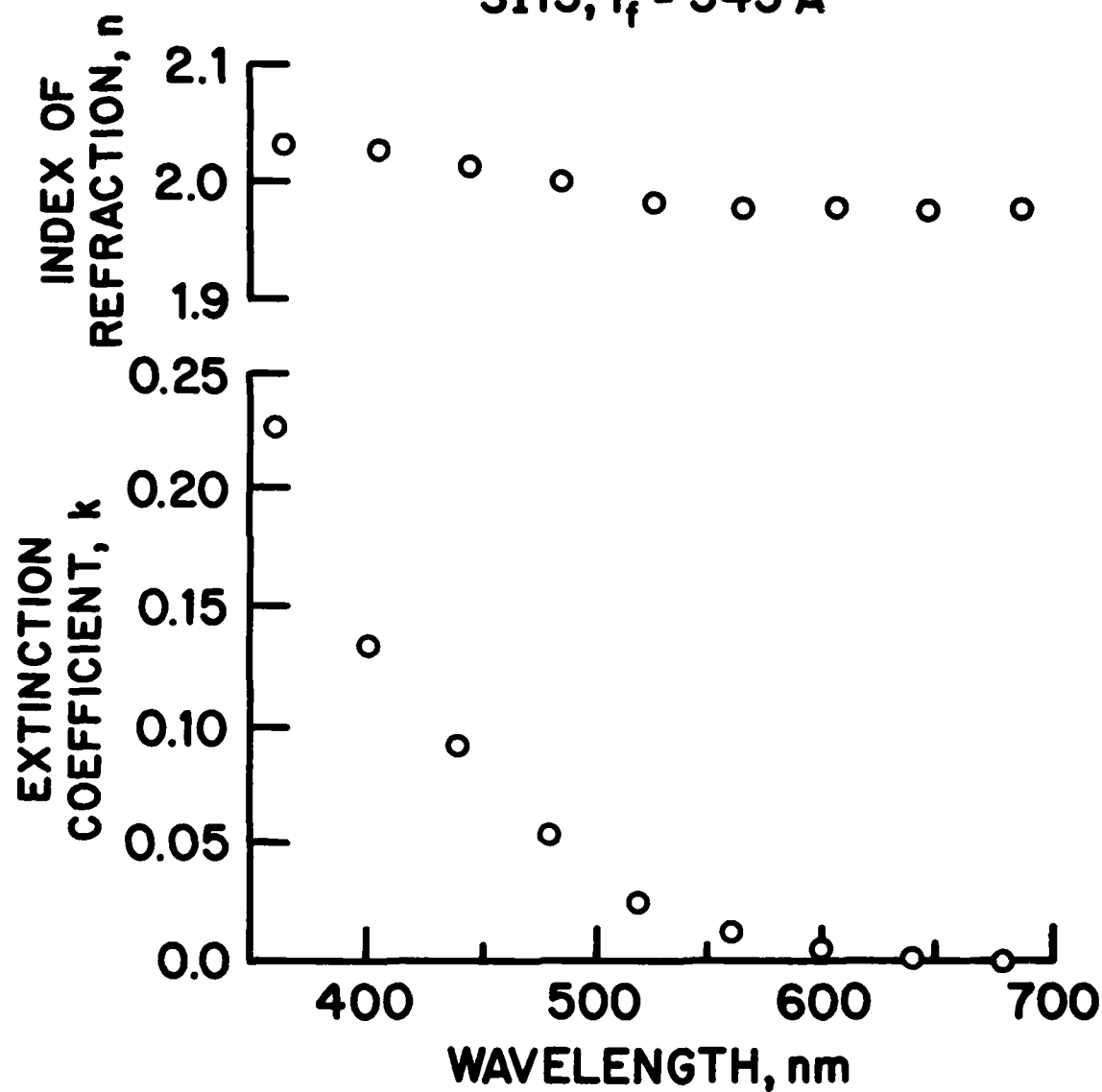
The Bruggeman effective medium approximation is used to analyze the spectra. Constituent media are assumed to be diamond, graphite, polyethylene, and voids. The general conclusion is that, DLC films are not mixtures of constituents, rather that DLC is a unique material with a unique band structure and optical properties. Data in the ultraviolet are needed to gain further information on interband transitions in these interesting materials.

#### References:

1. Workshop on Diamond-Like Carbon Coatings, BDM Corporation Technical Report BDM/A-82-242-TR under DARPA Contract MDA OP 3-81-C-013.
2. J.A. Woollam, V. Natarajan, J. Lamb, A.A. Khan, G.H. Bu-Abbud, D. Mathine, D. Rubin, and R.O. Dillon, Thin Solid Films, 119, 121 (1984).
3. R.O. Dillon, J.A. Woollam, and V. Katkamant, Phys. Rev. B15, 7229 (1983).
4. A.A. Khan, J.A. Woollam, and Y. Chung, J. Appl. Phys. 55, 4299 (1984).
5. D.E. Aspnes, and A.A. Studna, Applied Optics 14, 220 (1975).

## DLC ON SILICON

SI13,  $t_f = 343 \text{ \AA}$



Index of refraction and extinction coefficient vs. wavelength for methane rf plasma deposited DLC on silicon.

## TEMPERATURE DEPENDENT OPTICAL PROPERTIES OF SILVER SULFIDE THIN FILMS

R.L. Burton, H. Buhay, M. Nisar, J.L. Grieser, N.P. Murarka  
IIT Research Institute  
Microwave and Electro-Optics Department  
Chicago, Illinois 60616

The silver chalcogenide,  $\text{Ag}_2\text{S}$ , exhibits a crystallographic phase transition at  $T_c = 180^\circ\text{C}$  which affects its optical properties. The stable phase below  $T_c$ ,  $\beta\text{-Ag}_2\text{S}$ , has an ordered monoclinic structure with the sulfur ions arranged in a body centered cubic lattice. The stable phase above  $T_c$ ,  $\alpha\text{-Ag}_2\text{S}$ , is cubic with the B.C.C. arrangement of sulfur ions; however, the silver ions are randomly distributed on the interstices occupying 4 of 42 available point sites of the unit cell [1,2]. As the temperature increases the electrical conductivity increases by three orders of magnitude [3,4] due to the phase change. In the high temperature phase, excess silver atoms act as electron donors.

The infrared properties of the  $\beta$ -phase can be accounted [5] for by a fundamental absorption edge with a band gap energy  $E_g = 0.6\text{--}0.9\text{ eV}$  [5]. In this phase it transmits through much of the infrared ( $200\text{ cm}^{-1}$  to  $6000\text{ cm}^{-1}$ ). In the  $\alpha$ -phase, a well-defined plasma absorption edge forms [5] with a plasma frequency of approximately  $3300\text{ cm}^{-1}$ . In view of these bulk properties, thin films of silver sulfide may be useful for specialized applications.

Flash evaporation techniques for synthesizing  $\text{Ag}_2\text{S}$  thin films have been reported [1,2,6]. In this work results are presented for films prepared by a triode D.C. sputtering process which has been found to provide greater control and produced superior films. Sputtering targets used were made by hot pressing  $\text{Ag}_2\text{S}$  powder. Typical deposition rates were  $0.5\text{ }\mu\text{m/hr}$ . Several films were prepared in this manner on GaAs substrates.

Optical transmittance and reflectance measurements were made using a Perkin-Elmer Model 580B spectrophotometer. For these measurements the films were mounted in a vacuum furnace and the temperature varied using an Omega Model CN2010 programmable controller. The typical transmittance for a  $0.94\text{ }\mu\text{m}$  film at  $26, 160, 165, 170$  and  $190^\circ\text{C}$  are shown in Figure 1. Absorption due to  $\text{CO}_2$  appears in the spectra at  $\sim 2350\text{ cm}^{-1}$  since the instrument was not purged. Because  $\text{Ag}_2\text{S}$  transmits infrared radiation, interference fringes can be seen in

the spectra. Absorption due to free carriers is the dominant feature above  $T_c$ . Figure 2 shows the front surface reflectance at the same five temperatures. The most important feature of these curves is the metal-like plasma edge at low frequencies. As the temperature increases, a greater number of silver atoms become ionized into electron donors. This raises the electron concentration and causes the plasma edge to shift to higher frequencies. Absorption due to free carriers is lower at higher energies and all of the curves approach similar values for frequencies above  $4000\text{ cm}^{-1}$ .

From the optical data, the frequency dependence of the refractive index  $n$  and extinction coefficient  $k$  were computed by two methods. The first method involved a nonlinear regression analysis which compared the R and T spectra of the films to calculated values based on a Drude dispersion model [7]. The second method makes use of a technique of bivariate optimization adapted from the literature [8]. This method uses the transmittance, reflectance and back surface reflectance to find values of  $n$  and  $k$  that directly satisfy these measurements at every data point. The results of the two methods agreed excellently, except for small regions of the spectra where the bivariate method fails to find a solution.

The results for  $n$  and  $k$  are shown in Figures 3 and 4 respectively. The figures can be interpreted as describing the refractive index and extinction coefficient due to free carrier absorption at low frequencies and converging asymptotically toward  $n = 3.00$  and  $k = 0.0$  at  $4000\text{ cm}^{-1}$ . Of course the fundamental absorption edge starts to exhibit influence on  $n$  and  $k$  at frequencies above  $4000\text{ cm}^{-1}$ .

By assuming an effective mass value equal to the bulk value [9],  $m^* = 0.24 m_e$ , the electron concentration,  $N$ , and mobility,  $\mu$ , can be computed from the Drude parameters  $\omega_p$ ,  $\tau$ , and  $\epsilon_\infty$ . The results for  $N$  and  $\mu$  are given in Table 1. The film electron mobility is fairly constant with respect to temperature except for  $160^\circ\text{C}$  at which the observed plasma edge was difficult to fit with accuracy. Bulk values for electron mobility are in the range  $160\text{--}190\text{ cm}^2/(\text{V}\cdot\text{sec})$  [1]. The thin film mobilities were lower, typically  $\mu = 130\text{ cm}^2/(\text{V}\cdot\text{sec})$ , and varied for different films of  $\text{Ag}_2\text{S}$ . The electron concentration versus temperature is shown in Figure 5. This data agrees well with the bulk value [9] of  $3.6 \times 10^{19}$



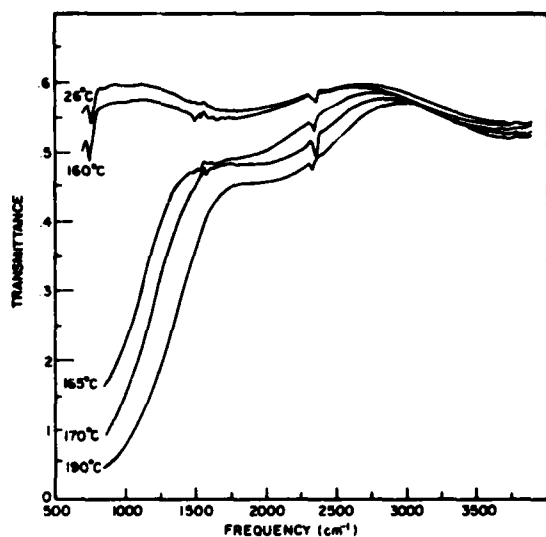


Figure 1. Transmittance of a silver sulfide film on a GaAs substrate at several temperatures.

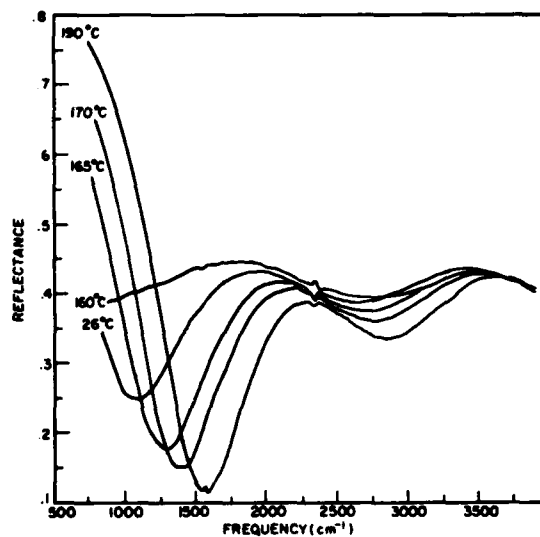


Figure 2. Reflectance of a silver sulfide film on a GaAs substrate at several temperatures.

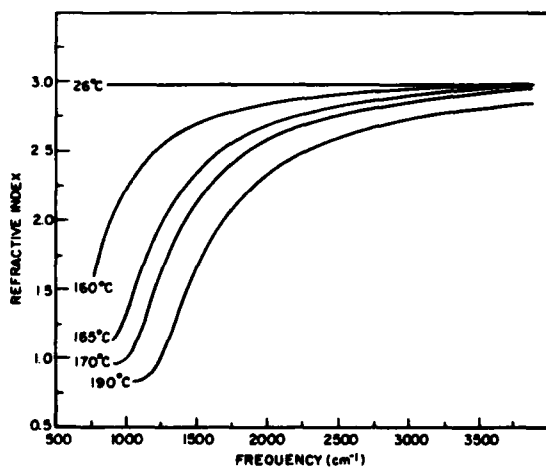


Figure 3. Refractive index of a silver sulfide film at several temperatures.

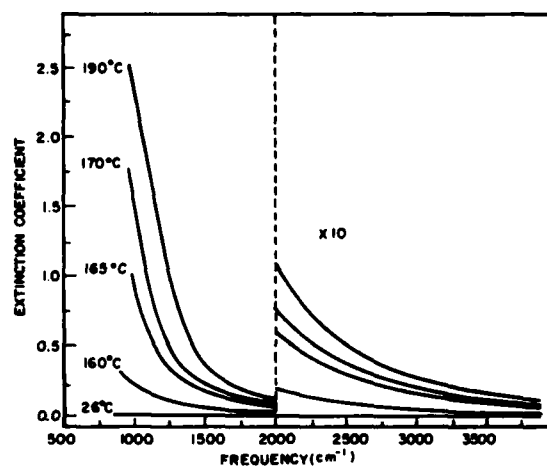


Figure 4. Extinction coefficient of a silver sulfide film at several temperatures.

( $\text{cm}^{-3}$ ) at  $185^\circ\text{C}$  for silver rich  $\text{Ag}_2\text{S}$ . Thus, it is concluded that the films are silver rich, although the target was initially stoichiometric. The latter may be accounted for by sublimation of sulfur at the surface of the target during the sputtering process.

Table 1		
$T(^{\circ}\text{C})$	$N(\text{cm}^{-3})$	$\mu \frac{\text{cm}^2}{\text{V-sec}}$
160	$1.21 \times 10^{19}$	180
165	$2.52 \times 10^{19}$	132
170	$3.13 \times 10^{19}$	136
180	$3.70 \times 10^{19}$	142
190	$4.03 \times 10^{19}$	134
200	$4.28 \times 10^{19}$	127

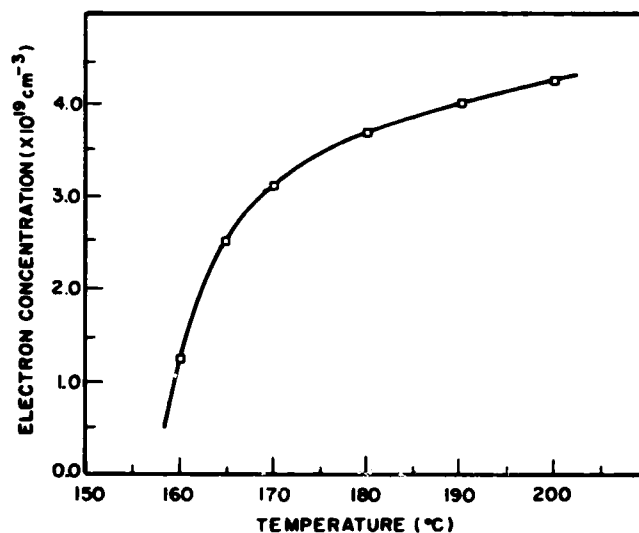


Figure 5. Electron concentration,  $N$ , as a function of temperature.

### References

1. H.P. Geserich and W. Suppanz, *Phys. Status Solidi* **35**, 381-387 (1969).
2. T.Y. Hsu, H. Buhay, N.P. Murarka, *Proc. SPIE* **259**, 38 (1980).
3. C. Wagner, *J. Chem. Phys.* **21**, 1819-1827 (1953).
4. M.H. Hebb, *J. Chem. Phys.* **20**, 185-190 (1952).
5. P. Bruesch, and J. Wulfschleger, *S.S.Comm.* **13**, 9-12, (1973).
6. T. Fleisch and R. Abermann, *Thin Solid Films* **42**, 255-263 (1977).
7. F. Wooten, *Optical Properties of Solids* (Academic Press, New York, 1972).
8. R.C. McPhedran, L.C. Botten, D.R. McKenzie and R.P. Netterfield, *Appl. Opt.* **23**, 1197-1205 (1984).
9. H.H. Dörner, H.P. Geserich, and H. Rickert, *Phys. Status Solidi* **37**, K85 (1970).

# MOLECULAR BONDING IN OPTICAL FILMS DEPOSITED BY ION-BEAM SPUTTERING\*

C. Y. She<sup>+</sup>

Physics Department, Colorado State University  
Ft. Collins, Colorado 80523

## Introduction

Recent demands in low-loss and low-scatter optical coatings have stimulated considerable activities in the investigation of dielectric films with high refractive index and low absorption. Of particular interest are new deposition methods on the one hand and novel diagnostic techniques on the other, which could be employed to elucidate the nature and property of the film at molecular levels. Over the past two or three years, work on ion-beam-sputter deposition has yielded dense dielectric films, such as titanium oxide, which are thought to be amorphous having desirable optical and mechanical properties.<sup>1</sup> More recently, the conventional technique of Raman spectroscopy has been modified and demonstrated to be a simple and effective method, satisfying the apparent need for evaluation of submicron-thick optical coatings.<sup>2</sup>

Despite the great success in crystalline solids, Raman spectroscopy has been applied only a few times, for example, to interrogate a semiconductor silicon film<sup>3</sup> via a very strong Raman line at  $520\text{ cm}^{-1}$  and an interfacial composition of an Al-GaAs structure;<sup>4</sup> encapsulated nonabsorbing films were, however, regarded as too weak for Raman study. Up to this point, x-ray diffraction, which works well only for thick films,<sup>5</sup> was used for structural characterization; its required long measurement time, typically hours, however, leaves much to be desired. Using a  $180^\circ$  backscattering geometry, Pawlewicz et al. recently were able to use Raman spectroscopy to characterize crystalline single-layer dielectric coatings with a measurement time a factor of 100 times less than that required for the x-ray diffraction method.<sup>6</sup> Very recently, we recognized that a major limiting factor in Raman study of thin films is the interference resulting from the Raman signal of the substrate. Using an oblique-incident technique, we were able to suppress this substrate interference by a factor of 50, making Raman spectroscopy a simple but effective nonintrusive method for structural characterization of submicron-thick films.<sup>2</sup> An amorphous coating was then characterized for the first time with a measurement time of only 500 sec.

Using Raman spectroscopy, we have studied the microscopic structure and molecular bonding of ion-beam sputtered optical films by the method of thermal and laser annealing. Transformation of amorphous titania coatings to crystalline anatase and/or rutile structures has been observed. We report these results and discuss their implications in this paper.

## Sample Preparation

Titania ( $\text{TiO}_2$ ) films are fabricated by sputtering a metallic Ti target with  $\text{O}_2$  and Ar ions from a Kaufman-type ion source.<sup>1</sup> The deposition chamber is

shown in Fig. 1. The secondary ion source is used for pre-sputtering and cleaning of the substrate. The sample (substrate) holder is rotating during the deposition process for film uniformity. Although the sample holder may be cooled or heated in principle, it was not controlled for the coatings used in this study. The temperatures were monitored during deposition, typically from 20°C to 170°C, resulting in amorphous titania films.

#### Laser Annealing

For laser annealing study,<sup>7</sup> a 240-nm-thick TiO<sub>2</sub> film was deposited on a 2-in-diameter <100> Si wafer by ion-sputtering, as described above. The coating was then laser annealed with a scanned Ar<sup>+</sup> laser beam 50 μm in diameter over 5 mm x 5 mm squares at different laser powers and scan speeds. Raman spectra of the laser annealed squares were recorded. Evidences of structural transformation became clear when these spectra are compared.

A typical Raman spectrum of TiO<sub>2</sub> as deposited on a Si wafer is shown in Fig. 2(a). Besides the strong Si peak at 520 cm<sup>-1</sup> and a weak feature at 300 cm<sup>-1</sup>, Raman spectra of the coating before annealing or of the areas between annealed squares are rather featureless indicative of amorphous structure. Raman spectra of the annealed titania with 6 W of laser power at different scan rates, 50 cm/s, 30 cm/s, and 15 cm/s are shown in Figs. 2(b)-2(d), respectively. Anatase peaks at 144 cm<sup>-1</sup>, 400 cm<sup>-1</sup>, and 635 cm<sup>-1</sup> can be seen clearly. As the laser annealing time at a given spot is increased by reducing the scan rate, crystalline anatase structure is more fully developed. Raman spectra of annealed titania coating on a Si wafer for shifts between 300 cm<sup>-1</sup> to 700 cm<sup>-1</sup>, at different laser powers, are shown in Fig. 3. It is quite evident from this figure that the amorphous coating has partially transformed into microcrystals of anatase structure after annealing. At higher annealing laser intensity, Raman spectra reveal the presence of rutile microcrystals in the coating as well. Qualitatively, this laser annealed amorphous-anatase-rutile transformation is consistent with the structure dependence of films on deposition substrate temperature.<sup>5</sup>

Compared to the as-deposited film of Fig. 2(a), these annealed samples show much higher background scattering which appears to be dependent on annealing laser intensity, but not on the scan rate. Visual inspection of annealed areas with a Nomarsky microscope indicates that with this beam diameter, the laser damages occur at 6 W and get worse at higher powers. As the annealing power is increased from 5 to 8 W at a constant scan rate, the anatase 144 cm<sup>-1</sup> peak intensity first grows and then decreases as rutile microcrystals begin to develop in the coating. With high annealing laser power, the film gets damaged and the background signal increases. This background is a measure of the surface scattering of the film. Even under these high scattering conditions, Raman spectroscopy is evidently still an effective probe for structural characterization of submicron-thick optical coatings.

#### Thermal Annealing

Amorphous titania films used for thermal annealing were deposited on Corning 7059 glass under different conditions. Type A films were obtained with lower ion beam current (0.4-0.8 mA/cm<sup>2</sup>) while type B films were made with beam

current greater than  $1 \text{ mA/cm}^2$ . The thicknesses are 2233 Å and 3117 Å, respectively, for type A and B films. As to be shown below, these films, although optically identical as deposited, crystallize differently upon thermal annealing. The as-deposited coating was annealed in an air furnace sequentially at 200, 300, 350, 400, 450, 500, and 600°C. At each temperature, the coating was annealed for 20 min in the furnace. It is then cooled slowly to room temperature for Raman scattering and other experimentation before the film is annealed to the next higher temperature.

Figure 4 shows the Raman spectra of these films subjected to annealing at various temperatures. Due to the lack of thickness, Raman spectra of the as-deposited films (20°C) are obscured by the broad features of the substrate at  $480 \text{ cm}^{-1}$  and  $790 \text{ cm}^{-1}$ ; its broad scattering shoulder is indicative of the amorphous nature of the film.<sup>2</sup> The spectra of annealed films at 200°C (not shown) and 300°C appear to be identical. For Type A films, upon reaching 350°C, there is a small bump at  $612 \text{ cm}^{-1}$  without any hint of the  $144 \text{ cm}^{-1}$  feature. This indicates crystallization with some rutile microcrystals, but no anatase. At 400°C, evidence of anatase is quite clear by the appearance of the peaks at  $144 \text{ cm}^{-1}$  and  $635 \text{ cm}^{-1}$  and additional shoulders at  $400 \text{ cm}^{-1}$  and  $515 \text{ cm}^{-1}$ . The concurrent presence of rutile growth is evident by the weak peaks at  $400 \text{ cm}^{-1}$  and  $612 \text{ cm}^{-1}$ . Subsequent annealing at 450°C, 500°C (not shown), and 600°C shows that the anatase peaks become more prominent while the rutile peaks remain constant. At 600°C and higher temperatures, the Raman intensity tends to be unchanged signifying the completion of the crystallization process. As shown in Fig. 4(b), a Type B film retains its as-deposited amorphous features up to 350°C, where it crystallizes into rutile structure without any anatase. Such evidence again comes from the appearance of the  $440 \text{ cm}^{-1}$  and  $612 \text{ cm}^{-1}$  rutile peaks. When the annealing temperature is increased further to 400 and 600°C, the rutile signal intensity increases along with the two-photon Raman modes of rutile at  $250 \text{ cm}^{-1}$  and  $690 \text{ cm}^{-1}$ .

If a similar Type A film is heated directly to 600°C, bypassing the lower temperature steps, it results in anatase crystallization without any detectable rutile, as illustrated in Fig. 5(a). If these Type A anatase films were further heated to 900°C or above, where rutile structure is thermodynamically more favorable,<sup>5</sup> the anatase films transform into anatase-rutile structure with rutile dominance, as shown in Fig. 5(b). The high background above  $500 \text{ cm}^{-1}$  is due to partial melting of the glass substrate.

The elastic light scattering of both types of films at various annealing temperatures has also been recorded simultaneously with the Raman spectra of Fig. 4. Using the scattering from MgO as a calibration, the percentage scattering can be determined. A dramatic two-order of magnitude increase in elastic scattering accompanying the film crystallization near 400°C has been found;<sup>8</sup> it suggests degradation upon heating and has obvious implications for use of these films as coatings for high-power laser mirrors.

Macroscopic optical transmission measurements of these coatings have also been made at each annealing temperature. An abrupt rise in refractive index and extinction coefficient has been found at a temperature between 300°C to 400°C for both types of films,<sup>8</sup> indicating crystallization at around 350°C. However, the microscopic differences between the two types of the films can be deduced only from the Raman data.

## Conclusions

Raman spectroscopy has been applied to probe the molecular structure of sub-micron-thick titania films deposited by ion-beam sputtering. Low-scattered amorphous optical coatings of different types have been characterized by Raman scattering for the first time. Under laser or thermal annealing, these amorphous coatings crystallize into microcrystals of anatase or rutile depending upon conditions of film deposition and subsequent annealing. Because it is a microscopic probe, Raman spectroscopy is capable of distinguishing different types of coatings with similar optical properties.

\*This work is supported by the Air Force Weapons Laboratory under Contract F29601-83-K-0079.

<sup>†</sup>On sabbatical at the University of Maryland and Laboratory for Physical Sciences, College Park, MD.

## Acknowledgement

The author acknowledges the contributions of L. S. Hsu, R. Rujkorakarn, and R. Solanki, who perform the experiment presented here.

## References

1. J. R. Sites, P. Gilstrap, R. Rujkorakarn, Opt. Engr. 22, 477 (1983).
2. L. S. Hsu, C. Y. She and G. J. Exarhos, Appl. Opt. 23, 3049 (1984).
3. S. R. Brueck, B-Y Tsaur, J. C. C. Fan, D. V. Murphy, T. F. Duetsch and P. J. Silversmith, Appl. Phys. Lett. 40, 895 (1982).
4. G. P. Schwartz and A. Y. Cho, J. Vac. Sci. Technol. 19, 607 (1981).
5. L. M. Williams and D. W. Hess, J. Vac. Sci. Technol. A1, 1810 (1983).
6. W. T. Pawlewicz, G. J. Exarhos and W. E. Conaway, Appl. Opt. 22, 1837 (1983).
7. L. S. Hsu, R. Solanki, R. Collins and C. Y. She, Appl. Phys. Lett. 45, 1065 (1984).
8. R. Rujkorakarn, L. S. Hsu and C. Y. She, 16th Boulder Damage Symposium, NBS special publication (to be published).

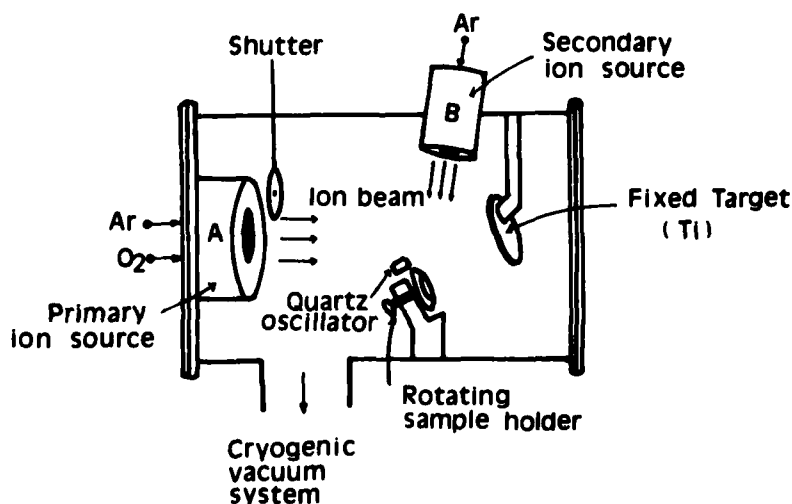


Fig. 1. Chamber for ion-beam sputtering of films.

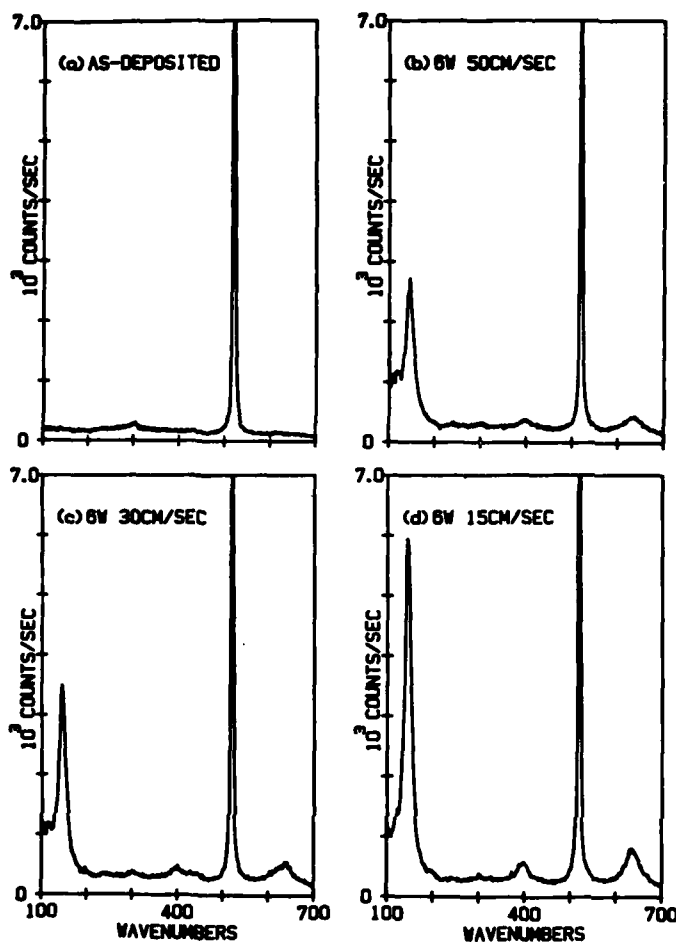


Fig. 2. Raman spectra of titania coatings on a Si wafer. (a) As deposited by ion sputtering showing amorphous structure. (b), (c), and (d) are results after annealing with a 6 W beam at different scan rates. Peaks at 300 and 520  $\text{cm}^{-1}$  are due to Si and peaks at 144, 400, and 635  $\text{cm}^{-1}$  are due to  $\text{TiO}_2$  in anatase phase.

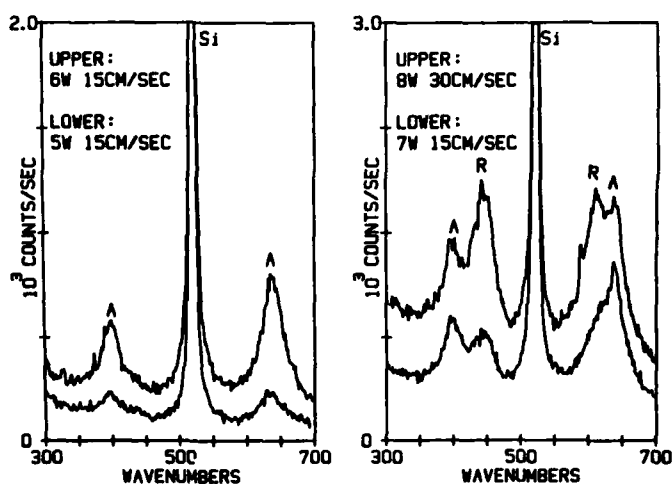


Fig. 3. Raman spectra of laser annealed  $\text{TiO}_2$  coatings on a Si substrate. Besides the strong Si peak at 520  $\text{cm}^{-1}$ , Raman spectrum of the coating before annealing is featureless (not shown) in this intensity scale. After annealing at different power levels, Raman peaks indicative of crystalline anatase (labeled A) and rutile (labeled R) structures are clearly evident.

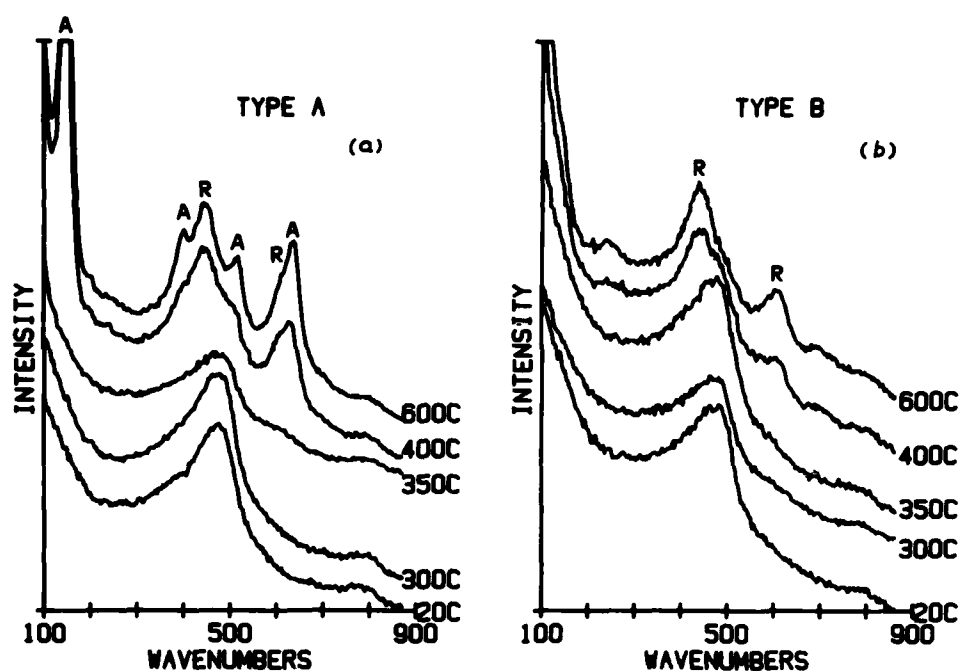


Fig. 4. Raman spectra for coatings annealed at various temperatures. (a) type A/glass and (b) type B/glass.

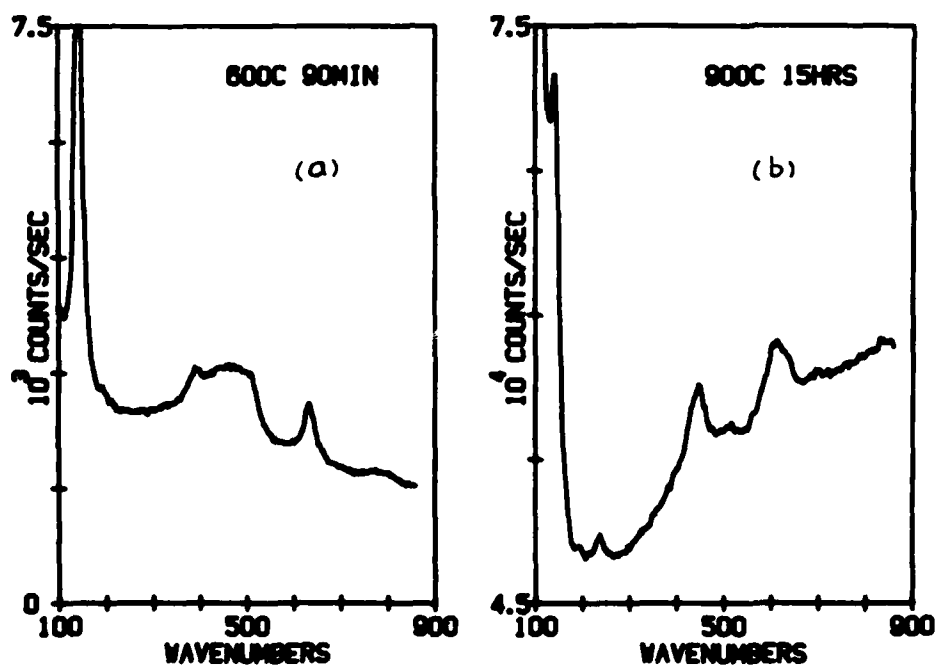


Fig. 5. Raman spectrum for type A/glass coatings annealed directly at (a) 600°C to form anatase and (b) 950°C to form anatase-rutile mixture.



## HIGHLY TRANSPARENT METAL FILMS: Pt ON InP

D. E. Aspnes

Bell Communications Research, Inc., Murray Hill, New Jersey 07974

Adam Heller, J. D. Porter, T. T. Sheng, and R. G. Vadimsky

AT&T Bell Laboratories, Murray Hill, New Jersey 07974

Highly transparent metal films are of potential interest in a number of areas of science and technology including light detection, photovoltaic energy conversion, catalysis, and photoelectrochemistry. In studies of light-activated hydrogen evolution on platinized semiconducting photocathodes,<sup>1</sup> it was discovered that the quantum yield of hydrogen-evolving semiconducting electrodes did not decline significantly with increasing platinum coverages, even for metric thicknesses as much as 50 nm where 99.9% of the transmitted light should have been absorbed. The observation of this anomalous transparency stimulated further investigation, and in a recent preliminary report<sup>2</sup> we described the preparation and characterization of the first substantially transparent supported metal films of significant thicknesses. We found that the essential characteristics giving rise to substantial transparency in metal films were porosity and microstructure, and that by controlling these properties, absorption and reflection losses could almost be eliminated. Here, we discuss in more detail the physical principles involved and present further results on Pt film/p-InP system.

The obvious reason that porosity reduces absorption losses in metal films is that porous films have less absorbing material per unit volume than dense films of the same thickness. Front-surface reflection losses also decrease because the refractive index of a film decreases along with its metal packing fraction,  $f_m$ . But the major factor in reducing absorption losses is microstructure, that is, spatial inhomogeneities on the scale of approximately 1 to 25 nm, or small compared to the wavelength of light in the medium. Losses can be reduced most effectively if the films are constructed of networks of small metal particles electrically isolated from each other. In physical terms, isolating the particles with insulating boundaries allows screening charge to develop at their surfaces. This screening charge excludes the photon fields from the metal particles and forces the fields into the spaces between the particles. To the extent that the fields do not penetrate the particles, absorption losses are reduced and transmittances correspondingly increased. The operation of wire-grid polarizers is based on the same principle. But in addition, the compression of photon fields into interstitial spaces between the metal particles causes a corresponding increase in the effective refractive index of the interstitial medium, permitting the metal films to perform simultaneously an antireflection function.

To illustrate these principles theoretically in simple terms, we consider a microscopically inhomogeneous two-phase composite in the Maxwell Garnett and Bruggeman approximations in the limit where the dielectric function of the metal,  $\epsilon_m$ , is much larger in magnitude than that,  $\epsilon_a$ , of the ambient. The ambient phase is assumed to fill the interstitial regions between particles. In this case it is straightforward to show from the

general two-phase effective medium expression<sup>3</sup> that the macroscopic dielectric function,  $\epsilon$ , of the composite is given by

$$\epsilon = \epsilon_a(1 + kf_m)/(1 - f_m) \quad (\text{Maxwell Garnett}); \quad (1a)$$

$$\epsilon = \epsilon_a(1/(1 - f_m/q)), \quad f_m/q < 1 \quad (\text{Bruggeman}); \quad (1b)$$

where  $q = 1/(1 + k)$  is the depolarization factor. The depolarization factor assumes the values 0, 1/3, 1/2, and 1 for no, isotropic 3-dimensional (spherical), isotropic 2-dimensional (cylindrical), and maximum screening, respectively. Minimum and maximum screening correspond to all boundaries parallel and perpendicular, respectively, to the applied field, and can be realized with laminar configurations. Note that  $\epsilon_m$  does not appear in either Eq. (1a) or (1b), and that  $\epsilon$  is increased over  $\epsilon_a$  by an amount depending on  $q$  and  $f_m$  up to the percolation thresholds of the respective microstructures. Thus to the extent that the magnitude of  $\epsilon_m$  is large compared to that of  $\epsilon_a$ , losses can be reduced to small fractions of those expected on the basis of bulk metal dielectric functions alone, and by controlling the metal packing fraction the refractive index of the film can be varied independently.

To establish the conditions under which transmittance of light into the substrate is optimized, it is necessary to work with the complete three-phase (semiconductor substrate-composite film-transparent ambient) model. The optical properties of this configuration can be expressed analytically<sup>4</sup> in terms of  $\epsilon_s$ ,  $\epsilon$ ,  $\epsilon_a$ , and  $d$ , where  $\epsilon_s$  is the substrate dielectric function, but the equations are cumbersome and better suited for numerical analysis. We therefore expand these equations to terms linear in  $d/\lambda$ , where  $\lambda$  is the wavelength of light in vacuo. Films encountered in practice are typically far too thick for this approximation to apply, but the expression nonetheless gives insight into the relative importance of screening and the ratio of metal to ambient dielectric functions. To first order in  $d/\lambda$ , the efficiency,  $\eta$ , of transmission through the film and all interfaces is given by

$$\eta \approx \frac{4n_a \text{Re}(n_s)}{|n_s + n_a|^2} \left\{ 1 + \frac{4\pi d}{\lambda} \frac{\text{Im}(n_s)[\text{Re}(\epsilon) - \epsilon_a] - \text{Im}(\epsilon)[\text{Re}(n_s) + n_a]}{|n_s + n_a|^2} \right\}, \quad (2)$$

where  $n_a^2 = \epsilon_a$ , etc. The first term in the numerator approximately describes the impedance-matching effect and the second absorption losses in the film. The first is always positive but vanishes if the dielectric function of the substrate is real; index-matching in this case becomes a quadratic function of  $d$ . The second is always negative, since absorption always represents a loss. Since  $n_s$  and  $n_a$  are essentially outside direct experimental control, the optimization strategy is to minimize film absorption by minimizing  $\text{Im}(\epsilon)$ .

If  $f_m$  is small enough to allow the Maxwell Garnett or Bruggeman expressions to be expanded to first order, then

$$\eta \approx \frac{4n_a \text{Re}(n_s)}{|n_s + n_a|^2} \left\{ 1 + \frac{4\pi d \epsilon_a f_m}{\lambda q |n_s + n_a|^2} \left[ \text{Im}(n_s) - \frac{\epsilon_a}{q |\epsilon_m|^2} \text{Im}(\epsilon_m(n_s + n_a)) \right] \right\}. \quad (3)$$

The efficiency is now optimized by maximizing both  $|\epsilon_m|$  and  $q$ . Since  $q = 1$  represents maximum screening, the importance of microstructure is immediately apparent.

We now consider a specific example that shows that the ideal conditions can be approached. A Pt film was electrochemically deposited on a previously prepared p-InP substrate in strong illumination under diffusion-limited conditions from a highly purified 1 M  $\text{HClO}_4$  solution containing  $1 \times 10^{-5}$  M Pt(IV) as  $\text{K}_2\text{PtCl}_6$ . Quantum efficiency measurements, performed using the sample as an actinometer to reduce protons in acid solution to neutral hydrogen, showed that the Pt film passed 92% of the incident light. Spectroellipsometric data for the dielectric response of the film, determined by solving the three-phase model implicitly, yielded  $d = 33.7 \pm 0.5$  nm and showed that the dielectric function of the deposited film was greatly reduced from that of the reference Pt spectrum (see Fig. 1). An independent analysis applied directly to the pseudoelectric function data yielded  $d = 32.6 \pm 0.8$  nm,  $f_m = 0.50 \pm 0.02$ , and  $q = 0.55 \pm 0.05$ . Scanning electron micrographs indicated that the surface was approximately 85% covered with spherical Pt particles about 50 nm in diameter. No fine structure was observable to the 20 nm resolution limit of the SEM, suggesting that the optical value of  $f_m$  was too small.

To resolve this discrepancy, we also examined the film by cross-sectional transmission electron microscopy. The results are shown in Fig. 2. These data revealed three levels of microstructure. The primary microstructure consisted of 2–10 nm microcrystals of dense Pt. the secondary microstructure consisted of linkages between these microcrystals to form branched chains. The tertiary microstructure consisted of collections of these chains into approximately spherical clusters of the order of 50 nm in diameter. The overall macrostructure was homogeneous, showing no detail under optical magnification. While an accurate quantitative comparison of the metal packing fractions determined independently by spectroellipsometry and by transmission electron microscopy is not feasible, the TEM results show that the spherical particles themselves are porous and have a complex microstructure with characteristic dimensions much smaller than  $\lambda$ . This observation explains why effective medium theory accurately describes the optical data under conditions where the small-dimensional assumption implicit in the quasistatic model is apparently violated. We suspect that a similar explanation may apply to many of the cases where apparent violations of the quasistatic dimensional limit also occur.

In these Pt films the various levels of microstructure are determined by interrelationships among the various metal nucleation and growth processes. The primary microstructure is principally related to the rate of lattice growth. The secondary microstructure depends on the rate of formation of viable nuclei on the surfaces of the growing microcrystals. The tertiary microstructure is determined by the number density and occupation rate of nucleation sites on the semiconductor substrate and by mass transport conditions in the ambient fluid established during film growth. The variables that control these growth processes are surface chemistry through solution composition, ion chemistry through solution complexes, mass transport rate, temperature, applied potential, and incident light intensity. We chose chemistries that tended to maximize nucleation and growth rate constants such as simple aquo coordination of interfaces and metal ions and low-to-moderate rates of mass transport so deposition took place under mass-transport-limited conditions established by a concentration gradient normal to the surface.

A detailed examination of effective medium theory shows that transparency for a given polarization direction comes at the price of poor dc conductance in that direction. This follows because nonconducting boundaries are needed for screening charge to develop. For the system studied here, high transmittance values in unpolarized light were achieved because electron transport occurred primarily along the surface normal, a consequence of the growth process involving transport of photoexcited electrons from the space charge region of the semiconductor to the surface of the growing film.

In many cases it is desirable, or even essential, to maintain a high dc conductance in a direction parallel to the surface. Here, the optimum configuration consists of parallel metal lines. The perpendicular polarization component passes virtually unattenuated, ignoring reflectance losses, while the parallel component is attenuated. Because transmittance is not improved significantly for non-normal incidence, some compromise between transmittance and dc conductance is necessary. While details will clearly depend on the specific situation, the transmittance will obviously be maximized by making the metal lines as thin as possible and using an overlying dielectric film for antireflection and protection of the microstructure.

## REFERENCES

1. A. Heller, *Science* 223, 1141 (1984).
2. J. D. Porter, A. Heller, and D. E. Aspnes, *Nature* (in press).
3. D. E. Aspnes, *Thin Solid Films* 89, 249 (1982).
4. R. M. A. Azzam and N. M. Bashara, *Ellipsometry and Polarized Light* (North-Holland, Amsterdam, 1977).

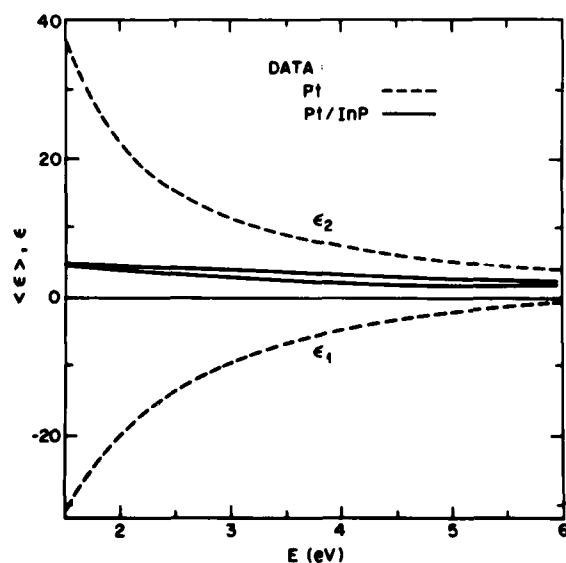


Fig. 1. Pseudodielectric function data for Pt and for Pt/InP.

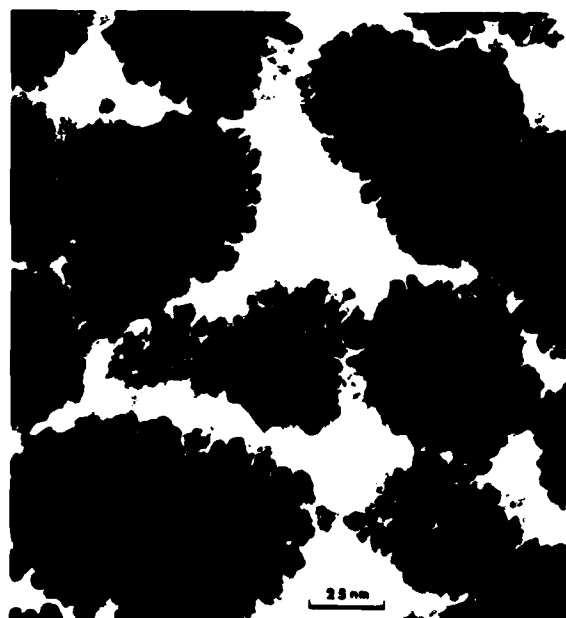


Fig. 2. TEM micrograph for the Pt/InP film of Fig. 1.

# Calculation of the Electronic Structure of $\text{As}_4\text{S}_4$ and $\text{As}_4\text{Se}_4$ Molecules

Davorin Babic and Sohrab Rabii  
Department of Electrical Engineering and  
Laboratory for Research on the Structure of Matter  
University of Pennsylvania  
Philadelphia, PA 19104

The recent developments in preparation of thin amorphous films of the arsenic chalcogenides by spin-coating from solution [1] have led to renewed interest in these materials for applications in the field of integrated optics as waveguides, couplers, or storage media. As part of our theoretical investigation of the electronic structure of these materials, we have undertaken to calculate the molecular structure for some of their existing molecules, namely  $\text{As}_4\text{S}_4$ ,  $\text{As}_4\text{Se}_4$ ,  $\text{As}_4\text{S}_6$  and  $\text{As}_4\text{Se}_6$ . In the present paper we report on our calculations for the first two molecules. Previous theoretical studies of these molecules include extended Huckel calculation on  $\text{As}_4\text{Se}_4$  [2], CNDO for  $\text{As}_4\text{S}_4$  and  $\text{As}_4\text{Se}_4$  [3], INDO for  $\text{As}_4\text{S}_4$  and  $\text{As}_4\text{Se}_4$  [4], and ab initio with Gaussian basis set for  $\text{As}_4\text{S}_4$  [5]. We have used the SCF-X $\alpha$ -scattered wave technique [6] to calculate the molecular energy levels, charge distributions, ionization potentials and

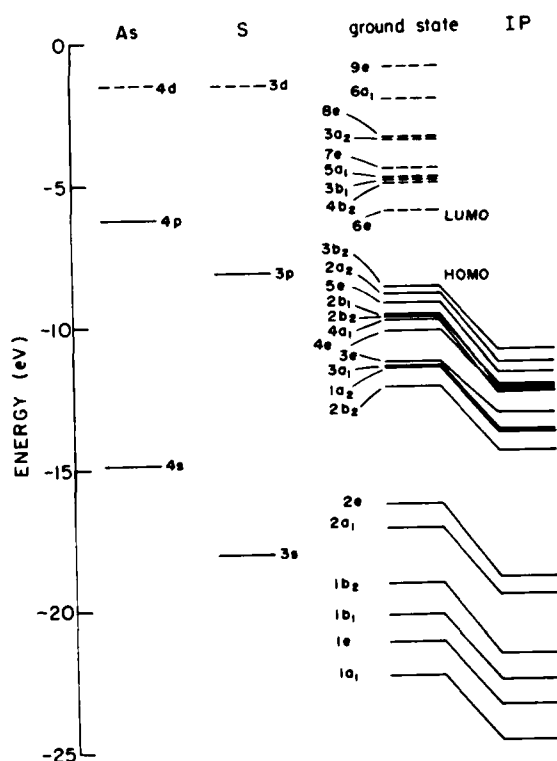
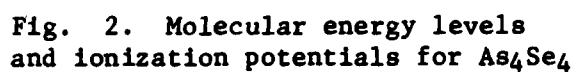


Fig. 1 Molecular energy levels and ionization potentials for  $\text{As}_4\text{S}_4$

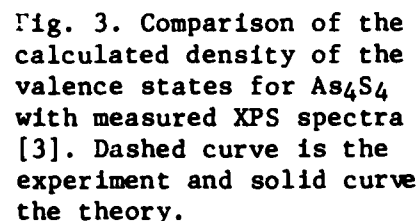
optical transition energies. Values of  $\alpha$  parameter for the exchange-correlation potential are taken from the work of Schwarz [7] and are 0.72475, 0.70665 and 0.70638 for S, As and Se respectively. The structural information for  $\text{As}_4\text{S}_4$  is taken from the gas-phase x-ray diffraction measurements of Lu and Donohue [8] and for  $\text{As}_4\text{Se}_4$  from the measurements of Goldstein and Paton on molecular crystals [9]. These molecules have the point group symmetry  $D_{2d}$ .

Figures 1 and 2 show the results of the ground state calculations for both molecules as well as the atomic calculations for the constituent atoms. In addition they show the ionization potentials for the occupied molecular levels calculated using the Slater's transition state concept [10]. The HOMO and LUMO for both molecules have  $b_2$  and  $e$  symmetries respectively. The HOMO is As-As bonding which is in agreement with [3] and its symmetry agrees with [5]. The charge distribution for LUMO is more



of a mixture of As and the chalcogen. The transition state concept was also used to calculate the transition energy for the allowed dipole transition between the HOMO and the LUMO. The energies are 2.73 and 2.59 eV respectively for  $\text{As}_4\text{S}_4$  and  $\text{As}_4\text{Se}_4$ . These values are consistent with the optical gaps of  $\sim 2.36$  and  $\sim 1.76$  eV for the  $\text{As}_2\text{S}_3$  and  $\text{As}_2\text{Se}_3$  glasses [11].

Since the corresponding solid phases of these compounds (realgar structure) are molecular crystals it is expected that a comparison of the theoretical results for the molecules are justified with the experimental measurement on the solid phase. We obtained a density-of-valence-states from our calculation by assigning to each state a Gaussian of width 0.5 eV and area equal to the degeneracy of the corresponding state centered at its ionization potential and adding the contributions to obtain a continuous curve. The results are compared in Figure 3 and 4 with the valence band XPS measurement of Salaneck et al [3]. As we can see



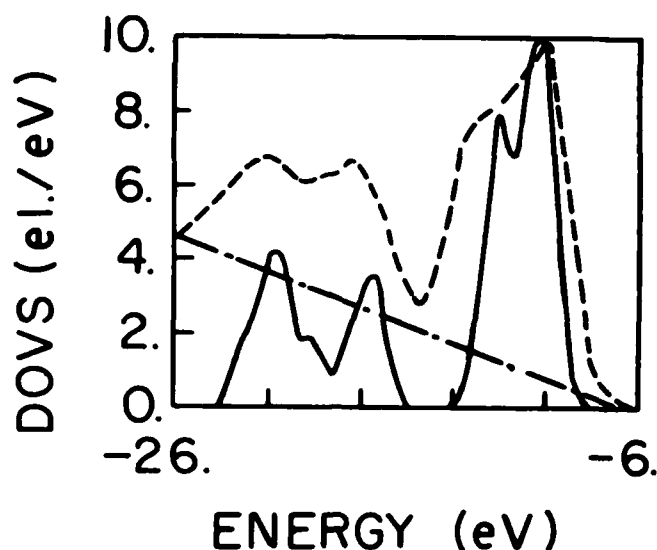


Fig. 4. Comparison of the calculated density of the valence states for  $\text{As}_4\text{Se}_4$  with measured XPS spectra [3]. Dashed curve is the experiment and solid curve the theory.

\* Supported by NSF/MRL DMR 82-16718 and AFOSR-84-0320

1. G.C. Chern and I. Lauks, J. Appl. Phys., 54, 6979 (1982).
2. I. Chen, Phys. Rev., B11, 3676 (1975).
3. W.R. Salaneck, K.S. Liang, A. Paton and N.O. Lipari, Phys. Rev., B12, 725 (1975).
4. K. Tanaka, T. Yamabe, A. Tachibana, H. Kato and K. Fukui, J. Phys. Chem. 82, 2121 (1978).
5. M.M. Palmer and R.H. Findlay, J. Mol. Struct. Theochem., 104, 327 (1983).
6. K.H. Johnson, Adv. Quantum Chem., 7, 143 (1973); J. Chem. Phys., 45, 3085 (1966).
7. K. Schwarz, Phys. Rev., B5, 2466 (1972).
8. C.S. Lu and J. Donohue, J. Am. Chem. Soc., 66, 818 (1944).
9. P. Goldstein and A. Paton, Acta Crystallogr., B30, 915 (1974).
10. J.C. Slater, J.B. Mann, T.M. Wilson and J.H. Wood, Phys. Rev., 184, 672 (1969).
11. N.F. Mott and E.A. Davis, Electronic Processes in Non-Crystalline Materials, (Clarendon Press, Oxford 1979) pp. 500-501.

## FREE-CARRIER ABSORPTION IN A THIN FILM SILVER SULFIDE GALVANIC CELL

R.L. Burton, H. Buhay, J.L. Grieser, N.P. Murarka

IIT Research Institute  
Microwave and Electro-Optics Department  
Chicago, Illinois 60616

$\text{Ag}_2\text{S}$  undergoes a crystallographic phase transition at a temperature  $T_c=180^\circ\text{C}$ . The electrical conductivity of the high temperature phase,  $\alpha\text{-Ag}_2\text{S}$ , is three orders of magnitude greater than the low temperature phase,  $\beta\text{-Ag}_2\text{S}$  [1,2]. As a result,  $\beta\text{-Ag}_2\text{S}$  transmits through much of the mid-infrared region, whereas  $\alpha\text{-Ag}_2\text{S}$  exhibits a distinct plasma absorption edge. Studies of the influence of the electron concentration on the electrical and optical properties of bulk  $\text{Ag}_2\text{S}$  have been reported [3-5]. Investigations of these properties were achieved by incorporating an  $\text{Ag}_2\text{S}$  sample in a galvanic cell structure. The structure of these bulk material galvanic cells is given by: Ag electrode/AgI/ $\text{Ag}_2\text{S}$ /Pt electrode. In a similar manner a thin film galvanic cell, with a design analogous to the bulk cell, has been made and used to vary the electron concentration in the silver sulfide film of the cell.

With a galvanic cell, an electrical current serves as a mechanism of controlling the  $\alpha\text{-Ag}_2\text{S}$  electron density and hence its infrared optical properties. The galvanic cell is in a fully charged state when all  $\text{Ag}^+$  ions have been removed. In this state the cell potential  $V_c \approx 200$  mV [1]. Further charging beyond this point will cause sulfur to plate out at the Pt electrode. Charging the galvanic cell from 0 to 200 mV shifts the position of the plasma edge [3]. Reversal of the current restores the initial concentrations of  $\text{Ag}^+$  and  $e^-$  in the  $\text{Ag}_2\text{S}$ .

The thin film silver sulfide galvanic cells studied were prepared in the following manner. Initially an  $\text{Ag}_2\text{S}$  layer was deposited on a GaAs substrate by D.C. sputtering from a target of hot-pressed  $\text{Ag}_2\text{S}$  powder. The  $\text{Ag}_2\text{S}$  layer was  $1.6\text{ }\mu\text{m}$  thick and only its central area was used in the optical measurements. AgI was evaporated over one edge of the  $\text{Ag}_2\text{S}$  layer to a thickness of  $2.0\text{ }\mu\text{m}$ . A Pt layer at a thickness  $0.5\text{ }\mu\text{m}$  was evaporated over the opposite edge. Finally, an Ag layer was evaporated over the AgI layer to a thickness of  $0.5\text{ }\mu\text{m}$ .

Reflectance and transmittance measurements were performed on a Perkin-Elmer Model 580B spectrophotometer over the range from  $250\text{ cm}^{-1}$  to  $4000\text{ cm}^{-1}$ . The



cell was mounted in a vacuum furnace and heated using an Omega Model CN2010 programmable temperature controller. All measurements were made with the cell at 185°C. In order to charge the cell a D.C. potential,  $V_{app}$ , was applied to the electrodes (Pt electrode positive). Upon application of the charging voltage, the cell current decayed steadily from a high initial value and approached zero after approximately 100 seconds. At this point, the voltage source was removed and the open circuit cell potential,  $V_c$ , was measured. For all cases, it was found that  $V_c = V_{app}$ . Spectral scans of reflectance and transmittance were then performed for cell potentials of 0mV, 50mV, 80mV, 110mV, and 150mV.

The transmittance and reflectance data are shown in Figures 1 and 2 respectively. As the cell is charged, the electron concentration within the  $Ag_2S$  layer is decreased. This reduces the degree of free carrier absorption and results in higher transmittance at lower energies as shown in Figure 1. For the same reason, the plasma edge in Figure 2 is shifted to lower energy.

In order to quantitatively characterize the measurements at different cell potentials, the reflectance spectra were analyzed by means of a fit to a dispersion formula derived from the classical Drude model of free carrier effects. The parameters of the fit are the asymptotic high frequency dielectric constant ( $\epsilon_\infty$ ), the electron mobility ( $\mu$  [cm<sup>2</sup>/vsec]), and the plasma frequency ( $\omega_p^2 = Ne^2/m^* \epsilon_0$  where  $N$  [cm<sup>-3</sup>] is the electron concentration and  $m^*$  is the effective mass, assumed equal to the bulk value  $m^* = 0.24m_e$ ) [3]. Analyses of the reflectivity spectra were performed by least squares adjustment of these parameters. The best fit values of electron concentration and mobility appear in Table 1 along with values for the bulk electron concentration. The corresponding refractive index and extinction coefficient computed from the best fit parameters are shown in Figure 3 and 4 respectively.

The electron concentrations in Table 1 agree with the bulk values reported by Dorner [3]. The electron mobility is fairly constant for all cell potentials and is also less than its bulk value of 160 cm<sup>2</sup>/V-s [3]. Figure 5 is a plot of electron concentration as a function of cell potential. Charging the cell to  $V_c = 150$ mV, reduces electron concentration by a factor of 5 and reduces the level of free carrier absorption. Repeated chargings and discharging yield reproducible results.

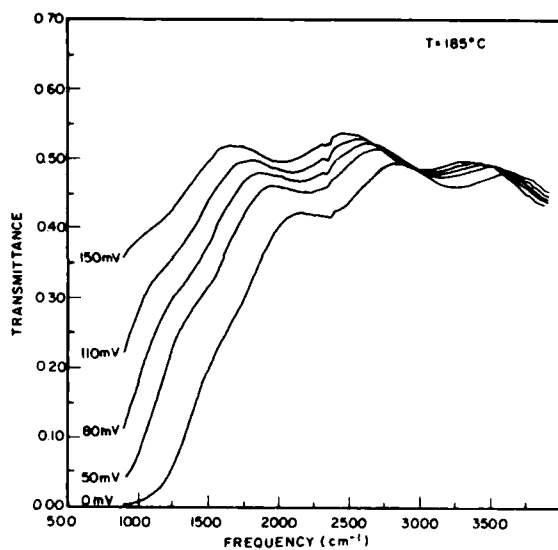


Figure 1. Silver sulfide film transmittance for five values of galvanic cell potential.

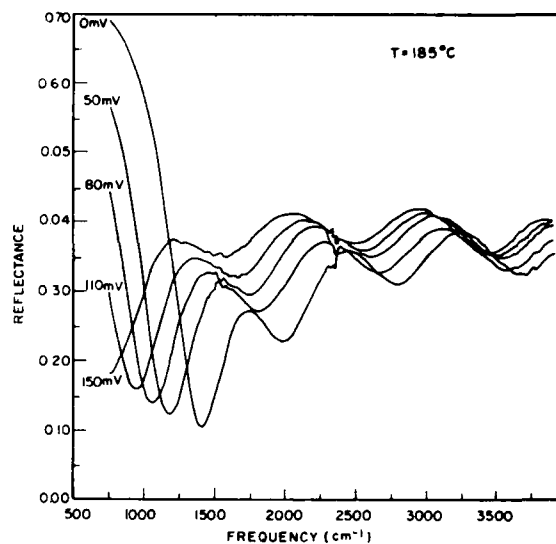


Figure 2. Silver sulfide film reflectance for five values of galvanic cell potential.

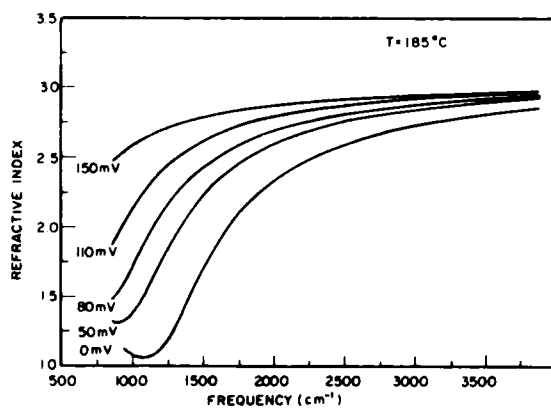


Figure 3. Silver sulfide film refractive index for five values of galvanic cell potential.

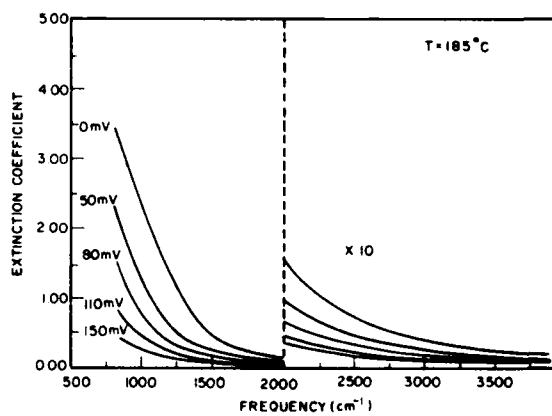
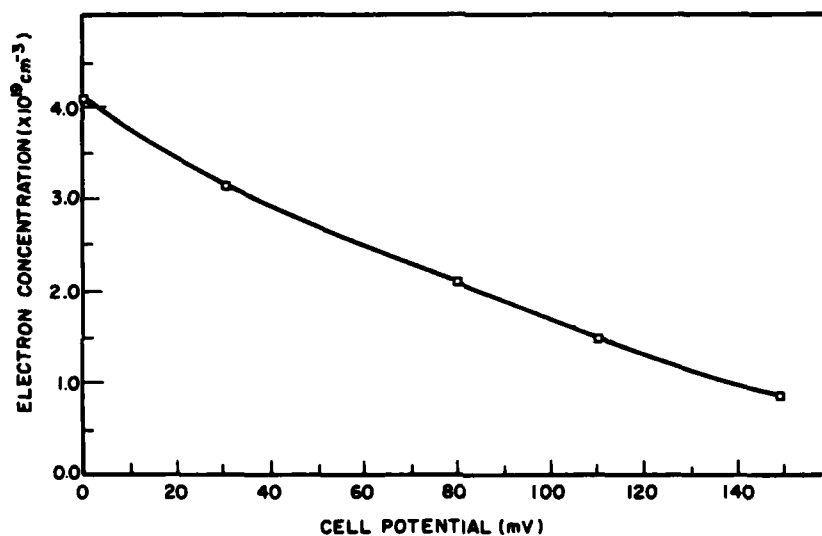


Figure 4. Silver sulfide film extinction coefficient for five values of galvanic cell potential.

TABLE 1

Cell Potential (mV)	Electron Mobility ( $\text{cm}^2/\text{V-s}$ )	Electron Concentration ( $\text{cm}^{-3}$ )	
		Film	Bulk [3]
0	102	$4.1 \times 10^{19}$	$3.6 \times 10^{19}$
50	99	$2.7 \times 10^{19}$	$2.3 \times 10^{19}$
80	100	$2.1 \times 10^{19}$	$1.8 \times 10^{19}$
110	99	$1.5 \times 10^{19}$	---
150	71	$0.85 \times 10^{19}$	$0.59 \times 10^{19}$

Figure 5. Electron concentration,  $N$ , as a function of cell potential.

### References

1. Carl Wagner, J. Chem. Phys. 21, 1819 (1953).
2. M.H. Hebb, J. Chem. Phys. 20, 185 (1952).
3. H.H. Dorner, H.P. Geserich, and H. Rickert, Phys. Stat. Sol. 37, K85 (1970).
4. G. Bornecaze, A. Lichanot and S. Gromb, J. Phys. Chem. of Solids. 34, 299 (1978).
5. G. Bonnacaze, A. Lichanot and S. Gromb, J. Phys. Chem. Solids. 39, 813 (1978).

## SYNTHESIS AND CHARACTERIZATION OF STOICHIOMETRIC CdPS<sub>3</sub>

J. Covino, P. Dragovich and C. Lowe-Ma  
Chemistry Division, Research Department  
Naval Weapons Center, China Lake, CA 93555

### INTRODUCTION

In recent years, there has been an increasing interest in the layer transition metal phosphorous trisulfide compounds. Their ability to intercalate such cationic species like alkali, metallocenium and ammonium ions,<sup>1</sup> along with their promising electrical, magnetic and optical properties,<sup>2</sup> make them an interesting class of compounds to study. Our initial studies focused on CdPS<sub>3</sub>. This material is optically transparent from 4000 cm<sup>-1</sup> to 500 cm<sup>-1</sup> (2.5-20 μm) with a fundamental absorption edge close to 454 cm<sup>-1</sup> (22 μm). Initial studies of CdPS<sub>3</sub> suggested that the material could be useful as an infrared transmitting material provided that the material strength could be increased.

Transition metal phosphorus trisulfide compounds, which generally form as thin platelet crystals, were first prepared and characterized by Klinger et al.<sup>3-5</sup> Their studies were primarily concerned with preparation and crystal structure determination. Klinger et al.<sup>5</sup> performed the single crystal structure determination of FePS<sub>3</sub> and found it to have a monoclinic unit cell (space group C2/m) with the lattice parameters  $a = 5.934 \text{ \AA}$ ,  $b = 10.28 \text{ \AA}$ ,  $c = 6.722 \text{ \AA}$ , and  $\beta = 107.16^\circ$ . The FePS<sub>3</sub> monoclinic structure is a distortion of the rhombohedral (trigonal space group R $\bar{3}$ ) structure found for FePSe<sub>3</sub>. The structure is related to that of CdCl<sub>2</sub>, with iron ions and phosphorous-phosphorous (P-P) pairs occupying the cadmium positions and sulfur or selenium ions occupying the chloride positions. In this structure, the iron ions and P-P pairs are approximately octahedrally coordinated in a distorted cubic close-packed lattice of anions (S or Se). The P-P bond lies on the octahedral threefold axis. Complete crystal structure determinations have been reported only for the layered compounds FePS<sub>3</sub> and FePSe<sub>3</sub>.<sup>4</sup> It should be noted that compounds having the MPX<sub>3</sub> (X = S, Se) stoichiometry can also crystalize with other structure types.<sup>6-11</sup>

In order to understand the structure of the CdPS<sub>3</sub> more clearly, the present work was initiated. In this work, single crystals and bulk powder of the systems CdPS<sub>3-x</sub>Se<sub>x</sub> (for  $x = 0, 1, 2$ , and  $3$ ) and Cd<sub>0.99</sub>Mn<sub>0.01</sub>P<sub>3</sub> have been synthesized. Detailed material characterization will be presented. Special emphasis will be placed on the X-ray diffraction data of this class of MPX<sub>3</sub> compounds and on how the present data, although internally consistent, does not agree with literature data. Some conclusions dealing with the crystal structure of CdPS<sub>3</sub> will be made.

### RESULTS AND DISCUSSION

The stoichiometry of the CdPS<sub>3-x</sub>Se<sub>x</sub> compounds reported in this work is shown in Table I.

TABLE I.

Theoretical stoichiometry	Experimental results
$\text{CdPS}_3$	Powders $\text{Cd}_{1.00} \text{P}_{1.02} \text{S}_{2.98}$
	Crystals $\text{Cd}_{1.00} \text{P}_{1.02} \text{S}_{3.00}$
	Literature <sup>13</sup> $\text{Cd}_{1.00} \text{P}_{.97} \text{S}_{3.20}$
$\text{CdPS}_2\text{Se}$	$\text{Cd}_{1.00} \text{P}_{1.05} \text{S}_{2.32} \text{Se}_{.84}$
$\text{CdPSSe}_2$	$\text{Cd}_{1.00} \text{P}_{1.09} \text{S}_{1.27} \text{Se}_{1.85}$

In comparing the analytical data for  $\text{CdPS}_3$  obtained in this study with analytical results on  $\text{CdPS}_3$  reported by Francis et al.,<sup>12</sup> it can be seen that the present samples are much nearer to the theoretical stoichiometry. The samples reported by Francis are either cadmium deficient or phosphorous deficient and sulfur rich, depending on how the formula is written.

Thermogravimetric analysis (TGA) of  $\text{CdPS}_3$  powder was performed. The TGA curve of the compound, in flowing nitrogen, showed virtually no weight loss below 500°C. After 500°C, a fairly abrupt decomposition to  $\text{CdS}$  was observed. This decomposition is consistent with the decomposition of the  $\text{MPS}_3$  as reported in the literature.<sup>12</sup>

X-ray powder diffraction data were obtained for all samples.  $\text{CdPSe}_3$  samples contained some  $\text{CdSe}$  (black material) which was identified in the powder patterns. The diffraction lines not due to hexagonal  $\text{CdSe}$ , definitely matched the reported powder pattern of  $\text{CdPSe}_3$ .<sup>13</sup> The Gandolfi film data for a single flake of the material with the nominal stoichiometry  $\text{CdPSe}_2\text{S}$  also matched the data for  $\text{CdPSe}_3$ <sup>13</sup> suggesting that both selenium-rich materials reported in this study were isostructural with  $\text{CdPSe}_3$ .

However, despite different synthetic attempts and reannealing, we were unable to prepare any  $\text{CdPS}_3$  which had a powder pattern matching the reported data for  $\text{CdPS}_3$ .<sup>13</sup> Our  $\text{CdPS}_3$  samples were composed of very pale orange to nearly colorless flake-like crystals. Table II has representative data of some 20 powder patterns run on  $\text{CdPS}_3$  samples. All of the X-ray diffraction data in Table II are from Gandolfi films of single flakes. These single flakes were not necessarily true "single crystals", but visually appeared to be single-phase. Although most of the reported hkl assignments for  $\text{CdPS}_3$ <sup>13</sup> can be matched to some of the X-ray lines reported in this study, our  $\text{CdPS}_3$  samples consistently exhibit far more lines than can be indexed based on the C2/m structure. Lifshitz and Francis<sup>14</sup> reported a structural phase transition for Mn(II)-doped  $\text{CdPS}_3$  somewhat below room temperature. On the same film, Gandolfi data were recorded for a flake of  $\text{Cd}_{0.99}\text{Mn}_{0.01}\text{PS}_3$  at approximately 50°C first and then at approximately 0°C. No differences in the two powder patterns were observed. This suggests that the observed anomalies in the X-ray data for the  $\text{CdPS}_3$  samples cannot be due to a structural phase transition taking place near room temperature. However, our X-ray data can be consistent with a lower symmetry structure of different symmetry.

TABLE II.

CdPS <sub>3</sub> JC1044-42 single flake		CdPS <sub>3</sub> JC1044-42 reannealed single flake		CdPS <sub>3</sub> PD1063-17 reannealed single flake		CdPS <sub>3</sub> PD 1063-30 reannealed single flake		CdPS <sub>3</sub> PD1063-52 single flake	
d	I	d	I	d	I	d	I	d	I
6.54	80	6.40	60	6.58	80	6.63	80	6.58	60
5.25	20	5.30	20	5.27	20	5.26	20 br	5.22	15 br
4.73	20	4.71	25	4.71	20	4.73	20 br	4.72	20 br
4.16	20	4.17	15	4.16	25	4.17	20 br	4.16	20
3.66	20	3.64	15	3.64	20	3.63	20	3.67	15
		3.19	5	3.20	5	3.17	10	3.20	5
3.08	100	3.08	100	3.08	100	3.08	100 br	3.08	100 br
2.96	5	2.96	5	2.96	5	2.96	5	2.96	5
2.80	30	2.80	30	2.79	10	2.79	20	2.81	30
2.63	100	2.63	90	2.63	100	2.63	100 br	2.63	100 br
2.44	30 br	2.44	60	2.46	20 br	2.44	30	2.46	30 br
2.35	5	2.36	5						
2.23	10	2.22	20	2.23	10	2.23	10	2.24	20
2.09	10	2.08	40	2.09	15	2.08	20	2.08	10
2.02	15			2.02	15	2.02	20	2.02	20
						1.956	5		
1.926	60	1.926	80	1.931	80	1.926	60	1.927	60
		1.874	5	weakline(s)				1.873	5
								1.843	5
1.795	80	1.796	100	1.795	80	1.797	80 br	1.796	80 br
1.731	40	1.733	80	1.732	60	1.734	60 br	1.729	45 br
1.696	5	1.696	5	1.696	10	1.701	5	1.697	10
1.647	5	1.647	10	1.650	10	1.648	5 br	1.645	5 br
		1.583	10						
1.549	30	1.552	60	1.551	40	1.564	30 br	1.547	20
1.483	40	1.485	70	1.483	40	1.484	40	1.482	25
		weaklines(s)		1.449	10 br	1.445	5	1.449	5
1.393	10 br	1.393	10	1.392	10	1.395	5	1.393	5
1.360	15	1.350	10	1.363	15	1.358	5 br	1.358	20
				1.344	5				
1.316	10 br	1.316	20	1.312	30	1.316	20	1.314	15
1.275	5	1.273	15	1.275	20	1.271	20	1.275	10
weakline(s)		1.231	15	weakline(s)				1.234	5
1.208	20	1.210	60	1.211	30	1.213	60	1.210	40
		1.191	5						
1.172	20	1.173	30	1.174	20	1.174	40		
1.142	40	1.142	40	1.143	30	1.143	30	1.142	60

d are in Å.

I are visually estimated intensities.

br = broad.

To check for differences in the local coordination of the Cd(Mn) in the CdPS<sub>3</sub> structure, the room temperature electron paramagnetic resonance spectrum of Mn(II)-doped CdPS<sub>3</sub> was recorded at 9 GHz. The data obtained in the present work was identical to that reported by Francis et al.<sup>14</sup> and is consistent with Mn(II) being in a site of rhombic or lower symmetry.

In order to investigate the number of sites that the Cd occupied in CdPS<sub>3</sub>, <sup>113</sup>Cd NMR was performed. The solid state <sup>113</sup>Cd NMR spectrum of bulk CdPS<sub>3</sub> powder showed only one cadmium(II) site. However, it is not conclusive evidence that only one cadmium site is present in CdPS<sub>3</sub>. Because of the noise to signal level, a second Cd could be present at a concentration of about 10% or less and, depending on its environment, might not be detectable. Alternatively, the Cd could be in only one kind of site, but the overall symmetry of the structure could have changed giving rise to the observed diffraction data.

There exists some intercalation data in the literature on both CdPS<sub>3</sub> and NiPS<sub>3</sub>. These two compounds have been assigned to the C2/m monoclinic space group, yet their intercalation chemistry is significantly different. Foot et al.<sup>15</sup> reported that NiPS<sub>3</sub> reacted readily with n-alkylamines, not at all with ammonia, and only partially with isopropylamine, while CdPS<sub>3</sub> appeared much less selective and reacted more quickly. This suggests a different intercalation process for the two compounds. The authors concluded that the nickel compound intercalates the amines via an electron transfer mechanism without any loss of Ni(II) from the structure, while the cadmium compound showed no sign of a mechanism involving electron transfer. Furthermore, Cd(II) ions were found in the liquid amines after the intercalation reaction in an amount equivalent to the intercalated amine. The authors attribute this to the difference in crystal-field stabilization energy between Cd<sup>2+</sup> (d<sup>10</sup>) and Ni<sup>2+</sup> (d<sup>8</sup>). Cd<sup>2+</sup> (d<sup>10</sup>) does not possess crystal field stabilization, whereas Ni<sup>2+</sup> (d<sup>8</sup>) does have a crystal field stabilization. However, the intercalation data can be better explained if the nickel and cadmium MPS<sub>3</sub> compounds have different crystal structures. The Cd(II) cations might be in a more labile site as compared to the Ni(II) cations.

## CONCLUSION

CdPS<sub>3</sub> has been synthesized with stoichiometry much closer to the theoretical value previously reported.<sup>14</sup> The present X-ray data for the CdPS<sub>3</sub> system, although reproducible from sample to sample, is not consistent with the C2/m structure assigned to this compound by Brec et al.<sup>13</sup> However, the presently reported data are consistent with a layer structure in which cadmium might be in a different environment or in more than one environment. If cadmium is in a second environment then it must be, as the <sup>113</sup>Cd NMR shows, only one Cd(II) site. Furthermore, as seen by the EPR data of Mn-doped CdPS<sub>3</sub> this cadmium site whether it be interstitial or defect cannot be substituted by Mn(II). Such structural differences could also explain the different intercalation chemistries of the cadmium and nickel MPS<sub>3</sub> compounds.

#### ACKNOWLEDGMENT

This work was supported in part by Contract No. N000148WR24182 from the Office of Naval Research. The authors would like to thank Robin A. Nissan, and Daniel C. Harris for their technical assistance and profitable discussions.

#### REFERENCES

1. R. J. Clement, *J. Chem. Soc., Chem Commun.* 647, (1980).
2. R. Brec, D. M. Schleich, G. Ouvrard, A. Louisy, and J. Rouxel, *Inorg. Chem.*, 18, 1814, (1979).
3. H. Hahn, and W. Klinger, *Naturwissenschaften*, 52, 494 (1965).
4. W. Klinger, R. Ott, and H. Hahn, *Z. Anorg. All. Chem.*, 396, 271 (1983).
5. W. Klinger, G. Eulenberger, and H. Hahn, *Z. Anorg. All. Chem.*, 401, 97 (1973).
6. Y. Mathey, A. Michalowicz, P. Toffoli, and G. Vlaic, *Inorg. Chem.*, 23, (7), 897 (1984).
7. R. Diehl, C. D. Carpentier, *Acta Crystallogr. Sect. B: Struct. Crystallogr. Cryst. Chem.*, B34, 1097 (1978).
8. C. Lowe-Ma, Final Report for NASA WO-8739 Contract NAS 7-918, December 1983.
9. R. Nitsche, *Mat. Res. Bull.* 5, 419 (1970).
10. C. D. Carpentier and R. Nitsche, *Mat. Res. Bull.* 9, 1097 (1974).
11. G. Dittmar and H. Schafer, *J. Naturforsch. Teil B29*, B12 (1974).
12. J. Boerio-Goates, E. Lifshitz, and A. H. Francis, *Inorg. Chem.* 20, 3019 (1981).
13. R. Brec, G. Ouvrard, A. Louisy, and J. Rouxel, *Ann. Chim. Fr.*, 5, 499 (1980).
14. E. Lifshitz, and A. H. Francis, *J. Phys. Chem.* 86, 4714 (1982).
15. P. J. S. Foot and G. Shaker, *Mat. Res. Bull.*, 18, 173 (1983).



# CHARACTERIZATION OF THIN SEMICONDUCTING FILMS ON TRANSPARENT SUBSTRATES

Bob Edgerton and David Shortt  
Energy Conversion Devices, Inc.  
1675 West Maple Road  
Troy, Michigan 48084

Uniform homogeneous layers of material deposited on a substrate can be described optically by a thickness and a complex index of refraction,  $n(\lambda) - ik(\lambda)$ . Alternately one can describe the absorption coefficient,  $\alpha(E)$ , as a function of the photon energy. If the complex index of refraction and the thickness are known for both the film and the substrate, then electromagnetic theory provides a basis for calculating the reflectance and transmittance spectra of the film (1). The challenge is to work this problem backwards. Given the two spectra, can one find a unique description of the dispersion in the optical properties as well as a thickness which satisfy the data?

The first step in our process is to choose a parameterized model to describe the optical properties. For some materials it would be appropriate to describe  $n$  and  $k$  with a small set of damped harmonic oscillators and/or free electrons (2). However, we have had success analyzing the data taken on amorphous silicon films by describing the index of refraction and the absorption coefficient independently. For the index of refraction,  $n(\lambda)$ , a four-term Cauchy power series was found to have a more appropriate shape than a single damped harmonic oscillator. For the absorption coefficient,  $\alpha(E)$ , a traditional approach for semiconductors is to match an exponential tail at low energies to some variant of a power law at higher energies (3). The resulting three-parameter function is described by the strength of the power law ( $S$ ), the threshold of the power law which is the bandgap ( $E_G$ ), and the inverse strength of the tail ( $T$ ).

$$n(\lambda) = n_1 + n_2/\lambda^2 + n_3/\lambda^4 + n_4/\lambda^6$$

$$\alpha(E) = S^2(E-E_G)^2/E \quad \text{for } E \geq E_M$$

$$\alpha(E) = \exp(T(E - E_M)) S^2(E_M - E_G)^2/E_M \quad \text{for } E < E_M$$

$$\text{where } E_M = \frac{1 + E_G T + \sqrt{(1 + E_G T)^2 + 4 E_G T}}{2 T}$$

An error function is defined to be the integrated rms deviation of the calculated spectra from the measured spectra (2). A simplex search algorithm proceeds to find a combination of the parameters that minimizes the error function (4). If there is uncertainty about the order of the interference, it is appropriate either to make a brief search over the thickness, holding the other parameters fixed, or to make several trial

calculations for different initial parameter choices and to compare them to the measured data. During a search, if a sufficiently low value of the error obtains, this first, or parameter, search yields smooth functional descriptions of the index of refraction, the absorption coefficient, and the film's thickness.

The second part of the process determines the values of the optical properties without recourse to a particular choice of parameterized model for describing the shape of the dispersion. This approach uses the thickness determined in the parameter search as a known constant. At each wavelength of interest we search for values of  $n$  and  $k$  which minimize the deviation between the measured and calculated reflectance and transmittance at that wavelength. For expedience, one chooses an acceptable error and a maximum number of allowed iterations before moving on to the next wavelength value. The second procedure yields a discrete set of optical properties rather than the continuous functions of the parameter search. Since each wavelength is treated separately, this procedure is model-independent; it gives optical properties consistent with the choice of thickness, the measured spectra, and the assumption of a uniform homogeneous layer on a known substrate. Plotting the resulting values of  $n(\lambda)$  and  $k(\lambda)$  or  $\alpha(E)$  in a variety of ways reveals the appropriateness of the models used in the parameter search. A study of trends in the data may suggest a different model to be implemented in a new parameter search.

The film used to illustrate this technique is a glow discharge deposition of amorphous silicon hydrogen alloy on Corning 7059 glass. The measured spectra appear in Fig. 1. The quality of the fit resulting from the search is shown in Fig. 2 by graphing the difference between the calculation and the measurement. The differences are less than 0.5%. The index of refraction and extinction coefficient resulting from the search are graphed in Fig. 3. Fig. 4 shows the results of the second search. The arrows indicate the spectral region in which agreement to three significant figures could not be obtained in several hundred iterations. Several regions of the spectrum show anomalous values that do satisfy the search criterium. Often the spectral region with no solution lies between two anomalous values, one high and one low. Different samples with different thicknesses produce anomalies like these in different regions of the spectrum. The index of refraction is most likely a smooth function, and the anomalies are probably a result of differences between the actual sample and the model describing it. Further interpretation of these anomalies will be the subject of future work.

Using the results for the absorption coefficient from the second search, one can plot various algebraic forms of  $\alpha$  vs.  $E$  and thus evaluate the appropriateness of the parameterized models. For the absorption model described above, we should observe a linear relation between the square root of  $\alpha E$  and  $E$  in the power law region. However, for the particular sample used, Fig. 5 shows slight curvature in this region. A plot of the square root of  $\alpha$  vs.  $E$  (Fig. 6) shows linearity over a wider energy region. When the parameter search is repeated using this more appropriate model, the resulting error is lower. The improved results appear in Fig. 7 with the new  $n$  and  $k$  in Fig. 8.

### Acknowledgments

We appreciate the interest and help of our colleagues, especially Vin Cannella, Joe Burdick, and finally Ralph Mohr, who expertly prepared a uniform sample.

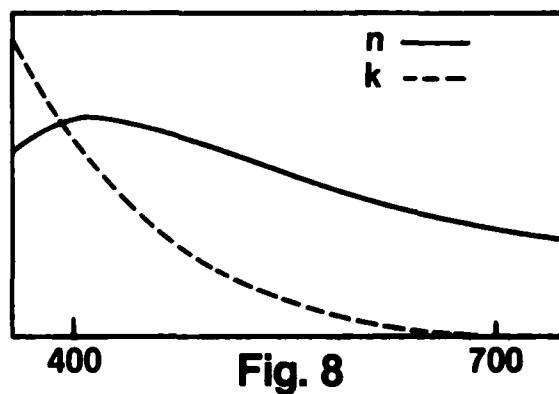
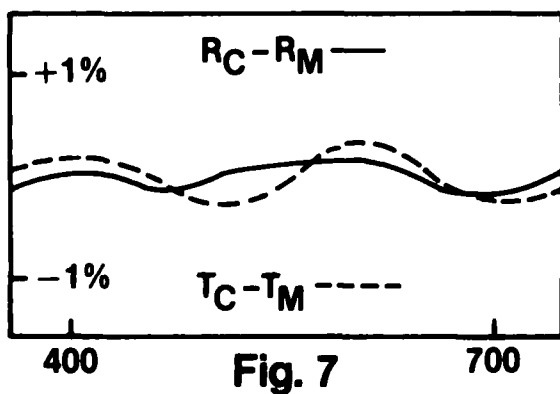
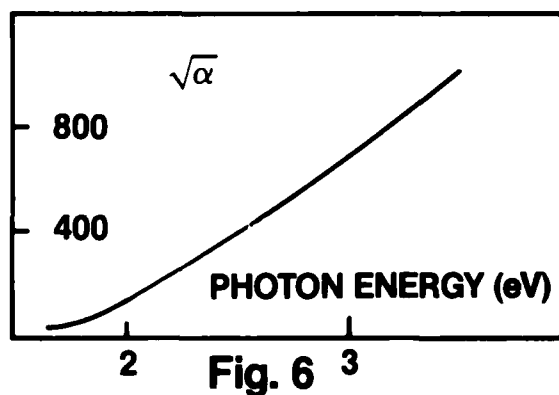
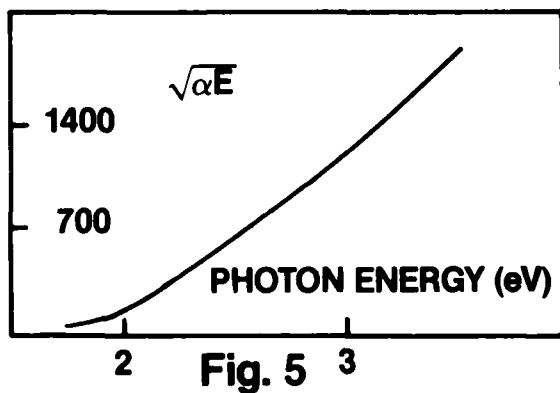
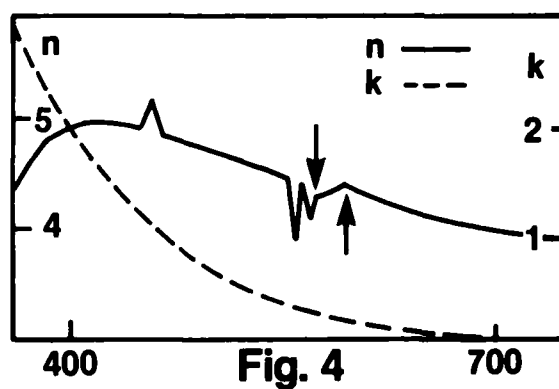
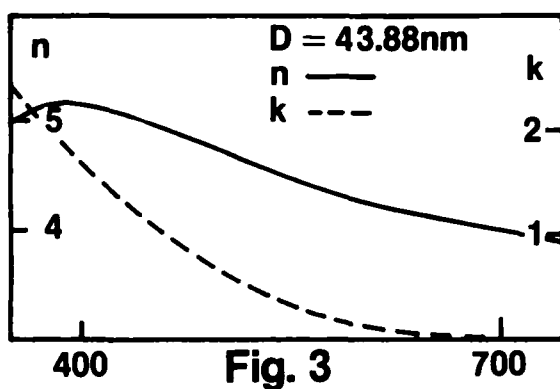
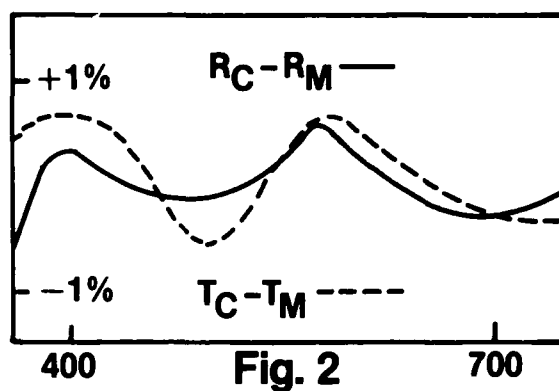
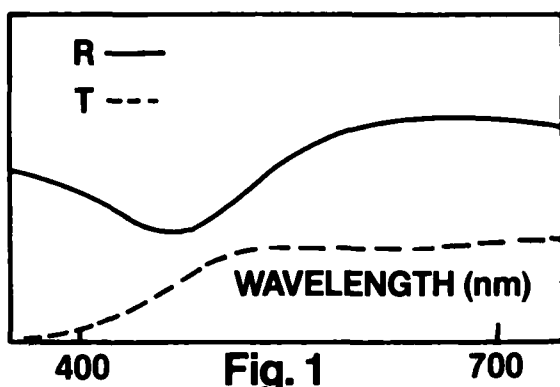
This work was partially supported by the Standard Oil Company (Ohio).

### References

- Ref. 1. O. S. Heavens, Optical Properties of Thin Solid Films, Butterworth Scientific Publications, London, 1955.
- Ref. 2. J. A. Dobrowolski, Applied Optics 22, 3191 (1983).
- Ref. 3. G. D. Cody, Hydrogenated Amorphous Silicon, J. Pankove, editor, Chapter 2, Vol. 21B, Semiconductors and Semimetals, Willardson and Beer, editors, Academic Press (1984).
- Ref. 4. J. A. Nelder, and R. Mead, Computer J. 7, 308-313 (1965).

### Figure Captions

- Fig. 1. Reflectance and Transmittance spectra (0 - 100%) of an amorphous silicon hydrogen film deposited by glow discharge on a Corning 7059 glass substrate.
- Fig. 2. Difference between the calculated spectra and the measured spectra after the simplex parameter search.
- Fig. 3. Values of  $n$  and  $k$  calculated from the values of the parameters determined in the search.
- Fig. 4. Values of  $n$  and  $k$  consistent with the thickness 43.88 nm. and the measured spectra.
- Fig. 5. Plot of the square root of  $\alpha E$  vs.  $E$ .
- Fig. 6. Plot of the square root of  $\alpha$  vs.  $E$ .
- Fig. 7. Differences between the calculated and the measured values after a second simplex search using the more appropriate model.
- Fig. 8. Values of  $n$  and  $k$  described by the parameters determined in the second parameter search using the new model.



# LASER PROPAGATION THROUGH FIBERS WITH BIQUADRATIC REFRACTIVE INDEX (CLOSED FORM SOLUTION)

Farag Z. El-Halafawy  
Dept. of Electronic Engineering  
Menouf, 23951 Egypt

and

Ahmed Y. Rezk and El-Sayed A. Al-Badawy  
Dept. of Engineering  
Alexandria University  
Alexandria, Egypt

In this paper, closed form equations for both trajectories and intensity profiles of a light beam traveling in a continuous media of biquadratic graded refractive index are derived avoiding the approximations made by [1] and [2].

Graded index fibers employed in optical communication or as sensors are manufactured with biquadratic (or nearly) refractive index of the form

$$n^2 = n_1^2 (1 - 2a \rho^2 + 2b \rho^4) \quad (1)$$

where both the parameters  $a$  and  $b$  are positive quantities,  $\rho = r/R$ , and  $R$  is the fiber radius.

Without loss of generality, meridional rays profiles are the solution of [3]

$$\frac{d^2 \rho}{d\eta^2} = \frac{1}{2n_o^2 N_o^2} \frac{dn^2}{d\rho} \quad (2)$$

where  $N$  is the direction cosine of the incident ray

$$\eta = z/R$$

and  $n_o$  denotes the refractive index at the incident point of  $r = r_o$ .

The use of equation (1) in equation (2) yields

$$\frac{d^2 \rho}{d\eta^2} = \frac{n_1^2}{n_o^2 N_o^2} (-2a\rho + 4b\rho^3) \quad (3)$$

The normalized radial position  $\rho_n$  and the normalized propagation distance  $\eta_n$  are defined as

$$\rho_n = \rho \sqrt{2b/a} = m\rho$$

where  $m^2 = 2b/a$  ( $< 2$ ) and  $\eta_n = \eta n_1/2n_0N_0a$ ; thus equation (3) reduces to the form

$$\frac{d^2 \rho_n}{d\eta_n^2} + \rho_n - \rho_n^3 = 0. \quad (4)$$

Multiplying equation (4) by  $\rho_n'$  and integrating, we obtain

$$\rho_n'^2 + \rho_n^2 - 1/2 \rho_n^4 = \rho_{n_0}'^2 + \rho_{n_0}^2 - 1/2 \rho_{n_0}^4 = \text{function of } r_0, \text{ say } A \quad (5)$$

where the lower suffix ( $n_0$ ) denotes the quantities at  $z = 0$  (launch conditions).

Equation (5) is re-arranged as follows:

$$\begin{aligned} \rho_n'^2 &= 1/2 \rho_n^4 - \rho_n^2 + A \\ &= 1/2 (\rho_n^2 - A_1^2)(\rho_n^2 - A_2^2) \end{aligned} \quad (6)$$

where  $A_1^2 A_2^2 = 2A$  and  $A_1^2 + A_2^2 = 2$ , with  $A_1 > A_2$ . The use of  $\rho_n = A_2 u$  and  $K = A_2^2/A_1^2$  in equation (6) yields

$$u'^2 = 1/2 A_1^2 (1-u^2)(1-K^2 u^2). \quad (7)$$

The separation of variables and the integration of equation (7) yields

$$\int_0^{\eta_n} \omega d\eta_n = \int_{u_0}^u \frac{du}{\sqrt{(1-u^2)(1-K^2 u^2)}}$$

or simply

$$\omega \eta_n = \text{sn}^{-1} u - \text{sn}^{-1} u_0$$

and hence

$$u = \text{sn}(\omega \eta_n + \text{sn}^{-1} u_0)$$

and finally

$$\rho_n = A_2 \text{sn}(\omega \eta_n + \phi_0) \quad (8)$$

where  $\omega$  and  $A_1/\sqrt{2}$  and  $\text{sn}$  denotes the Jacobian periodic elliptic function [4] of period  $4K$ , and  $\phi_0$  is the solution of  $\text{sn } \phi_0 = \rho_{n_0}/A_2$ . Both  $A_1$  and  $A_2$

and consequently the period  $4K$  are functions of both the launch conditions and the fiber parameters where

$$A_1^2 = 1 + \sqrt{1-2A} = f_1(r_o, a, b),$$

$$A_2^2 = 1 - \sqrt{1-2A} = f_2(r_o, a, b).$$

With respect to the intensity profiles and in the same spirit as [2] we have

$$I(\rho_n, \eta_n) = I(\rho_{n_o}, 0) \frac{\rho_{n_o}}{\rho_n} \left( -\frac{\partial \rho_{n_o}}{\partial \rho_n} \right)_{\eta_n} \quad (9)$$

where  $I(\rho_{n_o}, 0)$  is the initial intensity at the entrance of the fiber (i.e., at  $Z = 0$ ).

As the period  $4K$  is a function of the launch radial position for a certain fiber, thus there is a caustic volume of relatively high harm rather than a single focus. Equation (8) yields the maximum radial position  $\rho_{max}$  as a function of  $\rho_{n_o}$  under the form

$$\rho_{max} = A_2. \quad (10)$$

Thus, self-trapping can be achieved by optical fiber if

$$\rho_{max} = A_2 < \rho_n \text{ (at } r = a; \text{ i.e., } = 1)$$

i.e., if  $A_2 < m$  or  $A < m - m^2/2$  and, finally

$$\rho_{n_o}^2 + \rho_{n_o}^2 - 1/2 \rho_{n_o}^4 < m - m^2/2. \quad (11)$$

This equation couples the launch conditions and the fiber parameter  $m$  in order to achieve self-trapping conditions.

Equation (9) indicates that  $I(\rho_n, \eta_n)$  oscillates along the propagation path (the fiber axis) and makes a caustic volume of maximum power concentration which yields concentrated-strain regions acting as damage centers.

In conclusion, biquadratic-index media yields self-trapping if its parameters and the launch conditions are adjusted.

#### References:

- [1] P. K. Tien, J. P. Gordan, and J. R. Whinnery, Proc. IEEE, Vol. 43, No. 2, pp. 129-136, Feb. 1965.
- [2] P. M. Mejias, Appl. Opt., Vol. 20, No. 24, pp. 4287-4295, 15 Dec. 1981.
- [3] T. Okoshi, Optical fiber, Ch. 3, Academic Press, 1982.
- [4] M. Abramowitz and I. A. Stegun, Handbook of Mathematical Functions, Ch. 16, Dover Publ., NY, 1965.

## DENSIFICATION OF ZIRCONIA FILMS BY COEVAPORATION WITH SILICA

Albert Feldman and Edward N. Farabaugh  
Inorganic Materials Division  
National Bureau of Standards  
Gaithersburg, Maryland 20899

Optical films of zirconia have been receiving considerable attention because of their potential use as the high-index layer in multilayer optical coatings for the ultraviolet portion of the spectrum. Several problems are associated with electron-beam deposited zirconia films and these include index instability [1] and index inhomogeneity [2]. The index instability is caused by the adsorption and the desorption of water in the porous columnar structure of the zirconia films. Index inhomogeneity is due to the inhomogeneous structure in the films. Recent work has shown that the first several tens of nanometers of a film possess a cubic structure whereas the outmost layers possess a monoclinic structure [3].

One approach for producing bulk-like zirconia films that is receiving considerable attention at present is ion-assisted electron-beam deposition. This is because the method has successfully produced zirconia films having bulk-like densities and refractive indices that show insignificant sensitivity to water adsorption [1]. In this paper we demonstrate a similar effect when mixed zirconia:silica films are produced by coevaporation from independent electron-beam sources, and, in particular, we show that the admixture of a small amount of silica with the zirconia produces a film possessing a higher refractive index than a pure zirconia film. This work is based on earlier studies that had shown coevaporated zirconia:silica films to possess an amorphous structure as determined by x-ray diffraction as opposed to pure zirconia films which were composed of mixed polycrystalline phases of the monoclinic and tetragonal structures [4]. In addition, the mixed films had not shown the columnar structure found in pure zirconia films.

Films in the system  $(\text{ZrO}_2)_x:(\text{SiO}_2)_{(1-x)}$  were produced by coevaporation from two independent electron beam sources onto fused silica substrates at a substrate temperature of 300 °C. Each source was monitored by a separate quartz-crystal monitor. Six films were produced varying in composition from pure  $\text{ZrO}_2$  to pure  $\text{SiO}_2$ .

Table 1 lists some of the properties of the films produced. The volume fractions shown were computed from the thicknesses measured with the quartz-crystal monitors [5]. The results are based on the assumption that the volume occupied by each molecule is a fixed quantity. The quartz-crystal monitors were calibrated on the basis of stylus thickness measurements made on the pure films.

The thicknesses and refractive indices of the films were determined by two methods. In the first method, thicknesses were measured by means of a diamond-stylus surface profiling instrument. Using the measured thickness values, we computed the refractive indices from determinations of optic path. The optic path was computed from thin film channel spectra (CS) measurements that were analyzed on the basis of a newly developed technique [6].



In the second method, known as the method of m-line spectroscopy [7], the thicknesses and refractive indices of the films were computed by a least squares fit to measurements of the angles required to couple radiation from an argon-ion laser ( $\lambda=0.5145 \mu\text{m}$ ), by means of a prism coupler, into the thin film guided modes. The calculation assumed that the films were homogeneous, a condition that was not strictly met, as discussed below. Thus, the values of thickness and refractive index that were computed are to be considered effective values. These were found to be adequate for the purposes of this work.

Due to the relatively low refractive index of the prism used ( $n=1.973$ ), we were not always able to observe the lowest order guided modes; this resulted in ambiguity in the mode assignment. Observed modes were therefore assigned to progressively higher mode orders until the computed optic path values agreed most closely with the optic path values obtained from the channel spectra measurements. Only computations based on the transverse electric (TE) modes were used in the comparison, because, in the case of birefringent films with the optic axis normal to the film surface, TE modes and channel spectra depend on the same refractive index component. Analysis of the TM modes indicates that these films are indeed birefringent.

An examination of the shape of the channel spectra and the fit of the m-line spectra indicate that the films are inhomogeneous as well. This could account for some of the disagreement between the values in Table 1 obtained by the two methods. In general, both methods are in reasonably good agreement.

An examination of the refractive index values in Table 1 indicates that as we add  $\text{SiO}_2$  to  $\text{ZrO}_2$  the refractive index first increases and then it subsequently decreases. The initial increase is unexpected because  $\text{SiO}_2$  has a lower intrinsic refractive index than  $\text{ZrO}_2$ , and, hence, is expected to lower the refractive index of the film. The result is explained as follows: a film of electron beam deposited  $\text{ZrO}_2$  has a high porosity, thus, its effective refractive index is lower than the refractive index of bulk  $\text{ZrO}_2$ . The admixture of a small amount of  $\text{SiO}_2$  first causes a change in the polycrystalline structure of the film; additional amounts cause the films to approach a glassy state. These structural changes are accompanied by a decrease in porosity of the films resulting in an increase in refractive index that more than compensates for the decrease expected from the addition of  $\text{SiO}_2$ . However, after maximum densification occurs, the addition of more  $\text{SiO}_2$  does cause a decrease in the refractive index.

Evidence for densification of the films can be seen in the thickness values. If we sum the thicknesses of the individual components of a particular mixed film as measured with the quartz crystal monitors and compare this sum with the thickness as determined by the stylus measurement we find that the stylus value is always less.

Further evidence for the lower porosity of the mixed films was obtained from additional channel spectra measurements which are sensitive to the uptake of water in the films. Channel spectra of the films were measured several months after deposition and compared to the optical fringe count that was monitored during the film deposition. The spectra of mixed films showed good

agreement between the two measurements indicating good index stability whereas the pure zirconia film showed significant discrepancies. The films were then baked out in vacuum and new channel spectra were taken. Here again, the pure zirconia film showed the greatest instability. Additional channel spectra were taken on a fresh film of pure  $ZrO_2$  just after deposition, after several days of exposure to moist atmosphere, and after vacuum bakeout. We found a variation in refractive index of as much as 3.5 percent. Depending on the model used for computing refractive index in a mixed system, and assuming that index changes due to changes in stoichiometry during bakeout are negligible, the porosity to account for such a variation would fall in the range 11-33 percent.

This work was supported in part by the Air Force Office of Scientific Research.

We thank T. Vorburger and C. Glauque of the Micro and Optical Technology Group for the diamond stylus measurements of specimen thicknesses.

#### REFERENCES

- [1] P. J. Martin, H. A. Macleod, R. P. Netterfield, C. G. Pacey and W. G. Sainty, *Appl. Opt.* 22, 178 (1983).
- [2] E. E. Khawa and S. G. Tomlin, *Thin Solid Films*, 30, 361 (1975).
- [3] R. E. Klinger and C. K. Carniglia, *J. Opt. Soc. Am. A* 1, 1289 (1984).
- [4] E. N. Farabaugh and D. M. Sanders, *J. Vac. Sci. Technol. A* 1, 356 (1983).
- [5] R. Jacobsson, in *Physics of Thin Films*, Vol. 8, G. Hass, M. H. Francombe, and R. W. Hoffman, editors (Academic Press, New York, 1975).
- [6] A. Feldman, *Appl. Opt.* 23, 1193 (1984).
- [7] P. K. Tien, R. Ulrich, and R. J. Martin, *Appl. Phys. Lett.* 14, 291, (1969).

TABLE 1. Parameters of Mixed  $\text{ZrO}_2\text{:SiO}_2$  Thin Films

Specimen no.	Volume %		Sum Monitored t(um)	Stylus & CS*		m-lines	
	$\text{ZrO}_2$	$\text{SiO}_2$		t(um)	n	t(um)	n
428	100	0	1.13	1.13	1.92	1.13	1.90
430	86.5	13.5	1.04	0.95	2.04	0.94	2.05
431	70	30	0.96	0.65	1.98	0.66	1.95
438	51	49	0.85	0.69	1.79	0.69	1.78
439	32	68	0.80	0.72	1.65	0.66	1.64
429	0	100	0.70	0.70	--	--	--

\* channel spectra

## TEMPERATURE DEPENDENCE OF THE VUV OPTICAL SPECTRA AND BAND STRUCTURE OF $\text{Al}_2\text{O}_3$

R. H. French and R. L. Coble  
Mass. Inst. of Tech.  
Cambridge, MA 02139

A high temperature vacuum ultraviolet (VUV) spectrophotometer<sup>1</sup> has been built that is capable of measuring the reflectance and transmittance of samples from 6 eV to 15 eV (210 nm to 85 nm) in the VUV on samples heated without contamination from room temperature up to 1100 °C. The precision (reproducibility) of the measurements is 0.01 eV, the resolution of the monochromator is 0.1 eV while the spectrophotometer can resolve 0.3 eV wide spectral features of the sample. The temperature dependence of the electronic structure of single crystal  $\text{Al}_2\text{O}_3$  has been studied with this facility.

### Reflectivity Measurements at Room Temperature

At room temperature, the reflectivity shows three main features (see figure 1): a 9 eV exciton peak, superimposed on a 9 eV absorption edge, and, at higher energy, a 13 eV peak. The 13 eV peak shows features that depend on the crystallographic orientation of the sample. A doublet peak appears for light incident parallel to the c axis, while a peak and a shoulder are observed for light perpendicular to the c axis. The absorption edge is due to transitions to the Al 3s sub-band of the conduction band, while the main peak at 13 eV corresponds to transitions to the Al 3p sub-band of the conduction band. The valence band has a lower lying Al-O sub-band, with the top of the valence band being of O 2p character. Transmission measurements show the absorption edge to lie at 8.8 eV at room temperature. This corresponds to a direct (8.8 eV) optical band gap at room temperature. This measurement provides no information about the nature (direct or indirect) of the minimum band<sub>2</sub> gap of the material. These results are in agreement with band structure<sup>2</sup> and atomic cluster models<sup>3</sup> of the T = 0 K electronic structure of  $\text{Al}_2\text{O}_3$ .

### Temperature Dependent Reflectivity Measurements

With increasing temperature (see figure 2) the features in the reflectivity broaden and shift to lower energies. These changes are due to spreading of the electronic energy level bands and shifts of the band centers. This may be explained either from the electron-phonon interaction, or as arising from the superimposed effects of thermal expansion and atomic vibrations on the instantaneous bond lengths in the material. It was found that the different sub-bands have different temperature dependencies. Over the temperature range studied, (25 °C to 1100 °C), the shifts were found to be linear with temperature, second order terms were negligible. The experimentally determined values of the linear temperature coefficient  $\beta$ , expressed in eV/K are:

$$\begin{aligned}\beta \text{ ( Al 3s abs. edge )} &= 1.1 \times 10^{-3} \text{ eV/K} & \pm 1 \times 10^{-4} \\ \beta \text{ ( 9 eV Exciton Peak )} &= 1.0 \times 10^{-3} \text{ eV/K} & \pm 3 \times 10^{-5} \\ \beta \text{ ( 13 eV Al3p Peak )} &= 7 \times 10^{-4} \text{ eV/K} & \pm 4 \times 10^{-5}\end{aligned}$$

#### High Temperature Optical Properties and Electronic Structure

There have been many studies of the shift of the absorption edge with temperature for optical materials such as sapphire due to its use as a window material. Most of these measurements have been over limited temperature ranges and for energies below the fundamental absorption edge. The values of  $\beta$  for the absorption edge reported in the literature range from  $1.5 \times 10^{-4}$  to  $2 \times 10^{-3}$  eV/K. This is the first work to measure the optical spectra over such a wide temperature range, to such high temperatures and covering the energy range necessary to observe the basic optical features of the material. In addition, by measuring the shift of various features, both peaks and edges, one gains greater confidence in the reported results.

The various theories of the temperature dependence of electronic structure<sup>5</sup> can not at present theoretically predict the value of the temperature coefficient for  $\text{Al}_2\text{O}_3$ , but they all predict a change in the temperature dependence at the Debye temperature, and at the onset of anharmonic vibrations associated with melting. We have not been able to observe a change in the temperature coefficient even though the Debye temperature lies between 700 and 1000 °C.

The energies reported in this work correspond to optical energies that create carriers without lattice relaxation. It is this lattice stabilization energy which determines the difference between the optical and thermal band gap values. The room temperature band gap extrapolated to  $T = 0$  K, using the measured temperature coefficients, gives 9.1 eV for the  $T = 0$  K apparent optical band gap of  $\text{Al}_2\text{O}_3$ . The optical band gap energy at 1500 °C is 7.15 eV, as determined by extrapolation from these measurements.

#### Acknowledgements

This work was supported by the U. S. Department of Energy through contract number DE-AC02-76-ER02390

#### References

1. R. H. French, H. P. Jenssen, R. L. Coble, Proceedings of the 7th International Conference on Vacuum Ultraviolet Radiation Physics', August 8-12 1983, Annals of the Israeli Physical Society, **6**, p 51.
2. S. Ciraci, I. P. Batra, Phys Rev B, **28**, 2, July 15 1983, p 982.
3. J. A. Tossell, J Phys Chem Sol, **36**, (1975), p. 1273.
4. For a review of the literature see R. H. French, 'Electronic Structure of  $\text{Al}_2\text{O}_3$ : VUV Reflectivity Measurements from Room Temperature to 1100°C', Ph.D. Thesis, M. I. T. Cambridge Mass, 1985.
5. M. L. Cohen, D. J. Chadi, Handbook on Semiconductors Vol. 2. Optical Properties of Solids, North Holland, New York, 1980, p 155.

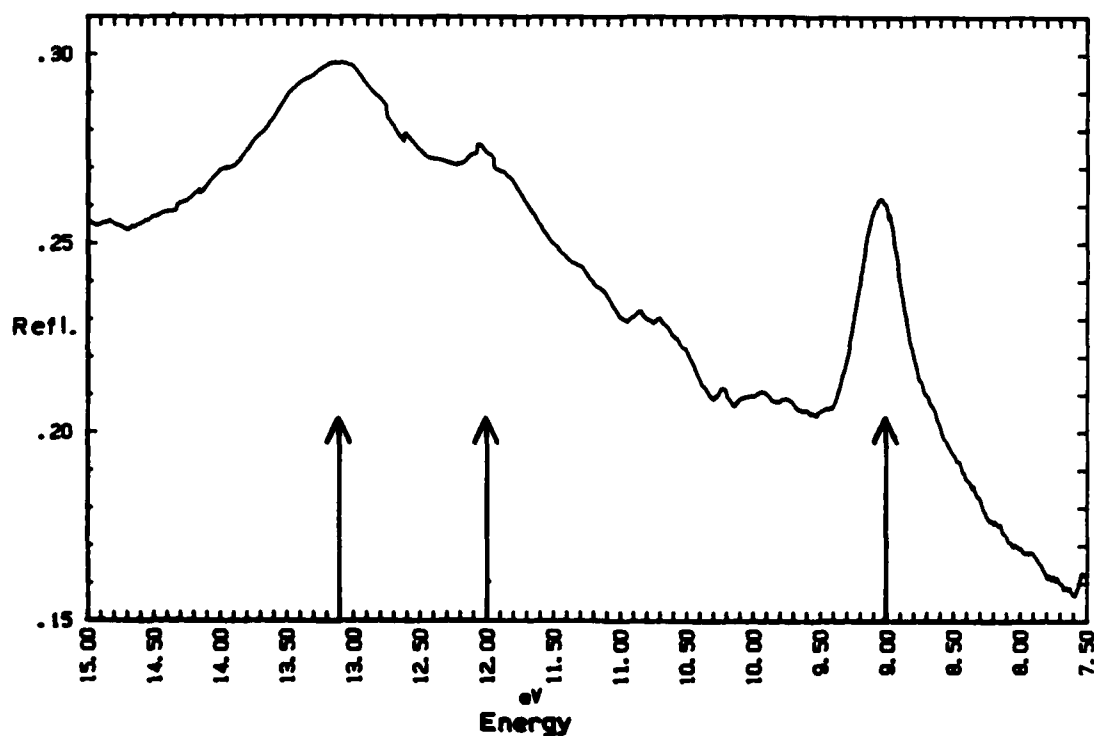


FIGURE 1a Reflectivity of  $\text{Al}_2\text{O}_3$ :  $\epsilon$  in plane,  $E$  perpendicular to the  $c$  axis,  $T$  equals 21 °C.

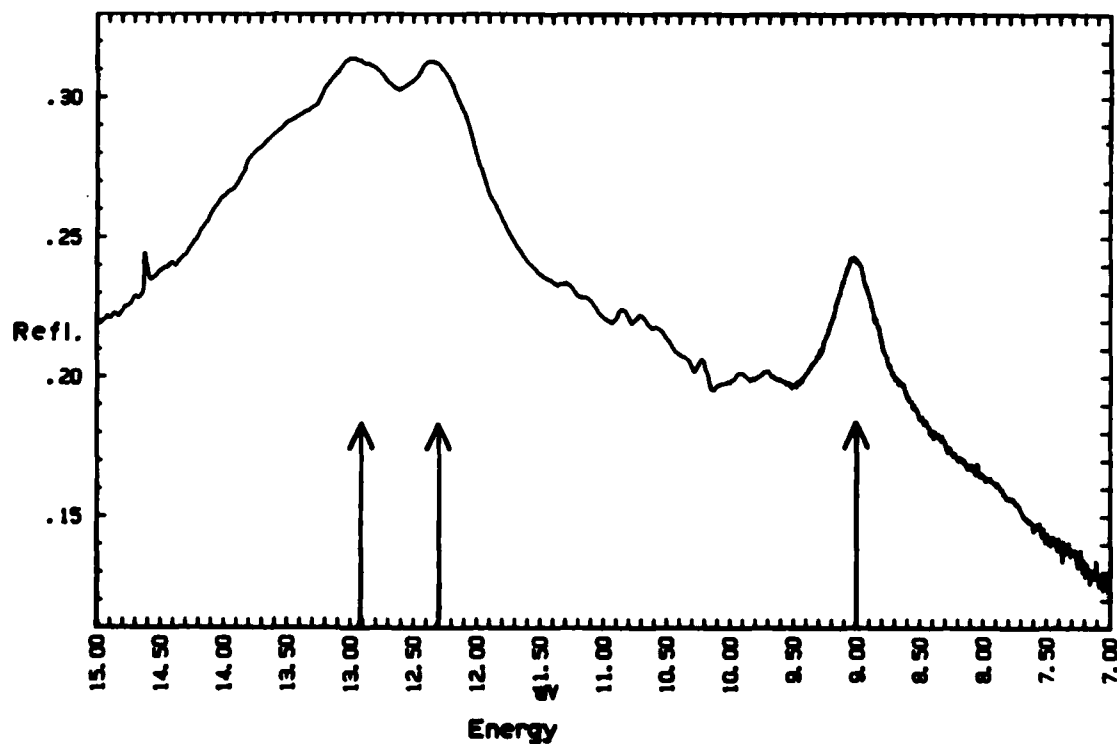
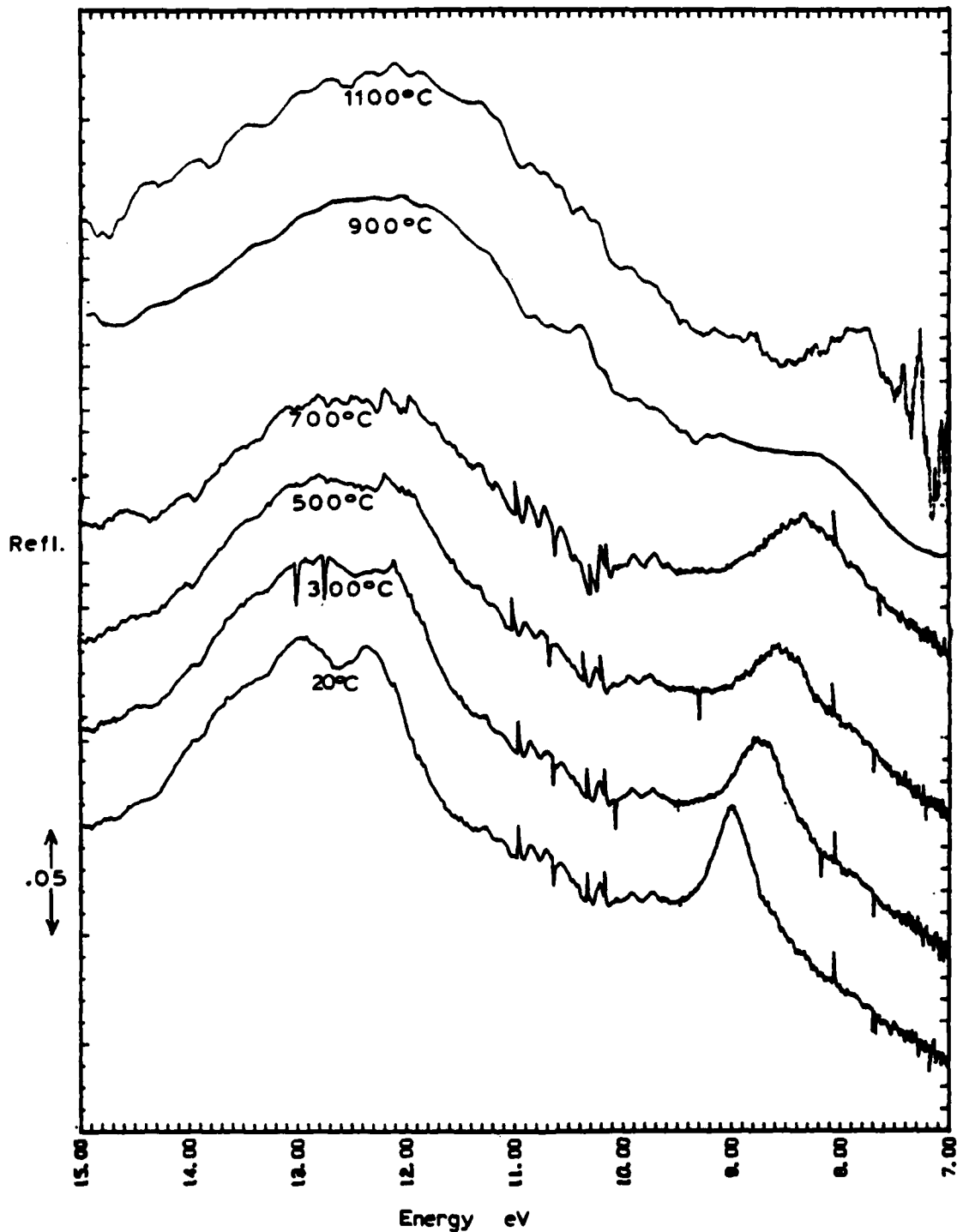


FIGURE 1b Reflectivity of  $\text{Al}_2\text{O}_3$ :  $\epsilon$  in plane,  $E$  parallel to the  $c$  axis,  $T$  equals 21 °C.



**FIGURE 2** Temperature dependent reflectivities of  $\text{Al}_2\text{O}_3:\text{T}$  (from bottom to top of figure) equals 21, 300, 500, 700, 900, and 1100 °C. Each division on R axis equals 0.01.

## RAMAN SPECTRA OF $\text{LiYF}_4$ CRYSTAL

F. Y. Gan and H. Y. Chen

Shanghai Institute of Optics and Fine Mechanics  
Academia Sinica, Shanghai, People's Republic of China

### Introduction

Rare earth ion doped  $\text{LiYF}_4$  crystals are well-known laser active materials; they produce the laser emissions in the range of 0.8-2.1  $\mu$  wavelength [1].  $\text{LiYF}_4$  host structure, a scheelite model, is a body-centre tetragonal with  $a = 5.175\text{\AA}$  and  $c = 10.74\text{\AA}$  [2]. The polarized fluorescence and absorption, excitation spectra, life-time, etc. of the crystal doped with  $\text{Nd}^{3+}$  have been studied in detail [3] and the crystal-field parameters have also been reported [4], but only a few works about its vibrational properties have been presented so far. The optical phonon spectra are rather important for development of tunable solid state lasers; for this reason we carried out the study of Raman spectra of this material, analysed its optical mode vibrations and finally compared with that of the sample doped with  $\text{Nd}^{3+}$ .

### Experiment

The sample we studied is a  $10 \times 10 \times 5\text{mm}$  polished lithium yttrium fluoride crystal prepared by gradient cooling method. The crystal axes were determined with X-ray diffraction methods. Using a 50mW He-Ne laser at  $6328\text{\AA}$ , we obtained the Raman spectra through a GDM 1000 double grating monochromator with the resolution of  $\pm 5\text{cm}^{-1}$ .

The incident beam is a linear polarized laser. When the crystal orientation was variated for a certain incident beam, the polarized Raman scattering light with the polarization parallel or vertical to scattering plane was observed. The DPT signs are used to mark the polarization characteristics; x, y, z indicate the crystal axes a, b, c respectively.

### Results and Discussion

Figures 1-3 represent the polarized Raman spectra of the  $\text{LiYF}_4$  crystal in  $y(\text{zz})x$ ,  $y(\text{xy})z$  and  $z(\text{xz})y$  direction, and the crystal axes x, y, z correspond to the a, b, c directions of the scheelite structure unit, respectively. Four main bands are observed in the spectra. The predominant peaks at  $260\text{cm}^{-1}$  in  $y(\text{zz})x$  and  $325\text{cm}^{-1}$  in  $y(\text{xy})z$  direction are polarized. Other bands are at about  $375\text{cm}^{-1}$  and  $440\text{cm}^{-1}$  and their polarizations are not very obvious.

As we know, in ionic crystals cations and anions are systematically arranged in close proximity to each other, and interactions between them will have a significant effect on the vibrational modes. The site-group and factor-group analysis are two available methods to study the vibrations of the crystalline lattice.  $\text{LiYF}_4$  belongs to  $\text{C}_4^6$  space-group and the site-group of  $\text{Y}^{3+}$  is  $\text{S}_4$ . In this structure geometry, we consider that the interaction between fluorine





Comparing the spectra of a  $\text{LiYF}_4$  crystal doped with  $\text{Nd}^{3+}$  ions with that of the pure host crystal, we have not found any difference; this fact means that with low doping concentration of  $\text{Nd}^{3+}$  ions there is no significant change of the vibrational states.

#### Conclusion

The site-group method can be used to study  $\text{LiYF}_4$  crystals. The vibrational modes A, Bz, Ex, Ey are determined at  $260\text{cm}^{-1}$ ,  $325\text{cm}^{-1}$ ,  $375\text{cm}^{-1}$  and  $440\text{cm}^{-1}$ , respectively. The vibrational spectra of a crystal doped with  $\text{Nd}^{3+}$  are just the same as that of the pure one.

#### Reference

- [1] A. A. Kaminskii, "Laser Crystals", p. 170.
- [2] G. Keller, J. Inorg. Nucl. Chem., 27, 900 (1965).
- [3] A. L. Harmer, A. Linz and D. R. Gabbe, J. Phys. Chem. Solids, 30, 1483 (1969).
- [4] D. Sengupta and J. D. Artman, J. Chem. Phys., 53, 838 (1970).
- [5] "Crystal Spectra", ed. by Nankai University.

## EPR STUDIES OF INFRARED-TRANSMITTING SULFIDE CERAMICS

Daniel C. Harris, Marian E. Hills, Josephine Covino,  
Charlotte K. Lowe-Ma and Robert W. Schwartz  
Chemistry Division, Research Department  
Naval Weapons Center  
China Lake, California 93555

Calcium lanthanum sulfide (nominally  $\text{CaLa}_2\text{S}_4$ ) and zinc aluminum sulfide ( $\text{ZnAl}_2\text{S}_4$ ) are potentially useful as infrared-transmitting ceramics. The former is prepared in our laboratory by heating coprecipitated metal carbonates under flowing  $\text{H}_2\text{S}$  at  $1000^\circ\text{C}$  for 1 day and the latter is made by heating the pure elements in a sealed, evacuated quartz ampoule at  $800\text{--}900^\circ\text{C}$  for 2-3 weeks. In an attempt to correlate optical properties with the presence of impurities and defects, we have been studying the electron paramagnetic resonance (EPR) spectra of powdered samples.

### $\text{CaLa}_2\text{S}_4$ and CaS

The EPR spectrum of  $\text{CaLa}_2\text{S}_4$ <sup>1</sup> is dominated by a distinctive six-line signal that is very similar to the published spectrum<sup>2</sup> of  $^{55}\text{Mn}^{2+}$  ( $I = 5/2$ , 100% natural abundance) in CaS. The metal ion environment in CaS is octahedral, while both metal ion environments in  $\text{CaLa}_2\text{S}_4$  have lower symmetry ( $S_4$ ). If  $\text{Mn}^{2+}$  is present as a substitutional impurity in  $\text{CaLa}_2\text{S}_4$ , the  $\text{Mn}^{2+}$  EPR spectrum should be different from that in CaS. Although our calcium lanthanum sulfide was made intentionally rich in lanthanum ( $\text{La}/\text{Ca} \approx 2.7$ ), it was possible that CaS was present as an impurity phase. The spectrum of CaS (Fig. 1) prepared in the same manner as  $\text{CaLa}_2\text{S}_4$  had a splitting pattern identical to the pattern observed for  $\text{Mn}^{2+}$  in  $\text{CaLa}_2\text{S}_4$ , verifying the presence of a CaS phase in the  $\text{CaLa}_2\text{S}_4$ . The spectrum of CaS in Fig. 1 also exhibits signals attributable to  $^{51}\text{V}^{2+}$  ( $I = 7/2$ , 100% natural abundance) and  $\text{Cr}^{3+}$ . The same  $\text{V}^{2+}$  signals were observed in one sample of  $\text{CaLa}_2\text{S}_4$ , but no  $\text{Cr}^{3+}$  was found in any samples of  $\text{CaLa}_2\text{S}_4$ .

When CaS was irradiated with 366 nm light at 77 K, peak a grew and six new signals appeared at fields ranging from 347 to 5376 G.<sup>3</sup> The new signals could be explained by photochemical oxidation of iron ( $\text{Fe}^{2+} + \text{acceptor} \rightarrow \text{Fe}^{3+} + \text{acceptor}$ ), since (1) the behavior was enhanced by  $\text{Fe}^{2+}$  doping and (2) nuclear hyperfine satellites due to  $^{57}\text{Fe}$  were observed near the strongest photogenerated signals. The broad peak a (16 G peak-to-trough) at  $g = 2.017$  in Fig. 1 is probably due to the electron acceptor site with its trapped electron.

Powered samples of  $\text{CaLa}_2\text{S}_4$  also exhibit a broad band similar to peak a, but at  $g = 2.022$  with a peak-to-trough width of 46 G. The intensity of the peak increases markedly when the material is irradiated with 366 nm light at 77 K, so we assign the signal to an electron acceptor site in  $\text{CaLa}_2\text{S}_4$ .

While studying the EPR spectra of CaS samples, another interesting feature was noted. There is a very weak peak labeled b at  $g = 2.003$  in Fig. 1. In a different preparation of CaS, a peak at the same position was the strongest

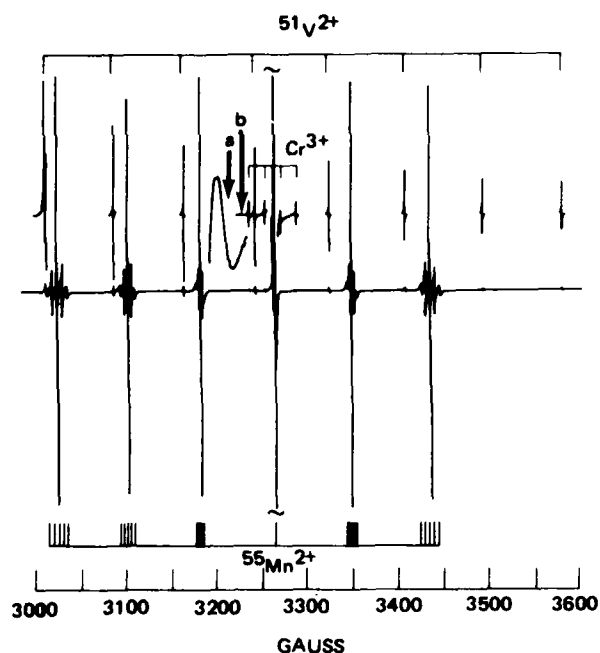


Fig. 1. EPR spectrum of CaS at 77 K. The strongest line of  $Mn^{2+}$  near 3266 G is off scale. Microwave power  $\approx 0.28$  mW and modulation amplitude  $= 0.32$  G. The upper trace is enlarged by a factor of 10. The broad peak a was recorded with power  $= 8.8$  mW and modulation amplitude  $= 2.5$  G. The very weak peak b was the most intense peak in another sample of CaS whose spectrum is shown in Fig. 2.

signal in the spectrum. A signal in CaS at this same g value has been noted before and assigned to an electron in a sulfur vacancy (an  $F^+$  center).<sup>4,5</sup> Indicated by asterisks in Fig. 2 are four of the eight lines expected for splitting by  $^{43}Ca$  ( $I = 7/2$ ). If signal b arises from an  $F^+$  center, the unpaired electron would interact with six equivalent  $Ca^{2+}$  ions. Since the natural abundance of  $^{43}Ca$  is only 0.13%, the intensity of each of the eight satellites should be  $6 \times 0.0013/8 = 0.0010$  of the total signal. The relative height of the outermost satellites compared to the central line in Fig. 2 is 0.0004. The

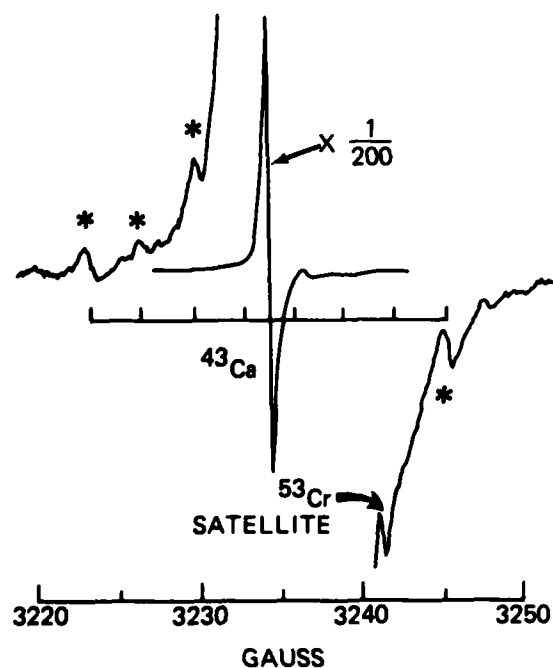


Fig. 2. EPR spectrum of defect in CaS at 77 K. Microwave power  $= 0.0044$  mW and modulation amplitude  $= 0.8$  G. Peaks marked by asterisks are part of the eight-line hyperfine pattern of  $^{43}Ca$ . The central line, whose gain is reduced by a factor of 200, is at position b in Fig. 1. The  $^{53}Cr$  satellite is the one at lowest field in Fig. 1.

poor agreement with the expected relative height might reflect a difference in linewidth between the central line and the satellites. The observed coupling constant is  $A = 3.2 \text{ G} = 3.0 \times 10^{-4} \text{ cm}^{-1}$ . This is smaller than the values near  $25 \times 10^{-4} \text{ cm}^{-1}$  for  $^{67}\text{Zn}$  coupling to an  $\text{F}^+$  center in  $\text{ZnS}$ <sup>6,7</sup> and values near  $40 \times 10^{-4} \text{ cm}^{-1}$  for  $^{135}\text{Ba}$  and  $^{137}\text{Ba}$  coupling to an  $\text{F}^+$  center in  $\text{BaS}$ .<sup>8</sup>

### $\text{ZnAl}_2\text{S}_4$

Two phases of  $\text{ZnAl}_2\text{S}_4$  have been characterized.<sup>9</sup> The  $\alpha$  phase, formed at  $900^\circ\text{C}$ , is reported to have the normal spinel structure. In this structure each S atom has  $\text{C}_3$  site symmetry and is 4-coordinate. The sulfur is bonded to one Zn atom and three Al atoms. The Zn atom is surrounded by four S atoms and the Al atom is attached to six S atoms. In the  $\beta$  phase, prepared at  $1050^\circ\text{C}$ , each S atom is 4-coordinate with two nearest neighbor Al atoms. The other two sites are occupied by one Zn atom and one vacancy in certain layers and by a random distribution of Zn atoms and vacancies in other layers. X-ray powder diffraction patterns of our samples showed predominantly  $\alpha$  phase with varying amounts of other unidentified impurities.

All preparations of  $\text{ZnAl}_2\text{S}_4$  exhibited a strong six-line EPR pattern attributable to  $\text{Mn}^{2+}$  in a nearly cubic (tetrahedral or octahedral) environment with a small axial distortion. Also present in the spectra was a pattern of at least 29 lines near  $g = 2.00$  with a coupling constant of 3.1 G. This could arise from one or more types of paramagnetic centers coupled to four to six equivalent  $^{27}\text{Al}$  nuclei ( $I = 5/2$ , 100% natural abundance). The paramagnetic species might be an  $\text{F}^+$  center or an  $\text{S}^-$  ion or a cluster of Al atoms with an odd number of electrons.

A few light yellow chunks of material selected from a typical gray preparation of  $\text{ZnAl}_2\text{S}_4$  proved to be  $\alpha\text{-ZnAl}_2\text{S}_4$  within the limits of X-ray powder diffraction. The EPR spectrum of this light yellow material showed  $\text{Mn}^{2+}$ , but not the 29-line pattern. The unidentified paramagnetic species that gives rise to the 29-line pattern is therefore located in one of the products other than  $\alpha\text{-ZnAl}_2\text{S}_4$ . The method of preparation and identification of the reaction products are under investigation.

### Summary

EPR spectroscopy has established that  $\text{CaS}$  is an impurity phase in  $\text{CaAl}_2\text{S}_4$  and has been used to identify transition metal impurities, paramagnetic defects and photochemical processes in these materials. Both  $\text{Mn}^{2+}$  and a paramagnetic center with coupling to several  $^{27}\text{Al}$  nuclei were observed in preparations of  $\text{ZnAl}_2\text{S}_4$ . These spectra may be useful in evaluating the quality of  $\text{ZnAl}_2\text{S}_4$  preparations and in the identification of impurity phases that are present.

### Acknowledgment

This work was supported, in part, by Contract No. N000148WR24182 from the Office of Naval Research. Some of the materials used in these studies were supplied by R. Gentilman and K. Saunders of the Raytheon Company.

### References

1. Covino, J., Harris, D. C., Hills, M. E., Loda, R. T., and Schwartz, R. W., Proc. Soc. Photoptical Instr. Eng. (SPIE) 505 (1984), in press.
2. Nair, P. G., Lingam, K. V., and Machwe, V. G., Proc. Indian Acad. Sci. A, 70, 53 (1969).
3. Harris, D. C., Covino, J., Hills, M. E., and Schwartz, R. W., J. Phys. Chem. Sol., in press.
4. Auzins, P., Orton, J. W., and Wertz, J. E., Proc. 1st Intl. Conf. Paramagnetic Resonance (Jerusalem 1962), 90 (1963).
5. Shanker, V., Gosh, P. K., and Reddy, T. R. S., Indian J. Pure Appl. Phys. 14, 193 (1976).
6. Schneider, J., and Räuber, A., Sol. State Commun. 5, 779 (1967).
7. Shono, Y., J. Phys. Soc. Jap. 47, 590 (1979).
8. Kolopus, J. L. and Lapeyre, G., Phys. Rev. 176, 1025 (1968).
9. Steigmann, G. A., Acta Cryst. 23, 142 (1967).

## ELASTIC PROPERTIES OF CHEMICALLY VAPOR-DEPOSITED ZnS AND ZnSe

Claude A. Klein and Charles B. Willingham  
Raytheon Company, Research Division  
Lexington, Massachusetts 02173

Material characteristics such as Young's modulus and Poisson's ratio play an important role in designing optical windows or assessing their performance from the point of view of thermally-induced distortion as well as pressure-induced fracture. For single-crystal cubic material, as in the case of ZnS and ZnSe, a complete description of the elastic properties requires fourth-rank tensors involving three elastic constants,<sup>1</sup> which are listed in Table 1. Both materials exhibit considerable anisotropy [ $C_{44} \neq 1/2 (C_{11} - C_{12})$ ], which implies that the elastic moduli of single crystals may assume a wide range of values depending on crystalline orientation. With chemically vapor-deposited (CVD) ZnS and ZnSe, measurements of the elastic properties reveal very little anisotropy, thus suggesting that these solids are made up of randomly-oriented polycrystalline aggregates. Various methods exist for deriving the properties of aggregates from the single-crystal elastic constants; the results of such calculations for polycrystalline ZnS and ZnSe are presented in Tables 2 and 3, in conjunction with a listing of measured property values. These values are not expected to change much with further development of the CVD process, albeit small plate-to-plate differences in elastic behavior undoubtedly will continue to occur.

The elastic properties of interest include Young's modulus (E), the shear modulus (G), the bulk modulus (K), Poisson's ratio ( $\nu$ ), the velocity of compressional waves ( $V_p$ ), and the velocity of shear waves ( $V_s$ ). For a single-phase aggregate of cubic material, it is known that the bulk modulus can be derived, unambiguously, from the single-crystal elastic constants:

$$K = 1/3 (C_{11} + 2C_{12}) \quad (1)$$

Furthermore, the shear modulus,

$$G = 1/2 (C_{11}^* - C_{12}^*) \quad (2)$$

falls between narrow bounds (the Hashin and Strikman averages<sup>2</sup>), which are tabulated in Ref. 3. Since these two moduli (K and G) suffice to completely characterize the elastic properties of a macroscopically isotropic solid, it is then a straightforward matter to obtain Young's modulus and Poisson's ratio in the Hashin or the Strikman limit:

$$E = \frac{9KG}{G + 3K} \quad (3)$$

and

$$\nu = \frac{3K - 2G}{2(G + 3K)} \quad (4)$$

Similarly, the two velocities can be obtained from

$$V_p = \left[ \frac{K + (4/3)G}{\rho} \right]^{1/2} \quad (5)$$

and

$$V_s = [G/\rho]^{1/2} \quad (6)$$

if  $\rho$  is the density of the aggregate. For polycrystalline ZnS and ZnSe with CVD densities of 4.09 and 5.26 g/cm<sup>3</sup>, respectively, Eqs. (1-6) in conjunction with the single-crystal elastic constants of Table 1 yield calculated elastic properties as listed

in Tables 2 and 3; note that the Hashin and Strikman limits do not differ significantly thus providing acceptable averages for randomly oriented aggregates.

Young's modulus and Poisson's ratio of both "standard" and "multispectral" grades of CVD ZnS have been measured at room temperature by means of strain gauges mounted on the tensile side of 4-point bend-test specimens. In addition, sound-velocity measurements were made in the longitudinal mode on specimens oriented parallel and perpendicular to the growth direction. A summary of this work<sup>4</sup> is presented in Table 2 in terms of average values and standard deviations. Compared to calculated values, these results show that the properties of as-deposited ZnS differ significantly (and consistently) from those expected on the basis of the Hashin-Strikman averaging procedure. Post-deposition treated material, however, behaves precisely as predicted for a randomly-oriented single-phase polycrystalline ZnS aggregate. It is not known what causes the discrepancy in the case of standard CVD ZnS but it should be pointed out that this material configuration always exhibits a hexagonal second-phase contribution in addition to a substantial concentration of structural imperfections.

Three teams,<sup>4-6</sup> at least, have carried out independent measurements of the elastic properties of CVD ZnSe (see Table 3). In Ref. 5, the moduli as well as Poisson's ratio were derived from ultrasonic velocity measurements and thus are indicative of dynamic conditions; the average value of Young's modulus (75.4 GPa) falls between the two theoretical bounds but turns out to be appreciably larger than typical values (70.3 GPa) derived from flexural testing.<sup>4</sup> Poisson's ratio, however, and the longitudinal velocity measured at Raytheon are in good agreement with theory. The technique used at the National Bureau of Standards<sup>6</sup> involves interferometric measurements on specimens under static uniaxial stress and provides elastic compliances, which in turn yield Young's modulus and Poisson's ratio simply from  $E = 1/s_{11}^*$  and  $\nu = -s_{12}^*/s_{11}^*$  since the material is essentially isotropic. In summary, it appears that the elastic properties of CVD ZnSe are almost independent of orientation and show no evidence of statistically significant variances with changes in the deposition process. Furthermore, they are compatible with calculated values derived from single-crystal elastic constants by means of standard averaging procedures for polycrystalline aggregates.

### References

1. J. F. Nye, *Physical Properties of Crystals* (Oxford U. Press, Oxford, 1957).
2. Z. Hashin and S. Strikman, *J. Mech. and Phys. Solids* **10**, 335 (1962) and **10**, 343 (1962).
3. G. Simmons and H. Wang, *Single-Crystal Elastic Constants and Calculated Aggregate Properties* (MIT Press, Cambridge, 1971).
4. Unpublished measurements (Raytheon Research Division, Lexington, Massachusetts).
5. S. Kulin, R. Salzbrenner, and H. Posen, in *Proc. Fourth Conf. Infrared Laser Window Materials* (ARPA, Arlington/VA, 1974), p. 678.
6. A. Feldman, D. Horowitz, R. Waxler, and M. Dodge, *Optical Materials Characterization: Final Report* (NBS-TN-993, Washington, 1979).



Table 1. Elastic constants (stiffnesses) of single-crystal ZnS and ZnSe at room temperature [D. Berlincourt, H. Jaffe, and L. Shiozawa, *Phys. Rev.* **129**, 1009 (1963)].

<u>Constant</u>	<u>ZnS</u>	<u>ZnSe</u>
C <sub>11</sub> (GPa)	104.62	80.96
C <sub>12</sub> (GPa)	65.34	48.81
C <sub>44</sub> (GPa)	46.13	44.05

Table 2. Elastic properties of CVD ZnS at room temperature.

<u>Property</u>	<u>Calculated</u>		<u>Measured</u>	
	"Hashin"	"Strikman"	"Standard"	"Multispectral"
Bulk modulus (GPa)	78.4	78.4		
Shear modulus (GPa)	33.4	32.4		
Young's modulus (GPa)	87.7	85.5	74.5±3.5	87.6±.7
Poisson's ratio (1)	0.314	0.318	0.29±.01	0.318±.001
Longitudinal velocity (km/sec)	5.484	5.455	5.35±.03	5.47±.01
Transverse velocity (km/sec)	2.858	2.816		

Table 3. Elastic properties of CVD ZnSe at room temperature.

<u>Property</u>	<u>Calculated</u>		<u>Measured</u>		
	"Hashin"	"Strikman"	ManLabs(a)	NBS(b)	Raytheon(c)
Bulk modulus (GPa)	59.5	59.5	65.3±.5		
Shear modulus (GPa)	30.2	28.8	28.8±.3		
Young's modulus (GPa)	77.6	74.5	75.4±.7	72.1±3.1	70.3±2.8
Poisson's ratio (1)	0.283	0.291	0.308±.003	0.32±.03	0.28±.01
Longitudinal velocity (km/sec)	4.356	4.315			4.38±.04
Transverse velocity (km/sec)	2.397	2.341			

(a) Ultrasonic velocities (Ref. 5)

(b) Interferometric technique (Ref. 6)

(c) Flexural testing (Ref. 4)

#### Additional Note

It has come to our attention that comprehensive measurements of the elastic properties of Raytran® ZnSe were also performed at General Electric Company and are documented in a Government Report dated August 1979.\* Ultrasonic measurements that were carried out in the longitudinal mode, at a frequency of 10 MHz, confirmed that the material is essentially isotropic, with  $V_p = 4.39 \pm .01$  km/sec, in accord with the result listed in Table 3. In-plane flexure tests at room temperature gave  $E = 10.1 \pm .15$  Mpsi ( $69.7 \pm 1.0$  GPa) and  $\nu = .29 \pm .01$ , whereas tensile tests, parallel and perpendicular to the deposition plane, yielded  $E = 10.3 \pm .3$  Mpsi ( $71.0 \pm 2.0$  GPa) and  $\nu = .28 \pm .01$ . These results are in good agreement with measurements that were carried out in our laboratory (see Table 3) and, thus, substantiate our observation that the "static" modulus of elasticity of chemically vapor-deposited ZnSe is lower than anticipated on the basis of standard averaging procedures.

---

\*J. Brazel, R. Fenton, J. Roetting, and R. Tanzilli, *Millimeter Wave Hardened Antenna Window Materials Development* (AD-A076769/9, NTIS, Springfield/VA).

## RADIATION EFFECTS IN A GLASS-CERAMIC (ZERODUR)

N. Koumvakalis  
Litton Systems, Inc.  
Guidance & Control Systems Division  
5500 Canoga Avenue  
Woodland Hills, California 91365 U.S.A.  
M. G. Jani and L. E. Halliburton  
Department of Physics  
Oklahoma State University  
Stillwater, Oklahoma 74074 U.S.A.

Zerodur [1] is a low-expansion glass-ceramic with important applications in laser-gyro guidance systems. The material contains by weight 70-75% crystalline quartz in the form of crystallites approximately 50 nm in diameter which are embedded in a glass matrix. The glass-crystal ratio is adjusted so that the resultant expansion coefficient at room temperature is near zero.

Ionizing radiation causes numerous effects in Zerodur. The most obvious is a change in the optical absorption, and this will have possible consequences in the thermal expansion behavior.. Thus, characterization of radiation-induced defects will help solve problems affecting Zerodur's performance in guidance systems and will provide an understanding of the basic properties of this unique class of materials.

Our Zerodur samples were optically polished at Litton. Dimensions were  $(2 \times 3 \times 7) \text{ mm}^3$  for the electron-spin-resonance (ESR) and  $(15 \times 15 \times 3) \text{ mm}^3$  for the optical samples. Radiation sources were a Van de Graaff accelerator (1.5-MeV electrons,  $10^5$  rads/min) and an x-ray tube (Machlett OEG-60, tungsten target). During the 77 K irradiation, the ESR sample was immersed directly in liquid nitrogen. Further details of the experimental technique and the apparatus are given in reference [2]. Optical absorption data were obtained using a Perkin-Elmer Model 330 spectrophotometer. For optical measurements at 77 K, a Sulfrian cryostat was used.

Figure 1 shows the ESR spectra of a Zerodur sample after electron irradiation at 77 K (trace a) and after subsequent warming-up to room temperature. Both spectra were measured at 77 K.

A number of spectral features are present after the 77 K irradiation. The sharp central line (g value = 1.9983) displays the line shape and long spin-lattice relaxation times (causing severe microwave power saturation effects) characteristic of the  $E_1'$  center in crystalline quartz [3].

The large negative  $g$  shift of the high-field broad band, centered at  $g = 1.9$ , indicates the presence of an electron trap. Results from recent studies of heavy-metal fluoride glasses [4] suggest that the electron trap is  $Zr^{4+}$  or  $Ti^{4+}$ . Both of these ions are present in Zerodur as nucleating agents in the form of  $TiO_2$  or  $ZrO_2$ . In trace b of Figure 1, the same spectral features are present although the intensity is reduced significantly. An ESR spectrum almost identical to trace b is produced after room temperature electron irradiation.

Figure 2 shows the optical absorption of Zerodur after electron irradiation at 77 K. The absorption increases with irradiation; each curve represents a different total dose. After 300 krad/s no indication of saturation was observed. The absorption band is peaked at 565 nm.

Figure 3 shows the optical absorption of Zerodur after electron irradiation at room temperature. In addition to the absorption band centered at 565 nm which grows in first, there is a second absorption band centered at 740 nm, growing at a slower rate.

The highest absorption curve corresponds to a dose of 16 Mrads. Both bands display saturation at this dose. Thermal anneal and optical bleaching data suggest that the 565 nm band and the  $E_1'$  ESR spectrum are correlated and that the 740 nm band (or a portion thereof) and the  $g = 1.9$  ESR spectrum are correlated.

Figure 4 shows the x-ray-induced luminescence of a Zerodur sample at 17 K. Its temperature dependence, depicted in the inset, indicates that unlike quartz [5] the observed emission is composed of only one band. At this stage the origin of the x-ray-induced luminescence is an open question.

In summary, a first look at the radiation-induced defects in Zerodur has been very informative. However, further work is necessary for a complete characterization of the material.

#### References

- [1] Zerodur (glass ceramic) manufactured by Schott Glass Works, Mainz, Germany
- [2] M. G. Jani and L. E. Halliburton, J. Appl. Phys. 56, 942 (1984)
- [3] M. G. Jani, R. B. Bossoli and L. E. Halliburton, Phys. Rev. B 27, 2285 (1983)
- [4] P. E. Fisanich et al., to be published in the J. Non-Cryst. Solids
- [5] P. J. Alonso et al., J. Appl. Phys. 54, 5369 (1983)

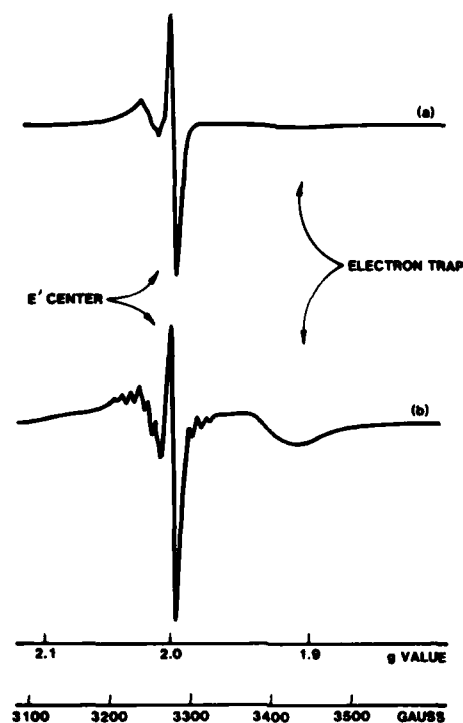


FIG. 1  
ESR spectra of  
Zerodur. In part  
a, the sample was  
electron-irradiated  
at 77 K; in part b,  
the sample was  
warmed up to room  
temperature and  
measured at 77 K.

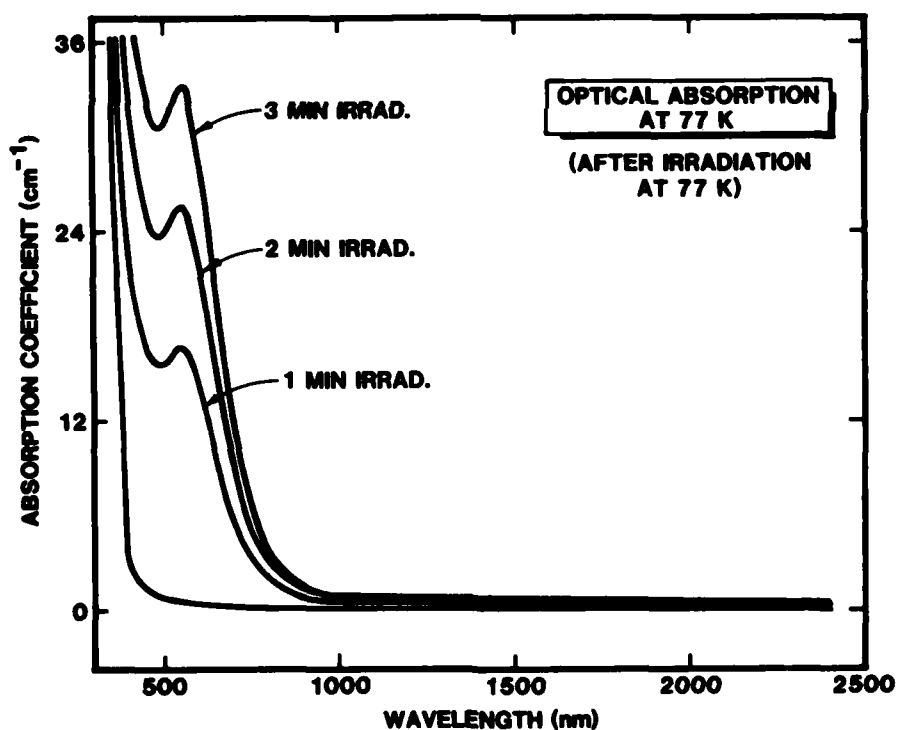


FIG. 2 Optical absorption of a sample electron-irradiated at 77 K. The label by each curve represents the accumulated dose.

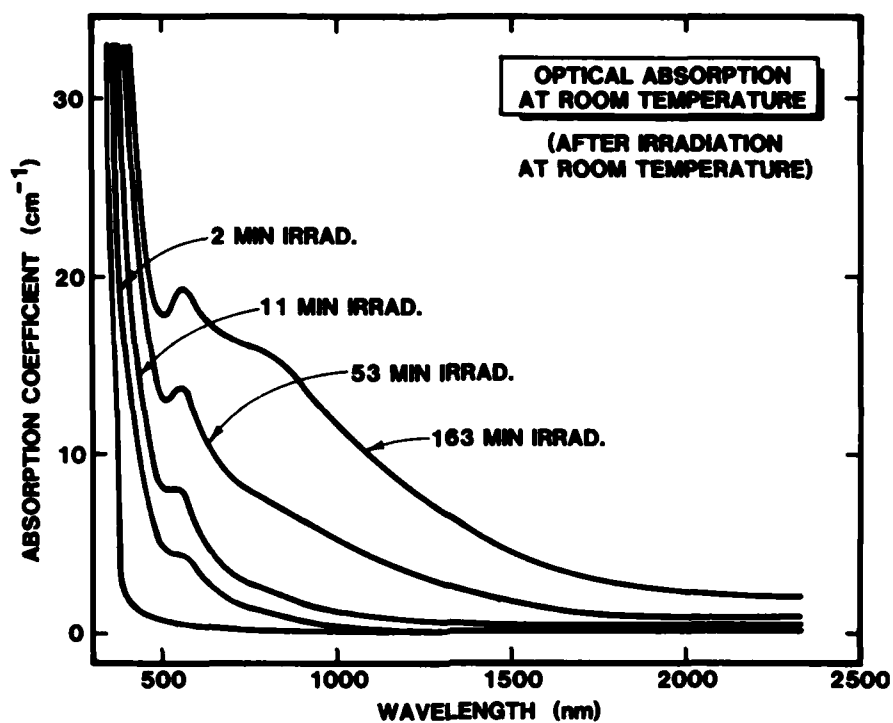


FIG. 3 Optical absorption of a sample electron-irradiated at room temperature. The label by each curve represents the accumulative dose.

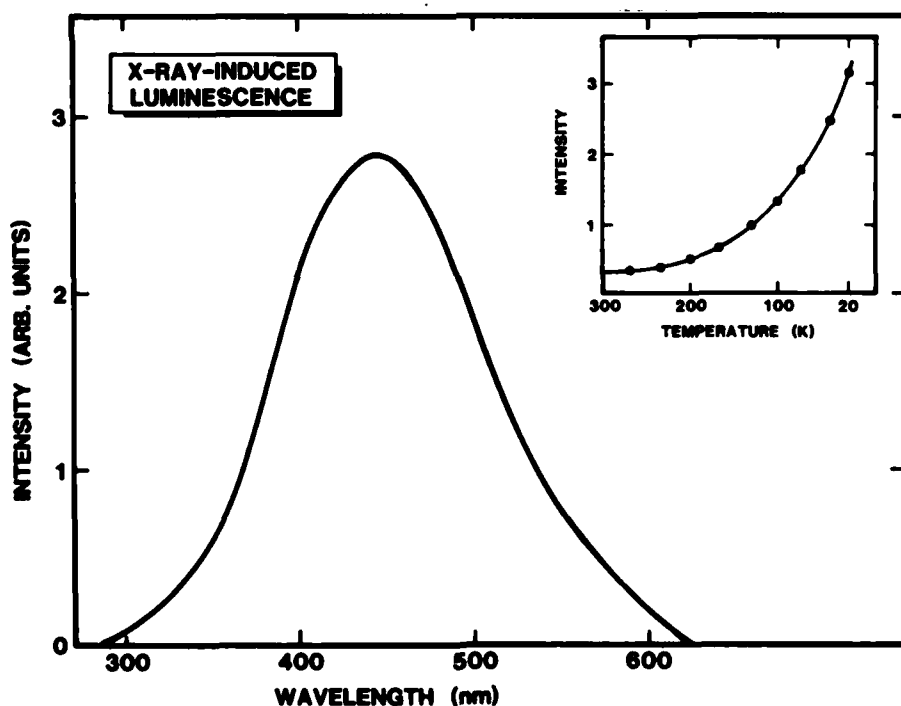


FIG. 4 X-ray-induced luminescence spectrum from an as-received sample taken at 17 K. The inset shows the temperature dependence.

## Infrared Characterization of Defect Centers in Quartz

Herbert G. Lipson  
Solid State Sciences Division  
Rome Air Development Center  
Hanscom AFB, Bedford, MA 01731

The radiation hardness and ageing properties of quartz oscillator devices depend strongly on the impurity and defect content of the synthetic quartz material. Low temperature infrared Fourier spectroscopy is a powerful tool for characterizing changes in quartz defect centers introduced by ionizing radiation and processing techniques such as electrodiffusion (sweeping). The technique of scanning large crystals normal to the growth or sweeping axis reported in this paper has revealed localized changes in defect center distribution produced by irradiation and the effect of impurity concentration on vacuum sweeping.

Transient and steady state radiation induced frequency shifts in quartz oscillator devices are partially attributed to radiation induced redistribution of point defect centers in the quartz used for the resonator disk. These disks are fabricated from pure z-growth bars and incorporate material produced during the entire growth cycle. The quality and impurity content of the nutrient used for crystal growth varies. In addition, during the growth period of several months, thermodynamic conditions change and introduce variations in quartz quality, aluminum impurity and hydroxyl concentrations between the seed and z-growth surfaces.

Specific point defect models for synthetic high quality quartz are well established and are reviewed in several publications.<sup>1-3</sup> The major defects are substitutional aluminum impurities in silicon sites, compensated with interstitial alkali metals to form  $Al-M^+$  ( $M = Li^+, Na^+ \text{ or } K^+$ ), and water molecules adjacent to oxygen sites to form as-grown  $OH^-$  centers. Room temperature ionizing radiation dissociates both  $Al-M^+$  and  $OH^-$  and two new centers are formed,  $Al-OH^-$  and aluminum holes,  $Al-h^+$ .  $OH^-$  in the crystal is the hydrogen source for  $Al-OH^-$ . The point defect structure of quartz is also modified by sweeping. Sweeping a crystal in an air atmosphere, at elevated temperatures, dissociates  $Al-M^+$ , saturates  $OH^-$  defects, and forms  $Al-OH^-$ . In this process, external water vapor provides hydrogen ions for  $Al-OH^-$  and at the same time, most of the alkali metal ions are physically "swept" out of the crystal. Sweeping a crystal in a vacuum atmosphere<sup>4</sup> also dissociates  $Al-M^+$  and forms  $Al-OH^-$ , but similar to irradiation, the hydrogen source is the

as-grown  $\text{OH}^-$ , which is reduced or depleted as the alkali metals are swept toward the cathode. Longer term vacuum sweeping also removes the  $\text{Al-OH}^-$ , leaving large regions of the crystal completely free of alkali and hydrogen defects. A completely vacuum swept material should contain  $\text{Al-h}^+$  as the basic defect and resonators fabricated from this material should have improved radiation hardness.

Infrared transmissions were measured between  $3100$  and  $3700\text{ cm}^{-1}$  with the focused beam of a Nicolet 170SX Fourier Spectrophotometer. The normal beam size was  $3\text{ mm}$  in diameter, but  $1.5\text{ mm}$  beams were also used to scan more localized regions. The sample mounted inside a dewar cooled to  $85\text{ K}$ , was moved across the spectrophotometer beam axis. Measurements were made normal to the  $z$ -growth or sweeping direction, that is, the incident unpolarized infrared beam is propagated parallel to the crystal  $y$ -axis. Beam positions are designated by the distance of the beam center from the  $+z$  face of the crystal. At  $85\text{ K}$ , the four principal bands associated with as-grown  $\text{OH}^-$  in synthetic quartz have vibration peaks at  $3348$ ,  $3396$ ,  $3438$  and  $3581\text{ cm}^{-1}$  and are usually designated  $S_1$ ,  $S_2$ ,  $S_3$  and  $S_4$ , respectively. The  $3581\text{ cm}^{-1}$   $S_4$  band has a strong narrow peak and easily determined background absorption and is used to monitor as-grown  $\text{OH}^-$ .  $\text{Al-OH}^-$  has peaks at  $3306$  and  $3366\text{ cm}^{-1}$ , designated  $e_1$  and  $e_2$ , respectively. The stronger  $e_2$  peak is used to monitor  $\text{Al-OH}^-$ . We are interested in evaluating only relative changes in as-grown  $\text{OH}^-$  and  $\text{Al-OH}^-$ , and for this purpose it is sufficient to compare absorption peak heights instead of integrated changes in band areas. Both the  $e_2$  and  $S_4$  bands have large dichroic ratios, with maximum strengths when the electric vector is normal to the optic  $c^-$ , or  $z$ -axis. With the beam aligned along  $y$ -axis maximum strength is obtained only with a properly oriented polarizer. The measurements reported in this investigation were made with unpolarized radiation, since the normally used wire grid type polarizer introduces large transmission losses in this spectral region.

The quartz samples were rectangular in shape and between  $1$  and  $2\text{ cm}$  in size with parallel  $x$ -,  $y$ - and  $z$ -faces. The quartz material was Premium-Q grade grown at SARP to which lithium salt was added to the nutrient and the  $\text{Na}_2\text{CO}_3$  mineralizer. The effects of radiation and vacuum sweeping are compared on samples of two different auto-claves, BH-A containing high aluminum and high  $\text{OH}^-$  impurity and D14-45 with relatively low aluminum and  $\text{OH}^-$ . The aluminum concentrations as determined from electron spin resonance (ESR) measurements are  $11\text{ ppm}$  for BH-A and  $1\text{ ppm}$  for D14-45.

Variations in the  $3581$  and  $3366\text{ cm}^{-1}$  peak heights obtained by scanning across samples of BH-A and D14-45 normal to the  $z$ -growth axis before and after irradiation are shown<sup>5</sup> in Figure 1 and 2. From Figure 1 for BH-A, the as-grown  $\text{OH}^-$  can be seen to vary from  $0.25$  to  $0.37\text{ cm}^{-1}$  with the highest concentration found in the center of the sample. Even though a  $0.8\text{ Mrad}$  irradiation reduced the as-grown  $\text{OH}^-$  uniformly across the crystal, a large variation in  $\text{Al-OH}^-$  is observed between the  $+z$  and  $-z$  faces. Further irradiation to the estimated saturation level of  $1.6\text{ Mrad}$  produces essentially



no change in  $\text{OH}^-$  or  $\text{Al-OH}^-$  between the center and  $-z$  face, and only small changes between the  $+z$  face and center. The differences in  $\text{Al-OH}^-$  produced in different sections of the crystal for the same  $\text{OH}^-$  decrease can be interpreted in terms of radiation induced hydrogen migration to compensate nonuniformly distributed  $\text{Al}^{3+}$  sites. An alternate explanation is that a second hydrogen source is present in addition to the as-grown  $\text{OH}^-$ . With no further change is as-grown  $\text{OH}^-$  over most of the crystal, the 1.6 Mrad  $\text{Al-OH}^-$  distribution reflects the  $\text{Al}^{3+}$  profile.

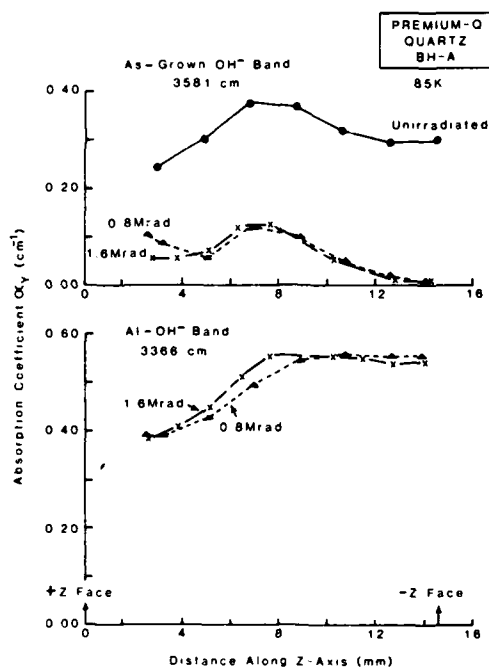


Figure 1. Peak absorption coefficient values for  $3581\text{cm}^{-1}$  and  $3366\text{cm}^{-1}$  bands before irradiation and after 0.8 and 1.6 Mrad  $^{60}\text{Co}$  irradiation doses for Premium-Q crystal BH-A. Beam normal to crystal z-axis

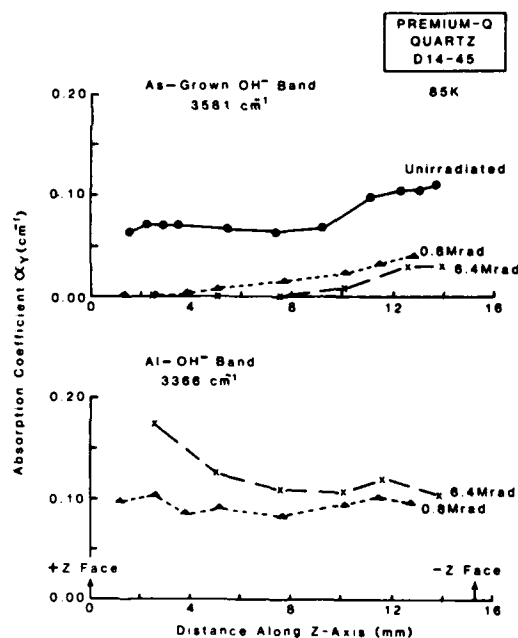


Figure 2. Peak absorption coefficient values for  $3581\text{cm}^{-1}$  and  $3366\text{cm}^{-1}$  bands before irradiation and after 0.8 and 6.4 Mrad  $^{60}\text{Co}$  irradiation doses for Premium-Q crystal D14-45. Beam normal to crystal z-axis

From Figure 2 for D14-45, it can be seen that the average  $\text{OH}^-$  level is about one-fourth of that of sample BH-A with the highest concentration toward the  $-z$  face of the crystal. A 0.8 Mrad irradiation depletes the as-grown  $\text{OH}^-$  close to the  $+z$  end and reduces it over the remaining part of the crystal. The relatively uniform  $\text{Al-OH}^-$  distribution produced by the 0.8 Mrad dose initially appears to indicate a uniform  $\text{Al}^{3+}$  distribution. Additional irradiation

up to the estimated saturation level of 6.4 Mrad further depletes or reduces the as-grown  $\text{OH}^-$ . A surprising feature is the increase in  $\text{Al-OH}^-$  toward the z-face of the crystal in  $\text{OH}^-$  depleted regions. As with sample BH-A, this implies either radiation induced migration to  $\text{Al}^{3+}$  sites or the presence of a second source of hydrogen. The situation for this sample may be further complicated by the presence of  $\text{Al-h}^+$  which has been observed in  $\text{OH}^-$  depleted regions of vacuum swept samples.<sup>6</sup>

The effect of impurity concentration on the progress of vacuum sweeping is demonstrated in Figures 3 and 4. Figure 3 shows the as-grown  $\text{OH}^-$  distribution and the movement of  $\text{Al-OH}^-$  through the crystal as alkali ions are replaced by hydrogen at  $\text{Al}^{3+}$  sites for sample BH-A after various total sweeping times. No significant changes in as-grown  $\text{OH}^-$  occur for short sweeping times up to 3.5 days. During this same sweeping period  $\text{Al-OH}^-$  forms across the crystal extending to about one third the distance between the anode and cathode. After 17.5 days of sweeping,  $\text{OH}^-$  is considerably reduced near the anode and is increased in other sections of the crystal. The  $\text{Al-OH}^-$  distribution follows a similar pattern, with a reduction near the anode and a strong increase toward the center of the crystal where the initial  $\text{OH}^-$  concentration was the largest. For this material with high aluminum and  $\text{OH}^-$  content vacuum sweeping proceeds slowly and formation of  $\text{Al-OH}^-$  across the entire crystal which indicates complete removal of alkali ions, does not occur during the 17.5 day time period.

Vacuum sweeping of sample D14-45 with low aluminum and  $\text{OH}^-$  content proceeds much more rapidly<sup>7</sup> as demonstrated in Figure 4. After 12 hours of total sweeping time as-grown  $\text{OH}^-$  is depleted near the anode and  $\text{Al-OH}^-$  is formed across the entire crystal. Sweeping 1 day eliminates  $\text{OH}^-$  over a section 4 mm from the anode and produces a significant decrease in  $\text{Al-OH}^-$  in this same region. After 4 days of sweeping  $\text{OH}^-$  is depleted over the half of the crystal closest to anode and  $\text{AlOH}^-$  is further reduced.  $\text{Al-h}^+$  is found in the  $\text{OH}^-$  depleted regions from ESR measurements. The possibility for complete vacuum sweeping is demonstrated in this sample where removal of alkali and hydrogen defects and replacement with aluminum-holes has been effected for a large section of the crystal.

#### References

1. A. Kats, Philips Res. Reports, 17 (1962).
2. D. B. Fraser; Physical Acoustics, Vol 5, W. P. Mason, editor, Academic Press, New York 59, (1968).
3. L. E. Halliburton, N. Koumuakalis, M. E. Markers, and J. J. Martin, J. Appl. Phys., 52, 3565 (1981).
4. J. C. King, Vacuum Electrolysis of Quartz, U.S. Patent 3,932,777, January 13, 1976.

5. H. G. Lipson and A. Kahan (submitted for publication in Journal of Applied Physics).
6. H. G. Lipson and A. Kahan and J. O'Connor, Proc. 37th Annual Frequency Control Symposium (AFSC) 169 (1983).
7. H. G. Lipson and A. Kahan, IEEE Transactions on Nuclear Science, NS-31, 1223 (1984).

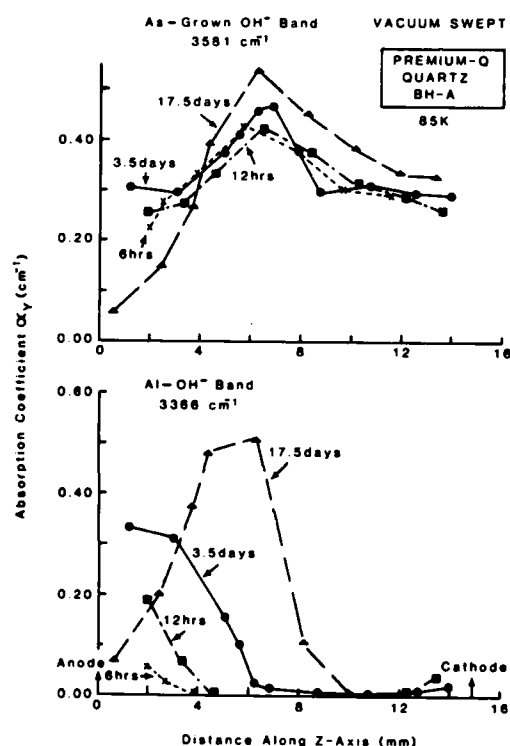


Figure 3. Peak absorption coefficient values for 3581cm<sup>-1</sup> and 3366cm<sup>-1</sup> bands between anode and cathode for 6 hrs, 12 hrs, 3.5 days and 17.5 days vacuum sweeping times measured normal to the sweeping axis. Premium-Q crystal BH-A

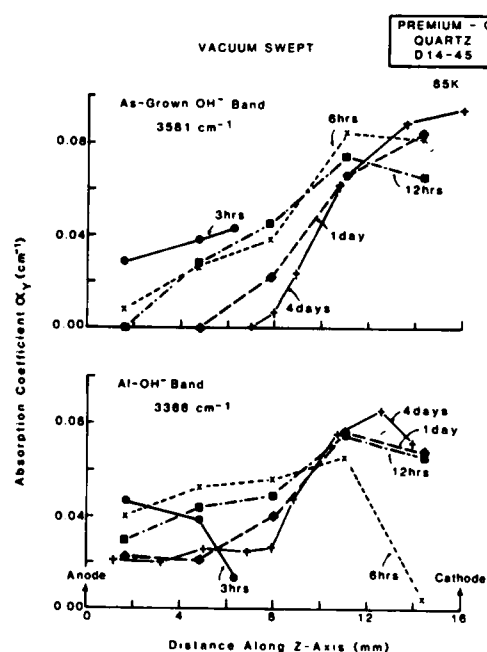


Figure 4. Peak absorption coefficient values for 3581cm<sup>-1</sup> and 3366cm<sup>-1</sup> bands between anode and cathode for 3 hrs, 12 hrs, 1 day and 4 days sweeping times measured normal to the sweeping axis. Premium-Q crystal D14-45.

THE IMPORTANCE OF ELECTRON-ELECTRON CORRELATION IN THE CALCULATION OF SECOND-ORDER NONLINEAR OPTICAL PROPERTIES OF ORGANIC MOLECULES. THE CASE OF UREA.

Brian M. Pierce

Hughes Aircraft Company  
Bldg. A-1, M/S 3C923  
P. O. Box 9399  
Long Beach, CA 90810

In studies of nonlinear optical organic molecules, the theoretical understanding of the relation between the electronic structure of the molecule and the molecular electronic component of the second-order nonlinear optical susceptibility (the hyperpolarizability tensor,  $\beta_{ijk}$ ) has been an important objective (1). The theoretical description of molecular electronic structure improves with the theoretical treatment of electron-electron correlation (EEC) in the molecule. Three general quantum mechanical molecular orbital (MO) formalisms (2) used to study molecular electronic structure, and ordered according to an improving treatment of EEC, are 1) the self-consistent-field (SCF)-MO method, 2) the SCF-MO method with single excitation configuration interaction (SCF-MO-SCI), and 3) the SCF-MO method with single and double excitation configuration interaction (SCF-MO-SDCI).

In published calculations of  $\beta_{ijk}$  for organic materials utilizing the results of molecular orbital calculations (1), the treatment of EEC was never extended beyond that of the SCF-MO and SCF-MO-SCI methods. It has been shown that EEC at the level of SCF-MO-SDCI is required to calculate with greater accuracy the third-order nonlinear optical property of molecular two-photon absorption for the  $\pi$ -electron singlet excited states in linear conjugated polyenes and related organic molecules (3,4). Therefore, it is necessary to assess the importance of EEC at the level of SCF-MO-SDCI in the calculation of  $\beta_{ijk}$  for organic molecules.

The organic molecule selected for our initial theoretical study was urea,  $(\text{NH}_2)_2\text{C} = \text{O}$ , because its nonlinear optical response has been the subject of extensive theoretical (5,6) and experimental (5,7-9) investigations.

The method of direct summation over singlet electronic states in a perturbation theory based expression was used to calculate  $\beta_{ijk}$  (10). The terms needed to evaluate this expression were calculated using CNDO- and INDO-SCF-MO procedures (4,11) combined with SCI and SDCI methods. The CNDO-SCF-MO-SCI (CNDO-SCI) and INDO-SCF-MO-SCI (INDO-SCI) calculations used the empirical Mataga electron-electron repulsion integral (4), whereas the CNDO-SCF-MO-SDCI (CNDO-SDCI) and INDO-SCF-MO-SDCI (INDO-SDCI) calculations employed both the empirical Mataga and Ohno (4) electron-electron repulsion integrals. Thus, six calculations of  $\beta_{ijk}$  for urea were performed that varied in the treatment of EEC in the molecule: CNDO-SCI, CNDO-SDCI with Mataga and Ohno integrals, INDO-SCI, and INDO-SDCI with Mataga and Ohno integrals. All six calculations were for an isolated urea molecule unperturbed by a solvent or crystalline

environment.

The parameterization of the CNDO and INDO formalisms is given in Ref. 4. All 96 singly excited configurations that can be generated from the valence electron molecular orbitals were used in calculations employing SCI. In calculations employing SDCI, all 96 singly excited configurations and the 200 lowest energy doubly excited configurations were used. Seventy-five singlet excited states were calculated for all six calculations of  $\beta_{ijk}$ . This number of states has been shown to ensure the convergence of the sum-over-states expression for the  $\beta_{ijk}$  of urea (5). The internal coordinates of urea used in the calculations were the same as those in Fig. 1(b) of Ref. 5. The molecule-fixed coordinate axes were such that urea lies in a z-x plane with the z-axis directed from the carbon atom to the oxygen atom.

The calculated values of  $\beta_{ijk}$  were used to compute several second-order nonlinear optical properties of urea: 1) the two linear electro-optic coefficients for a single crystal,  $r_{63} = r_{xyz}(\omega_1, 0)$  and  $r_{41} = r_{zxy}(\omega_1, 0) = r_{yzx}(\omega_1, 0)$  for  $\omega_1 = 632.8\text{nm}$ ; 2) the macroscopic susceptibility for second harmonic generation,  $d_{xyz}^{\text{SHG}}$ , for  $\omega_1 = \omega_2 = 1060\text{nm}$ ; and 3) the term  $\beta_z^* = \sum_{ij} \beta_{zij}$  for  $\omega_1 = \omega_2 = 1060\text{nm}$ .

Table I contains second-order nonlinear optical properties of urea measured experimentally and calculated in the present study and in other ab-initio-SCF-MO (6) and CNDO-SCI (5) studies. The CNDO-SCI study by Morrell, et al (5) is virtually identical to ours, and the small differences between the two sets of calculations are attributed to differences in parameterization. All calculated results in Table I are for an isolated urea molecule; whereas the experimental results are for single crystals of urea or for the molecule dissolved in a given solvent. Consequently, there are differences between the calculated and experimental results. The discrepancy between theory and experiment can be resolved by incorporating local field corrections (5) and the influence of hydrogen bonding (6) into the theoretical formalisms.

The salient conclusions concerning the comparison of our calculated results for urea against those of experiment and the sophisticated ab-initio-SCF-MO calculation (6) are as follows. 1) The INDO-SCI and INDO-SDCI formalisms describe the second-order nonlinear optical properties of urea better than the CNDO-SCI and CNDO-SDCI formalisms. The principal reason is that, unlike CNDO theory, INDO theory accounts for the difference in electrostatic interaction between two electrons in different orbitals on the same atom (11). 2) The CNDO-SDCI and INDO-SDCI calculations with the Ohno integral are better than those with the Mataga integral because the Ohno integral combined with an extensive SDCI treatment of EEC results in more accurate calculations of the ground state dipole moment and singlet excited state transition energies and oscillator strengths for urea (not shown). This finding is consistent with that of other theoretical studies of EEC at the level of SCF-MO-SDCI (12). 3) Although the ground state dipole moment and singlet excited state transition energies and oscillator strengths of urea calculated by the INDO-SCI method and the INDO-SDCI method with the Ohno integral are similar (not shown), the second-order nonlinear optical properties of urea in Table I calculated by the two methods are different. The magnitudes of these calculated second-order nonlinear optical properties decrease as the

treatment of EEC improves from the INDO-SCI method to the INDO-SDCI method with the Ohno integral. Thus, the treatment of EEC at the level of SCF-MO-SDCI has a significant impact on the calculation of second-order nonlinear optical properties for urea. This impact is expected to be greater for organic molecules with more extensive  $\pi$ -electron systems.

Dr. David B. Chang is thanked for interesting and helpful discussions.

1. The chapters by Garito, et. al and Badan, et. al and the references therein in Nonlinear Optical Properties of Organic and Polymeric Materials, D. J. Williams, Ed., American Chem. Soc., Washington, D.C., 1983.
2. H. F. Schaefer III, The Electronic Structure of Atoms and Molecules A Survey of Rigorous Quantum Mechanical Results, Addison-Wesley, Reading, MA, 1972.
3. R. R. Birge and B. M. Pierce, J. Chem. Phys., 70, 165 (1979).
4. R. R. Birge, J. A. Bennett, L. M. Hubbard, H. L. Fang, B. M. Pierce, D. S. Kliger, and G. E. Leroi, J.A.C.S., 104, 2519 (1982).
5. J. A. Morrell, A. C. Albrecht, K. H. Levin, and C. L. Tang, J. Chem. Phys., 71, 5063 (1979).
6. J. Zyss and G. Berthier, J. Chem. Phys., 77, 3635 (1982).
7. C. Cassidy, J. M. Halbout, W. Donaldson, and C. L. Tang, Opt. Commun., 29, 243 (1979).
8. J. M. Halbout, S. Blit, W. Donaldson, and C. L. Tang, IEEE J. Quantum Electron., QE-15, 1176 (1979).
9. I. Ledoux and J. Zyss, Chem. Phys., 73, 203 (1982).
10. C. Flytzanis, in Treatise of Quantum Electronics, Vol. Ia, H. Rabin and C. L. Tang, Eds., Academic, New York, 1975.
11. J. A. Pople and B. L. Beveridge, Approximate Molecular Orbital Theory, McGraw-Hill, New York, 1970.
12. K. Schulten, I. Ohmine, and M. Karplus, J. Chem. Phys., 64, 4422 (1976).

Table I. Calculated and Experimentally Measured Second-Order Nonlinear Optical Properties of Urea.

	Expt.	Theory							Other CND0- <sup>b</sup> SCI
		CND0- SCI	CND0- Mataga	SDCI Ohno	IND0- SCI	IND0- Mataga	SDCI Ohno	ab- <sup>a</sup> initio	
$r_{41}$ ( $10^8$ esu)	$5.6^b$	1.63	1.36	1.04	2.05	2.13	1.45	--	1.51
$r_{63}$ ( $10^8$ esu)	$2.5^b$	1.73	1.48	1.14	2.18	2.41	1.66	--	1.55
$d_{xyz}^{SHG}$ ( $10^9$ esu)	$3.4 \pm 1.0^c$	3.42	2.92	2.23	4.30	4.68	3.21	4.4	3.0
$\beta_z^*$ ( $10^{30}$ esu)	$+ 2.3^d$ $0.3 \pm 0.1^e$ $0.45 \pm 0.1^f$ $0.3 \pm 0.03^g$	-0.97	-0.71	-0.76	-1.60	-1.45	-1.30	-0.55	-0.92
$\beta_{zxx}^h$ ( $10^{30}$ esu)	--	-0.53	-0.45	-0.34	-0.68	-0.70	-0.50	0.6	--
$\beta_{zyy}^h$ ( $10^{30}$ esu)	--	0.04	0.02	0.01	0.03	0.02	-0.01	-0.08	--
$\beta_{zzz}^h$ ( $10^{30}$ esu)	--	-0.49	-0.27	-0.43	-0.94	-0.77	-0.79	-1.15	--

(a) Ref. 6

(b) Ref. 5

(c) Absolute value, Ref. 8

(d) In DMF solvent, Ref. 7

(e) In DMF solvent, Ref. 9

(f) In H<sub>2</sub>O solvent, Ref. 9

(g) In DMSO solvent, Ref. 9

(h) Nonzero  $\beta_{zjk}$  components with  $\omega_1 = \omega_2 = 1060\text{nm}$

# DIFFUSE MULTILAYER ANALYSIS USING A MULTIFLUX METHOD

S.O. Sari  
Rockwell International Science Center  
Thousand Oaks, CA 91360

The use of uniform material layers to form multilayer films forms the basis for an extensive coating technology. The transmissive and reflective properties of such structures are dominated by optical interference occurring among the layers. Comparatively less attention seems to have been given to treating stratified media consisting of random rather than uniform material layers. Within such structures, the optical scattering properties of each sublayer dominate the optical properties.

Some previous work on diffuse coatings has been concerned with investigations of surface-roughened layers and the form of diffuse scattering from one or more roughened interfaces.<sup>1</sup> Such analytical investigations have been based on lowest-order solutions to Maxwell's equations at a perturbed roughened interface, a calculational procedure which has been carried out by several different authors in recent years.<sup>2</sup> Our present objective is to point toward a possible alternative method for treating diffuse scattering from inhomogeneous materials. This procedure may be helpful for analyzing specialized coatings which are diffusely scattering. Examples would include aggregate suspensions, artificial dielectrics, solids containing scattering defects, paint layers or inhomogeneous recording materials.

The approach which we presently follow is the extended Kubelka-Munk theory developed some years ago by Mudgett and Richards.<sup>3</sup> In this framework, we assume a layer of scattering material having parallel interfaces to be oriented normal to the x-axis. Orthogonal (y,z) axes are assumed to lie in the plane of the interfaces. Diffuse flux pencils  $F(\Omega)$  propagating in the angular directions  $\Omega = (\theta, \phi)$  defined with respect to these axes are taken to be scattered among themselves through diffuse scattering or to external channels by optical absorption. A convenient approximation is to assume four distinct integrated fluxes propagating either along the positive or negative x-directions through the layer. These are taken as collimated specular fluxes  $F_S^+$  and  $F_S^-$ , and as integrated diffuse fluxes  $F_D^+$  and  $F_D^-$ , where  $F_D^\pm = \int_{\pm} d\Omega F_D(\Omega)$  is understood to be integrated over either the forward or reverse cone of diffuse radiation. Mudgett and Richards show<sup>3</sup> (their Eq. (51)) that the flux propagation can be written as

$$\frac{d}{dx} \begin{pmatrix} F_S^+ \\ F_D^+ \\ F_D^- \\ F_S^- \end{pmatrix} = \begin{pmatrix} -(K_1 + S_1 + S_2) & 0 & 0 & 0 \\ S_1 & -(K_2 + S_3) & S_3 & S_2 \\ -S_2 & -S_3 & (K_2 + S_3) & -S_1 \\ 0 & 0 & 0 & (K_1 + S_1 + S_2) \end{pmatrix} \begin{pmatrix} F_S^+ \\ F_D^+ \\ F_D^- \\ F_S^- \end{pmatrix}$$

(1)



where the  $S_i$  and  $K_i$  are cross-channel scattering and absorption coefficients, respectively, within the layer. We write this compactly as  $dF/dx = S \cdot F$ . For a layer of thickness  $L$ , we obtain the formal solution  $F(L) = \exp(SL) \cdot F(0) = \tilde{\sigma}(L) \cdot F(0)$ , where  $\tilde{\sigma}(L) = \exp(SL)$ .

We now consider a stack of such stochastically scattering layers, connected by smooth interfaces for which there is no specular-to-diffuse channel coupling. In this case, we can relate the fluxes for the medium on the left ( $i$ th medium) to the medium on the right ( $i+1$ th medium) by defining a transfer matrix  $\tilde{\tau}$  such that  $F_i = \tilde{\tau} \cdot F_{i+1}$ . Because of the absence of cross-channel coupling, the form of  $\tilde{\tau}$  is block diagonal and can be written as

$$\tilde{\tau} = \begin{pmatrix} 1/T & 0 & 0 & -R/T \\ 0 & 1/T_a & -R_a/T_a & 0 \\ 0 & R_a/T_a & (1-2R_a)/T_a & 0 \\ R/T & 0 & 0 & (1-2R)/T \end{pmatrix} \quad (2)$$

The interfacial Fresnel reflectance and transmission coefficients  $R$  and  $T$  satisfy the condition  $R+T = 1$ . Also,  $R_a$  and  $T_a$  are a solid angle and polarization averaged reflectance and transmission such that we again have  $R_a + T_a = 1$ . As an example,  $R_a = \int d\Omega R(\Omega) F_D(\Omega) / \int d\Omega F_D(\Omega)$ , where  $F_D(\Omega)$  is the incoming diffuse flux from either side of the interface. This procedure is approximately self-consistent when both of these averages are about the same. This will occur either when the distribution  $F_D(\Omega)$  is relatively narrow or when the interfacial index mismatch is not too large.

In the present model, incident and exiting fluxes  $F_n^+$  and  $F_x^+$  through an  $N$ -layer diffuse scattering stack can be written as

$$F_n^+(0) = \tilde{\tau}_1 \cdot \tilde{\sigma}_1(-L_1) \cdot \tilde{\tau}_2 \cdot \tilde{\sigma}_2(L_1-L_2) \cdot \dots \cdot \tilde{\sigma}_N(L_{N-1}-L_N) \cdot \tilde{\tau}_{N+1} \cdot F_x^+(L_N) \quad (3)$$

where  $0 < L_1 < L_2 < \dots < L_N$ . Each coordinate  $L_i$  along the  $x$ -axis determines the location of the  $i$ th interface between diffuse layers. We assume that the nonzero components of  $F_x$  are  $F_{xS}^+$  and  $F_{xD}^+$  so that no flux is incident from the exiting side. Let us also assume that a collimated impinging beam  $F_{nS}^+$  strikes the incident side. Then we may define a specular-to-diffuse integrated hemispherical reflectance and transmission as  $R_{SD} = F_{nD}^-/F_{nS}^+$  and  $T_{SD} = F_{xD}^+/F_{nS}^+$  and collimated specular components as  $R_{Sp} = F_{nS}^-/F_{nS}^+$  and  $T_{Sp} = F_{xS}^+/F_{nS}^+$ . If we define a total diffuse multilayer reflectance and

transmission by  $R_t = R_{Sp} + R_{SD}$  and  $T_t = T_{Sp} + T_{SD}$ , then  $R_t + T_t = 1$  in the absence of absorption. This will hold because all component matrices in Eq. (3) are flux conserving, assuming that  $K_1 = K_2 = 0$  for each layer. If positive absorption coefficients  $K_i$  occur for one or more layers, we will have  $R_t + T_t + A_s = 1$ . Here, the absorptivity  $A_s$  depends in lowest order only on those coefficients  $K_i$  which are nonzero. It is also possible to have a diffuse cone of radiation  $F_{nD}^+$  incident on the multilayer rather than  $F_{nS}^+$ . Then we will have a diffuse-to-diffuse channel coupling such that  $R_{DD} = R_{nD}^-/F_{nD}^+$  and  $T_{DD} = F_{xD}^+/F_{nD}^+$ . Because of solid angle restrictions, no diffuse-to-specular coupling ordinarily occurs. Moreover, excluding absorption, we again have  $R_{DD} + T_{DD} = 1$ . In the case of absorption, we again define an absorptivity  $A_D$  which depends to lowest order on nonzero  $K_i$  such that  $R_{DD} + T_{DD} + A_D = 1$ .

In the present discussion, we will restrict our application of the foregoing multiflux approach to a single weakly scattering layer having  $S_i L \ll 1$  and  $K_i L \ll 1$ . Suppose the density of individual particulate scatterers within the layer to be  $N_p$  and the particulate scattering cross section to be  $C(\Omega)$ . Then, we define

$$S_1 = N_p \int_+ d\Omega C(\Omega) \text{ and } S_2 = N_p \int_- d\Omega C(\Omega)$$

where integrations are over forward and reverse cones. Particularly interesting in this model are the hemispherical backscattering or hemispherical forward scattering. We may state these as

$$R_{SD} = \frac{(1-R_1)(1-R_{1a}) L \{S_1(R_2 + R_{2a}) + S_2(1 + R_2 R_{2a})\}}{(1-R_1 R_2)(1-R_{1a} R_{2a})} \quad (4)$$

and

$$T_{SD} = \frac{(1-R_1)(1-R_{2a}) L \{S_1(1 + R_{1a} R_2) + S_2(R_2 + R_{1a})\}}{(1-R_1 R_2)(1-R_{1a} R_{2a})} \quad (5)$$

Since all interfacial reflectances are  $< 1$ , we may show that  $1 + R_{1a} R_2 > R_2 + R_{1a}$  and  $1 + R_2 R_{2a} > R_2 + R_{2a}$ . Thus, if the individual particulate scattering coefficient  $S_2 > S_1$ , the diffuse reflectance  $R_{SD}$  will be  $> T_{SD}$ . On the other hand, if  $S_1 > S_2$ , then the diffuse transmittance  $T_{SD}$  will be  $> R_{SD}$  instead. Thus, simultaneous integrated hemispherical back and forward scattering measurements can yield some microparticulate defect scattering information through determination of the coefficients  $S_1$  and  $S_2$ .

This analysis may have applications to optical material studies such as ensemble microparticle drop sizing<sup>4</sup> or other related topics of current interest. It may serve as an adjunct to scattering models based on direct solutions to Maxwell's equations for various scattering geometries.

#### REFERENCES

1. J.M. Elson, Kirtland Weapons Laboratory, Technical Report No. AFWL-TR-75-210, Kirtland AFB, NM (1976).
2. See e.g., J.M. Elson and J.M. Bennett, Opt. Eng. 18, 116 (1979); E. Kretschmann and E. Kröger, J. Opt. Soc. Am. 65, 150 (1975).
3. P.S. Mudgett and L.W. Richards, Appl. Opt. 10, 1485 (1971).
4. See e.g., D.J. Holve and K.D. Annen, Opt. Eng. 23, 591 (1984).

## OPTICAL ABSORPTION IN THE BAND GAP IN HIGH PURITY SILICON

Randall T. Swimm  
Center for Laser Studies  
University of Southern California  
Los Angeles, CA 90089-1112

Calorimetric measurement of weak optical absorption of laser illumination by solid samples is a well established method. The possibility of applying such methods to the study of deep level impurities has been discussed in the literature (1,2), but little data has been published. In this paper, some of the many difficulties and constraints in applying calorimetry to the study of deep level impurities will be discussed.

The goal of the present study was to determine the energy of a deep level with respect to either the valence or conduction band edge. In order to do this it is necessary to measure the photoionization or photoneutralization cross section as a function of photon energy. In order to accurately determine the energy of the level, it is essential that the photo cross section be measured in the very low absorption limit near the threshold energy for transitions. This is because the absorption near the threshold is strongly influenced by coupling to the lattice, as shown by Ridley (3) using photoconductivity, and Monemar and Samuelson (4) using photoluminescence. The effect of this coupling must be included in the lineshape model used to analyze the data, and determine the level energy. Measurements of only the upper portion of the photo cross section cannot be relied upon to yield an accurate energy determination.

Extremely high sensitivities for calorimetry and closely related photoacoustic measurements have been reported - absorption coefficient capabilities of  $10^{-7} \text{ cm}^{-1}$ . However, such sensitivities are useless if background absorption levels are greater than the signal being sought. Calorimetric measurements of optical absorption in high purity silicon single crystals were carried out at room temperature in order to determine limiting background absorption levels.

Samples were cut from a boron-doped float-zone ingot grown by Wachter-Siltronjc. Sample resistivity was  $10^4 \Omega\text{-cm}$ , and minority carrier lifetime was  $5 \times 10^{-3} \text{ s}$ . Absorption measurements were carried out at two wavelengths.

One set of data was measured at a wavelength of  $1.9 \mu\text{m}$ , obtained by Raman shifting in hydrogen the  $1.06 \mu\text{m}$  radiation from a Q-switched Nd:YAG laser. An apparent absorption coefficient of  $1 \times 10^{-2} \text{ cm}^{-1}$  was measured at an incident intensity of  $3 \text{ MW/cm}^2$ . Subsequent measurements showed the absorption to be intensity dependent, consistent with multiple photon absorption.

A second set of data was measured at a wavelength of  $1.32 \mu\text{m}$ , obtained from a CW Nd:YAG laser. An absorption coefficient of  $1 \times 10^{-3} \text{ cm}^{-1}$  resulted. It is suspected that this absorption may be due to an indirect band-to-band process involving three phonons. This process has been shown to exist at photon energies above  $0.991 \text{ eV}$  by Anagnostopoulos and Sadasiv (5).

The relatively high background absorption found in these measurements, and the requirement of measuring the lowest possible absorption limit of the photo cross section imply that heavy doping will be required if the energies of deep level impurities in silicon are to be measured by calorimetric methods (including photoacoustic). The high background absorption suggests that it may not be possible to fully utilize the extremely high sensitivity of which calorimetric methods are capable.

This research was sponsored by the California Institute of Technology Jet Propulsion Laboratory.

1. D. Bimberg and A. Bubenzer, Appl. Phys. Lett. 38, 803 (1981)
2. G. Wetsel and F.A. McDonald, 1st Topical Meeting on Photoacoustic Spectroscopy, held Aug. 1979 at Ames Iowa, paper ThA5.
3. B.K. Ridley, J. Phys. C. Solid St. Phys., 13, 2015 (1980).
4. B. Monemar and L. Samuelson, Phys. Rev. B 18, 809 (1978).
5. C. Anagnostopoulos and G. Sadasiv, Phys. Rev. B 7, 733 (1973).

# PROPERTIES OF GUIDED MODES IN BIDIRECTIONAL ANISOTROPIC MEDIA

O. Schwelb

Department of Electrical Engineering

Concordia University

1455 de Maisonneuve Blvd. West

Montreal, Quebec, H3G 1M8

Guidance has been investigated in layered anisotropic media characterized by a permittivity or permeability tensor that is Hermitian and has one pair of off-diagonal elements, but is otherwise arbitrary. Depending on the location of the off-diagonal elements one distinguishes between polar, longitudinal and equatorial orientation. In polar orientation the nonzero off-diagonal element pair:  $\epsilon_{yz} - \epsilon_{zy}$ , corresponds to the plane of the interface, in our case the y-z plane. In longitudinal orientation  $\epsilon_{xy} - \epsilon_{yx}$  is the non-vanishing pair, corresponding to the plane perpendicular to the direction of propagation (x-y plane). Finally the equatorial configuration is associated with an optic axis in the plane of incidence (x-z plane).

Assuming  $\exp(j\omega t)$  time dependence and a wave vector  $\vec{k} = k_0[\kappa(n)\vec{a}_x + \beta\vec{a}_z]$ , where  $k_0 = \omega/\mu_0\epsilon_0$ ,  $\beta$  is taken to be real and  $\kappa(n)$  is a transverse guide index in region n, the polar and longitudinal orientations admit bidirectional wave propagation, i.e. the normalized wave members of the four partial waves satisfy the constraints  $\kappa_2(n) = -\kappa_1(n)$  and  $\kappa_4(n) = -\kappa_3(n)$ . The equatorial orientation is quasi-isotropic in the sense that TE and TM modes are separate, but the TM mode exhibits peculiarities of which more will be said later.

The layer transfer matrix  $G(x)$  is defined by

$$\vec{g}(x) = G(x)\vec{g}(0) \quad (1)$$

where the state vector is  $\vec{g}(x) = \text{col}[\eta_0^{-1/2}E_y(x), \eta_0^{1/2}H_z(x), \eta_0^{-1/2}E_z(x), -\eta_0^{1/2}H_y(x)]$  and  $\eta_0 = \sqrt{\mu_0/\epsilon_0}$ , and the normalized characteristic impedance of a medium is computed from

$$\eta_0^{-1/2}E_{\tau 1} = Z\sigma^T \eta_0^{1/2}H_{\tau 1} \quad (2)$$

where  $\sigma = \begin{bmatrix} 0 & -1 \\ 1 & 0 \end{bmatrix}$  and  $E_{\tau 1}$  ( $H_{\tau 1}$ ) is the incident electric (magnetic) field vector component in the plane of the interface.

It can be shown [1] that in a polar medium

$$G(x) = G_1(x) - G_2(x) \quad (3)$$

where

$$G_1(x) = \frac{1}{h_3 - h_1} \begin{bmatrix} h_3 C_1 & -jh_3 \kappa_1^{-1} S_1 & -C_1 & jw^{-1} \kappa_1^{-1} S_1 \\ -jh_3 \kappa_1 S_1 & h_3 C_1 & j\kappa_1 S_1 & -w^{-1} C_1 \\ h_1 h_3 C_1 & -jk_1 h_3 \kappa_1^{-1} S_1 & -h_1 C_1 & jh_1 w^{-1} \kappa_1^{-1} S_1 \\ -jwh_1 h_3 \kappa_1 S_1 & wh_1 h_3 C_1 & jwh_1 \kappa_1 S_1 & -h_1 C_1 \end{bmatrix} \quad (4)$$

$h_i = \epsilon_{zy}(\epsilon_{xx} - \beta^2) / [\epsilon_{xx}\kappa_i^2 - \epsilon_{zz}(\epsilon_{xx} - \beta^2)]$ ,  $i=1,3$ ,  $w = \epsilon_{xx} / (\epsilon_{xx} - \beta^2)$ ,  
 $C_i = \cos \kappa_i x$ ,  $S_i = \sin \kappa_i x$  and  $G_j(x)$  obtains from  $G_i(x)$  by interchanging  
indices 1 and 3. Note that  $\epsilon_{ij}$  is the  $ij$ -th element of the Hermitian  
relative permittivity tensor, and  $x$  is normalized with respect to  $k_0$ . From  
(3) it can be seen that  $H_z=0$  and  $dE_y/dx=0$  occur in the same  $x=x_0$  plane.  
Conversely,  $H_y=0$  and  $dE_z/dx=0$  also occur simultaneously in the same  $x=\text{const.}$   
plane. The values of the normalized transverse wave numbers can be  
calculated from

$$2\kappa^2 = (\epsilon_{yy} + \epsilon_{zz}) - (\epsilon_{xx} + \epsilon_{zz}) \frac{\beta^2}{\epsilon_{xx}} \pm \left\{ [(\epsilon_{yy} - \epsilon_{zz}) - (\epsilon_{xx} - \epsilon_{zz}) \frac{\beta^2}{\epsilon_{xx}}]^2 + 4|\epsilon_{yz}|^2 (1 - \frac{\beta^2}{\epsilon_{xx}}) \right\}^{\frac{1}{2}}. \quad (5)$$

The forward characteristic impedance matrix of a polar layer is given by

$$Z_f = \frac{1}{w\kappa_1\kappa_3(h_3 - h_1)} \begin{bmatrix} w(\kappa_3 h_3 - \kappa_1 h_1) & (\kappa_1 - \kappa_3) \\ wh_1 h_3 (\kappa_3 - \kappa_1) & (\kappa_1 h_3 - \kappa_3 h_1) \end{bmatrix} \quad (6)$$

and the backward characteristic impedance is simply the negative of this expression.

In a longitudinal medium the transfer matrix is also given by (3) but now

$$G_i(x) = \frac{1}{g_3 - g_1} \begin{bmatrix} g_3 C_i & -jg_3 \kappa_i^{-1} S_i & js^{-1} \kappa_i^{-1} S_i & -C_i \\ -jg_3 \kappa_i S_i & g_3 C_i & -s^{-1} C_i & j\kappa_i S_i \\ -jsg_1 g_3 \kappa_i S_i & sg_1 g_3 C_i & -g_1 C_i & jsg_1 \kappa_i S_i \\ g_1 g_3 C_i & -jg_1 g_3 \kappa_i^{-1} S_i & jg_1 s^{-1} \kappa_i^{-1} S_i & -g_1 C_i \end{bmatrix} \quad (7)$$

where  $g_i = \beta \epsilon_{zz} \epsilon_{xy} / [\epsilon_{zz}(\epsilon_{xx} - \beta^2) - \epsilon_{xx} \kappa_i^2]$ ,  $i=1,3$  and  $s=1/\epsilon_{zz}$ . The turning  
points in longitudinal configuration are such that either  $H_z=0$  and  $dE_y/dx=0$ ,  
or  $E_z=0$  and  $dH_y/dx=0$  occur simultaneously in the same transverse plane. The  
values of the normalized transverse wavenumbers can be obtained from

$$2\kappa^2 = (\epsilon_{yy} + \epsilon_{zz}) - |\epsilon_{xy}|^2 / \epsilon_{xx} - (\epsilon_{xx} + \epsilon_{zz}) \frac{\beta^2}{\epsilon_{xx}} \pm \left\{ [(\epsilon_{yy} - \epsilon_{zz}) - |\epsilon_{xy}|^2 / \epsilon_{xx}]^2 - (\epsilon_{xx} - \epsilon_{zz}) \frac{\beta^2}{\epsilon_{xx}} \right\}^{\frac{1}{2}} + 4|\epsilon_{xy}|^2 \epsilon_{zz} \beta^2 / \epsilon_{xx}^2 \right\}^{\frac{1}{2}}. \quad (8)$$

The forward characteristic impedance matrix of a longitudinal layer is

$$Z_f = \frac{1}{\kappa_1 g_3 - \kappa_3 g_1} \begin{bmatrix} g_3 - g_1 & \kappa_1 - \kappa_3 \\ sg_1 g_3 (\kappa_1 - \kappa_3) & s\kappa_1 \kappa_3 (g_3 - g_1) \end{bmatrix} \quad (9)$$

but now the backward characteristic impedance is related to  $Z_f$  via

$$Z_b = - \begin{bmatrix} 1 & 0 \\ 0 & -1 \end{bmatrix} Z_f \begin{bmatrix} 1 & 0 \\ 0 & -1 \end{bmatrix} \quad (10)$$

The TE mode in an equatorial medium is equivalent to that in an isotropic medium. The TM mode however "walks off" the z axis at an angle  $\delta$  given by [2]

$$\tan \delta = \operatorname{Re}(\epsilon_{xz})/\epsilon_{xx}. \quad (11)$$

The TM mode wave admittance in the forward direction is

$$Y_{TM} = \{j\beta \operatorname{Im}\epsilon_{xz} + [\Delta_{yy}(\epsilon_{xx} - \beta^2) - \beta^2(\operatorname{Im}\epsilon_{xz})^2]^{1/2}\} / (\epsilon_{xx} - \beta^2) \quad (12)$$

where  $\Delta_{yy} = \epsilon_{xx}\epsilon_{zz} - |\epsilon_{xz}|^2$ . When  $\operatorname{Re}\epsilon_{xz} = 0$  wave propagation is bidirectional, but the backward and forward wave admittances are not simply of opposite signature. When  $\operatorname{Im}\epsilon_{xz} = 0$  forward and backward wave admittances have opposite signature, but the guide does not support bidirectional wave propagation.

Bounds of  $\beta$  refer to those values of the real axial wavenumber, or effective guide index, at which either an external region attenuation coefficient ( $\alpha_1$ ) vanishes (cutoff), or an internal region transverse wave number ( $\kappa_1$ ) approaches zero (high frequency limit). In a lossless waveguide  $\alpha_1$  change from real to imaginary at cutoff, as the effective guide index decreases. This limit marks the frequency below which the guide becomes leaky. Since there is more than one limit condition, the highest  $\beta$  is critical. As the frequency increases, the rays approach the axial direction, the axial wavenumber approaches the free space wavenumber and  $\kappa_1$  vanishes.

In polar orientation, when  $\beta^2 = \beta_a^2 = \epsilon_{xx}$  and  $\epsilon_{yy} > \epsilon_{xx}$ , then  $\kappa_1^2 = \epsilon_{yy} - \epsilon_{xx}$  and  $\kappa_3^2 = 0$ . On the other hand, at the same value of  $\beta$ , when  $\epsilon_{yy} < \epsilon_{xx}$ ,  $\kappa_1^2 = 0$  and  $\kappa_3^2 = \epsilon_{yy} - \epsilon_{xx}$ . Therefore  $\beta_a$  is a high frequency limit condition. The other high frequency limit is at  $\beta^2 = \beta_b^2 = \epsilon_{yy} - |\epsilon_{yz}|^2/\epsilon_{zz}$ . At this value if  $(1/\epsilon_{xx} + 1/\epsilon_{zz})|\epsilon_{yz}|^2 > (\epsilon_{yy}/\epsilon_{xx} - 1)\epsilon_{zz}$ , then  $\kappa_1^2 = (1/\epsilon_{xx} + 1/\epsilon_{zz})|\epsilon_{yz}|^2 - (\epsilon_{yy}/\epsilon_{xx} - 1)\epsilon_{zz}$  and  $\kappa_3^2 = 0$ , whereas if the inequality points in the other direction, then  $\kappa_1^2$  and  $\kappa_3^2$  exchange roles. The same conditions apply to cutoff if primed quantities, referring to an external region, are used in the above expressions, and if the  $\kappa_1 \rightarrow -j\alpha_1$  substitution is made.

In longitudinal orientation one of the high frequency limits is at  $\beta^2 = \beta_a^2 = \frac{1}{2}(\epsilon_{xx} + \epsilon_{yy}) + [\frac{1}{2}(\epsilon_{xx} - \epsilon_{yy})^2 + |\epsilon_{xy}|^2]^{1/2}$ . If  $\delta_a = \epsilon_{yy} + \epsilon_{zz} - |\epsilon_{xy}|^2/\epsilon_{xx} - (\epsilon_{xx} + \epsilon_{zz})\beta_a^2/\epsilon_{xx} > 0$ , then at  $\beta = \beta_a$   $\kappa_1^2 = \delta_a$  and  $\kappa_3^2 = 0$ , whereas if  $\delta_a < 0$ , then at  $\beta = \beta_a$   $\kappa_1^2 = 0$  and  $\kappa_3^2 = \delta_a$ . The other high frequency limit is at  $\beta^2 = \beta_b^2 = \frac{1}{2}(\epsilon_{xx} + \epsilon_{yy}) - [\frac{1}{2}(\epsilon_{xx} - \epsilon_{yy})^2 + |\epsilon_{xy}|^2]^{1/2}$ . If  $\delta_b = \epsilon_{yy} + \epsilon_{zz} - |\epsilon_{xy}|^2/\epsilon_{xx} - (\epsilon_{xx} + \epsilon_{zz})\beta_b^2/\epsilon_{xx} > 0$ , then at  $\beta = \beta_b$   $\kappa_1^2 = \delta_b$  and  $\kappa_3^2 = 0$ , whereas if  $\delta_b < 0$ , then at the same value of  $\beta$   $\kappa_1^2 = 0$  and  $\kappa_3^2 = \delta_b$ . The cutoff conditions are given by the same expressions provided primed quantities are used and  $\kappa_1$  is interpreted as  $-j\alpha_1$ .

In conclusion explicit expression have been presented for the layer transfer matrix, for the characteristic impedance and for the bounds of the effective guide index for uniaxial media in polar and longitudinal orientation. Some properties distinguishing the equatorial orientation have also been mentioned.



- [1] O. Schwelb: Anisotropic stratified waveguides for electromagnetic waves: a matrix analysis, Internal Report, Dept. Electrical Eng., Concordia University, Montreal, Quebec, 1984.
- [2] D. Marcuse: IEEE J. QE-14, 736 (1978).

CALORIMETRIC MEASUREMENT OF OPTICAL ABSORPTION IN SAPPHIRE  
AT VISIBLE, NEAR IR, AND NEAR UV WAVELENGTHS

Antonio Balbin Villaverde\*, Randall T. Swimm, and Michael Bass

Center for Laser Studies  
University of Southern California  
Los Angeles, CA 90089-1112

In this paper calorimetric measurements of optical absorption in sapphire at visible, near IR and near UV wavelengths are reported. Single-crystal sapphire grown by Union Carbide was fabricated into rectangular prism samples and polished on all faces. Sample cross section was 1 cm square, and samples of thickness 0.5, 1.0, and 2.0 cm were measured. CW-laser irradiation from krypton ion, dye, Nd:YAG and Nd:YAlO<sub>3</sub> lasers was used, over a wavelength interval from 1.32  $\mu\text{m}$  to 0.35  $\mu\text{m}$ . Measurements were carried out at room temperature using a calorimeter which was been described previously [1].

Chromium is a ubiquitous impurity in sapphire, and was apparently present even though the samples were not intentionally doped. Fluorescence was observed when samples were pumped at wavelengths in the  $\text{Cr}^{+3}$  bands. The weak peaks in the absorption data at these absorption band wavelengths are due to the combined effect of nonradiative recombination, and indirect heating of calorimeter components by the radiated fluorescence. For this reason, it is difficult to estimate the chromium concentration.

A plot of  $\ln \alpha$  vs wavelength  $\lambda$ , where  $\alpha$  is the absorption coefficient in  $\text{cm}^{-1}$  yields a surprisingly linear behavior over the wavelength interval from 0.75  $\mu\text{m}$  to 0.35  $\mu\text{m}$ . However, this may be fortuitous, considering the presence of chromium absorption.

A plot of  $\ln \alpha$  vs photon energy  $\hbar\omega$  yields a reasonably linear behavior over a wider wavelength range, extending from 1.08  $\mu\text{m}$  to 0.35  $\mu\text{m}$  (1.15 eV to 3.50 eV). This result is consistent with an exponential absorption edge described by Urbach's rule, with some additional absorption in the chromium absorption bands.

An Urbach tail may be modelled [2] by the relationship

$$\alpha = A \exp[\sigma(\hbar\omega - \hbar\omega_0)/k_B T]$$

where  $h$  is Plack's constant,  $k_B$  is Boltzmann's constant,  $T$  is temperature and  $A$ ,  $\sigma$ , and  $\omega_0$  are fitting parameters.  $\hbar\omega_0$  is usually approximately equal to the lowest exciton energy, 9.5eV is the case of sapphire [3]. If the data are assumed to follow the behavior of Urbach's rule, then the slope of the measured data plotted in the figure results in a value for the parameter  $\sigma$  of 0.065. This is rather small, considering

that the value is usually of order unity.

In summary, the optical absorption of sapphire was measured calorimetrically in the wavelength interval from 1.32  $\mu\text{m}$  to 0.35  $\mu\text{m}$ . The data show reasonably linear behavior in a plot of the natural logarithm of the absorption coefficient versus photon energy, with some additional absorption due to residual chromium ions.

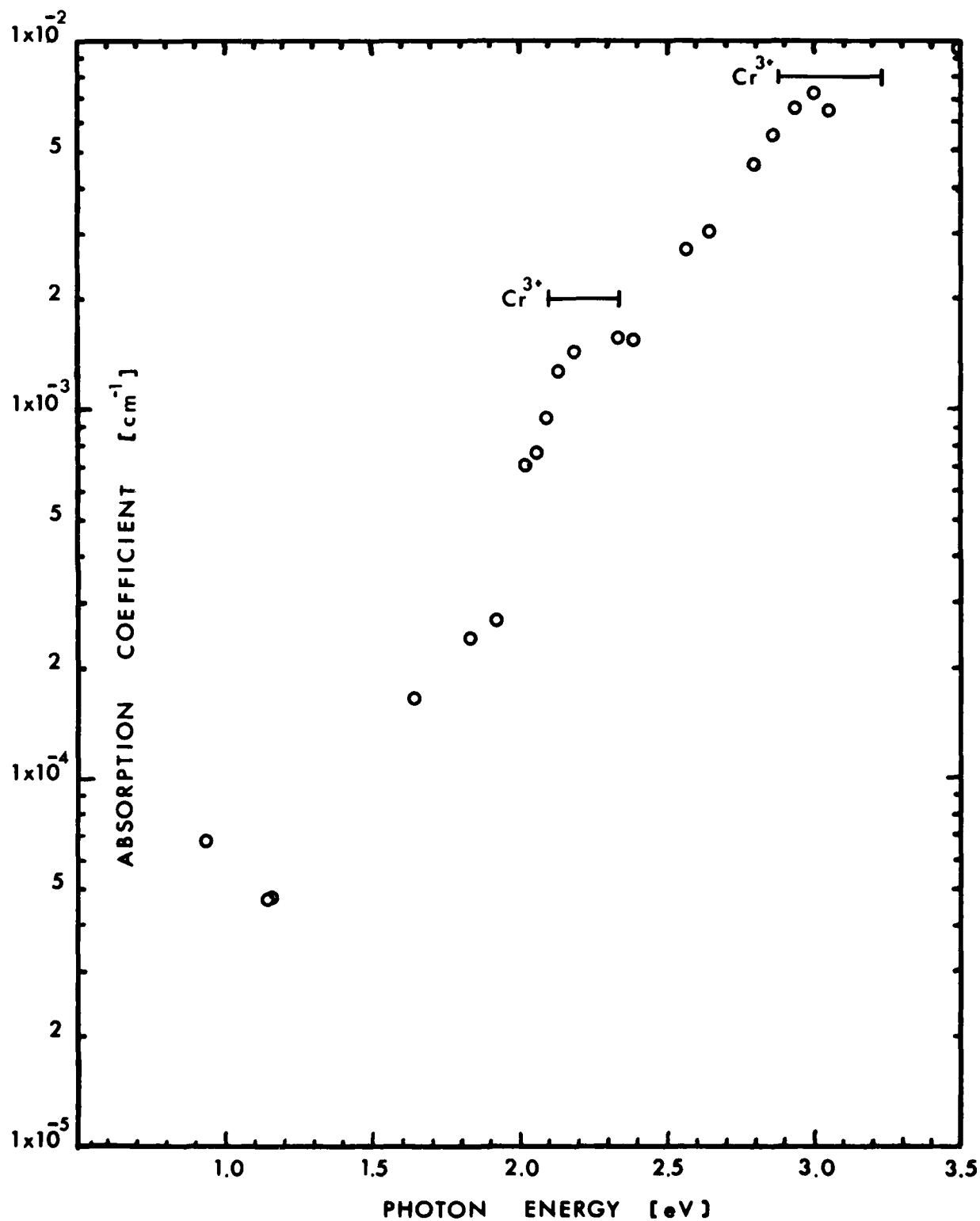
This research was sponsored by Lawrence Livermore National Laboratory.

1. R. T. Swimm, Y. Xiao and M. Bass, "A Calorimetric Study of Optical Absorption of Suprasil W-1 Fused Quartz at Visible Near IR and Near UV Wavelengths", accepted for publication in early 1985 in Applied Optics.
2. John D. Dow and David Redfield, Phys. Rev. B 5, 594 (1972) and references therein.
3. E. T. Arakawa and M. W. Williams, J. Phys. Chem. Solids 29, 735 (1968).

\*Antonio Balbin Villaverde, Instituto de Fisica, Depto Eletronica Quantica, Universidade Estadual de Campinas C.P. 6166, 13100 - Campinas - S.P. Brazil

Figure. Plot of Absorption Coefficient for Sapphire vs Photon Energy. Indicated lines show  $\text{Cr}^{3+}$  absorption bands. (Note that there is a data point in the upper right corner).

# SAPPHIRE ABSORPTION VS PHOTON ENERGY



OPTICAL PROPERTIES OF ION  
BEAM IRRADIATED MOLYBDENUM  
LASER MIRRORS AS STUDIED  
BY ELLIPSOMETRY<sup>+</sup>

John A. Woollam, George H. Bu-Abbud,  
and David L. Mathine  
Department of Electrical Engineering  
University of Nebraska, Lincoln, NE 68588-0511

David Poker  
Solid State Division  
Oak Ridge National Laboratory  
Oak Ridge, TN 37830

David Ingram and Peter Pronko  
Universal Energy Systems  
Dayton, OH 45432

Molybdenum mirrors are widely used in high energy lasers because of their desirable high temperature thermal properties such as high thermal diffusivity, low thermal expansion coefficient, and high laser damage threshold (1). It is also stiff so it can be attached to water cooled backs. However it is nearly impossible to diamond-turn the surface, and mechanical polishing is mainly used. Ion beam processing of materials is of considerable interest, and sizable literature in this field is developing (2). Heavy ion implantation into metal surfaces can radically change surface properties, as a result of chemical changes and enhanced atomic kinetics.

In this paper we report on implantation of Mo ions into polished molybdenum surfaces to investigate the effects of implantation of surface roughness, and optical reflectivity. The motivation is to develop ion beam techniques for improving the reflectivity and (surface smoothness) over a wide spectral range. Information on the index of refraction, and extinction coefficient as functions of wavelength are also obtained.

Three sets of mirrors were prepared from rolled sheet stock of molybdenum, and polished with a series of grits down to a final cloth lap using 1 micron diamond paste.

Samples were irradiated with 150 kv Mo ions with fluences of 0, 2, 4, 8, and  $16 \times 10^{15}$  ions  $\text{cm}^{-2}$  directed at separate sections of the sample. Thus the starting surfaces for the various fluences were identical. Each sample was held at a separate temperature: 25°C, 250°C, and 500°C respectively.

<sup>+</sup>Research supported by the College of Engineering, University of Nebraska, The Department of Energy, and the National Science Foundation.

Ellipsometric data were taken with both null and automated rotating analyzer systems for angles of incidence near the principle angle for each wavelength. Data were analyzed by comparing the measured ellipsometric parameters  $\psi$  and  $\Delta$  with those calculated assuming several possible geometrical models. The Marquardt algorithm was used to find the minimum of the sum of squares between measured and calculated  $\psi$ 's and  $\Delta$ 's (3).

The results are as follows: the reflectivity is found to increase as a function of fluence, but most of the increase is in the range up to  $4 \times 10^{15}$  ions/cm<sup>2</sup>. This statement is true no matter what wavelength is used in the 365 to 800 nm range, although the absolute value of reflectivity depends on wavelength of course. The fluence for maximum reflectivity is reached earlier for higher temperatures and shorter wavelengths.

We used the index of refraction and extinction coefficient data, along with the Bruggeman effective medium theory (EMA) to analysis what is happening physically at the surface (4). The following models were assumed:

1. A bare surface of unknown refractive index.
2. A bare surface consisting of molybdenum metal which is microscopically rough. (In the EMA, voids plus Mo are the assumed constituents).
3. A bare substrate including a mixture of voids, Mo, and MoO<sub>2</sub>. (ESCA measurements were used to identify the presence of small amounts of MoO<sub>2</sub>).

Several other models were tried by the sum of the squares of differences of experimental and calculated  $\psi$ 's and  $\Delta$ 's were unreasonably high.

The best fit to the data came by using Model 3, when the fraction of void was 0.2, Fraction Mo was 0.8, and fraction MoO<sub>2</sub> was less than 0.01. This fraction void is consistent with a microstructure of hemicylinders. As a function of fluence the fraction Mo reaches a maximum (fraction void reaches a minimum) for fluences in the 2 to  $4 \times 10^{15}$  ions/cm<sup>2</sup> range, consistent with the reflectivity reaching a maximum in the same range.

#### References

1. J.M. Bennett, S.M. Wong, and G. Kraus, *Applied Optics* 19, 35662 (1980)
2. *Metastable Materials Formation by Ion Implantation*, Materials Research Society Proceedings, Vol. 7, S.T. Picroux, and W.J. Choyke, Editors, 1982.
3. G.H. Bu-Abbud, N.M. Bashara, and J.A. Woollam, "Sensitivity Correlation Test of Variable Wavelength Variable Angle Ellipsometric Solutions", accepted for publication in *Thin Solid Films*, 1985.
4. D.E. Aspnes, J.B. Theeton, and F. Hottier, *Phys. Rev.* 320, 3292 (1979).

CRYSTAL FIELD ENERGY LEVELS AND OPTICAL ABSORPTION  
INTENSITIES OF  $\text{Ni}^{2+}:\text{MgF}_2$

Bing Zhang, Ji-Kang Zhu and Song-Hao Liu

Anhui Institute of Optics and Fine Mechanics, Academia Sinica  
P.O. Box 25, Hefei, Anhui, People's Republic of China

One-electron energy levels and wave functions of laser crystal  $\text{Ni}^{2+}:\text{MgF}_2$  with lower symmetric crystal fields  $D_{2h}$  are calculated by use of the spin-unrestricted MS-X $\alpha$  method. The calculated value of  $10D_q$  is in much better agreement with the experimental result than another theoretical value which was based on higher symmetric crystal field consideration<sup>[1]</sup>. By analyzing  ${}^3T_{2g}$  and  ${}^3T_{1g}$  energy levels related with laser operation the splitting values of  ${}^3T_{2g}$  and  ${}^3T_{1g}$  in lower symmetric crystal field have been derived. MS-X $\alpha$  calculation of magnetic dipole intensity by means of Karplus electronic charge partition method has been reported for the first time. The oscillator strengths of electric dipole coupled with vibration between ground state and  ${}^3T_{1g}$  state have been estimated. It is shown theoretically that  ${}^3A_{2g}-{}^3T_{2g}$  is magnetic dipole transition and  ${}^3A_{2g}-{}^3T_{1g}$  is electric dipole transition coupled with vibration. Comparisons between the calculated and experimental results of  $10D_q$  and oscillator strengths are shown in Tables 1 and 2.

[1] S. Larsson, J. W. D. Connolly, Chem. Phys. Lett., 20, 323 (1973).

Table 1. One-Electron Eigenvalues and  $10D_q$  for Crystal  $Ni^{2+}:MgF_2$

Energy Levels		Eigenvalues	$10D_q (cm^{-1})$		
Oh	$D_{2h}$	$(cm^{-1})$	This Work	Expt.	Calc.[1]
${}^3T_{2g}$	${}^3B_{3g}$	7594			
	${}^3B_{2g}$	7780	7795	7407	9500
	${}^3A_g$	8011			
${}^3T_{1g}$	${}^3B_{2g}$	9835			
	${}^3B_{3g}$	11105			
	${}^3B_{1g}$	11360			

Table 2. Magnetic Dipole Oscillator Strengths  $f$  of  ${}^3T_{2g}$

Energy Levels		$f (\times 10^{-6})$	$f (\times 10^{-6})$
Oh	$D_{2h}$	This Work	Expt.
${}^3T_{2g}$	${}^3B_{3g}$	4.4	
	${}^3B_{2g}$	4.5	5.0
	${}^3A_g$	4.6	



## STATUS OF OPTICAL CONSTANTS OF SOLIDS FROM X-RAY TO MM-WAVE REGION

E.D. Palik  
Naval Research Laboratory  
Washington, DC 20375

### INTRODUCTION

As editor of the Handbook of Optical Constants of Solids (1), I have obtained a bird's-eye view of the quantity and quality of optical constants for 37 solids of technological and physics interest. These include 11 metals - Al, Cu, Au, Ir, Mo, Ni, Os, Pt, Rh, Ag, W; 14 semiconductors - CdTe, GaAs, GaP, Ge, InAs, InSb, InP, PbSe, PbS, PbTe, Si, a-Si, SiC, ZnS; 12 insulators - As<sub>2</sub>Se<sub>3</sub>, As<sub>2</sub>S<sub>3</sub>, C(diamond), LiF, LiNbO<sub>3</sub>, KCl, SiO<sub>2</sub>, a-SiO<sub>2</sub>, SiO, Si<sub>3</sub>N<sub>4</sub>, NaCl, TiO<sub>2</sub>. Twenty one critiquers have examined the existing literature for these materials and have tabulated a single set of refractive index  $n$  and extinction coefficient  $k$  for as wide a spectral region as possible. Examples of a metal Ag, a semiconductor Si and an insulator a-SiO<sub>2</sub> (silica) are given in Fig. 1. Some effort is made to discuss the measurement techniques and the quality of the data. The problems encountered here with measurements and data are representative of all the solids studied. The Handbook also contains 11 chapters on how to determine  $n$  and  $k$  in various spectral regions.

### EXPERIMENTAL TECHNIQUES

The experimental techniques are numerous and change as the spectral region changes. In the x-ray region 1-500 Å (12500-25 eV) samples are generally evaporated thin films removed from backings, so that transmission/reflection measurements can be made with x-ray or synchrotron sources and spectrometers. For any material but especially for metals, external total reflection is done to determine  $n$  where it is only slightly less than unity, and  $n \gg k$  holds true. In the UV region 25-6 eV (500-2000 Å) reflectance of bulk samples is made, followed by Kramers-Kronig analysis with due consideration of frequency limits. For opaque solids ellipsometry or variable angle-of-incidence reflectivity are dominant over normal-incidence unpolarized reflectivity. In the near infrared generally near or below the fundamental band gap, a thin slab sample or a film on a substrate are used for transmittance and reflectance measurements. In the transparent region below the band gap thick samples can be used to determine  $k$  from a transmittance or a calorimetry measurement. Interestingly, the prism minimum-deviation technique is still the best for determining  $n$  to 5 significant figures. In fact, Ruben's data for NaCl of nearly 90 years ago (2) is in agreement with today's data (3) to 4 figures, usually. Measurement of interference-fringe spacing is the next best technique for determining  $n$ . As the optical-phonon region is approached in the far infrared, it is necessary to go to reststrahlen reflectivity measurements fitting with a Lorentz-oscillator model or Kramers-Kronig analysis if no thin films are available. Fortunately, asymmetric Fourier transform spectroscopy gives both phase and amplitude of  $R$  directly with no model or analysis assumptions (4). Techniques like ellipsometry and variable angle-of-incidence reflectance have not found general use in the infrared.

There are a number of special-purpose measurement techniques such as emittance (5), internal reflection critical-angle determination (6), launching and retrieval of guided modes for thin transparent films (7), interference effects to determine both  $n$  and  $k$  in thin films (8). Many of us have forgotten the

measurement of capacity of dielectrics well beyond the mm-wave region to determine the low-frequency real and imaginary parts of the dielectric function. While the mass absorption constant was measured for many elements in the x-ray region early in the century (9), it now proves to be convenient to use a model of Henke et al. (10) to calculate this quantity to obtain  $k$ . This model for chemical elements as well as compounds is based on the atomic scattering cross-section of the elements and allows calculation of the absorption edges in the x-ray to UV region before chemical bonding begins to perturb the valence electron states.

In addition to the chapters in the Handbook, there are a number of other reviews of the many ways to determine  $n$  and  $k$  (11-15).

#### SAMPLE PROBLEMS

While different experiments in different spectral regions give rise to a myriad of accuracy and precision problems, samples also vary from lab to lab. Problems include: 1) Bulk samples are mechanically polished with grit rather than chemically polished. This can affect the reflectivity minimum and maximum in the reststrahlen region and becomes more important as the wavelength gets shorter; 2) Bulk sample surfaces grow native oxides when polishing or cleaving is done in air. This problem is most important where the absorption edge of the dielectric layer 10-20 Å thick occurs (generally  $> 4$  eV). It also affects the ellipsometric determination of  $\epsilon_1$  and  $\epsilon_2$ , the real and imaginary parts of the dielectric function (16), and should be included in the modeling used to obtain the dielectric function or native-oxide-free surfaces should be measured in the first place (such as in laboratory UHV apparatus; 3) Roughness is also a layer which can be treated as an effective medium and if not considered, gives "psuedo" optical constants; 4) An especially bad actor is the deposited, evaporated or CVD grown film on a substrate. Authors invariably do not characterize films several different ways to determine stoichiometry, roughness, void fraction, crystallinity, etc., so the optical constants vary from lab to lab. This has been especially true of deposited metals (17). Any film grown on a substrate will be strained, so that the refractive index is affected (for example,  $\text{SiO}_2$  on Si (18)), or the band gap is shifted (19).

#### MODELS

Models are especially useful in accounting for a) refractive index in the transparent region (Sellmeier equation), b) dielectric function in the reststrahlen region (Lorentz oscillator), and c) dielectric function in the free-carrier plasma region (Drude model).

An ultimate Sellmeier equation which includes contributions of several higher-frequency interband transitions represented as classical oscillators as well as low-frequency lattice oscillators is

$$n^2 = 1 + \frac{A}{\pi} \ln \frac{E_1^2 - (\hbar\omega)^2}{E_0^2 - (\hbar\omega)^2} + \frac{G_1}{E_1^2 - (\hbar\omega)^2} + \frac{G_2}{E_2^2 - (\hbar\omega)^2} + \frac{G_3}{E_3^2 - (\hbar\omega)^2},$$

where  $E_0$  is the fundamental band gap and  $E_1$  and  $E_2$  are the next higher-lying band gaps, and  $E_3$  is the transverse optical phonon frequency. This formula has been used to fit a wide variety of semiconductors over a wide range of frequency from the fundamental band gap to the first reststrahlen band, generally reproducing the experimental data to 2-4 figures (20).

The Lorentz-oscillator model gives

$$\epsilon = \epsilon_1 + i\epsilon_2 = (n + ik)^2 = \epsilon_\infty \left[ 1 + \frac{\omega_L^2 - \omega_T^2}{\omega_T^2 - \omega^2 - i\Gamma\omega} \right],$$

where  $\omega_T$  and  $\omega_L$  are the transverse and longitudinal optical photon frequencies, respectively,  $\Gamma$  is the damping constant and  $\epsilon_\infty$  is the high-frequency dielectric constant. The corresponding values of  $k$  are probably good to one significant figure near the peak and poorer in the wings as measurements on thin films indicate (21). There are few examples of measurement of reflectivity  $R$  with both oscillator and Kramers-Kronig fits (22). For CdTe the results agree to  $\pm 30\%$ . The dc dielectric constant can be estimated by letting  $\omega \rightarrow 0$ .

Free-carrier absorption is often analyzed with the Drude model with

$$\epsilon = \epsilon_\infty \left[ 1 - \frac{\omega_p^2}{\omega(\omega + i\gamma)} \right].$$

For metals it is useful for extrapolating to longer infrared wavelengths where  $R > 0.95$ . The plasma reflection edge is fitted for semiconductors to obtain the plasma frequency  $\omega_p^2 = 4\pi N e^2 / m^* \epsilon_\infty$  and damping constant  $\gamma$  (23). Here,  $N$  is the free-carrier density and  $m^*$  is the effective mass. Then  $n$  and  $k$  can be calculated. This  $k$  is invariably too small as transmittance measurements show, because  $n$  generally dominates the reflectivity. Thus, measurement of  $R$  is a good way to get  $n$ ; measurement of transmission absorption is a good way to get  $k$ . Data near  $1 \mu\text{m}$  for Ag in Fig. 1(a) do not agree between two labs probably because of differences in sample preparation. Polarimetric measurements were used in each case (24,25). Generally, Si of high resistivity  $> 1000 \Omega\text{cm}$  is used to minimize free-carrier effects. However, some absorption shows up near  $100 \mu\text{m}$  in Fig. 1(b).

The Henke model does not include x-ray fine structure seen in experiments for Si near  $10^{-2} \mu\text{m}$  in Fig. 1(b). Note that M absorption edges of atomic Si are smeared into interband transitions as are O edges of Ag and M and L edges of Si and O for  $\text{SiO}_2$ . Absorption edges of c- and a- $\text{SiO}_2$  would be similar since chemical bonding does not affect core levels very much. It is just these differences, however, which are exploited in core-level spectroscopies.

#### SOME OBSERVATIONS

We find that room temperature in the literature is anything from 292 to 300 K. It is surprising how many authors neglected to report this number; it is usually important when you are measuring  $n$  to more than 4 significant figures or are measuring the band-edge absorption of a semiconductor.

In Fig. 1 we show values of  $n$  and  $k$  for Ag, Si and a- $\text{SiO}_2$ , plotted from detailed numerical tables. I had never seen  $k$  displayed over such a wide spectral region before. Since  $\alpha = 4\pi k/\lambda$ , and  $I/I_0 = (1-R)^2 \exp(-\alpha x)$  for the simple case of no multiple reflections, it is easy to see how thickness  $x$  must vary over such a wide range to do a transmission experiment. For example, a Si sample thin enough for  $I/I_0 = 0.2$  at  $10 \mu\text{m}$  ( $k = 10^{-5}$ ,  $n = 3.4$ ,  $R = 0.3$ ) is  $0.71 \text{ cm}$  thick, while at  $10^{-3} \mu\text{m}$  ( $k = 10^{-5}$ ,  $n \approx 1$ ,  $R \approx 0$ ), the sample must be  $0.013 \text{ cm}$  thick. Note that a film  $130 \mu\text{m}$  thick for x-ray measurements can be handled unsupported, whereas a film used to measure band-edge absorption ( $k=10^{-1}$ ) in the near infrared must be  $\sim 1 \mu\text{m}$  thick and is generally mounted on a substrate. Also, a film  $\sim 1 \mu\text{m}$  thick ( $k=1$ ) is needed to measure transmission at the TO frequency of GaAs, for example.

A collection of data from several labs over a wide spectral range cannot be easily massaged to give uniformity in accuracy. Most measurements were made to locate optical phonons or interband transitions rather than to determine  $n$  and  $k$ . Therefore, experimenters paid more attention to precision to resolve peaks in  $\alpha$ . Some general observations are; 1) Al, Si, GaAs, NaCl, SiO<sub>2</sub>,  $\alpha$ -SiO<sub>2</sub>, LiF have been worked upon over the widest spectral range by the largest number of workers; 2) Where minimum-deviation or interference-fringe techniques have been used, the values of  $n$  are good to 3-5 figures with a caution about temperature. Where transmission measurements have been performed, values of  $k$  are usually good to 1-2 figures, i.e., two measurements in two labs agree to 1-2 figures; 3) Kramers-Kronig analysis of near-normal incidence reflectivity of NaCl in the 6-15 eV region in two laboratories (26,27) disagree in  $n$  and  $k$  to  $\pm 20\%$  because the uncertainty in  $R$  is  $\pm 3\%$ ;  $k$  is generally too small in the ends of spectral regions especially if  $n \gg k$ ; 4) We feel that spectroscopic ellipsometry provides the most consistent numbers in the 1.5-6 eV region, especially when native oxides and roughness are accounted for and transmission data are used when  $k \ll n$ . We expect  $n$  and  $k$  are reliable to 2-3 figures; 5) In transparent regions where calorimetry is done (visible and near infrared),  $k$  is found to be  $\sim 10^{-6}$ , but numbers vary by factors of two from sample to sample. This absorption is probably due to impurities and structural defects, once surface effects are properly accounted for; 6) One of the main errors in the accuracy of the data quoted in the tables is in reading the graphs given in the literature. Authors often omit the fiduciary marks 2-9 on log scales. Some researchers kindly provided original numerical tables; 7) The least studied materials as far as workers and spectral range are concerned are Ir, Os, Rh, InP, InAs, LiNbO<sub>3</sub>, Si<sub>3</sub>N<sub>4</sub>; 8) Conspicuous by their absence in the Handbook are Cr, Fe, Zn, Sn, CdS, Se, Te, GaSb, KBr, MgF<sub>2</sub>, C (graphite), Al<sub>2</sub>O<sub>3</sub>. While data exist, no collection was made due to lack of critiquers.

While tables of  $n$  and  $k$  from x-ray to mm-wave region with  $n$  and  $k$  accurate to 3-4 figures are desirable, this is not the real experimental world. Throughout the tables,  $n$  in transparent regions is probably good to 3-4 figures, while in opaque regions it is good to 1-2 figures.  $k$  is good to 1-2 figures throughout (I have not found measurements of  $k$  from two laboratories in agreement to 3 figures).

#### OTHER COLLECTIONS OF $n$ AND $k$

Several reports on optical properties have proved useful during the preparation of the Handbook. They include; a) "The Refractive Index of Alkali Halides" by Li (3) in which the refractive index is fitted with a Sellmeier equation; b) "Optical Properties of Some Insulators in the Vacuum Ultraviolet Region" by Haelbich et al. (28) in which all the x-ray UV work of a number of insulators are listed; c) "Refractive Index of Optical Materials for the Infrared Region" by Moses (29) and d) "Optical Materials for Infrared Instrumentation" by Ballard et al. (30) give refractive index and other physical properties of many window materials; e) "Properties of Optical Materials" by Wolfe (31) cites many optical properties in numerous figures; f) "Optical Properties of Metals" by Hass and Hadley (32) is an old reliable source, while g) "Optical Properties of Metals" by Weaver et al. (33) is more up-to-date.

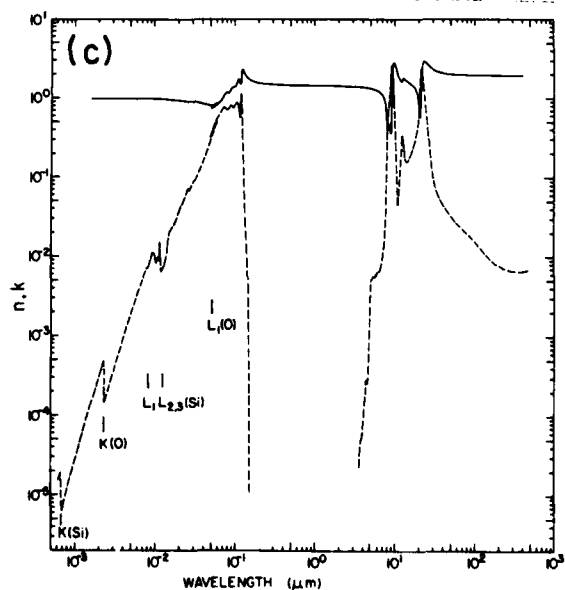
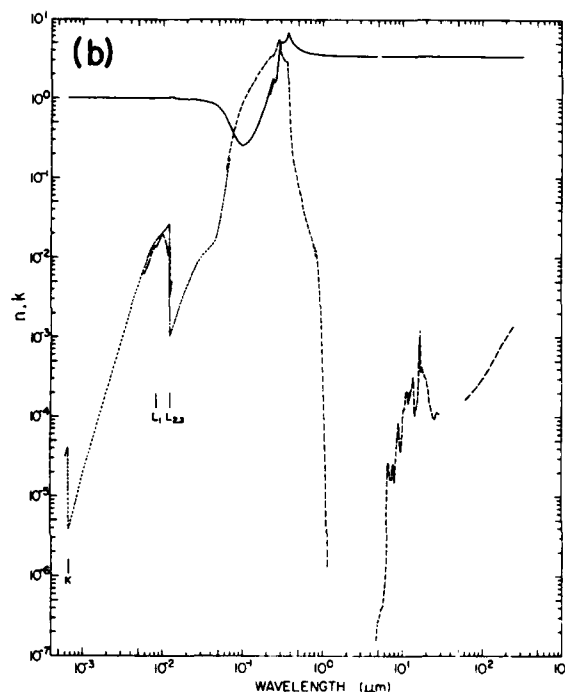
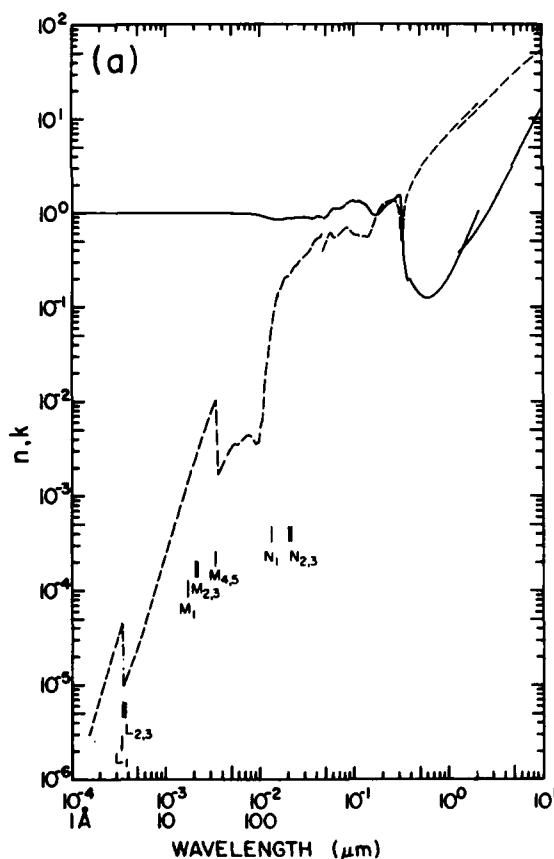
#### REFERENCES

1. Handbook of Optical Constants of Solids, (E.D. Palik, ed.), (Academic Press, New York, 1985).

2. H. Rubens and E.F. Nichols, *Ann. Phys. Chem.* 60, 418 (1897); H. Rubens and A. Trowbridge, *Ann. Phys. Chem.* 60, 724 (1897).
3. H.H. Li, *J. Phys. Chem. Ref. Data* 5, 329 (1976).
4. J.E. Eldridge and P.R. Staal, *Phys. Rev.* B16, 4608 (1977).
5. D.L. Stierwalt and R.F. Potter, in "Semiconductors and Semimetals", Vol. 3, p. 171, (R.K. Willardson and A.C. Beer, eds.), (Academic Press, New York, 1967).
6. D.C. Gupta, *Solid State Electr.* 13, 543 (1970).
7. E.D. Palik and R.T. Holm, *Opt. Eng.* 17, 512 (1978).
8. J. Shamir and P. Graff, *Appl. Opt.* 14, 3053 (1975); J. Shamir, *Appl. Opt.* 15, 120 (1976).
9. E.P. Bertin, "Principles and Practices of X-Ray Spectrometric Analysis", Chap. 2, (Plenum, New York, 1970).
10. B.L. Henke, P. Lee, T.J. Tanaka, R.L. Shimabukuro and B.K. Fujikawa, *Low Energy X-Ray Diagnostics-1981*, AIP Conference Proc. No. 75, (D.T. Attwood and B.L. Henke, eds.), (American Institute of Physics, New York, 1981).
11. E.E. Bell, in "Handbuch der Physik", Vol. 25, Part 2a, p. 1, (S. Flugge, ed.), (Springer-Verlag, Berlin, 1963).
12. F. Abeles, in "Progress in Optics", Vol. 11, p. 251, (E. Wolf, ed.) (North-Holland, Amsterdam, 1963).
13. H.E. Bennett and J.M. Bennett, in "Physics of Thin Films", Vol. 4, p. 1, (G. Hass and R.E. Thun, eds.), (Academic Press, New York, 1967).
14. O.S. Heavens, "Optical Properties of Thin Solid Films", (Dover, New York, 1965).
15. P.H. Berning, in "Physics of Thin Films", Vol. 1, p. 69, (G. Hass, ed.), (Academic Press, New York, 1963).
16. D.E. Aspnes, *J. Phys. (Paris)*, C10, 3 (1983).
17. E. Shiles, T. Sasaki, M. Inokuti and D.Y. Smith, *Phys. Rev.* B22, 1612 (1980).
18. E. Taft and L. Cordes, *J. Electrochem. Soc.* 126, 131 (1979).
19. G.G. Macfarlane, T.P. McLean, J.E. Quarrington and V. Roberts, *Phys. Rev. Lett.* 2, 252 (1959).
20. A.N. Pikhlin and A.D. Yas'kov, *Sov. Phys. Semicond.* 12, 622 (1978); *Fiz. Tekh. Poluprovodn.* 12, 1047 (1978).
21. S. Iwasa, I. Balslev and E. Burstein, in *Seventh Intern. Conf. Phys. Semicond.*, Paris 1964, (Dunod, Paris and Academic Press, New York, 1964), p. 1077.
22. A. Manabe, A. Mitsuishi and H. Yoshinaga, *Japan. J. Appl. Phys.* 4, 581 (1965).
23. R.T. Holm, J.W. Gibson and E.D. Palik, *J. Appl. Phys.* 48, 212 (1977).
24. B. Dold and R. Mecke, *Optik* 22, 435 (1965).
25. P. Winsemius, F.F. van Kampen, H.P. Lengkeek and C.G. van Went, *J. Phys.* F 6, 1583 (1976).
26. D.M. Roessler and W.C. Walker, *J. Opt. Soc. Am.* 57, 835 (1967); *Phys. Rev.* 166 599 (1968).
27. T. Miyata and T. Tomiki, *J. Phys. Soc. Japan* 24, 1286 (1968); 22, 209 (1967).
28. R.P. Haelbich, M. Iwan and E.E. Koch, "Physik Daten, Physics Data", (Fach-Information Zentrum, Karlsruhe, 1977).
29. A.J. Moses, "Refractive Index of Optical Materials in the Infrared Region", Report on Contract F33615-68-C-1225, Air Force Systems Command, Hughes Aircraft Company, Culver City, CA, 1970).

30. S.S. Ballard, K.A. McCarthy and W.L. Wolfe", Optical Materials for Infrared Instrumentation", Report from Infrared Information and Analysis Center, University of Michigan, Willow Run, Laboratories, Ann Arbor, MI 1959.
31. W.L. Wolfe, in "Handbook of Optics OSA", Section 7, (McGraw-Hill, New York, 1978).
32. G. Hass and L. Hadley, in "AIP Handbook", Section 6, (McGraw-Hill, New York, 1972).
33. J.H. Weaver, C. Krafka, D.W. Lynch and E.E. Koch, "Physik Daten, Physics Data", "Optical Properties of Metals," Vol. 18-1, (Fach-Information Zentrum, Karlsruhe, 1981).

Fig. 1 Log-log plot of  $n$  (—) and  $k$  (----) vs. wavelength in  $\mu\text{m}$  for Ag(a), Si(b) and a-SiO<sub>2</sub>(c).



## OPTICAL CONSTANTS AT X-RAY WAVELENGTHS\*

D. Y. Smith, A. E. Williamson<sup>†</sup>, and T. I. Morrison  
Argonne National Laboratory  
Argonne, IL 60439

The present paper is a preliminary report on optical properties of selected elements at x-ray wavelengths as derived from measured absorption spectra. Need for such data is an outgrowth of the world-wide development<sup>1</sup> of synchrotron radiation sources; the reflectance is of interest for designing grazing-incidence mirrors,<sup>2</sup> and knowledge of optical constants is required to calculate the properties of multilayer elements,<sup>3</sup> as well as to analyze differential absorption and anomalous scattering experiments.<sup>4</sup>

Generally, the only optical data available at x-ray wavelengths are for bulk absorption. In principle the other optical properties may be derived from these using the Kramers-Kronig relation<sup>5</sup>

$$n(\omega) - 1 = \frac{2}{\pi} P \int_0^{\infty} \frac{\omega' k(\omega') d\omega'}{\omega'^2 - \omega^2}, \quad (1)$$

that connects the real and imaginary parts of the complex refractive index,  $N(\omega) = n(\omega) + ik(\omega)$ .

The x-ray photoelectric mass absorption cross section  $\mu(\omega)$ , the quantity usually tabulated, is related to the extinction coefficient  $k(\omega)$  by

$$k(\omega) = c\rho\mu(\omega)/2\omega, \quad (2)$$

where  $c$  is the speed of light in vacuum and  $\rho$  is the density of the material.

The primary difficulty in applying Eq. (1) is that knowledge of  $k(\omega)$  for all  $\omega$  is required. While good absorption data are generally available for hard x-ray energies, UV and soft x-ray data are often uncertain or fragmentary. This uncertainty at low energies would seem of minor importance for hard x-ray processes. However, we have found that systematic underestimates of oscillator strength in the low-energy portion of the data<sup>6</sup> we analyzed, gave errors in  $n(\omega)-1$  exceeding 30-35% at  $\hbar\omega > 5$  keV for roughly half the elements.

An important point evident from Eq. (1) is that the low-energy absorption contributes a smoothly varying component to  $n(\omega)$  at high energies. This contribution is proportional to the integrated oscillator strength at low energies, but is insensitive to its distribution. Thus, if the net absorption strength in the region of uncertainty can be estimated, a Kramers-Kronig analysis can be made despite the lack of reliable low-energy spectra.

A major guide for estimating the unknown or uncertain oscillator strength is

---

\*This work supported by the U.S. Department of Energy.

<sup>†</sup>Present address: Department of Physics, University of California, Berkeley, California 94720.

the Thomas-Reiche-Kuhn f-sum rule<sup>7,8</sup>

$$\int_0^{\infty} \omega k(\omega) d\omega = \pi^2 \mathcal{N} e^2 / m, \quad (3)$$

where  $\mathcal{N}$ ,  $e$ , and  $m$  are the electron number density, charge, and mass, respectively. Provided reliable x-ray absorption data at high energies are available, their contribution to the f sum may be calculated and the remaining oscillator strength assigned to the low-energy region so that Eq. 3 is satisfied. In the cases in which the absorption of individual electron shells (or groups of shells) can be identified separately, an even more powerful guide is provided by partial f sums<sup>9</sup>. An example of this procedure is given by Shiles *et al.*<sup>10</sup>

In the present study, the photoelectric cross sections above 10 eV as compiled by Biggs and Lighthill<sup>6</sup> from experimental and theoretical sources were used. These consist of piece-wise continuous four-term polynomial fits to the absorption in regions bounded by the various absorption edges, a form particularly convenient for analytic integration of Eq. 1. To estimate the net absorption strength  $S$  below 10 eV we have used the f-sum rule, assuming the absorption to be concentrated at a single frequency  $\omega_v$ ;

$$k(\omega) = S \delta(\omega - \omega_v), \quad 0 < \hbar\omega < 10 \text{ eV}, \quad (4)$$

where  $\hbar\omega_v < 10 \text{ eV}$ . By Eq. (1)

$$\omega_v S = \pi^2 e^2 \mathcal{N} / m - \int_{10 \text{ eV}}^{\infty} \omega k(\omega) d\omega. \quad (5)$$

The properties at x-ray wavelengths are virtually independent of  $\omega_v$ , but experience with materials for which UV refractive index data are available indicates that  $\hbar\omega_v \sim 9.5 \text{ eV}$  is a reasonable choice.

The absorption below 10 eV is dominated by the most loosely bound electrons; hence,  $S$  is expected to be roughly equal to the number of valence electrons. In approximately half of the elements this expectation held for Biggs and Lighthill's cross sections.<sup>6</sup> In these cases the refractive index was calculated directly from Eq. 1 using  $S$  determined via Eq. 5. In the remaining half of the elements -- particularly the transition elements --  $S$  was significantly greater than the number of outer-shell electrons. From a study of partial f sums it became clear that this arose from a deficiency in absorption strength between 10 and 1000 eV. In most cases this deficiency could be ascribed to an underestimate of absorption by weakly bound d or f electrons. For these elements the low-energy data were scaled to make their integrated oscillator strength approximately equal to the occupation number of the shells involved in the absorption. This reduced  $S$  to approximately the number of valence electrons as expected. The optical constants were then calculated using the modified data. The results are best presented in terms of the complex atomic scattering factor for forward scattering:

$$f_1(0) = (m\omega^2 / 4\pi\rho e^2) [1 - \epsilon_1(\omega)], \text{ and } f_2(0) = (m\omega^2 / 4\pi\rho e^2) \epsilon_2(\omega), \quad (6)$$

where  $\epsilon(\omega) = \epsilon_1(\omega) + i\epsilon_2(\omega)$  denotes the complex dielectric function. Representative results for metallic platinum are given in Fig. 1.



AD-A161 247

OM85 BASIC PROPERTIES OF OPTICAL MATERIALS SUMMARIES OF  
PAPERS(U) NATIONAL BUREAU OF STANDARDS GAITHERSBURG MD  
A FELDMAN MAY 85 NBS-SP-697 AFOSR-RR-85-0902

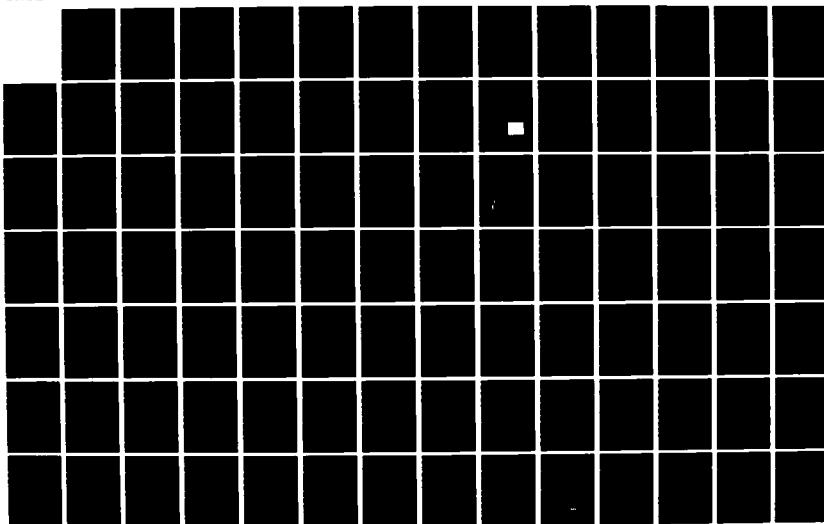
3/4

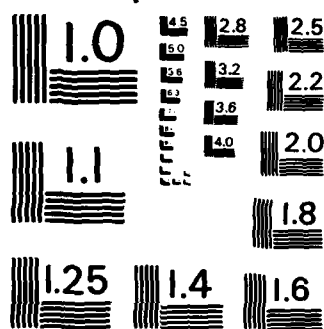
UNCLASSIFIED

AFOSR-ISSA-85-00052

F/G 20/6

NL





MICROCOPY RESOLUTION TEST CHART  
NATIONAL BUREAU OF STANDARDS-1963-A

## Platinum Z=78

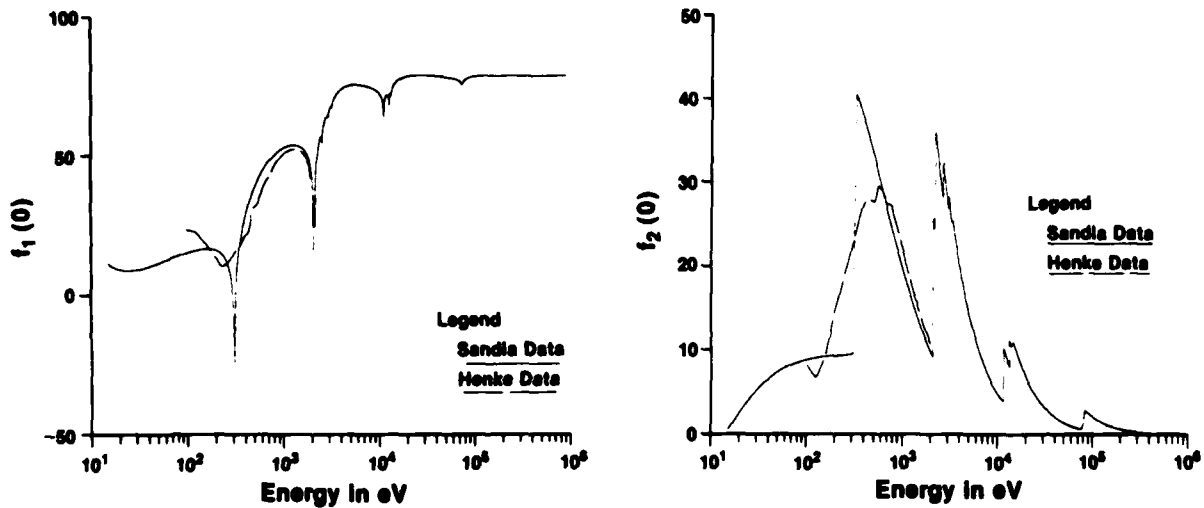
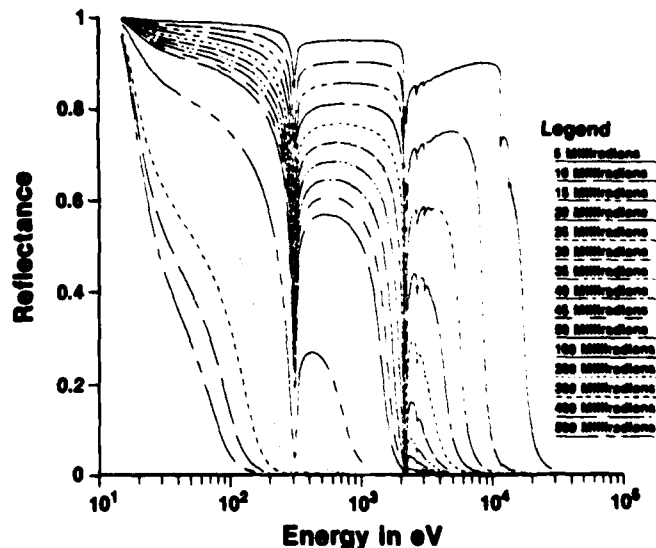


Fig. 1 The real and imaginary parts of the atomic scattering factor for forward scattering by metallic platinum. The solid curve was calculated from the cross-section data of Biggs and Lighthill, Ref. 6, in which the region below  $\sim 1$  keV was treated approximately. The results of Henke *et al.*, Ref. 11, who studied the low-energy region in detail are shown for comparison.

The optical properties relevant to reflecting optical elements are the reflectance, critical angle for total external reflection, Brewster's angle, etc. Experience<sup>4</sup> indicates that, at the energies of interest here, continuum electrodynamic theory holds approximately even though the x-ray wavelengths approach atomic dimensions. In particular, the reflectance as a function of angle may be calculated using the Fresnel equations.<sup>12</sup> The results for the reflectance of a smooth platinum surface for unpolarized light are given in Fig. 2. (In practical mirrors these results must be reduced by a factor accounting for surface roughness, see Ref. 13.)

Fig. 2 The reflectance for unpolarized x-rays of a smooth surface of metallic platinum as calculated from the forward scattering factors given in Fig. 1 via the Fresnel equations. Angles are measured relative to the surface.

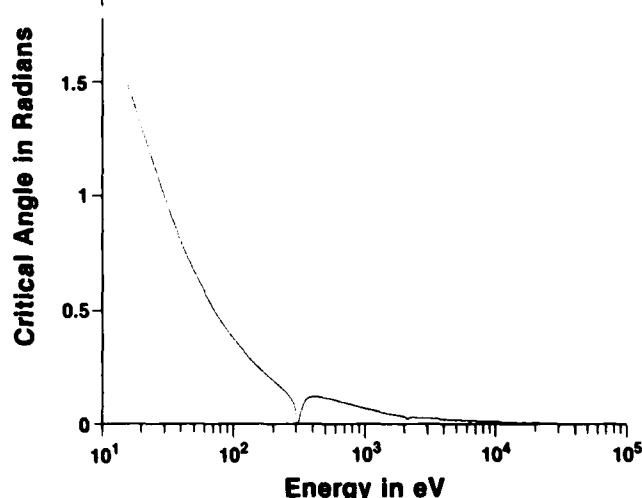


The critical angle for total external reflection  $\theta_c$  (as measured relative to the surface) is given by

$$\theta_c(\omega) = \cos^{-1} n(\omega), \quad (7)$$

in the absence of absorption. Values of  $\theta_c(\omega)$  for our exemplary substance platinum are given in Fig. 3. For  $k \neq 0$  the reflectance, while not total, approaches unity for grazing angles less than  $\theta_c$  provided the photon energy is not near an absorption edge,<sup>4,14</sup> cf. Fig. 2.

Fig. 3 The critical angle (measured relative to the surface) for total external reflection for a smooth metallic platinum surface calculated via Eq. 7 from the forward scattering factors given in Fig. 1.



#### References and Footnotes

1. Current Status of Facilities Dedicated to the Production of Synchrotron Radiation, National Research Council (National Academy Press, Washington, 1983).
2. W. Gudat and C. Kunz, in Synchrotron Radiation, C. Kunz ed. (Springer, Berlin, 1979).
3. E. Spiller, in Low Energy X-Ray Diagnostics-1981, D. T. Attwood and B. L. Henke, APS Conf. Proc. No. 75, (American Institute of Physics, New York, 1981).
4. R. W. James, The Optical Principles of the Diffraction of X-Rays, (Cornell, Ithaca, 1965).
5. J. S. Toll, Phys. Rev. **104**, 1760 (1956).
6. F. Biggs and R. Lighthill, Analytical Approximations for X-Ray Cross Sections II, Sandia Report SC-RR-71 0507, (Sandia National Laboratory, Albuquerque, 1971).
7. H. A. Bethe and E. E. Salpeter, Quantum Mechanics of One- and Two-Electron Atoms, (Springer-Verlag, Berlin, 1957).
8. For the purposes of this preliminary study the non-relativistic  $f$ -sum rule is sufficient. In more detailed work involving heavy elements, core electrons should be treated relativistically. The largest relativistic correction to the  $f$  sum arises from the mass-velocity effect. This may be thought of as reducing the contribution of an electron to the  $f$  sum by a factor  $[1 - (5/3mc^2) T_0 + O(v^4/c^4)]$ , where  $T_0$  is the expectation value of the electron's kinetic energy in the ground state and  $v$  is its velocity; See J. S. Levinger, M. L. Rustig, and K. Okamoto, Phys. Rev. **106**, 1191 (1957). This correction has been discussed independently in connection with anomalous scattering factors by D. T. Cromer and D. Liberman, J. Chem. Phys. **53**, 1891 (1970), and M. S. Jensen, Phys. Lett. A **74**, 41 (1979).
9. D. Y. Smith and E. Shiles, Phys. Rev. B **17**, 4689 (1978).
10. E. Shiles, T. Sasaki, M. Inokuti, and D. Y. Smith, Phys. Rev. B **22**, 1612 (1980).
11. B. L. Henke, P. Lee, T. J. Tanaka, R. L. Shimabukuro, and B. K. Fujikawa, Atomic Data and Nuclear Data Tables **27**, 1 (1982).
12. F. Stern, in Solid State Physics, edited by F. Seitz and D. Turnbull (Academic, New York, 1963), Vol. 15.
13. D. H. Bilderback and S. Hubbard, Nucl. Instrum. Methods **195**, 91 (1982).
14. For further details, see J. A. Prins, Z. Physik **47**, 479 (1928).

## VACUUM ULTRAVIOLET LOSS IN MAGNESIUM FLUORIDE FILMS

O. R. Wood, II and P. J. Maloney  
AT&T Bell Laboratories  
Holmdel, New Jersey 07733

and

H. G. Craighead and J. E. Sweeney  
Bell Communications Research  
Holmdel, New Jersey 07733

Because  $\text{MgF}_2$  is transparent to wavelengths as short as 1100 Å in the VUV,<sup>1</sup> it finds extensive use for lenses and windows in this region. Major applications can be found in UV lasers, spectroscopy and space astronomy. Another important use of  $\text{MgF}_2$  is as an evaporated coating onto aluminum,<sup>2,3</sup> where it greatly increases the VUV reflectance and also retards oxidation. In practice the reflectance obtainable by this means is limited to 83 - 85%<sup>4,5</sup> at 1216 Å because of the high loss of the evaporated material,<sup>6</sup> which is  $10^4$  times that of single crystal  $\text{MgF}_2$ . If the loss were as low as single crystal material,<sup>7</sup> a reflectivity of 94% would be possible,<sup>4,8</sup> exceeding any known value at this wavelength.

We have investigated the excess loss in evaporated films and found<sup>9</sup> that it is due to scattering from inhomogeneities and absorption from the low energy tail of an exciton band. Both of these mechanisms were found to be strongly dependent on the degree of crystallinity of the film, which is largely determined by the substrate temperature during deposition. Our study has allowed us to produce films with extinction coefficients as low as 0.005, several times better than previously reported. Our study included a series of measurements from 1050 to 1600 Å of the optical constants of evaporated  $\text{MgF}_2$  films deposited on single crystal LiF substrates. These films were produced over a wide range of deposition rates and substrate temperatures. Transmission electron microscopy was used to determine the grain size of the resulting polycrystalline evaporated film.

Our measurements of the optical constants of  $\text{MgF}_2$  films (1000 Å thick) at 1216 Å deposited on room temperature LiF substrates at different rates are shown in Table I, together with the optical constants of a  $\text{MgF}_2$  crystal. Independent of deposition rate, the  $\text{MgF}_2$  films are characterized by a lower index of refraction and an extinction coefficient some 10,000 times higher than the single crystal material. As was found in the earlier work,<sup>6</sup> the highest deposition rates resulted in the highest losses. In contrast to the earlier work on  $\text{MgF}_2$ -overcoated aluminum mirrors, however, no improvement in the optical properties of these films

Table I. Optical Constants of  $\text{MgF}_2$  Film Deposited onto Room Temperature LiF Substrate Vs Deposition Rate

Evaporation rate (A/sec)	Refractive index	Extinction coeff.
2	1.69	0.046
5	1.70	0.053
14	1.71	0.041
150	1.69	0.064
Crystalline	1.73	0.000003

with increasing deposition rates was seen for deposition rates in the 2 - 45 A/sec range. This dependence suggests that the film growth process is more important than impurity incorporation.

We have found that when impurities are inconsequential the degree of crystallinity (i.e., the polycrystalline grain size) determines film absorption regardless of how the crystalline state was obtained. We have further found that the losses observed in evaporated  $\text{MgF}_2$  films in the wavelength range from 1050 to 1600 Å can be fully accounted for by a simple model that includes absorption by the low energy tail of an exciton band and scattering from inhomogeneities at the surface and in the body of the film. Such a model can account for the wavelength dependence of the absorption coefficient of the films deposited at various substrate temperatures and gives a value for the band gap energy,  $E_g = 12.3$  eV, that agrees with previous measurements.<sup>10</sup> Furthermore, in the region where the absorption coefficient appears to obey the Urbach relation [ $k \sim \exp(E/E_g)$ ] the model leads to values for the characteristic energy,  $E_g$ , that are close to those of other materials.<sup>11</sup> Previous attempts to explain the observed wavelength dependence of the absorption coefficient led to values for  $E_g$  that varied from 10.95 (for the most crystalline films) to 8.8 eV (for amorphous films, gave abnormally large values of the characteristic energy and led to explanations based on the presence of impurities.<sup>12</sup>

We now see that the attempt by Hutcheson et al.<sup>5</sup> to significantly improve the VUV reflectance of  $\text{MgF}_2$ -overcoated mirrors by varying the deposition rate and substrate temperature, and that gave little change in reflectance when the substrate temperature was increased from 40 to 100 °C, and a decrease in reflectance at higher substrate temperatures was probably unsuccessful because of the conflicting growth requirements of the two films. A low loss  $\text{MgF}_2$  film can best be produced at high substrate temperatures, whereas, a high reflectance aluminum film is destroyed at high temperatures.<sup>13</sup> One solution to the problem of fabricating a high reflectance mirror in the VUV would be to overcoat a freshly evaporated Al film with a crystalline (i.e., low loss) layer of  $\text{MgF}_2$ . This might be accomplished through the use of pulsed laser annealing to heat the film and at the same

time minimize heating of the aluminum layer. Another possibility might be to modify the microstructure by methods other than heating such as low energy ion bombardment during deposition. On the other hand, these techniques probably could not be used to fabricate a low loss Al-MgF<sub>2</sub> interference filter for the VUV. The large surface roughness of a low loss MgF<sub>2</sub> layer, particularly one with a large grain size, would result in coupling to the surface plasmon<sup>14</sup> and would severely limit the performance of an Al-MgF<sub>2</sub> multilayer. Even so, it is thought that the understanding of the important film parameters and loss mechanisms gained in this study could eventually lead to improved performance of MgF<sub>2</sub> coated optics in the VUV.

#### References

1. A. Duncanson and R. W. H. Stevenson, Proc. Phys. Soc. London 72, 1001 (1958).
2. G. Hass and R. Tousey, J. Opt. Soc. Am. 49, 593 (1959).
3. P. H. Berning, G. Hass and R. P. Madden, J. Opt. Soc. Am. 50, 586 (1960).
4. L. R. Canfield, G. Hass and J. E. Waylonis, Appl. Opt. 5, 45 (1966).
5. E. T. Hutcheson, G. Hass and J. T. Cox, Appl. Opt. 11, 2245 (1972).
6. G. Hass and J. B. Ramsey, Appl. Opt. 8, 1115 (1969).
7. D. L. Steinmetz, W. G. Phillips, M. Wirick and F. F. Forbes, Appl. Opt. 6, 1001 (1967).
8. W. R. Hunter, J. Opt. Soc. Am. 54, 208 (1964).
9. O. R. Wood, II, H. G. Craighead, J. E. Sweeney and P. J. Maloney, Appl. Opt. 23, 3644 (1984).
10. G. Stephan, Y. LeCalvez, J. C. Lemonier and S. Robin, J. Phys. Chem. Solids 30, 601 (1969).
11. N. F. Mott and E. A. Davis, Electronic Processes in Noncrystalline Materials (Clarendon, Oxford, 1979), p. 275.
12. A. S. Barriere and A. Lachter, Appl. Opt. 16, 2865 (1977).
13. Yu. I. Dymshits, V. A. Korobitsyn and A. A. Metelnikov, Sov. J. Opt. Technol. 46, 649 (1979).
14. E. Spiller, Appl. Opt. 13, 1209 (1979).

## SURFACE EROSION INDUCED BY ELECTRONIC TRANSITIONS

Richard F. Haglund, Jr. and Norman H. Tolk  
Department of Physics and Astronomy  
Vanderbilt University  
Nashville, TN 37235

The problem of damage to ultraviolet optical materials has been and continues to be a major source of concern in the design and operation of high-power lasers. Little fundamental understanding exists of the atomic-level mechanisms which operate to produce this damage. However, recent experiments have shown that irradiation of optical materials by electrons and photons at energies characteristic of high-power and high-energy laser systems is an efficient cause of surface erosion. The experiments described here are intended to illuminate the basic mechanisms associated with energy absorption, distribution and localization leading to electronically induced desorption, and to determine the role of defects in these processes.

In ultraviolet laser systems currently operating or under design, laser fluences range up to several J/cm<sup>2</sup>. The significance of these flux levels can be put into context by observing that, for a KrF laser (248 nm), 1 J/cm<sup>2</sup> of laser output corresponds to a flux of some 10<sup>14</sup> photons per surface site on the optical components experiencing the laser irradiation. In electron-beam-pumped lasers, Bremsstrahlung X-rays produced by the deceleration of submegavolt pump-beam electrons, as well as scattered or diffusing low-energy electrons, will also irradiate nearby optical surfaces. It is becoming clear that each of these sources of radiation is efficient in producing Desorption Induced by Electronic Transitions (DIET), and that the most abundant products of DIET processes are not ions but neutral atoms and molecules. These kinds of processes may well be the most plausible microscopic physical mechanisms responsible for the observed macroscopic optical damage.

In our experiments, controlled doses of low-energy electrons or synchrotron uv photons are delivered to clean surfaces under ultra-high vacuum conditions. Desorption products are identified by the characteristic line radiation either from excited states or from fluorescence induced by laser pumping of ground-state atoms and molecules. Substantial research has been performed over the past decade on desorbing ions.<sup>1</sup> However, our recent work has shown that the overwhelming majority of desorbed particles are neutral atoms and molecules, with yields often several orders of magnitude larger than corresponding ion yields.

In the initial experiments, the excitation source was an electron beam incident on single-crystal surfaces of NaCl and LiF.<sup>2</sup> By using varying collection geometries, it was easy to distinguish the atomic emission line spectra of the desorbed neutrals from the broad-band cathodoluminescence of the substrate. Results of these experiments on several alkali halide surfaces are shown in Fig. 1. The characteristic features of the experiments include a gradually-rising yield of neutral excited-state alkalis as a function of electron energy, with some features corresponding to threshold energies for various electronic transitions.



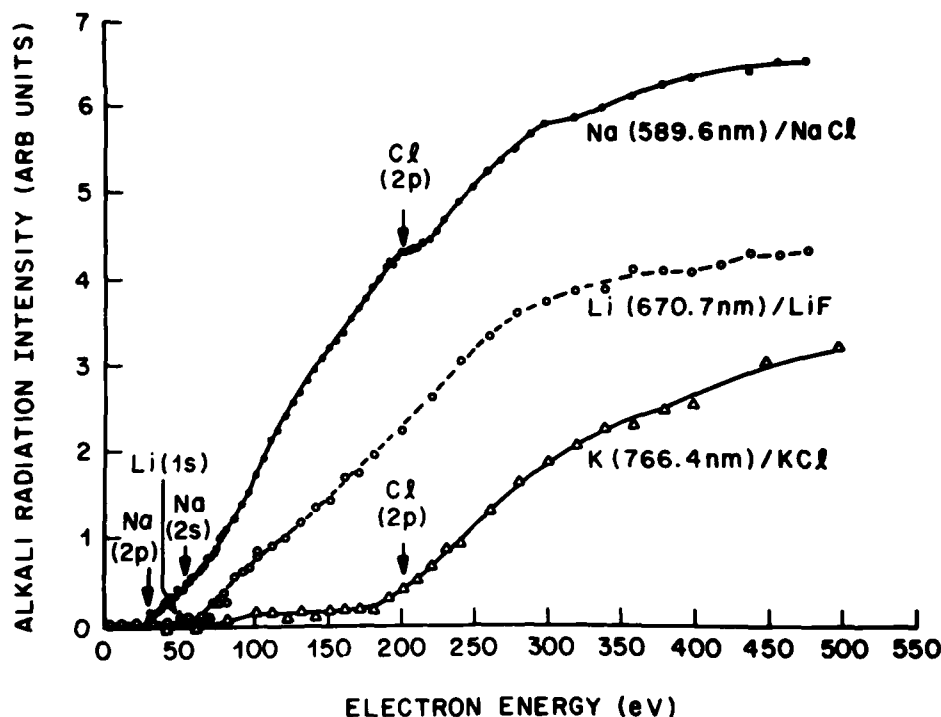


Fig. 1 Yield of excited-state neutral alkali atoms desorbed from single-crystal alkali-halide surfaces under electron bombardment, shown as a function of electron energy.

This same detection method was subsequently extended to photon-stimulated desorption of excited neutrals.<sup>3</sup> The excitation source for these experiments was the Tantalus storage ring at the University of Wisconsin Synchrotron Radiation Center. Experiments were performed with photons in the energy range from 40-200 eV, using a grazing-incidence "Grasshopper" monochromator.

Figure 2 shows the optical emission intensity of desorbed excited Li atoms as a function of the primary-beam photons, compared to the similar curve for  $\text{Li}^+$  ions and to the LiF photon absorption coefficient. In particular, the main excitonic structure of the Li K-edge is evident in all three curves. The comparison of the three curves affords important insights into the nature of the desorption process for this particular crystal. Similar photon-stimulated desorption experiments have also been undertaken on  $\text{Al}_2\text{O}_3$  and  $\text{TiO}_2$ .

In our most recent experiments the goal has been to detect desorbed ground-state neutral atoms emitted due to electron beam irradiation.<sup>4</sup> This has been accomplished using a tunable dye laser to excite Na and Li desorbing from clean alkali halide surfaces. Because typical counting rates in these laser-induced fluorescence measurements are greater than  $10^5$  Hz, this method clearly overcomes the signal-level difficulties which have discouraged the development of neutral-species detection based on quadrupole mass spectro-

metry. The ground-state yields indicate substantial efficiencies for stimulated desorption -- of order  $10^{-3}$  for ground-state Li neutrals desorbing from LiF crystals, for example.<sup>5</sup>

The mechanisms responsible for these electronically induced desorption phenomena are now believed to be associated with the production of excitons and defects which migrate to the surface and release energy during the desorption process. The resulting DIET affects the material by producing (1) macroscopically visible cratering; (2) microscopic pools of metal which can act as optical absorption sites for subsequent photon irradiation; and (3) ejected gas-phase halide (e.g., fluorine) atoms which can then interact chemically with surrounding gases and surfaces. All of these processes can occur in pure, defect-free crystals under electron and photon irradiation.

A number of questions are being addressed in current and planned experiments in order to obtain a more complete picture of fundamental erosion mechanisms in optical materials. The yields for neutral atoms desorbed at low electron and photon energies are being measured to establish threshold mechanisms. Differing temperature dependences of the yield for excited and ground-state Li desorbed from LiF have been observed; it may be possible to establish a relationship to defect mobilities by measuring at very low temperatures. Significant yields of excited neutral hydrogen have been observed in both electron- and photon-stimulated desorption experiments, and ways to measure the ground-state yield are being sought as well. Finally, the intensity dependence of the photon-stimulated desorption yields at selected wavelengths needs to be measured.

However, the present work clearly establishes erosion induced by electronic processes in surfaces as an efficient mechanism for changing surface composition and probably surface structure in optical materials.

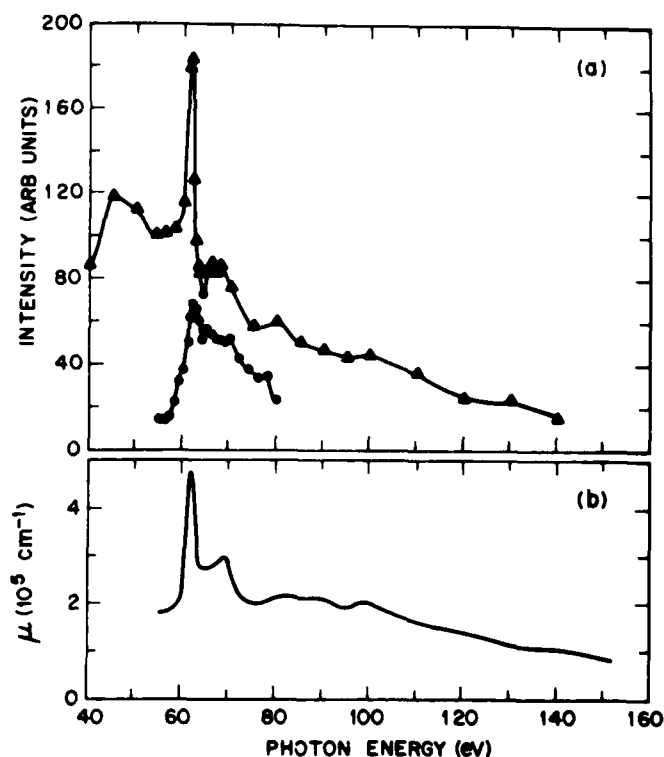


Fig. 2 Excited-state neutral yields for Li desorbed by photon bombardment from LiF (upper curve in (a));  $10^4 \times$  Li ion yield under the same conditions (lower curve in (a)); and the photon absorption curve for LiF (curve (b)).

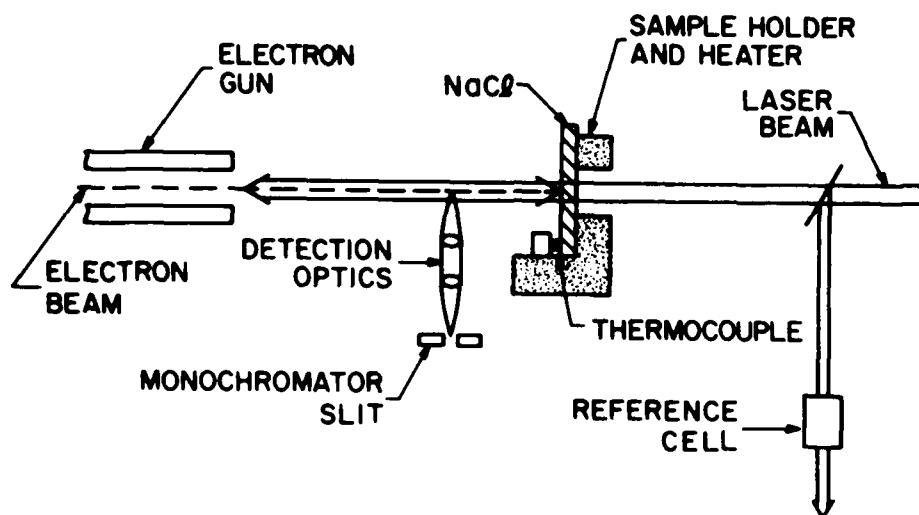


Fig. 3 Schematic of experimental geometry for detecting neutral ground-state atoms desorbing from crystal surfaces under electron bombardment. The tunable dye laser illuminates a portion of the transparent NaCl surface irradiated by the electron beam; the de-excitation radiation from neutral atoms excited by the laser is detected in a monochromator. Movement of the NaCl target manipulator allows measurement of the fluorescence yield as a function of distance from the target surface.

#### REFERENCES

1. For a recent review, see M. L. Knotek, *Physics Today* 37 (9), 24 (1984).
2. N. H. Tolk, L. C. Feldman, J. S. Kraus, R. J. Morris, M. M. Traum and J. C. Tully, *Phys. Rev. Letters* 46, 134 (1981).
3. N. H. Tolk, M. M. Traum, J. S. Kraus, T. R. Pian, W. E. Collins, N. G. Stoffel and G. Margaritondo, *Phys. Rev. Letters* 49, 812 (1982).
4. N. H. Tolk, P. Bucksbaum, N. Gershenfeld, J. S. Kraus, R. J. Morris, D. E. Murnick, J. C. Tully, R. R. Daniels, G. Margaritondo and N. G. Stoffel, *Nucl. Instr. and Meth. in Physics Research* B2, 457 (1984).
5. R. F. Haglund, Jr., N. H. Tolk, D. E. Murnick, R. R. Daniels, P. G. Pappas and N. G. Stoffel, to be submitted to *Surface Science*.

## DIELECTRIC FUNCTION AND INTERBAND TRANSITIONS IN SEMICONDUCTORS

M. Cardona

Max-Planck-Institut für Festkörperforschung  
7000 Stuttgart 80, Federal Republic of Germany

The optical constants (dielectric function) of semiconductors in the region of interband transitions have been intensively studied during the past 25 years. Nevertheless available data are incomplete and often inaccurate. The advent of automatic rotating analyzer ellipsometry pioneered by Aspnes and coworkers [1-3] has changed this situation and made possible the rapid collection of data. The resulting data are so accurate that they allow repeated differentiation with respect to the frequency. The derivative spectra enhance the so-called critical point structure which can be directly related to the band structure of the material. Thus this procedure has partly replaced the modulation techniques in which the derivatives of the spectral dependence of some optical parameter (e.g., transmissivity or reflectivity) with respect to an external modulated agent (e.g., electric field, pressure, strain) are measured [4]. An interesting form of modulation spectroscopy which has been profusely used in the past 15 years is resonance Raman scattering [5].

The derivative spectra obtained from ellipsometric data are, in principle, equivalent to those obtained through Kramers-Kronig transformation of wavelength modulated reflectivity spectra [4]. They are, however, more accurate since they avoid errors due to spectral dependence of the light source and Kramers-Kronig transformation of the data.

The derivative spectra of optical functions are easier to interpret than those obtained from modulation spectroscopy since they involve only the theory of the optical functions and not the effect of external perturbations on these functions. Nevertheless conventional modulation spectra are still useful. Electroreflectance, for instance, enhances structures due to bands with small effective masses. Such is the case of the lowest direct gap  $E_0$  of tetrahedral semiconductors. It is easily seen in electroreflectance while it is hardly observable because of its low strength, in the derivative spectra.

In a rotating analyzer ellipsometer linearly polarized light is reflected on a sample at oblique incidence (angle  $\approx 70^\circ$ ). The state of polarization of the reflected light (ellipticity and orientation of the ellipse) is measured with an analyzer rotating at the frequency  $\psi$  followed by a photomultiplier. The signal thus has the form:

$$I = A + B \cos(2\Omega t + \psi). \quad (1)$$

Fourier analysis of the signal yields the parameters  $\psi$  and  $B/A$  which can be used to determine numerically  $\epsilon_1(\omega)$  and  $\epsilon_2(\omega)$ . Because of the speed of the instrument one can take measurements for different surface treatments so as to optimize the surface quality following certain criteria (e.g., sharpness of a given critical point). Results obtained in this manner for Ge [6] are shown in Fig. 1. Typical second derivative spectra of  $\epsilon_1(\omega)$  and  $\epsilon_2(\omega)$  are

shown in Fig. 2 for gray tin ( $\alpha$ -Sn) [7]. In this figure the points are experimental while the lines are fits with theoretical critical point (cp) shapes to the rich structure observed. Typical cp shapes are:

$$\begin{aligned}\Delta\epsilon &= Ce^{i\psi}(\omega - \omega_g + i\Gamma)^{1/2} & (3d) \\ \Delta\epsilon &= -Ce^{i\psi}\ln(\omega - \omega_g + i\Gamma) & (2d) \\ \Delta\epsilon &= Ce^{i\psi}(\omega - \omega_g + i\Gamma)^{-1/2} & (1d),\end{aligned}\tag{2}$$

where we have distinguished between one-, two-, and three-dimensional critical points. The fits yield for every critical point the parameters  $C$  (strength),  $\omega_g$  (critical energy),  $\Gamma$  (Lorentzian broadening due partly to electron-phonon interaction and partly to interaction with defects such as substitutional donors and acceptors), and phase angle  $\psi$  which represents, in a phenomenological way, excitonic effects. This angle is a multiple of  $\pi/2$  in the absence of excitonic effects.

As seen in Fig. 1 the critical points shift to lower energies and broaden with increasing  $T$ . The shift in  $\omega_g$  vs.  $T$  obtained ellipsometrically for the  $E_1$  critical points of Ge and Si is shown in Fig. 3 [8] and compared with calculations of the effect of the electron-phonon interaction on the corresponding conduction and valence band levels (dashed line). The solid line represents this calculation plus the effect of thermal expansion. Excellent agreement with experiment is found. Similar work has recently been performed for the broadening parameters  $\Gamma(T)$  [9]. The electron-phonon interaction effects are composed of two contributions, the so-called Debye-Waller term, which arises from second-order terms in the electron-phonon Hamiltonian, and the self-energy which arises from first-order terms taken in second order perturbation theory. The Debye-Waller terms are real and contribute to the energy shift of the cp. The self-energy terms are complex: the real part contributes to the energy shift while the imaginary part determines the broadening parameter.

Ellipsometry can also be used to study the effect of impurities on the dielectric function and the critical point parameters. Figure 4 shows the spectra of four heavily doped silicon samples compared with those of undoped Si [10]. Red shifts and broadenings of the  $E_1$  and  $E_2$  critical points are seen. The impurity induced red shifts of  $\omega_g$  obtained from fits with Eqs. (2) are represented in Fig. 5 and compared with the result of theoretical calculations. These calculations follow similar lines as those for the temperature shifts [10]. The perturbing potential is taken to be the Coulomb potential of one impurity screened by the free carriers. The first order perturbation terms, which would yield opposite shifts for donors and for acceptors, are negligible. Second order perturbation theory expressions, when multiplied by the carrier concentration, yield the shifts shown by the solid lines in Fig. 5. For a given concentration of either donors or acceptors these shifts are nearly the same, small differences being due to differences in the screening of electrons and of holes.

Ellipsometry is also being used for the investigation of the effect of alloying on the interband critical points [11,12]. Figure 6 shows results for the

$E_1$ ,  $E_1 + \Delta_1$ , and  $E_2$  gaps of  $\text{Hg}_{1-x}\text{Cd}_x\text{Te}$  [12]. One of the most interesting aspects of these data is the so-called bowing or deviation from the linear dependence of cp-energies on  $x$ . Part of this deviation can sometimes be accounted for with the virtual crystal approximation (VCA), in which the crystal potential is taken to contain the average potential of the disordered atoms (Hg and Cd in this case). Additional contributions are due to potential fluctuations related to the chemical and topological disorder [13] (by topological disorder it is meant the variation of bond lengths due to the cation disorder). The VCA contribution and that of the potential fluctuations have often the same sign and order of magnitude.

Particularly interesting is the study of magnetic semiconductors such as  $\text{Cd}_{1-x}\text{Mn}_x\text{Te}$ . As shown in Fig. 7 the  $E_1$ ,  $E_1 + \Delta_1$  energies decrease with increasing  $x$  while the opposite is true for the  $E_0$  gap. This effect must be attributed to the admixture of Mn 3d states to the valence and conduction bands. In particular, such admixture is symmetry forbidden for the conduction state of the  $E_0$  gap. This is no longer the case for the  $E_1$  gap.

Ellipsometry can also be used for the investigation of anisotropic materials [14]. As an example we show in Fig. 8 data obtained for GeS with polarizations parallel to the two crystal axes which lie in the cleavage plane [15]. Data for the third polarization direction, perpendicular to the cleavage plane, are also obtained, although less accurately than those of Fig. 8, with ellipsometry [15]. One notices in Fig. 8 considerable differences in the positions of cp structure for the two polarization directions. These differences, while in principle due to polarization selection rules for the interband transitions, have not been unambiguously explained. We note the strong sharpening of some of the cp structures of Fig. 8 obtained at low temperatures. This sharpening emphasizes the advantage of performing ellipsometric measurements at low temperatures in order to resolve cp structure. Such measurements are still lacking for many common semiconducting materials.

#### REFERENCES

1. D.E. Aspnes, in *Optical Properties of Solids: New Developments*, ed. by B.O. Seraphin (North Holland, Amsterdam, 1976), p. 799.
2. D.E. Aspnes and A.A. Studna, *Phys. Rev. B* **27**, 985 (1983).
3. P.S. Hauge, *Surf. Sci.* **96**, 80 (1980); **96**, 108 (1980).
4. M. Cardona, *Modulation Spectroscopy* (Academic Press, N.Y. 1969).
5. M. Cardona, in *Light Scattering in Solids II* (Springer, New York, 1982).
6. L. Viña, S. Logothetidis, and M. Cardona, *Phys. Rev. B* **30**, 1979 (1984).
7. L. Viña, H. Höchst, and M. Cardona, *Phys. Rev.*, in press.
8. P. Lautenschlager, P.B. Allen, and M. Cardona, *Phys. Rev.*, in press.
9. P. Lautenschlager, to be published.
10. L. Viña and M. Cardona, *Phys. Rev. B* **29**, 6739 (1984).
11. S.M. Kelso, D.E. Aspnes, M.A. Pollak, and R.E. Nahory, *Phys. Rev. B* **29**, 6739 (1982).
12. L. Viña, C. Umbach, M. Cardona, and L. Vodopyanov, *Phys. Rev. B* **29**, 6752 (1984).

13. P.A. Fedders and C. Myles, Phys. Rev. B 29, 802 (1984); K.C. Haas, R.J. Lampert, and H. Ehrenreich, Phys. Rev. Letters 52, 77 (1984).
14. D.E. Aspnes, J. Opt. Soc. Am. 70, 1275 (1980).
15. P. Lautenschlager, S. Logothetidis, L. Vina, and M. Cardona, to be published.
16. S. Logothetidis, L. Vina, and M. Cardona, Phys. Rev. B, in press.

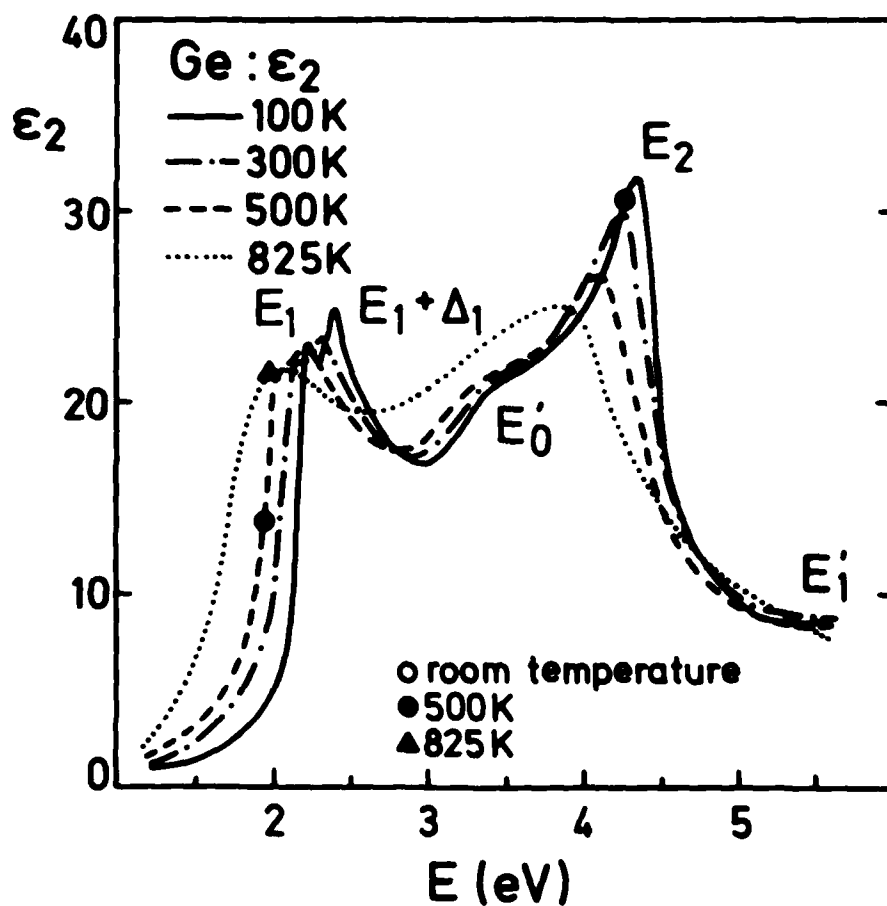


Fig. 1. Imaginary part  $\epsilon_2$  of the dielectric function of undoped Ge at several temperatures showing the  $E_1$ ,  $E_1 + \Delta_1$ ,  $E_0'$ ,  $E_2$ , and  $E_i'$  critical points. A red shift and broadening of critical points with increasing temperature is clearly observed.

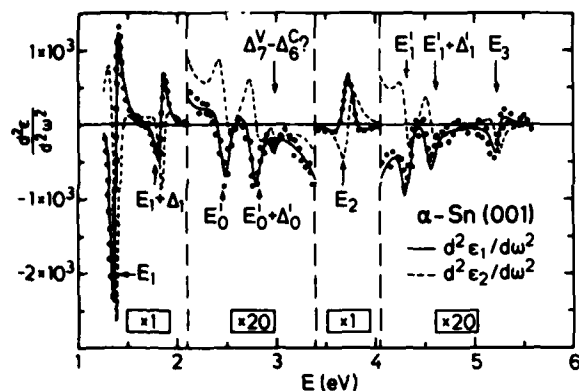


Fig. 2: Second derivative of the dielectric function of  $\alpha$ -Sn. The points are experimental for  $\epsilon_2$ . The lines are critical point fits.

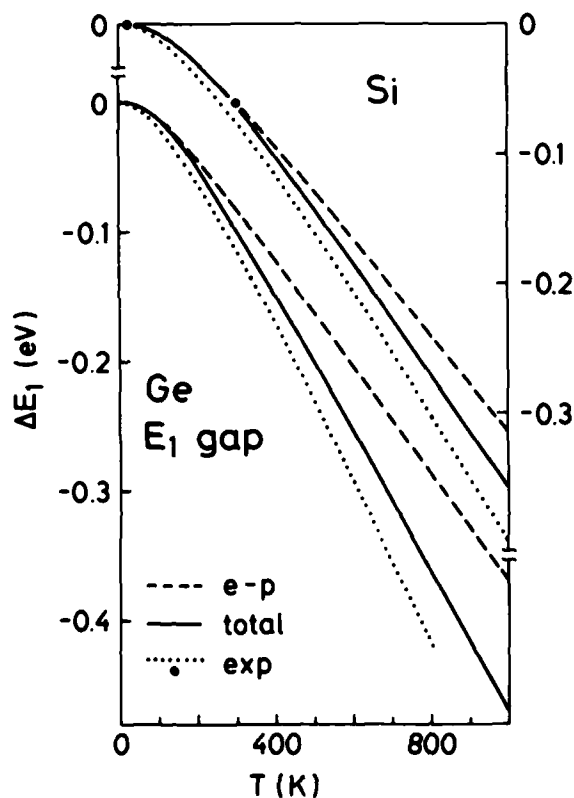


Fig. 3: Temperature dependence of the  $E_1$  critical point energies of Ge and Si. The dashed line gives calculated electron-phonon effects, the solid line includes thermal expansion.

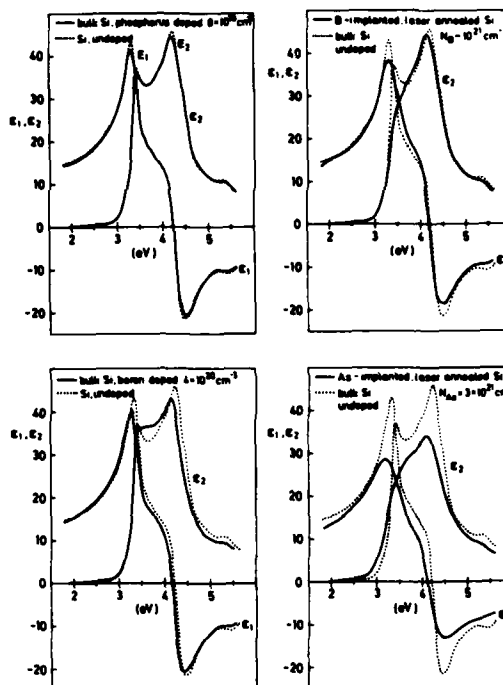


Fig. 4: Dielectric function of pure and heavily doped Si.

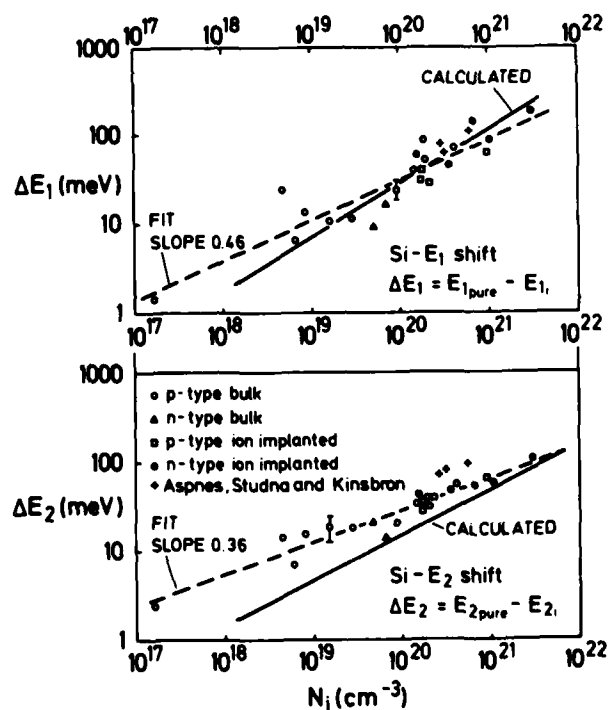


Fig. 5: Shift with doping of the critical point energies of  $E_1$  and  $E_2$  of silicon.



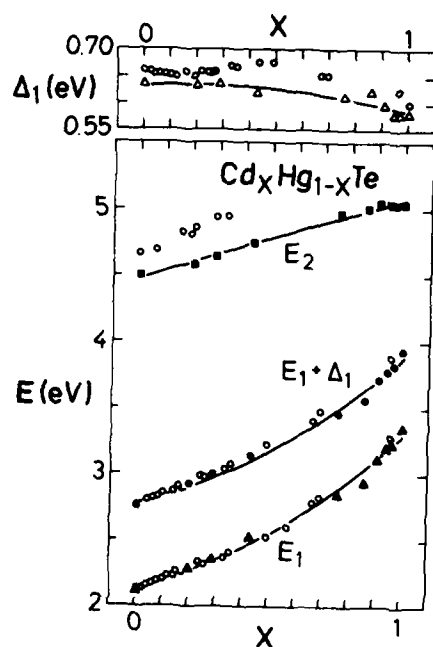


Fig. 6: Dependence of critical point energies  $E_1$ ,  $E_1 + \Delta_1$ ,  $E_2$ , and of  $\Delta_1$  on concentration  $x$  for  $\text{Cd}_x\text{Hg}_{1-x}\text{Te}$ .

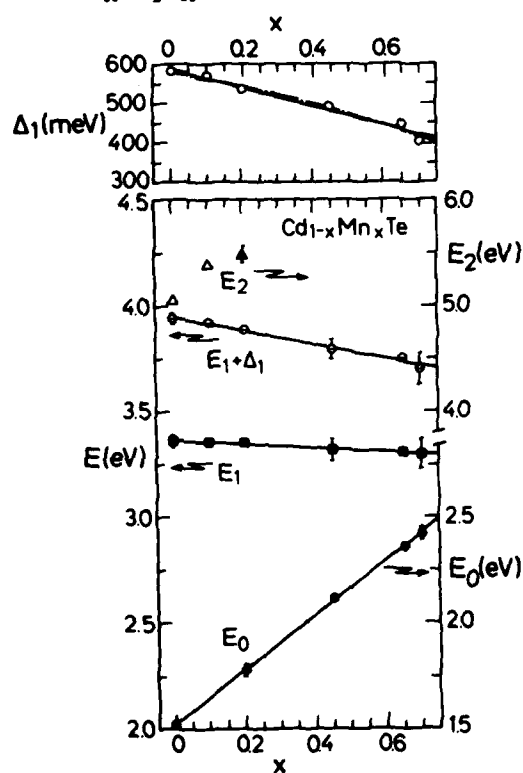


Fig. 7: Dependence on  $x$  of critical point energies  $E_0$ ,  $E_1$ ,  $E_1 + \Delta_1$ , and of  $\Delta_1$  for  $\text{Cd}_{1-x}\text{Mn}_x\text{Te}$ .

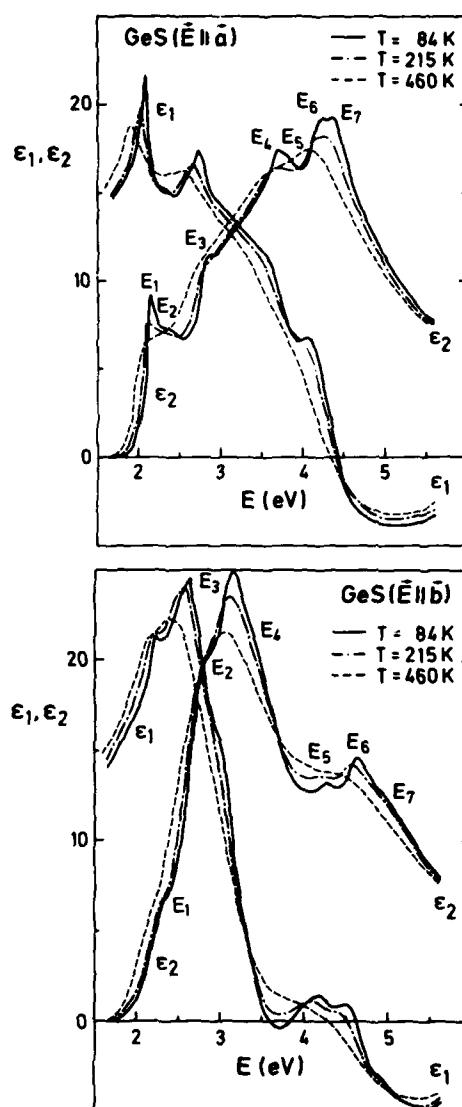


Fig. 8: Dielectric functions of GeS for polarizations parallel to the  $a$  and  $b$  axes at several temperatures.

# BAND STRUCTURE AND DENSITY OF STATES CHANGES FOR DOPED GALLIUM ARSENIDE

Herbert S. Bennett  
Semiconductor Devices and Circuits Division  
National Bureau of Standards  
Gaithersburg, MD 20899

## Introduction

Lasers, opto-electronic devices, and transistors have high carrier and/or doping concentrations in their active regions during operation. Such high concentrations produce changes in the band structure, density of states, and optical properties. These changes then influence considerably the performance of optical materials at 300 K in advanced applications for optical signal processing, computing, and communications.

This paper contains calculations of the changes in the band structure and density of states for both n-type and p-type doped GaAs. These band structure changes may be applied to optical properties such as absorption, luminescence, and refractive index. The application to absorption is given here.

Past interpretations of optical absorption measurements in heavily doped GaAs to give the dependence of the direct bandgap,  $E_G(exp)$ , on doping density use intrinsic values for the band structure and density of states. However, in heavily doped GaAs, the dopant ion-carrier and many-body (majority-carrier exchange and minority-carrier correlation) interactions greatly distort the band structure and the density of states. These interactions result in energy shifts of the band edges and distorted bands and density of states. Such modifications to the band structure have technological implications for the optical and electronic behavior of GaAs devices.

This paper shows that reducing the uncertainty in how the band structure and density of states change with carrier and/or doping concentration requires improved optical measurements on doped GaAs at 300K. Such measurements are essential for estimating many-body interactions. These interactions are of the same order of magnitude as the one-body (dopant ion-carrier) interactions and greatly alter the dependence on doping density,  $N$ , and carrier density of the input parameters used in numerical simulations of optical and electronic devices.

## Optical Absorption

According to the one-electron model, the optical absorption coefficient for transitions between a valence band and a conduction band has the form [1],

$$\alpha(E) = \frac{\pi e^2 \hbar}{\epsilon_0 m_0^2 c n_r E} \int_{-\infty}^{+\infty} \rho_c(E_f) \rho_v(E_i) |M(E_f, E_i)|^2 (f_0(E_i) - f_0(E_f)) dE_f, \quad (1)$$

where  $c$  is the speed of light,  $\hbar$  is Planck's constant divided by  $2\pi$ ,  $m_0$  is the free-electron mass,  $\epsilon_0$  is the permittivity of free space,  $E$  is the photon energy,  $n_r$  is the index of refraction,  $\rho_c$  and  $\rho_v$  are the densities of states per unit volume and unit energy in the conduction and valence bands, respectively, and  $M$  is the effective matrix element of the momentum operator between valence band states at energy  $E_i = E_f - E$  and conduction band states at energy  $E_f$ . The Fermi-Dirac distribution function,  $f_0(E_f) = 1/[1 + \exp((E_f - E_F)/k_B T)]$ , gives the probability that a state of energy  $E_f$  is occupied by an electron. The Fermi energy, Boltzmann constant, and temperature are denoted by  $E_F$ ,  $k_B$ , and  $T$ . The total absorption coefficient for GaAs is given by a sum of terms like Eq. (1) for each of the three valence bands.

Whenever carrier densities or ionized dopant densities,  $N$ , exceed  $8 \times 10^{16} \text{ cm}^{-3}$  for n-type and  $10^{19} \text{ cm}^{-3}$  for p-type GaAs at 300K, the above one- and many-body interactions lead to appreciable changes in the band structure and carrier density of states  $\rho_c$  and  $\rho_v$ . These changes must be included in the interpretation of optical measurements. They also affect greatly the performance of optical materials for the above mentioned applications. The self-energy formalism of Klauder [2,3] is applied to the dopant ion-carrier interactions in the effective mass approximation for GaAs. This formalism yields numerical procedures for computing the distorted bands and density of states. These perturbations and distortions are due to the effects of large dopant densities and/or carrier concentrations. Because theories for the many-body effects of majority-carrier exchange and minority-carrier correlation do not exist for carrier densities intermediate between the non-degenerate and degenerate cases in GaAs at 300 K, estimates for these energies are obtained as follows. When optical absorption measurements are available, these estimates are obtained from the relation  $E_{mb} = E_G(\text{exp}) - 1.424 \text{ eV} - E_{ic}$ , where  $E_{mb}$  is the energy shift of the bandgap associated with many-body interactions and  $E_{ic}$  is the energy shift of the bandgap associated with one-body interactions. The latter are calculated by the Klauder formalism. When optical absorption measurements are not available, then  $E_{mb}$  is estimated by degenerate theory.

The optical absorption measurements [1,4] are interpreted in terms of the above distorted bands and density of states from the Klauder self-energy formalism. The latter yield values for Fermi energies and band edges which differ from those obtained by earlier interpretations of the experiments. When applied to heavily doped GaAs, this self-energy formalism for dopant ion-carrier interactions and the estimates for the above many-body effects give the modified band structure and the dependences of the Fermi energy,  $E_F(N, T)$ , the screening radius,  $r_s(N, T)$ , and the effective intrinsic carrier concentration,  $n_{ie}(N, T) = \sqrt{\bar{n}\bar{p}}$ , on the ionized doping density,  $N$ , and temperature,  $T$ . The equilibrium electron and hole concentrations are denoted by  $\bar{n}$  and  $\bar{p}$ .

These calculations incorporate the Thomas-Fermi expression for the screening radius and the charge neutrality condition,  $N = \bar{n} - \bar{p}$ , to compute self-consistently  $E_F$  and  $r_s$ , for given values of  $N$  and  $T$ . The input parameters for the above calculations are the values at 300 K of the unperturbed effective masses  $m_c = 0.067m_0$  and  $m_v = 0.572m_0$ , intrinsic bandgap energy  $E_G = 1.424 \text{ eV}$ , and static dielectric constant  $\kappa = 12.9$ .

Ideally, the procedure would be as follows. First, the values of  $E_F(N, T)$  and the perturbed densities of states  $\rho_c$  and  $\rho_v$  from the Klauder formalism would be inserted in Eq. (1). Then, the bandgap  $E_G(N, T; \text{exp})$  in Eq. (1) would be varied until satisfactory agreement occurs

between the calculated and measured absorption coefficients. However, the published data and our knowledge of the energy dependence of the momentum matrix element,  $M$ , are not adequate to accomplish this. Instead, the bandgaps given in references 1 and 4 are shifted by the differences between the Fermi energies used in these references and the Fermi energies obtained from the above Klauder formalism. This latter procedure is justified since the bandgap values interpreted from absorption measurements are much more sensitive to the value of the Fermi energy than to distortions in the density of states.

The above 300 K formalism is a compromise between two conflicting goals: 1) calculating the band structure changes as rigorously as possible; and 2) having the 300 K results incorporated readily and economically into numerical simulations of GaAs devices. The 0 K many-body theories [5,6] do meet the second goal but generally are not correct unless the device or sample is fully degenerate. In order to meet goal 2, it is necessary to use the Yukawa potential to describe the screening of carriers at 300 K.

The hole and electron concentrations at thermal equilibrium are given by

$$\bar{p} = \int_{-\infty}^{+\infty} (1 - f_0(E)) \rho_v(E) dE \quad \text{and} \quad \bar{n} = \int_{-\infty}^{+\infty} f_0(E) \rho_c(E) dE. \quad (2)$$

The quantities  $\rho_c$  and  $\rho_v$  are, respectively, the perturbed densities of states for the distorted conduction and valence bands which result from doping the semiconductor. The calculations of  $\bar{p}$  and  $\bar{n}$  from Eq. (2) require, at the least, the above estimates for the many-body effects.

### Band Structure Changes

Numerically integrating the products in Eq. (2) of the perturbed densities of states and the appropriate Fermi-Dirac distributions over the distorted bands gives  $\bar{p}$  and  $\bar{n}$  separately as functions of  $N$ . Then, multiplying  $\bar{p}$  and  $\bar{n}$  together yields  $n_{ie}^2(N)$ . Tables I and II show the results for the band structure changes as functions of  $N$  from this self-energy approach. The unperturbed intrinsic carrier density,  $n_i$ , in these tables is the limit of  $n_{ie}$  as  $N$  approaches zero.

Table I. Band structure changes for n-type GaAs as a function of donor density,  $N_D$ , at 300 K. The many-body energy,  $E_{mb}$ , is estimated by comparison with optical absorption measurements which are interpreted in terms of distorted bands and density of states.

$N_D$ ( $10^{18} \text{ cm}^{-3}$ )	$r_s$ ( $a_0$ )	$E_F$ (eV)	$E_{mb}$ (eV)	$E_{ic}$ (eV)	$E_G(\text{exp})$ (eV)	$n_{ie}/n_i$
10.0	65.8	0.28	-0.04	-0.10	1.28	0.16
3.0	82.2	0.13	-0.03	-0.06	1.34	0.75
0.6	127.0	0.03	-0.003	-0.04	1.38	0.96

Table II. Band structure changes for p-type GaAs as a function of acceptor density,  $N_A$ , at 300 K. The many-body energy,  $E_{mb}$ , is estimated from degenerate theory.

$N_A$ ( $10^{19} \text{ cm}^{-3}$ )	$r_s$ ( $a_0$ )	$E_F$ (eV)	$E_{mb}$ (eV)	$E_{ic}$ (eV)	$E_G(\text{theory})$ (eV)	$n_{ie}/n_i$
12.0	15.0	-0.19	-0.07	-0.06	1.29	0.97
8.0	16.2	-0.14	-0.06	-0.05	1.31	1.36
5.5	17.6	-0.11	-0.05	-0.04	1.33	1.65

The Bohr radius is  $a_0 = 0.529 \times 10^{-8} \text{ cm}$ ; the Fermi energy  $E_F$  is relative to the majority-carrier distorted band edge; and the bandgap narrowing is  $\Delta E_G = E_{ic} + E_{mb}$ . The decreases in  $n_{ie}/n_i$  from the value of unity for large values of  $N$  arises because the Fermi-Dirac statistics dominates over the other interactions in this regime. Degeneracy makes  $E_F$  rise more rapidly into the majority band with increasing carrier density. This effect compensates the effect of bandgap narrowing in the evaluation of integrals such as those in Eq. (2). When it becomes dominant in GaAs, then the minority-carrier density decreases more rapidly with increasing  $N$  than the majority-carrier density increases. Hence, the net result is that  $n_{ie}$  decreases for increasing values of  $N$  in the highly degenerate regime.

### Conclusions

Calculations of optical and electronic device operation, fabrication process parameters, device performance, and degradation mechanisms for GaAs which is heavily doped or which has high carrier concentrations must consider many-body interactions. Because computationally efficient theories for these interactions do not exist, comparisons with correctly interpreted optical measurements are essential for obtaining estimates of these terms. The example of the optical absorption serves to illustrate the relations among basic optical properties, carrier densities, band structure, and the performance of optical materials.

### Acknowledgments

The author acknowledges the many contributions of his colleagues at the National Bureau of Standards to this work.

### REFERENCES

1. H. C. Casey, Jr. and F. Stern, J. Appl. Phys. **47**, 631(1976).
2. J. R. Klauder, Ann. Phys. **14**, 43(1961). The third level approximation is used here. This approximation provides a medium in which a number of completed scatterings occur to second order in the scattering potential.
3. J. R. Lowney and H. S. Bennett, J. Appl. Phys. **54**, 1369 (1983).
4. H. C. Casey, Jr., D. D. Sell, and K. W. Wecht, J. Appl. Phys. **46**, 250 (1975).
5. R. A. Abram, G. N. Childs, and P. A. Sauderson, to be published in J. of Physics C (London), January 1985.
6. G. D. Mahan, J. Appl. Phys. **51**, 2634 (1980).

## MICRO-RAMAN STUDY OF LASER-INDUCED DAMAGE

Philippe M. Fauchet,<sup>(a)</sup> Ian H. Campbell<sup>(a)</sup> and Fran Adar<sup>(b)</sup>

<sup>(a)</sup>Department of Electrical Engineering and Computer Science, Princeton University, Princeton, NJ 08544

<sup>(b)</sup>Instruments S.A. Incorporated, Metuchen, NJ 08840

In most laser systems, damage to optical components is the major factor that limits scaling towards higher energy density. Although laser-induced damage in solids has been an active field of research for many years, we do not have a satisfactory understanding of the physics involved in these processes. This situation is in part due to the lack of non-destructive, quantitative probes that can be used *in situ*. In this paper, we show that Raman scattering is such a probe and can be used successfully in a wide range of practical situations.

Raman scattering is a probe of structural properties. In our experiments, incident probe photons are scattered off lattice vibrations and the backscattered Stokes signal is analyzed with a Ramanor U-1000 double-grating spectrometer. A spatial resolution of 1  $\mu\text{m}$  is achieved by passing the CW Argon laser beam and the scattered light through a microscope objective. All Raman spectra (peak and width) are reproducible to 0.1  $\text{cm}^{-1}$ . The spectral resolution of the entire apparatus can be as good as 0.2  $\text{cm}^{-1}$  although it is routinely set at 2 to 3  $\text{cm}^{-1}$ . The spectra discussed below consist of data spaced by 0.1  $\text{cm}^{-1}$  with 2 or 4 second exposure times.

The damaging beam is produced by a modelocked Nd:YAG laser. The samples discussed below are irradiated with modelocked trains of 20 1.06  $\mu\text{m}$  pulses. Experiments are in progress with single picosecond pulses in the gigawatt range at 1.06  $\mu\text{m}$ , 532 nm and 355 nm. To date, we have performed experiments on thin films or bulk samples (single crystal, polycrystal or amorphous). Here, we only discuss our results on silicon, which is a well-characterized material and thus can be used to calibrate our method. Results obtained on other materials will be presented later.

In Figure 1, we show a high-resolution Nomarski microphotograph of the surface of a silicon-on-insulator (SOI) sample after irradiation with 600 identical laser shots having an energy density that is half the measured single shot threshold. If the illumination sequence is stopped at 300 shots or less, no damage is visible. Even at 600 shots, a preliminary inspection with 160 X magnification revealed no damage. At 1200 shots, a more or less uniform surface damage is observed. We took micro-Raman spectra of this heterogeneously damaged region, as well as of many other areas (either virgin or irradiated with different numbers of shots at various energy densities). Figure 2 shows spectra taken at different locations in the area shown in Figure 1. The variations in the central frequency, linewidth and asymmetry of the lineshape clearly indicate that the structure has been altered. The magnitude of the effects shows the power of Raman spectroscopy. Similar experiments performed on other materials (including silicon-on-sapphire and amorphous silicon layers) show changes in the spectra that are also easily detected.

The undoped SOI samples were grown at 625 °C by low pressure chemical vapor deposition to a thickness of 1  $\mu\text{m}$ . At room temperature, the silicon is under tensile stress because the film and the substrate have different thermal expansion coefficients. Furthermore, the film is microcrystalline [2]. If laser damage is associated with local melting and subsequent regrowth, we can expect that the stress and microcrystallite properties will be affected. For our geometry, the stress will shift the central frequency  $\omega_0$  and the

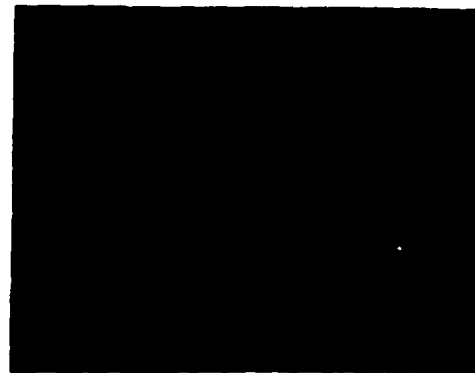
microcrystallite size will alter  $\omega_0$  as well as the linewidth  $\Gamma$  and lineshape  $\Gamma_a/\Gamma_b$ . As shown in Figure 3, we clearly observe changes in these quantities upon laser irradiation. We estimate the uncertainty on  $\omega_0$  and  $\Gamma$  to be less than  $\pm 0.2 \text{ cm}^{-1}$  and that on  $\Gamma_a/\Gamma_b$  to be  $\pm 0.05$ .

After laser damage, we observe a reduction in  $\Gamma_a/\Gamma_b$  and  $\Gamma$ , and a reduction in the Stokes shift. According to Richter et al. [3], the reduction in linewidth and asymmetry of the lineshape would indicate larger microcrystallites, while from Anastassakis et al. [4], the smaller Stokes shift would indicate an increased tensile stress. A complete quantitative interpretation of these and other spectra (including the amount of stress and microcrystallite size) is presently under way. However, it is already clear that Raman scattering is an excellent probe of the structural changes produced by laser-induced damage. It is more sensitive and quantitative than Nomarski microscopy. Furthermore, we have preliminary indications, from theory and experiments, that Raman scattering can be sensitive to the subtle subthreshold transformations which occur prior to visible damage in a multipulse exposure sequence [5].

We thank C. Paddock for her help with the laser and Dr. N. Johnson for providing us with the SOI samples.

1. J. Gonzalez-Hernandez, D. Martin and R. Tsu, in Spectroscopic Characterization Techniques for Semiconductor Technology, F.H. Pollak and R.S. Bauer editors, SPIE Proceedings Vol. 452, 1984, pp. 44-50.
2. N. Johnson, private communication.
3. H. Richter, Z.P. Wang and L. Ley, Solid State Commun. **39**, 625 (1981).
4. E. Anastassakis, A. Pinczuk, E. Burstein, F.H. Pollak and M. Cardona, Solid State Commun. **8**, 133 (1970).
5. P.M. Fauchet, Phys. Lett. **A93**, 155 (1983).

Fig. 1: High-resolution Nomarski microphotograph of a  $53 \mu\text{m} \times 41 \mu\text{m}$  area at the center of a spot illuminated with 600 laser shots at one half single shot damage threshold. The light, worm-like, micron-size features are localized damage spots that do not appear even after 300 laser shots.



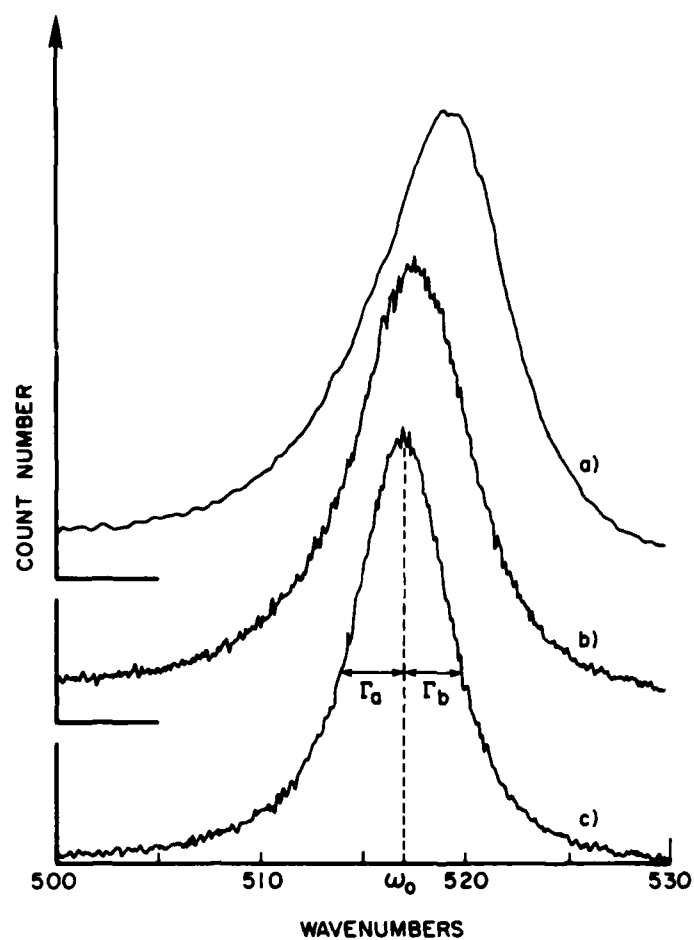


Fig. 2: Stokes line of a) virgin SOI; b) and c) two different locations in the area of fig. 1. The central frequency  $\omega_0$ , linewidth  $\Gamma(=\Gamma_a + \Gamma_b)$  and asymmetry (as measured by the ratio of the half-width half-maxima  $\Gamma_a/\Gamma_b$ ) change continuously from the center of one of the worm-like features to a worm-free region. The spectra are excited at  $5145\text{\AA}$  with a  $1\text{ }\mu\text{m}$  spatial resolution.



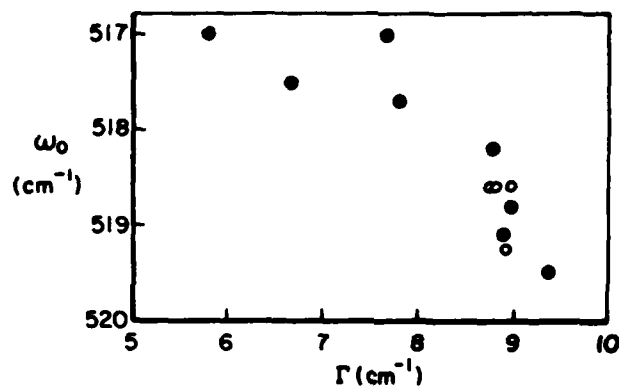


Fig. 3a: Central frequency and linewidth of virgin SOI (o) and at various locations in the area of fig. 1 (•). The data taken in the neighborhood of worm-like features yield lower  $\Gamma$ /lower  $\omega_0$ .

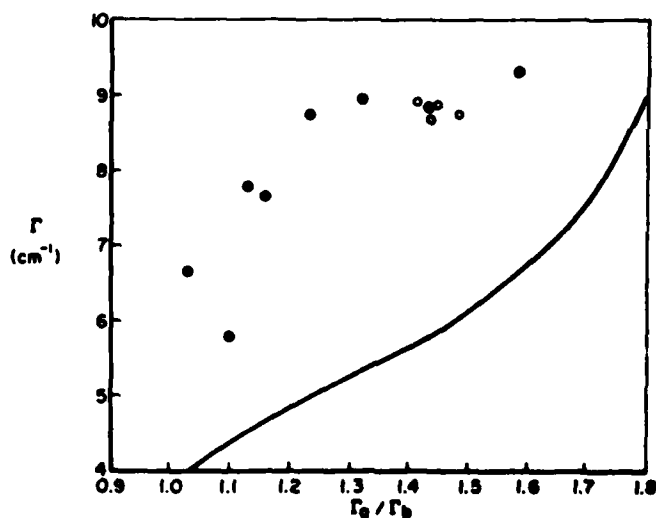


Fig. 3b: Linewidth versus asymmetry for the same spectra. The full line is the theoretical prediction based on a model where the increase in  $\Gamma$  and  $\Gamma_a/\Gamma_b$  is due to the gradual relaxation of the q-vector selection rule when the microcrystallite size decreases.

D. S. Chemla

AT&T Bell Laboratories, Holmdel, N.J., U.S.A.

## INTRODUCTION

Recently analog and digital optical processing have attracted much attention. However the operation of optical devices such as switches or modulators requires very large optical or electro-optical nonlinearities. These can be found in semiconductors at excitonic transition resonances (1). In bulk semiconductors excitonic resonances are only observed at low temperatures. It has recently been shown that excitonic effects are enhanced in ultra-thin semiconductor layers due to the quasi two-dimensional carrier confinement (2). The combination of an increased exciton binding energy (3) and a slightly reduced overall exciton-phonon interaction result in the observation of clear and well resolved exciton peaks in the absorption spectra of GaAs/AlGaAs multiple quantum well structures (MQWS) at room temperature (4).

The nonlinear optical effects involving room temperature excitons are extremely interesting to investigate for practical as well as fundamental reasons. From the point of view of applications MQWS exhibit at room temperature very large nonlinear optical and electro-optical effects at wavelengths, power levels and speeds compatible with laser diodes and electronics. In addition MQWS are prepared by advanced semiconductor technology (5), and therefore they have the potential to be incorporated in integrated systems. From a more fundamental viewpoint, MQWS form a model system to study the effects of reduced dimensionality on excitonic behavior. Furthermore, the room temperature excitons found in MQWS, are in the very unusual situation where;

$$\hbar\Omega_{LO} > kT > E_b$$

In this equation,  $\hbar\Omega_{LO} \sim 36 \text{ meV}$  is the GaAs LO-phonon energy,  $kT \sim 25 \text{ meV}$  at room temperature and  $E_b \sim 10 \text{ meV}$  is the exciton binding energy. Under these conditions excitons generated by resonant optical excitation are ionized in a very short time by phonon collisions. This provides a unique opportunity to study the dynamics of the transformation of excitons into an electron-hole (e-h) plasma and to investigate the nonlinear optical effects associated with both species.

## 1. OPTICAL NONLINEARITIES OF GaAs/AlGaAs MULTIPLE QUANTUM WELL STRUCTURES

The low temperature linear absorption in MQWS has been reviewed in Ref. (2) and the room temperature linear absorption has been discussed in Ref. (6). The confinement of an e-h pair in ultra-thin semiconductor layers increases the exciton binding energy (3,7,8) resulting in the observation of well resolved resonances in the room temperature absorption spectra of MQWS (4,9,10,11). This is shown in Fig. 1. where the 300 K absorption spectra of a  $3.2 \mu\text{m}$  thick high quality GaAs sample is compared to that of a MQWS sample. A small bump is seen at the edge of the GaAs spectrum, it corresponds to the remains of the excitonic resonance. The MQWS spectrum show two clear resonances for the heavy and the light hole excitons, followed by the flat two-dimensional continuum and the onset of the next subband transitions. This type of absorption spectrum is very well described by two Gaussian absorption lines corresponding to the two excitons and a two-dimensional continuum with the appropriate Sommerfeld enhancement factor for the

interband transitions (6). In the insert of Fig. 1. is shown the variation as a function of the temperature of the width of the heavy hole exciton peak, it is well described by a semi-empirical fit, shown by the solid line, involving two terms; a constant inhomogeneous line width,  $\Gamma_0 \sim 2 \text{ meV}$  (12,13,14) and a term proportional to the density of LO-phonons (9,6). The coefficient giving the temperature-dependent broadening,  $\Gamma_{ph} \sim 5 \text{ meV}$ , is smaller than that of bulk GaAs,  $\Gamma_{ph} \sim 7 \text{ meV}$  (15). From this dependence one can deduce a mean time for ionization by thermal LO-phonon collision of about 400 fs. Since at room temperature  $kT \sim 2.5 \times E_b$ , almost no excitons can reform from the electrons and holes created by the thermal phonons ionization (6). *Therefore, although excitonic resonances are observed at room temperature the gas of excitons resonantly generated through photon absorption is very short lived; it transforms into a free e-h plasma in less than 0.5 ps.*

Under optical excitation, as free e-h are generated they screen the Coulomb interaction causing the renormalization of the single particle states, with however very little shift of the exciton energy because of its neutrality (16). Nevertheless, the binding energy of the exciton with respect to the normalized band gap decreases, the e-h correlation diminishes progressively and the height of the absorption peak decreases. Eventually the correlation is completely lost and the exciton peak disappears leaving a step like absorption continuum edge near the exciton original position. This edge is much more difficult to saturate and can be shifted further to low energy if more carriers are generated. The large optical nonlinearity observed in MQWS with cw and ps sources results from conjunction of two factors; the concentration of a large oscillator strength in a narrow energy band and the screening of the Coulomb interaction by a charged plasma that modifies and eventually destabilizes the excitonic states.

Saturation of excitonic absorption in MQWS has been observed with cw laser excitation at resonance (4,9) and well above the exciton energy well in the continuum (6). The intensity dependence of the exciton peaks of the two samples (whose absorption spectra are given in Fig. 1.) are shown in Fig. 2a. and 2b., respectively for the GaAs sample and the MQWS. The solid curves are semi-empirical fits based on the model discussed in the previous paragraph. For GaAs the saturation is well described by a constant (  $\sim$  not saturable) background plus a saturable species with a saturation intensity  $I_s \sim 4.4 \text{ kW/cm}^2$ . The fit for the MQWS involve two saturable species one with a very small saturation intensity  $I_s \sim 580 \text{ W/cm}^2$  and the other one more difficult to saturate,  $I_s \sim 44 \text{ kW/cm}^2$  (9). According to our model these results can be interpreted in terms of the bleaching of the excitonic absorptions for the two samples, followed, in the case of the MQWS, by the saturation of the renormalized two dimensional continuum as it is shifted down in energy. In the case of GaAs, the interband transitions in the three-dimensional continuum show no saturation, at least up to the intensities reached in our experiments. This interpretation is well supported by the shapes of the spectra observed with a low intensity tunable cw dye laser with or without the excitation of a cw diode laser delivering about  $800 \text{ W/cm}^2$ , and emitting at 42 meV above the exciton peak (6). Examples of these spectra are shown in Fig. 3. Under excitation the exciton peaks have disappeared, and the absorption spectrum observed is a step-like edge which has exactly the same shape as the two dimensional continuum used to describe the interband transition in the unexcited spectrum.

The absorptive and dispersive part of the optical nonlinearity at low excitation has been measured by forward degenerate four wave mixing (DFWM) using a picosecond dye laser (17). In these experiments the nonlinear transmission induced by the pump beam on the probe beam and the diffraction efficiency of the coherent gratings generated by pump-probe interference can be simultaneously measured. In addition to the linear transmission the same set-up gives access to the recombination life time,  $\tau \sim 30 \text{ ns}$ , and to the diffusion coefficient,  $D \sim 13 \text{ cm}^2/\text{s}$ . An example of the experimental data is shown in Fig. 4a,b,c for the linear transmission, the differential nonlinear transmission, and the DFWM signal respectively. From the spectra of Fig. 4a and 4b and an adapted Kramers-Krönig inversion it is possible to obtain the spectra of the changes of absorption coefficient per e-h pair  $\sigma_{eh}$  and of refractive index per e-h pair  $n_{eh}$  (6) these are shown in Fig. 5. They determine completely the optical nonlinearity in the fundamental absorption region. A severe test of the accuracy of this determination is that the two complex spectra of Fig. 5 should reproduce

the measured DFWM diffraction efficiency of Fig. 4c. The comparison of the experimental data of Fig. 4 with the theoretical predictions based on the spectra of Fig. 5 is shown in Fig. 6, the agreement is excellent (6). The measured nonlinearities are very large, more than one order of magnitude larger than that of GaAs and six order of magnitude that of Si at room temperature.

To demonstrate the potential use of MQWS for nonlinear optics with cw laser diodes; DFWM experiments were performed in a  $1.25\mu\text{m}$  MQWS using a commercial diode laser as the sole light source (18). Internal diffraction efficiency of about  $5 \times 10^{-4}$  was measured with pump power as low as 2.5 mW ( $I_p \sim 20 \text{ W/cm}^2$ ) and probe power of 0.1 mW ( $I_t \sim 0.8 \text{ W/cm}^2$ ). It should be mentioned that such experiments are usually performed on thick samples with high power lasers.

Optical bistability using MQWS as the nonlinear element in a Fabry-Perot etalon, has been demonstrated (19).

More recently saturation of excitonic absorption in MQWS has been used to mode-lock laser diodes. Pulses as short as 1.6 ps and reliable operation have been obtained (20).

The dynamics of the exciton ionization by thermal phonons has been studied with the recently developed femtosecond spectroscopic techniques (21). The changes in the absorption spectrum of MQWS samples under excitation resonant with the heavy hole exciton or under non-resonant excitation in the continuum, have been measured with a resolution of 150 fs (22,23). In order to avoid any interference with band gap renormalization effects a moderate excitation was used in both cases. It was found that after a transient evolution which last approximately 0.5 ps, the changes are very similar to those observed with cw or ps lasers. However the transient regime ( $t < 0.5$  ps) is highly dependent on the nature of the excitation. For the non-resonant case a smooth evolution of the spectrum takes place, from the unpumped spectrum to that observed at long times ( $t > 1$  ps). Conversely in the case of resonant pumping one observes a very efficient bleaching of the exciton absorption that recovers partially in  $300 \pm 100$  fs. Typical spectra under resonant pumping and at various probe delays, are compared to the unexcited spectrum on Fig. 7. The time dependence of the height of the heavy hole exciton peak for the two excitation conditions is shown in Fig. 8. The smooth variation found for non-resonant pumping follows quite well the integral of the pump pulse, showing that the effects are proportional to the number of e-h pairs generated in the continuum. The behavior in the resonant pumping case corresponds to the instantaneous generation of a species that, in  $300 \pm 100$  fs, transforms into free e-h pairs, which have the same effects as in the non-resonant pumping case (22,23). The experiment is interpreted as the first observation of the exciton saturation due to the generation of excitons that occupy the lowest lying energy states of the system, followed by the thermal phonon ionization of these excitons into free e-h pairs. The saturation induced by the resonantly generated excitons is indeed large, and can be used for applications in ultra-fast optical devices.

## II. ELECTRO-ABSORPTION IN GaAs/AlGaAs MULTIPLE QUANTUM WELL STRUCTURES

MQWS absorption is also very sensitive to perturbation by electrostatic fields. The reason for such sensitivity is that the energies associated with the carrier confinement in the layers or with the Coulomb attraction between electrons and holes are small, typically  $\sim 10 \text{ meV}$ , and that the corresponding envelope wave functions are large, of the order of  $\sim 100 \text{ \AA}$ . Therefore the application of rather small fields, of the order of  $10 \text{ mV}/100 \text{ \AA}$  i.e.,  $10^{+4} \text{ V/cm}$ , well within the range that can be applied to semiconductors will cause large changes of the absorption spectra (24-27). Large changes of the luminescence efficiency with applied field have also been observed at low temperatures (28,29).

By symmetry it is expected that fields parallel and perpendicular to the layers will produce different effects. For a field parallel to the layers there is no effect on the confinement but the relative motion of the electron and the hole is perturbed as in the case of the Stark effect, with however some changes due to the lowered dimensionality of excitons in MQWS (30). For a field perpendicular to the layers the confinement energy of the electron and the hole are affected, and

since the two particles are pushed away from one another and squeezed against the walls of the potential well the exciton binding energy is also changed.

The design of samples to distinguish between the two geometries is quite important. In the case of field parallel to the layers photolithography used to define proper electrode geometry. The main observed effect is a broadening of the exciton peak which is due to the reduction of the exciton lifetime by the field ionization. This is shown in Fig. 9. At an applied field of  $1.6 \times 10^4$  V/cm the two peaks have substantially broadened, and they are no more resolvable at  $5 \times 10^4$  V/cm. The low field ionization rate has been calculated for two dimensional excitons by the same method as in the case of the Hydrogen atom (31). It is smaller than in three dimensions because of the increased binding energy and because of other effects related to the lowered dimensionality, the results are in qualitative agreements with the measurements.

To apply fields perpendicular to the layers special samples have been prepared; they consist of a MQWS in the intrinsic region of a p-i-n diode (25). The p and n regions are made of AlGaAs transparent at the energy of the fundamental gap of the MQWS. The diode is operated back-biased to vary the field across the MQWS and yet avoid large currents and thermal effects. The dominant effect is a shift of the whole spectrum with a small broadening of the exciton peaks. However these remain well resolved at fields as large as  $10^5$  V/cm, i.e., more than fifty times the classical ionization field. At such field shifts 2.5 times the binding energy are observed. Typical spectra under various static fields are shown in Fig. 10. At field larger than  $10^5$  V/cm the excitons are no longer resolvable. The interpretation of these observations is the following. As the static field is applied the potential seen by the electrons and the holes in the GaAs layers becomes that of a skewed well and the energy levels of the individual particles are shifted down. Simultaneously the wave functions are compressed against the walls of the well; the charge distribution is thus modified resulting in a variation of the binding energy of the excitons. If the field is further increased, the less-confined particles, i.e., the holes finally tunnel out owing to the finite depth of the well, so that the resonances can no longer be resolved. No adjustable parameters are used and the agreement with the measured shifts is very good (26). In this calculation the usual discontinuities at the band edges (i.e.,  $0.15 \times E_g$  for the valence band and  $0.85 \times E_g$ ) for the conduction band have been used (2); an almost perfect agreement is obtained if a larger discontinuity at the valence edge is taken ( $\sim 0.40 \times E_g$ ) as recently suggested (32). The reason why excitons are still observed at field much larger than the ionization field is that the large potential barriers prevent the particles from escaping from one another. This remarkable property is specific to MQWS; it allows us to move an abrupt absorption edge into a region of the spectra where the sample is transparent in the absence of field.

The intrinsic speed of the effect is very high since it corresponds to the response of the electronic envelope functions. In practice the limits are set by the RC constant of the circuit in which the MQWS is incorporated (25). Recently high speed modulation of laser diode has been achieved using a p-i-n MQWS  $0.965 \mu\text{m}$  thick in form of a  $95 \mu\text{m}$  mesa with a  $25 \mu\text{m}$  optical window. When the device is driven by electrical pulses of -8V and 125 ps duration, optical pulses  $\sim 131$  ps are produced (27). A schematic of the device and the optical response compared to the electrical excitation pulse are shown in Fig. 11. A modulation of 2.3 dB was measured. The overall response time of the device is well accounted for by the characteristics of the electric circuit. Deeper modulation and faster responses should be obtained with thicker MQWS and smaller device area.

A bistable optical switch based on a novel principle, has been demonstrated using the p-i-n MQWS devices; it is called Self-Electro-Optic-Effect-Device or SEED (33). It presents several attractive features: it requires no cavity, it has a very small switching energy, it operates over a broad band of wavelengths and eventually with incoherent light sources. When a reverse bias is applied to the p-i-n MQWS, the structure also acts as an efficient photodetector. The bistable optical switch consists of a series resistor and a constant voltage supply that are used to bias a p-i-n MQWS. A light beam at a wavelength close to the peak of the exciton at zero bias is sent through the sample and the bias is applied. The absorption spectrum is shifted so that the transmission is high. As the intensity of the incident beam is increased, the photocurrent passing through the

resistor induces a reduction of the voltage applied to the device, which in turn increases the absorption by shifting the spectrum thus further increasing the photocurrent and so on. This process provides the feedback mechanism for optical bistability (33). An example of the optical hysteresis loop obtained with a SEED is shown in Fig. 12. The SEED used in these experiments was rather large (about  $600\ \mu\text{m}$  in diameter), nevertheless the measured switching energy per unit area is remarkably low,  $W_{so} \sim 4\ \text{fJ}/\mu\text{m}^2$  for optical incident energy and  $W_{st} \leq 18\ \text{fJ}/\mu\text{m}^2$  for the total switching energy (electrical plus optical) substantially lower than any previously reported bistable optical device. Even lower switching energy should be possible for smaller devices, the physical limit for a  $(\lambda/n)^2$  device is  $\sim 1\ \text{fJ}/\mu\text{m}^2$ , comparable to that of electronic switches.

## CONCLUSION

We have presented some recent progress made in the investigation and the utilization of the excitonic resonances observed at room temperature in GaAs/AlGaAs multiple quantum well structures. Novel nonlinear optical and electro-optical effects are observed which result from the lowered dimensionality of the electrons in ultra-thin semiconductor layers. Room temperature excitonic peak are not only interesting for the applications, they also exhibit the most unusual properties owing to their extremely short life time and their transformation into free e-h pairs.

Finally, we would like to stress that although the GaAs/AlGaAs alloys form a model system from which extremely high quality MQWS have already been made, MQWS made with other semiconductors should soon be available with comparable quality. In addition, quantum wells represent only one type of microstructure soon it will be possible to prepare novel microstructures and investigate their even more exciting physical properties.

## ACKNOWLEDGEMENTS

The work that has been reviewed in this article has been performed at the AT&T Bell Laboratories in close collaboration with D. A. B. Miller, A. C. Gossard, P. W. Smith, T. C. Damen, T. H. Wood, C. A. Burrus, W. H. Knox, R. L. Fork and C. V. Shank.

## REFERENCES

- [1] D. S. Chemla, A. Mariani, *Progress in Quantum Electronics*, 8, 1 (1982).
- [2] R. Dingle, "Confined Carrier Quantum States in Ultra Thin Semiconductor Heterostructures," in *Festkörperprobleme XV*, p. 21, Ed. H. J. Queiser, Pergamon/Vieweg Braunschweig (1975).
- [3] R. C. Miller, D. A. Kleinman, W. T. Tsang, A. C. Gossard, *Phys. Rev.*, B24, 1134 (1981).
- [4] D. A. B. Miller, D. S. Chemla, P. W. Smith, A. C. Gossard, W. T. Tsang, *Appl. Phys.*, B28, 96 (1982).
- [5] A. C. Gossard, "Molecular Beam Epitaxy of Superlattices in Thin Films" in "Thin Films Preparation and Properties," ed. K. N. Tu and R. Rosenberg, Academic Press, NY (1983).
- [6] D. S. Chemla, D. A. B. Miller, P. W. Smith, A. C. Gossard, W. Wiegmann, *IEEE JQE-20*, 265 (1984).
- [7] G. Bastard, E. E. Mendez, L. L. Chang, L. Ezaki, *Phys. Rev.*, B26, 1974 (1982).
- [8] R. L. Greene, K. K. Bajaj, *Sol. State Commun.*, 45, 831 (1983).
- [9] D. A. B. Miller, D. S. Chemla, D. J. Eilenberger, P. W. Smith, A. C. Gossard, W. T. Tsang, *Appl. Phys. Lett.*, 41, 679 (1982).
- [10] Y. Ishibashi, S. Tarucha, H. Okamoto, *Inst. Phys. Conf. Ser. No. 63, Proceeding of Int. Symp. GaAs and Related Compounds, Japan 1981*, pp. 587-588 (1982).
- [11] S. W. Kirchoefer, N. Holonyak, K. Hess, D. A. Gulino, H. G. Drickamer, J. J. Coleman, P. D. Dapkus, *Appl. Phys. Lett.*, 40, 821 (1982).

- [12] C. Wiesbuch, R. C. Miller, R. Dingle, A. C. Gossard, Sol. State Commun., *37*, 219 (1981).
- [13] R. C. Miller, D. A. Kleinman, W. A. Norland, A. C. Gossard, Phys. Rev., *B22*, 863 (1980).
- [14] C. Wiesbuch, R. Dingle, A. C. Gossard, W. Wiegmann, J. Vac. Sci. Technol *17*, 1128 (1980).
- [15] V. I. Alperowich, V. M. Zalekin, A. F. Kranchinko, A. S. Terekhev, Phys. Stat. Sol., *B77*, 466 (1976).
- [16] H. Haug and S. Schmitt-Rink Progr Quantum Electronics, *9*, 3 (1983).
- [17] D. A. B. Miller, D. S. Chemla, D. J. Eilenberger, P. W. Smith, A. C. Gossard, W. Wiegmann, Appl. Phys. Lett., *42*, 925 (1983).
- [18] D. A. B. Miller, D. S. Chemla, P. W. Smith, A. C. Gossard, W. Wiegmann, Optic Letter, *8*, 477 (1983).
- [19] See, for example H. M. Gibbs, S. S. Tarng, J. L. Jewell, D. A. Weinberger, K. Tai, A. C. Gossard, S. L. McCall, A. Passner, and W. Wiegmann, Appl. Phys. Lett. *41*, 221 (1982).
- [20] Y. Silberberg, P. W. Smith, D. J. Eilenberger, D. A. B. Miller, A. C. Gossard, W. Wiegmann, Optic Letters *9*, 507 (1984).
- [21] R. L. Fork, C. V. Shank, R. Yen, C. A. Hirlimann, IEEE *JQE-19*, 500 (1983).
- [22] W. H. Knox, R. L. Fork, M. C. Downer, D. A. B. Miller, D. S. Chemla, C. V. Shank, A. C. Gossard, W. Wiegmann, Proceedings of the "Ultrafast Phenomena" Monterey, CA (1984).
- [23] W. H. Knox, R. L. Fork, M. C. Downer, D. A. B. Miller, D. S. Chemla, C. V. Shank, A. C. Gossard, W. Wiegmann, to be published.
- [24] D. S. Chemla, T. C. Damen, D. A. B. Miller, A. C. Gossard and W. Wiegmann, Appl. Phys. Lett. *42*, 864 (1983).
- [25] T. H. Wood, C. A. Burrus, D. A. B. Miller, D. S. Chemla, T. C. Damen, A. C. Gossard and W. Wiegmann, Appl. Phys. Lett. *44*, 16 (1984).
- [26] D. A. B. Miller, D. S. Chemla, T. C. Damen, A. G. Gossard, W. Wiegmann, T. H. Wood and C. A. Burrus, Phys. Rev. Lett. *53*, 2173 (1984).
- [27] T. H. Wood, C. A. Burrus, D. A. B. Miller, D. S. Chemla, T. C. Damen, A. C. Gossard, and W. Wiegmann, to be published.
- [28] E. E. Mendez, G. Bastard, L. L. Chang, L. Esaki, H. Morkoc and R. Fisher, Phys. Rev. *B26*, 7101 (1982).
- [29] R. C. Miller and A. C. Gossard, Appl. Phys. Lett. *43*, 954 (1983).
- [30] J. D. Dow and D. Redfield, Phys. Rev. *B1*, 3358 (1970).
- [31] D. A. B. Miller, D. S. Chemla, T. C. Damen, A. C. Gossard, W. Wiegmann, T. H. Wood and C. A. Burrus, to be published.
- [32] R. C. Miller, A. C. Gossard, D. A. Kleinman, O. Munteanu, Phys. Rev. *B29*, 3740 (1984).
- [33] D. A. B. Miller, D. S. Chemla, T. C. Damen, A. C. Damen, A. C. Gossard, W. Wiegmann, T. H. Wood, C. A. Burrus, Appl. Phys. Lett. *45*, 13 (1984).

## FIGURE CAPTIONS

- Figure 1 Room temperature absorption spectra of a  $3.2\ \mu\text{m}$  thick high purity GaAs sample and of a MQW sample consisting of 77 periods of  $102\text{\AA}$  GaAs layers and  $207\text{\AA}$   $\text{Al}_{.28}\text{Ga}_{.72}\text{As}$  layers.  
Insert: Temperature dependence of the line width of the  $n = 1$  heavy hole exciton. The solid line corresponds to fit discussed in the text.
- Figure 2 Intensity dependence of the absorption at the peak of the exciton resonance for the GaAs (curve (a)) and MQW (curve (b)) samples whose absorption spectra are shown in Figure 1. The solid line corresponds to the empirical fits discussed in the text.
- Figure 3 Absorption spectra of a MQW sample consisting of 65 periods of  $96\text{\AA}$  GaAs layers and  $98\text{\AA}$   $\text{Al}_{.3}\text{Ga}_{.7}\text{As}$  layers with (solid line) and without (dashed line) a pumping beam from a cw laser diode operating  $42\text{ meV}$  above the first exciton resonance. The intensity of the pumping beam is  $I = 800\text{ W/cm}^2$ . The fast oscillations in these spectra are Fabry-Perot fringes in a thin glass plate covering the sample.
- Figure 4 Raw data obtained by pump-probe experiments on the sample described in Figure 3. (a) linear transmission; (b) nonlinear transmission; diffraction efficiency on the light induced grating. For (b) and (c) the pump and probe beam powers were  $\sim 300\ \mu\text{W}$  and  $\sim 60\ \mu\text{W}$  respectively.
- Figure 5 Spectra of the imaginary and real parts of nonlinearity of the MQW sample.  $\sigma_{eh}$  and  $n_{eh}$  describe respectively the change of absorption and the change of refractive index induced by one electron-hole pair.
- Figure 6 Comparison of the experimental data of Figure (6), corrected for the small variations of the laser power, with the semi empirical fit for the linear absorption (a) and nonlinear absorption (b). The sold curve in (c) is obtained by the Kramers-Krönig inversion discussed in the text.
- Figure 7 Comparison of the absorption spectrum of an unexcited MQWS to the spectra after excitation by an ultra short pump pulse at resonance with the heavy hole exciton.
- Figure 8 Dynamic of the absorption of the heavy hole exciton peak for resonant and non resonant femtosecond pumping.
- Figure 9 Absorption spectra for electric fields  $E$  parallel to the quantum well layers. (a)  $E \approx 0$ ; (b)  $E \approx 1.6 \times 10^4\text{ V/cm}$ ; (c)  $E \approx 4.8 \times 10^4\text{ V/cm}$ .  
The insert shows figuratively the distortion of the electron-hole Coulomb potential with the applied field.
- Figure 10 Absorption spectra for electric fields  $E$  perpendicular to the quantum well layers (a)  $E \approx 1 \times 10^4\text{ V/cm}$ ; (b)  $E \approx 4.7 \times 10^4\text{ V/cm}$ ; (c)  $E \approx 7.3 \times 10^4\text{ V/cm}$ .  
The insert shows figuratively the distortions of the quantum well potentials with the applied field.
- Figure 11 Schematic of the p-i-n MQWS modulator. Comparison of the electric pulse applied to the modulator and the optical pulse generated by the modulator.
- Figure 12 Theoretical and measured optical transmission of the optical bistable SEED.



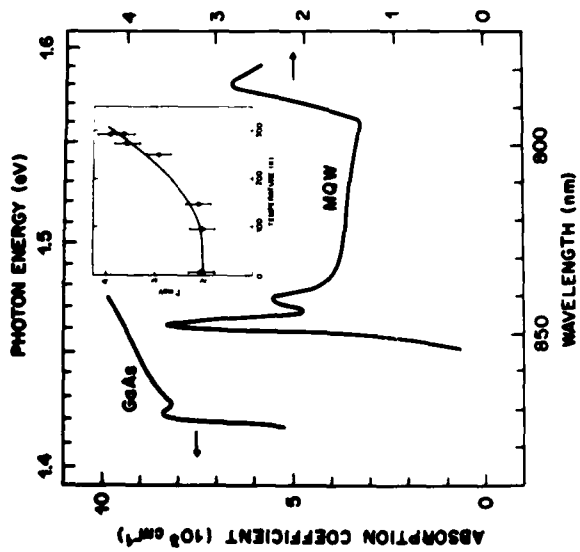


FIGURE 1

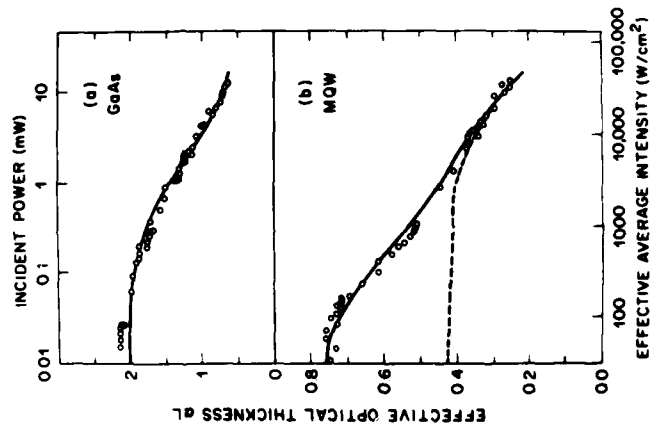


FIGURE 2

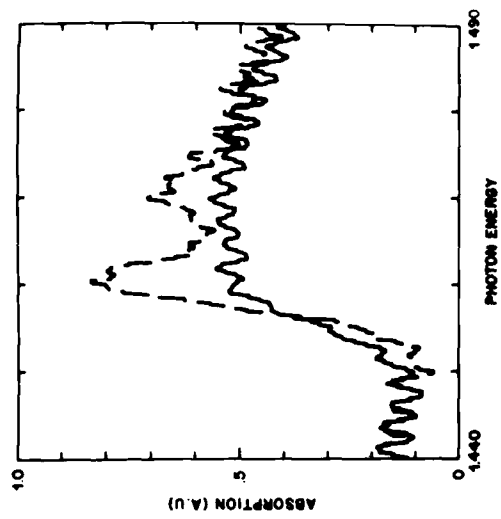


FIGURE 3

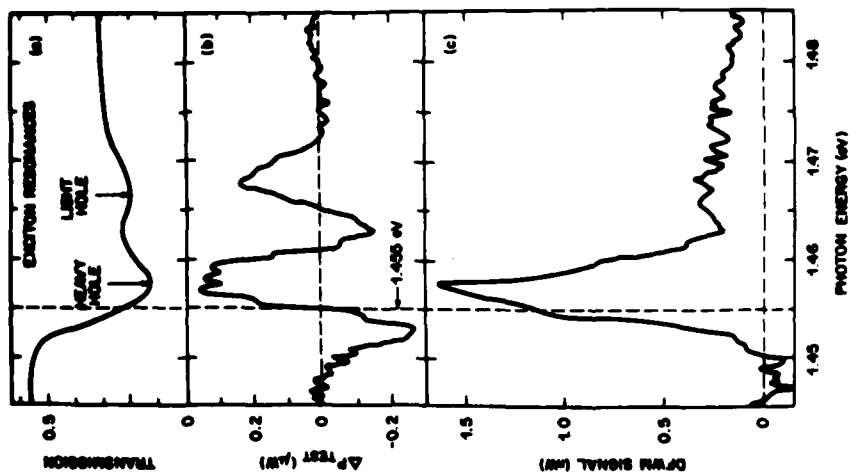


FIGURE 4

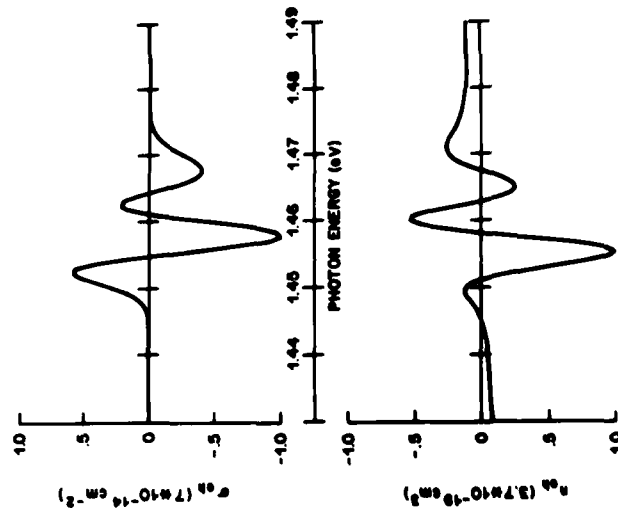


FIGURE 5

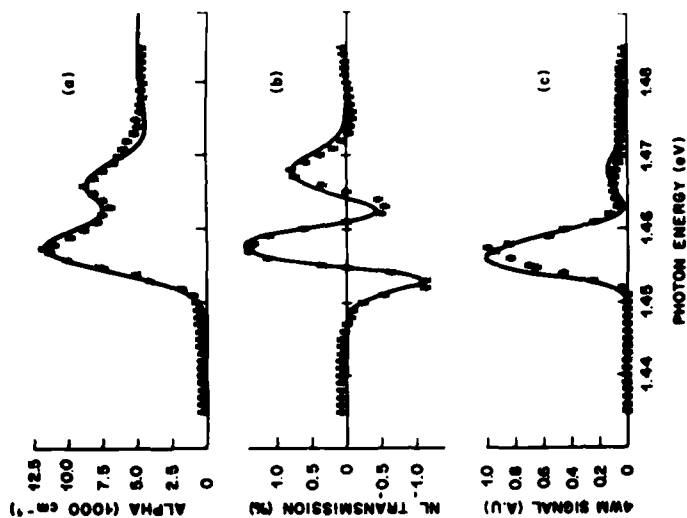


FIGURE 6

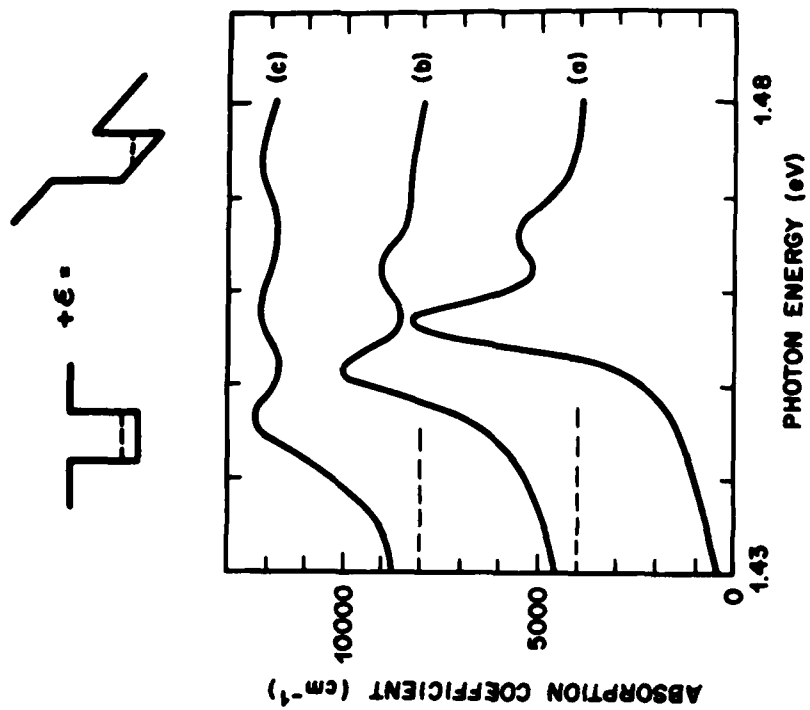


FIGURE 9

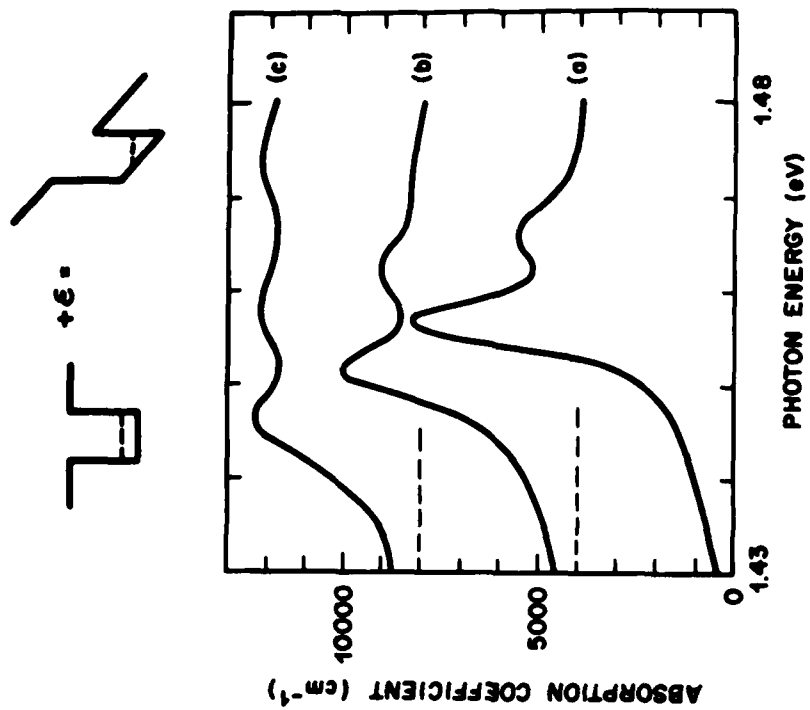


FIGURE 10

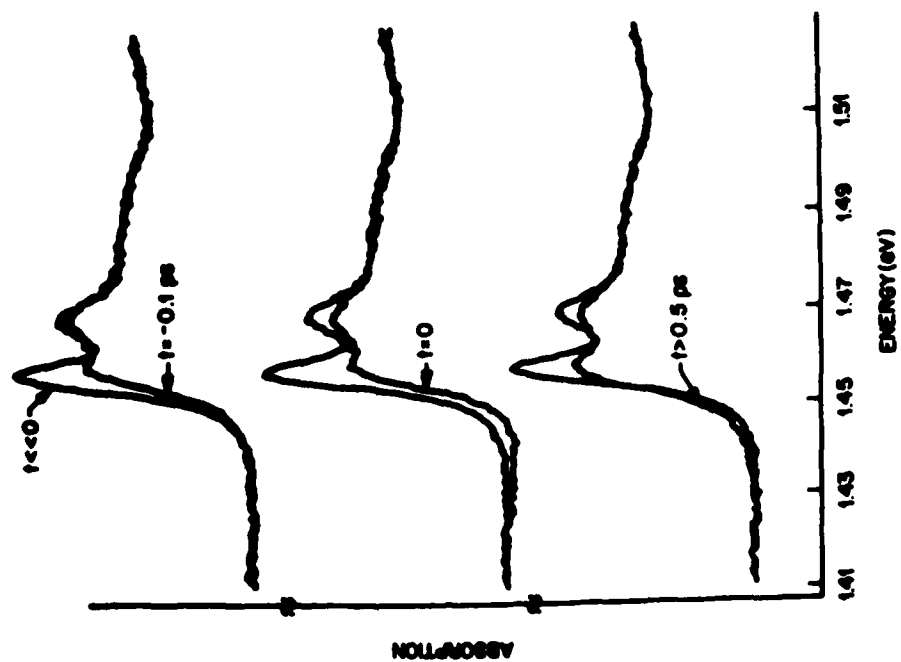


FIGURE 7

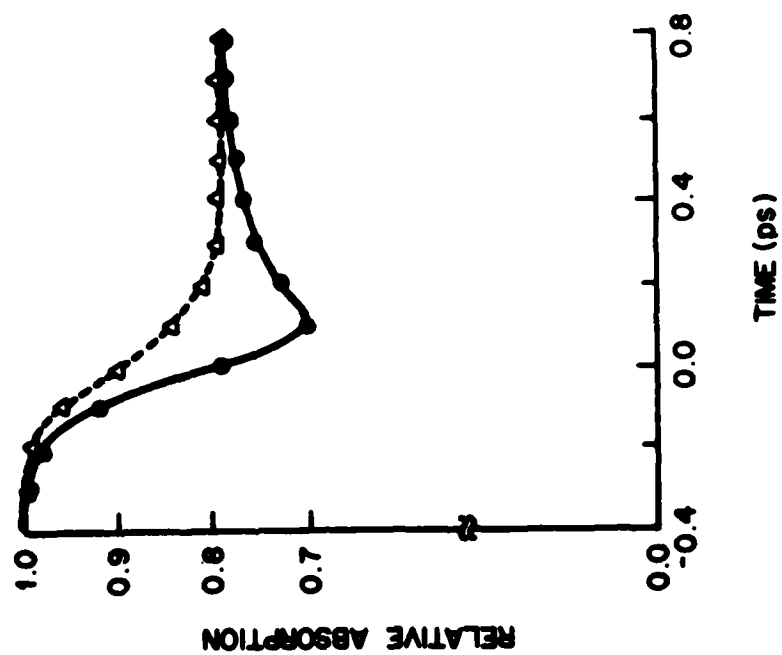


FIGURE 8

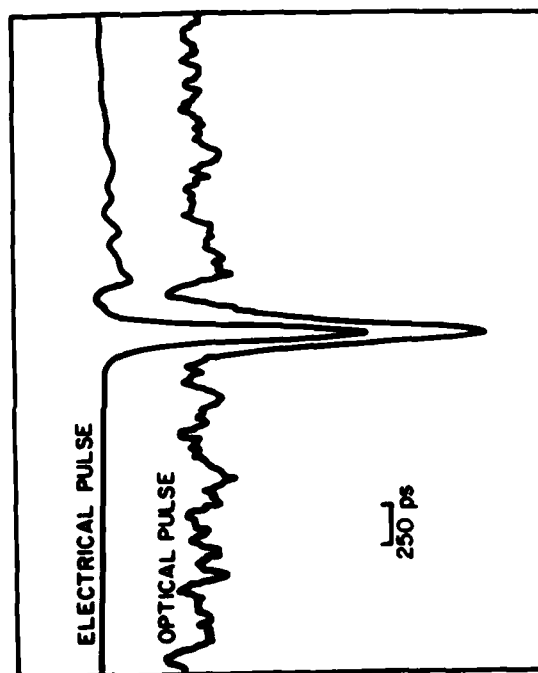
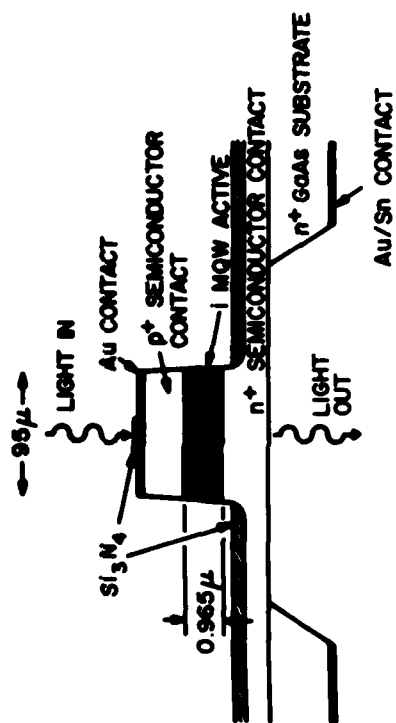


FIGURE 11

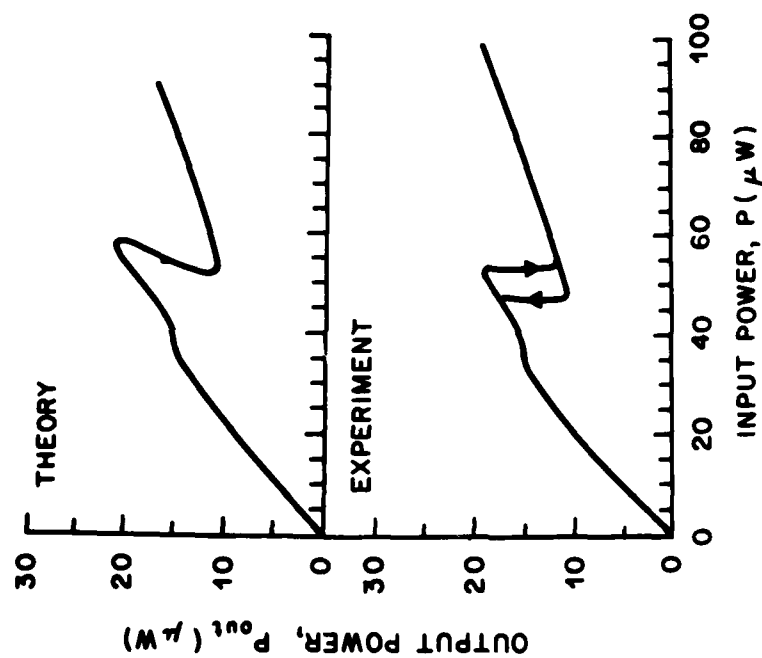


FIGURE 12

## PHOTOREFLECTANCE IN GaAs/AlGaAs MULTIPLE QUANTUM WELLS

O.J. Glembocki, B.V. Shanabrook, N. Bottka, W.T. Beard and J. Comas  
Naval Research Laboratory  
Washington, DC 20375

Photoreflectance (PR) is a contactless form of electromodulation spectroscopy in which the built-in surface field is periodically modulated by the photoinjection of electron-hole pairs. Photoexcited minority carriers recombine with surface state charge and thereby reduce the built-in electric field.<sup>1,2</sup> As in electroreflectance (ER), this modulation produces "third derivative-like" features in the optical dielectric function, in the vicinity of critical points. Consequently, even at room temperature, one observes very sharp differential reflectance lines related to the joint density of states of the material being studied.<sup>3</sup> Because of this ER and PR have proven to be sensitive room temperature probes of interband transitions in bulk semiconductors. However, there have been few ER or PR studies of microstructural systems.

Recently, we demonstrated that photoreflectance is a sensitive probe of interband transitions in GaAs/Al<sub>x</sub>Ga<sub>1-x</sub>As multiple quantum wells (MQW) and modulation doped heterojunctions exhibiting a two dimensional electron gas.<sup>4</sup> In this paper, we describe the photoreflectance technique and review the results of the MQW work of Ref. (4).

The experimental arrangement for photoreflectance is similar to one used in ER measurements. Shown in Fig. 1 is a schematic diagram of an ER spectrometer modified to perform PR measurements. The modulation is accomplished by mechanically chopping a laser of photon energy greater than the band gap of the sample. The reflectance measurement is performed with a probe beam of white light dispersed by a monochromator and then reflected from the sample. The reflected beam is passed through a filter which blocks the laser light and is detected by a photomultiplier (PMT) or some other suitable detector. The signal from the PMT is processed by a lockin amplifier tuned to the modulation frequency of the chopper. A servo mechanism on the high voltage power supply of the PMT is used to maintain a constant DC current in the phototube, allowing us to directly obtain  $\Delta R/R$ . In our system, a quartz halogen lamp and a 1/4 m Jarrell-Ash monochromator provided the probe beam. The detector was either a PMT with an S-1 response or a Si diode cell. In the later case, the servo mechanism was not used and  $\Delta R/R$  was obtained from independent measurements of  $\Delta R$  and  $R$ . The modulation was produced with a 1/2 mW HeNe laser chopped at 150 HZ.

Our samples were made by the molecular beam epitaxy (MBE) technique. The MQW structures consisted of approximately 30 periods of GaAs/Al<sub>x</sub>Ga<sub>1-x</sub>As layers grown on semi-insulating GaAs substrates and clad with either 200 Å thick GaAs or 1000 Å thick Al<sub>x</sub>Ga<sub>1-x</sub>As films. The Al<sub>x</sub>Ga<sub>1-x</sub>As layers separating the quantum wells were about 125 Å thick. The well width,  $L_z$ , was estimated by several methods including the use of the growth rates of the MBE films, photoluminescence and resonant Raman scattering measurements.

Shown in Fig. 2 are the 300 K photoreflectance spectra obtained from Ref. (4). The topmost trace is for a single undoped GaAs/Al<sub>0.17</sub>Ga<sub>0.83</sub>As

heterojunction, covering the spectral range between the direct gaps of the GaAs and  $\text{Al}_x\text{Ga}_{1-x}\text{As}$  components, i.e., the  $E_0 (\Gamma_{8,v} + \Gamma_{6,c})$  transitions. The lowest energy line near 1.42 eV results from the GaAs  $E_0$  transition, while the sharp feature located at 1.65 eV is the  $E_0$  transition from the  $\text{Ga}_{0.83}\text{Al}_{0.17}\text{As}$  thin film. The latter line allows us to obtain  $x$ .

The bottom three traces of Fig. 1 are PR spectra of the MQW samples. There are several general features to note. First, each spectrum contains a weak GaAs PR line. This line was observed in all of our samples, regardless of the type of cladding layer (GaAs or  $\text{Al}_x\text{Ga}_{1-x}\text{As}$ ). The GaAs signal originates from the buffer layer, which is typically grown between the quantum wells and the substrate material.<sup>4</sup> This indicates that the built-in modulating field reaches across all of the quantum well layers. Second, we see that each spectrum has a line near 1.70 eV corresponding to the  $E_0$  transitions in the  $\text{Al}_x\text{Ga}_{1-x}\text{As}$  films. From this line we obtain  $x$  for each sample.

The quantum well (QW) nature of our samples is evident in the numerous PR structures observed between the  $E_0$  transitions of the GaAs and  $\text{Al}_x\text{Ga}_{1-x}\text{As}$ . The strongest features increase in number and their energy separations decrease with increasing quantum well width, a behavior expected from parity allowed QW interband transitions.<sup>5</sup> There are also weaker structures located between the strong lines. In Ref. (4) these lines were identified by comparing their energy positions to predicted results of a finite square well calculation of the subband structure. The fraction of the band gap difference between GaAs and  $\text{Al}_x\text{Ga}_{1-x}\text{As}$  taken up in the conduction band was assumed to be  $Q_e=0.7$ . In Fig. 2, we have marked the calculated energy positions of parity allowed interband transitions, from heavy ( $h_1, \dots, h_n$ ) and light ( $l_1, \dots, l_n$ ) hole states to conduction subband states. This shows that the strong features are due to  $h_n$  transitions while the weaker ones are due to  $l_n$  transitions. Shown in Fig. 3 is a comparison of the calculated and experimental values of the transition energies  $h_n-h_1$  for all of our samples. Values relative to  $h_1$  were used to partially account for excitonic effects on the transitions. The agreement between experiment and theory is good.

In Ref. (4) the value of  $Q_e$  was varied and it was found that the best agreement between experiment and theory for interband transition energies was obtained using  $Q_e = 0.6$ . Consistent with recent findings,<sup>6,7</sup> this value of  $Q_e$  is smaller than the 0.85 initially suggested by Dingle.<sup>5</sup> Our value of  $Q_e$  is in excellent agreement with the 0.57 of Miller et al..<sup>7</sup> It is interesting to note that the values of  $x$  used in the experiments of Refs. (7) and (6) were 0.3 and 0.54 respectively, while in our case they were approximately 0.2 and 0.03. The differences among the reported values of  $Q_e$  suggest that it may be a function of  $x$ .

The  $l_n$  transitions are typically much less in intensity than the  $h_n$  features, consistent with previous work.<sup>3,6</sup> By using bulk conduction and valence band wave functions we estimated<sup>4</sup> that the  $l_n$  PR lines should be about a factor of 3 less intense than the  $h_n$  transition, in reasonable agreement with the experimental results.

In conclusion, we see that photoreflectance is a powerful, contactless room temperature probe of the optical properties of multiple quantum wells. Its contactless nature extends modulation spectroscopy to samples prepared on

on semi-insulating substrates. In MQW samples we observed the  $E_0$  transitions from the AlGaAs barrier and the allowed  $h_n$  and  $l_n$  interband transitions from the quantum wells. Our experimental results for the transition energies agree with a square well calculation of the QW states using  $Q_e = 0.60$ . Therefore, a single PR spectrum can provide information about the  $x$  value of the AlGaAs layers, the quality of the quantum wells from spectral line widths and (given  $Q_e$ ) the well width from the allowed QW transitions.

#### REFERENCES

1. J.L. Shay, Phys. Rev. B2, 803(1970).
2. D.E. Aspnes, Solid State Commun. 8, 267(1976).
3. F.H. Pollak, SPIE Proceedings, 276, 142 (1981).
4. O.J. Glembocki, B.V. Shanabrook, N. Bottka, W.T. Beard and J. Comas, submitted to, Appl. Phys. Lett.
5. R. Dingle, W. Wiegmann and C.H. Henry, Phys. Rev. Lett., 33, 827(1974).
6. D. Arnold, A. Ketterson, T. Henderson, J. Klein and H. Morkoc, Appl. Phys. Lett., 45, 1237(1984).
7. R.C. Miller, D.A. Kleinman and A.C. Gossard, Phys. Rev. B29, 7085(1984).
8. M. Erman, J.B. Theetan, P. Frijlink, S. Gaillard, F.J. Hia and C. Alibert, J. Appl. Phys. 56, 3241(1984).

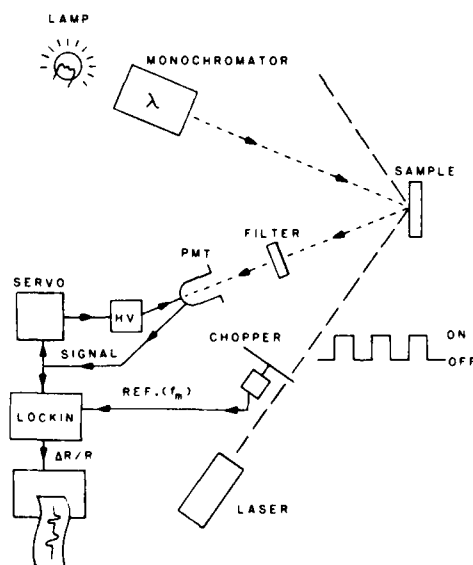


Figure 1. A schematic diagram of the photorefectance apparatus.



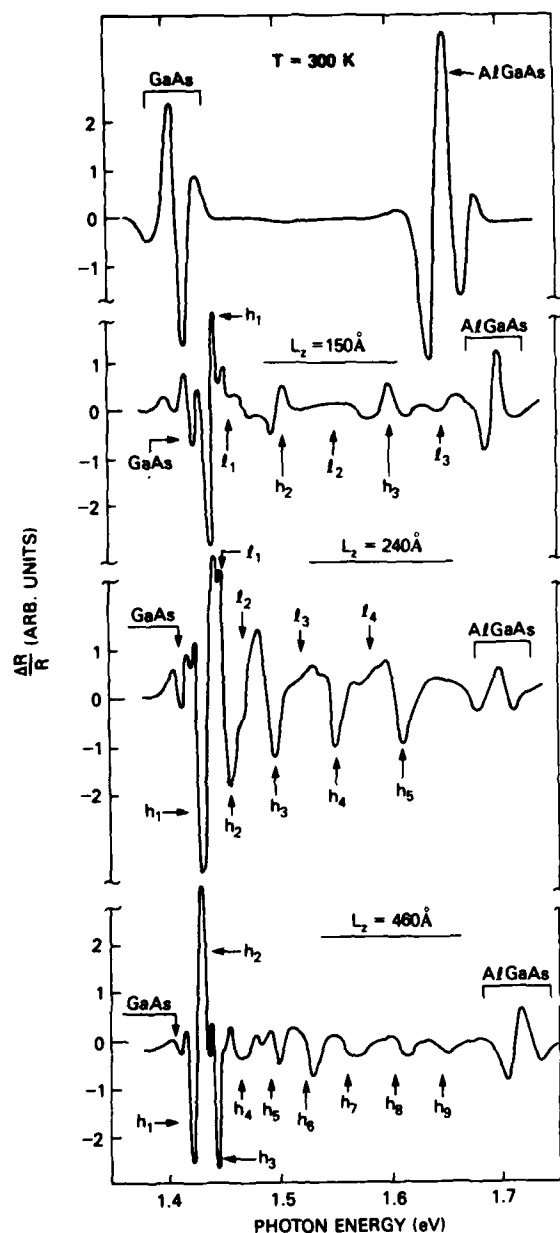


Figure 2. Photoreflectance spectra for an undoped  $\text{GaAs}/\text{Al}_x\text{Ga}_{1-x}\text{As}$  heterojunction (top trace) and three multiple quantum well samples with  $x \approx 0.2$ . The arrows labeled  $h_1, \dots, h_n$  ( $l_1, \dots, l_n$ ) correspond to the calculated values of allowed interband transitions between heavy (light) hole valence and conduction subbands

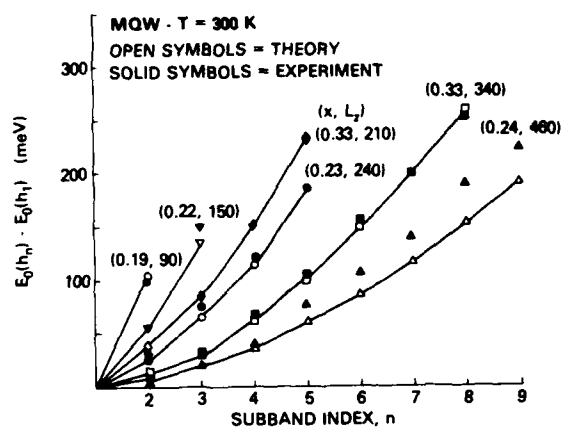


Figure 3. Theoretical (open) and experimental (solid) values of the  $h_n$  transition energies taken relative to  $h_1$ . Values of  $x$  and  $L_z$  for each sample are in parenthesis. The lines are drawn only as a guide to the eye.

# PICOSECOND CARRIER DYNAMICS IN a-Si

A. I. D'Souza, M. G. Roe, P. E. Wigen  
 Department of Physics, The Ohio State University  
 174 West 18th Avenue, Columbus, Ohio 43210  
 and  
 R. Messier  
 Materials Research Laboratory  
 The Pennsylvania State University  
 University Park, Pennsylvania 16802

**Experiment:** A mode locked argon ion laser is used to synchronously pump a cavity dumped dye laser in a picosecond spectrometer. A block diagram of the spectrometer is shown in Figure 1. The cavity dumped dye laser is operated at a wavelength of 600 nm, an average output power of 14 mW, and a repetition rate of 0.4 MHz. The pulses have a FWHM of 15 ps and a peak power of 2300 W/pulse. The output beam is divided by a beam splitter with 95% of the power used as a pump beam, incident normally on the sample. The remainder is again split with one portion monitored by a PMT, giving a real time monitor of any changes in laser power. The balance is used as a probe beam which is passed through a delay line determining the time interval between arrival of pump and probe pulses at the sample. The pump and probe beams are focussed on the sample with spot diameters on the order of 30  $\mu\text{m}$  to 40  $\mu\text{m}$ , resulting in a peak power density of approximately  $2.4 \times 10^8 \text{ W/cm}^2$ . The probe spot is maintained at a smaller diameter than the pump spot in order to assure proper overlap. The analyzer is initially set crossed to the reflected beam insuring that the signal PMT

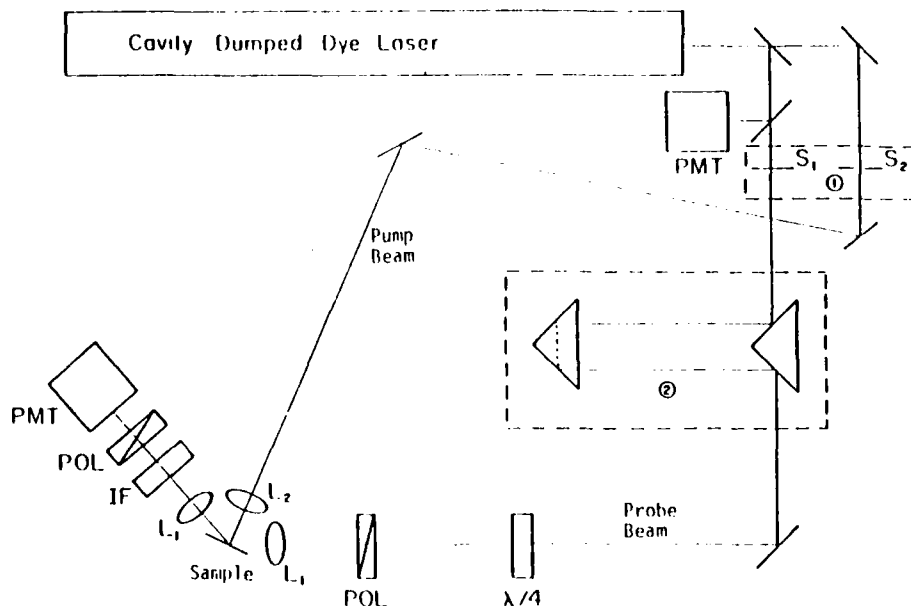


Figure 1. The experimental setup. Stepper motors control the shutters, Box #1 and the delay line, Box #2. The symbols are PMT photomultiplier detectors, POL polarizers,  $L_1$  lenses, IF interference filter, and  $\lambda/4$  quarterwave phase plate.

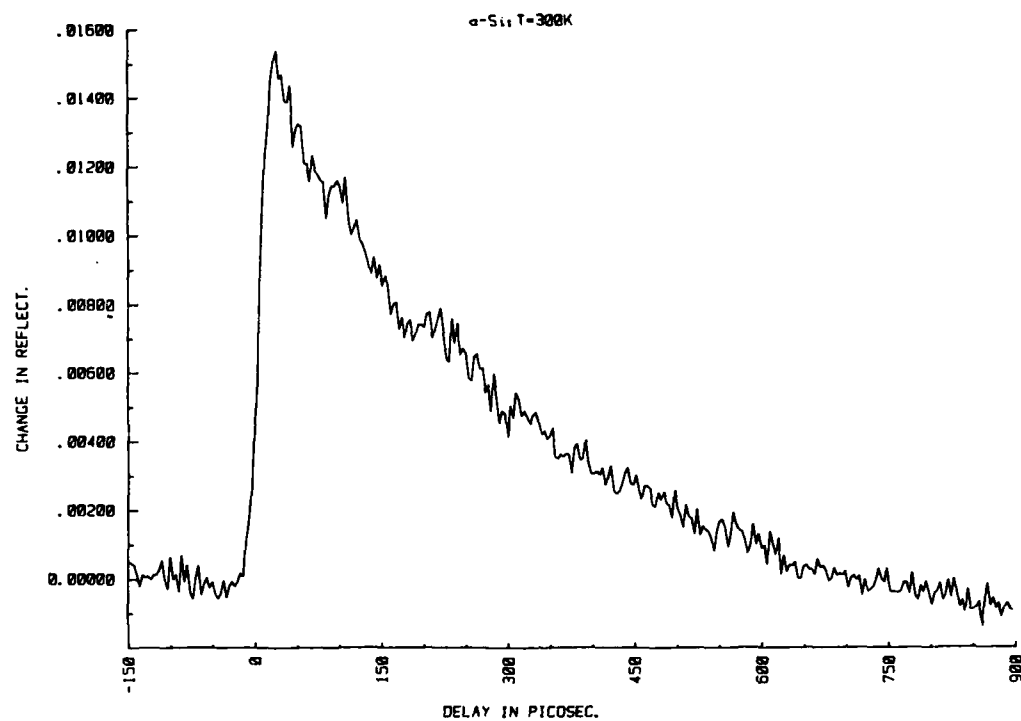


Fig. 2. Change in reflectance as a function of delay time in picoseconds

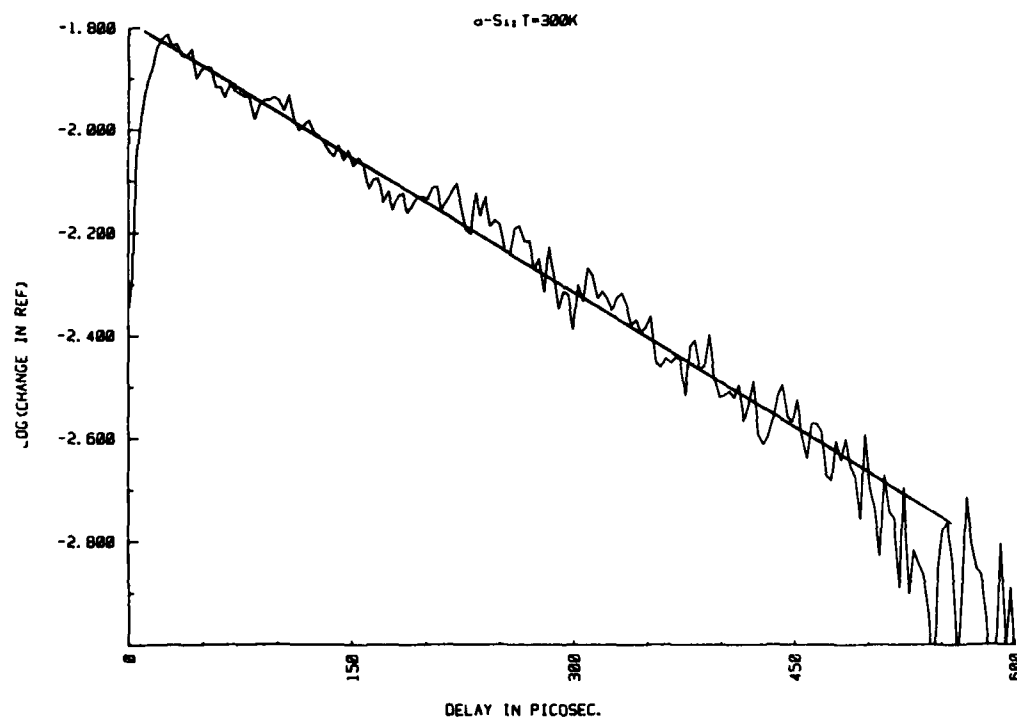


Fig. 3. Semilog plot of the log (change in reflectance) as a function of delay time in picoseconds.

will measure changes in reflectance of the sample due to changes in the electronic properties induced by the pump beam.

**Sample:** Films of a-Si of thickness 1  $\mu\text{m}$  were prepared by rf diode sputtering under fixed Ar pressure of 7 mTorr [1] on substrates of fused silica. The band gap was determined from optical absorption measurements, by extrapolation of  $(\alpha h\nu)^{1/2}$  vs.  $(h\nu)$  curves to  $\alpha = 0$ . [2]. The band gap  $E_0$  was measured to be 1.32 eV.

**Discussion:** Changes in reflectance as a function of time in the range -150 ps to +900 ps were measured by using a pump-probe technique. Typical data is shown in Figure 2. Photons of energy 2.1 eV excite  $4.4 \times 10^{20}$  carriers/cm<sup>3</sup> from the valence band to a point high in the conduction band. This carrier density was calculated using a reflectance R of .35 and an absorption coefficient  $\alpha = 10^5 \text{ cm}^{-1}$ . The hot electrons are assumed to decay down to the localized states near the conduction band edge in 0.7 ps [3]. Since the pulses have a FWHM of 15 ps, this process is too fast to be observed in this experiment. The initial condition is then assumed to be that of the excited carriers near the conduction band edge. Figure 3 shows a semi-log plot of the data in Figure 2. The plot is linear, indicating an exponential decay of the change in reflectance with time. The decay time constant is determined, from the slope of the semi-log plot, to be  $\tau = 270$  ps. Since the change in reflectance is, to first order, proportional to the conduction band carrier density n, [4] n satisfies an equation of the form:

$$\frac{dn}{dt} = -\frac{n}{\tau}$$

The decay of carriers from the conduction band is therefore a single body process.

A rough sketch of the density of states in the gap for a-Si is shown in Figure 4 [5]. The large density of states in the gap enhances the percolation of charge carriers through the defect states in the gap into the valence band. This is the proposed non-radiative single body process that dominates the decay in a-Si at T = 300 K as opposed to a radiative two-body process normal in single crystal materials. The near absence of radiative recombination [5] is consistent with photoluminescence experiments performed

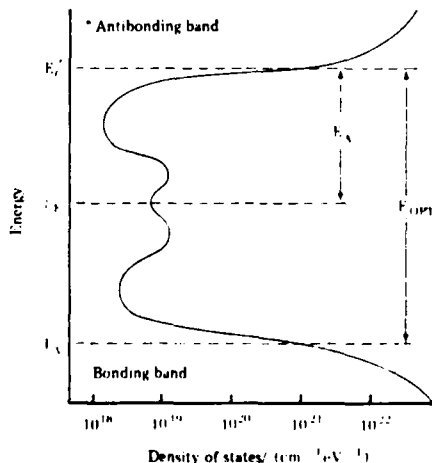


Fig 4. Density of states as a function of energy. (Reference 5)  $E_c^*$  and  $E_v^*$  define the mobility edges.

on sputtered a-Si:H. These experiments indicate that photo-luminescence intensity tends to zero as the partial pressure of hydrogen during growth of the samples tends to zero.

Experiments performed on a-Si:H indicate decay processes different from that observed in a-Si. The decay is no longer exponential, suggesting the existence of competing processes such as radiative recombination. Other decay processes are currently being studied.

In conclusion, the observations suggest that the large density of states in the gap in a-Si provides a fast and easy non-radiative channel for the decay of charge carriers out of the conduction band. This conclusion is derived from the exponential decay in the reflectance which is interpreted as indicating the dominance of monomolecular non-radiative recombination, with bimolecular radiative recombination relatively unimportant in sputtered a-Si at  $T = 300$  K up to 900 ps.

#### References:

- [1]. J. S. Lannin, L. J. Pilione, S. T. Kshirsagar, R. Messier and R. C. Ross; Phys. Rev. B26,3506 (1982).
- [2]. R. C. Ross and R. Messier; J. Appl. Phys. 52,5329 (1981).
- [3]. J. Tauc, Physica 117B & 118B (1983) 889-893.
- [4]. D. G. McLean; Ph.D. Dissertation, The Ohio State University (1984).
- [5]. S. R. Ovshinsky and D. Adler; Contemp. Phys. 19,109 (1978).
- [6]. M. A. Paesler and W. Paul; Phys. Mag. B, 41,393 (1980).

# PHOTOREFRACTIVE AND NONLINEAR-OPTICAL PROPERTIES OF NEW ELECTROOPTIC MATERIALS

Peter Günter  
Laboratory of Solid State Physics  
Swiss Federal Institute of Technology  
ETH Hönggerberg  
CH-8093 Zürich, Switzerland

In this paper we will present a review of both photorefractive and nonlinear-optical materials for optoelectronic applications. The materials requirements for nonlinear optical laser frequency conversion using the electronic hyperpolarizabilities and optical signal processing using the photorefractive effect shall be discussed. Some representative examples of newer photorefractive and nonlinear optical materials, its properties and applications will be described.

In recent years ferroelectric materials with their large electro-optic coefficients have found new optical applications in the field of phase conjugate optics, image processing and dynamic holography. These applications are based on the photoinduced refractive index changes or photorefractive effect which is due to the linear electro-optic effect driven by photoinduced space-charge fields. The light induced changes of refractive indices in electro-optic crystals are based on the spatial modulation of photocurrents by non-uniform illumination. The electrons or holes which are excited from impurity centers by light of suitable wavelength, are upon migration, retrapped at other locations leaving behind positive or negative charges of ionized trap centers. The resulting space-charge field between the ionized donor centers and the trapped charges modulates the refractive indices via the electro-optic effect.

In photoconductive materials the photocurrent along one dimension ( $z$ ) with electrons as carriers is given by:

$$j(z,t) = \frac{e\phi\alpha}{h\nu} I(z,t) \cdot L_d - \frac{\phi\mu\tau\alpha kT}{h\nu} \frac{dI(x,t)}{dz} \quad (1)$$

where  $L_d = \mu\tau E_0$  is the drift length,  $e$  the electronic charge,  $\phi$  the quantum efficiency for exciting an electron,  $\alpha$  the absorption constant,  $h\nu$  the photon energy,  $\mu$  the electron mobility,  $\tau$  the lifetime of photoexcited electrons,  $I(z,t)$  the light intensity distribution and  $E_0$  the applied electric field. The space-charge build-up process is mainly affected by  $\mu\tau$  and  $\alpha, \phi$ . The latter two quantities being strongly wavelength dependent.

Laser-induced dynamic phase gratings can be recorded by means of this photorefractive effect. The main requirements for photorefractive materials used in "real-time" recording and processing are:

- a) short recording time constants and
- b) large refractive index changes.

It has been shown in Refs. 1 and 2 that photoinduced grating recording using the migration of photoinduced charge carriers by an external electric field is

most efficient. The grating recording time constant  $T$  for small drift length can be determined from the relaxation time of charged dielectric layers separated by half a fringe spacing:

$$T = \frac{h\nu}{e} \frac{\epsilon\epsilon_0}{\Phi\mu\tau} \frac{1}{\alpha I_0} \quad (\epsilon: \text{dielectric constant}) \quad (2)$$

Therefore short recording times are found in electro-optic materials with large drift length  $L_d = \mu\tau E_0$ , i.e. in materials with large lifetime of photo-induced carriers. This parameter is mainly determined by the defect concentration (donor- or trapping concentration). (Table 1).

The maximum refractive index changes depend on the value of the photoinduced space-charge field and the electro-optic coefficient  $r_{ij}$  of the material. The maximum possible space-charge field  $E_q$  is limited by the concentration of trapping centers  $N_A$  <sup>1</sup>:

$$E_q = \frac{e N_A \Lambda}{2\pi\epsilon\epsilon_0} \quad (3)$$

For a peak field  $E_q = 10^4$  V/cm, a fringe spacing  $\Lambda = 1 \mu\text{m}$ , and a dielectric constant  $\epsilon=50$ , the required trap density would be  $N_A = 1.7 \cdot 10^{16} \text{ cm}^{-3}$ . This value is comparable to the ones determined in  $\text{BaTiO}_3$ ,  $\text{KNbO}_3$  and  $\text{Bi}_{12}\text{SiO}_{20}$  <sup>1</sup>. In Table 1 the electro-optic coefficients and peak refractive index changes are listed in addition to the photoconductivity parameter  $\mu\tau$ . Table 1 also shows, that photoconductive ferroelectrics with large electro-optic coefficients (e.g.  $\text{KNbO}_3:\text{Fe}^{2+}$ ,  $\text{BaTiO}_3$ ,  $\text{Ba}_2\text{NaNb}_5\text{O}_{15}$ ,  $\text{Ba}_{1-x}\text{Sr}_x\text{Nb}_2\text{O}_6$ ) are extremely interesting for photorefractive applications such as optical phase conjugation and "real-time" image processing.

The materials requirements for nonlinear optical laser frequency conversion using the electronic hyperpolarizabilities in inorganic crystals is discussed in the second part of this contribution. It is shown, that high quality materials with large nonlinear optical coefficients and the possibility of phase matching between interacting beams have been found, in which low power laser light (e.g. from  $\text{Ga}_{1-x}\text{Al}_x\text{As}$  laser diodes) can be efficiently converted to the second-harmonic.

For the ideal case of second-harmonic generation of plane monochromatic waves, neglecting pump depletion, the second harmonic intensity is given by:

$$I(2\omega) = \frac{2\omega^2 \ell^2}{c^3 \epsilon_0} \frac{d_{\text{eff}}^2}{n^3} I^2(\omega) \left( \frac{\sin \Delta k \ell / 2}{\Delta k \ell / 2} \right)^2 \quad (4)$$

where  $\ell$ ,  $\omega$  and  $c$  are the crystal length and the vacuum speed of light respectively and  $\Delta k = k_2 - 2k_1$  is the phase mismatch. As seen from (4),  $d_{\text{eff}}^2/n^3$  can be used as a figure of merit for frequency doubling (see Fig. 1 for a comparison of materials). Phase matching ( $\Delta k=0$ ) is possible e.g. in birefringent materials by a suitable choice of the direction of propagation and polarization

of the fundamental wave. For extremely long interaction lengths one would like to use collinear phase matching (PM), where the fundamental and second harmonic beams generally propagate along a main axis of the index ellipsoid. Adequate birefringence for PM is the most restrictive requirement. Room temperature operating and  $90^\circ$  noncritical phase-matching are particularly important to eliminate the use of temperature controllers for compactness and to ascertain long effective interaction length without walk-off for high efficiencies. The group symmetry of the doubling crystal must be such, that non-zero tensor elements exist for the proper phase matchable polarizations. Some nonlinear optical materials which fulfill these requirements for  $\text{Ga}_{1-x}\text{Al}_x\text{As}$  and  $\text{InGaAsP/InP}$  double heterostructure laser radiation will be discussed.  $\text{KNbO}_3$  is such a material with large nonlinear optical coefficients ( $d_{32} = 21 \text{ pm/V}$ ,  $d_{31} = 16 \text{ pm/V}$  and  $d_{33} = 33 \text{ pm/V}$ ) and the possibility of  $90^\circ$  noncritical phase matching for frequency doubling  $\text{Al}_x\text{Ga}_{1-x}\text{As}$  diode and (Styryl-9) dye laser radiation ( $840 \text{ nm} < \lambda_{\text{pm}} < 950 \text{ nm}$ ) at room temperature <sup>3,4</sup>. Up to  $P_{2\omega} = 0.35 \text{ mW}$  blue light ( $\lambda = 430 \text{ nm}$ ) could be generated in a  $5.74 \text{ mm}$  long crystal with a  $\text{Ga}_{1-x}\text{As}$  laser diode  $P_\omega = 155 \text{ mW}$ ). Frequency doubling experiments with dye lasers (e.g. Styryl-9) and  $\text{KNbO}_3$  within or out of the laser cavity are described <sup>5</sup>.

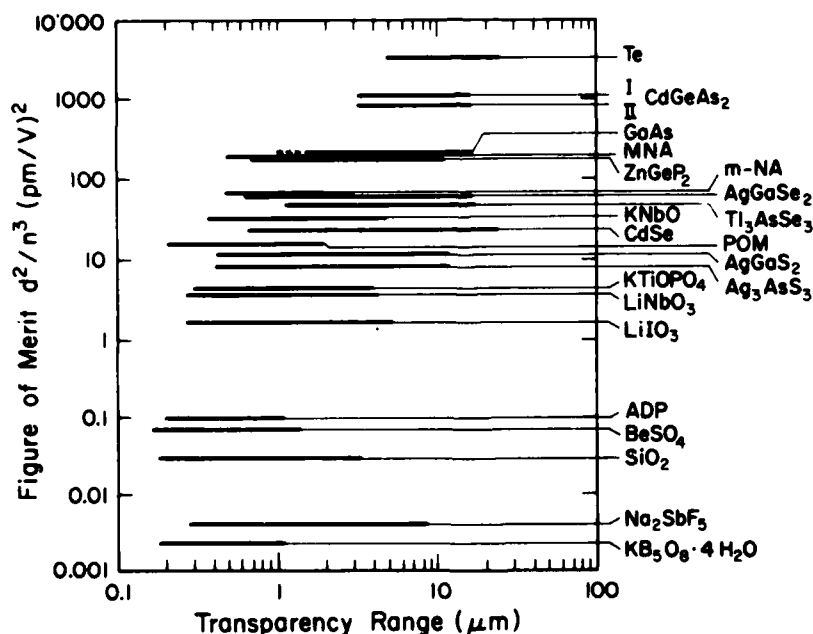


FIGURE 1: Figure of merit  $d^2/n^3$  and transparency range for nonlinear optical materials (including organic crystals).  
POM: 3-methyl-4-nitropyridine-1-oxide  
MNA: 2-methyl-4-nitroaniline  
m-NA: metanitroaniline)



TABLE 1: Photoconductive electro-optic materials

Material	$\mu\tau$ ( $10^{-7} \frac{\text{cm}^2}{\text{V}}$ )	EO coef- ficient $r_{ij}$ ( $\frac{\text{pm}}{\text{V}}$ )	T (S)	$10^3 \cdot \Delta n$
$\text{Bi}_{12}\text{SiO}_{20}$	1	5	-	
$\text{Bi}_{12}\text{GeO}_{20}$	0.8	3.4	30*	0.01
$\text{KNbO}_3:\text{Fe}$	0.3	64, 380*	0.001-0.1*	0.3
$\text{K}(\text{NbTa})\text{O}_3 (T_c=40^\circ\text{C})$	0.01	500	-	-
$\text{BaTiO}_3$	0.001	80,1640*	40*	0.1-1
$\text{LiNbO}_3$	$10^{-5}$	31	100	1
$\text{Ba}_{.25}\text{Sr}_{.75}\text{Nb}_2\text{O}_6$	0.8	45	-	0.03

$\Delta n$ : Peak steady-state refractive index change

\* : depending on crystal orientation. \* ( $\lambda = 600 \text{ nm}$ )

#### References

1. P. Günter, Physics Reports 93, 199-299 (1982)
2. P. Günter, Optics Letters 7, 10 (1982)
3. P. Günter, SPIE (Proceedings of ECOSA'80) Vol. 236, 8-18 (1981)
4. J.-C. Baumert, P. Günter and H. Melchior, Optics Commun. 48, 215 (1983)
5. J.-C. Baumert, J. Hoffnagle and P. Günter, Appl. Optics (to be published)

# MEASUREMENT OF DEFECT AND TRANSPORT PROPERTIES OF ELECTRO-OPTIC MATERIALS USING THE PHOTOREFRACTIVE EFFECT

M. B. Klein and George C. Valley  
Hughes Research Laboratories  
3011 Malibu Canyon Road  
Malibu, CA 90265

In this paper, we use steady state beam coupling as a function of grating period at 442 nm to obtain data on the sign of the dominant photocarrier, the concentration of empty traps and the effective electro-optic coefficient for several samples of  $\text{BaTiO}_3$ ,  $\text{Ba}_2\text{NaNb}_5\text{O}_{15}$  (BNN) and  $\text{Sr}_{1-x}\text{Ba}_x\text{Nb}_2\text{O}_6$  (SBN).

We assume an energy level model in which a single species X, in two valence states X and  $X^+$ , is responsible for the photoactive energy states in the bandgap of each sample. We denote the concentration of X as N, and that of  $X^+$  as  $N^+$ . We allow for the photo-generation of both electrons and holes, through the ionization of X or  $X^+$ , respectively.

In our experiments, we used a cw He-Cd laser to measure the intensity gain  $\Gamma$  as a function of grating period  $\Lambda$  for each sample. The grating normal was aligned parallel to the c-axis, and in most  $\text{BaTiO}_3$  experiments the beams were s-polarized in order to avoid the complications of beam fanning [1]. For each crystal the c-axis direction was set so that the weak probe beam was amplified at the expense of the strong reference beam. By measuring the sense of the resulting c-axis orientation, and using the convention developed by Feinberg, et. al. [2], we were able to determine the sign of the dominant photocarrier in each crystal.

We have developed an expression for the beam coupling gain as a function of grating period, taking into account the explicit contribution from both holes and electrons, and the possibility of incomplete poling of our crystals. The model contains two lumped experimental parameters which can be determined for each sample by fitting our gain expression to the experimental points. The first parameter is an effective electro-optic coefficient, defined as

$$r_{\text{eff}} = \bar{\sigma} F r_{\text{ang}},$$

where  $\bar{\sigma}$  is the normalized conductivity, F is the fractional poling and  $r_{\text{ang}}$  is the appropriate combination electro-optic coefficients and angular factors for a fully poled crystal. The second experimental parameter is an effective trap density, written as  $NN^+/(N+N^+)$ .

In Fig. 1 we show typical gain data for each of the three materials studied. Through curve fitting techniques, this data yields values of effective electro-optic coefficient and effective trap density for each sample. The solid curves in each case represent a best fit to the data. In Table I we present our results for the sign of the dominant charge carrier, the effective trap density, the effective electro-optic coefficient, and the fractional poling times the normalized conductivity for seven crystals of  $\text{BaTiO}_3$ . Through non-photorefractive measurements [3] on the same crystals, we have shown  $N \ll N^+$ , so that  $NN^+/(N+N^+) \approx N$ , the concentration of level X. Other measurements of this parameter in  $\text{BaTiO}_3$  [2,4] give values similar to ours. We believe that the reduction in the values of  $F\bar{\sigma}$  from unity (as obtained in a perfectly poled crystal with a single dominant charge carrier) is primarily due to the comparable contribution of electrons and holes to the photoconductivity. The results of the same analysis for BNN and SBN will also be presented.

#### References

1. J. Feinberg, J. Opt. Soc. Am. **72**, 46 (1982).
2. J. Feinberg, D. Heiman, A.R. Tanguay, Jr. and R.W. Hellwarth, J. Appl. Phys. **52**, 1297 (1980).
3. M.B. Klein, S.P.I.E. Conference on Analog Optical Processing and Computing, Cambridge, MA, 25-26 October, 1984, Paper 519-22.
4. S. Ducharme and J. Feinberg, J. Appl. Phys. **56**, 839 (1984).

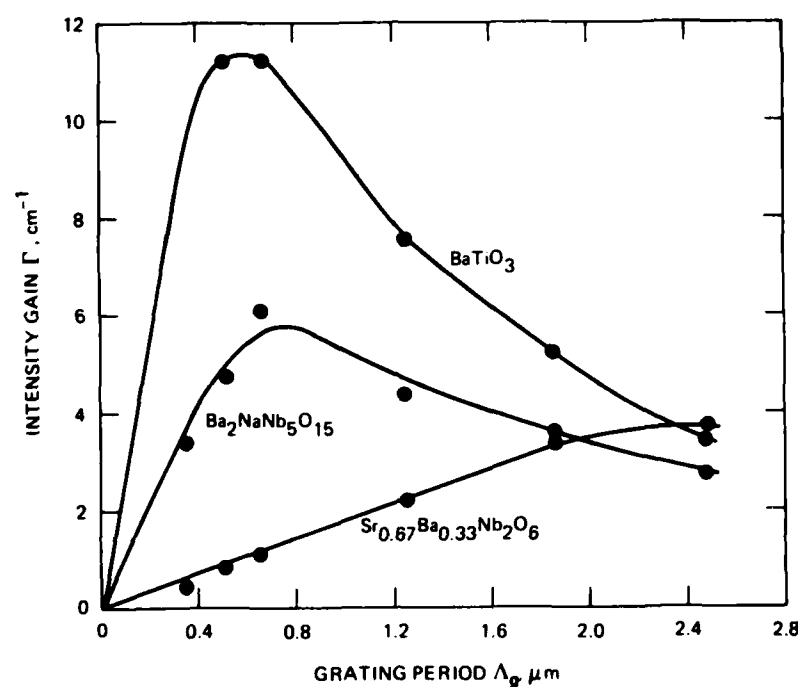


Figure 1. Intensity gain vs. grating period for  $\text{BaTiO}_3$ , BNN and  $\text{Sr}_{0.75}\text{Ba}_{0.25}\text{Nb}_2\text{O}_6$  at 442 nm.

CRYSTAL	SIGN OF DOMINANT PHOTOCARRIER	$\frac{NN^+}{N + N^+}$ $\text{cm}^{-3}$	EFFECTIVE E-O COEFFICIENT $r_{\text{eff}}$ (PM/VOLT)	$F\bar{\sigma} = r_{\text{eff}}/r_{13}$
G/L	+	$4.4 \times 10^{16}$	7.3	0.30
R1	+	8.1	9.5	0.40
R2	-	2.8	-7.9	-0.33
GB3	+	6.1	9.7	0.41
K2	+	8.7	12.0	0.50
SC	+	4.2	8.3	0.35
GB4	+	3.0	4.2	0.18

Table I. Sign of the dominant photocarrier, effective trap density, effective electro-optic coefficient and fractional poling times the relative conductivity for seven crystals of  $\text{BaTiO}_3$ .

# ANALYSIS OF SCATTERING PATTERNS AND DECAY DYNAMICS OF PHOTOREFRACTIVE GRATINGS IN $\text{LiNbO}_3$ CRYSTALS

Jacek K. Tyminski, Richard C. Powell, H.C. Chow,  
and Michael J. Kleiwer  
Department of Physics, Oklahoma State University  
Stillwater, OK 74078

One technique for studying the Photorefractive effect (PRE) in crystals is to establish and probe holographic gratings with crossed laser beams. Generally the gratings are assumed to have a sinusoidal shape and the measurement which is made is the scattering efficiency of the probe beam at the Bragg condition. We report here the development of a new technique for studying the PRE based on the analysis of small angle scattering patterns. This technique allows for the inclusion of multiple Fourier components in the geometric shape of the grating in interpreting the data. The results of applying this type of analysis to  $\text{LiNbO}_3$  crystals with several different types of defect properties show that the measured scattering patterns are extremely sensitive to the microscopic properties of the grating. In addition, the dynamics of charge relocation in the PRE were investigated by monitoring the decay curve of the scattered probe beam during erasure for a variety of samples and experimental conditions. The results were interpreted in terms of the recently proposed hopping model.<sup>1</sup>

The crossed laser beams used to write a holographic grating produce an electric field pattern in the crystal in the form of a sine wave. However, the final shape of the photorefractive pattern established by the laser-induced charge relocation will generally not have exactly the same shape as the laser pattern due to the geometric effects of the spatial distributions of the donor and trap defect sites and possible asymmetric charge relocation dynamics. This situation is enhanced when more than one type of defect contributes to either donor or trapping kinetics. Previous investigations of the PRE in solids have not addressed the effects of these deviations from pure sine wave gratings either theoretically or experimentally.<sup>2,3</sup> This information is important in developing an understanding of the properties of the chemical and structural defects which contribute to the PRE characteristics of a material.

The samples used for this investigation were single crystals of  $\text{LiNbO}_3$  containing different types of defects. One was a nominally pure crystal which we subjected to a series of thermal annealing treatments in either air or a vacuum for oxidation and reduction. The effects of these treatments on the concentration and valence states of lattice defects and the valence states of chemical impurities has been determined previously by electron paramagnetic resonance measurements.<sup>4</sup>

Another sample was treated with benzoic acid to introduce deep traps into the crystal.<sup>5</sup> Also a crystal doped with Cu (which enhances the PRE) and one doped with Mg (which decreases the PRE) were studied. These samples provide a wide variety of defect distributions which is necessary for enhancing our understanding of the effects these distributions have on the PRE characteristics.

The 442 nm emission from a 16 mW He-Cd laser was used to write and erase the photorefractive holograms. Holograms were established using several different crossing angles for the write beams in order to determine the effect of grating spacing on the PRE properties. The 632 nm emission from a 6 mW He-Ne laser was used to probe the grating without damaging the hologram. The scattered signal beam was detected by a RCA C31034 photomultiplier tube and recorded with the help of a EG&G/PAR lock-in amplifier to improve the signal-to-noise ratio. The charge relocation associated with the PRE reached steady state conditions in 2 to 5 minutes. The variation of the scattering efficiency of the probe beam as a function of scattering angle was measured by slightly rotating the sample holder base. The charge relocation dynamics were determined by monitoring the time dependence of the grating erasure. The erasure was accomplished by redirecting the He-Cd laser beam to provide uniform illumination of the crystal. The experiments were performed at several temperatures to determine the effects of thermal activation on the charge relocation dynamics.

For the simplest case of a single set of donor and acceptor traps, a sinusoidal grating, and one type of charge relocation dynamics, the grating erasure gives an exponential signal decay with the decay rate given by<sup>1</sup>

$$K = 2Rd^2Nq^2 / (e\epsilon_0 k_B T) + 2Rd^2 [4\pi \sin(\theta/2) / \lambda]^2 \quad (1)$$

where  $\theta$  is the write beam crossing angle,  $N$  is the average concentration of the photocarriers contributing to the photorefractive effect,  $q$  is their charge, and  $R$  is the rate of charge relocation over a distance  $d$ . After measuring  $K$  as a function of  $\sin^2(\theta/2)$ , the slope and intercept of the experimental data can be used to obtain the charge concentration and relocation rate parameters. The results of our measurements show the erasure decay patterns to be biexponential decays with the two decay rates varying differently for different defect distributions. This is attributed to the presence of two types of charge carriers contributing to the PRE. In addition, the temperature dependence results show the effective charge densities to be affected by filling and emptying shallow traps.

The angular scattering patterns were generally found to have several major scattering maxima which included the Bragg peak, peaks having positions and erase rates consistent with harmonics of the Bragg peak, and peaks whose properties could not be related to those of the Bragg peak. Small angle scattering patterns were measured around each of these major scattering

maxima. These patterns varied from intense, narrow central peaks with weak, damped side lobes, to weak central peaks with strong side lobes, to very broad central peaks no visible side lobe oscillations. The type of pattern varied with write beam crossing angle and with partial erasure conditions. The coupled wave theory of holographic gratings<sup>2</sup> was extended to include higher order harmonics and subharmonics in the scattering patterns. The results were used to develop a computer program for fitting the observed angular scattering patterns. This procedure provided information concerning the geometric shape and modulation depth of the gratings.

**ACKNOWLEDGMENTS:** This work was sponsored by the U.S. Army Research Office.

#### REFERENCES

1. J. Feinberg, D. Heiman, A.R. Tanguay, Jr., and R.W. Hellwarth, J. Appl. Phys. **51**, 1279 (1980).
2. H. Kogelnik, Bell Sys. Tech. J. **48**, 2909 (1969).
3. P. Bunter, Phys. Repts. **93**, 199 (1982).
4. K.L. Sweeney and L.E. Halliburton, Appl. Phys. Lett. **43**, 336 (1983).
5. J. Jackel, A.M. Glass, G.E. Petereson, C.E. Rice, D.A. Olson and J.J. Veselka, J. Appl. Phys. **55**, 269 (1984).

# Use of optical phase conjugation for understanding basic material properties

R.W. Hellwarth  
Departments of Electrical Engineering and Physics  
University of Southern California  
Los Angeles, CA 90089-0484  
(213)743-6390

When nearly counter-propagating monochromatic optical beams whose complex field amplitudes are  $G_i$  and  $H_i$  ( $i=x,y,z$ ) overlap an image-bearing beam of amplitude  $E_i$  in a transparent material, the nonlinear polarization density can generate a fourth beam whose complex amplitude  $F_i$  in some plane is related to  $E_i$  in the same (or a slightly displaced) plane by

$$\sum_j K_{ij} E_j^* + N_i \quad (1)$$

Here  $K_{ij}$  is a complex constant matrix and  $N_i$  is a non-conjugate or noise background assumed to be small. For ideal phase-conjugation,  $K_{ij} = K \delta_{ij}$ ,  $N_i = 0$  and

$$F_i = K E_i^* \quad (2)$$

in one plane, the conjugate "reflectivity" or "gain" being  $|K|^2$ . However, the more general case described in (1) is often referred to as phase-conjugation, as we will here. The particular geometries of the "four-wave mixing" of beams  $E$ ,  $F$ ,  $G$ , and  $H$  that lead to (1) produce a signal  $F_i$  whose dependence on the sixteen possible combinations of beam polarization, and on beam angles and frequencies, gives much information on the process mediating beam mixing.

Phase-conjugation by four-wave mixing requires the beam frequencies to obey

$$\omega_F = \omega_G + \omega_H - \omega_E \quad (3)$$

and the beam wavevectors (or subsets of them when complex images are propagating) to obey the "phase-matching" condition

$$|\vec{k}_G + \vec{k}_H - \vec{k}_E - \vec{k}_F| \leq L^{-1} \quad (4)$$

where  $L$  is the length of the region over which the  $F$  beam interacts with the others. A great advantage of phase-conjugation as a spectroscopic probe is the ease of satisfying



(4) for a wide range of input angles and frequencies. When all frequencies are equal (degenerate four-wave mixing) and G and H are perfectly counter-propagating, then any direction of input beam E results in a perfectly phase-matched output F.

In the simplest class of phase-conjugation experiments the two beams E and G interfere to create intensity variations (moving or stationary) which in turn cause a variation in the refractive index seen by beam H. This variation is often called an index "grating". The H beam scatters from this grating to generate the F beam. This may be called the (tensor) volume holographic process for phase-conjugation. The beams can be on simultaneously or in various time sequences. We will describe how this single-grating process has been used to obtain the most accurate measurements of impurity density, conduction band diffusion lengths, and trap excitation cross-sections in photorefractive bismuth silicate and barium titanate. Results for electron-hole pairs in semiconductors will also be described. This process gives often the simplest and most accurate method of measuring thermal conductivities of slightly absorbing transparent media. It is also the basis for another coherent Raman spectroscopic technique (Raman-induced phase conjugation) which has advantages and disadvantages relative to coherent anti-Stokes Raman spectroscopy and other well-known laser spectroscopic techniques.

In another class of phase-conjugation experiments, there are two gratings formed simultaneously, one by interference of beams E and G, the other by interference between beams E and H. The interference of the two beams formed by the scattering of H and G respectively from these gratings gives a precisely calibrated comparison of the relative phases, index tensor, and amplitude of the two gratings. We will describe how this process can be used to measure the diffusion of optically-excited ions in transparent media, as well as the alteration in optical polarizability of the excited states.

We will also describe other forms of phase-conjugation in which optical intensity gratings play no role. One depends on resonant two-photon absorption by beams G and H. Another depends on spatial variations in the state of polarization of the optical field. These have yielded accurate spectroscopic data where two-photon induced fluorescence is absent, and also evidence on the nature of atomic collisions in vapor.

MEASUREMENT OF DIELECTRIC PROPERTIES OF  $\text{KTa}_{1-x}\text{Nb}_x\text{O}_3$   
AT MILLIMETER WAVELENGTHS

D. Rytz and M.B. Klein  
Hughes Research Laboratories, Malibu, California 90265

B. Bobbs, M. Matloubian and H. Fetterman  
Dept. of Electrical Engineering  
UCLA  
Los Angeles, Ca 90024

Mixed crystals of  $\text{KTa}_{1-x}\text{Nb}_x\text{O}_3$  or KTN are well known ferroelectrics whose transition temperatures  $T_c$  can be adjusted between  $-273$  and  $430^\circ\text{C}$  by varying the Nb concentration  $x$ . In the present work, we report on dielectric measurements in the 60-95 GHz range for crystals with  $x = 0.20, 0.09, 0.025, 0$  and  $T_c = -103, -183, -238^\circ\text{C}$  respectively (for  $x=0$ , i.e. pure  $\text{KTaO}_3$ , there is no transition). The crystal growth of these samples is described by Rytz and Scheel (1982) and the phase transition properties are reviewed by Kugel et al. (1984).

The measurement technique utilizes samples with plane parallel faces mounted between the flanges of two standard rectangular metal waveguides. The sample thus acts as a Fabry-Perot etalon, yielding a fringe pattern when the phase factor  $2\pi nL/\lambda$  is varied ( $n$  is the microwave refractive index and  $L$  is the sample thickness). The use of free-standing samples eliminates the mechanical problems associated with mounting the sample inside the waveguide, and facilitates the interchange of samples. In particular, high values of dielectric constant and/or loss tangent can be accurately measured by using samples with sufficiently small thickness. In our experiments, we have varied the phase factor by two different means, and analyzed the resulting fringe pattern in transmission to obtain the dielectric constant and the loss tangent. First, by using a swept frequency source we varied  $\lambda$ , and thus obtained the dielectric properties as a function of frequency between 60 and 85 GHz. Second, by varying the temperature (and thus the refractive index) at a fixed frequency of 94 GHz, we obtained data on the temperature variation of the dielectric constant and the loss tangent between  $20^\circ\text{C}$  and  $200^\circ\text{C}$ .

The Fabry-Perot fringe pattern (in transmission) is described by :

$$I_{\text{trans}}/I_{\text{inc}} = (1-R)^2 \tau / ((1-R\tau)^2 + 4R\tau \sin^2(2\pi nL/\lambda)) \quad (1)$$

where  $R$  is the reflection coefficient,  $\tau = \exp(-\alpha L)$ , and  $\alpha$  is the absorption coefficient. The coefficient  $R$  is taken as the Fresnel reflection from an air-dielectric interface, modified by the change in phase velocity resulting from the presence of the metallic waveguide walls (Bridges et al. 1982).

For each sample, we began the experimental sequence by

analyzing the transmission fringe pattern at room temperature, using a swept frequency source. The refractive index (and thus the dielectric constant) was obtained from the spacing between fringe peaks, and the absorption coefficient was obtained from the fringe contrast, or the peak transmission. Finally, the loss tangent was obtained from the absorption coefficient and the refractive index using

$$\tan \delta = \lambda \alpha / 2\pi n \quad (2)$$

A typical measured fringe pattern is shown in Fig. 1. Note the excellent fringe visibility and the lack of dispersion over the measured frequency range. We find that the loss tangent values obtained from the fringe contrast agree very well with those obtained from the peak transmission, thus giving firm support to our Fabry-Perot analysis.

After a sample was measured as a function of frequency, the transmission variation with temperature was recorded by inserting the waveguides holding the sample into a cylindrical furnace. Typical transmission plots are displayed in Fig. 2, and the resulting values of loss tangent are plotted vs. temperature in Fig. 3. For all the Nb concentrations but one ( $x=0.025$ ), the data points have been obtained with more than one sample. The scattering observed for  $x=0.20$  and  $0.09$  can be explained by concentration inhomogeneities.

Our experimental findings may be related to the phonon properties of KTN. In a simple harmonic oscillator model :

$$\tan \delta = \gamma_s \omega / (\Omega_s^2 - \omega^2) \quad (3)$$

where  $\omega$  is the angular frequency corresponding to  $\lambda$ ,  $\Omega_s$  the soft mode frequency and  $\gamma_s$  the damping of the soft mode. In Table 1, we give relevant figures for  $\Omega_s$  and  $\gamma_s$  at room temperature and compare the loss tangent obtained from Eq. (3) to the value measured at 94 GHz. The agreement is reasonable for  $x=0.09$ ,  $0.025$  and  $0$ . For the highest concentration  $x=0.20$ , the soft mode is overdamped at room temperature (Kugel et al. 1984) and therefore  $\gamma_s / \Omega_s > (2)^{1/2}$ . From Eq. (3), one can estimate  $\gamma_s > 90 \text{ cm}^{-1}$ . The variation of soft mode properties with temperature and the comparison of our high frequency measurements with static measurements will also be discussed.

One of the authors (DR) acknowledges financial support from the Swiss National Science Foundation.

## REFERENCES

- Bridges, W.B., Klein, M.B., and Schweig, E., IEEE Trans. MTT-30 (1982) 468.
- Kugel, G., Vogt, H., Kress, W., and Rytz, D., Phys. Rev. B30 (1984) 985.
- Rytz, D., Fontana, M.D., Servoin, J.L., and Gervais, F., Phys. Rev. B28 (1983) 6041.
- Rytz, D., and Scheel, H.J., J. Cryst. Growth 59 (1982) 468.
- Vogt, H., and Uwe, H., Phys. Rev. B29 (1984) 1030.

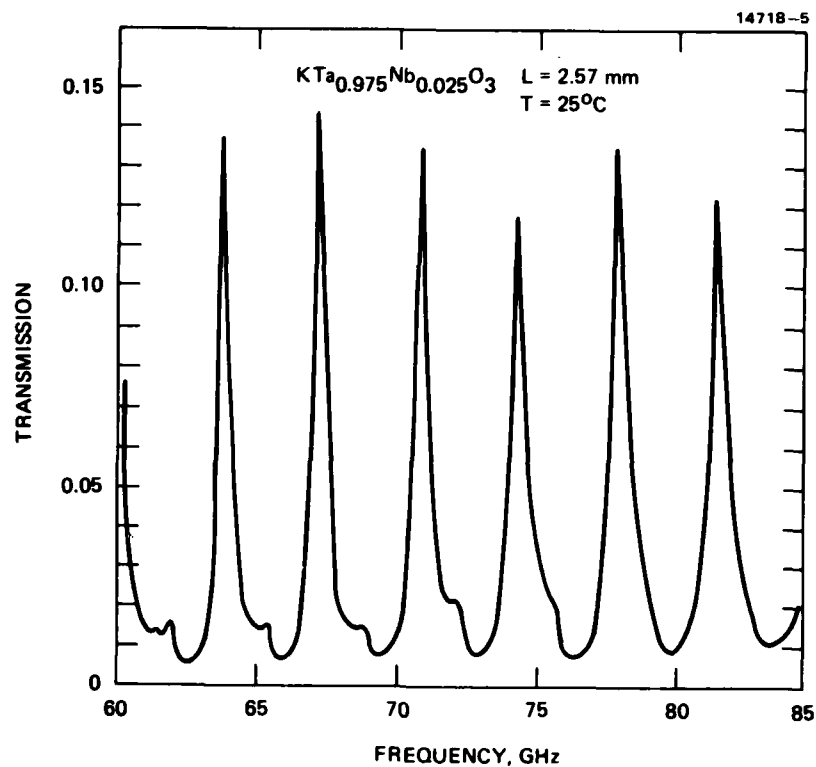


FIGURE 1 : Fabry-Perot transmission pattern recorded at room temperature as a function of frequency. The measured dielectric constant is 287 and the measured loss tangent is 0.005.

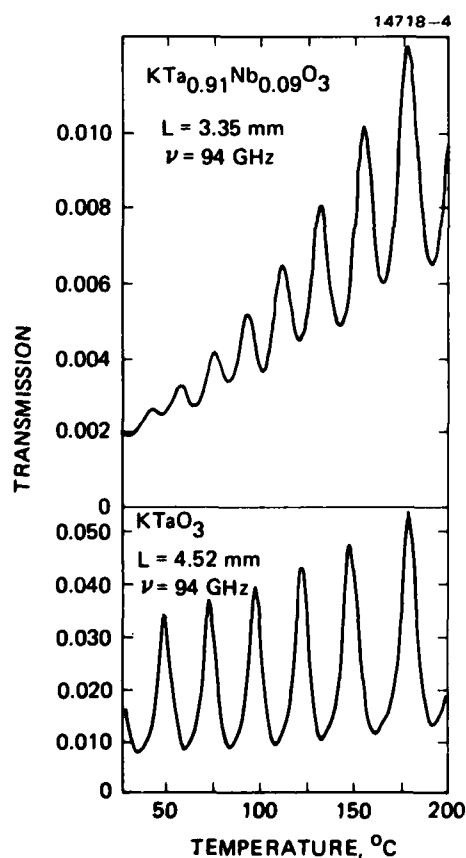


FIGURE 2 : Fabry-Perot transmission pattern at 94 GHz as a function of temperature.

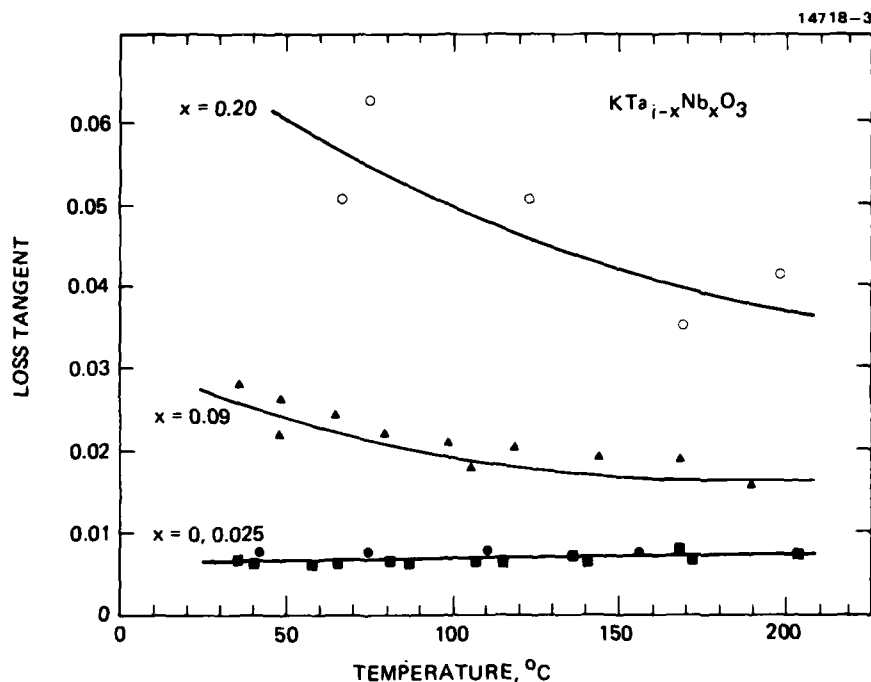


FIGURE 3 : Temperature dependence of the loss tangent in KTN.

14718-1

KTa <sub>1-x</sub> Nb <sub>x</sub> O <sub>3</sub>	REFERENCE	$\Omega_S$ (cm <sup>-1</sup> )	$\gamma_S$ (cm <sup>-1</sup> )	$\tan \delta = \frac{\gamma_S \omega}{\Omega_S^2 - \omega^2}$	$\tan \delta$ AT 94 GHz
x = 0	VOGT AND UWE (1984)	81	20	0.010	0.007
x = 0.018	RYTZ, et al. (1983)	86	32	0.014	
x = 0.02	KUGEL, et al. (1984)	83	24	0.010	
x = 0.025					0.007
x = 0.09	KUGEL, et al. (1984)	~55	~30	0.031	0.030
x = 0.20	KUGEL, et al. (1984)	OVER-DAMPED			0.07

TABLE 1 : Soft phonon frequency  $\Omega_S$  and damping  $\gamma_S$ , calculated loss tangent (see Eq. (3)) and measured loss tangent at room temperature.

# REFRACTIVE INDICES AND THERMO-OPTIC COEFFICIENTS OF NONLINEAR CRYSTALS ISOMORPHIC TO $\text{KH}_2\text{PO}_4$

K. W. Kirby, C. S. Hoefler and L. G. DeShazer  
Hughes Research Laboratories  
3011 Malibu Canyon Road  
Malibu, CA 90265

Crystals of the potassium dihydrogen phosphate (KDP) group are widely used in laser technology. These tetragonal isomorphs have the composition  $\text{MH}_2\text{XO}_4$ , where M may be K, Rb, Cs or  $\text{NH}_4$ ; X may be P or As; and H may be replaced by deuterium D, fully or partly. They encompass sixteen crystals potentially useful in state-of-the-art optical devices. These devices are second harmonic generators, sum and difference frequency mixers, electro-optical switches, and phase modulators. The refractive indices and their thermal behavior were measured for eleven of these nonlinear crystals (Table 1). These parameters are needed to establish the phase matching geometry and thermal behavior of a nonlinear crystal in the frequency upconversion operation in high-power laser systems.

The ordinary and extraordinary indices of refraction were measured at twelve wavelengths spanning the visible and near infrared region from 404 to 1064 nm. The measurements were obtained by the method of minimum deviation using a Zeiss spectrometer designed for this technique. The overall angular accuracy of the instrument is  $\pm 5$  arc seconds, which translates to a systematic uncertainty in the refractive index of  $\pm 3 \times 10^{-5}$ . A small hot stage stabilizes the prism temperature at about 6 C above room temperature to avoid both water adsorption on the crystal faces and thermal variation of the refractive indices during the measurement run. The prism temperature was measured by a thermocouple attached to the top of the prism, and showed  $\pm 0.5$  C stability over an eight hour day. Crystal prisms having 1  $\text{cm}^2$  faces and  $50^\circ$  apex angle were furnished by Interactive Radiation Inc. The measured indices of refraction were fitted to a two resonance Sellmeier formula

$$n^2 = A + CB/[\text{C}\lambda^2 - 1] + D\lambda^2/[\text{E}\lambda^2 - 1]$$

with deviations between measured and calculated values consistent with the estimated systematic error.

We observed that the indices of refraction of three KDP crystals varied with crystal supplier, with index differences as much as  $6 \times 10^{-4}$  in the visible spectrum (Table 2). The differences correlated to variations in the lattice parameters of these crystals determined by standard x-ray techniques (Table 3). The index of refraction decreased as the lattice parameters increased, which is expected from dispersion

theory. We speculate that the changes in lattice parameters arise from variations in the inclusion of crystalline defects during the crystal growth process. We are currently examining this conjecture with relation to the growth rate.

The thermo-optic coefficients  $\alpha_n = n^{-1}dn/dT$  and the thermal expansion coefficients  $\alpha_\ell$  perpendicular to the optic axis were measured using a double interferometric technique involving the simultaneous use of the Twyman-Green and Fizeau configurations. Crystal plates 8x11x12 mm were held in a gimbal mount in a vacuum oven which provided a linear heat ramp to the crystal from 25 to 40 C. The chamber was evacuated to  $10^{-6}$  torr to eliminate index contributions due to air. The chamber was placed in one arm of a Twyman-Green interferometer. Fringe changes from this interferometer are caused by path length changes in the arm containing the crystal. The Fizeau interferometer was formed by the front and rear faces of the sample which was polished to provide 2 or 3 fringes of wedge between the two surfaces. Phase shifts measured with this interferometer are caused by optical path length changes in the sample. The coefficients  $\alpha_n$  and  $\alpha_\ell$  are determined from the simultaneous solution of the two equations that describe the phase shifts for the two interferometers.

The quantities actually determined by the experiment are  $\Delta T_T$  and  $\Delta T_F$ , the temperature change needed to move one fringe in the Twyman-Green and Fizeau interferograms. Each fringe pattern is magnified and sampled by a pinhole placed in front of photomultiplier detectors. As the sample is heated the motion of each pattern across its pinhole is recorded on a chart recorder.  $\Delta T_T$  and  $\Delta T_F$  are then determined from the record and used to calculate  $\alpha_n$  and  $\alpha_\ell$  using the relations

$$\alpha_\ell = (\lambda/2L)(\Delta T_T^{-1} - \Delta T_F^{-1})$$

$$\alpha_n = (\lambda/2L)\{\Delta T_T^{-1} - [(n-1)/n]\Delta T_F^{-1}\}$$

where  $\lambda$  is the wavelength of light and  $L$  is the length of the sample. This measurement is made for light polarized parallel ( $\pi$ ) and perpendicular ( $\sigma$ ) to the optic axis for three wavelengths (441.6, 632.8 and 1152 nm). The signs of the temperature changes are chosen such that  $\alpha_\ell$  determined from the above equation does not depend on polarization or wavelength. The wavelength variation of the  $\alpha_n$  coefficients was compared to the theoretical formula [1], and the necessary constants were determined in order to be able to calculate the values of  $\alpha_n$  in the range from 440 to 1150 nm.

We acknowledge helpful discussions with David Eimerl, LLNL, and Stephen C. Rand, HRL, and the experimental assistance of James E. Brown, HRL, in performing the interferometer measurements. This research was partially supported by Lawrence Livermore National Laboratory.

# REFERENCE

1. Y. Tsay, B. Bednow and S.S. Mitra, Phys. Rev. B8, 2688 (1973).

Table 1. Listing of nonlinear crystals and refractive indices at wavelengths of Nd:YAG laser harmonics

Acronym	Formula	Pol	Wavelength (Angstroms)		
			3547	5321	10642
KDP	$\text{KH}_2\text{PO}_4$	Ord	1.531114	1.512125	1.493807
		Ext	1.485358	1.470396	1.459882
KD*P	$\text{KD}_2\text{PO}_4$	Ord	1.525282	1.507339	1.493102
		Ext	1.483432	1.468282	1.458221
ADP	$\text{NH}_4\text{H}_2\text{PO}_4$	Ord	1.547578	1.526734	1.505719
		Ext	1.498635	1.481351	1.467922
AD*P	$\text{NH}_4\text{D}_2\text{PO}_4$	Ord	1.540189	1.520750	1.504601
		Ext	1.512196	1.494977	1.481440
CDA	$\text{CsH}_2\text{AsO}_4$	Ord	1.602576	1.573174	1.551442
		Ext	1.578136	1.551465	1.535613
CD*A	$\text{CsD}_2\text{AsO}_4$	Ord	1.597533	1.569171	1.549921
		Ext	1.576096	1.549586	1.534122
ADA	$\text{NH}_4\text{H}_2\text{AsO}_4$	Ord	1.610849	1.580123	1.555052
		Ext	1.550872	1.525129	1.508105
AD*A	$\text{NH}_4\text{D}_2\text{AsO}_4$	Ord	1.603119	1.573608	1.552381
		Ext	1.546980	1.521465	1.505873
RDP	$\text{RbH}_2\text{PO}_4$	Ord	1.528293	1.509970	1.492026
		Ext	1.496667	1.480662	1.469535
RD*P	$\text{RbD}_2\text{PO}_4$	Ord	1.556300	1.537537	1.521639
		Ext	--	--	--
RDA	$\text{RbH}_2\text{AsO}_4$	Ord	1.590975	1.562495	1.540502
		Ext	1.549174	1.525049	1.510470



Table 2. Comparison of refractive indices of KDP crystals from two different suppliers

$\lambda$ (Å)	Pol	Inrad	Clev. Cry.	$\Delta n$ ( $\times 10^5$ )
4799.91 Cd	Ord	1.51570	1.51598	28
	Ext	1.47314	1.47325	11
5085.82 Cd	Ord	1.51365	1.51392	27
	Ext	1.47150	1.47183	33
5893. Na	Ord	1.50897	1.50955	58
	Ext	1.46808	1.46860	52
6438.47 Cd	Ord	1.50671	1.50702	31
	Ext	1.46644	1.46687	43

Table 3. Lattice parameters of the different KDP crystals

Crystal source	Lattice parameters (Angstroms)		a/c ratio
	a	c	
Inrad	7.460	6.965	1.071
Clev. Cry.	7.451	6.950	1.072

BISMUTH SILICON OXIDE: SAMPLE VARIABILITY  
STUDIED WITH THERMALLY STIMULATED  
CONDUCTIVITY AND THERMOLUMINESCENCE

Brian W. Holmes  
Department of Physics  
San Jose State University  
San Jose, California 95192

Jacques E. Ludman  
Charles L. Woods  
RADC/ESOP  
Hanscom AFB, MA 01730

## 1. Introduction

Bismuth silicon oxide (BSO) is widely used in optical data processing, reversible, real-time holography, and optical phase conjugation. The optical characteristics (such as wavefront reflectivity) vary significantly, even for identically prepared crystals.<sup>/1/</sup> The manufacture of uniform and improved BSO crystals may well depend on a better understanding of the fundamental processes responsible for its photosensitivity.

In BSO and other photorefractive materials, absorbed light causes electrons to diffuse through the crystal or to drift under an applied electric field. Electrons tend to be trapped in regions of weaker illumination, and the resulting uneven charge distribution causes variations in the refractive index, due to the electro-optic effect. However, the centers responsible for electron trapping in BSO have not been identified.<sup>/2/</sup>

We studied electron trapping in BSO using thermally stimulated conductivity (TSC) and thermoluminescence (TL). These techniques<sup>/3/</sup> entail irradiating samples at low temperatures (filling the electron traps), followed by warming. During warming, electrons are released from the traps, contributing to the conductivity when they are promoted to the conduction band, and contributing to luminescence when they lose energy via a luminescent center. In this study, we survey a number of different BSO crystals, in order to assess sample variability as revealed in TSC and TL.

## 2. Experimental details

Of the nine crystals studied, one was from Crystal Technology and the rest were from Itek. The Itek crystals were from different growth runs. The crystals were cut in 0.5 x 0.5 cm<sup>2</sup> and 1.0 x 1.0 cm<sup>2</sup> samples. Thicknesses varied from 0.08 to 0.17 cm. Often several small and large samples of the same crystal were available for comparison. Electrical contact was made using ultrasonic indium soldering; contacts were ohmic.<sup>/4/</sup>

Samples fitted on a copper mount inside an optically accessible dewar. The copper mount was in thermal contact with a liquid nitrogen reservoir and a heater. A copper-constantan thermocouple monitored the temperature. The BSO samples were electrically isolated from the copper mount by thin teflon tape; teflon fittings pressed the samples against the copper mount, ensuring good thermal contact.

Samples were irradiated at liquid nitrogen temperatures using unfiltered light from a mercury lamp. This produces light near 350nm, corresponding to the band gap of BSO./5/ All samples were exposed for ten minutes; longer exposure did not alter the TSC and TL spectra. The heating rate was 0.8 K/sec. Samples were biased at 10 volts during warming. TSC was measured using a Keithley 103B electrometer. TL was measured using a cooled RCA 7102 phototube; sensitive in the infrared. Data were collected on x-y recorders, giving TSC and TL as a function of thermocouple voltage.

### 3. Results

Figure 1 gives TSC and TL for one of the samples. All samples studied showed three major peaks. Peak 1 has a peak temperature ( $T_m$ ) near 160 K; peak 2 has  $T_m$  near 235 K; peak 3 has  $T_m$  near 298 K. Peak 2 is always double; peak 1 is double for some of the samples, making the measurement of  $T_m$  uncertain for this peak; and there is evidence for other minor peaks.

3a. Peak temperatures -  $T_m$  values obtained for TSC and TL show systematic variations. Neglecting  $T_m$  for peak 1 (since this peak is sometimes double), we note that TL peaks at lower temperatures than TSC for all samples. For peak 2, the average temperature shift is 1.8 K; for peak 3, the average temperature shift is 6.2 K. These temperature shifts are probably due to the quenching of the luminescence at higher temperatures /5/.

b. Peak heights - The peak heights are not directly comparable. For TSC, peak heights depend on heating rate, applied voltage, and sample thickness. For TL, peak heights depend on heating rate, sample size, phototube characteristics, and experimental geometry.

However, we note the following

consistent pattern: peak 3 is higher than peak 2 for TSC, and peak 3 is smaller than peak 2 for TL. This may also be attributed to the quenching of the luminescence at higher temperatures; however, this feature is not present in the TSC and TL spectra reported earlier by Lauer./4/

3c. Thermal activation energies - The thermal activation energies  $E_A$  can be calculated from TSC and TL curves using initial rise techniques./4,6/ Expressing these energies as multiples of  $kT_m$  for peaks 2 and 3, we obtain  $E_A = 26 kT_m$ , consistent with Lauer's earlier measurement./4/ There is no significant difference between TSC and TL. If this relation holds for peak 1, then the three major peaks represent electron traps with thermal activation energies of 0.36, 0.53, and 0.67 eV below the conduction band.

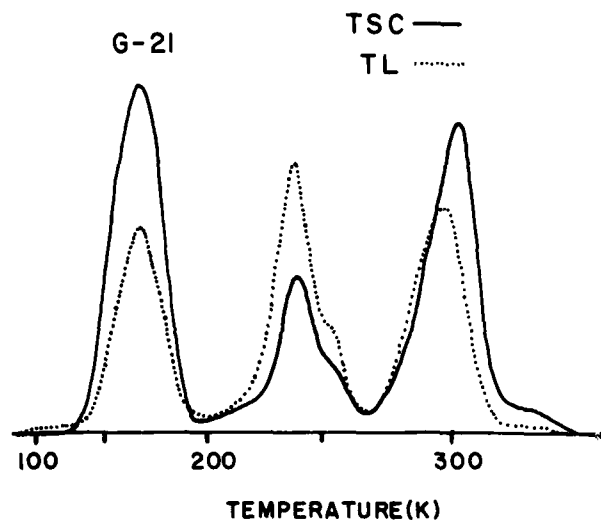


Fig. 1 - TSC and TL for a BSO sample. The vertical scales are arbitrary.

3d. Sample consistency - Different samples of the same crystals were studied. In this case, TL results differ for large and small samples, owing to geometrical factors. For TSC, however, the results for large and small are quite similar, since the large and small samples had the same thicknesses. Figure 2 gives TSC spectra for large and small samples of the same crystal. Typically, large and small crystals agree on peak positions, and the agreement on peak heights is within 10%.

3f. Sample variability - Different crystals, while yielding similar  $T_m$  values, show considerable variation in peak heights. Table 1 gives peak heights measured for TSC in eight different samples. It can be seen that peak 1 heights vary by a factor of 3.4; peak 2 by a factor of 2.2; and peak 3 by a factor of 2.5. It can also be seen that the height variations are not obviously correlated; that is, a crystal which has a high peak 1 will not necessarily have a high peak 2 or 3.

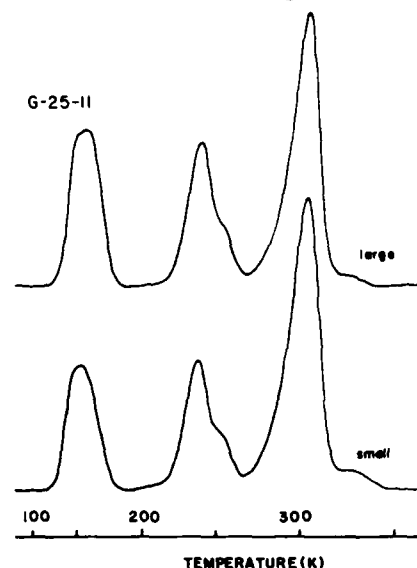


Fig. 2 - Comparison of TSC for large and small samples of a BSO crystal. (Not the same crystal in Fig. 1.)

Sample	Peak 1	Peak 2	Peak 3
G-9	3.00	0.73	1.56
G-21	2.14	1.11	2.03
G-25-11	1.33	1.41	3.00
G-27-6	0.89	1.20	1.90
Q-2-22	1.09	0.61	1.46
Q-17-18	2.27	0.63	1.22
J-2	1.68	0.77	1.48
C.Tech.	1.61	0.98	2.16

Table 1 - Peak heights (in nanoamperes) for TSC in different BSO crystals.

#### 4. Discussion

Since the TSC and TL spectra results from the release of electrons from traps in BSO, it would be valuable to learn what the density of these electron traps is. Our results do not give this information directly. One can integrate under a TSC curve to obtain the number of electrons passing through the electrometer; however, the limited drift range for electrons in BSO/5/ means such a calculation will greatly underestimate the trap density. More important, from the standpoint of applications of BSO, is the fact that the traps studied in TSC and TL are probably not responsible for the trapping which produces photorefractivity./2/ These latter traps are likely to be deeper than the shallow traps studied here, which release electrons at room temperatures or below. However, the variation in peak heights we measure surely reflects a variation in trap densities by a factor of three or more. A similar variation in the concentration of photorefractive traps centers has

been inferred from studies of wavefront reflectivity; and an even larger range of variability has been reported in bismuth germanium oxide./1/

In summary, although TSC and TL do not give information regarding the specific nature of electron trapping in BSO, these studies do provide additional evidence of the variability of BSO crystals. Supplementary studies, such as EPR, optical absorption, photoluminescence, and four-wave mixing will be needed to give more information on the fundamental character of the electron traps, and to show how the variations in TSC and TL relate to variations in the centers responsible for photorefractivity.

#### 5. Acknowledgments

We are pleased to acknowledge the assistance and advice of R. Aldrich of Itek, and C. Pitha of RADC/ESOP, Hanscom AFB, MA. This work was conducted while BWH was a fellow in the 1984 USAF-SCEEE Summer Faculty Research Program.

- /1/ Y. Ja, Opt. Quant Elec. 16, 355-8 (1984).
- /2/ M. Peltier & F. Micheron, J. App. Phys. 48(9), 3683-90 (1974).
- /3/ See P. Bräunlich (ed.), Thermally Stimulated Relaxation in Solids (Springer-Verlag, New York, 1979).
- /4/ R. Lauer, App. Phys. Lett. 42(5), 2147-9 (1971).
- /5/ S. Hou, R. Lauer, & R. Aldrich, J. App. Phys. 44(6), 2652-8 (1973).
- /6/ R. Chen, J. App. Phys. 40(2), 570-85 (1969).

## MATERIALS REQUIREMENTS FOR OPTICAL LOGIC AND BISTABLE DEVICES

N. Peyghambarian and H. M. Gibbs  
Optical Sciences Center  
University of Arizona  
Tucson, Arizona 85721

Semiconductors are attractive materials not only because of device applications but also because of their unique physical properties.<sup>1</sup> They exhibit large optical nonlinearities near the band edge due to the excitons, biexcitons, electron-hole plasma, carrier, and thermal effects. They provide adequate absorption ( $\alpha l \approx 1$ ) in a very short ( $l \approx 1 \mu\text{m}$ ) length. As a result, a large nonlinear phase shift, of the order of  $\pi/2$ , is obtained for logic operation, with  $\text{kW}/\text{cm}^2$  intensities in micrometer lengths.

When an optical nonlinear material is sandwiched between two partially reflecting mirrors, a nonlinear etalon is formed. Nonlinear etalons can perform various optical logic operations such as AND, OR, and NOR. The principle of such operations is the shifting of the Fabry-Perot transmission peak in response to input pulses. The nonlinear medium must be such that the absorption of one input pulse changes the refractive index at the probe wavelength enough to shift the transmission peak of the etalon by about one instrument width. For example, if the etalon is initially tuned to the probe wavelength, a NOR gate operation results if the control pulse can detune the etalon from the probe wavelength. The speed of the gate can be very rapid, allowing picosecond decision making at a gigahertz repetition rate without thermal problems. A GaAs-AlGaAs optical NOR gate has recently been demonstrated to respond in 1 ps with very low switching energy.<sup>2</sup>

Individual pixels can be defined by dividing the beam and focusing on different spots on the device or by plasma etching an array of devices. Already, an array of  $1\text{-}\mu\text{m}$ -diameter cylinders spaced  $5 \mu\text{m}$  apart has been constructed in a GaAs wafer of millimeter dimension by plasma etching, but switching of pixels in the array has not yet been tried.

Optical bistability, which is referred to as the existence of two stable output intensities for the same input intensity, has been realized in many semiconductors.<sup>1</sup> In bulk GaAs and GaAs-AlGaAs multiple-quantum-well superlattices, the nonlinearity arising from the presence of the free-exciton resonance has produced room-temperature optical bistability with a few milliwatts of power.<sup>3,4</sup> The biexciton resonance in CuCl is responsible for subnanosecond optical bistability at cryogenic temperatures.<sup>5,6</sup> The index change caused by thermal effects in ZnS and ZnSe interference filters has produced bistability at room temperature with a visible light source using  $\approx 50 \text{ kW}/\text{cm}^2$  intensity and  $\approx 10 \mu\text{s}$  switching times.<sup>7</sup> In this talk, we focus our attention on these materials because of their greater potential to be used as practical devices, however, a survey of other materials will be given.<sup>1</sup>

The larger the nonlinear refractive index,  $n_2$ , the lower the switching power. For excitonic nonlinearities, the switching intensity is the intensity required

to saturate the exciton resonance. The saturation intensity is smaller for a larger exciton radius or smaller exciton binding energy. Smaller electron-phonon interaction reduces the exciton broadening and causes observation of the exciton feature at higher temperatures close to the ambient. Therefore, a moderate exciton binding energy with a small electron-phonon interaction is ideal for low-power switching operation at room temperature. Nonlinear spectroscopy reveals characteristics of the materials and their suitability for device applications. We will show nonlinear transmission and luminescence spectra obtained in a pump-probe technique with femtosecond pulses<sup>1</sup> and discuss their use in characterizing some materials.

The switch-on time of a bistable device is limited by how fast the exciton feature saturates. Since the exciton screening occurs in a fraction of a picosecond<sup>2</sup> and the cavity build-up time is also  $\approx 1$  ps, a switch-on time of  $\approx 1$  ps is expected and has been demonstrated in GaAs-AlGaAs devices.<sup>3</sup> However, the switch-off time is limited by how fast the exciton feature recovers, which depends on the carrier lifetime and is usually on the order of a nanosecond in semiconductors at room temperature.

In conclusion, semiconductor optical bistable etalons lend themselves naturally to parallel logic operations, taking advantage of parallel propagation and imaging properties of light. They should be useful for such applications as multiplexing, encoding, and spatial modulation.

This research is supported by a National Science Foundation grant No. ECS 8020303 and by the Air Force Office of Scientific Research (United States Air Force) and the Army Research Office (United States Army) under contract No. F49620-80-C-022.

## REFERENCES

1. N. Peyghambarian and H. M. Gibbs, invited article for the special issue of JOSA B on Excitonic Nonlinear Optical Processes in Semiconductors (1985); also N. Peyghambarian and H. M. Gibbs, invited paper for the special issue of Opt. Eng. on Optical Computing (Jan. 1985).
2. A. Migus, A. Antonetti, D. Hulin, A. Mysyrowicz, H. M. Gibbs, N. Peyghambarian, and J. L. Jewell, Appl. Phys. Lett. Jan. 15, 1985.
3. H. M. Gibbs, S. S. Tarng, J. L. Jewell, D. A. Weinberger, K. Tai, A. C. Gossard, S. L. McCall, A. Passner, and W. Wiegmann, Appl. Phys. Lett. 41, 221 (1982).
4. S. S. Tarng, H. M. Gibbs, J. L. Jewell, N. Peyghambarian, A. C. Gossard, T. Venkatesan, and W. Wiegmann, Appl. Phys. Lett. 44, 360 (1984).
5. N. Peyghambarian, H. M. Gibbs, M. C. Rushford, and D. A. Weinberger, Phys. Rev. Lett. 51, 1692 (1983); also, R. Levy, J. Y. Bigot, B. Honerlage, F. Tomasini, and J. B. Grun, Solid State Commun. 48, 705 (1983).
6. S. W. Koch and H. Haug, Phys. Rev. Lett. 46, 450 (1981); also E. Hanamura, Solid State Commun. 38, 939 (1981); and D. Sarid, N. Peyghambarian, and H. M. Gibbs, Phys. Rev. B., Rapid Commun. 28, 1184 (1983).
7. G. Olbright, N. Peyghambarian, H. M. Gibbs, A. Macleod, and F. Van Milligan, Appl. Phys. Lett. 45, 1031 (1984); also, S. D. Smith, J. G. H. Mathew, M. R. Taghizadeh, A. Walker, B. S. Wherrett, and A. Hendry, Opt. Commun. 51, 357 (1984).
8. C. V. Shank, R. L. Fork, R. F. Leheny, and J. Shah, Phys. Rev. Lett. 42, 112 (1979); also N. Peyghambarian, H. M. Gibbs, J. L. Jewell, A. Antonetti, A. Migus, D. Hulin, and A. Mysyrowicz, Phys. Rev. Lett. 53, 2433 (1984).



## Mirrorless Optical Bistability in CdS

J.W. Haus  
Physics Dept.  
Rensselaer Polytechnic Institute  
Troy, NY 12181

C.C. Sung  
Physics Dept.  
University of Alabama in Huntsville  
HUNTSVILLE, AL 35899

C.M. Bowden  
Research Directorate  
US Army Missile Lab  
US Army Missile Command  
Redstone Arsenal, AL 35898-5248

and

J.M. Cook  
Physics Dept.  
Middle Tennessee State University  
Murfreesboro, TN 37132

### Summary

Recently, Dagenais and Sharfin<sup>1</sup> have reported whole-beam optically bistable behavior in uncoated platelets of CdS. This phenomenon was observed at milliwatt power levels when the incident laser frequency was tuned just below the resonance of the  $I_2$  bound-exciton. Using a qualitative model, they successfully correlated the temperature dependence of the absorption with the observed bistable behavior.

Our research extends their qualitative model by eliminating several unnecessary assumptions.<sup>2</sup> The first point to consider, is that the previous treatment assumed a constant temperature across the sample; this is valid only for small absorption and small sample lengths. The second point concerns the heat dissipation outside the active volume; because the large heat conductivity of CdS at low temperature, we assume in our model that the variation of temperature over a cross-sectional area normal to the incident laser field is small and can be neglected. Thus, the heat dissipation through the end faces determines the temperature variation across the material. The third point is the inclusion of the boundary conditions for both heat conduction and the electromagnetic field at each end of the sample.

Our results clearly demonstrate the importance of the temperature boundary conditions. Even small changes in the boundary thermal resistances can significantly alter the results. Also we find the existence of a second optically bistable hysteresis which has not been reported as yet. We show how such devices can be used as multiplexers and as composite optical logic elements<sup>3</sup> (AND, XOR and negation XOR gates) for use in optical computing and optical communications.

The role of the temperature-induced absorption in CdS which leads to bistable output intensities is explained as follows. The initial tuning of the incident laser frequency is below the bound-exciton resonance, as the input intensity increases, the temperature of the medium rises and the absorption resonance is shifted toward the laser frequency, thus the absorption increases. The result is a further increase in the temperature in the medium due to the extra absorbed energy and this mechanism provides positive feedback. In our treatment, the temperature is no longer homogeneous, therefore the exciton resonance frequency is also inhomogeneous and this yields a more complex behavior. At a certain input intensity, a runaway behavior is observed where the exciton resonance frequency overshoots the laser frequency at the input face; this causes a sudden increase in absorption inside the sample and a resulting low transmission. As the input field is further increased the resonance frequency distribution in the medium is shifted to lower values until the highest resonance frequency in the distribution lies below the laser frequency. Again, the transmission changes abruptly, but this time to a larger value. As the input intensity is reduced, the switching points can, depending on the initial detuning between the laser and exciton resonance frequency, occur at a lower value of the intensity.

1. M. Dagenais and W.F. Sharfin, Appl. Phys. Lett. 45, 210 (1984).
2. J.W. Haus, C.C. Sung, C.M. Bowden and J.M. Cook, submitted to J. Opt. Soc. Amer. B (1984).
3. J.W. Haus, C.M. Bowden and C.C. Sung, "Composite Logic Gate Element and Multiplexer for Optical Computing and Optical Communications" patent applied November, 1984.

## NONLINEAR OPTICAL EFFECTS IN LIQUID CRYSTALS

D. Armitage and S. M. Delwart  
Lockheed Missiles & Space Company, Inc.  
Research and Development Division  
3251 Hanover Street  
Palo Alto, California 94304

Liquid crystals are birefringent materials with fluidity comparable to water. Device potential arises from the influence of electric, magnetic or optic fields on the optic axis orientation. The response time is viscous limited. However, the more viscous smectic phases have storage properties.

The birefringence is directly related to the order parameter of the fluid and is therefore sensitive to temperature, particularly near a phase transition. At the nematic to isotropic phase transition, the refractive index ( $n$ ) discontinuity approximates 0.1. This is a weak first order transition with latent heat approximately  $1 \text{ J/cm}^3$ . These properties make the nematic phase an interesting solvent in a thermal dye cell. The thermal response is not viscous limited. It can be shown that when submillisecond response is demanded the thermal process is more efficient than the viscous limited orientation response.

The value according to mean-field theory is also plotted. The well known inadequacy of the theory close to the transition point is revealed. The extraordinary axis value are always greater than the ordinary axis values, in accordance with theory. These results are representative of nematics. Although there is some variation in behavior close to the transition, it is unlikely that substantially higher values will be found.

A further advantage of nematics follows from the use of pleochroic dyes. The dye is oriented by the nematic and results in a polarization-dependent absorption, which can be exploited by orthogonally polarized write and read beams such that minimum absorption of the read beam occurs.

Experiments were performed with 5CB doped with L-dye D81 (EM Chemicals). A  $10\text{-}\mu\text{m}$  period grating was written with a 10-ns doubled YAG pulse. The grating dynamics were probed with a HeNe readout beam. Figure 2 shows the evolution of the first-order diffraction intensity. Nematic theory suggests a functional form  $[1 - \exp(-t/\tau)]^2$ , which is verified experimentally. Figure 3 shows the temperature dependence of  $\tau$ . The higher  $dn/dT$  of the nematic is accompanied by a significant delay time approaching 100 ns.

In the isotropic phase the response time is essentially the thermalization time of the dye. An improved value for the order parameter response should result from subtracting the dye thermalization time. This is shown against reduced temperature in Fig. 4, and implies the form  $\tau = (T_{NI} - T)^{-0.7}$ . The same behavior is seen in the ultrasonic experiments (Ref. 5).

The order parameter response derived from this experiment is about a factor of 2 greater than that associated with ultrasonic attenuation (Ref. 4). However, the differing thermodynamic situation could account for the discrepancy.

The cell was generally operated at 1 percent diffraction efficiency, which should require according to Fig. 1 a write energy of  $1 \text{ mJ/cm}^2$  at  $T_{NI} - T = 1^\circ\text{C}$ . Fluctuation in the write pulse prevented verification of this prediction to better than a factor of 2.

The thermal grating is accompanied by an acoustic grating, but output oscillations from this source are beyond the response time of the system (Ref. 5). The response is much stronger when the grating is modulated across the nematic-isotropic transition, where the index discontinuity approaches 0.1. The grating decay time increases by a factor of  $10^3$  to approximately 10 ms. This is due to a quenching of the grating through the isotropic-nematic transition, which results in a disoriented nematic with a viscoelastic decay process.

The nematic phase is turbid, with a  $1/e$  optical attenuation length approaching  $100 \text{ }\mu\text{m}$ . This makes it difficult to achieve the high-efficiency thick-phase grating condition, which is possible in clear liquids. At infrared wavelength, nematics are favored since other solvents lose path length advantage.

#### REFERENCES

1. F. Rondelez, W. Urbach, and H. Hervet, Phys. Rev. Lett. 61, 1058 (1978)
2. I. C. Khoo and S. Shepard, J. App. Phys. 54, 5491 (1983)
3. D. Armitage and S. M. Delwart, Int. L. Cryst. Conf. (1984), Mol. Cryst. Liq. Cryst. (1985)
4. S. Candau and S. V. Letcher, Advances in Liquid Crystals V3, ed. G. H. Brown (Academic, 1978)
5. I. C. Khoo and R. Normandin, J. App. Phys. 55, 1416 (1984)

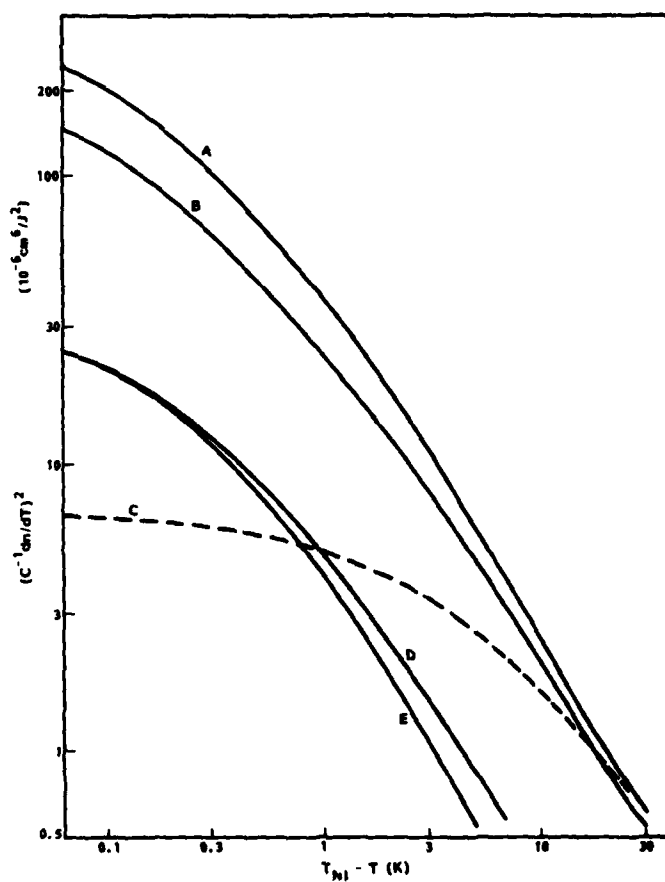


Fig. 1 (A) MBBA  $n_e$ , (B) 5CB  $n_e$ , (C) Mean-Field Prediction for "(B)", (D) MBBA  $n_o$ , (E) 5CB  $n_o$

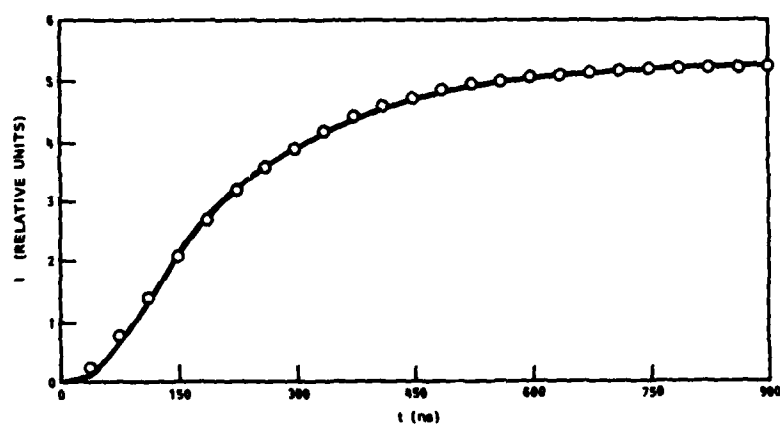


Fig. 2 Oscilloscope Recording of First-Order Diffraction Intensity from 5CB at  $T_{NI} - T = 2^\circ\text{C}$ . Circles are calculated from  $5.3 [1 - \exp(-t/\tau)]^2$  with  $\tau = 150$  ns

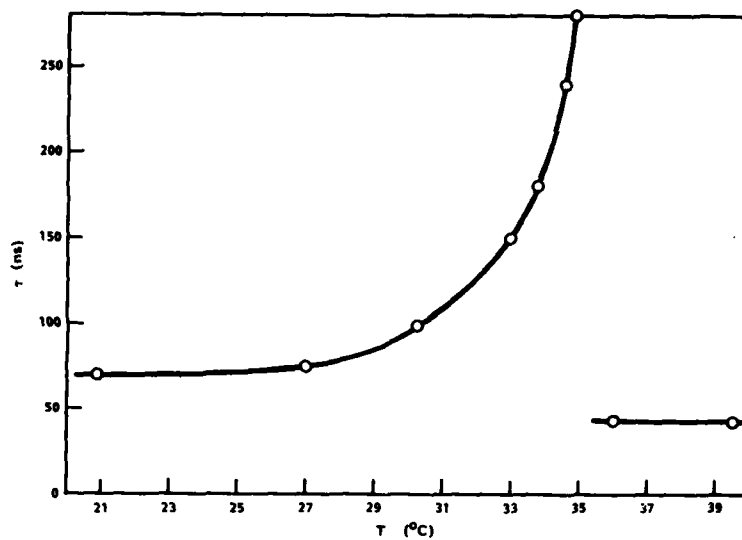


Fig. 3 Response Time as Function of Temperature T Through Nematic-Isotropic Transition  $T_{NI} = 35^{\circ}\text{C}$

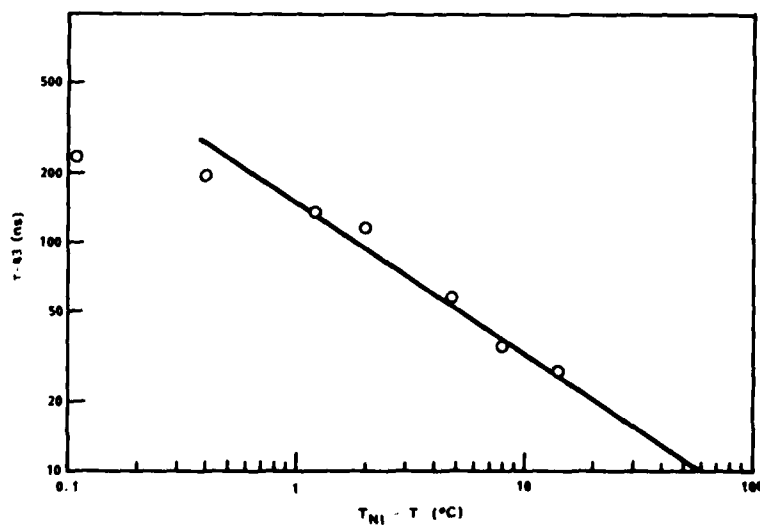


Fig. 4 Nematic Response Time Minus Isotropic Response Time (dye thermalization time) Against Reduced Temperature

A STUDY OF SECOND HARMONIC GENERATION COEFFICIENTS  
AND  
ULTRAVIOLET ABSORPTION EDGE OF BARIUM BORATE CRYSTAL

Ji-Kang Zhu, Bing Zhang, and Song-Hao Liu

Anhui Institute of Optics and Fine Mechanics, Academia Sinica  
P.O. Box 25, Hefei, Anhui, People's Republic of China

Barium borate ( $\beta$ -BaB<sub>2</sub>O<sub>4</sub>) is a new type of non-linear optical crystal which was made by China for the first time. Its transparent range 190-3000nm and SHG coefficient of macroscopic crystal  $\chi_{111}^{(2\omega)} = 4.6 \times 10^{-9}$  e.s.u. have been shown by experiments. CNDO/S calculated value of  $\chi_{111}^{(2\omega)}$  which was in good agreement with the experimental one was obtained by Chen et al.[1] However, their ultraviolet absorption edge 90nm was far from the experimental result and unbelievable (the best UV crystal LIF has its ultraviolet absorption edge 104nm).

In this paper we report one-electron energies and wave functions of barium borate by use of EHMO theory. Both the calculated values of SHG coefficient and ultraviolet absorption edge for barium borate crystal are in quantitative agreement with the experimental results. The comparison between EHMO, CNDO/S and experimental values is show in table 1.

Table 1. Comparison between calculated and experimental values of  
SHG coefficient  $\chi_{111}^{(2\omega)}$  and ultraviolet edge  $\lambda\mu$

	EHMO	CNDO/S	EXPT.
$\chi_{111}^{(2\omega)} (10^{-9} \text{ e.s.u.})$	5.39	3.78	4.60
$\lambda\mu \text{ (nm)}$	188	90	190

Since there has been dispute on the position of ultraviolet absorption edge we also calculate it by use of more accurate MS-X $\alpha$  method and the calculated result supports the EHMO calculation mentioned above. The factors which determine the positions of ultraviolet absorption edges and the values of SHG coefficients are discussed briefly.

- [1] Chuangtion Chen, et al., a report on International Conference on Quantum Electronics, 1984.

# SOLITON TRANSMISSION IN INHOMOGENEOUS MEDIA WITH W-TAILORED REFRACTIVE INDEX

Farag Z. El-Halafawy  
Fac. of Electronic Eng.  
Menouf, 23951, Egypt

El-Sayed A. El-Badawy, Mohammed A. El-Gammal,  
and Mostafa H. Aly  
Fac. of Eng.  
Alexandria University  
Alexandria, Egypt

In this paper, a method for soliton transmission in inhomogeneous media with W-tailored refractive index is modeled and parametrically analyzed. Two kinds of inhomogeneities are simultaneously considered: (a) Biquadratic variation of the refractive index (W-tailored radial profile), and (b) Boundary conditions of the cladded fiber.

The achievable bit rate of such important transmission was shown [1] to comfortably match with and could be made an order of magnitude better than that of the best linear transmission.

The refractive index,  $n$ , is W-tailored under the biquadratic nonlinear form,

$$n(\rho, \lambda, E) = n(\lambda) [1 - \alpha \rho^2 + m \alpha \rho^4] + n_2 |E|^2 \quad (1)$$

where  $\rho = r/R$  and  $R, \lambda, E$ , and  $n_2$  are respectively fiber radius, carrier wavelength, electric field, and nonlinear coefficient of the refractive index. The parameters  $\alpha$  and  $m$  control both the values of minimum and maximum refractive index and the radial position of the first  $\rho_{\min}$  where:

$$n_{\max} = n(\lambda) (1 - \alpha + \alpha m), \quad n_{\min} = n(\lambda) (1 - \alpha/4m), \quad \text{and } \rho_{\min}^2 = 1/2 m$$

The wave equation for the electric field,  $E$ , is given by [2]

$$\nabla^2 E - \frac{1}{c^2} \frac{\partial^2 \bar{D}_L}{\partial t^2} = \frac{2n_2 \eta_0}{c^2} \frac{\partial^2}{\partial t^2} (|E|^2 \bar{E}) \quad (2)$$

where the electric field in the fiber  $E(r, z, t)$  is given by

$$E(r, z, t) = \text{Re} [\phi(z, t) U(\rho) \exp [j(qz - \omega t)]] \quad (3)$$

where  $U(\rho)$  is the solution of the steady state wave equation for the linear inhomogeneous medium,



$$[\nabla_{\perp}^2 - p^2 + k_0^2 (1 - 2\alpha p^2 + 2\alpha m p^4)] U(p) = 0 \quad (4)$$

where  $P$  is the eigenvalue of the propagation constant and

$$k = (w + w_0) n(w + w_0), w = 2\pi c/\lambda, \text{ and } k_0 = \lim_{w \rightarrow 0} k$$

the solution of Eq.(4) is assumed under the series form,

$$U(p) = \exp(-p^2/2) \sum_{i=0}^{\infty} a_{2i} p^{2i} \quad (5)$$

with  $a_0 = 1$ . It is found that  $a_{2i}$ 's ( $i > 1$ ) are functions of  $a_2$ ,  $\alpha$ , and  $m$  where  $a_2 = 0.5 + (p^2 - k_0^2) R^2/4$

$P_0^2$  was calculated through the perturbation theory to the third order [3] under the form.

$$P_0^2 = k_0^2 - 2k_0 \sqrt{2\alpha}/R + 2m/R^2 + 4.5m^2/R^3 k_0 \sqrt{2\alpha+79} m^3/8\alpha R^2 k_0^2 \quad (7)$$

The function  $\Phi(z,t) = \Phi(\eta)$  possesses a light solitary solution of the form

$$\Phi(\eta) = \Phi_0 \operatorname{sech}(\eta) \quad (8)$$

$$\text{where } \Phi_0^2 = \frac{Vg^{-2} - Q(k_0' + k_0'')}{(n_2/n_0) k_0^2 \tau^2 \delta}$$

with a propagation velocity  $Vg$ ,

$$Vg = P_0 / Q k_0 k_0' \quad (10)$$

where  $\eta = (Vg\tau - z)/Vg\tau$ ,  $\tau$  is the pulse duration,  $k_0'$ ,  $k_0''$  are the derivatives of  $k$  w.r.t.  $w$ ,  $Q = 1 - \alpha + \frac{1}{2}\alpha m$ , and  $\delta$  is a function of  $R$ ,  $\alpha$ , and  $m$ ,

$$\delta = \int_0^\infty U(p) dp^2 \quad (11)$$

It is not the same as reported by [2].

The peak power  $P_0$  is given by [1]

$$P_0 = \frac{1}{2} Vg \epsilon_0 n_0^2 S \Phi_0^2$$

where  $\epsilon_0$  is the permittivity of free space and  $S$  is the cross sectional area of the fiber core.

A sample of the calculations based on this model will be discussed. The variations of the peak power  $P_0$  and the group velocity  $Vg$  with the parameter  $\alpha$  at different values of  $m$  and the assumed set of parameters are displayed respectively in Figs. 1 and 2. From these figures and the other obtained data, it is found that both  $P_0$  and  $Vg$  possess exponential correlations with the parameter  $\alpha$ . The results clarified in Fig. 3, where the radius  $R$  appears as a parameter, assert that, at any assumed set

of parameters , there is a threshold value  $\alpha_{th}$  to achieve a stable soliton transmission where  $\alpha_{th}$  increases as the fiber radius increases , Fig. 4.

In conclusion, to design a W-tailored refractive index fiber for stable soliton transmission of high bit rate , minimum power and high group velocity, the parameter  $\alpha$  must be of minimum value while the parameter  $m$  must be of maximum value .

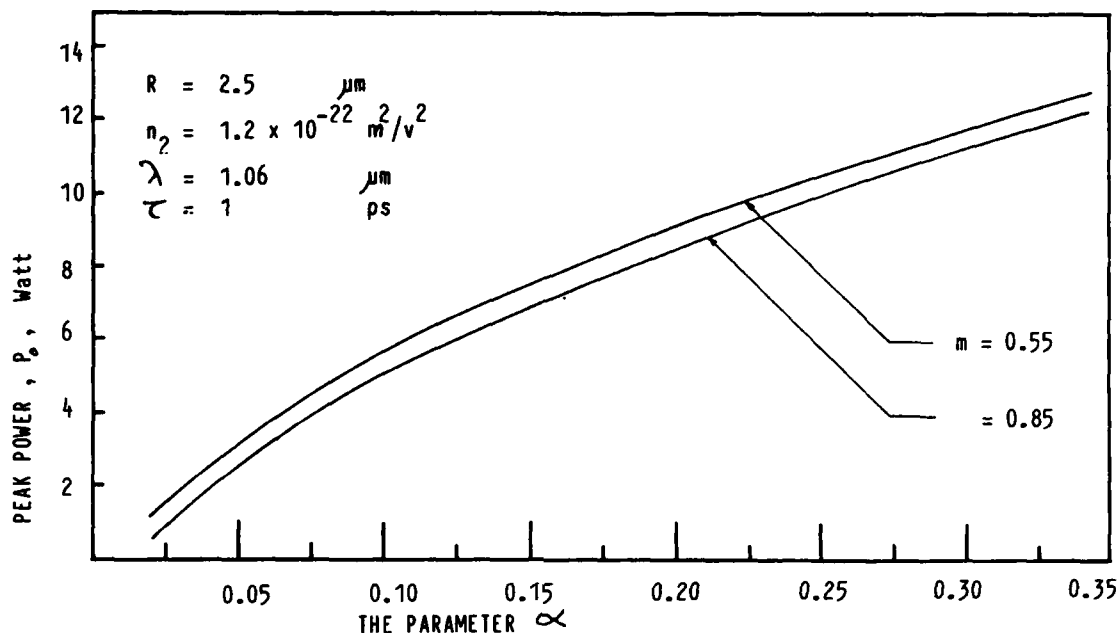


Fig.1. Variation of  $P_0$  with  $\alpha$  for different values of  $m$  and the assumed set of other parameters .

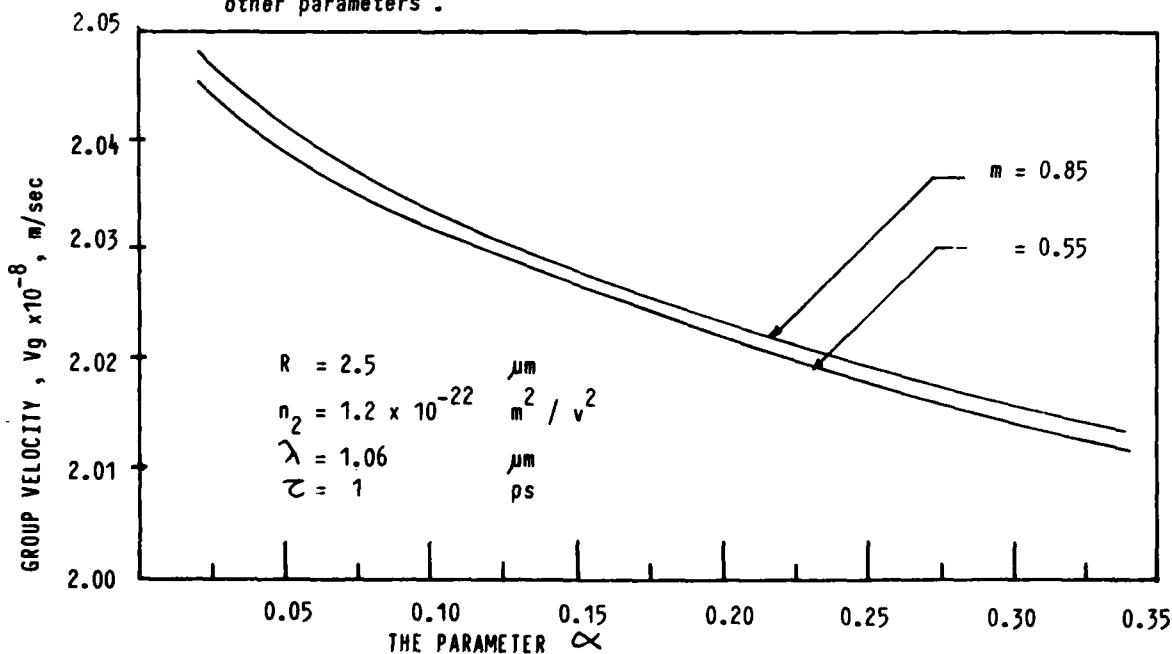


Fig.2. Variation of  $V_g$  with  $\alpha$  for different values of  $m$  and the assumed set of other parameters .

- [1] A. Hasegawa and Y. Kodama, Proc. IEEE, Vol. 69, No 9, PP. 1145 - 1150, Sep. 1981.
- [2] M. Jain and N. Tzoar, J. Appl. Phys., Vol. 49, No.9, PP. 4649 - 4654, Sep. 1978.
- [3] G. Jacobsen and J.J.R. Hansen, Appl. Opt., Vol.18, No. 16, PP. 2837 - 2842, 15 Aug. 1979.

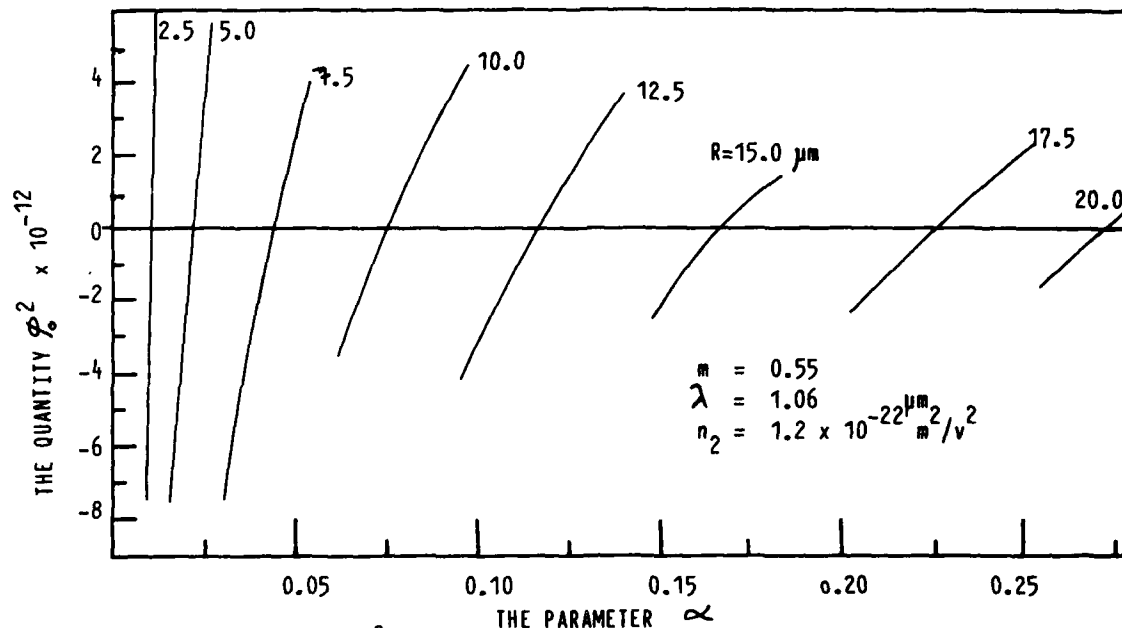


Fig.3. Variation of  $\phi_0^2$  with  $\alpha$  for different values of R and the assumed set of other parameters.

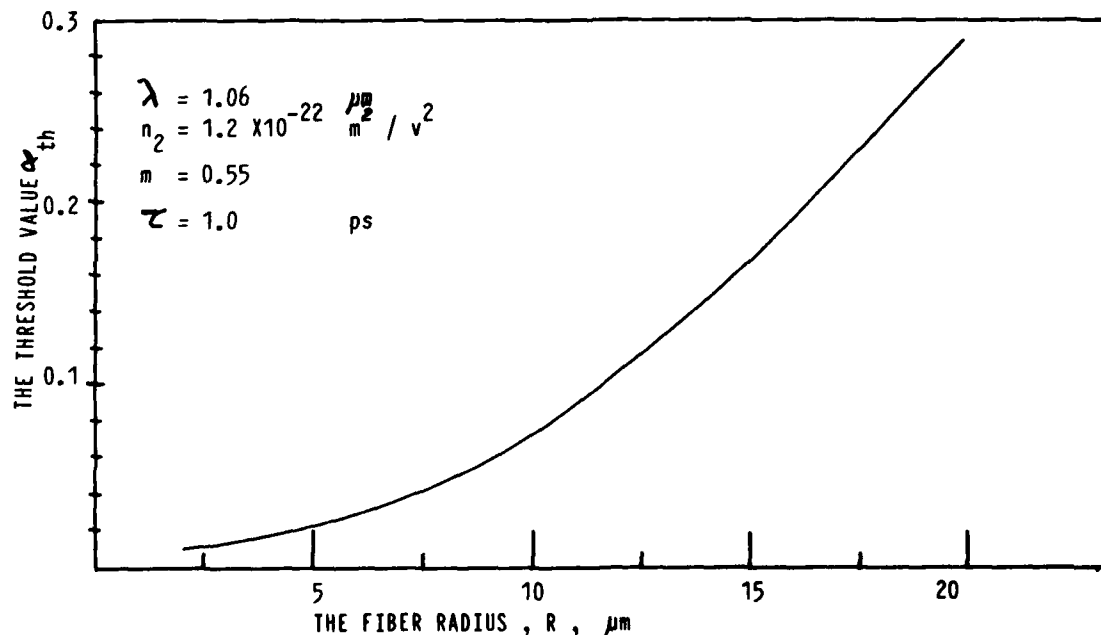


Fig.4. Variation of  $\alpha_{th}$  with R at the assumed set of parameters.

## COMPARISON OF VIBRATIONAL SPECTRA OF HEAVY METAL FLUORIDE GLASSES WITH THOSE OF "COMMON" GLASSES\*

Bernard Bendow  
The BDM Corporation  
Albuquerque, NM 87106

Heavy metal fluoride (HMF) glasses have generated considerable interest recently<sup>1</sup> as potential materials for laser hosts, mid-IR optical fibers, and multispectral windows, domes, lenses and filters. A wide variety of HMF glasses have been synthesized, but only a few, such as fluorozirconate (FZ)-type glasses (fluorozirconates and fluorohafnates), have been investigated in detail. FZ-type glasses are composed primarily of  $ZrF_4$  or  $HfF_4$ , in combination with  $BaF_2$  and a variety of tertiary components such as  $LaF_3$ ,  $ThF_4$  and alkali-fluorides. Rare earth (RE) glasses based on  $ThF_4$  and  $BaF_2$  in combination with  $ZnF_2$ ,  $YbF_3$ ,  $YF_3$ ,  $AlF_3$  and/or  $LuF_3$ , have also attracted considerable interest due to their extended IR transparency and improved chemical resistance relative to FZ glasses. Another family of glasses which has generally received less attention than FZ and rare-earth fluoride glasses, is the transition metal (TM) fluoride glasses. Typical compositions consist of combinations of the fluorides of bivalent metals such as Mn, Co, Ni, or Zn; trivalent metals such as Cr, Ga, or In; and other constituents such as  $PbF_2$  and  $AlF_3$ .

Vibrational spectroscopy, including polarized Raman scattering and fundamental IR reflectivity (Reststrahlen spectra), has been used to study the structure and bonding of many glasses<sup>2</sup>, and to determine the origins of observed IR edge characteristics. In this paper, we review the spectra obtained to date for heavy metal fluoride glasses, and compare them with the spectra of simple halide, oxide and chalcogenide glasses.

The fundamental vibrational spectra of single component halide glasses such as  $ZnCl_2$  and  $BeF_2$  are quite similar to those of simple oxide and chalcogenide glasses. An inspection of figures 1-3, which display spectra for  $SiO_2$ ,  $BeF_2$ , and  $ZnCl_2$ , reveals two peaks in the IR reflectivity and one dominant, highly polarized peak in the Raman spectrum. These peaks are smaller in number and generally much broader than those of their crystalline analogues--an expected consequence of the breakdown of selection rules in vitreous materials. The dominant Raman line may be attributed to symmetric stretch vibrations of the bridging atom (O, F, Cl) along the bisector of the angle that it makes with its two nearest neighbors. The high frequency infrared mode represents "rigid cage" or sublattice-type motion of (O, F, Cl) relative to (Si, Be, Zn).

The Raman spectra of a few simple glasses containing two different kinds of bonds have been measured, and they show two highly polarized Raman lines of roughly equal strength, one at low frequencies and the other at high frequencies; some examples are  $P_2O_5$  and the alkali oxide glasses, and again the motions are symmetric stretches. Thus, it appears that the number of dominant, highly-polarized Raman lines gives the number of well-defined but different bonds in the main framework of the glass structure.

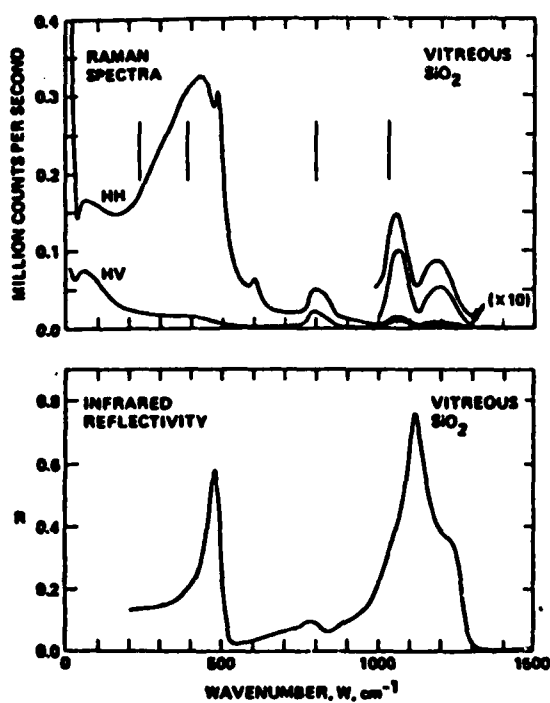


Figure 1. Raman and IR Spectra of  $\text{SiO}_2$

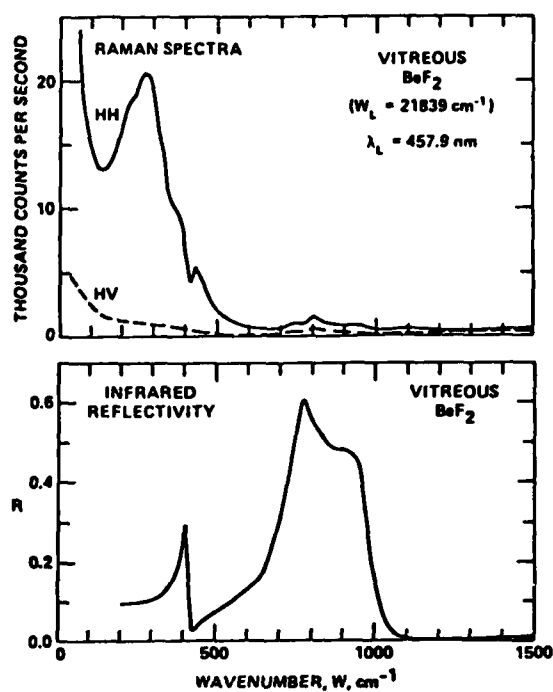


Figure 2. Raman and IR Spectra of  $\text{BeF}_2$

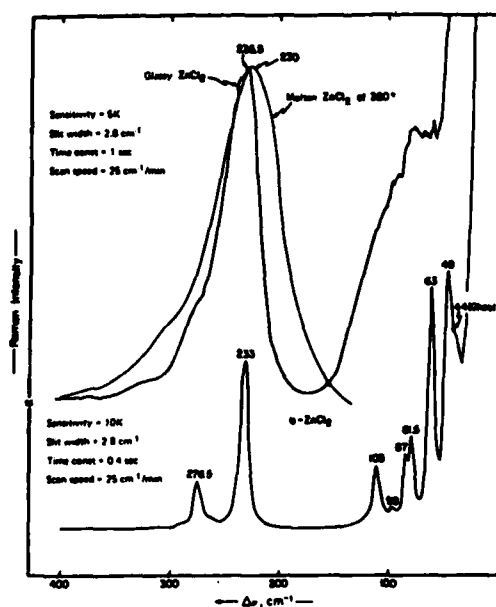
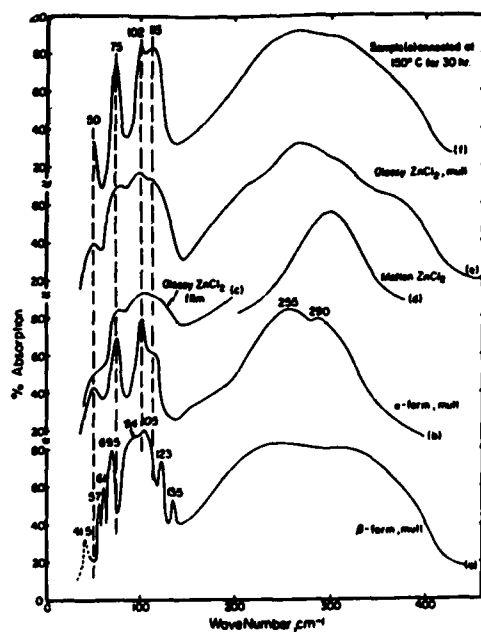


Figure 3. Raman and IR Spectra of  $\text{ZnCl}_2$

The fundamental vibrational spectra of fluorozirconate-type glasses indicated in figures 4-7 are similar to those of "simple" glasses because they display a small number of relatively broad peaks<sup>3</sup>. Notably, despite the multiple components in the glass, only a single highly polarized mode dominates the Raman spectrum, suggesting a single principal bond in the glass. A major difference between these and other glasses is that the Raman line falls in between the high frequency LO-TO mode pair of the glass--a behavior characteristic of crystalline fluorides such as  $\text{BaF}_2$ . This feature and the narrowness of the Raman line suggest that the ionic bonding of the individual constituents may be retained in the vitreous state as well. Other characteristics worthy of note include a relatively high peak reflectivity of the fluorozirconates, indicating large coupling to light, and an insensitivity of the spectra to the choice of tertiary components. A more detailed analysis of  $\text{HfF}_4$  compared to  $\text{ZrF}_4$ -based glass spectra (see figure 7) suggests, among other things, that the lower frequency peak in the reflectivity is due primarily to Hf/Zr-F bending modes, as opposed to Ba-F

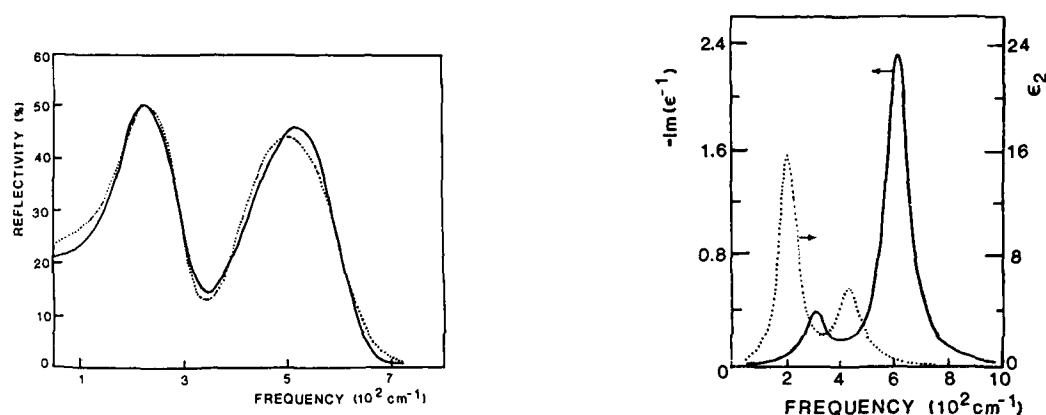


Figure 4. Reflectivity Spectrum and Derived  $\epsilon_2$  and  $-\text{Im}\epsilon^{-1}$  for the Fluorohafnate Glass HBT

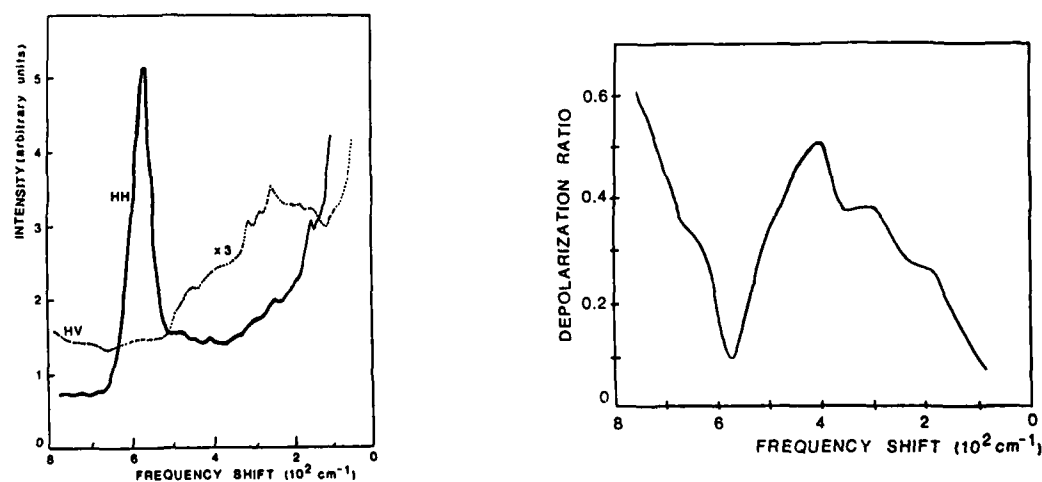


Figure 5. Raman Spectrum and Depolarization Ratio for HBT Glass

stretching modes; that the Hf-F force constant is larger than that of Zr-F; and that the oscillator strength of the high frequency vibration is higher for  $ZrF_4$ -based glasses. Comparisons with molten salt spectra imply coordination numbers for Zr with F in the range of 6 to 8, which is in agreement with the results of molecular dynamics calculations and X-ray data.

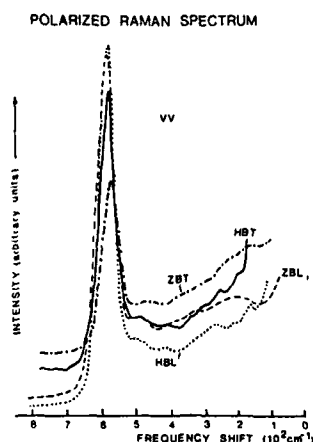


Figure 6. Raman Spectrum (VV-Polarized) of Typical Fluorozirconate and Fluorohafnate Glasses

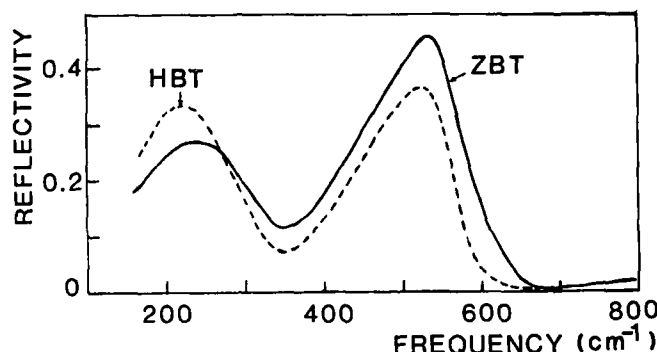


Figure 7. Reflectivity of Fluorohafnate Glass HBT Compared to its Fluorozirconate Analogue ZBT

The IR spectra of other glasses based on Th/Ba fluorides display<sup>4</sup> characteristics similar to fluorozeirconates, except that peak reflectivities are lower in the compositions investigated to date, indicating smaller coupling to light (figure 8). When significant amounts of aluminum are incorporated into the glass, a third distinct peak emerges in the IR reflectivity (figure 9). Available Raman spectra<sup>5</sup> for these glasses display much broader features than those of fluorozeirconates (figures 10 and 11). The results suggest that these glasses are more highly disordered than fluorozeirconates, and that a multiplicity of bonds exists in the glass. Preliminary data suggest that Ba/Th fluoride glasses having large amounts of  $AlF_3$  are the most disordered, as evidenced by a flattening of their depolarization ratios as a function of frequency (figure 12).

The Raman and IR spectra of transition metal fluoride glasses<sup>6</sup> are similar to those of fluorozeirconates, displaying essentially two-mode behavior in both Raman and IR (see figures 13 and 14).

A comparison of the vibrational spectra of the various HMF glasses suggests that FZ-type glasses, whose spectra are most similar to those of crystalline fluorides, are the most highly "ordered" of the HMF glasses, and presumably contain well-defined structural units consisting of Zr or Hf with F. The TM fluoride glasses are somewhat less ordered than FZ glasses, but also possess distinct structural units, in this instance based on TM ions with F. The RE fluoride glasses are the "most disordered" of the HMF glasses, containing the broadest distribution of local structural configurations. While glasses without  $AlF_3$  appear to possess some distinct structural units comprised of RE ions with F, glasses containing large amounts of  $AlF_3$  display spectra characteristic of highly disordered systems without clearly identifiable local structural units.

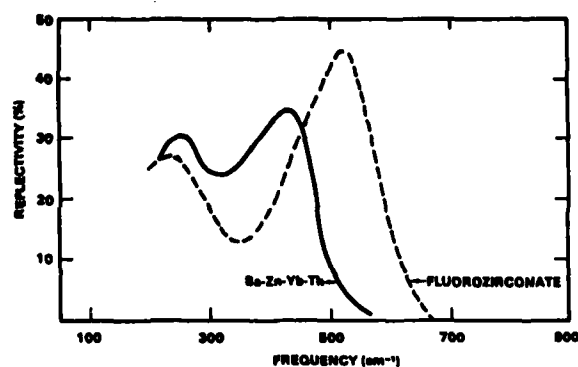


Figure 8. Comparison of Reflectivity of Fluorozirconate and Th/Ba Fluoride Glass

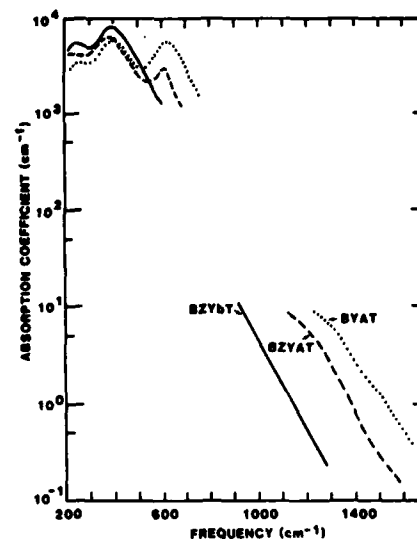


Figure 9. Fundamental and IR Edge Absorption of Several Th/Ba Fluoride Glasses Containing 0 (BZYbT), 14(BZYAT), and 29 (BYAT) mol %  $\text{AlF}_3$

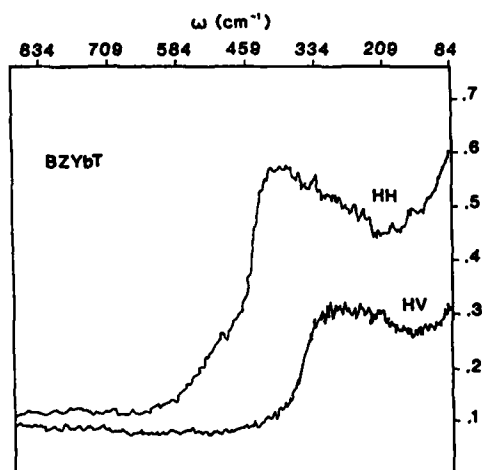


Figure 10. Raman Spectrum of BZYbT Glass

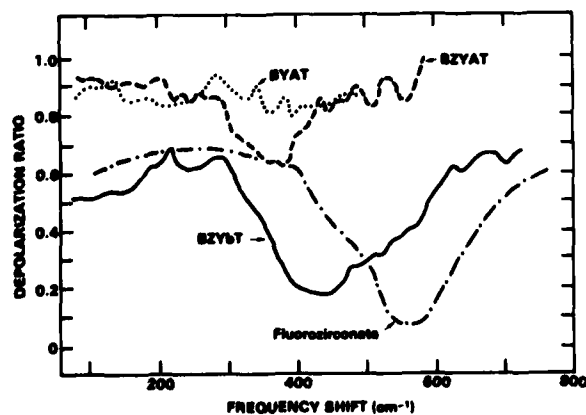


Figure 12. Depolarization Ratio for Several Ba/Th Fluoride Glasses

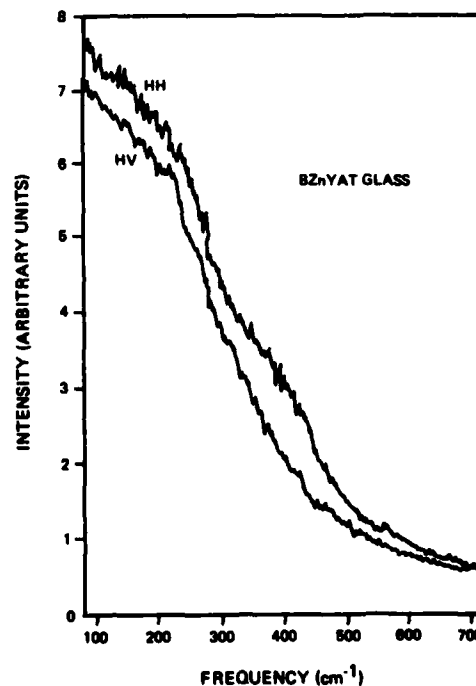


Figure 11. Raman Spectrum of BYAT Glass



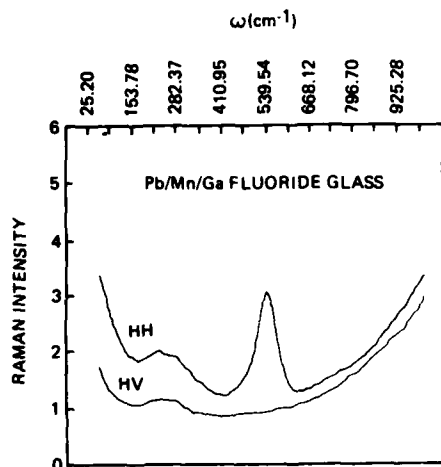
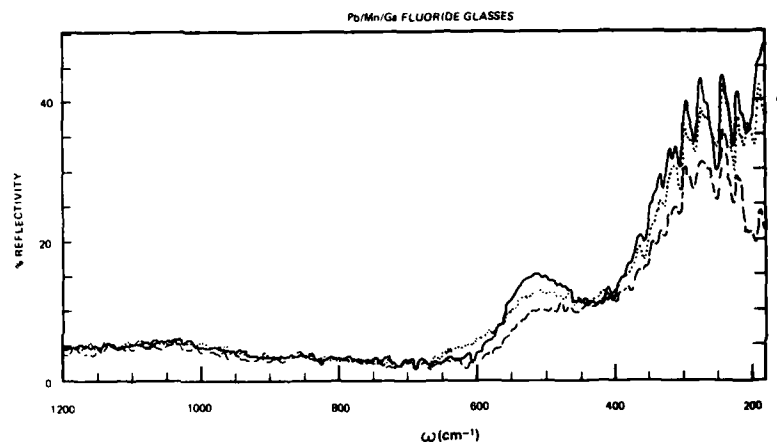


Figure 13. Raman Spectra of Typical Transition Metal Fluoride Glasses

Figure 14. Reflectivity Versus Frequency for Transition Metal Fluoride Glasses



The position and strength of the peaks in the fundamental spectra correlate well with observed IR edge behavior of fluoride glasses. For example, as indicated in figure 9, the deleterious effect of aluminum on the IR transmission edge is related directly to the appearance of high-frequency Al-F vibrational modes in the fundamental spectrum.

In summary, HMF glasses display a rich diversity of vibrational characteristics, some similar to highly ordered (nearly-crystalline) solids, others similar to "common" glasses, and still others similar to highly disordered solids such as amorphous semiconductors.

\*Supported by Air Force Weapons Laboratory under Contract No. F39601-81-0012.

1. D. Tran, G. Sigel and B. Bendow, J. Lightwave Tech. 5, 566 (1984).
2. J. Wong and C. Angel, "Glass Structure by Spectroscopy" (Marcel Dekker, NY, 1976).
3. B. Bendow, M. Drexhage et al, Sol. State Commun. 37, 485 (1981); and B. Bendow, P. Banerjee et al, J Amer. Ceram. Soc. 65, C8 (1982).
4. B. Bendow, P. Banerjee et al, J. Amer. Ceram. Soc. 66, C64 (1983).
5. B. Bendow, P. Banerjee et al, to be published.
6. B. Bendow, P. Banerjee et al, J. Amer. Ceram. Soc. 67, C136 (1984).

## THE VERDET CONSTANT OF OPTICAL GLASSES

Hans J. Hoffmann, Werner W. Jochs, Gudrun Przybilla  
Schott Glaswerke, Hattenbergstrasse 10, D-6500 Mainz,  
Fed. Rep. Germany

A magnetic field can rotate the plane of vibration of linearly polarized electromagnetic waves propagating in an optical medium. In a standard Faraday configuration, a linearly polarized wave propagates in a transparent medium parallel to the magnetic field vector. Then the angle of rotation  $\alpha$  is given by

$$(1) \quad \alpha = V \cdot l \cdot B$$

with the absolute value  $B$  of the magnetic flux density, the distance  $l$  of the wave travelled in the sample and the Verdet constant  $V$  being the factor of proportionality. The sign of the Verdet constant  $V$  - and that of the rotation angle - is positive (negative) if the rotation is clockwise (counter-clockwise) looking parallel to the vector  $B$  of the magnetic flux density irrespective of the propagation vector of the wave being parallel or antiparallel to  $B$ .

A relation for the Verdet constant as a function of wavelength was first derived by Becquerel [1]. He obtained

$$(2) \quad V = - \frac{e}{2mc^2} \lambda \frac{dn}{d\lambda}$$

with the charge  $e$  and the mass  $m$  of the electron, the velocity  $c$  of light in vacuum, the wavelength  $\lambda$  of the electromagnetic wave and the dispersion  $dn/d\lambda$  of the refractive index. Equation (2) has been derived on the premise of classical physics that the rotation frequency of electrons changes by the Larmor frequency  $\omega_L = eH/2mc$  in a magnetic field  $H$ . In order to obtain a rather reasonable agreement between experimental results and formula (2), however, one has to introduce into (2) the correction factor  $\gamma$  ("magneto optic anomaly").

Unfortunately Becquerel's equation (2) - even with the factor  $\gamma$  - cannot generally be justified on the basis of quantum mechanics. L. Rosenfeld [2] calculated a quantum mechanical expression of the Faraday rotation angle for the monoatomic case. His formula can be reduced to (2) under rather special conditions, only. A thorough discussion of the limitations is given by Van Vleck [3]. Special limiting cases of Rosenfeld's expression have been recently discussed with respect to glasses [4-6]. Experimental results, however, could not be evaluated quantitatively, since there are too many unknown parameters.

In order to avoid these difficulties, we developed recently a simple new dispersion formula [7]. We started from the Sellmeier-

type equation for the refractive index  $n$

$$(3) \quad n^2 - 1 = A \frac{N}{v} f \frac{\lambda^2 \lambda_0^2}{\lambda^2 - \lambda_0^2}$$

with just one term representing electronic oscillators with suitably averaged parameters: the mean density  $N/v$  of dispersion electrons, the mean oscillator strength  $f$ , the mean resonance wavelength  $\lambda_0$  and the constant  $A$ .

From (3) one can derive the approximate relation

$$(4) \quad V(\lambda) = \frac{\pi}{\lambda} \frac{(n^2 - 1)}{2n} \left( a + \frac{b}{\lambda^2 - \lambda_0^2} \right)$$

with the fitting parameters  $a$  and  $b$  for the Verdet constant as a function of wavelength.

To test this equation, we determined experimentally the Verdet constant  $V(\lambda)$  of different glasses in the visible spectral region by measuring the rotation angle  $\alpha$  induced by a magnetic field. For that purpose, linearly polarized monochromatic light (interference filters with FWHM of about 10nm) propagated along the axis of cylindrical glass samples (length: 100mm). The axis of the samples was oriented parallel to the magnetic flux density vector in the homogeneous field within a solenoid. The maximum flux density was about  $3 \cdot 10^{-2} \text{ T}$ . The temperature of the samples was  $295 \pm 2 \text{ K}$ .

The rotation angle  $\alpha$  of the plane of polarization could be measured with an accuracy of  $5'$  making use of a half-shade plate. This corresponds to an absolute error of about  $0.5 \text{ rad/T}\cdot\text{m}$ . In addition, there is a relative uncertainty of 3 to 4% for the experimental data of  $V$ , mainly due to the error of the magnetic flux density.

Typical results for an arbitrary choice of different glasses are shown in Fig. 1a and b by the data points.

The data for different glasses at about 440nm vary between 0 and 70  $\text{rad/T}\cdot\text{m}$ . The values of  $V(\lambda)$  decrease monotonically with increasing wavelength  $\lambda$  in nearly all cases. For SF-glasses the Verdet constant increases monotonically with the PbO content. The largest values of  $V$  were measured for heavy flint glass SF 59. This glass has an extremely large content of PbO, namely about 80 weight %. Because of its large Verdet constant, this glass type is an excellent candidate as Faraday rotator material.

On the other hand, the Verdet constants of the glasses SF 64 and SFL 56 are nearly zero. The plane of polarization of an electromagnetic wave is nearly unaffected by a magnetic field. To our knowledge the absolute values for SFL 56 are the smallest data of  $V$  reported for any glass in the literature until now.

Exoept for glass SFL 56 and for glass-ceramics ZERODUR we fitted the data by equation (4). The mean resonance wavelengths  $\lambda_0$  of

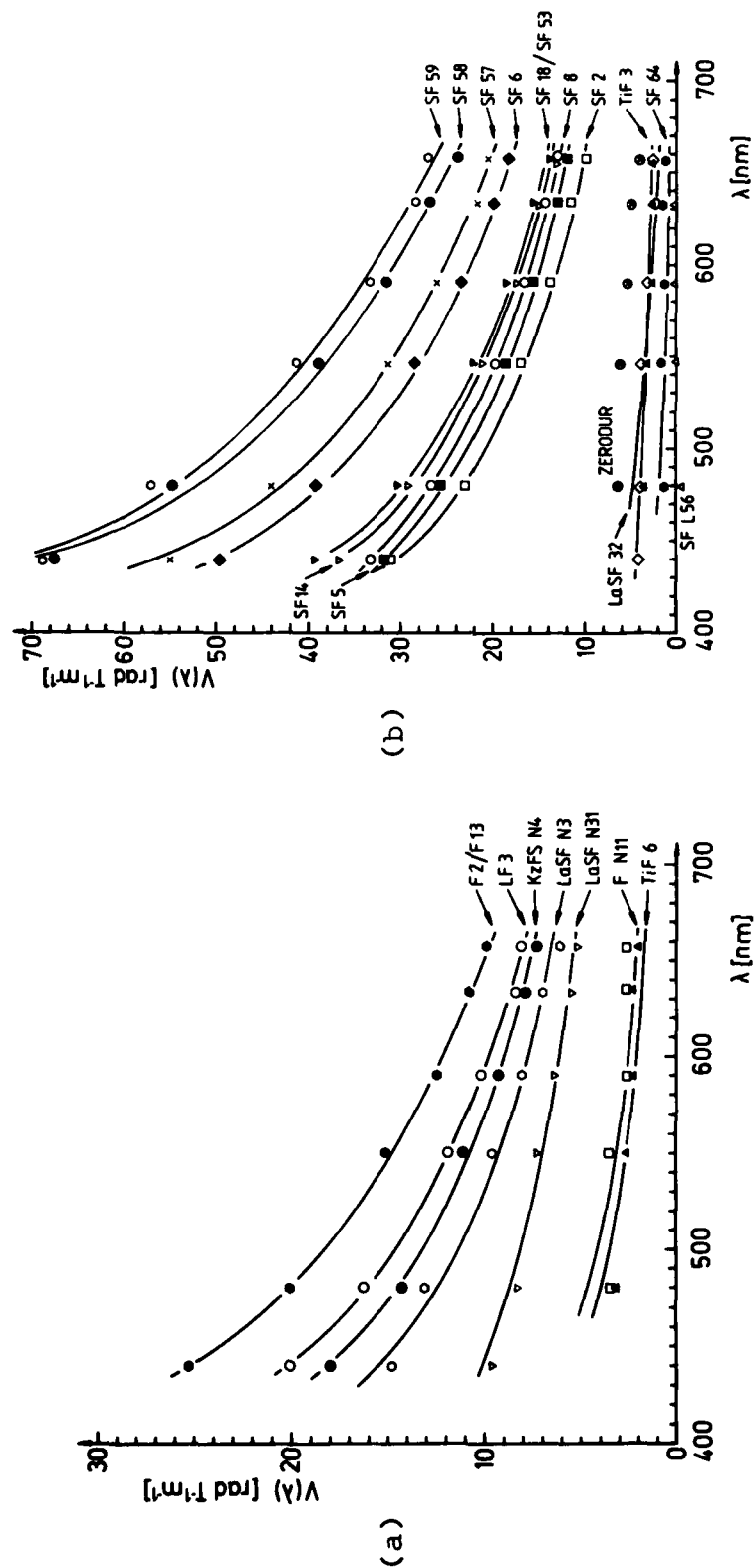


Fig. 1a and b: The Verdet constant  $V$  of different glasses and of ZERO DUR as a function of wavelength  $\lambda$  in the visible spectral region. The experimental results are shown by the data points and the solid curves represent the results of fitting calculations according to equation (4).

the different glasses were determined from a fit of the known dispersion curves  $n(\lambda)$  by equation (3) in the visible spectral region. Thus, we had to determine for a fit of  $V(\lambda)$  by (4) only the parameters  $a$  and  $b$ . This was achieved by a linear regression of  $V(\lambda)2n/(n^2-1)$  as a function of  $1/(\lambda^2-\lambda_0^2)$ . The full curves in Fig. 1a and b show the results of this fitting procedure. In fact, we obtained a good fit within the experimental accuracy of the Verdet constant for all glasses investigated by us [7].

For comparison with (4) we fitted our data also by Becquerel's formula (2) with the magneto-optic anomaly factor  $\gamma$  as fitting parameter. A fit with suitable factor  $\gamma$  is possible within reasonable deviation of the fitting curve from the experimental data points. In most cases, however, the experimental data can be fitted better by our equation (4) than by (2). This is not surprising since there are two fitting parameters in (4) whereas there is only one in (2).

In order to understand why a fit of the experimental data by (2) can be successful irrespective of its theoretical shortcomings, we estimate the dominant dependence of  $V$  upon  $\lambda$  according to (2) and (4). Calculating  $dn/d\lambda$  from (3) and inserting into (2) yields  $V \sim 1/\lambda^2$ , if one neglects  $\lambda_0^2$  as compared to  $\lambda^2$ . On the other hand, according to (4)  $V(\lambda)$  is given by a superposition of two terms proportional to  $1/\lambda$  and  $1/\lambda^3$ , respectively, neglecting  $\lambda_0^2$  as compared to  $\lambda^2$  as well. Since both terms have the same sign, they can obviously be approximated by only one term proportional to  $1/\lambda^2$  in a relatively small interval of wavelength. Thus, in order to discriminate between the validity of (2) or (4) from the quality of fitting alone, one needs experimental data of the Verdet constant in a larger interval of  $\lambda$ .

#### References

- [1] H. Becquerel Compt. Rend. 125, 679 (1897)
- [2] L. Rosenfeld Zeits. f. Physik 57, 835 (1930)
- [3] J. H. Van Vleck The Theory of Electric and Magnetic Susceptibilities, Oxford University Press (1932)
- [4] N. F. Borrelli J. Chem. Phys. 41, 3293 (1964)
- [5] L. D. Pye, S. C. Cherukuri, J. Mansfield and T. Loretz J. Non-Crystalline Solids 56, 99 (1983)
- [6] M. J. Weber Faraday Rotator Materials Report M-103 Lawrence Livermore National Laboratory, Ca., (1982)
- [7] Hans J. Hoffmann, Werner W. Jochs, Gudrun Przybilla to be published

## TEMPERATURE DEPENDENCE OF MAGNETOOPTIC EFFECTS IN MID-INFRARED FIBERS

Heihachi Sato, Yuji Azumai and Mitsunori Saito\*

Department of Electrical Engineering, National Defense Academy,  
Yokosuka 239, Japan.

\*Research and Development Department, Horiba Ltd., Kyoto 601,  
Japan.

Recently, mid-infrared fiber is getting important for its various applicational feasibilities such as power transmission, sensing, welding, machinery and medicine. Among many candidates KRS-5 and As-S fibers are very promising because of not only being flexible but also their low loss characteristics at the mid-infrared wavelengths covering that of high power CO and CO<sub>2</sub> lasers. So far, many researchers have reported about the propagation property and low-loss mechanism, involving fabrication processes[1]-[3]. The authors have also studied mainly on the magneto-optic effects of KRS-5 fiber and crystal at room temperature[4],[5]. In the present paper low temperature properties of KRS-5 and As-S fibers will be emphasizingly described about their magneto-optic effects such as the Faraday- and Voigt effects at CO<sub>2</sub> 10.6  $\mu\text{m}$  and He-Ne 3.39  $\mu\text{m}$  laser lines.

Experimental schematic diagram is typically illustrated in Fig.1 for measuring temperature dependence of IR fibers on the Faraday effect. A CO<sub>2</sub> laser or a He-Ne 3.39  $\mu\text{m}$  laser was used as an optical source, because these fibers have almost minimum loss points which just correspond to the operation wavelengths of the above lasers. The linearly polarized beam was focused onto the fiber through a ZnSe or CaF<sub>2</sub> lens. The fiber placed inside a hollow solenoid magnet variable up to 2 kilogauss was cooled down up to about -110  $^{\circ}\text{C}$  through the brass heat-sink by liquid nitrogen. The temperature was also measured by a thermocouple(not shown in the figure) at the center portion of the magnet. The transmitted beam was detected through a ZnSe polarizer.

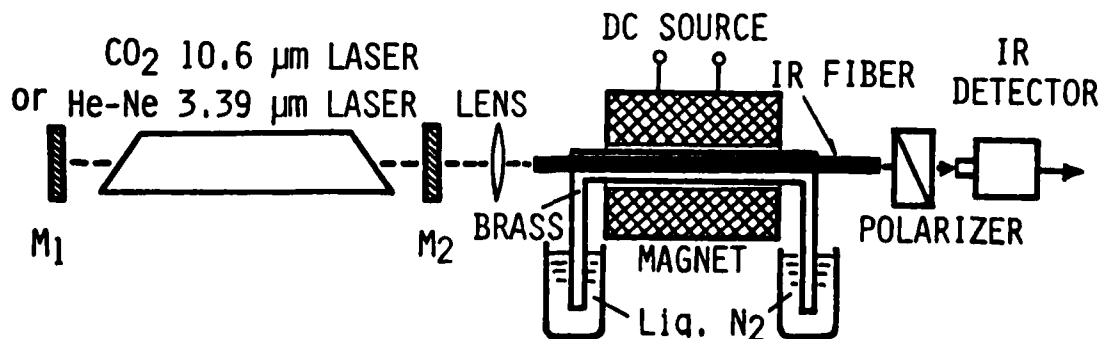


Fig. 1 Experimental setup for the Faraday effect.

zer(II-IV : PAZ-6) by a power meter (Coherent M201) or an InAs detector (Judson). For the measurements using a CO<sub>2</sub> laser a grating was used instead of the flat mirror M<sub>1</sub>. For measuring the Voigt effect a transverse dc magnetic field was applied instead of the longitudinal field, variable up to 800 gauss. Because of using an effective dewar lower temperature was obtained up to -190 °C in case of the Voigt-effect measurement using KRS-5 fiber.

About 3 ° of the Faraday rotation at room temperature became 10 ° - 11 ° for both KRS-5 and As<sub>2</sub>S<sub>3</sub> fibers under the applied field 2 kG and the effective length 7.5 cm. From the measurements of the Faraday rotation the temperature dependence of these fibers upon the Verdet constant  $V$  is depicted in Figs. 2 and 3 for KRS-5 and As<sub>2</sub>S<sub>3</sub> fibers, respectively. It is seen that the Verdet constant tends to increase rapidly with decrease of temperature; and that both fibers follow  $A + B/T$  characteristics ( $T$  : temperature,  $A$  and  $B$  : constants). The values of  $V$  at room temperature was well consistent with that obtained theoretically by using known refractive indices[6] as

$$V = -(e/2mc^2)\lambda (dn/d\lambda), \quad (1)$$

where  $e$  and  $m$  are, respectively, the charge and mass of electron,  $c$  the light velocity in vacuum,  $n$  the refractive index and  $\lambda$  the wavelength.

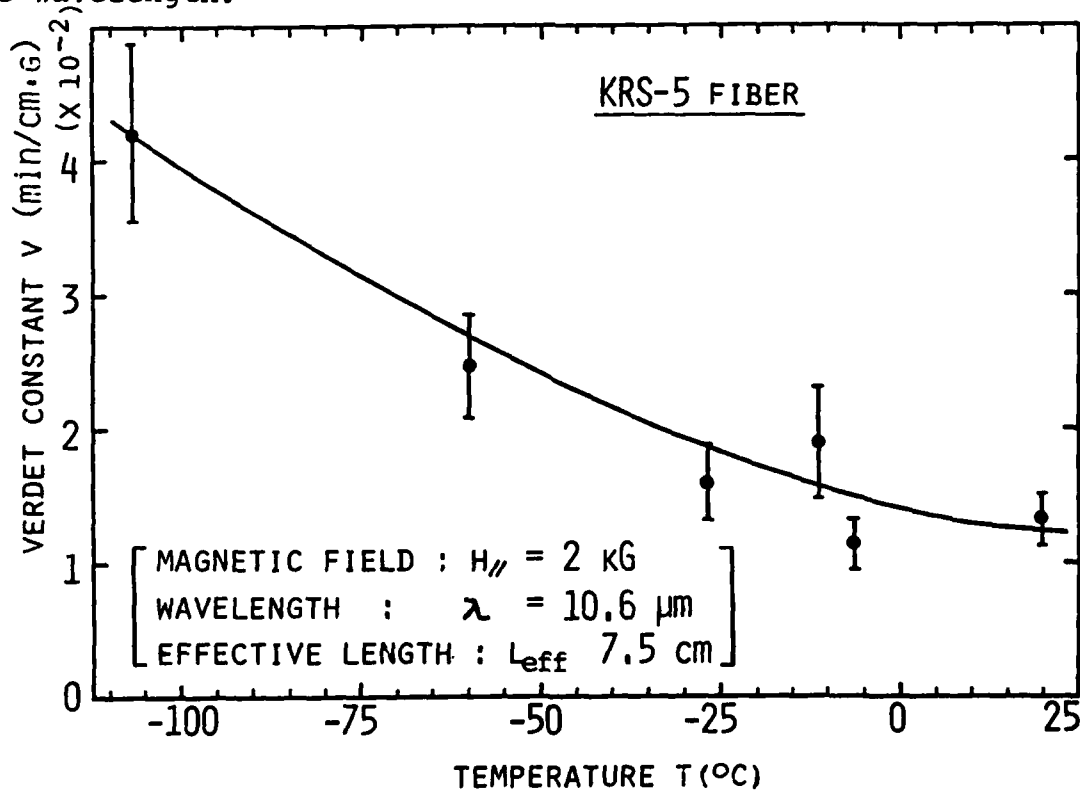


Fig. 2 Temperature dependence of KRS-5 fiber on the Verdet constant.

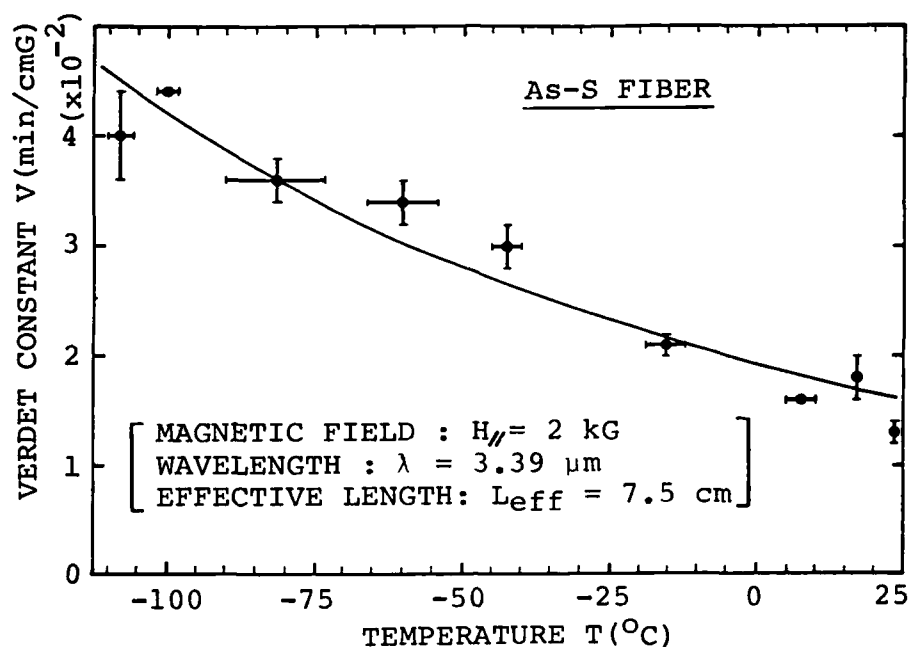


Fig. 3 Temperature dependence of  $\text{As}_2\text{S}_3$  fiber on the Verdet constant.

The temperature dependence of KRS-5 on the Voigt constant  $C$  is shown in Fig. 4 using a  $\text{CO}_2$   $10.6 \mu\text{m}$  laser line. It can be seen that the Voigt constant also significantly increases at low temperature. Almost one order enhancement was recognized at  $-160^\circ\text{C}$  in comparison with that of room temperature. By cooling down the birefringent retardation is enhanced with increase of the applied field, in addition to increase of the natural retardation. However, the natural birefringence tends to saturate at about  $-100^\circ\text{C}$  and tends to keep constant. The Voigt constant at room temperature was also compared with the theoretical estimate using known parameter as

$$C = -(e^2/16\pi mc^2)\lambda^3(d^2n/d\lambda^2), \quad (2)$$

being consistent well each other.

From the obtained temperature dependence of both Verdet- and Voigt constants it was found that these follow roughly  $A + B/T$  dependence. Especially, the temperature dependent term  $B$  is strongly related to the angular momentum quantum number  $J$  and the Lande splitting factor  $g$ [7] as

$$B = \tilde{a}(J + 1)g\mu_B/3k_B, \quad (3)$$

where  $k_B$  is the Boltzmann constant,  $\mu_B$  the Bohr magneton and  $\tilde{a}$  the constant. Thus, the obtained results gives us some information to analyze the above parameters. On the other hand, since cooling techniques using liquid nitrogen is, so far, getting popular without any difficulty, increase of these constants must be great benefit not only for designing magneto-optic devices and sensing elements for magnetic field or electric current, but also gives us fundamental informations to evaluate dispersion



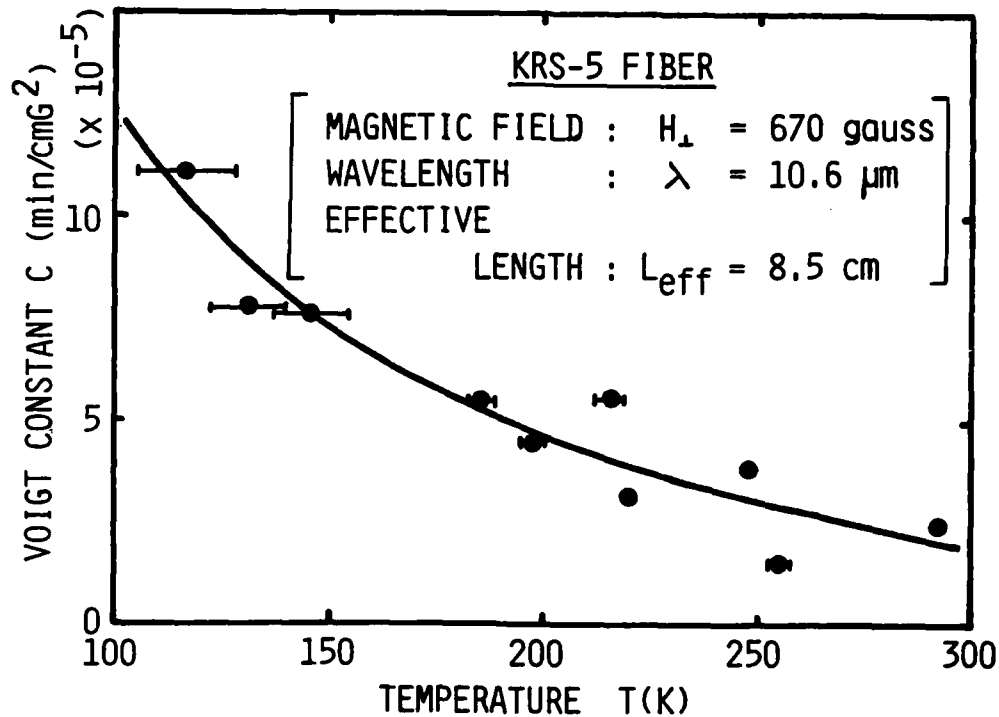


Fig. 4 Temperature dependence of KRS-5 fiber on the Voigt constant.

property at low temperature. As seen from Eqs.(1) and (2) the temperature dependence of  $dn/d\lambda$  and  $d^2n/d\lambda^2$  can be readily evaluated in the experiments, so that this allows us to find the coefficients of a Sellmeier fit. More about this point will be discussed.

#### References

- [1] J. A. Harrington et al, Adv. Ceram. 2, 94(1981).
- [2] S. Sakuragi et al, Opt. Lett. 6, 629(1981).
- [3] J. A. Harrington et al, Opt. Lett. 8, 223(1983).
- [4] H. Sato et al, Opt. Lett. 8, 180(1983).
- [5] H. Sato et al, Appl. Opt. 23, 2633(1984).
- [6] W. G. Driscoll, Ed., Handbook of Optics (McGraw Hill, New York 1978), p 7 - 108.
- [7] C. Kittel, Introduction to Solid State Physics (Wiley, New York, 1976), p 438.

## OPTICAL CHARACTERIZATION OF DEVITRIFICATION FOR $\text{Cr}^{3+}$ -DOPED Zr-Ba-La-Al FLUORIDE GLASS

W.J. Miniscalco, L.J. Andrews, B.T. Hall, and D.E. Guenther  
GTE Laboratories Incorporated  
40 Sylvan Road  
Waltham, MA 02254

The past decade has seen an enormous increase in activity in the area of heavy metal fluoride glasses. These glasses contain no oxygen and are distinguished from the fluoroberyllates by the absence of beryllium. In addition to their scientific interest as a largely unexplored glass-forming system, heavy metal fluoride glasses are of technological interest because they have high optical transmission from the UV to the mid-IR ( $\geq 7 \mu\text{m}$ ). One potential application is as optical fiber for both communications and energy transmission in the mid-IR. Since these glasses can be doped with transition metal and rare earth ions, other promising applications are as solid state laser hosts and magneto-optic devices.

An important consideration in all applications is the relatively poor stability of these glasses compared to oxide glasses as indicated by their extremely narrow working ranges. Even for the best compositions the crystallization temperature is seldom more than 100 C higher than the glass transition temperature. To further understand the stability of heavy metal fluoride glasses, we have undertaken an investigation of crystallization using primarily optical techniques. The work has concentrated on a Zr-Ba-La-Al fluorozirconate glass (ZBLA) which has been doped with probe ions whose optical spectra are sensitive to their local environment. The strength and symmetry of the crystal field at the site occupied by these ions affect the positions of their electronic states. The  $d \rightarrow d$  transitions of transition metal ions are particularly sensitive because their electron-lattice coupling strengths range from intermediate to strong. The peak positions, bandwidths, and oscillator strengths of the optical transitions for a given transition metal ion vary greatly depending upon the particular glass or crystalline host. Major spectral changes associated with devitrification have been reported by Andrews *et al.* for  $\text{Cr}^{3+}$ -doped oxide glasses and ceramics [1]. More recently Tanimura *et al.* have observed that crystallization has a significant effect upon the emission spectrum of  $\text{ZBLA}:\text{Er}^{3+}$  [2]. However, Feuerhelm *et al.* found only minor changes for  $\text{Mn}^{2+}$  in the same glass [3]. The dopants we have investigated include the transition metals  $\text{Cr}^{3+}$ ,  $\text{Fe}^{3+}$ ,  $\text{Fe}^{2+}$ , and  $\text{Mn}^{2+}$ , as well as the rare earths  $\text{Nd}^{3+}$ ,  $\text{Eu}^{3+}$ , and  $\text{Ce}^{3+}$ . We have established that it is possible to determine whether these ions reside at amorphous or crystalline sites on the basis of their photoluminescence spectra. For this glass  $\text{Cr}^{3+}$  is a particularly sensitive probe of its environment and not only indicates the presence of trace amounts of crystalline phase in the glass, but can also be used to identify the types of crystals present.

AD-A161 247

OM85 BASIC PROPERTIES OF OPTICAL MATERIALS SUMMARIES OF  
PAPERS(U) NATIONAL BUREAU OF STANDARDS GAITHERSBURG MD  
A FELDMAN MAY 85 NBS-SP-697 AFOSR-RR-85-0902

4/4

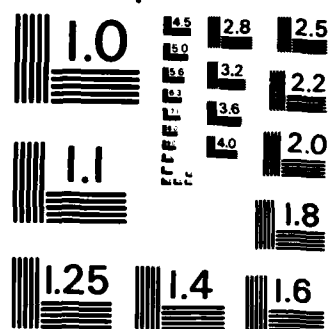
UNCLASSIFIED

AFOSR-ISSA-85-00032

F/G 20/6

NL





MICROCOPY RESOLUTION TEST CHART  
NATIONAL BUREAU OF STANDARDS-1963-A

The glass investigated had the composition 58 m/o  $\text{ZrF}_4$ , 34 m/o  $\text{BaF}_2$ , 5 m/o  $\text{LaF}_3$ , and 3 m/o  $\text{AlF}_3$ . Dopant concentrations ranged from  $\leq 100$  ppm to 1 m/o. High purity commercially available fluoride starting materials were used and  $\text{NH}_4\text{HF}_2$  was added to maintain fluoridation since the glasses were melted and poured in air. After annealing at 300 C, the samples were cut and polished for the optical investigations. Absorption spectra were measured for the more concentrated dopants. Room temperature photoluminescence spectra were obtained using cw argon and krypton ion lasers as excitation sources. The samples were then subjected to heat treatment and the photoluminescence spectra measured again. To assist in assigning the crystalline phases corresponding to the different  $\text{Cr}^{3+}$  emission spectra, polycrystalline samples of  $\text{BaZrF}_6\text{:Cr}$  were synthesized by slow cooling or quenching in liquid nitrogen to form the different crystalline phases possible for this compound. Phases of  $\text{BaZrF}_6$  and  $\text{BaZr}_2\text{F}_{10}$  are believed to nucleate and grow when ZBLA is devitrified upon reheating [4,5,6]. Emission spectra were measured for the polycrystalline samples and correlated with those observed for the glass. In addition, powder x-ray diffraction patterns were measured for the crystalline phases and compared to those observed for the devitrified glasses.

Figure 1 compares the  $\text{Cr}^{3+}$  photoluminescence spectrum of (a) untreated ZBLA, (b) a sample which has been heated for 2 hr at 375 C, and (c) a sample which has been heated for 30 min at 426 C. The spectral changes are quite dramatic. We have tentatively assigned curves (a) and (b) to emission from the phases reported to be dominant in published x-ray diffraction studies of devitrified ZBLA. The heat treatment at 375 C has been observed to produce primarily  $\beta\text{-BaZrF}_6$  for similar compositions [4,5,6] and the emission band (b) which peaks at  $\approx 890$  nm indicates that this phase provides a very low crystal-field-strength site for  $\text{Cr}^{3+}$ . Although narrower than (a), this band is still excessively wide on the short wavelength side, most probably as a result of  $\text{Cr}^{3+}$  sites in other crystalline phases. The emission intensity is more than an order of magnitude higher than for the untreated glass, implying a significantly larger quantum efficiency for  $\text{Cr}^{3+}$  in this phase. After treatment at 426 C the emission band (c) is narrowed and shifted to shorter wavelength, peaking at  $\approx 780$  nm. This indicates that  $\text{Cr}^{3+}$  has been incorporated into a phase with a higher field site, most likely either  $\alpha\text{-BaZrF}_6$  or  $\beta\text{-BaZr}_2\text{F}_{10}$  [6]. The narrowing of the band implies that the luminescence is predominately from a single site. Moreover, the emission is  $>1500$  times brighter than from the untreated glass. The luminescence band for untreated ZBLA is atypical and extremely broad even for a glass. One explanation is an unusually broad range of crystal field strengths for a single  $\text{Cr}^{3+}$  site in the glass. Another possibility is that of multiple sites, including the presence of trace quantities of crystalline phase in the untreated glass. Neilson *et al.* have reported microcrystals of  $\alpha\text{-BaZrF}_6$  in untreated ZBLA [5]. Emission from this phase, curve (c), would broaden the band on the short wavelength edge. The higher quantum efficiency for this phase would make the glass luminescence spectrum extremely sensitive to minute quantities.

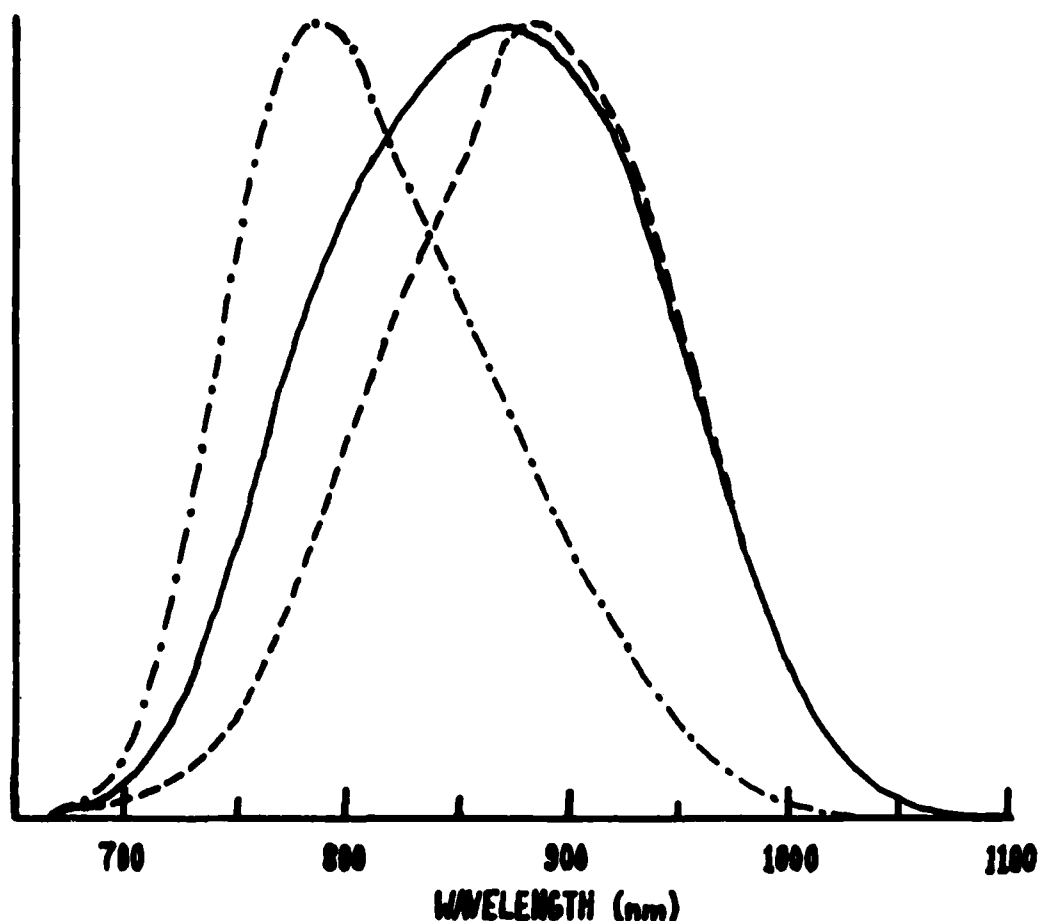


Figure 1

Photoluminescence spectra for  $\text{Cr}^{3+}$ -doped ZBLA subjected to different heat treatments. Curve (a) — is for the untreated glass; curve (b) --- is for a sample held for 2 hr at 375 C; curve (c) -·- is for a sample held for 30 min at 426 C. All samples were excited at 647.1 nm.

Although self-consistent, the above assignment of the emission spectra remains open to question since we cannot exclude the possibility that  $\text{Cr}^{3+}$  is preferentially incorporated into phases present in only small amounts. The luminescence could, in principle, emanate from phases present in such small quantities as to be undetectable by x-ray diffraction. Accordingly, we have attempted to synthesize single phase polycrystalline samples of  $\text{BaZrF}_6:\text{Cr}^{3+}$  to verify the above assignments. The emission spectrum for the sample treated at 426 C corresponds most nearly to that of  $\text{BaZrF}_6$  synthesized by melting at 850 C, holding for 3 days at 512 C, and rapidly cooling to room temperature. The x-ray pattern for this polycrystalline sample is identical to that published by Laval *et al.* and attributed by them to  $\alpha\text{-BaZrF}_6$  [7]. The luminescence spectrum for ZBLA heat treated at 375 C is most similar to that of a polycrys-

talline sample quenched from 654 C. The x-ray pattern for this latter crystalline sample corresponds closely to that reported by Mehlhorn and Hoppe although they synthesized their sample by slow cooling [8]. We have also synthesized samples by slow cooling (10 days), and find x-ray patterns very similar to those of the quenched samples although their photoluminescence spectra are quite different. In all cases, the polycrystalline emission spectra have been broader than expected, implying that we have not yet succeeded in synthesizing single phase material.

In conclusion, we have observed radical changes in the photoluminescence spectrum of Cr-doped ZBLA. These changes indicate that, depending upon the heat treatment applied,  $\text{Cr}^{3+}$  is being incorporated into different crystalline phases which have sites with significantly different crystal field strengths and quantum efficiencies. A general correspondence has been found between emission from these phases and that from polycrystalline samples, but the results are still inconclusive. This ambiguity is probably due to the presence of multiple phases in both the glass and polycrystalline samples combined with the difference in sensitivity between x-ray diffraction and optical probe ion spectroscopy. A phase which is present in trace quantities may not be observable in an x-ray diffraction pattern. However, if the optical probe ion is preferentially incorporated into this phase with a higher quantum efficiency than in the majority phase, the luminescence spectrum will reveal or even be dominated by the trace phase. Since it is not always possible to resolve the emission spectra from different phases under cw excitation, we are now investigating these materials using time-resolved spectroscopy which provides additional discrimination based upon variations in excited state lifetime. It is a pleasure to acknowledge helpful discussions with R. M. Klein, R. C. Folweiler, and M. G. Drexhage, who also provided a sample.

- [1] L.J. Andrews, A. Lempicki, and B.C. McCollum, Chem. Phys. Lett. 74, 404 (1980); and L.J. Andrews et al., "Development of Materials for a Luminescent Solar Concentrator," Final Report for DOE Contract No. DE-AC02-78ER-04996, January 1983.
- [2] K. Tanimura, M.D. Shinn, and W.A. Sibley, Phys. Rev. B 30, 2429 (1984).
- [3] L.N. Feuerhelm, S.M. Sibley, and W.A. Sibley, J. Solid State Chem. 54, 164 (1984).
- [4] M.C. Weinberg, G.F. Neilson, and G.L. Smith, J. Non-Cryst. Solids 56, 45 (1983).
- [5] G.F. Neilson, G.L. Smith, and M.C. Weinberg, Mat. Res. Bull. 19, 279 (1984).
- [6] N.P. Bansal, R.H. Doremus, A.J. Bruce, and C.T. Moynihan, Mat. Res. Bull. 19, 577 (1984).
- [7] J.-P. Laval, D. Mercurio-Lavaud, and B. Gaudreau, Rev. Chim. Minérale 11, 742 (1974).
- [8] Von B. Mehlhorn and R. Hoppe, Z. anorg. allg. Chem. 425, 180 (1976).

## OPTICAL STUDY OF Ge-P-Te AND Ge-Se-Te CHALCOGENIDE GLASSES

L. Boehm, A. Bornstein, and S. Arie  
Solid State Physics Department,  
Soreq Nuclear Research Center, Yavne 70600, Israel

### 1. Introduction

Chalcogenide glasses have been thoroughly investigated, especially in connection with their electronic properties and their promise as IR windows in the 8-12 $\mu$ m region [1]. For the purpose of the present study, the major attraction of chalcogenides lies in their promise as IR materials for infrared optical fibers. Such fibers are needed in applications using high-power CO<sub>2</sub> laser for surgery as well as in cutting and heat treatment of metals. These fibers will also play an important role in the development of many infrared devices in the field of image relaying and remote sensing.

In this study we present the preparation and optical characterization of two glass systems containing relatively high amounts of Te. Such glasses are expected to be transparent up to 20 $\mu$ m and may serve as preforms for drawing IR fibers.

### 2. Experimental Procedure and Results

Starting materials are semiconductor grade germanium, selenium, and tellurium of 99.9999% purity, subjected to a special process of purification by which oxides are separated by zone refining. Red phosphorous 99.99% pure (Cerac Corp.) was used. Melting is conducted in charges of 90g in evacuated, sealed silica tubes of 8.0mm diameter and 200mm length. Before use, the tubes are carefully cleaned with HNO<sub>3</sub>-HF solution and fused to 1000°C, under vacuum. The melting temperature is 950°C, and the melt is homogenized by continuous axial rotation of the tube for approximately 40 hours. Then the tube is air-cooled in the vertical position, by which the melt solidifies in the form of a glass cylinder. The glasses are cut and polished before conducting physical measurements. X-ray diffraction showed that all samples were glassy. Inspection with a scanning electron microscope showed homogeneity with no particles and phase separation (detection limit 3 $\mu$ ) in contrast to previously reported [2] results for the Ge-Se-Te system.

#### 2.1 Chemical analysis by EDS and WDS methods

Since we are synthesizing complicated ternary systems, and the properties of the glasses (mainly the index of refraction) are composition-dependent, chemical analysis of the prepared samples was performed. Two main techniques are used, both based on the X-ray spectrum emitted from an excited atom: EDS (Energy Dispersive Spectrum) and WDS (Wavelength Dispersive Spectrum). The two techniques differ in the way the X-rays are accumulated and identified. The EDS technique analyzes all elements simultaneously, but the poor energy



resolution of the Si-Li detector used causes errors in the quantitative analysis of elements adjacent in the periodic table such as Se and Ge. This is why the WDS technique was used for elements in the system Ge-Se-Te; this technique has a much better resolution. A more detailed description of the techniques will be presented in a forthcoming study. In both methods, standards composed of the investigated elements are used. Table 1 presents the chemical analysis of the glass Ge-P-Te performed by the EDS method. In Table 2, the analysis of the glass Ge-Se-Te is presented as measured both by the EDS and WDS techniques.

The results show that the amount of phosphor present in the Ge-P-Te glass is much less than weighed, although the glass obtained is homogeneous. Such a low amount of phosphor enabled us to obtain a stable glass phase in the alloy system Ge-Te, which is known to have the tendency to crystalize [3].

From Table 2 it is obvious that the EDS technique is not accurate enough for analyzing the glass Ge-Se-Te, as there is an overlap both between the emitted lines Ge-K and Se-K, and between Ge-L and Se-L. Therefore, the WDS method was used. As seen, the glass obtained has the same composition as the weighed starting materials.

Table 1. Chemical Analysis of Ge-P-Te Glass by EDS

Element	Composition weighed in at%	Composition of polished glass
Ge	20.0	23.44 ± 1.40
P	10.0	3.04 ± 0.64
Te	70.0	73.52 ± 1.30

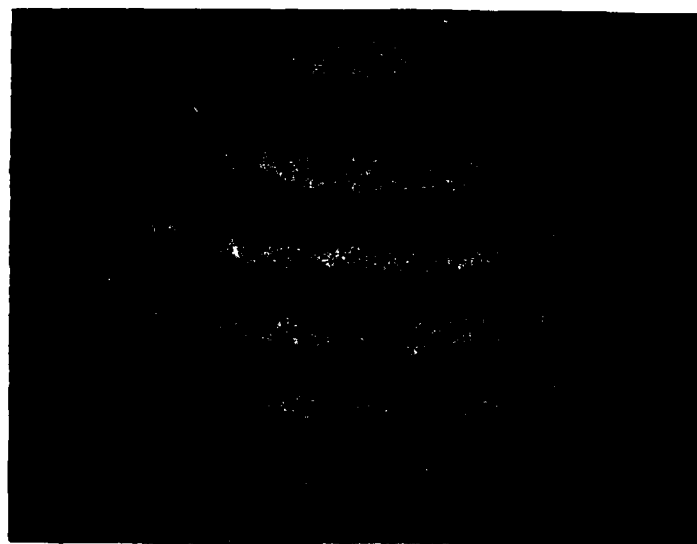
Table 2. Chemical Analysis of Ge-Se-Te Glass

Element	Composition weighed in at%	Composition obtained by	
		WDS technique	EDS technique
Ge	20.0	19.88 ± 0.6	15.1 ± 1.2
Se	50.0	50.19 ± 4.0	59.0 ± 1.3
Te	30.0	30.18 ± 0.6	25.8 ± 1.0

## 2.2 Optical measurement

Interferometric mapping of refractive index inhomogeneity was used to diagnose optical imperfections in components. Such inhomogeneity arises from the existence of stresses or impurities in the sample. When it exists, it distorts the wavefront and impairs optical performance. For such measurements each surface has to be flat within one visible fringe, to separate surface irregularities from volume inhomogeneities. Picture 1 shows an interferogram of the glass  $\text{Ge}_{20}\text{Se}_{50}\text{Te}_{30}$  12mm in diameter and 10mm thick. It was calculated that the inhomogeneity in the index of refraction ( $\Delta n$ ) of the sample is  $4 \times 10^{-4}$  which indicates that the glass has no crystallization or other imperfections. This result is consistent with those obtained by the SEM measurements.

The IR spectra were measured on polished samples at room temperature, with a Nicolet 5DX FT-IR Spectrometer having a resolution of  $4\text{cm}^{-1}$ . Figure 1 shows the IR spectra of 1.5mm thickness of the two glasses,  $\text{Ge}_{20}\text{Se}_{50}\text{Te}_{30}$  and  $\text{Ge}_{23.5}\text{P}_{3.0}\text{Te}_{73.5}$ . As can be seen, the Se based glass is transparent up to  $15\mu\text{m}$ , while the glass based on Ge-Te is transparent up to  $20\mu\text{m}$ .



Picture 1. Interferogram of the Glass  $\text{Ge}_{20}\text{Se}_{50}\text{Te}_{30}$

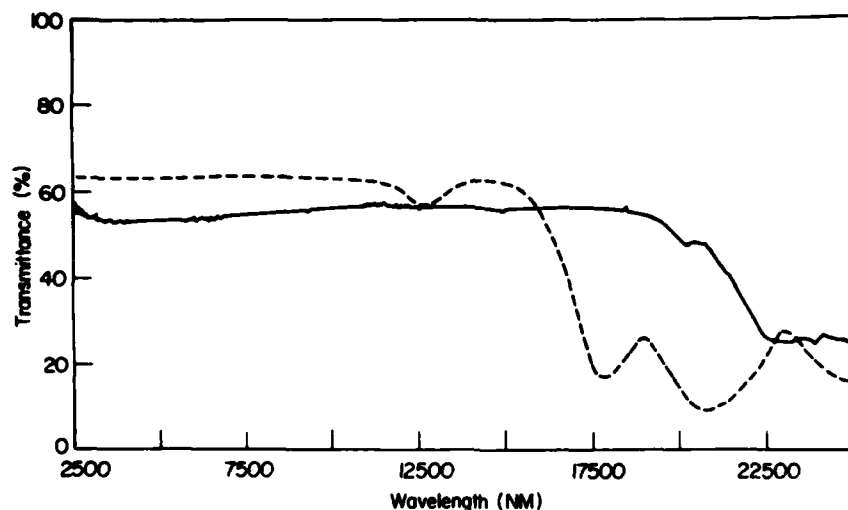


Figure 1. Emission Spectra of Ge-P-Te Glass (unbroken line) and Ge-Se-Te (broken line), 1.5mm thickness

### Discussion and Conclusion

We succeeded in preparing a stable glass in the system Ge-Te by adding a small amount of phosphor (around 3 at%). It is known [3] that such alloys containing high amounts of Te tend to crystallize. This glass shows no absorption up to  $430\text{cm}^{-1}$ . The glass  $\text{Ge}_{20}\text{Se}_{50}\text{Te}_{30}$  shows a weak absorption band at  $780\text{cm}^{-1}$ , due to Ge-O stretching vibration [4]. It arises from an oxide layer or absorbed oxygen formed at the surface layer of the Ge element used in this preparation. The absorption bands at  $560\text{cm}^{-1}$  and  $475\text{cm}^{-1}$  presumably result from Ge-Se and Se-Se stretching, respectively.

We conclude that both glass systems are promising materials for application in IR systems such as fiberoptics or IR components.

Special care should be taken in fabricating the glasses from high-purity materials in a controlled atmosphere.

### Acknowledgements

The authors are grateful to Dr. K. Shilo and Dr. Y. Noter for the interferometric measurements.

- (1) J. A. Savage, P. J. Weber, and A. M. Pitt, *Infrared Physics*, **20** 313 (1980).
- (2) S. Bordas, M. Geli, Y. Casas-Va'zquez, N. Clavaguera, and M. T. Clavaguera-Mora, *Revue Physique Appliquée* **12** 677 (1977).
- (3) D. Rerewnicka, P. G. Zielinski, and H. Davies, *J. Material Science Letters* **1** 87 (1982).
- (4) S. Maruno and M. Noda, *Rep. Asahi Glass Found. Ind. Technol.* **35** 367 (1979).

# AUTHOR INDEX

	Page		Page
Adar, F. . . . .	198	Dragovich, P. . . . .	110
Aly, M. H. . . . .	256	Edgerton, B. . . . .	115
Andrews, L. J. . . . .	274	El-Badawy, E-S. A. . . . .	119, 256
Arakawa, E. T. . . . .	58	El-Gammal, M. A. . . . .	256
Arie, S. . . . .	278	El-Halafawy, F. Z. . . . .	119, 256
Armitage, D. . . . .	251	Elson, J. M. . . . .	21
Ashley, J. C. . . . .	58	Farabaugh, E. N. . . . .	122
Aspnes, D. E. . . . .	5, 99	Fauchet, P. M. . . . .	198
Azumai, Y. . . . .	270	Feldman, A. . . . .	122
Babic, D. . . . .	103	Fetterman, H. . . . .	234
Barber, P. W. . . . .	11	Flory, F. . . . .	84
Bass, M. . . . .	164	French, R. H. . . . .	126
Beard, W. T. . . . .	214	Gan, F. X. . . . .	130
Bendow, B. . . . .	260	Georger, J. P. . . . .	40
Bennett, H. E. . . . .	32	Gibbs, H. M. . . . .	246
Bennett, H. S. . . . .	194	Glembocki, O. J. . . . .	214
Bobbs, B. . . . .	234	Grieser, J. L. . . . .	89, 106
Boehm, L. . . . .	278	Guenther, D. E. . . . .	274
Bohn, P. W. . . . .	71	Günter, P. . . . .	222
Bornstein, A. . . . .	278	Haglund, R. F., Jr. . . . .	184
Boyd, J. T. . . . .	65	Hall, B. T. . . . .	274
Bottka, N. . . . .	214	Halliburton, L. E. . . . .	141
Bowden, C. M. . . . .	249	Harris, D. C. . . . .	133
Bu-Abbud, G. H. . . . .	86, 167	Haus, J. W. . . . .	249
Buhay, H. . . . .	89, 106	Heller, A. . . . .	99
Burton, R. L. . . . .	54, 89, 106	Hellwarth, R. W. . . . .	232
Campbell, I. H. . . . .	198	Hills, M. E. . . . .	133
Cardona, M. . . . .	188	Hoefer, C. S. . . . .	238
Carter, G. M. . . . .	40	Hoffman, H. J. . . . .	266
Chang, R. K. . . . .	11	Holmes, B. W. . . . .	242
Charlwood, L. . . . .	80	Hryniewicz, J. V. . . . .	40
Chemla, D. S. . . . .	202	Inabe, T. . . . .	54
Chen, H. Y. . . . .	130	Ingram, D. . . . .	167
Chen, Y. J. . . . .	40	Jackson, H. E. . . . .	65
Chew, N. G. . . . .	80	Jani, M. G. . . . .	141
Chow, H. C. . . . .	229	Jochs, W. W. . . . .	266
Coble, R. L. . . . .	126	Kaminow, I. P. . . . .	1
Comas, J. . . . .	214	Kannewurf, C. R. . . . .	54
Cook, J. M. . . . .	249	Kirby, K. W. . . . .	238
Covino, J. . . . .	110, 133	Klein, C. A. . . . .	137
Craighead, H. G. . . . .	181	Klein, M. B. . . . .	226, 234
Cullis, A. G. . . . .	80	Kleiber, M. J. . . . .	229
D'Souza, A. I. . . . .	218	Koumvakalis, N. . . . .	141
Delwart, S. M. . . . .	251	Lamb, J. D. . . . .	86
Deniau, G. . . . .	84	Lewis, K. L. . . . .	80
DeShazer, L. G. . . . .	238	Lieberman, A. G. . . . .	17
Dirk, C. W. . . . .	46	Lipson, H. G. . . . .	145

	Page		Page
Liu, S-H. . . . .	169, 255	Sari, S. O. . . . .	154
Lowe-Ma, C. K. . . . .	110, 133	Sato, H. . . . .	270
Ludman, J. E. . . . .	242	Savage, J. A. . . . .	80
Lynch, D. W. . . . .	24	Schwartz, R. W. . . . .	133
Macleod, H. A. . . . .	74	Schwelb, O. . . . .	160
Maloney, P. J. . . . .	181	Segall, B. . . . .	28
Marks, T. J. . . . .	54	Shanabrook, B. V. . . . .	214
Mathine, D. L. . . . .	167	She, C. Y. . . . .	93
Matloubian, M. . . . .	234	Sheng, T. T. . . . .	99
McCarthy, W. J. . . . .	54	Shortt, D. . . . .	115
Messier, R. . . . .	218	Simon, H. J. . . . .	60
Miniscalco, W. J. . . . .	274	Smith, D. Y. . . . .	28, 177
Morrison, T. I. . . . .	177	Sung, C. C. . . . .	249
Murarka, N. P. . . . .	89, 106	Sweeney, J. E. . . . .	181
Nisar, M. . . . .	89	Swimm, R. T. . . . .	158, 164
Oh, J. E. . . . .	86	Thakur, M. K. . . . .	40
Palik, E. D. . . . .	171	Tolk, N. H. . . . .	184
Felletier, E. . . . .	84	Tripathy, S. K. . . . .	40
Peyghambarian, N. . . . .	246	Twieg, R. J. . . . .	46
Pierce, B. M. . . . .	150	Tyminski, J. K. . . . .	229
Pitt, A. M. . . . .	80	Vadimsky, R. G. . . . .	99
Poehler, T. O. . . . .	50	Valley, G. C. . . . .	226
Poker, D. . . . .	167	Villaverde, A. B. . . . .	164
Porter, J. D. . . . .	99	Wagniere, G. . . . .	46
Potember, R. S. . . . .	50	Wigen, P. E. . . . .	218
Powell, R. C. . . . .	229	Williams, M. W. . . . .	58
Primak, W. . . . .	36	Williamson, A. E. . . . .	177
Pronko, P. . . . .	167	Willingham, C. B. . . . .	137
Przybilla, G. . . . .	266	Wood, O. R., II . . . . .	181
Rabii, S. . . . .	103	Woods, C. L. . . . .	242
Rezk, A. Y. . . . .	119	Woollam, J. A. . . . .	86, 167
Roe, M. G. . . . .	218	Young, D. W. . . . .	58
Rubner, M. F. . . . .	40	Zhang, B. . . . .	169, 255
Rytz, D. . . . .	234	Zhu, J-K. . . . .	169, 255
Saito, M. . . . .	270		

U.S. DEPT. OF COMM. <b>BIBLIOGRAPHIC DATA SHEET</b> (See instructions)	<b>1. PUBLICATION OR REPORT NO.</b> NBS/SP-697	<b>2. Performing Organ. Report No.</b>	<b>3. Publication Date</b> April 1985												
<b>4. TITLE AND SUBTITLE</b> OM85 Basic Properties of Optical Materials, Summaries of Papers (Topical Conference on Basic Properties of Optical Materials)															
<b>5. AUTHOR(S)</b> Albert Feldman, Chairperson, Editorial Committee															
<b>6. PERFORMING ORGANIZATION</b> (If joint or other than NBS, see instructions) National Bureau of Standards Department of Commerce Gaithersburg, MD 20899		<b>7. Contract/Grant No.</b> AFOSR-ISSA-KS-00052	<b>8. Type of Report &amp; Period Covered</b> Final												
<b>9. SPONSORING ORGANIZATION NAME AND COMPLETE ADDRESS</b> (Street, City, State, ZIP) <table border="0"> <tr> <td>National Bureau of Standards</td> <td>Air Force Office of Scientific Research</td> <td>American Physical Soc.</td> </tr> <tr> <td>Department of Commerce</td> <td></td> <td>335 East 45th Street</td> </tr> <tr> <td>Gaithersburg, MD 20899</td> <td>Bolling Air Force Base</td> <td>New York, NY 10017</td> </tr> <tr> <td></td> <td>Washington, DC 20332</td> <td></td> </tr> </table>				National Bureau of Standards	Air Force Office of Scientific Research	American Physical Soc.	Department of Commerce		335 East 45th Street	Gaithersburg, MD 20899	Bolling Air Force Base	New York, NY 10017		Washington, DC 20332	
National Bureau of Standards	Air Force Office of Scientific Research	American Physical Soc.													
Department of Commerce		335 East 45th Street													
Gaithersburg, MD 20899	Bolling Air Force Base	New York, NY 10017													
	Washington, DC 20332														
<b>10. SUPPLEMENTARY NOTES</b> Library of Congress Catalog Card Number 85-600534 <input type="checkbox"/> Document describes a computer program; SF-185, FIPS Software Summary, is attached.															
<b>11. ABSTRACT</b> (A 200-word or less factual summary of most significant information. If document includes a significant bibliography or literature survey, mention it here) This Special Publication contains summaries of papers to be presented at the Topical Conference on Basic Properties of Optical Materials to be held at the National Bureau of Standards in Gaithersburg, Maryland on May 7-9, 1985. The conference is sponsored by the National Bureau of Standards, the Air Force Office of Scientific Research, and the American Physical Society in cooperation with the Optical Society of America and SPIE-The International Society for Optical Engineering. This publication contains summaries of 70 papers which include 17 invited papers. The purpose of the conference is to bring together researchers from industry, academia, and government to discuss the physical and structural properties of optical materials as they affect optical performance. The scope of the conference includes the measurement and theory of basic properties of optical materials in bulk and in thin film form and the dependence of these properties on atomic structure, morphological structure, impurity content, and inhomogeneity.															
<b>12. KEY WORDS</b> (Six to twelve entries; alphabetical order; capitalize only proper names; and separate key words by semicolons) Glasses; infrared; modulated structures; nonlinear optics; metals; organics; optical constants; optical waveguides; photorefractive effect; polymers; semiconductors; thin films; ultraviolet															
<b>13. AVAILABILITY</b> <input checked="" type="checkbox"/> Unlimited <input type="checkbox"/> For Official Distribution. Do Not Release to NTIS <input checked="" type="checkbox"/> Order From Superintendent of Documents, U.S. Government Printing Office, Washington, D.C. 20402 <input type="checkbox"/> Order From National Technical Information Service (NTIS), Springfield, VA. 22161		<b>14. NO. OF PRINTED PAGES</b> 294 <b>15. Price</b>													

# **NBS** *Technical Publications*

## **Periodical**

**Journal of Research**—The Journal of Research of the National Bureau of Standards reports NBS research and development in those disciplines of the physical and engineering sciences in which the Bureau is active. These include physics, chemistry, engineering, mathematics, and computer sciences. Papers cover a broad range of subjects, with major emphasis on measurement methodology and the basic technology underlying standardization. Also included from time to time are survey articles on topics closely related to the Bureau's technical and scientific programs. As a special service to subscribers each issue contains complete citations to all recent Bureau publications in both NBS and non-NBS media. Issued six times a year.

## **Nonperiodicals**

**Monographs**—Major contributions to the technical literature on various subjects related to the Bureau's scientific and technical activities.

**Handbooks**—Recommended codes of engineering and industrial practice (including safety codes) developed in cooperation with interested industries, professional organizations, and regulatory bodies.

**Special Publications**—Include proceedings of conferences sponsored by NBS, NBS annual reports, and other special publications appropriate to this grouping such as wall charts, pocket cards, and bibliographies.

**Applied Mathematics Series**—Mathematical tables, manuals, and studies of special interest to physicists, engineers, chemists, biologists, mathematicians, computer programmers, and others engaged in scientific and technical work.

**National Standard Reference Data Series**—Provides quantitative data on the physical and chemical properties of materials, compiled from the world's literature and critically evaluated. Developed under a worldwide program coordinated by NBS under the authority of the National Standard Data Act (Public Law 90-396).

NOTE: The Journal of Physical and Chemical Reference Data (JPCRD) is published quarterly for NBS by the American Chemical Society (ACS) and the American Institute of Physics (AIP). Subscriptions, reprints, and supplements are available from ACS, 1155 Sixteenth St., NW, Washington, DC 20056.

**Building Science Series**—Disseminates technical information developed at the Bureau on building materials, components, systems, and whole structures. The series presents research results, test methods, and performance criteria related to the structural and environmental functions and the durability and safety characteristics of building elements and systems.

**Technical Notes**—Studies or reports which are complete in themselves but restrictive in their treatment of a subject. Analogous to monographs but not so comprehensive in scope or definitive in treatment of the subject area. Often serve as a vehicle for final reports of work performed at NBS under the sponsorship of other government agencies.

**Voluntary Product Standards**—Developed under procedures published by the Department of Commerce in Part 10, Title 15, of the Code of Federal Regulations. The standards establish nationally recognized requirements for products, and provide all concerned interests with a basis for common understanding of the characteristics of the products. NBS administers this program as a supplement to the activities of the private sector standardizing organizations.

**Consumer Information Series**—Practical information, based on NBS research and experience, covering areas of interest to the consumer. Easily understandable language and illustrations provide useful background knowledge for shopping in today's technological marketplace.

Order the above NBS publications from: Superintendent of Documents, Government Printing Office, Washington, DC 20402.

Order the following NBS publications—FIPS and NBSIR's—from the National Technical Information Service, Springfield, VA 22161.

**Federal Information Processing Standards Publications (FIPS PUB)**—Publications in this series collectively constitute the Federal Information Processing Standards Register. The Register serves as the official source of information in the Federal Government regarding standards issued by NBS pursuant to the Federal Property and Administrative Services Act of 1949 as amended, Public Law 89-306 (79 Stat. 1127), and as implemented by Executive Order 11717 (38 FR 12315, dated May 11, 1973) and Part 6 of Title 15 CFR (Code of Federal Regulations).

**NBS Interagency Reports (NBSIR)**—A special series of interim or final reports on work performed by NBS for outside sponsors (both government and non-government). In general, initial distribution is handled by the sponsor; public distribution is by the National Technical Information Service, Springfield, VA 22161, in paper copy or microfiche form.

**END**

**FILMED**

**12-85**

**DTIC**